Vladimir State University
named after Alexandr and Nikolay Stoletovs

XII RGC

PROCEEDINGS

of the 12th Russian-German Conference on Biomedical Engineering

Suzdal, 2016

THE MINISTRY OF EDUCATION AND SCIENCE

VLADIMIR STATE UNIVERSITY
NAMED AFTER ALEXANDER AND NIKOLAY STOLETOVS

FRIEDRICH-ALEXANDER-UNIVERSITÄT ERLANGEN-NÜRNBERG

UDK 61:57; 615.47
B63

Volume Editors

Prof. Dr. Lyudmila T. Sushkova
Prof. Dr. Sergei V. Selishev
Prof. Dr. Zafar M. Yuldashev
Prof. Dr. Sergei I. Schukin

Proceedings of the 12th Russian-German Conference on Biomedical Engineering. – Suzdal.: VlSU, 2016
ISBN 978-5-905527-12-8

Proceedings of the 12th Russian-German Conference on Biomedical Engineering in Suzdal are presented. Papers are grouped on plenary session and 4 topic sections: Processing and analysis of biomedical data, signals and images; Mechatronics, implants, artificial organs & Diagnostics and analysis in surgery; Modeling and computer aided medicine; Biomedical engineering and biomaterials.

The book is useful for researchers and engineeris, students and postgraduates specializing in the field of biomedical engineering.

INFORMATION SUPPORT

"Biomedical Engineering" ("Медицинская Техника")

The priority of "Biomedical Engineering" is strengthening and widening of multidisciplinal contacts in the field of medical equipment. The journal publishes fundametal articles and the results of applied researchs and developments

http://www.mtjournal.ru/

"Biomedical Radioelectronics"
("Биомедицинская радиоэлектроника")

The journal publishes articles on bio-material science, biomedical technologies, and the interaction of physical fields and radiation with biological objects, as well as the development of new electronic devices for use in biology, biomedical technology, and medicine.

http://www.radiotec.ru/catalog.php?cat=jr6

"Biotechnosphera" ("Биотехносфера")

The magazin is aimed to scientists, leading specialists of academic, research and engineering organizations of medical-technical field, for healthcare stuff and other persons, who invlolved into biomedical engineering.

http://www.polytechnics.ru/magazine/bts.html

“Dynamics of Complex Systems – XXI century”
(“Динамика сложных систем — XXI век”)

International scientific magazine. The main objective of the magazine consists in representation of research results in investigation of dynamic processes into complex technical systems (mechanical, information technologies and computers, radioengineering and electronics, physical systems, control systems).

http://www.radiotec.ru/catalog.php?cat=jr16

“Technologies of Living Systems"
("Технологии живых систем")

"Tekhnologii zhivykh sistem" is a scientific and technical journal elucidating fundamental and applied problems of life sciences. Established in 2004.

http://www.radiotec.ru/catalog.php?cat=jr14

INTERNATIONAL PROGRAM COMMITTEE

President:

Prof. Dr. Joachim Hornegger - the President of FAU, Erlangen-Nurnberg, Germany

Co-President:

Prof. Dr. Yuri V. Gulyaev - Dr.Phys.-Math.Sci, professor, scientific advisor of Institute of Radio-engineering and Electronics of RAS, academician, member of RAS presidium, head of solid state electronics and radiophysics department at the Moscow Institute of Physics and Technology

Co-President:

Prof. Dr. Lyudmila T. Sushkova - head of biomedical and electronical systems and technologies department of Vladimir State University named after Alexander and Nikolay Stoletovs, Russia

Head of the Organizing Committee:

Prof. Dr. Valeriy G.Prokoshev - first prorector, scientific and innovating activity prorector of Vladimir State University named after Alexander and Nikolay Stoletovs

Committee Members:

Prof. Dr. Leonhardt - RWTH Aachen University, Aachen, Germany
Prof. Dr. Glasmacher - Leibniz Universität Hannover, Hanover, Germany
Prof. Dr. Mayr - Technische Universität München, Germany
Prof. Dr. Feussner - Klinikum rechts der Isar der Technischen Universität München, Munich, Germany
Prof. Dr. Bauernschmitt - University of Ulm, Ulm, Germany
Prof. Dr. Navab - Institut für Informatik I16, Technische Universität München, Germany
Prof. Dr. Liepsch - professor at department of Buildting Services Engineering and Print and Media Technology of Munic University of Applied Sciences, Germany
Prof. Dr. Kiryukhin - honoured doctor of Russia, head of Healthcare department of Vladimir region administration, Russia
Prof. Dr. Selishev - head of biomedical system department at National Research University of Electronic Technology, Russia
Prof. Dr. Chichkov - head of nanotechnology department, Lazer Centrum Hannover, Germany
Prof. Dr. Schukin - dean of "Biomedical Technique" faculty, head of medical-technical informational technologies deaprtment at Bauman University, Moscow, Russia
Prof. Dr. Medvedev - head of pharmacy department at Moscow State University, Russia
Prof. Dr. Niemann - honoured professor of VlSU, Erlangen, Germany
Prof. Dr. Shapovalov - Saint Petersburg Electrotechnical University "LETI", Russia
Dr. Shestopalov - assistant professor, education work prorector at "LETI", Saint-Petersburg, Russia
Prof. Dr. Yuldashev - head of biotechnical systems department at Saint Petersburg Electrotechnical University "LETI", member of Russian medical-technical science academy, Russia
Prof. Dr. Potrakhov - head of electron devices and systems department at "LETI", Saint-Petersburg, Russia
Prof. Dr. Zaichenko - head of medical radioelectronics department at SUAI, Saint-Petersburg, Russia
Prof. Dr. Spiridonov - head of biomedical technical systems department at Bauman University, Russia
Prof. Dr. Naraykin - head of applied mechanics department at Bauman University, Russia
Prof. Dr. Korenevskiy - head of biomedical engineering department at SWSU, Kursk, Russia

CONTENT

Section 2
PROCESSING AND ANALYSIS OF BIOMEDICAL DATA, SIGNALS AND IMAGES

PLENARY SESSION

Kybernetic modeling of human body system

J. Mau
H Heine University Düsseldorf, Buschstr.9, 47800 Krefeld

Introduction

For a functional perspective, human body system's physiological and operational design motifs follow from its mission and from the roles of its life context, cf. Fig. 1 (left): it shows physical human body as *bio-sphere*, its 'habitat' as *eco-sphere* and its social and socio-economic conditions as *socio-sphere*; specific *driving forces* for dynamics of interactions between any particular "bio-sphere" body, its environment and its social space are implied. Here, individual's bio-sphere *operations*, or activities, are in foreground [1]:

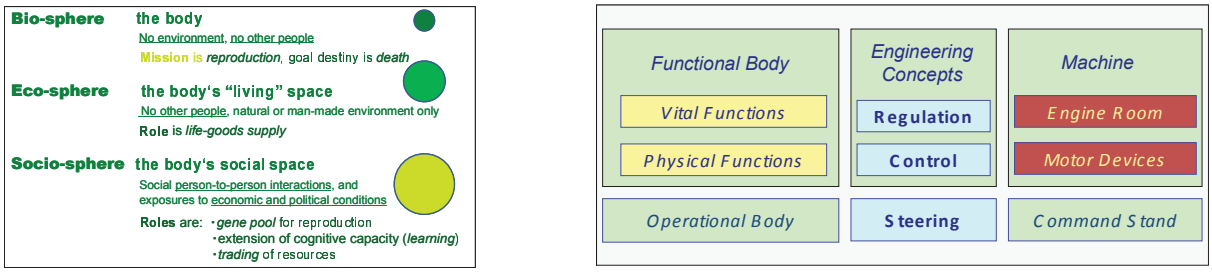

Fig. 1: Human body: Life-sphere (left) and functional (right) decompositions; analogous technical concepts.

Firstly, manual and locomotor physical activity and sexual activity which together are referred to as 'physical (re-)production', and secondly, mental activity in solving cognitive tasks making and enacting volitive decisions; both express in *behavior*, as the perception of bio-sphere operations by its eco-sphere and socio-sphere context.

The analogy between the living and the machine - a paraphrase to the subtitle of Wiener's seminal book [2] - is shown in Fig. 1 (right) which reviews parts of [3]: Human body has two main components, *functional body* and *operational body* - the former of two compartments, one of *vital functions* that provide energy or power, and another of *productivity functions* that are under command by *operational body*. This matches the situation in an engineered device, a machine's engine room, motor devices for production, human operator's command stand.

In clinical context, functional core body is seen in the disabled deprived of physical (re-)productive activity, though possibly still operationally enabled, while a person in *coma* may be reduced to a *vegetative state* of persisting minimal vital physiological functions that just serve the 10^{14} body cells to survive; both physical and operational activity are disabled. Fig. 2 (right) shows the full spectrum of competences according to operational body's command upon whole-body behavior, as levels of recovery from acute stroke.

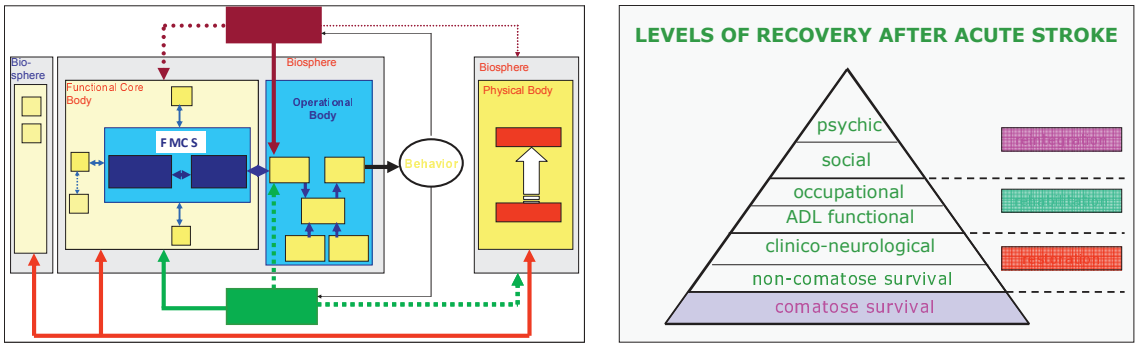

Fig. 2: Physical, functional, and operational body, and feed-back from eco- and socio-sphere on behavior (left);possible extent of impairments and recovery, applicable to all brain diseases. ADL=activity of daily living(right)

Returning to Fig. 1 (right), pertinent engineering control concepts are *feed-back control*, sometimes also called *regulation*, to keep a set point, balance out disturbances and thus ensure good internal operating conditions, and *control* to initiate or modify processes that aim to achieve a target under changing requirements which includes set point changes for regulation. *Steering* is a concept at a higher level: it is 'making operative decisions' given input information on operational goals, operational rules and the current set of operational options for the system, hence a typical human operator's task. As in the machine, steering requires sensory equipment which signals a situation, a director's role of processing received information, and command lines that transmit appropriate signals to devices that execute operational decisions. Steering is the mission of *operational body*, then.

Functional Body

In Fig. 2 right, total body system is an aggregate of three units, *functional core body* $\mathcal{F}$ of vital bodily functions, *functionally extended body* $\mathcal{P}$ of physical (re-)production, and *physical body* $\mathcal{Z}$ of cellular "material". Each unit is an aggregate by itself, composed of units with distinct tasks: energy sub-system (***E***), transportation sub-system (***T***), the sub-system for internal security (***H*** for "Homeland Security"), and the body's xenobiotic residential sub-system, ***X***, physical manual or locomotor production sub-system, ***P***, reproductive sub-system, ***R***.
As human body hormone system and nervous system jointly manage and control all body functions, together they are referred to as Functional Management and Control System (***FMCS***), cf. [1] for more detail.

Operational body

Basically, human body bio-sphere life fitness is determined from its sensory, cognitive and motor function capacities which involve the sensory nervous system, the mind, and motor cortex nervous system; the capacity of each and in combination is always conditional on prevailing physiological situation of functional body [1]. More specifically, operational body is understood as an aggregate of two units, a sub-system ***K*** for bio-sphere's communication with its world outside, and a sub-system ***D*** for processing of signals received from ***K***.
K takes the role of a "Signal Corps": it receives messages from eco- and socio-sphere through its devices, i. e. the senses for sound / airpressure, light / heat, smell / taste / chemical exposures, local touch, and transmits these via *afferent* nervous pathways for processing by ***D***; denote this part of ***K*** by $\boldsymbol{S}_{\text{aff}}$. Upon orders received from ***D*** via *efferent* nervous pathways, ***K*** will also send out messages to outer world engaging *functional body*'s options to produce sounds (e.g. speech), mimics, body language, and physical gestures; denote this part of ***K*** by $\boldsymbol{S}_{\text{eff}}$.

In its operational interpretation of received signals, ***D*** takes the steering role of reviewing and weighing currently available response options subject to two competences that rest in bio-sphere's *personality*: (i) *intellectual capacity,* ***r***, of *rationale* decision-making (abstracting, categorizing, systematic structuring), and in (ii) *motivational potentials* ***m*** of making *emotional* decisions based on affections, desires, visions, etc.; any decision is passed on to ***K*** for 'sending' the message to world outside. This way, ***K*** and ***D*** form an *operational unit* that responds to received messages with some operational activity; ***K*** engages also physical functions to make expression while ***D*** does not.
An intuitive summarizing notation for operational body is then $\mathcal{O} = \{ \boldsymbol{S}_{\text{eff}}\, \boldsymbol{D}\, \boldsymbol{S}_{\text{eff}} \mid \mathcal{F}, \mathcal{P}, \mathcal{Z}; \boldsymbol{r}, \boldsymbol{m} \}$; when noticed in eco-sphere or socio-sphere compartments of human body life-sphere, $\mathcal{O}$ is perceived as *behavior* $\mathcal{B}$.

Reverse Built-up
Conceptually, one can understand a *functional aggregate* (FA) as an ensemble composed of *functional units* (FU) made to work together in a coordinated way with regard to a distinct functional task within the whole system. Both FA's and FU's are *logical units* (LU), though with FU $\in$ FA $\Rightarrow$ level(FU) = level(FA) + 1.
Remark: As with data file system administration across several hardware storage devices [4], LU's may not have a direct correlate with *physical units* (PU) in wiring complex systems according to a prescribed *functional logic* [3]; in the same way of thought, *kybernetik* characterizes a system's "*Schaltgefüge*", the structure of couplings for control of its internal energy (mass, information) transfer dynamics, irrespectively from its physical realization [5]. The following is a more elaborate presentation of an approach indicated in [3].

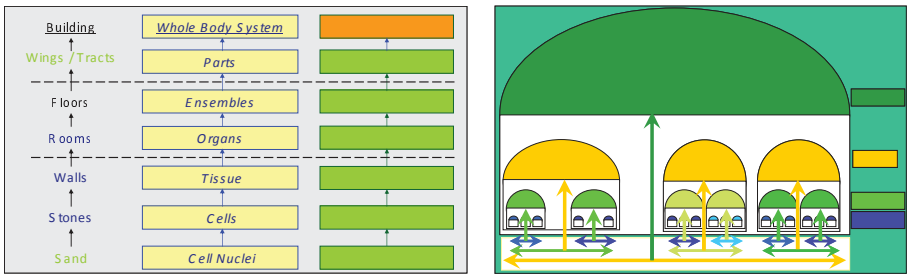

Fig. 3: Physical units (PU) at seven "levels" in holistic modeling of human body system (left), and built-up in logical units (LU) with their within-level interactions as emergent properties (right).

In Fig. 3 (left), seven functional levels are suggested for kybernetic modeling of whole human body system, with their functional correspondences in a complex building and in body's anatomy; the red box (level 0) indicates higher level interaction of human body bio-sphere in eco-and socio-sphere, actually the case for *behavioral kybernetics*. Dashed horizontal lines separate (from bottom to top) material components from dedicated functional units and aggregates, and from larger segments some of which may temporarily be suspendable.
In Fig. 3 (right), horizontal double-arrows indicate interacting LU's within an FA; their *emergent properties* - depicted as "vertically uprising" arrows - express as LU properties for interaction at the next higher level - in other words, the interactions among LU's at level n+1 generate the emergent properties for level n. More precisely, emergent properties of an FA expressing at level n are the interactions among its FU's at level n+1. (Note: Color of horizontal double-arrow indicates interaction of only LU's with cap of same color.)

For example, level-1 LU's are vital functions $\mathcal{F}|\mathcal{Z}$, physical (re-)production functions $\mathcal{P}|\mathcal{Z}$, and operational functions $\mathcal{O}|\mathcal{Z}$. Each is a functional unit of functional aggregate "whole human body"; the properties of "whole human body" bio-sphere in interaction with its eco- and socio-sphere at level 0 are determined as emergent properties (dark green cap) from interaction of its three constituent functional units, $\mathcal{F}|\mathcal{Z}$, $\mathcal{P}|\mathcal{Z}$, $\mathcal{O}|\mathcal{Z}$, each with an orange cap, at level 1. By definition, "dark green cap" properties are *behavior*, $\mathcal{B}$ = ($\mathcal{F}$, $\mathcal{P}$, $\mathcal{O}$)$|\mathcal{Z}$. *Reverse built-up* of whole human body system across all levels follows by induction. It remains to get a usable definition of interaction between FU's of an FA.

Kybernetic Modeling

Interaction within a system is understood as energy (mass, information) transfers between system components; their dynamics due to prevailing *driving forces* are controlled by *Schaltgefüge*, the structure of couplings that is independent of physical realization, it is in the focus of *kybernetic modeling*. In context of Fig. 3 (right) level 1, one may use $\mathcal{k}\{\ \mathcal{F}, \mathcal{P}, \mathcal{O}\ |\mathcal{Z}\}$ to denote *Schaltgefüge* for horizontal orange-colored double-arrow and address the system of involved regulation (looped feed-back) and controls in expression of interactions as emergent properties visible at whole-body level 0, $\mathcal{B}$ = ($\mathcal{F}$, $\mathcal{P}$, $\mathcal{O}$)$|\mathcal{Z}$.

Specifically, *kybernetic modeling* of $\mathcal{k}\{\ \mathcal{F}, \mathcal{P}, \mathcal{O}\ |\mathcal{Z}\}$ will first devise the *structure of functional dependencies* between

- a person's ability to make decision about how and when to act: operational capacity of $\mathcal{O}|\mathcal{Z}$,
- the body's ability to physically enact the decision: locomotor capacity of $\mathcal{P}|\mathcal{Z}$, and
- the body's ability to meet performance requirements: availability of physiological resources of $\mathcal{F}|\mathcal{Z}$,

based on level-1 *functional logic* [3; Fig. 1] and then use it as blueprint of a proper automation engineering wiring diagram for $\mathcal{k}\{\ \mathcal{F}, \mathcal{P}, \mathcal{O}\ |\mathcal{Z}\}$; by the *kybernetic paradigm*, independence of physical realization, this step may use wiring diagrams of *functionally comparable* engineered systems, i. e. systems that implement the same functional logic.

Application

In practice, it will involve human body's physiological FMCS and account for *operational control* effectuated by feed-backs from eco-sphere environment or socio-sphere settings with impact on human body operations, see Fig. 2 left. On ethical grounds, one will gain most insight from diseases of human body FMCS, i. e. primarily from $\mathcal{B}$-effects and pathophysiology of disorders of cerebral control (e.g. strokes, vascular dementia, degenerative dementia, Parkinson's disease, multiple sclerosis and epilepsy), and concurrent disorders in functional body [6], and from staging of competence as in Fig. 2 (right). For an example, with "Ø", "–", "+" for "none", "reduced", "mainly normal", respectively, staging as "viable" may be seen in ($\mathcal{F}$, $\mathcal{P}$, $\mathcal{O}$) = (−−−, Ø , Ø), (−−, − , Ø), (+ , +/−, −), (+ , (+), +/ −), explicitly named "vegetative", "highly dependent", "moderately dependent" and "practically independent" stagings, respectively, and ($\mathcal{F}$, $\mathcal{P}$, $\mathcal{O}$) = (+, (+) , (+)), (+, +, (+)), and (+, +, +) as "fit for work", "(socially) presentable", and "self-motivated" stagings, respectively; cf. Fig. 2 (right).

Discussion

An approach based on different concepts is noteworthy, as it links molecular level and organ level properties directly [7]; the present approach presents a multi-scale modeling framework for control structures, instead.

References

[1] J. Mau in, *Advances in Cognitive Neurodynamics (V)*, R. Wang and X. Pan eds. (Springer Science+Business Media Singapore, 2016) Chapter 59.

[2] N. Wiener, *Cybernetics or Control and Information in the Animal and the Machine*, (Massachusetts Institute of Technology, Boston, 1961).

[3] J. Mau, *Bioautomation - re-engineering human body system controls*, (Международная конференция и молодёжная школа «Информационные технологии и нанотехнологии», 17 - 19 июня 2016, Самара).
[4] F. J. Kauffels, *Rechnernetzwerk-Systemarchitekturen und Datenkommunikation*,(Bibliograph. Institut & F.A. Brockhaus, Zurich, 1989)
[5] H. Sachsse, *Einführung in die Kybernetik*, (Vieweg, Braunschweig, 1974).
[6] K. Toyoda ed., *Brain, Stroke and Kidney*, (Karger, Basel, 2013).
[7] G.Y. Wang, *Analysis of Complex Diseases. A Mathematical Perspective*, (Taylor & Francis, Boca Raton, FL, 2014).

Application of telemedicine in Emergency Medical Services of Aachen, Germany: principle and benefits

***M. Czaplik*[1], *R. Rossaint*[1], *S. Bergrath*[1], *F. Hirsch*[1], *S.K. Beckers*[1,2], *J.C. Brokmann*[3]**

1. Department of Anaesthesiology, University Hospital RWTH Aachen, Germany
2. Fire Department and Emergency Medical Service, Germany
3. Emergency Department, University Hospital RWTH Aachen, Germany

Background: The task of emergency medical services (EMS) is to immediately initiate medical treatment or transportation to hospital in cases of accidents or severe diseases. Indeed, diverse acute events such as myocardial infarction and stroke necessitate prompt decisions and medical therapy. Even other conditions like acute pain badly need an early relief. Although most European countries bank on paramedic systems with well-educated ambulance men, competences and authorities are strictly regulated and limited as compared to physicians'. In German EMS, in about half of the emergencies, doctors, so-called emergency physicians (EP), are involved [1]. They are dispatched concurrently with the ambulance (but in a separate car) in cases when a life-threatening situation seems to be apparent or dispatched afterwards when paramedics need medical assistance. Due to national legal provisions and economic reasons, the network of ambulance locations is denser than the network of EMS physician units. If "only" an ambulance is sent to the site, the crew evaluates the patient's condition after their arrival. If the condition is more severe than so far expected or special medications (e.g. analgesics) are necessary, additionally an EMS physician is sent to the site. Therefore, in many cases the ambulance paramedic team arrives several minutes prior to the arrival of a physician and initiates emergency measures. The proportion of EP supported missions varies regionally from less than 30 % to more than 60 % [2]. Due to demographic changes, the amount of old patients and the incidence of chronic diseases is ever-increasing. Therefore, on the one hand, the number of emergency missions is escalating yearly by about 3 to 4 % all over Germany with increasing treatment complexity. On the other hand, the number of physicians is limited, so that qualified personnel is lacking - particularly in rural regions with consequently rising waiting periods for the EP and falling qualification standards. Coincidentally, experience of medical staff in managing severely ill and severely injured patients is considerably lower in rural regions due to the far lower number of such emergency cases. However, quality depends on both formal qualification and experience [3-5]. Several studies have shown that at least critically ill patients benefit from treatment by an EMS physician [6]

The application of telemedicine and especially of tele-consultation can be of crucial worth in managing the balancing act between ensuring a high quality and conserving resources. Therefore, telemedical procedures have become increasingly important in emergency and acute care settings; however, these applications are often restricted to research and pilot

projects but broad implementation into routine care is lacking [7]. In the city of Aachen a telemedical rescue assistance system (TRAS) was developed and further developed in a number of sequent research projects. It is based on organisational, medical and technical modules and consists of connected medical devices, safe and secure high-tech communication technology and a checklist-based medical documentation system ensuring a high guideline-adherence.

Nowadays, TRAS is established in daily routine and available on all ambulances 24/7. In this paper a brief technical overview of the system is given as well as some results regarding medical capabilities, structural effects and technical performance during the last two years of application.

Methods: TRAS enables telemedical support of the paramedics by a tele-EP on-site (e.g. at the patient's habitation) and during the transportation in the ambulance. Therefore, two independent working communication devices are provided using several mobile networks each. One of them is integrated into the car, the other one is embedded in the bag of the patient monitor and defibrillator unit (Corpuls C3, GS Stemple, Germany) that is always taken along to the patient. Whereas the C3 is connected to the portable communication device, a video camera (integrated into the ambulance ceiling) and a printer is connected to the in-car communication box. The paramedics use Bluetooth headsets ensuring a hands-free communication with the tele-EP (figure 1). For initiating a call to the EP, only one button-press is necessary. A Smartphone is applied to take picture or short video sequences on-scene. All data including real-time ECG transmission, video data and periodically measured vitals are encrypted and sent to a so-called tele-EP centre for evaluation. The tele-EP is qualified and authorized to instruct the paramedics e.g. to administer drugs, so that an immediate medical treatment can be initiated even though the doctor is not present on-site.

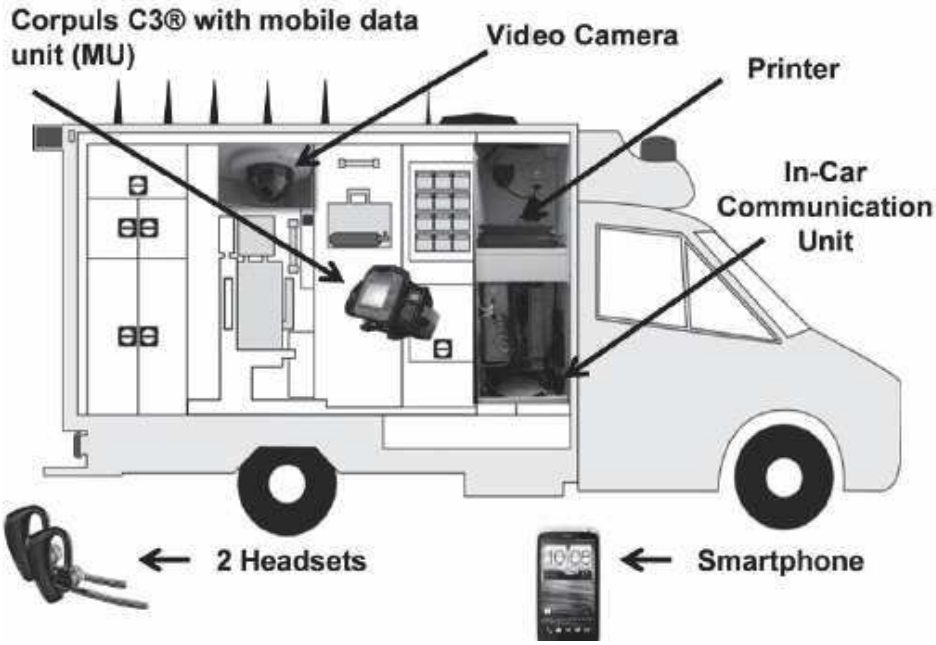

Figure 1: Hardware components of the telemedical rescue assistant system. The conventional ambulance is equipped with diverse technical features.

Results: Although technical performance of TRAS is reliable, adaptation of all stakeholders to the new processes was necessary. As a matter of fact, acceptance differed from person to person but rose steadily from quarter to quarter. Whereas the total of number of tele-EP-directed emergency missions was 193 in the first quarter after establishment into

clinical routine (2nd quarter of 2014), nowadays more than 600 missions are supported by the tele-EP each quarter. Therefore training of EMS personnel and dispatch personnel was necessary and further optimisation of technical equipment – software and hardware. Up to date more than 4.100 missions were conducted by telemedical support since April, 2014 with no adverse event or complication. In most cases, TRAS was used in order to reduce the time interval to medical therapy with consequently improved patient safety (figure 2).

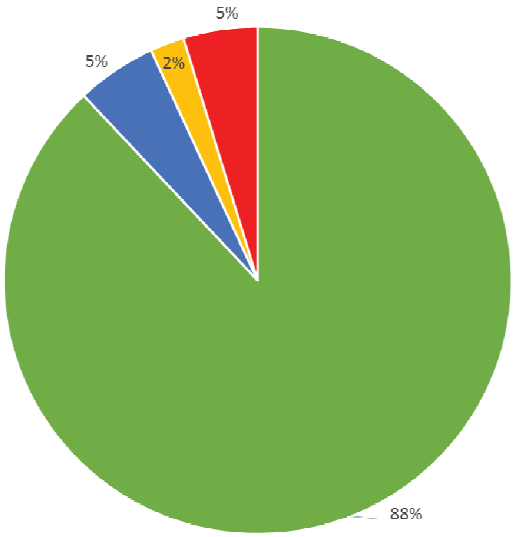

Figure 2: Categories of telemedically supported missions. Green: paramedics and tele-EP alone, blue: dispatch of conventional EP during tele-EP consultation ("emergency upgrade by tele-EP"), red: tele-consultation between EP and tele-EP (hand-over, second opinion), orange: tele-consultation to bridge EP travel time.

In most consultations, the tele-EP was connected with the requisitioning paramedic within 20 seconds. The mean duration of emergency missions operated by the tele-EP is significantly lower (32 min) as compared to the conventional EP at the City of Aachen (54 min) or the German mean value (56 min). Nowadays already 28 % of all physician-directed emergency missions are carried out by the tele-EP. Furthermore, 35 % of all physician-accompanied inter-hospital transfers are performed telemedically. In consequence, the percentage of physician-directed emergency missions fell from 33 % (2013/14) to 24 % (2015). Today it is almost 50 % below the German mean (44 %).

Discussion: Telemedicine in emergency medicine is technically feasible and will be an important integrative component of German EMS in future. It can contribute to guarantee a resource-saving medical treatment of high-quality. However, telemedicine cannot replace physicians or paramedics on-scene since manual skills are required in a number of emergency missions. By building up regional or transregional telemedical centres, further economic advantages can be achieved. Furthermore, telemedicine can provide medical support even in remote areas where medical care (e.g. with general practitioners) is sparse.

References

[1] Behrendt, H. "Time comparison of current performance by emergency medical services in the Federal Republic of Germany (part II)", German Interdisciplinary Journal of Emergency Medicine **7**:59-70 (2004).
[2] Messelken, M, Kehrberger, E, Dirks, B, Fischer, M. "The quality of emergency medical care in baden-württemberg (Germany): four years in focus", Dtsch Arztebl Int. **107**:523-30 (2010).

[3] Gries, A, Zink, W, Bernhard, M, Messelken, M, Schlechtriemen, T. “Realistic assessment of the physician-staffed emergency services in Germany”, Anaesthesist **55**:1080–1086 (2006).
[4] Schuster, M, Pints, M, Fiege, M. “Duration of mission time in prehospital emergency medicine: effects of emergency severity and physicians level of education”, Emerg Med J **27**:398–403 (2010).
[5] Moecke, H, von Knobelsdorff, G. “The anesthesiologist in prehospital and hospital emergency medicine”, Curr Opin Anaesthesiol **21**:228–232 (2008).
[6] Timmermann, A, Russo, SG, Hollmann, MW. “Paramedic versus emergency physician emergency medical service: role of the anaesthesiologist and the European versus the Anglo-American concept”, Curr Opin Anaesthesiol **21**:222–227 (2008).
[7] Amadi-Obi, A, Gilligan, P, Owens, N, et al. “Telemedicine in pre-hospital care: A review of telemedicine applications in the pre-hospital environment”, Int J Emerg Med **7**: 29 (2014).

Intelligent remote health monitoring system for patients with chronic diseases

***A. Anisimov*[1], *E. Pustozerov*[1], *Z. Yuldashev*[1]**
1. Saint Petersburg State Electrotechnical University “LETI”, Russia

Relevance. The problem of telemedicine systems development for diagnostic purposes and its broad integration into clinical practice is becoming extremely relevant today due to a number of objective and subjective reasons: firstly, the increase of world population, especially the elderly people who require much more of doctors attention, secondly, decreasing rate of healthcare costs for medical care per individual even with the increase of financial support of the health system, thirdly, necessity of expanding access and improve quality of health services.

An effective solution of this problem can be achieved by improving the technology of telemedicine monitoring of the health status of people especially for socially significant diseases, prevention of diseases and prediction of the risk of exacerbation of chronic diseases.

Objective of the study. The goal of the study is to develop a multi-level intelligent system of remote monitoring of the person’s health status and forecasting the risk of exacerbation of chronic diseases. Socially significant diseases are the diseases that are most prevalent in society and cover wide strata of the population; they require significant financial and personnel resources. With insufficient treatment these diseases often become chronic. Therefore, the solution of monitoring problems and forecasting the risk of exacerbation of chronic diseases contributes also to the solution of the treatment problems of socially significant diseases.

To achieve this objective we formulated and solved the following problems:

- substantiation of the technology and the structure of the system for continuous remote monitoring of the person's health status and prediction of future exacerbation of the disease;
- formation of a set of indicators for description of patient’s health status and prediction of future disease exacerbation;
- substantiation and development of the wearable patient device structure;

Solutions.

1. Substantiation of the technology and the structure of the continuous remote monitoring system of the person’s health status and prediction of future disease exacerbation. To monitor the state of human health and to predict the disease exacerbation the system is required to solve the complex of problems related to registration of signals, which characterise the activity of the body's systems, processing and analysis of biomedical information, assessment of the current state of the human body, revealing of dynamic changes and prediction of acute conditions. It is obvious that for the solution of complex tasks the

system should have a multilevel hierarchical structure, each level of which should provide optimal solutions to specific tasks.

The first level of the hierarchical monitoring system (wearable patient device) provides the solution for the task of objective and reliable registration of complex biomedical signals and indicators of body systems activities. Minimization of method errors of signals registration can be achieved by reducing the effect of registration devices on the functioning of body systems and on patient's life activities. Sensors on the wearable patient device should have minimum size and weight to provide non-invasive evaluation of indicators, be biologically compatible, not affect the spatial-temporal distribution of the registered biomedical signals [1]. To ensure continued reliable registration of biomedical signals a wearable device should have long battery life (up to several days). That means that the wearable device is not advisable to use for signals pre-processing: complex handling of biomedical signals necessitates using of high-performance CPU, and as a result, we have increased electric current consumption and reduced of battery life. Using intelligent algorithms for recording and transmission of biomedical signals on the second level of the system – the level of biomedical signals recept can significantly reduce current consumption and increase the autonomy of the device. Intellectualization is based on usage of a limited set of recorded biomedical signals to monitor the status of individual norms (e.g., ECG and respiration). In case of detection of functional changes in the activity of body systems the wearable device can connect additional registration channels of biomedical signals, change algorithms and register parameters of biomedical signals to improve accuracy and reliability of the assessment of the patient's health condition. The transmission power of the signals by the radio channel from the wearable device to the receiver should not exceed tens of mW. This contributes to additional enhancement of the work autonomy of the wearable device. The main function of the first-level system can be formulated as follows: accuracy and reliability of registration and transmission of signals in conditions of long autonomous work.

The second level of the system is signals receiver. It provides preliminary processing of biomedical signals, estimation of diagnostically important indicators of patient health, assessment of the current health condition, administration of operating mode and changes the settings of the wearable device recording channels. The analysis of indicators of the body systems functioning, formation of the signals alerts for the patient about changes in his/her health condition and transmission of biomedical information by WLAN channel to the server of any medical institution which performs the monitoring of the health status and prognosis of exacerbation of chronic diseases are also provided on this level. In order to effectively use memory, the receiver storage time for diagnostically important indicators of the health status should not exceed a week. Recording and storing of these parameters for a longer period of monitoring of the patient's health state is carried out on the server of the medical institution. To solve all the tasks specified above the second level of the system must have a high-performance CPU. Taking into consideration the current level of the computer technologies development it is implemented on a smartphone or a tablet computer using a stand-alone or network power source [2]. The main function of the second-level of the system can be formulated as follows: an accurate assessment of the current state of the patient and transfer of biomedical information to the third level for implementation of long-term monitoring and forecasting of the health condition of the patient.

The third level of the systems is presented by cloud-based tools and technologies of the medical institution server which performs the monitoring of the patient health status. It provides a detailed analysis of the dynamics of the functional state of body systems, an integral assessment of health status, an adjustment of indicators of individual norms of the monitored patient and the criteria for diagnostics of diseases and prediction of their exacerbation, the formation of informational messages for a physician about patient's health

threat of functional changes in body systems. The objective function of the system's third level can be formulated as follows: long-term monitoring of the patient health status and prognosis of the disease exacerbation.

The fourth level of the system is formed by a microprocessor system of the attending (family) physician and implemented on the portable (tablet) or desktop computer. The doctor receives detailed information about the patient's current condition, about the dynamics of changes in health status during the long-term monitoring and about the forecast of the patient's health state in the next days. Typical solutions for using medical technologies and medicines could be recommended for the doctor to normalize the condition of the patient in case of threatening his life and health functional disorders. Communication between second, third and fourth levels of the monitoring system is implemented by using the WLAN communication channel. The medical institution server receives a biomedical information about the patient's current health condition from the second level of the system, and in the opposite direction – to the patient receiver it sends updates of software modules which were specified as a result of long-term monitoring criteria for the assessment of the patient current state and control commands to implement an intellectual mode of recording and processing of biomedical signals.

The use of the WLAN channel between the server of the medical institution and the doctor's computer provides the physician access to patient data, monitoring patient's health status, medical advisory accompanying the patient with no restrictions in space and time. The doctor can adjust the monitoring program, methods of assessing current status and forecasting of the health status of the patient by using cloud-based tools. The objective function of the fourth-level system can be formulated as follows: monitoring of the patient health status and decision making by the family physician, patient medical care performed by the doctor.

In accordance with the above rationale, we propose the following architecture of the intelligent system of remote monitoring of patient health condition (Fig. 1).

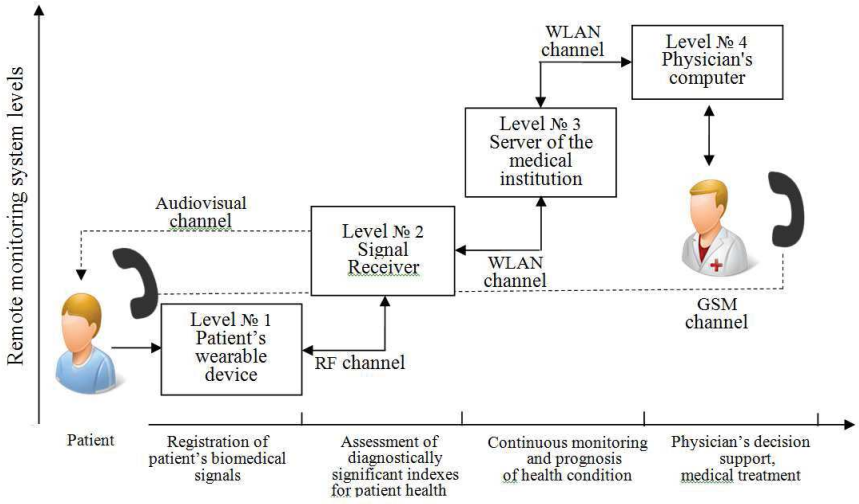

Fig. 1 Intelligent system of remote monitoring of patient health condition architecture

2. Forming a set of indicators for description patient's health status and prediction of future disease exacerbation.

The process of the patient's current state evaluation and diagnosis of diseases, proceeded by a doctor, is a process of finding a model (description) from a previously known set of state models (including diseases) which is the most similar to the current model of the patient's condition. Therefore, the accuracy of formation of the current model of patient's condition, disease models, feasibility and optimality of search algorithms and models comparing, making decision, diagnostic criteria objectivity have a significant influence on

accuracy of the disease diagnosis. The models of the patient's health state (healthy and with different diseases) are described by a set of diagnostically significant parameters.

The set of these parameters for various diseases commonly doesn't match. The following approach is recommended to create a complex of significant indicators for the diagnosis of diseases. A group of physicians with large clinical experience in the profile of the specific disease is formed. This group provides expert evaluation of the indicators importance for the diagnosis of specific disease. Further, a database for the state of physiological norm and a specific disease is formed according to the results of clinical trials on a representative sample of different groups of patients using the proposed set of indicators [3]. While gathering groups, researcher should take into account age and gender differences between patients, their present illnesses.

The experimental data are used for factor analysis to determine the factors (indicators) that have the greatest power in the identification of diseases, and ranking these factors by significance level. Power of diagnostically significant factors is used to formalize models (mathematical, table), and the level of significance of the factors used to organize intelligent monitoring process. It provides monitoring of a patient current state with a limited number of the most significant indicators (with a high level of significance) in the background of the system operation, and in case of deviation of the current patient health state from the area of individual standards should connect another channels for recording biomedical information for the evaluation of additional model indicators. Thus, the set of indicators used in the patient's condition models, let us to determine the composition of the measuring channels for biomedical signals recording and the sequence of their connection.

For the diagnosis of a large number of functional disorders we need to use channels for registration of different signals in remote health monitoring systems: ECG, arterial blood pressure, pulse wave, respiration and body temperature.

3. Substantiation and development of the wearable patient device structure.

The functionality of the intelligent system for remote monitoring of the person's health status is largely determined by the functionality of wearable device measuring channels, since it provides recording of biomedical information, which is used for evaluation of the person's current health status, monitoring and prediction of disease exacerbation [4]. In order to provide improved technical and metrological characteristics of measuring channels, it is recommended to use highly integrated Analog Front End (AFE) modules for medical purposes, intended for registration of ECG, EEG, EMG biopotentials, SO_2, pulse wave, respiration rate and temperature. Most modern AFE modules have onboard various serial digital interfaces like UART and SPI, which allow us to offer the following unified structure of the wearable device (Figure 2).

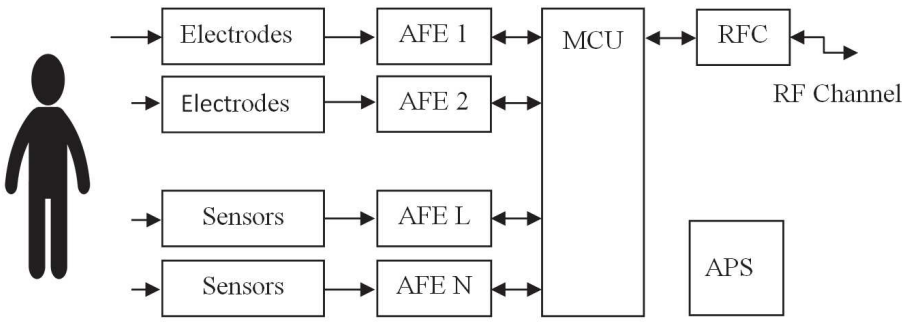

Fig. 2 Unified structure of the wearable device

The wearable patient device contains the set of electrodes and sensors for signal registration from patient, N channel AFE modules, microcontroller (MCU) for collecting digital data from the measuring channels and control their operation modes, radio channel (RFC) for transmission/reception of signals from the second level of the system, and

The aim of the present work is to develop a numerical model for geometric evaluation of a mutual inductance with parallel computing on GPU in order to reduce time expenditures.

Mutual inductance between two infinitely thin circular filaments can be described using so called Neumann's formula:

$$M_F = \frac{\mu_0}{4\pi}\oint_{l_t}\oint_{l_r}\frac{d\vec{l}_t d\vec{l}_r}{r_{tr}} = \frac{\mu_0 R_t R_r}{4\pi}\int_0^{2\pi}\int_0^{2\pi}\frac{\cos(\varphi_r-\varphi_t)d\varphi_r d\varphi_t}{r_{tr}}\ , \tag{1}$$

here μ_0 is magnetic permeability of a vacuum, R_t and R_r are filaments radii and r_{tr} is distance between filaments elements $d\vec{l}_t$ and $d\vec{l}_r$:

$$\begin{cases} r_{tr} = \sqrt{(x_t-x_r)^2+(y_t-y_r)^2+(z_t-z_r)^2} \\ x_t - x_r = \rho + R_t\cos\varphi_t\cos\varphi - R_r\cos\varphi_r \\ y_t - y_r = R_t\sin\varphi_t\cos\varphi - R_r\sin\varphi_r \\ z_t - z_r = d + R_t\cos\varphi_t\sin\varphi \end{cases}, \tag{2}$$

here d is an axial distance between the coils, ρ is a lateral distance between the filaments and φ is an angle between the filaments planes.

Integral (1) cannot be obtained analytically in general case, when $d,\rho,\varphi \neq 0$. Simplest way to calculate it is by using rectangle method. Therefore, following expression for mutual inductance can be written:

$$M_F = \frac{\mu_0 R_t R_r}{4\pi}\sum_{n=1}^{N}\sum_{k=1}^{K}\frac{\cos(\varphi_k-\varphi_n)\Delta\varphi_t\Delta\varphi_r}{r_{kn}} = \frac{\mu_0\pi R_t R_r}{NK}\sum_{n=1}^{N}\sum_{k=1}^{K}\frac{\cos(\varphi_k-\varphi_n)}{r_{kn}}\ , \tag{3}$$

here $\Delta\varphi_t = 2\pi/N$, $\Delta\varphi_r = 2\pi/K$, $\varphi_k = 2\pi k/K$, $\varphi_n = 2\pi n/N$.

Equation for two coils with number of a windings N_{wt} and N_{wr}:

$$M_C = \frac{\mu_0}{4\pi}\sum_{i=1}^{N_{wt}}\sum_{j=1}^{N_{wr}}M_{F_{ij}} = \frac{\mu_0}{4\pi}\sum_{i=1}^{N_{wt}}\sum_{j=1}^{N_{wr}}R_{t_i}R_{r_j}\int_0^{2\pi}\int_0^{2\pi}\frac{\cos(\varphi_{r_j}-\varphi_{t_i})d\varphi_{r_j}d\varphi_{t_i}}{r_{t_i r_j}}\ . \tag{4}$$

It should be noted that coils in IMDs inductive powering usually have pancake shape, so radii of filaments are not equal to each other in contrast to the case of cylindrical coils. Finally, substituting (3) in (4) one can obtain:

$$M_C = \mu_0\pi\sum_{i=1}^{N_{wt}}\sum_{j=1}^{N_{wr}}\frac{R_{t_i}R_{r_j}}{N_i K_j}\sum_{n_i=1}^{N_i}\sum_{k_j=1}^{K_j}\frac{\cos(\varphi_{k_j}-\varphi_{n_i})}{r_{k_j n_i}}\ . \tag{5}$$

Expression (5) is generalized in terms of filaments discretization. If every filament in coils is divided into a same number of elements, it can be simplified as follows

$$M_C = \frac{\mu_0\pi}{NK}\sum_{i=1}^{N_{wt}}\sum_{j=1}^{N_{wr}}R_{t_i}R_{r_j}\sum_{n_i=1}^{N}\sum_{k_j=1}^{K}\frac{\cos(\varphi_{k_j}-\varphi_{n_i})}{r_{k_j n_i}}\ . \tag{6}$$

For geometric evaluation of a coils couple it is necessary to obtain a set of mutual inductance values $M_C(P) = [M_C(P_1), M_C(P_2), ..., M_C(P_{N_P})]$ for N_P values of a parameter or set of parameters (e.g., d,ρ,α). Altogether, in order to obtain mutual inductance as a function of geometric parameters one need to perform $N_p N_{wt} N_{wr} NK$ calculations of a basic function

$\cos(\varphi_{k_j} - \varphi_{n_i}) / r_{k_j n_i}$. In case of a coils couple for an inductive IMD powering number of a basic function calculation can reach $10^7...10^8$ for a uniform wire filaments and $10^9...10^{10}$ for a Litz wire. Described procedure is time consuming, but can be effectively dealt with the help of parallel computing methods.

One of the popular and cost-effective parallel computing method is using of graphical processing unit (GPU). In our work we performed calculations on the NVIDIA Tesla C2075 unit (448 CUDA cores, 1,15 GHz). It should be noted that the main drawback of a GPU computing is low speed of reading and writing data, thus it is necessary to perform a geometric evaluation in one access to the GPU. At the same time, a set of parameters usually has a relatively small number of elements (that said, 10...20) in comparison to the number of a GPU parallel threads N_T (that said, 1024). So, effective parallelization can be achieved using following procedure:

1°. Establish a super-index $g = 1...N_T$ as a GPU-array $g = [1,2,...,N_T]$. It is necessary because all data must be translated to GPU and super-index must be used for calculation of parameters and indexes values inside parallel threads.

2°. Determine a number of a parallel threads for every point in a $M_C(P)$ as a

$$N_{ST} = [N_T / N_P], \tag{7}$$

here $[\bullet/\bullet]$ is an integer division. In order to achieve maximum efficiency it is desirable to choose $N_P = 2^x < N_{ST}$, usually it is sufficient to have 8...32 points in geometric parameter set.

3°. Calculate the value of a parameter inside *g*-th parallel thread as a

$$P_g = P_{\min} + \left[\frac{(g-1)}{N_{ST}}\right]\frac{(P_{\max} - P_{\min})}{N_p - 1}. \tag{8}$$

4°. Divide every low level sum into N_{ST} parallel threads and calculate intermediate value inside every single thread as follows

$$M'_t(P_g) = \sum_{i=1}^{N_{wt}}\sum_{j=1}^{N_{wr}} R_{t_i} R_{r_j} \sum_{n_i=1}^{N}\sum_{k_j=K'}^{K''} \frac{\cos(\varphi_{k_j} - \varphi_{n_i})}{r_{k_j n_i}}, \tag{9}$$

here $K'' = (g - N_{ST}[(g-1)/N_{ST}])[K/N_{ST}]$, $K' = K'' - [K/N_{ST}] + 1$, $t = 1..N_{ST}$.

5°. Obtain value $M_C(P_g)$ as a sum

$$M_C(P_g) = \frac{\mu_0 \pi}{NK}\sum_{t=1}^{N_{ST}} M'_t(P_g). \tag{10}$$

Proposed method was implemented using MATLAB coding. Examples of calculations using the method are presented on fig. 1. Values of mutual inductance were calculated for typical inductive IMD powering. Distance between coils centers is 18 mm, radii of a coils is 35 mm, radii of a windings is 0.5 mm, number of windings is 3 (given in fig. 1, a) and 15 (given in fig. 1, b) for two examples. Evaluation was performed for angular displacement in range of 0...32 degrees with the step equal to 2 degree. Every winding was split into 256 elements.

In order to validate parallel procedure it was compared to the sequential summing on a host CPU. It can be seen on fig. 1 that both methods are in perfect agreement. It should be noted that increment of number of windings affects geometric properties of a coils couple. In fig.1,

a, dependencies have a local maximum in a region of interest. In fig 1, b, mutual inductance is a monotonic function of angle.

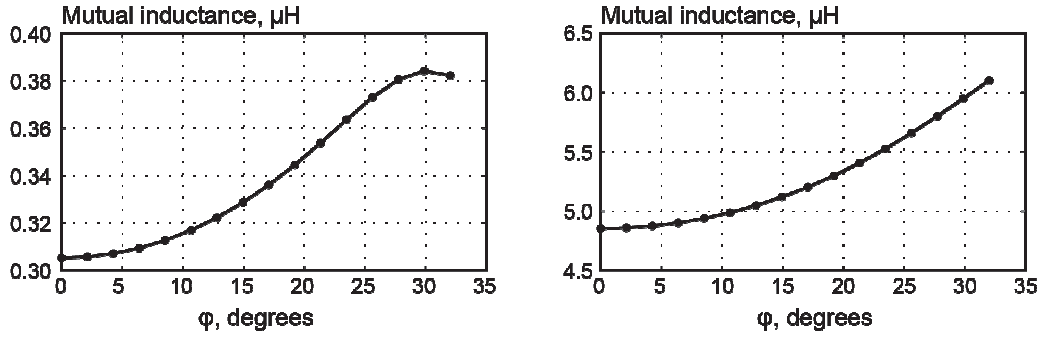

a) b)

Fig.1 Mutual inductance as a function of an angular displacement for coils couple with 3 (left) and 15 (right) windings. Distance between coils centers is 18 mm, radii of a coils is 35 mm, radii of a windings is 0,5 mm. Results of a numerical modeling with sequential (solid line) and parallel (dots) computing.

Investigation of the calculation speed-up was performed and results are presented in fig. 2. It can be seen that proposed method is about 50...80 times faster than sequential calculation on a host CPU for wide variety of a problem discretization values.

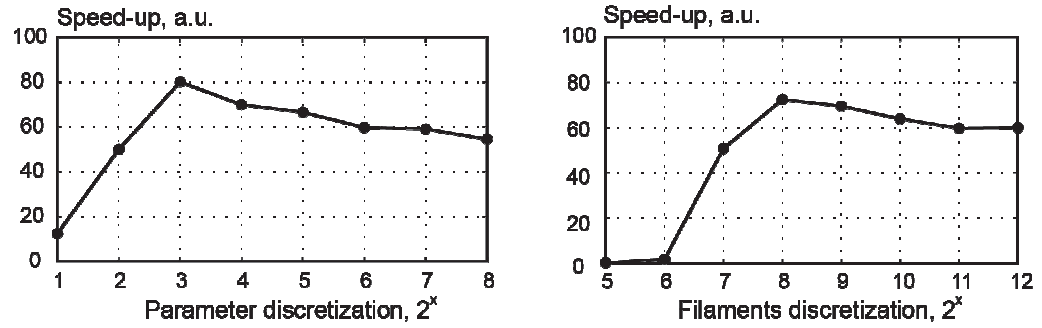

a) b)

Fig.2 Speed-up of calculation with parallel computing using GPU in comparison to sequential calculation on a host CPU as a function of a geometric parameter discretization (left) and filaments discretization (right).

Geometric evaluation of a coils couple is an important part of an IPU design. Numerical calculation is a flexible instrument for such evaluation and thus plays a key role in the design procedures. One of the main problems here is a high time-cost of a calculation. Proposed method of a mutual inductance geometric evaluation with parallel computing on GPU is an acceptable solution of a problem. It provides nearly real-time possibilities for evaluation of coils with single wires filaments.

Usually coils in IPU have about 10...20 filaments. With proposed method it takes about 20...50 seconds to obtain one set of a mutual inductance values versus geometric parameters with 16...32 elements and discretization of a coils filaments of $2^8...2^{10}$. So, it is possible to perform extensive numerical modelling aimed at design optimization. Geometric evaluation usually should be performed for every parameter (e.g., distance, lateral displacement, angular displacement) and its combinations. That means that number of a mutual inductance geometric sets during the design procedure can reach $2^8...2^{10}$. It is a significant amount of data, but it can be obtained in the course of one-two days with the help of the proposed method. Our future works should be aimed at computer aided processing of such a data. Another direction of the studies is coils form-factor analysis, i.e., the calculation of a mutual

inductances value for various numbers of windings and for various coils radii for a given geometry.

References

[1] B. Wilson, M. Dorman, "Cochlear implants: Current designs and future possibilities", JRRD, **45(5)**, 695-730 (2008).
[2] A. Foletti, A. Durrer, E.Buchser, "Neurostimulation technology for the treatment of chronic pain: a focus on spinal cord stimulation" Expert Rev Med Devices **4(2)**, 201-214 (2007).
[3] B. Pelletier, S. Spiliopoulos, T. Finocchiaro, F. Graef, K. Kuipers, M. Laumen et al., "System overview of the fully implantable destination therapy—ReinHeart-total artificial heart". Eur J Cardiothorac Surg **47**, 80-86 (2015).
[4] A.A. Danilov, G.P. Itkin and S.V. Selishchev, "Progress in methods for transcutaneous wireless energy supply to implanted ventricular assist devices", Biomed. Eng., **44-4**, 125-129 (2010).
[5] A.A. Danilov, E.A. Mindubaev, "Space-frequency approach to design of displacement tolerant transcutaneous energy transfer system" PIER M; **44**, 91-100 (2015).
[6] [online] http://www.fastfieldsolvers.com/products.htm#fasthenry2.
[7] [online] https://www.comsol.com/comsol-multiphysics.

SECTION 1

MECHATRONICS, IMPLANTS, ARTIFICIAL ORGANS. DIAGNOSTICS AND ANALYSIS IN SURGERY

Velocity fluctuation and wall vibration measurements in cerebral aneurysms before and after stenting

D. Liepsch[1], A. Balasso[1], S.V. Frolov[2], S.V. Sindeev[2], M. Fritzsche[3]
[1] Department of Neuroradiology, Klinikum rechts der Isar, Technische Universität München, Munich, Germany
[2] Tambov State Technical University, Tambov, Russia; [3]Polytec GmbH, Waldbronn, Germany

Introduction

Endovascular aneurysm repair procedures such as the insertion of coils or stents are often used to reduce the risk of rupture. The combination of coils with stents is highly effective because a reduced amount of thrombotic material can escape into the aneurysm. There is also a better chance of complete occlusion of the aneurysm. The factors which can contribute to the development of cerebral aneurysms include: influence of blood flow, blood pressure, wall elasticity and wall properties, pusatility, the non-Newtonian flow behavior of blood, velocity and wall vibrations and flow shear stresses acting on the vessel walls. The goals of our study were to measure wall vibrations and to investigate ways of reducing the factors which contribute to aneurysm rupture. Because the type of stents used plays an important role in the success of treatment, two different stent types were tested. Physiologically (one-to-one, true-to scale) transparent models with a compliance similar to that of human vessels were used.

Methods

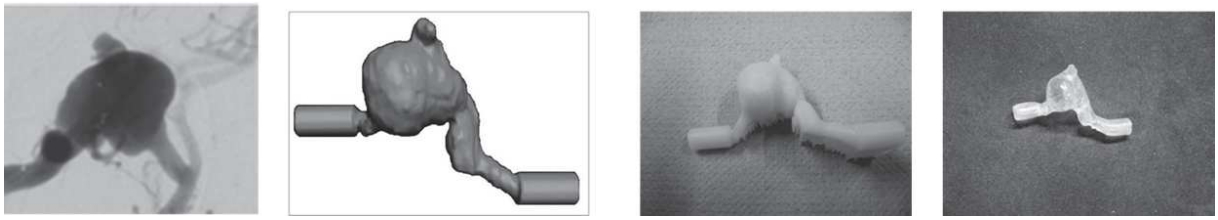

Fig. 1 CTA, 3D-reconstruction, wax model and silicone model of an aneurysm.

Flow visualization was done in the models with a photoelasticity apparatus. Dyes were used to visualize steady flow; a birefringent solution was used for unsteady flow and particles were also added. Further velocity measurements were done with LDA and a laser Vibrometer.

Results

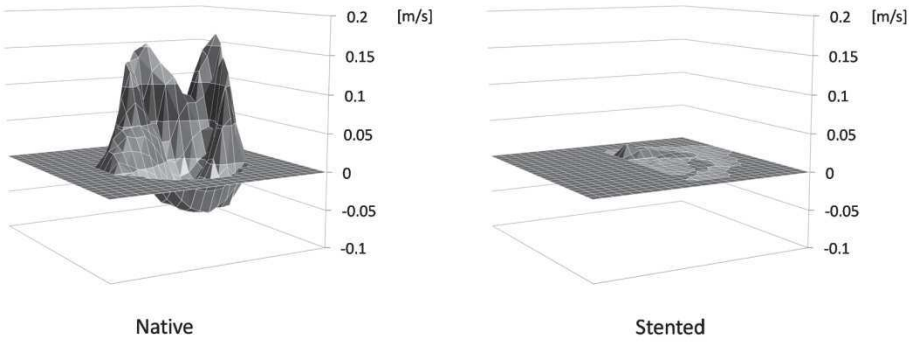

Fig 2 Velocity component of the fluid in flow direction measured over a cross section in the center of the aneurysmal sac at systole: left native, right stented aneurysm.

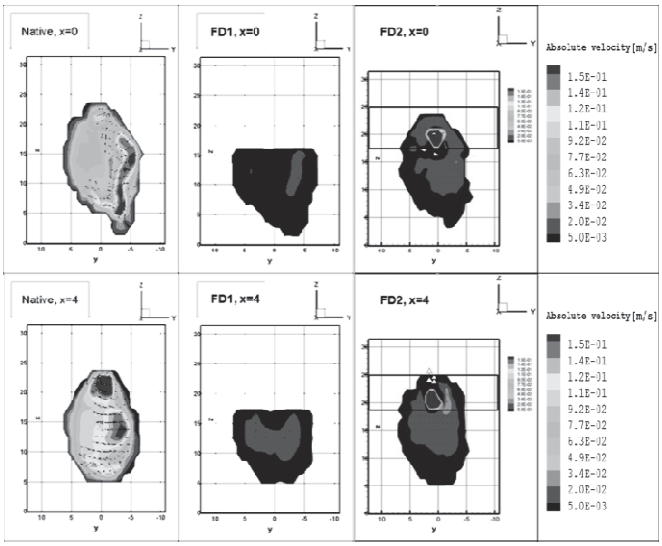

Fig. 3 Aneurysmal velocity magnitude over two cross sections before (left) and after implantation of flow diverter FD1 (center) and flow diverter FD2 (right).

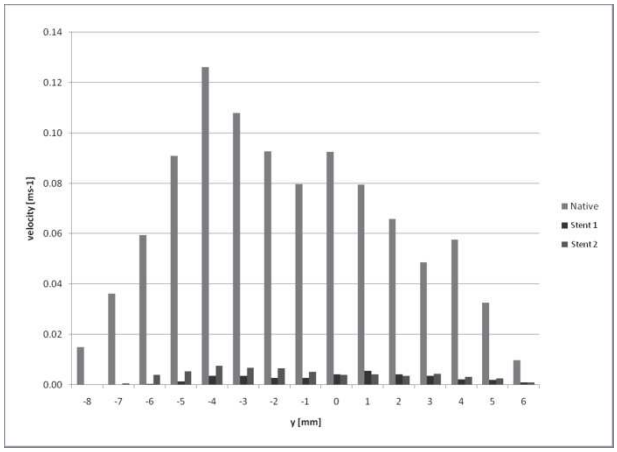

Fig. 4 Aneurysmal mean velocity calculated on longitudinal planes (aneurysm center in y=0) after stenting with two different flow diverters.

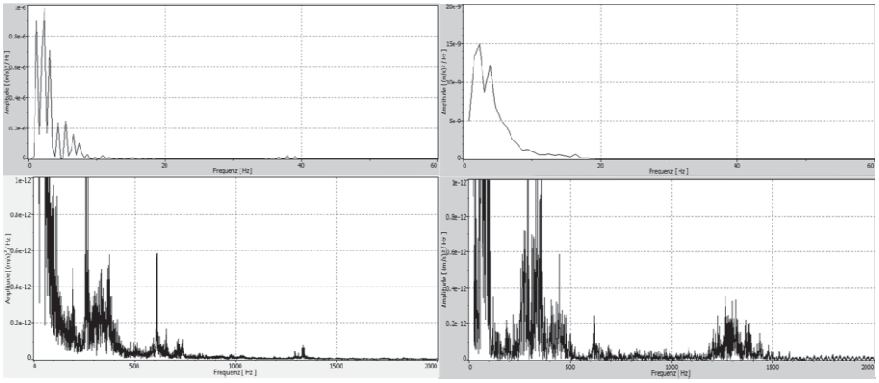

Fig. 5 Power spectral density measured at a point on the bottom (left) and on the lateral wall (right) of an aneurysm. The pictures above show the PSD in the frequency range 0-60 Hz, below in the range 0-2000 Hz.

Discussion

Low shear inside aneurysms may provide the conditions for the formation of thrombogenic areas and it remains to be investigated how these areas are affected by stent placement. Recorded vibrational frequencies up to and exceeding 550Hz are important and must be investigated in more detail in the cerebral arterial system, especially in areas prone to aneurysm. It is well known that vibrations cause resonance at specific frequencies, unique to each material. It may be theorized that vibrations in an aneurysm, up to a specific as yet unidentified frequency or critical resonance frequency, may contribute to aneurysm rupture.

Conclusions

- Frequencies exceeding 550 Hz have been measured in models of human cerebral arteries.
- Further studies with modified flow conditions (flow rate, pressure range and beat frequency) are needed in the cerebral arterial areas prone to aneurysm.
- Thrombogenic areas may be created at low shear rates inside aneurysms and these may be affected by stent placement.
- Vortices have been observed within aneurysm and may cause velocity fluctuations.
- The intensity of vibrations is small than the average pulse intensity. With increasing aneurysm size, small additional vortices with a high turbulence degree arise.
- Energy exchange causes wall vibrations.
- The highly disturbed flow in aneurysms may cause vibrations of the wall and lead indirectly to rupture.

Novel tissue engineering methods for bile duct reconstruction

I. Klabukov

I.M. Sechenov First Moscow State Medical University, Trubetskaya St. 8/2, Moscow, 119991, Russia

Iatrogenic bile duct injuries following cholecystectomy for gallstone disease represent a serious and challenging surgical complication. Intraoperative bile duct injures requiring its repair observed in 0.05–2.7% of patients, who underwent cholecystectomy due to cholelithiasis. Lots of patients require reconstructive bile duct surgery given that cholecystectomy is the second most common surgery in the abdominal region, and more than 1 mln operations are made all over the world per year. The standard surgery includes suturing

of the duct with small intestine, but such a reconstruction can lead to liver abscess, biliary cirrhosis and increased risk of cholangiocarcinoma [1]. No one method was proposed as the best option for the repair and native reconstruction of common bile duct (Fig.1), though the use of bioengineered matherials and methods is keeping an experimental surgery research.

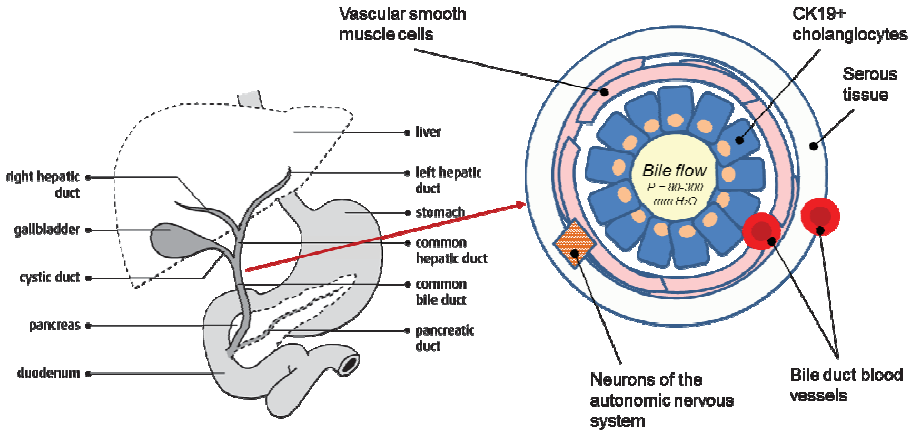

Fig.1 Location of the Common Bile Duct (CBD) and schema of CBD's multilayer structure.

In early studies was theoretically analyzed of methods for creating a three-dimensional universal tissue-engineering graft of the common bile duct and consider the possibility of creating fragments of tissue engineered bile duct, which involves the use of tissue-engineering structures, consisting of a matrix of cells and signaling molecules [1,2]. Used electrospinning methods were prepared of several experimental samples for forming biocompatible tissue-engineered constructions of the bile duct using four polymers: polycaprolactone (PCL), a copolymer of D,L-lactide-co-glycolide of composition 75:25 (PDLGA), a copolymer of L-lactide with ε-caprolactone of composition 70:30 (PLC), and cellulose diacetate. The samples were two-layer structures having an impermeable to bile layer. Characteristics of PCL inner layer were the same for all samples. Determination of optimum parameters were based on the results of experiments on MTT assays with two standardized lines of stromal (3T3) and epithelial (MCF7) cells. Biodegradation kinetics test of experimental biocompatible samples was carried out in various mediums: water, phosphate buffer, Fenton reagent, bile, a nutrient solution with or without serum, as well as in the presence of eukaryotic cells [2]. Are supposed, the bile duct repair with the multilayer construction will contribute to formation of physiologically equivalents of tissue without any focuses of disease (Tab.1).

№	Causes of the diseases	Pathologies
1	Injures of the epithelial layer of cholangiocytes	Fibrosis, stenosis, biliary strictures; Cholangitis.
2	Injures of bile duct blood vessels	Ischemia; Stenosis, strictures; Infections.
3	Injures of bile duct innervation	Dyskinesia.

Tab.1 Impact of injures of multilayer structure components on tissue-specific bile duct pathologies.

Although the first surgery with the use of polymeric tube for its partial epithelialization during 3 weeks were carried out in 1913 by Propping [3], it was necessary to create the instrumentation tools for tissue engineering based on achievements of cell biology (immunohistochemistry, flow cytometry, induced pluripotency), microbiology (nucleic acid

amplification from single cell, metagenome analysis), biotechnology (grows factors, transcription factors, gene therapy vectors) and biochemistry (electrospinning method). Actually, electrospinning is the most promising and technological method to obtaining fibrous and porous biocompatible materials [4]. In addition, state-of-the-art research tools for bioengineer-surgeon includes techniques with adequate physiological models from selecting animals to genetically-engineered humanizing mini-pigs. Was found the biomechanical properties of mini-pig bile ducts aged 7 to 10 months close to the same parameters in humans in early experimental studies on animals [5]. During the reconstruction of extrahepatic duct mini-pigs using a collagen matrix, functionalized by rhFGF, the formation of a complete monolayer CK19+ cells noted 8 weeks after surgery [6]. Use of a biodegradable copolymer of polylactic acid (PLA) and PCL (50:50), reinforced with polyglycolic acid fibers, in the reconstruction of the bile duct required 6 months for epithelium regeneration in the case of a full prosthesis [7], and 4 months using the patch (with size 20 mm x 10 mm) [8].

Studies on the biodegradation of specimens biocompatible in different mediums, particularly in the bile, showed the feasibility of further use as carcass material PCL, cellulose diacetate and PLC (retain their structural properties of more than 2 weeks). The study revealed the strength characteristics about the same ratio values of the longitudinal and transverse strength obtained on the scaffold of native and decellularized bile ducts, as well as the values of Young's modulus. As a result of screening using the MCF7 and 3T3 cell lines and methods using light microscopy and MTT assay revealed the most biologically suitable materials. Through the instrumentality of electrospinning copolymers of lactic acid were produced and been choosed the best samples of the materials for the tubular tissue-engineering bile duct graft development: PCL (inner layer) and PLC (outer layer) [2]. Thus, with the help of electrospinning copolymers of lactic acid were produced and been studied the best samples of the materials for formation of the tubular tissue-engineering graft with surfaced epithelialization and intra-layered vascularization.

Creating an artificial matrix for different cells types is a complex problem related to the selection of non-toxic polymer and method for material forming, activation exogenous extracellular matrix with specific properties, and long-term biological effects of ready-to-use cell-engineered graft. Conclusions about the usefulness of a particular polymer can be made only after the cell growth studies on scaffolds made of degradable biomaterials (electrospinning parameters influence the morphology of the material), and studies in model medium as well as *in vivo*. The work was supported by Ministry of Education and Science of the Russian Federation (grant No. 14.604.21.0133, ID RFMEFI60414X0133).

References

[1] Dyuzheva T.G. et al. “Prospects for tissue engineered bile duct (Review),” Genes & Cells, **XI** (1), 43 (2016). [in Russian]

[2] Klabukov I.D., Dyuzheva T.G., Lyundup A.V., Tenchurin T.H., Shepelev A.D., Mamagulashvili V.G., Chvalun S.N. *In: Programma i nauchnye trudy nauchnoj konferencii molodyh uchenyh po medicinskoj biologii FGBU FNKC fiziko-himicheskoj mediciny FMBA,* E.N.Ilina and E.S.Kostrykova eds. (FRCC PCM, Moscow, 2016). [in Russian]

[3] S.P. Fedorov, *Zhelchnye kamni i khirurgiia zhelchnykh putei*, 2nd ed. (Medgiz Publ., Moscow, 1934).

[4] Agarwal S., Wendorff J. H., Greiner A., “Use of electrospinning technique for biomedical applications,” Polymer, **49**(26), 5603 (2008).

[5] Li W. C. et al. “Comparison of biomechanical properties of bile duct between pigs and humans for liver xenotransplant,” Transplantation proceedings, **45**(2), 741 (2013).

[6] Li Q. et al. “Extrahepatic bile duct regeneration in pigs using collagen scaffolds loaded with human collagen-binding bFGF”, Biomaterials, **33**(17), 4298 (2012).

[7] Miyazawa M. et al. “A Tissue-Engineered Artificial Bile Duct Grown to Resemble The Native Bile Duct,” American journal of transplantation, **5**(6), 1541(2005).

[8] Aikawa M. et al. “A novel treatment for bile duct injury with a tissue-engineered bioabsorbable polymer patch,” Surgery, **147**(4), 575 (2010).

The aspects of needle-electrode insertion during electrical impedance quality controlling of venipuncture.

I.A. Kudashov[1], S.I. Shchukin[1]

[1] *Bauman Moscow State Technical University, Moscow, Russian Federation*

In medicine to obtain intravenous access for blood sampling of venous blood during the process of venipuncture the needle is inserted at an angle almost parallel to the skin surface [1].

The aim of this work is to study the effect of needle-electrode insertion at an angle to the calculation of the influence of non-uniform needle insertion speed, whereas the equation of vertical shaft inserted from the surface has been used to calculate the current spread [2,3].

$$Z = \frac{\rho}{2\pi l} \ln \frac{4l}{d}$$

where Z - spreading resistance (ohms); l - the length of inserted needle shaft (mm); d-diameter of the needle electrode (mm); ρ - Resistivity of the medium (Ohm • m).

The length of the inserted needle electrode to the vein vertically is different from inserted it at an angle. However, the conducted study shows that electrical impedance value due to the inserting of a needle electrode at an angle differ greatly from the value by inserting it vertically to a depth of 5 mm. This is due to the geometry of the end of the needle electrode, which corresponds to the injection needle (Fig. 1). The injection needle has a beveled surface at the end with 10-15 °, the bevel length is 5 mm. When the needle electrode is inserted at an angle, the contact area becomes greater than the vertical insertion , so larger values of electrical impedance can be considered during vertical insertion.

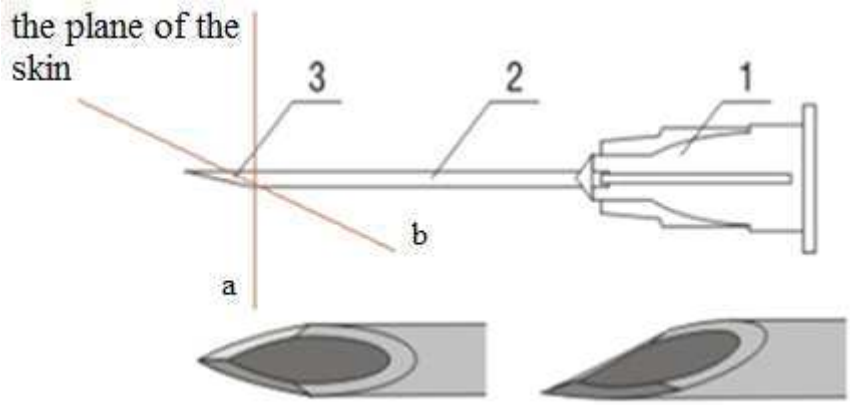

Fig. 1 The geometry of the electrode needles.
1 - cannula needle, 2 - needle, 3 - bevel needle
a - vertical insertion of a needle, b - the insertion of the needle at an angle of 10-15 °

However, the values are stabilized and became similar when the electrode needle was inserted to the biological tissue to a depth of more than 5 mm. The measured values are shown in Table 1.

Table 1: Effect of the needle bevel to measure electrical impedance

Depth, mm	Vertical insertion, Ohm	Insertion at angle, Ohm
1	500,0	144,0
3	200,5	108,2
5	127,0	89,0
7	93,0	85,3
10	74,0	68,0

The results of this study show the comparability of vertical insertion of needle electrode to the biological tissue and the insertion of a needle electrode at an angle. Values of electrical impedance become closer during insertion of the needle electrode at 5 mm, which corresponds to 1 mm depth of biological tissue when the needle electrode is inserted at an angle.

References

[1] Egorova M. Venepunktia and blood sample preparation. The practice of medicine. Moscow, 2014. P. 3-9
[2] Zaborovskiy, A. I., "Electrical Prospecting". Moscow 1963. 429 p.
[3] I. Kudashov, S. Shchukin, O. Belaya, S. Perov. The features of the controlling venipuncture electrical impedance method. Biomedical electronics, 2015. P. 15-19

Analysis and simulation force-position control linear actuator with driving system for below knee amputees

Dhirgaam A. Kadhim

Kerbala University/ College of Engineering/ Prosthetic & Orthotics Engineering Department/ 56001 Kerbala/Iraq

dhirgaamk@yahoo.com

dhorgam.khadim@uokerbala.edu.iq

1. Introduction

Today's commercially available below-knee prostheses are completely passive during stance, and consequently, their mechanical properties remain fixed with walking speed and terrain. These prostheses typically comprise elastic bumper springs or carbon composite leaf springs that store and release energy during the stance period, e.g. the Flex-Foot or the Seattle-Lite [1-2]. Lower extremity amputees using these conventional passive prostheses experience many problems during locomotion. For example, transtibial amputees expend 20-30% more metabolic power to walk at the same speed than able-bodied individuals, and therefore, they prefer a slower walking speed to travel the same distance. Thus, their self-selected walking speed is normally 30-40% lower than the mean speed of intact individuals [3] Also, many clinical studies report that amputees exhibit an asymmetrical gait pattern [4-5].. These biomechanical results may explain why transtibial amputees require more metabolic energy to walk than intact individuals. Using a conventional passive prosthesis, a leg amputee can only supply energy through the hip joint to power center of mass dynamics, producing a pathological gait pattern [6]. Tasks such as walking are difficult when each footfall is seen as a collision with the ground by the rigid limb, especially on uneven or

unknown surfaces. In unknown, unstructured human environments, low impedance (compliant) force controlled actuation improves safety [7]. Actuation for robotics is a demanding task, requiring high torque and low speed, large peak power output for short periods, accurate feedback sensing, and suitability in shape, size and mass. Most robots use high impedance (stiff) position controlled actuators typical of industrial robot arms[8].In this paper, linear ball-screw actuator with spring is reproduced to be used as driver of the proposed ankle-foot prosthetic. The results of force and force-position control are presented. Also, a variable force-position control strategy is performed to reproduce the typical values of ankle joint's stiffness and damping presented by humans during the walking.

2. Methods

I. Actual prototype of Ankle–Foot Prosthesis and Component Selection and Implementation

The ankle–foot prosthesis used for this study, shown in Fig. (1a) ,. This prosthesis is a successor to the series of prototypes developed in the Bio mechatronics Group of the MIT Media Laboratory. It is a completely self-contained device having the weight (1.8 kg) and size of the intact biological ankle–foot complex.

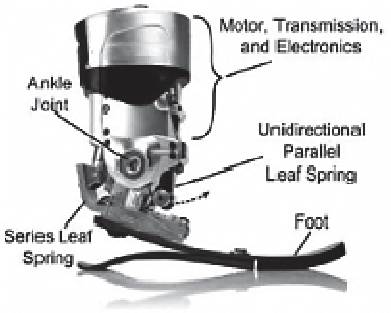

Fig. 1a prototype of Ankle–Foot Prosthesis with labeled components

Fig. 1b Components of actuator Ankle–Foot Prosthesis.

The first step in the design is to select an actuator and a transmission to satisfy the torque/power-speed requirements of the human ankle (Fig.1b). In the design, a DC brushed motor from Maxon, Inc (RE-40) was used because its peak power output(500 W) is much larger than the measured peak power in human ankle during walking (350 W). Furthermore, it only weighs 0.45 kg and its stall torque and the maximum angular velocity of the motor are up to 2.5 Nm and 7580 rpm, respectively [9].

II. Structure of Linear DC-BallScrew Actuator in Series with Spring

The current actuator (Fig.2) that used for Ankle–Foot Prosthesis has a DC geared motor connected to a ball screw through gear box drives the linear motion. The ball screw nut is coupled to the output through die compression spring.

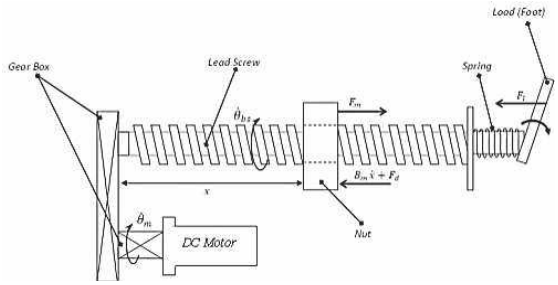

Fig. 2 Structure of Linear Actuator in Series with Spring.

III. Dynamic Modelling of The Actuator System

For the purposes of simulation and controller design, it is appropriate to develop a mathematical model of the linear motor system. For this reason, a diagram of the basic linear motor with spring in series is given in Figure 2, Hence, the equation of motion for the system given :

$$M\ddot{x} = F_m - B_m\dot{x} - F_d - F_l \quad (1)$$

With $F_l = k_s(x - x_l)$ (2)

Where: F_m – The force produced by DC motor; F_d – The general external disturbances; F_l – The load force; B_m – The Damping coefficient of DC Motor; k_s – The Spring Stiffness; x – The linear displacement of the ball screw nut; x_l – The linear displacement of the load; M – The total mass of the load (including the motor thrust block and linear bearings). As can be seen, Eq. (1) represents a very basic mathematical model of the linear motor with spring in series. The term F_d represents all disturbance forces acting on the system. As some of these forces are not strictly external, such as coulomb friction and periodic cogging forces, a more accurate model would include additional terms representing the inherent system disturbances. However, since all of these factors are seen by the motor as general disturbances, it is fair to treat them this way in a basic model. One of the aims of this paper is to quantify the inherent disturbances that significantly affect system performance. From these results it would be possible to build a more accurate system model as below:

$$\left[M_n + \left[\frac{2\pi}{P}\right]^2\left[J_{bs} + \left[\frac{N_2}{N_1}\right]^2 J_m\right]\right]\ddot{x} = \frac{2\pi}{P}\left[\frac{N_2}{N_1}\left[T_m - B_m\dot{\theta}_m - T_{dism}\right]\right] - \frac{2\pi}{P}\left[B_{bs}\dot{\theta}_{bs} - T_{disbs}\right] - B_n\dot{x} - k_s(x - x_l) - F_{dis} \quad (3)$$

Where: M_n - The mass of the moving nut; J_m and J_{bs} -The motor and ball screw inertias respectively; P – The pitch of the ball screw; N_2 , N_1 – The number of teeth on the motor and ball screw gear respectively; B_n, B_{bs} – The viscous friction coefficients of the nut and ball screw respectively; x – The linear displacement of the ball screw nut.

θ_m, θ_{bs} – The angular displacements of the motor and ball screw respectively; T_m –The motor torque; T_{dis} –The disturbance forces at the nut; T_{dism}, T_{disbs} – The disturbance torques at the motor and ball screw respectively.

IV. Proposed Control System

The position based- impedance control and force-tracking impedance control are combined and adapted to be used in the variable impedance of the ankle-foot prosthetic. The desired impedance is defined as the relationship between the load applied force (Ankle foot force) F_l and the load position (Ankle foot position) x_l . It can be given as:

$$F_l - F_l^d = M_d\ddot{x}_l - K_d(x_l^d - x_l) - B_d(\dot{x}_l^d - \dot{x}_l) \quad (4)$$

Where F_l^d is a desired force to be applied to the load, $\dot{x}_l^d, x_l^d$ are the desired velocity and position defined in the Cartesian space, respectively, and $\dot{x}_l, x_l$ are the load velocity and position in Cartesian space, respectively. The M_d, K_d, B_d are the desired inertia, stiffness and damping for the load. The reference or target load acceleration $u = \ddot{x}_l$ is then given by:

$$u = M_d^{-1}(B_d\dot{e}) + K_d e + F_l - F_l^d \quad (5)$$

where $\dot{e} = \dot{x}_1^d - \dot{x}_1, e = x_1^d - x_1$ are the velocity and position errors, respectively. Thus, u can be used as the command signal to an inner position control loop in order to drive the robot accordingly to the desired position.

$$u_f = m_d^{-1}(b_d\tilde{x}_1^v - \dot{x}_1) + k_d(x_1^v - x_1) + F_1^n \quad (6)$$

Where $x_1^v, \dot{x}_1^v$ and u_f are the virtual position, velocity and load acceleration, respectively, while , , m_d, b_d, K_d are appropriate elements of M_d, b_d, k_d defined in (4) in the constrained direction. The contact force F_1^n during steady-state contact with the surface is given by: $F_1^n = k_d(x_1^v - x_1)$ (7)

Considering for simplicity the ground that foot touches it modeled by a linear spring with stiffness k_e the contact force load is given by: $F_1^n = k_e\delta x_1$ (8)

This leads to the following steady-state position and contact force:

$$x_{1_{ss}} = \frac{k_d x_1^v + k_e x_e}{k_d + k_e} \quad (9) \qquad F_{1_{ss}}^n = \frac{k_d k_e}{k_d + k_e}(x_1^v - x_e) \quad (10)$$

It is possible to apply a desired force load F_1^d on the system while simultaneously achieving the desired impedance by estimating the desired virtual position x_1^v as: $x_1^v = x_e + F_1^d\left(\frac{k_e + k_d}{k_e k_d}\right)$ (11)

Moreover, when the environment stiffness is unknown, it is also possible to obtain the virtual position from F_1^d, F_1^n and δx_1. In this case, by substitution of k_e in (11) the following virtual position x_1^v is obtained:

$$x_1^v = \begin{cases} x_e + \frac{F_1^d}{k_d}, & if\ F_1^n = 0 \\ x_e + F_1^d\left(\frac{k_d\delta x_1 + F_1^n}{k_d F_1^n}\right), & if\ F_1^n \neq 0 \end{cases} \quad (12)$$

This is valid for contact and non-contact condition. This approach enables the classical impedance controller. The block diagram of impedance control with force is presented in below figure.

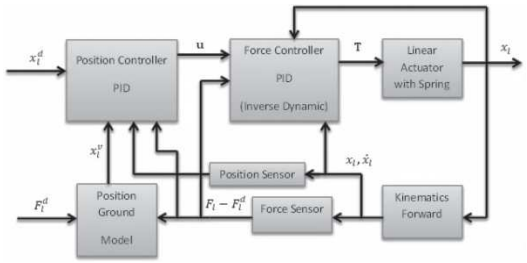

Fig. 4 Block diagram of impedance control with force.

1. Simulation Results

The simulation of overall suggested system, including the linear ball-screw actuator in series with spring, posion and force controllers, feedback position and force sensor is shown in Fig. 5 , based on this model the sub-system model of linear ball-screw actuator, can be built, this sub-system will be used to built another sub-systems, inverse dynamics model, forward kinematics model , model of position an force load contact with ground

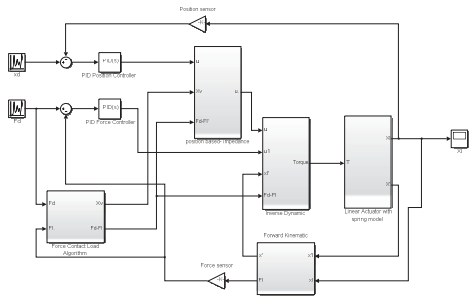

Fig. 5 Matlab/Simulink force- position control of the system.

The values of k_s^d and B_d are introduced in the Fig. 5 which computes the desired position for the load. The linear actuator with spring that connected to the ankle-foot prosthesis the results for the different behaviors of the device can be seen in Figs. 6(a) to 6(d). Fig. 6(a) shows the actuator behaving like a spring of k_d = 2Ns/mm , and with coefficient damping $B_d = 0$ for position, load force, torque and angular velocity. The figs. 7(a) to 7(d) show the same variables in previous fig. 6 but, when actuator operatized with parameters like a spring of k_d = 30 Ns/m , and with coefficient damping $B_d = 15$ Ns/m ,Note that the load force have high fluctuations relative to input desired value corresponds to the position by low fluctuations. In Figure 8(a) to 8(d) can be seen the system approach to optimum satiability with parameters like a spring of k_d = 10 Ns/m , and with coefficient damping $B_d = 8$ Ns/m.

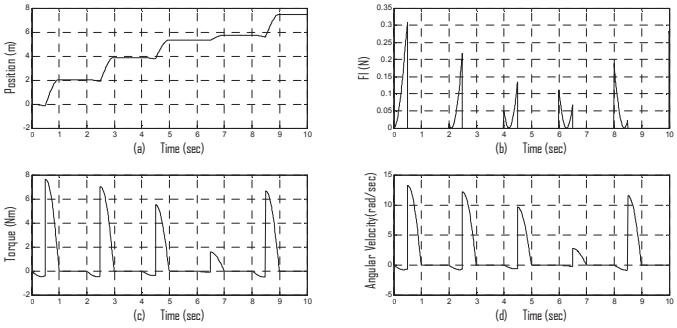

Fig. 6 Control Linear Actuator With Spring

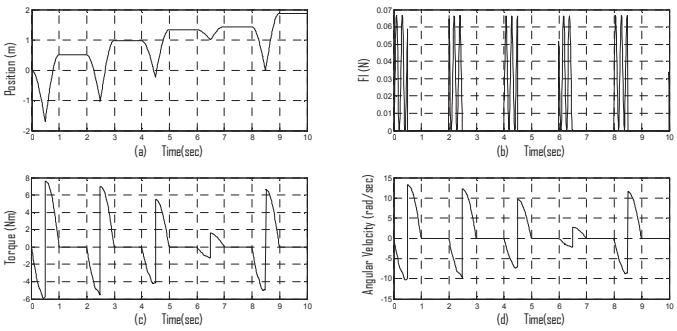

For Different Impedances Values [k_d = 10 Ns/m, $B_d = 0$] .
Fig. 7 Control Linear Actuator With Spring

For Different Values [k_d = 30 Ns/m, B_d = 15 Ns/m] .

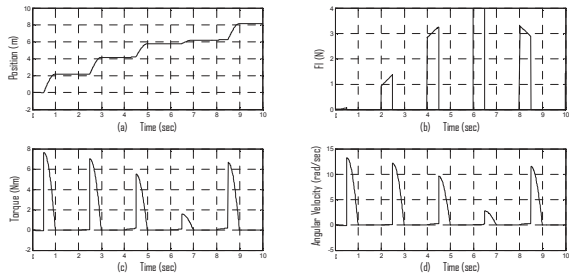

Fig. 8 Control Linear Actuator With Spring For Different Impedances Values [k_d = 10 Ns/m, B_d = 8 Ns/m] .

2. Conclusions

This study has successfully simulated algorithm for force-position controlling an ankle-foot prosthesis with linear elastic actuator. The ball-screw linear actuator with spring in series it is possible to implement the force and impedance control with different impedance parameters and achieve performance similar to biological systems. The results indicate that this rule system has potential for direct application in micro-processor controlled prosthetics. Matlab/Simulink has exhibited utility in modeling the complex nature of human gait, and provided a medium for evaluating the functionality of the algorithm. Matlab/Simulink is an indispensible tool in computational modeling, and provides great utility in accelerated modeling and evaluation of control mechanisms.

References

[1] www.ossur.com.

[2] S. Ron, Prosthetics and Orthotics: Lower limb and Spinal. Lippincott Williams & Wilkins, 2002.

[3] N. H. Molen, "Energy/speed relation of below-knee amputees walking on motor driven treadmill," Int. Z. Angew. Physio, Vol. 31, pp.173, 1973.

[4] D. A. Winter and S. E. Sienko, "Biomechanics of below-knee amputee gait," Journal of Biomechanics, Vol. 21, No. 5, pp. 361-7, 1988.

[5] H. B. Skinner and D. J. Effeney, "Gait analysis in amputees," Am J Phys Med, Vol. 64, pp. 82-89, 1985.

[6] A. Ruina, J. E. Bertram, and M. Srinivasan, "A collisional model of the energetic cost of support work qualitatively explains leg sequencing in walking and galloping, pseudo-elastic leg behavior in running and the walk-to-run transition," Journal of Theoretical Biology, Vol. 237, Issue 2, pp. 170-192, 2005.

[7] Zinn, M., O. Khatib, B. Roth, and J.K. Salisbury, Playing It Safe. IEEE Robotics and Automation Magazine, 2004. 11(2): p. 12-21.

[8] www.maxon.com .

[9] S. K. Au, J. Weber, and H. Herr, "An ankle-foot emulator system for the study of human walking biomechanics," Proc. IEEE Int. Conf. on Robotics and Automation, Orlando, FL, pp. 2939-2945, May 2006.

The design of artificial ventricles for mock circulation loop

A.O. Porfiryev, A.A. Pugovkin, D.V. Telyshev

National Research University of Electronic Technology / Department of Biomedical Systems, Moscow, Russia

Artificial ventricles (AVs) have complex structure and different design [1]. The differences consist in the body form and material design, the selection of artificial heart valves and variations of the ventricle membrane. At present heart artificial ventricles of the standard volumes equal to the average natural stroke volume (72 ml, 80 ml and 120 ml) are commercially available [2, 3]. However, ventricular volume can reach 300 ml in the heart

failure condition [4]. Commercial pneumatic AV [5-7] are limited not only by volume, but also by artificial valves and ventricle membrane used in the design. Undoubtedly, such AVs provide the acceptable hydrodynamic characteristics and they can be used in the mock circulation loops (MCLs). The disadvantage of such systems is the inability to increase the ventricular volume and to use different artificial heart valves. Therefore, in this work it was required to ensure the versatility of the designed artificial ventricles.

Commercial AVs are intended for intracorporeal or extracorporeal medical use. [8]. These ventricles are designed to minimize blood damage and thrombosis, which increases their cost. For the artificial ventricles used in the MCL, such parameters are not crucial.

During out research two prototypes of AV were realized and tested (Figures 1 and 2).

AV with external heart valves manufactured with accordance to all necessary requirements shown on Figure 1a. For the creation of a 3D AV models the CAD computer program was used (Solidworks Corp., Waltham, Massachusetts, USA) The body of AV consists of two hemispherical parts. Pneumatic part has a hole for a fitting connection with a pneumatic control system, and hydraulic part has two holes for cut-in fitting connection with a hydraulic circuit of MCL, one hole for connecting the rotary or centrifugal blood pump and one hole for connecting a pressure sensor. The body of the prototype model is made of organic glass by blowing method with thickness of 3 mm. To connect AV body with artificial heart valves special chambers were developed and manufactured. These chambers are shown on Figure 1b. The material of the AV membrane is two-component silicone rubber on the platinum catalyst (Elastosil RT 620 A/B; Wacker Chemie AG, Munich, Germany). The advantage of this material is the ability to make membranes of any thickness under laboratory conditions in accordance with the necessary requirements. This material is elastic, strong, transparent and is vulcanized at the room temperature. Main characteristics of the material are presented in the table. Membrane with thickness of 1 mm was used in tests.

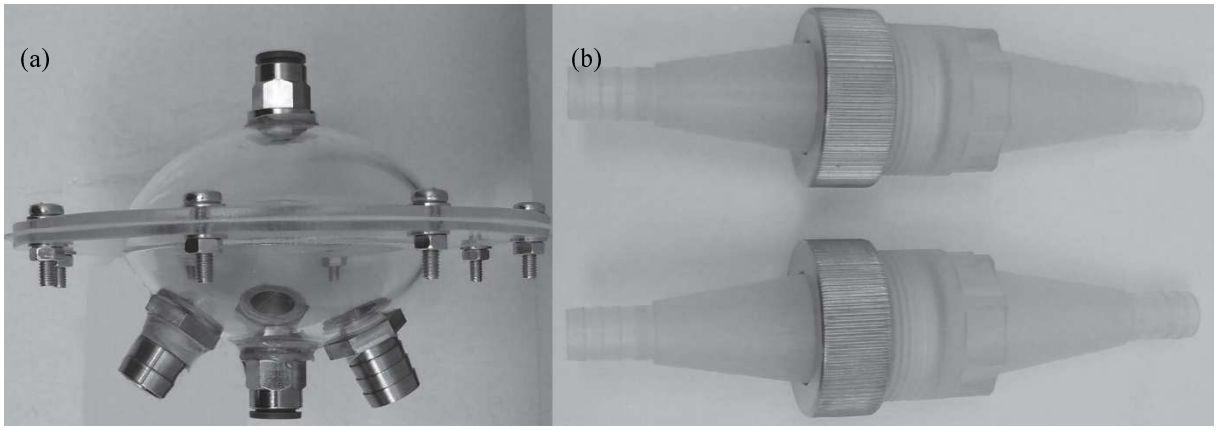

Fig. 1 Image of AV with external heart valves (a) and special connecting chambers (b).

Another design of AV is a ventricle with the built-in heart valves. The body made of translucent organic glass consists of two parts. The hydraulic part (Fig. 2a) has two holes with seats for the artificial heart valves, pneumatic part (Fig. 2b) has a hole for the fitting connection to pneumatic control system. The total volume of the ventricle is 100 ml. When designing it was considered that inlet valve diameter should be larger, than outlet valve diameter since filling of ventricle occurs mostly passively from the low pressure area in a definite time. Increase of resistance of the inlet valve with a small diameter can disturb the AV function more than outlet valve characteristics mismatch. Additional inserts (Fig. 2d) under seats of aortal and mitral valves with a diameter of 23 mm and 25 mm, respectively, were designed for this purpose. These inserts protect valves from possible damage when

twisting the fitting (Fig. 2c) designed and manufactured for this AV. Connection of two ventricle parts is implemented with 8 screw-nut couples.

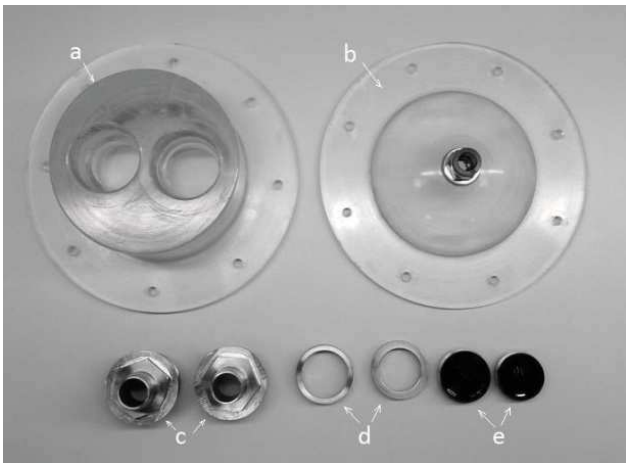

Fig. 2 Image of AV with built-in heart valves: a – hydraulic part, b – pneumatic part, c – fittings, d – inserts, e – valves.

Silicone membrane of two-part silicone Mold Super 10 on the tin catalyst with a thickness of 1 mm was made for testing. The main characteristics of the material are presented in the table. It was decided to use bileaflet mechanical heart valves (MedEng, Russia). Its distinctive feature is the design of the locking element in the form of two symmetrically located semi-district shutters that fastening to the prosthesis frame by means of hinged connection. Advantage of such valves is the lowest profile (among mechanical valves), existence of the central bloodflow via the valve, and also elimination of a "small hole zone" that is responsible for thrombosis and dysfunction of rotary-disk structures. The diameter of the aortic and mitral valves is 21.6 and 23.6 mm, respectively.

Table. The main characteristics of silicone compounds

Material / Characteristic	Elastosil 620 A/B	Super Mold 10
Density, g/cm^3	1,1	1,08
Shore hardness A	15	10
Elongation at break, %	900	520
Tensile at break, MPa	6,5	1,8

Medos VAD with 80 ml volume was used as an AV reference. The material of the Medos VAD individual components (body, membrane, valves) is polyurethane of different hardness and elasticity. The direction of flow in a circulation loop through Medos VAD is controlled by bulbous artificial tricuspid valves.

The tests were conducted on the MCL, the hydraulic circuit of which is shown on Figure 3. The hydraulic circuit consists of membrane type AV, two closed reservoirs, reproducing the parameters of the aorta and vena cava, two ultrasonic flow meters and four pressure sensors. All elements of the hydraulic circuit are interconnected by flexible laboratory PVC tubing with inner diameter of 12.7 mm (TYGON E-3603; Compagnie de Saint-Gobain, Courbevoie, Ile-de-France, France). Distilled water of 3000 ml total volume was used as the fluid in the hydraulic circuit.

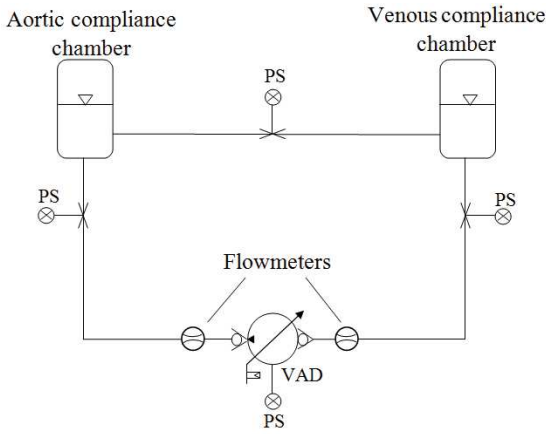

Fig. 3 Schematic of mock circulation loop. VAD, ventricular assist device; PS, pressure sensor.

Control of AV work during tests was carried out by means of the pneumatic control system consisting of a servovalve (LRPA4-34-2-B-00; Camozzi, Brescia, Italy), pumps to create pressure (K40PSN oilless air pump; M-Technology CO., LTD, Korea) and depression (K30PSN oilless air pump; M-Technology CO., LTD, Kopea) and an electronic control system which is based on generation of the control signal which is set by means of the

$$s(t) = A \cdot g(t)$$

A $g(t)$

$$g(t) = \begin{cases} 0, & t < 0 \\ \sin^2\left(2\pi \frac{t}{T_{cc}}\right), & 0 \le t \le \frac{T_{cc}}{2} \\ 0, & t > \frac{T_{cc}}{2} \end{cases}$$

T_{cc}

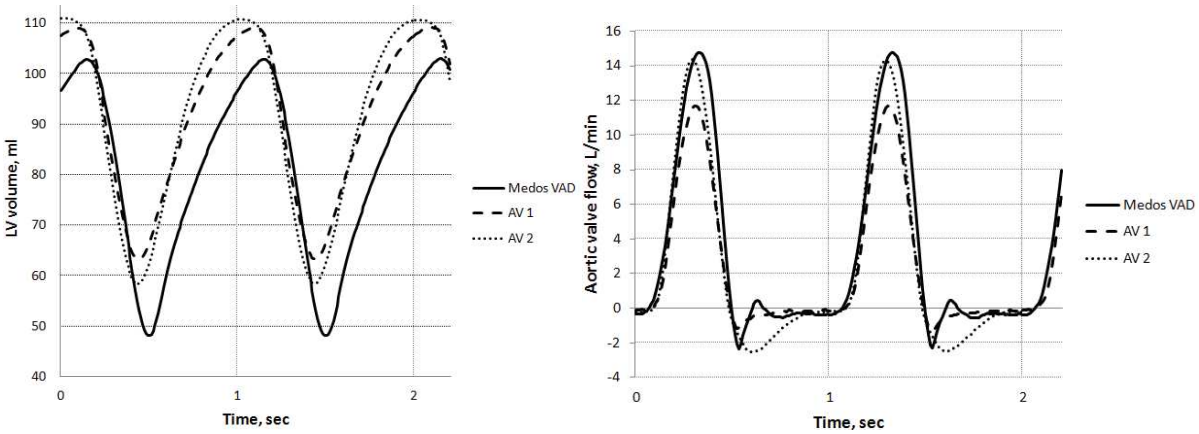

Fig. 4 Ventricular volume (a) and aortic valve flow (b).

The viscous losses across the special connecting chambers can be the reason of the low volume changes corresponds to the stroke volume in AV 1. That problem was solved in AV2. Developed AV prototypes shown reliable results in compare to Medos VAD and can be used in the MCL.

References

[1] A.C Alba; D.H. Delgado. The Future is here: ventricular assist devices for the failing heart. Cardiovascular Ther. 7(9):1067-1077 (2009).

[2] J.A. DiNardo, D.A. Zvara. Anesthesia for cardiac surgery (Massachusetts, Blackwell, 2008).

[3] T. Akutsu, H. Koyanagi. Heart replacement: artificial heart 5 (Springer, Japan, 1996).

[4] R.G. Masters. Surgical options for the treatment of heart failure (Kluwer Academic Publishers, Netherland, 1993).

[5] J.M. Anton. Mechanical Ventricular Support – A 2013 Update. (Society of Cardiovascular Anesthesiologists, 2013).

[6] S. Takatani. Beyond implantable first generation cardiac prostheses for treatment of end-stage cardiac patients with clinical results in a multicenter. Ann Thorac. Cardiovasc. Surg. Vol. 8, No. 5 (2002).

[7] L.E. Rodriguez. Ventricular assist devices (VAD) therapy: New technology, new hope? (Methodist Debakey Cardiovasc., 2013).

[8] V. Patlolla. The effect of ventricular assist devices on post-transplant mortality. Journal of the American College of Cardiology, Vol. 53, No. 3 (2009).

Definition of grasp degree at purpose of artificial limb control in real time

M. V. Markova[1], A. V. Kobelev[1], S. I. Shchukin[1]

1. BMSTU, Moscow, Russia

Introduction

Development of the artificial limb control technique, which is most repeating process of the operation of lost extremity and is intuitively clear to the patient, is an actual problem of prosthetics design. It will help to reduce the time for artificial limb exploitation training and to increase the accuracy of movements classification.

Surface electromyography (sEMG) signals have been used in numerous studies for the classification of wrist gestures and implemented in the different prosthetic hands for amputees. But it is difficult to determine kinetic parameters because sEMG signals are not proportional to the associated movement [1]. It also requires additional signal processing and time to obtain useful information [2], which makes impossible anthropomorphic prosthetic control.

The use of the impedance signal in a task of gestures classification and movements parameters determination can resolve the designated problems and can form the basis of artificial limb anthropomorphous control system. It is possible to draw a conclusion about muscle tension and the nature of the realized movement, based on amplitude and a form of impedance changes.

Several researchers including T. Nakamura et al. [3] showed that impedance could be used to detect lower limb motion.

This work is dedicated neuromuscular interface, which is based on electrical impedance and sEMG registration together from one electrode system. Analysis of neuromuscular signals will implement an anthropomorphic control of the various movement patterns.

Methods

The task of this study is to define the grasp degree in real time. The 2-channel impedance measurement system was used. The voltage-to-current converter generated AC current levels in the lower mA range at frequencies from 50 kHz up to 1 MHz [4].

Each electrode system consists of 4 electrodes, two current carrying (CC) and two potential unit (PU) electrodes.

Electrode systems were located on the antagonist muscles which provide flexion and extension. Impedance was measured together with sEMG from potential unit (PU) electrodes.

The mechanism of signals forming can be described as follows. We can present the two-channel impedance signal registered from antagonists muscles on the phase plane with value of the impedance from the lower electrode on a horizontal axis (flexor muscle) and with value of the impedance from the top electrode on a vertical axis (extensor muscle). Each point of a phase portrait characterizes an impedance of system at a certain time (fig. 1).

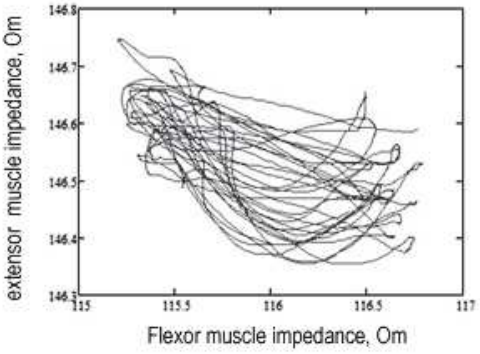

Fig. 1 The 2-channel impedance phase portrait

There is a relaxation of the top muscles of a forearm (extensor muscle) while the grasp movement, therefore reduction of their thickness and increase in an impedance. Contraction of the lower muscles of a forearm (flexor muscle) by analogy leads to reduction of an impedance. Such condition of system characterizing full grasp will be described on a phase portrait by an extreme left point. The state of full opening (the minimum impedance of the top muscles and the maximum impedance of the lower muscles) is characterized on a phase portrait by an extreme right point.

Points between two extreme states describe the intermediate position of a hand. Thus, the movement from an extreme left point to the extreme right characterizes opening of a hand, and the movement from extreme right to an extreme left point – grasping of a hand. The intermediate position of the phase portrait point corresponds to an intermediate stage of an artificial limb movement.

Results

It is found that muscle contraction leads to proportional changing in active and reactive impedance components. This is reflected in anti-phase impedance signals behavior from antagonist muscles during wrist grasp process. Experimentally established difference between

"grasp" and "rotation" signals. Impedance signals are in-phase during wrist rotation process. This difference makes it possible to determine wrist grasp and rotation in real time.

Additional information about nature of the movement can be received in the joint analysis of impedance and EMG signals.

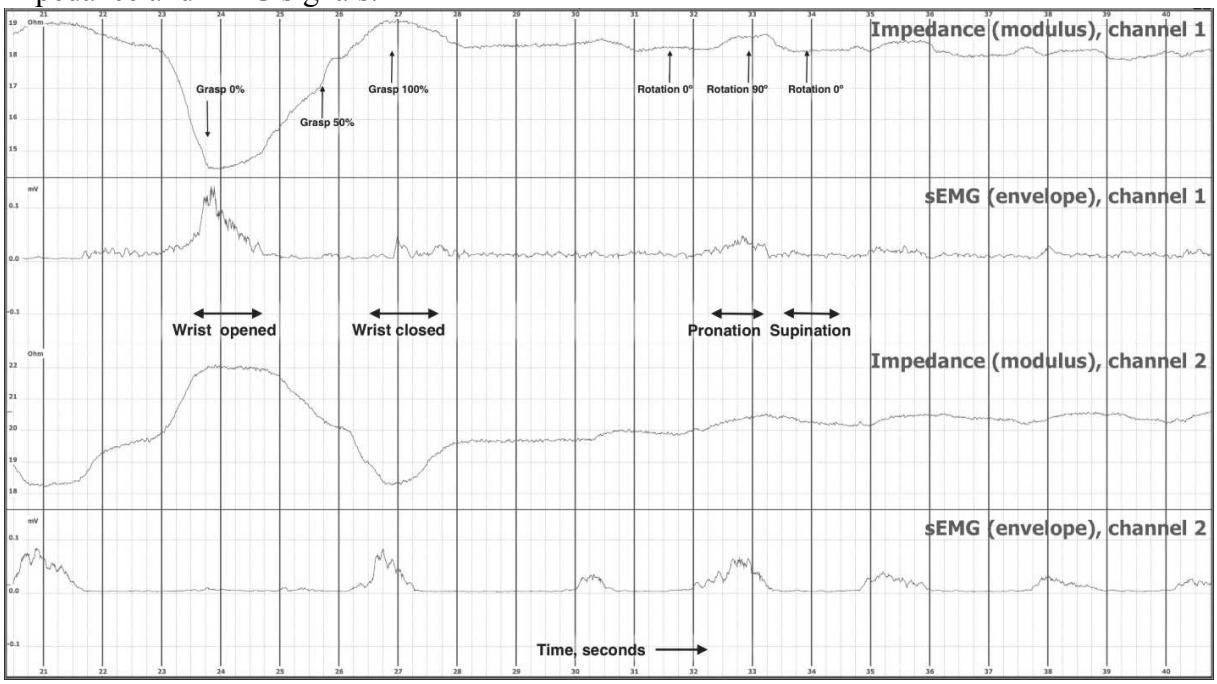

Fig. 2 Typical impedance and EMG signals during grasp and rotation movements

The typical impedance and EMG signals are shown in figure 2.

Conclusion

The calibration is needed to get an absolute wrist grasp value or rotation angle for each individual. Time delay for signal processing does not exceed 120 ms, which makes the interface anthropomorphic. Anthropomorphic control significantly increases prosthesis usability and reduces required time to learn for disabled person.

The use of an impedance signal is the perspective direction in a task of an active artificial limb control. In further work it is necessary to investigate possibility of distinction of such signals as grasp /opening of a hand, the pronation/supination, the flection/extension and determine parameters of these movements, and also to study the joint analysis of impedance and EMG signals for decrease an error to movements classification.

References

[1] Adrian M.J., Cooper J.M., Biomechanics of Human Movement, 2nd Ed., McGraw-Hill, Boston, 1994, pp. 43-48.

[2] Koike Y., Kawato M., "Human interface using surface EMG signals", Trans. Inst. Electr., Infor. and Comm.. vol. 2, pp. 363-370, 1996.

[3] Nakamura, T., Kusuhara, T., and Yamamoto, Y., "Impedance characteristics and data processing for analysis of human movement", Proc. XII Int. Conf. Elect. Bio-Imp., Oslo, Norway, 2001,pp. 641-644.

[4] S. Grimnes and Ø. G. Martinsen, Bioimpedance and Bioelectricity Basics. San Diego, CA: Academic Press, 2000.

Accelerometric system of goniometric control of the locomotors apparatus of the human

A.V. Grecheneva[1]
1. Belgorod National Research University, Belgorod, Russia

In modern medical systems of goniometric control need to ensure measurement accuracy within 1.8%. To improve the accuracy, efficiency and reliability of goniometric measurements need to replace the traditional goniometers on the electronic inertial systems, based on accelerometers [1].

The aim is to create a new approach to achieving high precision goniometric measurements, through the development of biomechanical control system of locomotors apparatus of man, based on the accelerometer sensor.

The basic idea of the accelerometric measurement method of articular displacement is to expand the operations of vector algebra, used to solve the problem of calculating the parameters of angular limb movements, by adding in an algebraic set of trigonometric operations calculate the angular variables, obtained by converting the acceleration values for each of the axes of the two accelerometers [2]. The vector of complete acceleration $\vec{a}$ is determined by measuring the four acceleration values in two coordinate systems: a_{x1}, a_{y1}, a_{x2}, a_{y2}, obtained with the help of digital accelerometers fixed on the neighboring links diagnosable joint (Figure 1).

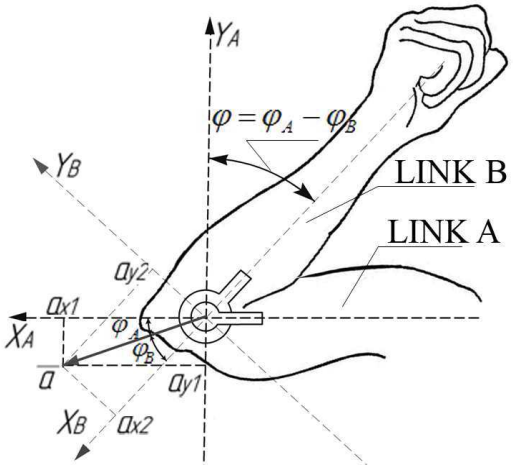

Fig. 1 The accelerometric method of measuring the angle of rotation

As a result of measurement of acceleration values for each of the accelerometer in the two coordinate systems, are obtained at the output of the four signals proportional to the acceleration $\vec{a}$ of the general point O of the kinematic pair:

$$tg\varphi = \frac{a_{y1}a_{x2}/k_{y1}k_{x2} - a_{x2}a_{x1}/k_{x2}k_{x1}}{a_{x1}a_{x2}/k_{x1}k_{x2} - a_{y1}a_{y2}/k_{y1}k_{y2}}. \quad (2)$$

In case the technical implementation of this approach, there are difficulties of its practical application, due to the need for eviction of the arc tangent in the transformation process, obtained from the accelerometers of acceleration value, in the angular values. The solution to this problem is to use phase metrical method.

Figure 2 is a block diagram of the construction principle of the accelerometric goniometer, which is a part of the measuring path goniometric control system.

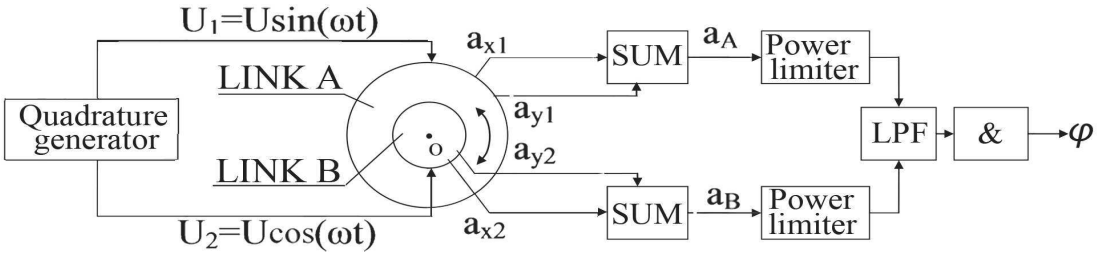

Fig. 2 Phase metric method of measuring the angle of rotation.

The operating principle of this method is based on the direct conversion of signals from two-component accelerometers in phase sine wave. This is accomplished by multiplying of the accelerometers signal on the signal of AC source $U_1 = U \cdot \sin \omega t$ и $U_2 = U \cdot \cos \omega t$ [3, 4, 5]. When adding the signals in the adders and phase detection for link A and link B respectively we get:

$$U_A = Uk_{x1}(1+\Delta k_1)a\cos(\omega t + \varphi_A + \varphi_{K1}), \quad U_B = Uk_{x2}(1+\Delta k_2)a\cos(\omega t + \varphi_B + \varphi_{K2}). \tag{3}$$

where U, ω - the amplitude and frequency of the quadrature signal generator; φ_{K1} and φ_{K2} the phase mismatch of the measurement branches.

Since the serial connection circuit of accelerometers is selected, the transform coefficients are, respectively: $k_{x1}=k_{y1}$ and $k_{x2}=k_{y2}$, hence the phase error measuring branches $\varphi_{K1}=\varphi_{K2}=0$. The output of main phase detector signal is generated proportional to the angle φ of bio kinematic pairs without affecting instability coefficients transmitter branches.

In the digital accelerometric goniometer phase measurement is based on the measurement of time intervals (Figure 3).

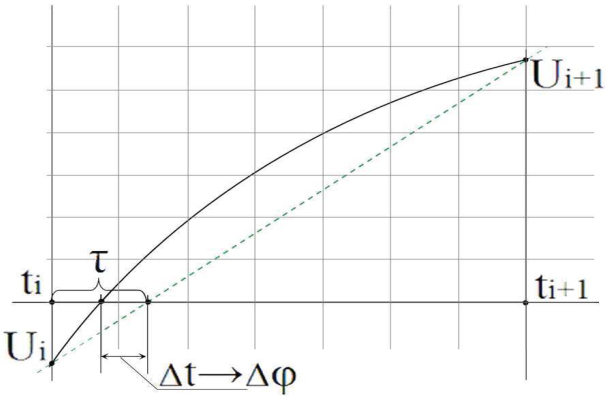

Fig. 3 The digital signal of accelerometric goniometer.

In traditional algorithms between samples $U_i(t_i)$ and $U_{i+1}(t_{i+1})$ used linear approximation $U(t) = kt + b$ to describe the actual process in the interval of adjacent samples:

$$U(t) = U_m \cdot \sin(\omega t + \varphi), \tag{4}$$

where $\omega = 2\pi f$ - reference oscillator frequency; φ - measured phase.

In this case the angle of rotation bio kinematic couples in the accelerometric goniometer is determined by the difference between the measured and the reference signal phases U^0:

$$\alpha = 2\pi \cdot m\left(\frac{U_i}{U_{i+1} - U_i} - \frac{U^0{}_i}{U^0{}_{i+1} - U^0{}_i}\right), \quad (5)$$

where m - the ratio of the oscillator frequency and the sampling frequency, $m = \frac{F}{f_d}$.

In developed accelerometric system of goniometer control can be distinguished the two functional parts: the measuring system tract; the unit of data collection and control (Figure 4).

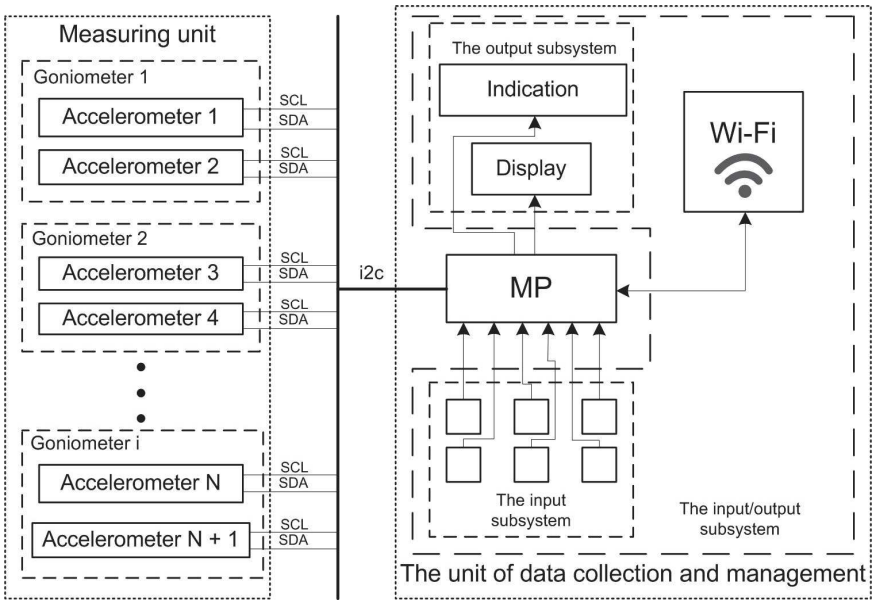

Fig. 4 Block diagram of the accelerometric system of goniometric control.

The measuring unit includes a set of goniometers, connected in series. The design of each of the goniometer consists of two miniature accelerometers. Each accelerometer is mounted on the skin of a patient in the diagnosable joint (joints) by double-sided adhesive tape based on silicone.

The unit of data collection and control is a printed circuit board, placed in a plastic case. To him using a wired i2c network connected sensors included in the measuring unit. Also, it is equipped with a USB connector and Wi-Fi module for performing data transfer on the PC or server. This block carries out processing, and providing information in digital form in real time.

Scalable control unit allows you to connect several different functionally systems in block actuators. Depending on the configuration and software such systems can be: the executive lever-restrictive mechanisms allowing limited movement of limbs; the compression system, to relieve fatigue after exercise; the mechanical support system to help reduce the load on the complex musculoskeletal system of man and others.

Thus, the practical implementation of the system goniometric control based on the accelerometer, presented in this article, allow:

- diagnose all types of joints (knee, elbow, ankle, intervertebral, the joints between the phalanges, hip and shoulder, etc.) in any plane of motion (frontal, sagittal and horizontal), thanks to the universality and adaptability of the system design;
- increase the accuracy and sensitivity measurements and stability of the system to the operating conditions;

- minimize the cost of the system through the use of new techniques for constructing goniometric systems based on MEMS accelerometers.

This work was supported by grant RFBR 16-38-00704 mol_a

References

[1] Erokhin AN "Functional state of orthopedic trauma patients: diagnostics and correction in the process of treatment and rehabilitation" // The genius of orthopedics. 2008. №4.
[2] Grecheneva AV Kuzichkin OR, Dorofeev NV, IS Konstantinov The use of the accelerometer in the goniometric measurement system of scientific and technical magazine "Information systems and technologies", ISSN 2072-8964, № 4 (90) 2015 July-August, pp. 5-10.
[3] Dorofeev NV, OR Kuzichkin Problems multiplicative instability of differential transmitters of the electromagnetic field. \ Questions electronics. 2010. Vol.1. №1. pp. 117-122.
[4] Kuzichkin OR, NV Dorofeev Eliminating multiplicative instability of differential transducers parameters. \ Methods and communication devices and information processing, Vol. 10, M .: Radio Engineering, 2008 pp. 79-82.
[5] No. 64342 (RF) G01V7 / 14. Device forming a differential transducer / output OR Kuzichkin, NV Dorofeev (RF), appl. 20.12.06 .; publ. 27.03.2007.

Osteoblasts growth study on the surface of nanocomposite coating for artificial knee ligament

N.N. Zhurbina[1], U.E. Kurilova[1], A.Yu. Gerasimenko[1], I.A.Suetina[2], M.V. Mezentseva[2], E.M. Eganova[3]

[1]National Research University of electronic technology, 124498, Moscow, Russia
[2]Ivanovsky Institute of Virology, 123098, Moscow, Russia
[3]Institute of Nanotechnology of Microelectronics of the Russian Academy of Sciences, 115487, Moscow, Russia

Nowadays one of the main problems in orthopedics is damage of knee ligaments. The best materials to replace damaged ligaments are autografts. However, their use is limited by number of contraindications, as well as their possible physiological remodeling in a long-term period. Available artificial implants of knee ligament in their turn have considerable structural and biological shortcomings. To improve the properties of synthetic ligaments we proposed to use tissue engineering techniques. These methods allow to partially or fully restore the physical, mechanical and biological function of damaged or lost organs by stimulating the regeneration of three-dimensional tissue structure [1]. Tissue engineering concept is based on the creation of artificial tissue-engineering structures (scaffolds) providing cell proliferation support and biological tissues growth [2]. It was found that carbon nanotubes (CNTs) dispersed in an artificial biological matrix are an promising material for tissue-engineering scaffolds creation [3-5]. We have been developing the knee ligament implant with a nanocomposite coating, which is a tissue-engineering scaffold based on CNTs. This work aims to study the coating biocompatibility with bone cells.

As a basis for creating the knee ligament implant we used synthetic fiber material in form of a seamless tube or strip made of polyethylene terephthalate fibers (PET). The PET has such advantages as mechanical and chemical properties to use as a knee ligament implant. However, an implant structure is not promote attachment and growth of biological cells, which leads to long-term post-operative recovery.

To improve the structural and biological characteristics of ligament implant we offered laser method of tissue-engineering construction forming on implants' surface. The construction or scaffold is based on carbon nanotubes biocompatible nanomaterials. By power ultrasonic treatment CNTs are uniformly distributed in the volume of a biocompatible matrix

– bovine serum albumin (BSA), thereby a porous, strong and lightweight material is obtained. We used in study a single-walled (SWCNTs) and multi-walled (MWCNT) nanotubes, and their mass fraction was from 0.1 to 1 g/l. In the first stage of nanomaterial manufacturing, CNTs were mixed with disstilled water with a magnetic stirrer and ultrasonic homogenizer. The use of these devices has allowed to obtain a homogeneous CNT water dispersion without large nanotubes agglomerates, which presence can lead to poor coating properties. Then powder BSA, acting as a biological matrix, was added to the dispersion. The mixture was stirred using a magnetic stirrer and ultrasonic bath.

For the formation of tissue-engineering scaffold the aqueous dispersion of CNTs and BSA was applied to the synthetic ligaments surface by ultrasonic method, then the sample was placed on the installation for laser processing. We used the continuous infrared diode laser with a wavelength of 810 nm and an output power from 3 to 5 Wt for samples irradiation. Ultrasonic method of nanocarbon dispersion applying provides uniform coating of implant surface. The aqueous component of CNTs and BSA dispersion had evaporated during laser irradiation, and under the influence of an electric field of directed coherent laser radiation, self-organization of nanotubes was carried out. Thus, the carbon nanotube scaffold was formed on the surface of artificial knee ligament implant.

The method of optical microscopy was used to study the proliferative activity of bone cells – osteoblasts, incubated on the surface of the nanocarbon scaffold samples. Experimental samples were placed in a 24-well plate and were sterilized under UV light for 1 hour. Then, 2 ml of cell suspension were added to each well. Osteoblast suspension was obtained by differentiation of mesenchymal stem cells (MSC) in the culture DMEM medium (modified Dulbecco Eagle) supplemented with 10% fetal bovine serum. The plate was placed in the CO^2 atmosphere of incubator at a temperature of 37 ° C. After a certain time, the samples were removed from the incubator, and cells fixation on the samples surface was carried out with glutaraldehyde solution for microscopic research.

Images obtained with an optical microscope, allow to study the proliferative activity of osteoblasts on the surface of the experimental samples (figure 1).

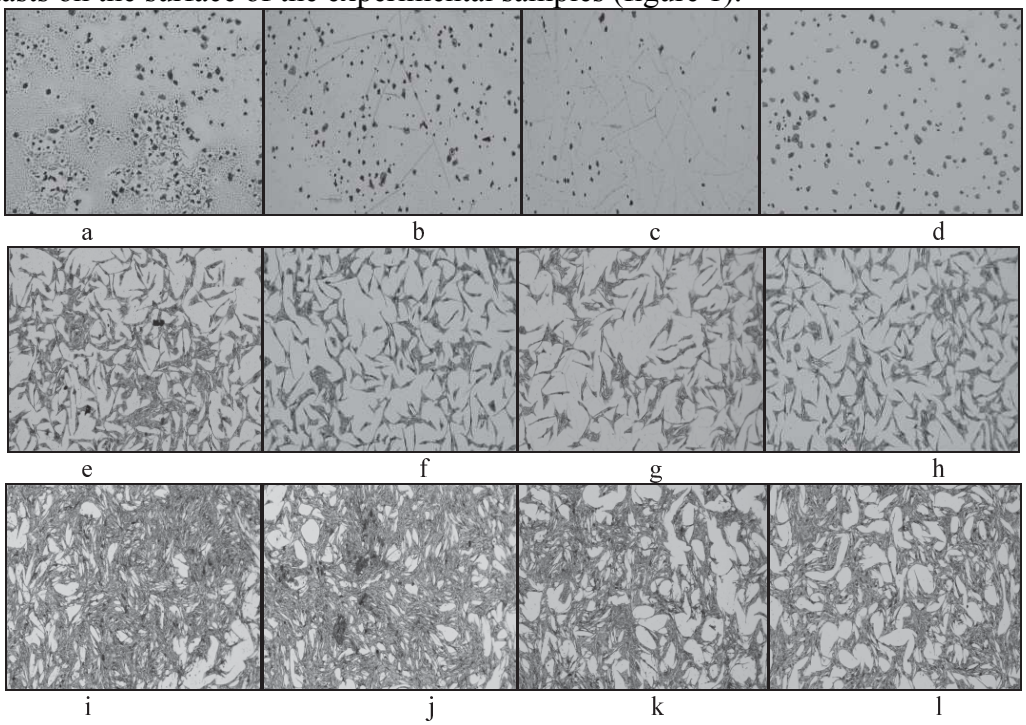

Fig.1 Osteoblasts microscopic images on the surface of MWCNTs (a,e,i), SWCNTs (b,f,j), BSA (c,g,k) and control (d,h,l) samples after 3 (a-d), 24 (e-h) and 72 (i-l) hours of incubation

Results showed that after 3 hours of incubation, almost all cells retain a rounded shape, which means that their growth has not started yet. On the BSA-based sample we observed significantly fewer cells than on the other samples. The most cells are uniformly distributed over the control sample, which may be explained by the absence of cracks and pores on this sample. After 24 hours of incubation, there is cell spreading on the sample surface, the cells are stretched, getting an oblong shape. In the center of the cell the nucleus can be seen. The greatest number of cells observed on a sample of three-dimensional structure based on MWCNTs, and the lowest – on the sample based on BSA.

After 72 hours of incubation, the cells filled large samples surface, their size and number increased. However, the distribution of cells on the samples surface is not uniform, which may be caused by cracks, pores and other irregularities of the samples. The number of cells in experimental samples in each time period is comparable to control and in some areas even exceeds it.

The atomic force microscopic method was used to detailed study of cells structure on the samples surface. In comparison with control sample, cells on the nanocomposite coatings surface have normal structure without any negative changes (figure 2).

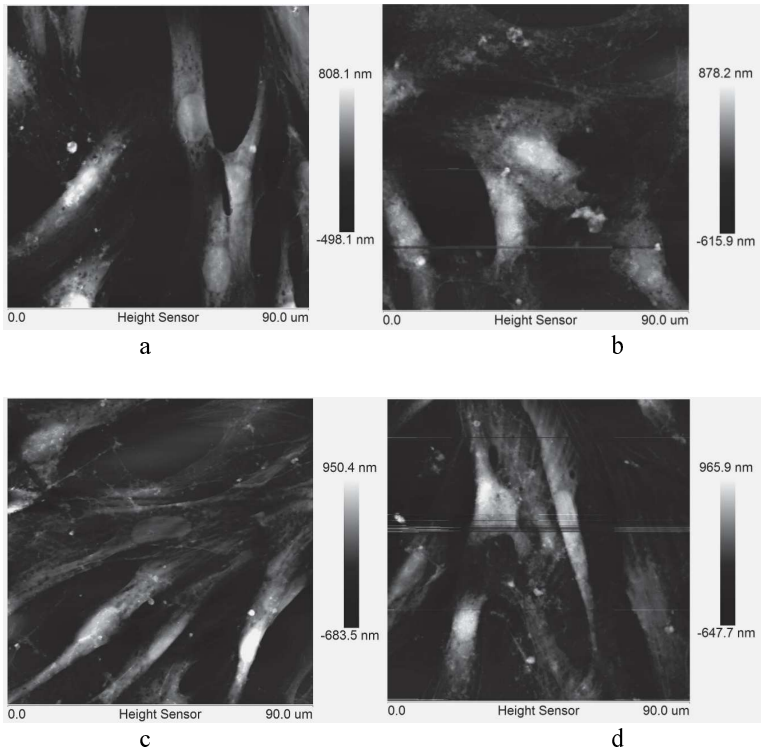

Fig.2 AFM images of osteoblasts on the surface of SWCNT-based coating (a) in comparison with control sample (b) after 48 h of incubation, and on the surface of MWCNT-based coating (c) in comparison with control sample (d) after 72 h of incubation

Thus, we have been studied osteoblasts proliferative activity on the surface of nanocarbon coatings for artificial knee ligaments, which showed absence of effect, inhibited the growth of bone cells on the experimental samples surface. Cells proliferative activity and their structure on all samples was similar to control samples, and in the later stages of incubation cell number was greater than in controls on some nanocomposite coatings areas. The result of the experiment can talk about advantages of nano-carbon coating use for knee ligament implants to improve the biological cells growth.

This work was provided by the Ministry of Education and Science of the Russian Federation (Agreement 14.575.21.0089, RFMEFI57514X0089).

References

[1] D.J. Mooney, A.G. Mikos, "Growing new organs", Scientific American. **280**, 38-43 (1999).
[2] M.C. Peters, D.J. Mooney, "Synthetic extracellular matrices for cell transplantation", Materials science forum. **250**, 43-52 (1997).
[3] E. Hirata et al., "Development of a 3D collagen scaffold coated with multiwalled carbon nanotubes", Journal of Biomedical Materials Research Part B: Applied Biomaterials. **90(2)**, 629-634 (2009).
[4] A. Martino, M. Sittinger, M.V. Risbud, "Chitosan: a versatile biopolymer for orthopaedic tissue-engineering", Biomaterials. **26(30)**, 5983-5990 (2005).
[5] A. Abattategi, M.C. Gutierrez, C. Moreno-Vicente, M.J. Hortiguela, V. Ramos, J.L. Lopes-Lacomba, M.L. Ferrer, F. Monte, "Multiwall carbon nanotube scaffolds for tissue engineering purposes", Biomaterials. **29**, 94-102 (2008).

Study of biomechanical parameters of vascular prostheses using a thermostatic bath

***G.V. Savrasov*[1], *N.V. Belikov*[1], *I.V. Khaydukova*[1]**
1. BMSTU,str. Baumanskaya 2nd, 5, 105005 Moscow, Russia

I. Introduction

In the development and in vitro mechanical tests of vascular prostheses the important aspect is the prediction of elastic and viscoelastic properties of their behaviour in vivo.

Strength parameters of vascular prostheses vary non-linearly and are highly dependent on the applied load [1]. Different methods of measuring the Young's modulus after cyclic preload of samples was observed in a large number of papers on the tensile tests of vessels, but none of them had studied the effect of the presence of liquid medium and the matching of temperature conditions on the results [2,3,4]. Papers on the analysis of the effect of temperature conditions, however, should be noted [5,6], but there was no attempt to standardize the methodology of biomechanical tests and further advices on testing conditions were not formulated.

In particular, measurement of the elastic properties should be carried out without viscoelastic properties, which is achieved by a series of preliminary load tests. During these tests, elastic hysteresis is registered to determine when the viscoelastic properties disappear.

Thus, when comparing the elastic-strength characteristics of the prosthesis, statistically significant difference was marked between the values measured in normal conditions and in conditions matching the internal environment of the body [1]. The same trend was found in the blood vessels when tested in a thermostatic chamber [7]. Thus, the assumption was made on the influence of the test environment on measuring the magnitude of the elastic hysteresis.

Elastic hysteresis is defined as follows: $\Psi = \frac{\Delta U}{U}$, where U is the energy of elastic deformation.

During normal behavior of the vascular prosthesis material stresses are considerably below the elastic limit. Thus, it is useful to measure the elastic hysteresis.

This paper studies the influence of temperature and environment on hysteresis of vascular prostheses.

II. Materials and methods

In the study of the hysteresis of vascular prostheses tests were conducted on a tensile testing machine Instron 3365. The preparation of samples was performed as previously

described [1]. Tests were conducted in BioPuls 3130-100 Instron thermostatic bath (Fig. 1, left). Saline was used as the liquid medium in the bath (0.9% NaCl isotonic solution) at a temperature of 20 and 37 ± 1°C.

Samples of prostheses in form of double-sided blades, fixed in the jaws, were stretched up to the elongation threshold of 3 mm, in which the strain reached 25%. This value corresponds to the assumed linear deformation area recorded in the study of elastic properties of a PTFE prosthesis [1].

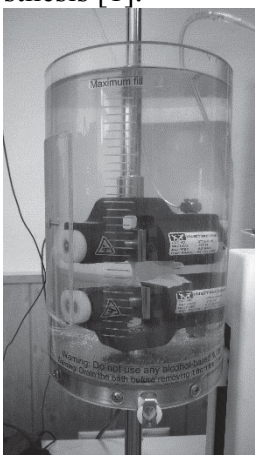

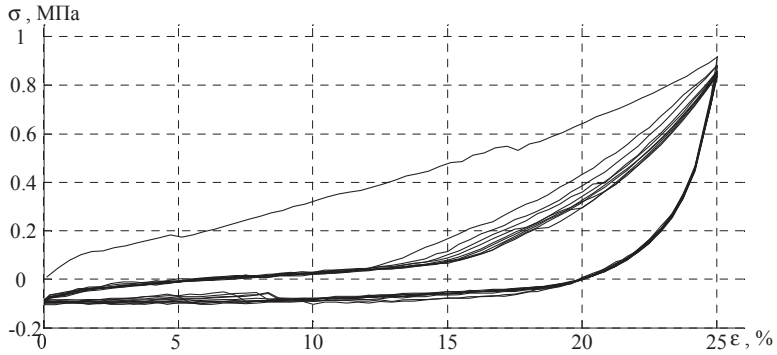

Fig. 1 Testing machine Instron 3365 with thermostatic bath (left), Example of elastic hysteresis of prostheses (right).

Then 10 cycles of load were performed. During the test force and elongation were recorded.

Data processing was performed in Matlab software. During the processing the stress-strain relation of the sample was examined.

III. Results

During the analysis of the stress-strain relation a sharp change in the slope of the hysteresis curve in the 2nd and subsequent cycles was found, which may indicate a transition in the plastic deformation zone. (Fig. 1, right)

Elastic hysteresis values were divided into groups according to the type of vessel, the temperature of the test and the number of cycle.

Compliance of mechanical characteristics with the normal distribution within each group, was verified by the Shapiro-Wilk criterion with significance level $\alpha = 0{,}05$. In each group, the sample did not fit a normal distribution.

Groups that differed only by the temperature of the test were compared in pairs according to the Mann Whitney criterion. Statistically significant difference was found between each group of the elastic hysteresis values in each type of prosthesis in each cycle with a significance level of 0.05.

Graphs of elastic hysteresis values of thin- and thick-walled prostheses at different temperatures at test to 25% strain are presented in Fig. 2 and 3

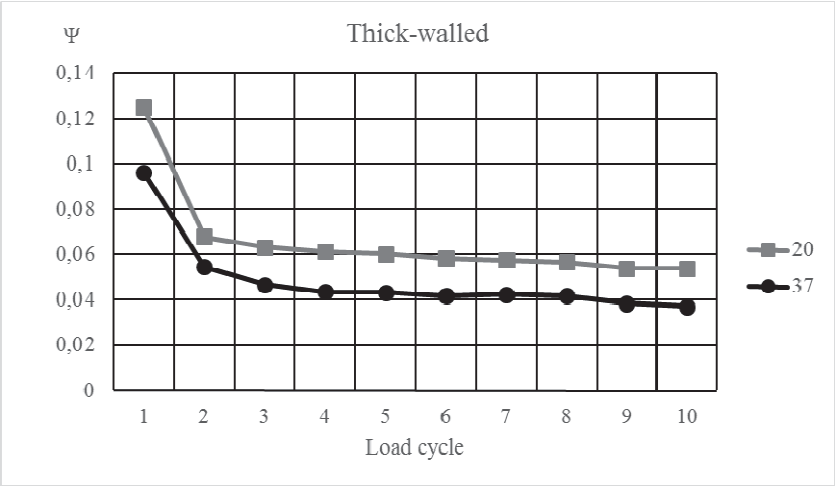

Fig. 2 Elastic hysteresis values of thick-walled prostheses at different temperatures at 25% strain

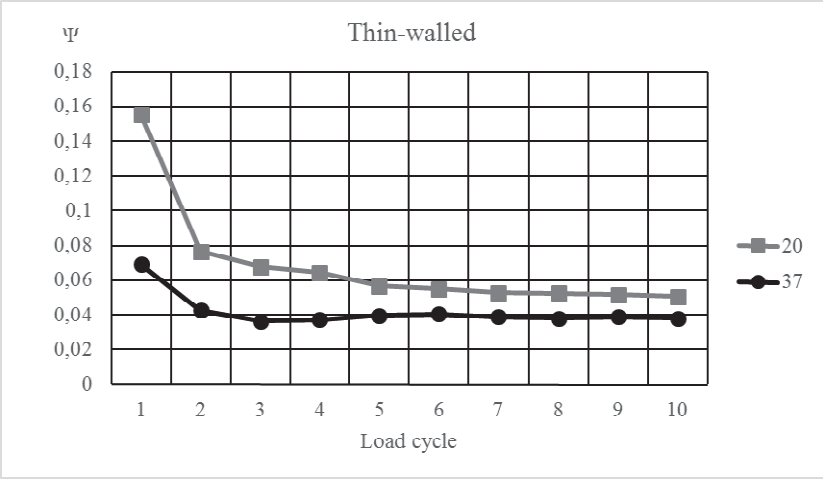

Fig. 3 Elastic hysteresis values of thin-walled prostheses at different temperatures at 25% strain

IV. Conclusions

In this paper we investigated the dependence of the elastic hysteresis of vascular prostheses on the temperature, which can fully reflect the behaviour of the material in the body.

There were statistically significant differences between the elastic hysteresis values in each test cycle, indicating the substantial dependence of the parameter characterizing the viscoelastic properties of the prosthesis on the temperature. Thus, taking into account previous results, which show the temperature dependence of other biomechanical prosthesis characteristics [1] the need for biomechanical tests in the environment that is maximally close to human body is essential.

Since the graphs showed possible transition to the plastic deformation zone, further studies of the prosthesis behaviour in the body include lower loads that will confirm the absence of transition to this area. However, we should ensure that the maximum stress in the sample is not lower than the stress occurring in the prosthesis at the maximum blood pressure.

References

[1] G.V. Savrasov, N.V. Belikov, I.V. Khaydukova. "Comparative analysis of the characteristics of vascular prostheses in different temperature testing regimes". Scientific-technical conference "Medical-technical

technology guard health". Crimea. – Research Institute of Radio Electronics and Laser Technology of BMSTU, 132-137 (2015)
[2] D. Tremblay, T. Zigras, R.A. Cartier et al. "Comparison of Mechanical Properties of Materials Used in Aortic Arch Reconstruction". Ann Thorac Surg. **88(5)**, 1484-91 (2009).
[3] D.P. Sokolis. "Passive mechanical properties and constitutive modelling of blood vessels in relation to microstructure". Med Biol Eng Comput. **46(12),** 1187-99 (2008)
[4] D.P. Sokolis, H Boudoulas, P.E. Karayannacos. "Assessment of the aortic stress–strain relation in uniaxial tension". J Biomech. **35(9)**, 1213-23 (2002)
[5] R.J. Okamoto, J.E. Wagenseil, W.R. DeLong et al. "Mechanical Properties of Dilated Human Ascending Aorta". Ann Biomed Eng. **30(5)**, 624-35 (2002)
[6] G.V. Guinea, J.M. Atienza, M. Elices, et al. "Thermomechanical behavior of human carotid arteries in the passive state". AJP-Heart Circ Physiol. **288**, H2940–H2945 (2005)
[7] G.V. Savrasov, N.V. Belikov, I.V. Khaydukova, A.P. Bashlay. "Determination of biomechanical characteristics of blood vessels using a thermostatic bath" Proceedings of the 11-th German-Russian-Conference on Biomedical Engineering., Aachen, Germany (2015)

The automated system of biomechanics control of a human spine

***N.V. Dorofeev*[1], *A.V. Grecheneva*[2], *O.R. Kuzichkin*[3]**

1. *Murom Institute (branch) Federal state budgetary Educational Institution of Higher Professional Education «Vladimir State University named after Alexader Grigoryevich and* Nickolay Grigoryevich Stoletovs»,*Murom, Russia*
2. Belgorod National Research University, Belgorod, Russia
3. Belgorod National Research University, Belgorod, Russia

In the existing medical rehabilitation methods in pathological changes in the functional state of the spine key reason for the purpose of rehabilitation procedures is the presence of pain syndrome. Pain is the basis for hospitalization, medical appointments actions aimed at rehabilitation, and often for the adoption of expert solutions (diagnosis). Therefore, indications for rehabilitation assigned to patients that have a partial violation or substantial loss of functionality, that is, with the spine pathology with pain syndrome and neurological manifestations. In practice, this means carrying out rehabilitation effects only in patients in acute and recovery.

Diseases of the spine accompanied by impaired mobility of vertebral joints. For example, in studies carried out on soldiers of the Air Force of the Ministry of Defense of Russia, which characterized by a high degree of physical fitness and health requirements of the relevant high level was detected in 56% cases the presence of disorders of the spine functions. At the same violation of the biomechanics of the spine revealed in 61.3 ± 3.5% of the number of all the patients, and in 19% of violations was in the nature from moderate to severe degree.

For this reason, an important part of solving the problem of diagnosis of spinal diseases and their treatment is the development of an automated method goniometric spine control, which has high accuracy, sensitivity, which is a simple and accessible method for assessing the functionality of the spinal column.

As a method of goniometry in the automated control system it is proposed to use accelerometer method of bending angle measurement for assessing spine configuration and range of motion in the sagittal, frontal and horizontal planes [1]. This instrumental method to the research of the curvature and mobility of the spine is built on the principle of measuring the full acceleration vector of two accelerometers attached to the vertebrae controlled spine segments. This goniometric angle $\alpha = \alpha_1 - \alpha_2$ on the basis of relations between the components

of the vector of the linear acceleration of the spine movement and displacement of the accelerometers can be determined by formulas:

$$\alpha = \sin\left[\frac{\left(\frac{a_{x2}a_{y1}}{K_{x2}K_{y1}}\right)-\left(\frac{a_{y2}a_{x1}}{K_{y2}K_{x1}}\right)}{\left(\frac{a_{x1}}{K_{x1}}\right)^2+\left(\frac{a_{y1}}{K_{y1}}\right)^2}\right],\ \alpha = \cos\left[\frac{\left(\frac{a_{x2}a_{x1}}{K_{x2}K_{x1}}\right)+\left(\frac{a_{y2}a_{y1}}{K_{y2}K_{y1}}\right)}{\left(\frac{a_{x1}}{K_{x1}}\right)^2+\left(\frac{a_{y1}}{K_{y1}}\right)^2}\right], \quad (1)$$

where a_{x1}, a_{y1}, a_{x2}, a_{y2} - values of acceleration of the accelerometer 1-st accelerometer 2-dimensional coordinate system, $K_{x1}, K_{y1}, K_{x2}, K_{y2}$ - the transform coefficients of corresponding accelerometers.

In the standard goniometry of the spine are reference points corresponding to the ends of the spinouts processes of the S4, L4, C7 and Th7 segments of the vertebrae.

This method provides a differentiated picture of movements in different parts of the spine. At the same time due to the small size and high precision of accelerometer sensor, significantly increases system flexibility and reliability of the results (for additional digital processing of recorded signals). In addition, this method is passive (does not use additional exposure, such as in ultrasound or X-ray method) and has no negative effects on humans. And because of the compactness of the accelerometer have the ability to easily connect the accelerometer module to the other modules of the system.

Existing systems control of biomechanics spine only measure kinematic parameters of the skeletal system, without taking into account the patient's neurophysiological parameters [2]. So process of diagnosis and rehabilitation is slower due to the absence of biofeedback. Consequently, when the organization of goniometric spine control, is of great importance the study of the central control mechanisms targeted physical activity [3,4]. This aspect is taken into account in the design of automated goniometric control system (Figure 1).

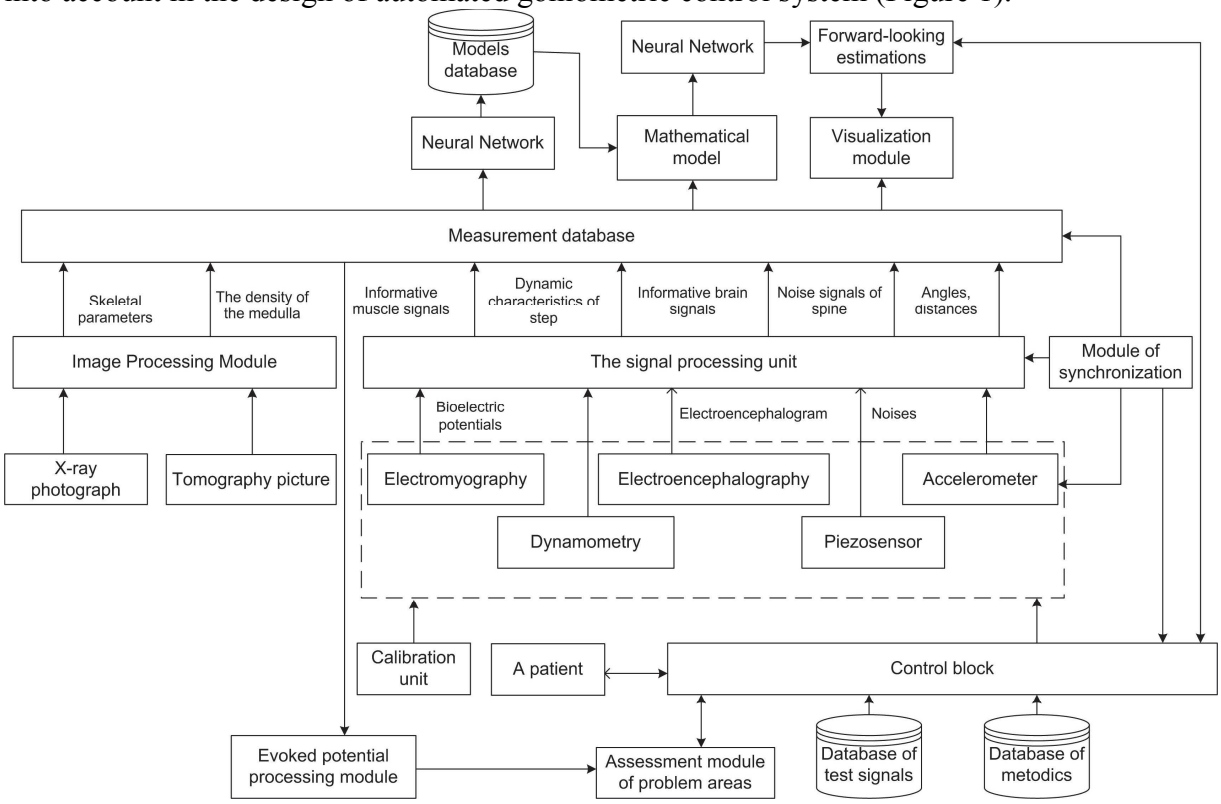

Fig. 1 A generalized structural scheme of the system of spine diagnostics and rehabilitation.

Information model, after the processing of the neural network will be entered in the database of models, thus, will be formed a statistics and selected the optimal operating parameters of the system rehabilitation for patients with a variety of neurophysiological features. According to the physiological parameters model of the patient, will be determined by the maximum pain thresholds and minimum thresholds of sensitivity upon the rehabilitation of the musculoskeletal system. With the help of neural network algorithms and algorithms for systems of decision support (DSS) based on database of the measurements, the database of the evoked potentials and the diseases database, determined an approximate diagnosis of the patient.

The accelerometer measurement method as a basis for building automated goniometric spine control system is used to optimize medical biomechanical research. Also, to achieve the optimum operation of the system is possible by forming a recruitment goniometric criteria. On this basis, it is necessary to define the criteria of acceptable values that characterize established statistical range of physiological fluctuations of parameters bio kinematic rules and degrees of functional disorders of the spine (Table 1).

Table. 1 Range of physiological fluctuations standards and degrees of spinal disorders in goniometric studies.

The position of the spine	Angle (º)	Normal	The degree of functional disorders					
			Slight		Moderate		Pronounced	
			Less	More	Less	Less	Less	More
Free vertical position	α	7-13	5-6	14-16	3-4	17-18	≤2	≥19
	β	10-15	8-9	16-18	6-7	19-20	≤5	≥21
	γ	9-14	7-8	15-17	5-6	18-19	≤4	≥20
Maximum flexion (degrees)	α	60-80	51-59	-	41-50	-	≤40	-
	β	90-115	81-89		61-68		≤60	
	γ	130-155	121-129		111-120		≤110	
Maximum extension (degrees)	α	0-3	4-6	-	7-8	-	≥9	-
	β	35-52	25-34		17-24		≤16	
	γ	36-50	26-35		16-25		≤15	
The slopes of the sides (degrees)	bs	30-40	20-29	-	10-19	-	≤9	-
	bd	30-40	20-29		10-19		≤9	

where α - angle of inclination of the sacrum, β - angle of inclination of the lower thoracic-lumbar department, γ - angles of thoracic spine in the free upright posture; bd and bs - angles to the vertical in the lower thoracic-lumbar and thoracic parts of the right and left respectively.

These criteria will help to determine the optimal values of the technical parameters of the accelerometric goniometer system: sampling frequency accelerometer signal converters required sensitivity of the sensor, and others. Also, it will improve the adaptability of the mathematical models underlying the accelerometer, goniometer system, and increase the reliability of the diagnosis.

Practical implementation of the described in this article automated biometric system of a human spine based on the accelerometer control method, will allow:

- Without the use of additional effects on the body to diagnose and maintain a constant dynamic movement control segments of the spine and musculoskeletal system as a whole in real time;
- Increase the effectiveness of diagnostics and rehabilitation of the spine;
- Reduce the risk of traumatic and as a consequence the time of rehabilitation, due to methodology for assessing and monitoring the permissible degree of bending of the spine, vertebral abnormalities in the rehabilitation process and under the influence of physical activity;
- Timely adjustments to the load overload and exclude the risks of traumatic, due to optimization of the rehabilitation process on the basis of the patient's physical abilities and data of control.

This work was supported by grant RFBR 16-08-00992 A

References

[1] Tsaplev A.V., Kuzichkin O.R., Dorofeev N.V. Accelerometer method of measuring the angle of rotation of the kinematic mechanisms of nodes. // Applied Mechanics and Materials Vol. 770 (2 015) pp 592-597.

[2] Vitenzon AS, KA Petrushanskaya The concept of the use of artificial correction movements in orthopedics, traumatology and prosthetics // Journal of Traumatology and Orthopedics. Priorov. - 2003. - № 4.

[3] Hecht BM, Kasatkina LF, Samoylov MI et al. Electromyography in the diagnosis of neuromuscular diseases. - Taganrog: TSURE, 1997. - 370

[4] Drew T, Kalaska J, Krouchev N. / Muscle synergies during locomotion in the cat: a model for motor cortex control // J Physiol. - 2008.- Vol. 586, N5. - P. 1239-1245.

Application of microfocus X-ray analysis for an assessment of the position of an electrode in the cochlear implantation

A. Yu. Gryaznov[1], N.E. Staroverov[1], Diab Khasan Mokhamad Ali[2]
V.N. Sokolova[2] , A. Y. Vasilev[3], N. N. Potrakhov[1]

1 – Saint-Petersburg State Electrotechnical University «LETI», 5 Professora Popova st., Saint-Petersburg, Russia

2 – FSBI «Scientific clinical Center of Otorhinolaryngology», korp. 2, 30 Volokolamskoe shosse, Moscow, Russia.

3 – Moscow State Medical University of Medicine and Dentistry named after A. I. Evdokimov, Ministry of Healthcare of Russia,
9a Vucheticha ul., Moscow, Russia.

Nowadays intraoperative control of position of an electrode during cochlear implantation using X-ray inspection has no systematic approach. Using of various methods of radiation diagnostics is hard because of technical difficulties. In particular, using the CT for position monitoring of an electrode requires relocation of the patient to the tomograph that extends time of the operation and causes receiving higher radiation load by the patient.

As the object of the research (electrode) can't be located closely to the detector, when using an X-ray source with an extensive focal spot only blur images (fig. 1) can be received.

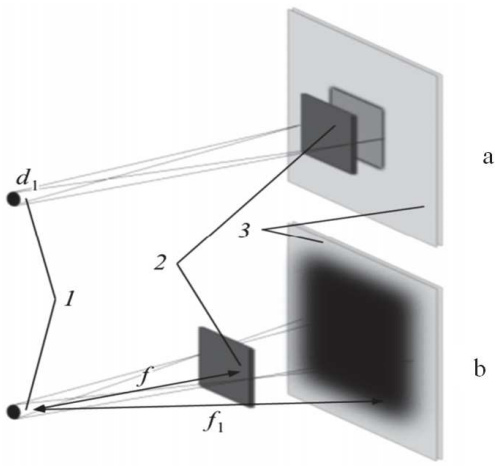

Fig. 1 X-ray optical scheme of method with an X-ray source with extended focal spot: a - contactly, b – with enlarged image; 1- X-ray source, 2 - object, 3 - plane of the receiver.

The usage of the microfocal X-ray source that is giving the chance of receiving the sharp enlarged pictures, allows to solve the arising problem. The usage of the digital image receiver decreases radiation dose of the patient. [1,2]

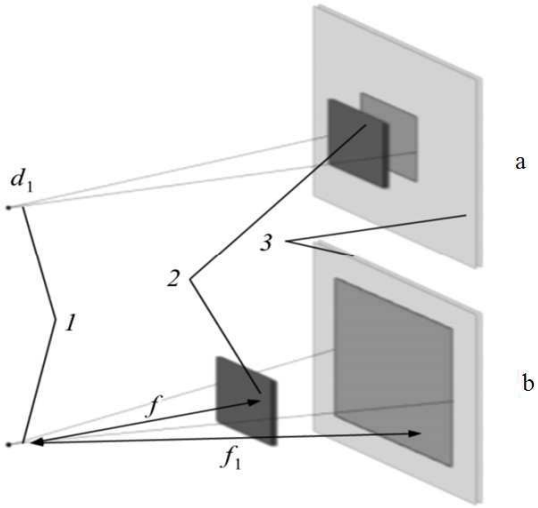

Fig. 2 X-ray optical scheme of shooting with an X-ray source with dot focal spot: a - contactly, b – with enlarged image; 1- X-ray source, 2 - object, 3 - plane of the receiver.

The purposes of this research were the selection of projection's options and determination of technical requirements of shooting with the microfocal X-ray device RAP100 in case of an assessment of position of the cochlear implant's electrode.

For the experiment test-objects were prepared, based on the fragment of a human skull and a pig's head with the entered electrodes of the cochlear implant. In the process, used electrodes Digisonic SP manufactured by Neurelek (France). The size of the electrodes' set: length – 26 mm, diameter in the base and in an extreme point – 1,07 mm and 0,5 mm, distance between electrodes – 0,7 mm.

The device RAP100 with a diameter of the focal spot less than 50 microns was the X-ray source. The CR system with plates with a photostimulated luminophor was the detector.

The quality of the received images was estimated on the image contrast of a temporal bone structures and possibility to visualize the electrode located in a cochlea of a temporal bone

[3]. For control of an electrode's position the following regimens were picked up: current of a X-ray tube 120 mkA (uA), voltage of 70 kV, exposition time 5 sec.

During the performance of researches it was revealed that the projections used today in the radiographic analysis such as X-ray analysis in a Stenvers X-ray view [4], X-ray analysis in a transorbital X-ray view and others, don't allow to obtain enough diagnostic information. The usage of the microfocal X-ray source gives the chance to receive the enlarged pictures with satisfactory sharpness (fig. 3) in a transorbital X-ray view.

a b

Fig. 3. X-ray analysis in a transorbital X-ray view: a - X-ray film of a skull with established electrode, b - the scheme of shooting.

However contrast of the pictures received in a transorbital X-ray view is insufficient and can be increased by making change in scheme of shooting. The usage of a X-ray tube with the transition anode allows to enter the hollow anode of a X-ray tube into a mouth of the patient, increasing contrast of the X-ray image. In this projection test-object pictures (fig. 4) were received, based on the head of a pig with the entered electrode.

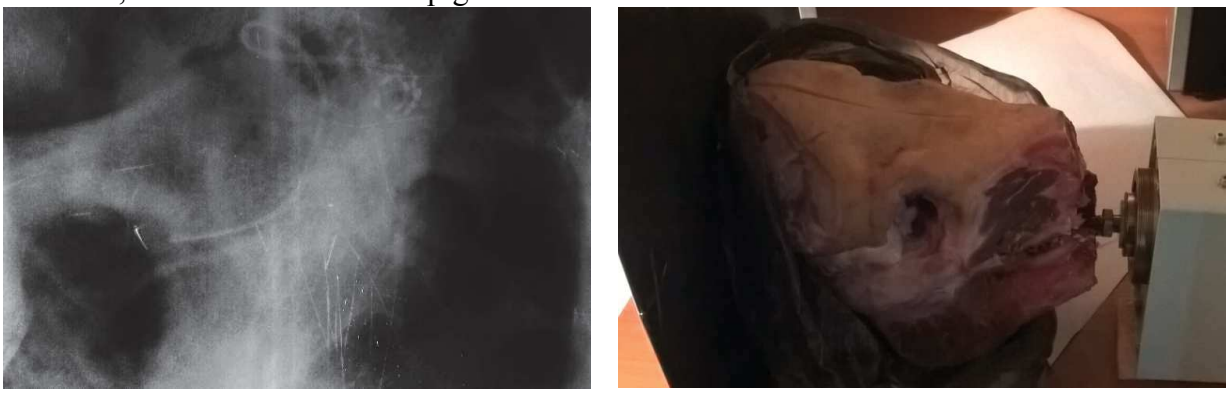

a b

Fig. 4. X-ray analysis in the offered view (projection):
a - X-ray fimage of the pig's head with established electrode, b - the scheme of shooting.

Conclusion. Application of the microfocal X-ray analysis in the cochlear implantation is perspective because gives the chance to receive the sharp images of an electrode that is allowing to define its precise location. The shooting method with introduction of the taken-out anode into a mouth of the patient allows to achieve essential increase of contrast in comparison with traditional projections.

References

[1] Potrakhov N. N., Gryaznov A. Yu. The microfocal X-ray analysis in medical diagnostics. SPb. SpbSETU, 2012, 104 P.

[2] Potrakhov N. N. The microfocal X-ray analysis in stomatology and maxillofacial surgery. SPb., 2Technomedia», 2007, 184 P.

[3] Cosetti MK, Troob SH, Latzman JM, Shapiro WH, Roland JT Jr, Waltzman SB. An evidence-based algorithm for intraoperative monitoring during cochlear implantation. Otol Neurotol 2012. P.169-76.

[4] Potrakhov N. N., Gryaznov A. Yu. Method of an assessment of informational content of the visualized dental x-ray images//Medical equipment, 2009, №1, pp. 16-18.

Mobile device for hemodialysis

S.A. Egorov

Penza State Technological University, pr-d Baydukova 1A Penza, Russia

Kidney is a natural filter cleaning the blood of human. According to the World Health Organization more than 500 million people in the world there are signs of impaired renal function. Particularly difficult situation with renal insufficiency was formed in Russia. More than half of Russians is subject to bad habits and lead an unhealthy lifestyle that is directly related to kidneys status. In identifying renal failure patients for the whole life tied to an artificial kidney machine. The procedure is performed three times a week on average for four hours while the patient is stationary. In addition, the Russian dialysis centers are open is not in everyone, even a large settlement. It turns out that the patient can spend the whole day to the procedure. These "walk" often cannot afford even physically healthy people, what can we say about people living only through regular hemodialysis procedures.

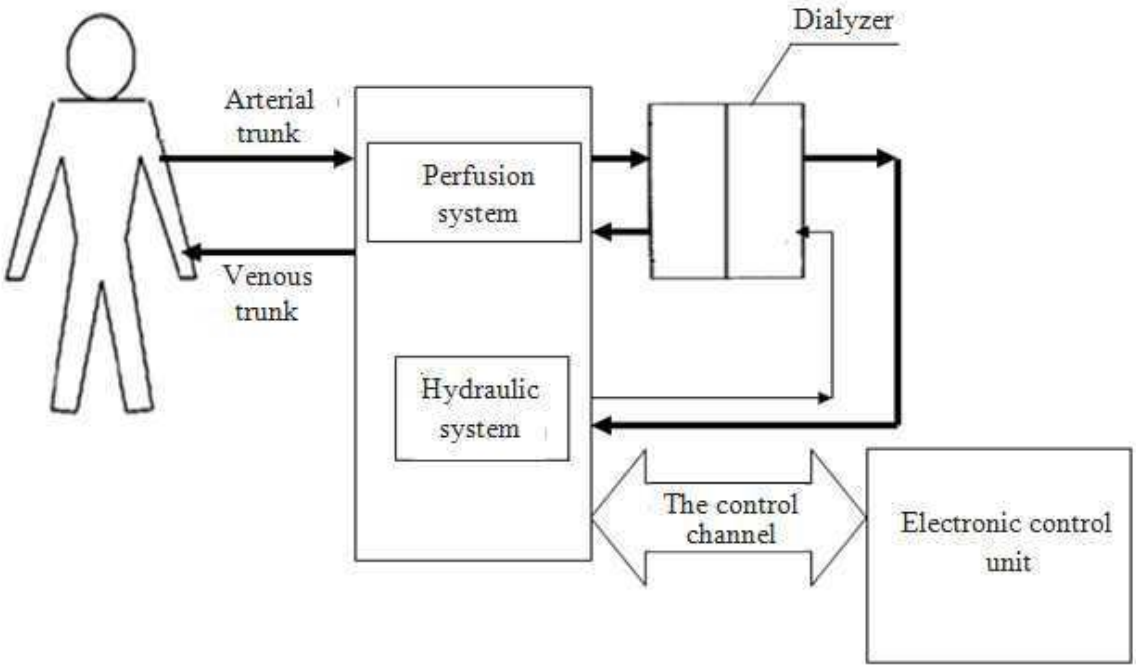

Fig. 1 The scheme of the "mobile device for hemodialysis

Hemodialysis is a mechanical cleansing of blood by diffusion and convection from waste, salts and liquids required for patients with kidney sick's. Hemodialysis is the most

common way to treat severe forms of kidney failure. During hemodialysis removes substances found in the blood by diffusion and convection, which depend on the properties of the hemodialysis membrane [2].

Currently, the Department of "Information Technology and Management in medical and biotechnical systems" work is underway to create a mobile device for hemodialysis. It is expected that the developed device will have a small weight and size parameters that allow its positioning on the belt. The device will be connected to the patient through a catheter, which will lead an active lifestyle.

The structure of the developed device includes the following main components: a dialyzer with blood highways; Hydraulic system comprising a blood pump; electronic control unit and perfusion system.

The electronic control unit is the brain of the machine, controls the operation of all its systems, controls the operation of units and components, monitors all hemodialysis parameters.

Perfusion system provides a controlled continuous or discrete patient blood samples (arterial sampling), its movement through the dialyzer and return the purified blood to the patient's body (venous return). Dialyzer removes low molecular weight substances from colloidal solutions due to diffusion and osmotic pressure difference on both sides of the semipermeable membrane of cellophane. Potassium ions, sodium, calcium, chloride, urea molecule, creatinine, ammonia, and other easily penetrate through the pores of cellophane. At the same time larger protein molecules, blood cells and bacteries cannot overcome the barrier of cellophane.

Hydraulic system performs the following tasks: preparing a dialysis liquid coming from the concentrate and purified water by mixing one part concentrate and 34 parts water; It produces vented prepared dialysis fluid to avoid hitting tiny air bubbles in the dialysis machine; It heats the dialysis fluid; is supplying dialysis fluid tothe dialyzer; conducting ultrafiltration; withdraws from the dialyzer the dialysis liquid; conducts internal disinfection of device before and after hemodialysis [4].

This version of the device, of course, will give way to a stationary power, but also the tactics of its application is offered completely different. The developed device will have a weight of about five kilograms, it will be designed to only personal use, and its characteristics will not only provide a more physiologic mode, but also reduce the diet restrictions.

References

[1]. Ivanitskii M.F. “Human anatomy” (Moscow, 2010).

[2]. Charles B. Carpenter, J. Michael Lazarus “Dialysis and kidney transplantation in the treatment of patients with renal insufficiency” (Moscow, 2004).

[3]. Stetsyuk E.A. “Modern hemodialysis” (Moscow, 2007).

[4]. Sapozhnikov D.B., Smirnov A.V. “Apparatus for hemodialysis: description of the main components” (Donis, 2010).

System of life-support in the extreme situations

N.U.Kosenok[1]
1. 440039 Russia, Penza, pr. Baidukova / ul. Gagarina, 1a / 11

Human condition under the influence of various environmental factors may deteriorate, which is reflected in the results of individual and collective activities. Enhancing Human Security in the modern world require, is a system for monitoring physiological status and location. Elderly people and those whose activities are connected with extreme physical and psychological stress, are potential-telyami require such systems.

In the Russian context, with the extent of the territory, more distance-s to help high-tech centers, the inability to rapidly increase, of their number to deal with, the lack of social infrastructure for the devel-opment of quality health services everywhere, life support system can become a strategic solution to many social problems. Therefore, optionally-walk distance assessment of the functional status of patients at risk and people engaged in extreme situations.

Create a wearable system for continuous remote control personified, Rowan basic human vital functions related to the solution of a wide range of technical problems. Universal devices for remote medical monitoring are not available, and automatic gauges basic physio-logical parameters, received recognition from clinicians unsuitable "O-field conditions."

A significant obstacle that arise when trying to use to monitor the dynamics of the functional state of the human standard meters, is the need to be placed on the body sufficiently massive metal detectors, multiple circular electrode and compressing an artery cuff.

Life support systems being developed in the form of a draft instrument com-plex, including biometric sensors and software equipment. But-pendent part provides basic physiological parameters: bullet-sa; respiratory rate; percent oxygen saturation; mean arterial pressure; skin temperature. The system evaluates the parameters of the position and movement of the body position, the motor activity and the location (on the GPS and GSM) (Figure 1).

The system is an undershirt clothes (see Figure 1) with the location-mi therein thermo sensor, electrocardiograph, pulsoksimerom, sensors are installed with the possibility of contact with the body section control-Rui object (determining skin temperature, heart rate, percentage of blood oxygen saturation), and also plethysmograph and an accelerometer, inclinometer, (respectively controlling the respiratory rate, body position and activity).

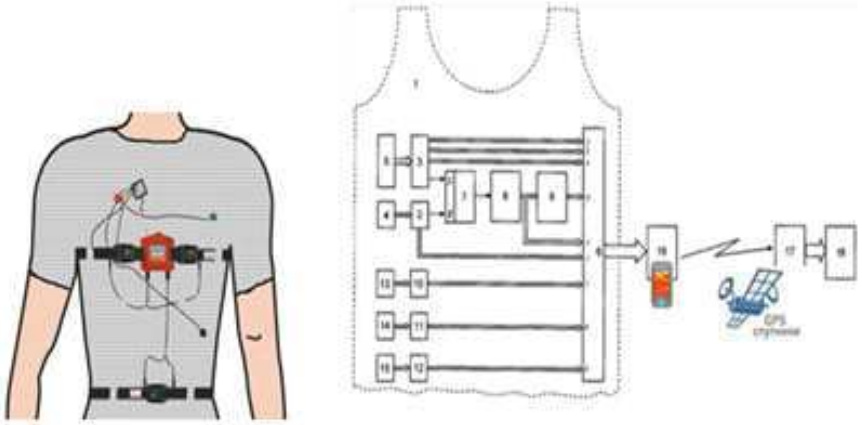

1 – wear

2,3 – nformation outputs from electrocardiograph and pulseoximeter

4 – electrocardiograph

5 – pulseoximeter

6 – the processing unit of the primary information

7 - RS-trigger

8 – timer

9 - блок расчета артериального давления

10,11,12 - induction the outputs from the thermometer, the induction plethysmograph and accelerometer – inclinometer

13 – thermometer

14 - induction plethysmograph

15 - accelerometer – inclinometer

16,17 - transmit-receive device measurement data through communication channels GPRS

18 - the data collection server

Fig. 1 The composition of the underwear clothing

The main principle of operation of the data collection and transmission system - it is a minimum of user interaction. All communication settings occur automatically.

For data transmission system uses GSM communication channel. The user must have the device (or a simple cell phone) supporting technolo-gies Bluetooth, to ensure the collection of data from the biometric system.

Messenger establishes a connection to a database located on the deleted-SG server via GPRS. The server provides access to information User The-telja by means of any internet browser

Fig. 2 The principle of operation of elements of the system of life support

Authorization object on the server takes place according to his telephone number. If the machine with the number registered in the database, the server will allocate to it a separate port for communication. User access to the server via the Internet browser. For information, the user must go through the authorization process. Upon successful login the user will go to the main page that allows you to view data on the movement and biometric information for each point in a given time interval.

To display the path used Google Map card supported function switch type (map, satellite, hybrid) and zoom.You can display data about their movements over a given period of time-ne. For each path, use the following information: time with Stu accurately to

a thousandth of a second; height above sea level; the speed of movement; breathing rate; position of the body; physical activity (talking, running, standing); temperature; arterial pressure; pulse; the percentage of blood oxygen saturation; the battery charge level.

The novelty of the project is as follows.

1. Modification of constructive solutions special clothing, a complex-ating means removal of the biological specimen data. Combining in modern sensors of various types, are mass-produced and certified.

2. Complex technique of monitoring the physiological condition of the person in real-time, synchronous processing algorithms and systematize data, and convert them to be transmitted through the GPS-channels in points PRIE-ma for analysis and rapid response.

The developed system has advantages over the existing analogous.

1. life support system includes measuring instruments physiological and logical parameters of the human condition, the TRD-governmental measured data via GPRS and data collection server. Arrange transceiver-tion has the ability to automatically transmit and receive files from digital data to the server upon the filing and remove power from the instrument, the buffer-tion of data in the event of disconnection and automatic data retransmission server to verify their integrity.

2. Hand-held instrument complex is a meter-rate ture, electrocardiograph, pulse oximeter sensors are installed with the possibility of contact with the opportunity-sensitive parts of the body (which determine skin temperature, heart rate, blood oxygen saturation percentage), as well as being a plethysmograph and akselerometr- inclinometer, (respectively controlling the respiratory rate, body position and activity).

3. The instrument is provided with a set of USB port or analog vyho-house, and a transceiver module comprises hardware and data storage in a GSM network or Ethernet server and wireless data collection module for data from the devices on the hardware module, and the wireless Internet -Water data modules are made for Bluetooth networking standard and are equipped with an interface for connecting devices.

Thus, in the article the project biotechnical system life-support in the form of portable complex for continuous remote con-trol and the physiological state of a person's location.

References

[1] Kosenok NY Modern aspects of safety when using personal body armor. Journal. Global Security, number 3. - M .: WASCS, 2010. - 116 p. (Pp 67-78).

[2] Istomina TV, Kosenok NY Biotech autonomous life support system. The utility model application from 28.10.2013g.

Kosenok Nikita Y., VPO Penza The State Technological University, komers777777@mail.ru, +79875163976, postgraduate.

SECTION 2

PROCESSING AND ANALYSIS OF BIOMEDICAL DATA, SIGNALS AND IMAGES

ECG analysis algorithms for smartphone based cardiac monitor

A.N. Kalinichenko[1], **S.V. Motorina**[1], **A.V. Uskov**[2]
1. Saint Petersburg Electrotechnical University, St. Petersburg, 5 Prof. Popova str., Russia
2. Medical project CardioQVARK Cardiomonitor, Moscow, Russia

Introduction.

Development of the mobile communication technology makes it possible to create compact and easily available smartphone based devices that provide real-time control of human physiological parameters and also translation of registered data to medical centers where they can be reviewed by doctors. The possibility like this is especially important for the cardiac patients supervision. As in case of the mobile based devices use, the conditions of physiological signals acquisition (first of all ECG) differ much from the conditions typical for standard ECG equipment, the task of special ECG processing algorothms development becomes urgent. This work is devoted to the description of ECG analysis algorithms complex oriented to the use in mobile cardiac monitoring systems.

Smartphone based cardiac monitor.

The described algorithmic complex was developed for the use in mobile cardiac monitor CardioQVARK [1], based on IPhone series 5/5S or 6. This device represents a portable case into which smartphone is inserted. On the rear side of the case two electrodes are placed for the ECG acquisition from fingers of both arms that corresponds to the standard ECG lead I. ECG signal is acquired with sampling frequency 20000 Hz and 16-bit resolution. Bandwidth of the signal is from 0.2 Hz to 5000 Hz. Registered signal is first preprocessed in the smartphone and displayed in real-time mode at the screen. Then the signal is decimated to 1000 Hz and transferred via Internet to the cloud service where additional analysis of the signal is implemented and also the ECG and its analysis results are saved in database. The data from service are available both to the patient and to the doctor with the use of special clients application that can be installed at smartphone, clipboard computer, notebook or desktop computer.

The following main functions of ECG processing and analysis are realized in this system:

- heart rate control and measuring of RR-intervals (distances between two adjacent heartbeats);
- pacemaker spikes detection (if they are present);
- cardiac arrhythmia recognition;
- heart rate variability (HRV) parameters estimation.

ECG analysis algorithms.

Common structure of the ECG analysis process.

The algorithms of ECG processing and analysis are distributed between the mobile device and the cloud service. The part of the preprocessing procedures that is implemented in the real-time mode is realized at the smartphone while most of the ECG analysis algorithms are

concentrated in the cloud service software. So in case of some algorithms modernization, most part of the ECG analysis program has to be updated only at the cloud service.

ECG processing and analysis algorithms realized at the smartphone.

If a patient has implanted pacemaker, it is very important to use a method of ECG acquisition and processing that provides the pacemaker spikes detection and visualization. As most of the modern pacemakers use bipolar mode that is characterized by very small amplitude of pacemaker spikes (typically about several millivolt and 0.2 -1 ms duration), routinely used standard ECG acquisition equipment doesn't provide reliable detection and display of the pacemaker spikes [2, 3]. The use of very high sampling frequency 20000 Hz and wide frequency range in the described above mobile ECG monitor permits not only detection of the spikes but also estimation of their parameters.

At the first stage of the spikes detection procedure estimation of the current mean amplitude of QRS-complexes is implemented. This mean amplitude is needed for further adjusting of some thresholds used in the detection algorithm. The spikes detection procedure itself includes the following stages:

- pacemaker spikes search, based on a criteria of two steep jumps presence separated by a plateau having duration between 0.15 and 1.0 ms;
- estimation of the detected pulse parameters (duration and amplitude);
- deleting of the spike with the use of linear interpolation;
- compensation of the signal jump (just after the spike) caused by the pacemaker electrodes polarization; this procedure is based upon polynomial approximation.

The pacemaker spike detection algorithm caused the signal delay 80 ms. Fig. 1 illustrates the spike detection process and further signal correction.

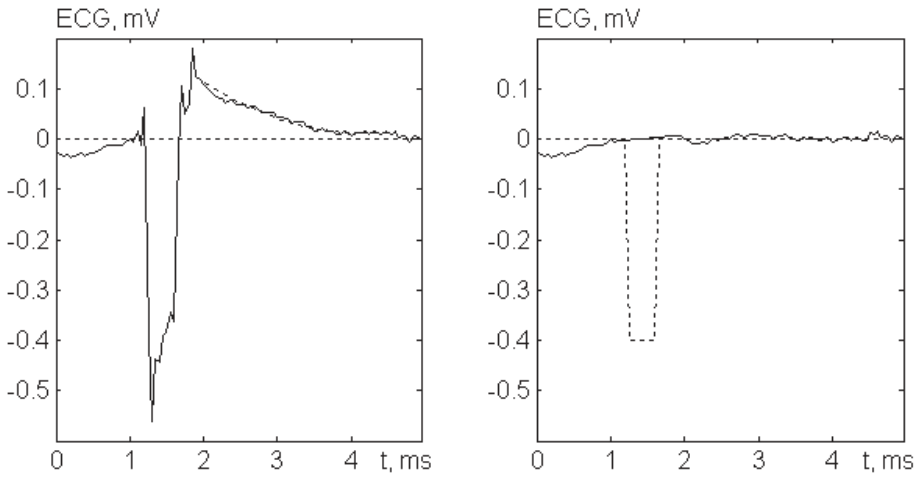

Fig. 1. Illustration of the spike detection algorithm and further signal correction. Left plot: a fragment of raw signal containing a pacemaker spike (solid line) and polynomial curve used for the polarization jump compensation (descending dotted line). Right plot: the same signal fragment after the pulse deleting and the jump compensation (solid line). Dotted line shows the detected pulse restored with the use of its parameters.

To prepare the ECG for display on the smartphone screen the signal is filtered by two digital filters: notching (removing AC interference) and low-pass (smoothing) filter. If some pacemaker spikes were detected, they are inserted in the signal as vertical lines having the high equal to the measured amplitude of the spikes (Fig. 2).

After the spikes detection procedure the signal is decimated to 1000 Hz with preliminary smoothing and then translated to the cloud service in parallel with the detected spikes parameters.

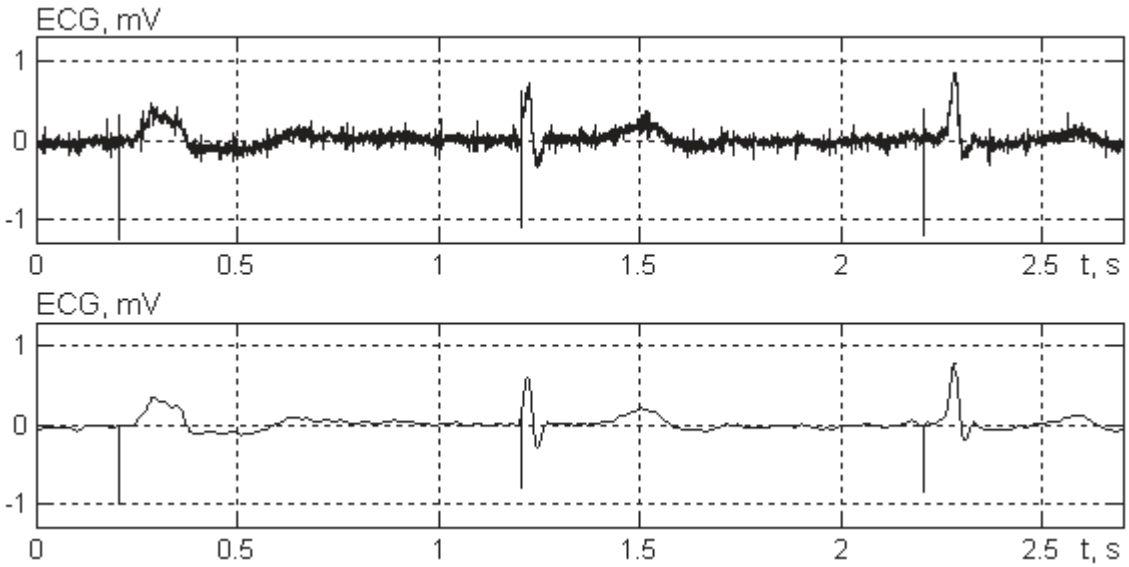

Fig. 2 Raw wide-range ECG signal with sampling frequency 20000 Hz in which pacemaker pulses take place (upper plot) and the same signal after the correction of the segments containing spikes, smoothing, decimation and restoring of the detected pulses (lower plot).

ECG analysis at the cloud service.

The ECG signal with sampling frequency 1000 Hz transmitted from the smartphone is stored in the cloud service database both in original and filtered forms. The signal filtering is implemented with the use of comb filter (removing DC component, AC interference and its harmonics) and low-pass filter with cutoff frequency about 35 Hz.

The unfiltered signal with sampling frequency 1000 Hz is used then as an input for the further ECG analysis stages [4-7]. First the noise level of the signal is estimated. If the noise level is too high, the corresponding ECG fragment is excluded from the further processing. If the signal is considered as noiseless, it is filtered by adaptive AC interference filter and smoothing filter. After this preliminary filtering the signal is passed through high-pass filter with cutoff frequency 5 Hz and differentiating filter to accentuate the signal components related to QRS-complex. Absolute values of the obtained signal samples are used as an input of QRS detection procedude [4, 5] that represents a logical algorithm based on threshold rules. This algorithm is adaptive to the current ECG amplitude and to the mean current heart rate. The begining and the end points of each detected QRS-complex are then determined and also a reference point used for RR-interval estimation.

All detected QRS-complexes are grouped into clusters with the use of dynamical clusterization algorithm [4, 5] based on the following three indices characterizing the complexes similarity:

- linear decision rule using four QRS features (duration, amplitude, square and shift relative to the baseline);
- correlation based index;
- spectrum based index.

Each of the obtained clusters is labeled as “normal”, “pathological” or “indefinite”.

RR-interval values and results of QRS forms classification are used further for the recognition of arrhythmia (premature ventricular beats and premature supraventricular beats). Arrhythmia recognition algorithm is based on a set of empirically derived decision rules [4]. The cardiac rhythm irregularity analysis including detection of atrial fibrillation is implemented by separate algorithm based on graphical representation of some regularities in RR-intervals values and order [8].

The analysis of HRV is also based on the RR-intervals sequence and the QRS classification results. Only the intervals between adjacent "normal" QRS-complexes (so called NN-intervals) are used for the HRV parameters estimation. The NN-interval values themselves as well as heart rate control function derived from these intervals with the use of spline interpolation are used for the HRV parameters calculation. The most widely used HRV indices both in time and frequency domains are determined by this procedure [9,10].

Results and conclusion

The pacemaker spikes detection algorithm was tested with the use of real ECGs set including 83 recording, each 300 s long. Following pacing modes underwent analysis: AAA (n=6), VVI (n=11), DDD (n=66), including biventricular pacing (n=17). Total number of the verified pacemaker spikes was 37921. The algorithm correctly detected 37276 spikes (98.3 %) while showed 531 false positives (1.4 % of the total pulses number).

Standard arrhythmia database MIT/BIH [11] was used for the QRS-complex detection and arrhythmia recognition algorithms testing. QRS detection algorithm showed sensitivity 98.90 % and specificity 99.88 % while for the ventricular premature beats these indices had values 87.2 % and 92.1 % correspondingly.

Atrial fibrillation recognition algorithm was tested with the use of Atrial Fibrillation Database [11] and showed sensitivity 93.22 % and specificity 95.57 % [8].

Today all algorithms presented here are included into the software of mobile cardiac monitoring system CardioQVARK. The whole volume of data stored in the system database is permanently reviewed in order to reveal ECG analysis mistakes that take place in some situations. The results of this review are used for the further enhancement of the algorithms quality.

References

[1] CardioQVARK project site: www.cardioqvark.ru.

[2] Maya E. Guglin, Neeta Datwani, Electrocardiograms with pacemakers: accuracy of computer reading. In: Journal of Electrocardiology, Vol. **40**. p. 144–146. (2007).

[3] Andersson, Hedvig; Hansen, Marco Bo; Thorsberger, Mads; Biering-Sørensen, Tor; Nielsen, Jonas Bille; Graff, Claus; Pehrson, Steen; Svendsen, Jesper Hastrup / Diagnostic accuracy of pace spikes in the electrocardiogram to diagnose paced rhythm. In: Journal of Electrocardiology. Vol. **48**, No. **5**. p. 834-839. (2015).

[4] Барановский А.Л., Калиниченко А.Н., Манило Л.А. и др. *Кардиомониторы. Аппаратура непрерывного контроля ЭКГ*. Под ред. А.Л. Барановского и А.П. Немирко - М.: Радио и связь, 1993. - 248 с.

[5] Немирко А.П., Манило Л.А., Калиниченко А.Н. *Математические методы анализа биомедицинских данных*. СПб.: Изд-во СПбГЭТУ «ЛЭТИ», 2013. - 175 с.

[6] R. M. Rangayyan, *Biomedical Signal Analysis: A Case-Study Approach*, (IEEE Press, Wiley-Interscience, New York, 2002).

[7] G. D. Clifford, F. Azuaje, and P. McSharry, *Advanced Methods And Tools for ECG Data Analysis*, (Artech House, Norwood, MA, 2006).

[8] Моторина С.В., Калиниченко А.Н., Немирко А.П. Выбор метода кластеризации для алгоритма выявления мерцательной аритмии - "Биотехносфера". № **4(40).** с. 2 -5. (2015).

[9] Heart rate variability. Standards of measurement, physiological interpretation, and clinical use. Task Force of the European Society of Cardiology and the North American Society of Pacing and Electrophysiology. Eur Heart J. **17(3)**. p. 354-81 (1996).

[10] Баевский Р.М., Иванов Г.Г., Гаврилушкин А.П., Довгалевский П.Я., Кукушкин Ю.А., Миронова Т.Ф., Прилуцкий Д.А., Семенов А.В., Федоров В.Ф., Флейшман А.Н., Медведев М.М., Чирейкин Л.В. Анализ вариабельности сердечного ритма при использовании различных электрокардиографических систем (часть 1) Вестник аритмологии. № **24**. с. 65-86. (2002).
[11] Physionet: the research resource for physiologic signals: www.physionet.org.

Detection of heart rate characteristics as an approach to distinguish between mental stress and physical activity

W. D. Scherz[1] ***and Ralf Seepold***[1]
1. HTWG Konstanz, Ubiquitous Computing Lab, DE-78462 Konstanz, Germany

Introduction

The raising self-awareness of health care and analysis of bio vital data is an upcoming topic in modern society, the notion and the understanding of stress has also changed in the last years. Stress is generally recognised as a factor with negative impact but stress should be divided in different categories and should not be seen as the peak of a dramatic event. Stress can be caused by the events of a day that elevate activity and require some response. Stress also has positive effects, for example, it helps us to estimate faster danger and takes decision on escaping or confronting. Stress appeared as a mechanism that allows us to react fast and effectively in dangerous situations. Being under stress, a body reorganises the biological priorities and functions to reach a maximal performance while in danger [2]. This reaction also happens in the daily life when circumstances require fast responses, so as consequence the body constantly stays in this mode. Some well-known effects of constant stress are failure to respond in an adequate way to fiscal, mental and emotional demands [3, 4, 5, 6] and changes of the structure and parts of the brain [7].

Long-term high stress can lead to medical problems like burnout and cardiac diseases [8, 9]. It has consequences for the modern society: increasing number of people with limitations leads to a growth of treating and healing costs.

The effects of the physical activities on the body also include change of heart rate (HR), blood pressure, etc. As by stress, physical activity effects can be divided in immediate effects, like changes in heart rate during physical activity, and those that appear in case of repeated physical activity [10].

In our previous research and during the development of a mobile system for measuring stress that uses an ECG signal, heart rate and heart rate variability for calculating stress, we had difficulties to distinguish between stress and physical activity. Both stress and physical activity have very similar effects like changes in the heart rate, vision, blood pressure, secretion of hormones, etc. [7, 11]. Both physical activity and stress, changes the behaviour of the heart rate and HRV.

This paper is focuses on the hypothesis that it is possible to differentiate between stress and physical activity by analysing heart rate and HRV and the resulting characteristics. The heart rate and the HRV can be simply obtained from a non-invasive mobile ECG. In the following section, the methodology and the data collection will be presented, followed by the possible options that can be used for differentiation between stress and physical activity.

Methodology

The proposed approach of this work consists basically of the measurement and the analysis of the data that is measured. The participants will be submitted to an exam with three different stages. At the first stage the data will be recorded while the participant is resting (RS). At the second stage, the participant will have to do some physical activity while the data is recorded (PS). At the third stage, the participant will have to take part in different stress tests (SS).

During these three stages RS, PS and SS the ECG and HR data of the participants will be collected and the participants will be under observation. At the first stage the participant will have to be resting and relaxing. The data that is collected during RS is important because it will be used for comparison with the other datasets. The duration of the RS is 15 minutes. At the second stage (PS) the physical activity will be monitored. The participants will have to perform different exercises on several difficulty levels using an exercise bike. At the beginning is the warm-up, then intense exercise and cool down. Each of these exercise units takes 5 minutes. It is important that for the PS the condition of each participant has to be taken in consideration. For the SS, we will use different cognitive demands. The stressors chosen for SS are the Stroop test [12], the Trier test [13] and arithmetical operations that have to be solved in limited time.

The participants are all students, aged from 18 to 40. None of them is an athlete or smoker. For gathering the data the ECG of the Bioharnes 3 from Zephyr is used. To improve the contact area and electrical characteristics of the electrodes, an electrode gel is applied.

Data Analyses / Discussion

As previous studies have shown, physical activity can be detected wrongly as *stress*, therefore, it is important to find a method to differentiate between them. The approach that is presented still has to be evaluated and validated with larger test groups, however first tests return convincing results: The method is composed of using two different principles that could be used to determinate physical activity. The first option is detection of fast changes in the heart rate [10, 14, 15]. These changes are expected to depend on the insensitivity of the physical activity. As shown in Fig. 1 where a peak appears and it shifts up the the RR intervals at the second 320. Another option that is taken under consideration is the Fourier spectrum analysis. The behaviour HF and LF will be analysed. Fig.1 (right part) shows the spectrogram.

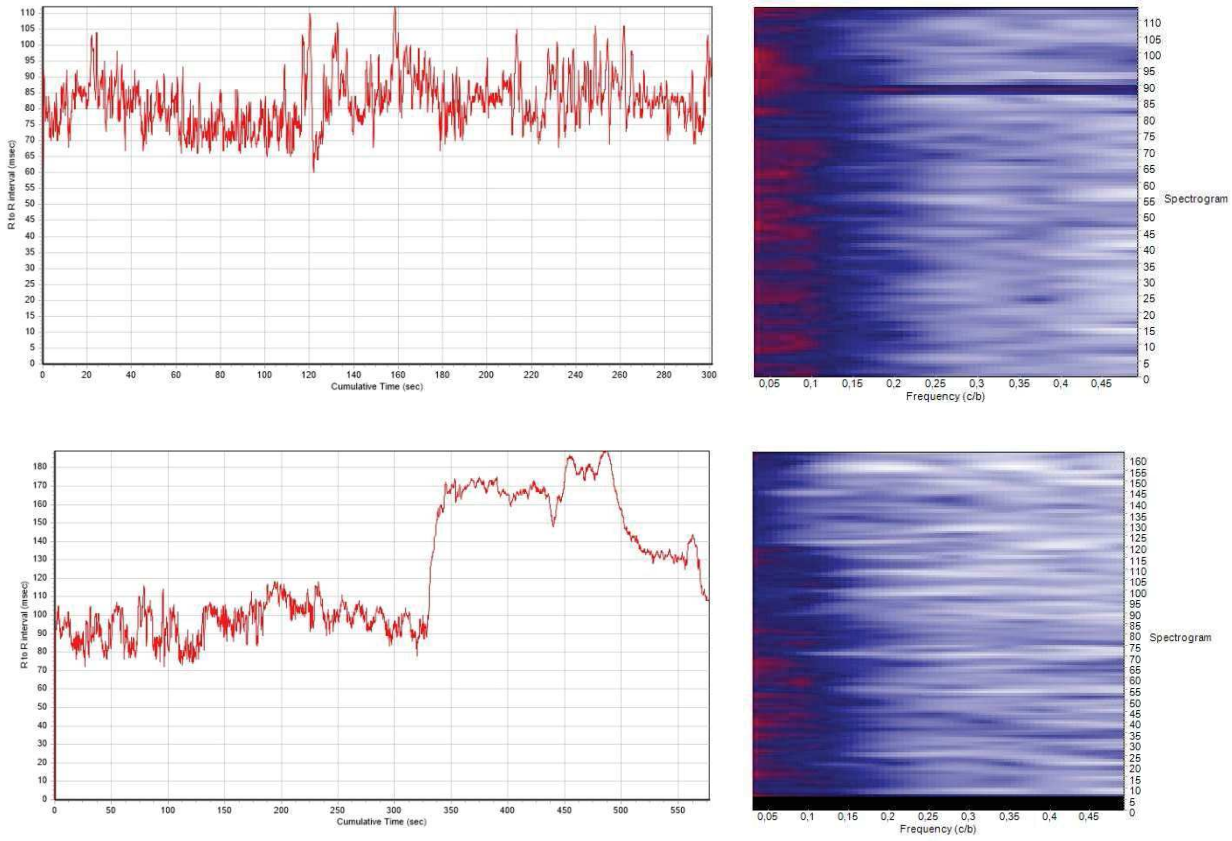

Fig. 1 the (upper) first pair of graphics shows the data of a participant while resting and avoiding any physical activity except of walking or standing up. The (lower) second pair of

graphics shows the same participant executing a physical activity of 10 minutes. On second 320 there is a clearly visible jump that marks the period when the physical activity was very intensive.

System overview

The system is based on a client server architecture. The server handles all the data and performs all computation. The client is composed of a mobile sensor that collects the ECG signal for calculation. The data can be uploaded manually to the system after the test has finished or the ECG module can be constantly connected over Bluetooth with a smartphone or PC and an application will upload the data to the server. The advantage of having the ECG module constantly connected is that a feedback and observation of the data in real-time mode is possible.

Conclusion

Physical activity and stress have similar characteristics. For a system that should detect stress it is important to be able to differentiate between stress and activity in order to avoid false information by false detection. When studying the differences of the participants' data while being under stress, physical activity and resting, it can be shown that the heart rate analysis is potentially a powerful method and indicator for detecting physical activity. Also the Fourier spectrum analysis could be used to indicate physical activity. To further validate this preliminary result, bigger studies with more participants have to be performed. For future studies it is also important to consider that the participants should be categorised depending of their physical condition.

The results presented here are preliminary, we will continue analysing the heart rate to validate these results.

References

[1] B. S. McEWEN und T. SEEMAN, „Protective and Damaging Effects of Mediators of Stress," *Annals of the New York Academy of Sciences,* pp. 30-47, 06 02 2006.
[2] X. V. N. V. K. T. C. M. A. D. L. Arthur S. P. Jansen, „Central command neurons of the sympathetic nervous system: basis of the fight-or-flight response," in *Science* , Bd. Vol. 270 , 1995, pp. 644-646.
[3] J. C. A. R. S. a. N. M. M. J. Martínez Fernández, „A Sensor Technology Survey for a Stress Aware Trading Process," *IEEE Trans. On Systems, Man and Cybernetics Part C: Applications and reviews,* Bd. 42, Nr. 6, pp. 809 - 824, 11 2012.
[4] J. Martínez Fernández, J. C. Augusto, R. Seepold und N. Martínez Madrid, Why Traders Need Ambient Intelligence, Germany: Springer Berlin Heidelberg, 2010.
[5] J. Martínez Fernández, J. C. Augusto, G. Trombino, R. Seepold und N. Martínez Madrid, „Self-Aware Trader: A New Approach to Safer Trading," in *Journal of Universal Computer Science*, 2013.
[6] B. Roozendaal, B. S. McEwen und S. Chattarji, „Stress, memory and the amygdala," *Nature Reviews Neuroscience 10,* pp. 423-433, 06 2009.
[7] S. J. Lupien, B. S. McEwen, M. R. gunnar und C. Heim, „Effects of stress throughout the lifespan on the brain, behaviour and cognition," *Nature Reviews Neuroscience 10,* pp. 434-445, 06 2009.
[8] K. Orth-Gomér, S. Wamala, M. Horsten , K. Schenck-Gustafsson, N. Schneiderman und M. Mittleman, „Marital stress worsens prognosis in women with coronary heart disease: The Stockholm Female Coronary Risk Study," in *Journal of the American Medical Association*, 2000.
[9] Y. Mei, M. D. Thompson, R. A. Cohen und X. Tong, „Autophagy and oxidative stress in cardiovascular diseases," in *Biochimica et Biophysica Acta (BBA) - Molecular Basis of Disease*, 2015.
[10] B. Gutin, P. Barbeau, S. Owens, C. R. Lemmon, M. Bauman, J. Allison, H.-S. Kang und M. Litaker, „Effects of exercise intensity on cardiovascular fitness, total body composition, and visceral adiposity of obese adolescents," *American Society for Clinical Nutrition,* Bd. 75, Nr. 5, pp. 818-826, May 2002.
[11] T. Kidd, L. A. Carvalho und A. Steptoe, „The relationship between cortisol responses to laboratory stress andcortisol profiles in daily life," *Biological Psychology,* pp. 34-40, 25 02 2014.

[12] J. R. Stroop, „Studies of interference in serial verbal reactions," *Journal of Experimental Psychology,* pp. 643-662, 1935.
[13] C. Kirschbaum, K.-M. Pirke und D. H. Hellhammer, „The 'Trier Social Stress Test'- A Tool for Investigating Pyschobiological Stress Responses in a Laboratory Settings," *Neuropychobiologie,* pp. 78-81, 1993.
[14] Y. Arai, J. P. Saul, L. H. Hartley, L. S. Lilly, R. J. Cohen und W. S. Colucci, „Modulation of cardiac autonomic activity during and immediately after exercise," *American Journal of Physiology - Heart and Circulatory Physiology,* pp. H132-H141, 01 1989.
[15] B. F. Robinson, S. E. Epstein, G. D. Beiser und E. Braunwald, „Control of heart rate by the autonomic nervous system: studies in man on the interrelation between baroreceptor mechanisms and exercise," *Circulation Research,* pp. 400-411, 4 04 1966.

Development of the method for evaluation of the component human body composition based on bioimpedance of trunk.

***A.D.Efremova*[1,2], *D.A.Prilutskiy*[2], *N.N. Rybkin*[2]**
1. National research university MIET, Moscow, Russia
2. Medical computer systems Ltd, Moscow, Russsia

Bioimpedance analysis (BIA) is effective solution for estimating body composition and extracellular and intracellular fluid analysis for diseases detection. Measuring part of the method BIA consists of passing through body areas (segments) a low and safe electrical current at one or more frequencies, measuring the voltage drop and calculating of full body impedance - bioimpedance. Analysis of the bioimpedance is based on an assumption about the relationship between the measured values of resistance and the composition of the body segments. Essentially BIA body composition is based on differences in conductivity constituent of various tissues due to their content of water and electrolytes. The main measured components are fat and fat-free mass, skeletal muscle mass and total body fluid. The multifrequency BIA allows estimation of the extracellular and intracellular fluids volume, and the phase angle. This is based on the property of cells and their membranes, as they do not conduct a low-frequency current. Changing any of component can carry serious consequences for human health. For example, excess body fat promotes the development of diseases such as hypertension, heart disease, diabetes, cancer and others. Moreover, maintaining an optimum percentage of water in the body contributes to the normal functioning of the body and reduces the risk of many chronic non-infectious diseases [2].

The main objective in this work is the development of analytical relationships linking the composition of the component model of the human body with the results of the measurement of the complex impedance of the trunk. A feature of the work is a way of measuring the impedance.

Typically, BIA used specific four-electrode scheme connection, when two pairs of closely placed current and voltage electrodes connect to wrist or ankle. While ECG is recorded from the 6 standard leads (I–aVF), using only 4 electrodes from patient's wrists and ankles. So, the scheme of BIA electrodes connection was modified. Current electrodes were placed to L (left arm) and N (right leg) standard ECG positions and voltage electrodes were placed to R (right arm) and L (left leg) standard ECG positions. Using of standard BIA scheme doesn't allow measuring the impedance of trunk accurately, as the body impedance is determined by limbs up to 90% and by trunk up to 10% only. Trunk active impedance of adults is in range of 15…30 Ohm. In our scheme the cross-sectional area is the central part of body. In fact, the impedance is measured in trunk (torso + abdomen) [1].

Having conducted research in the field of existing methods of calculating the body composition component by bioimpedance analysis and taking into account the selected circuit and method for measuring the body impedance the analytical relationship were developed for anthropometric parameters, bioelectric parameters and body composition components. And coefficients were selected empirically. Anthropometric parameters are very important in calculation of the component composition, so example ratio length of the trunk relative to body length: KL = 29,5 if the body type 1 (asthenia), KL = 31,0 if the body type 2 (normostenichesky) or KL = 33,5 if the body type 3 (hypersthenic). Trunk weight ratio relative to body weight: KW = 43,0. Developed equations with coefficients were realised in PC software in the next algorithm by 5 steps: Step 1 - data entry such as sex, age, height, weight. Step 2 - measurement of resistance and reactance of 95 points in the range of 5 ... 100 kHz. Step 3 - the calculation of anthropometric parameters such as body mass index (BMI), body length, body weight. Step 4 - Calculation of bioelectric parameters such as impedance at a frequency of 50 kHz, and the phase angle. Step 5 - the body composition calculation component in a certain sequence. Extracellular fluid (EXF) is computed initially, further the total water (TW), intracellular fluid (ICF), fat-free mass and body fat mass are calculated for trunk. Used equations for calculation EXF and TW of body trunk:

$$EXF = K_{ecf} \times \left(\frac{Lt^2 \times \sqrt{Wt}}{R_{ecf}}\right)^{\frac{2}{3}}$$

$$TW = K_{TW} \times \frac{Lt^2}{R_{TW}} + K_{Wt} \times Wt + K_A \times A + K_G \times G$$

where Recf = R [f5] and Rtw = R [f100], and R [f5] and R [f100] - body resistance at low and high frequencies, respectively, K – selected coefficients, A - full years, G - gender: G = 0 if a woman, G = 1 if male.

According to the proposed scheme of measurement was designed the special four-electrode PC biomedical amplifier by company Medical computer systems Ltd. The amplifier is connected to personal computer via the USB and corresponds safety standards IEC60601-1 and IEC60601-2-25. PC software application allows to do 3 or 5 minutes records of 6 lead ECG for analyze by dispersion mapping (DM) method and analyze the heart rate variability (HRV). Further the active and reactive bioimpedance components are measured at 95 points in range 5…100 kHz, graphs are plotted and component composition of the human body is calculated by developed method. The comparative clinical trials proved that the measured impedance and the calculated parameters obtained by developed device generally corresponds to the results obtained by popular BIA analyzers ABC-Medass and Diamant-AIST from the same volunteers in one time. 47 volunteer patients of different sex and age were tested in experimental bioimpedance trials.

As result, the developed device allow to do a few different examinations at the same time due to of using of common electrodes for ECG and BIA so it produces a new possibility for more effective and precision medical diagnostic, for example during screening examination. Additionally the important advantage of this device is more precision evaluation the impedance measurement of vitally important body organs (heart, lung, livers etc), because the main measurement segment in this scheme is trunk.

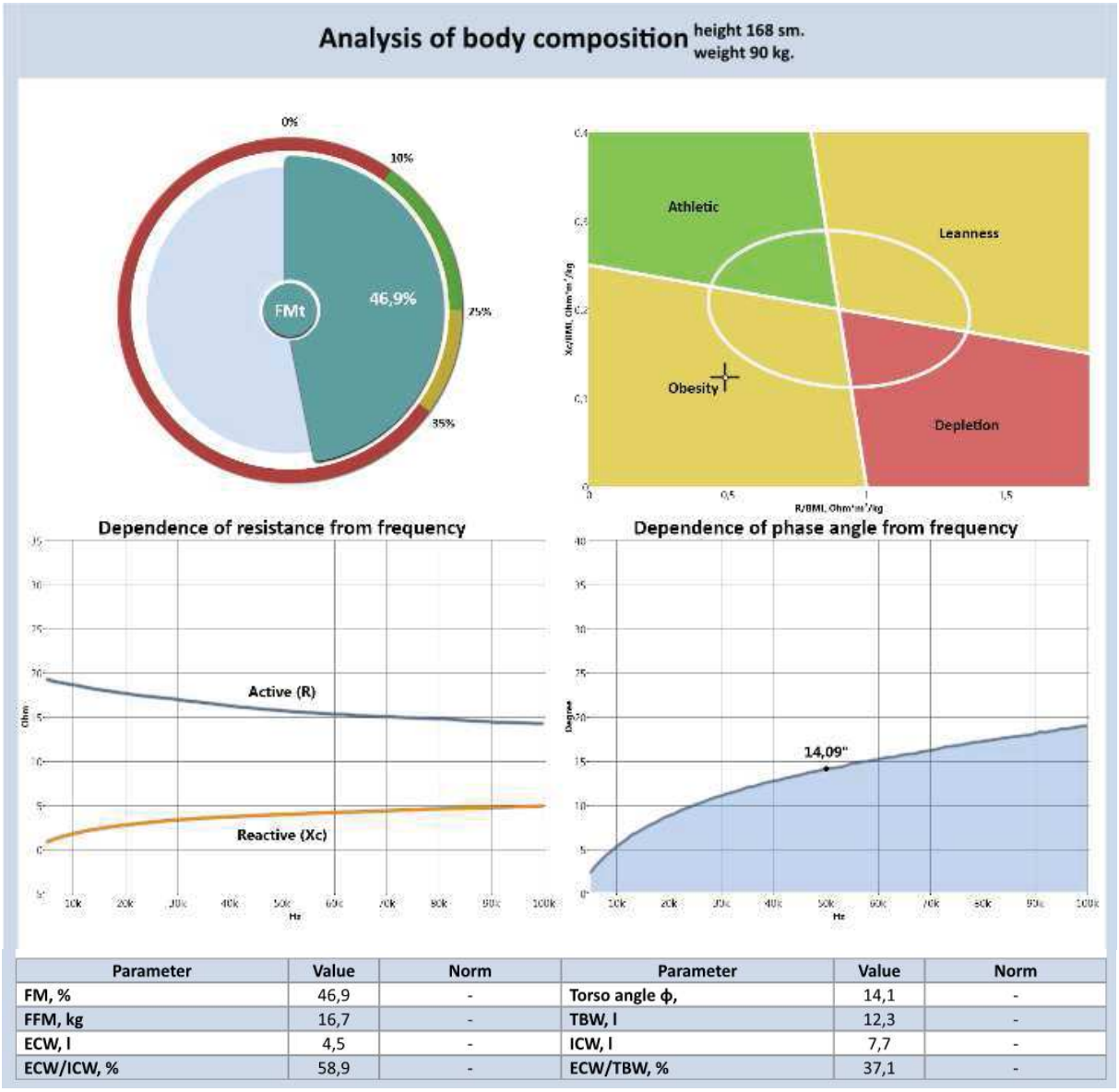

Parameter	Value	Norm	Parameter	Value	Norm
FM, %	46,9	-	Torso angle ϕ,	14,1	-
FFM, kg	16,7	-	TBW, l	12,3	-
ECW, l	4,5	-	ICW, l	7,7	-
ECW/ICW, %	58,9	-	ECW/TBW, %	37,1	-

Fig. 1. Example of BIA report obtained on developed device, man 20 years old.

References

[1] A.D.Prilutskaya, S.V.Selischev, D.A.Prilutskiy, N.N. Rybkin. "*Bioimpedance measurement from standard ECG electrodes position*." 1st Russian-German Conference (RGC) on Biomedical Engineering, (Hanover, 2013).

[2] Jukka A. Salmi. "*Body composition assesment with segmental multifrequency bioimpedance method*." Journal of sport sciency & medicine. Vol. 2 supplementum 3, (2003).

[3] Kenneth R Foster, Henry C Lukaski. "*Whole-body impedance-what does it measure?*" American Society for Clinical Nutrition, (1996).

[4] Henry C. Lukaski. "Assessment of body composition using tetrapolar bioelectrical impedance analysis." Journal Bristol-Myers Nutrition Symposia 1990 Vol. 9 pp. **303-315**

Near-infrared transillumination images of the periodontal tissues segmentation

A.V. Kolpakov[1], I.N. Spiridonov[1]

[1] Bauman Moscow State Technical University/Department of Biomedical Techniques, chair BME-1 "Biotechnical system and devices" Moscow, Russian Federation

Introduction

According to previous research results the basis for the early lesion detection in periodontal tissues is visual imaging of the inflammation area by transillumination in the NIR wavelength range 650 – 1200 nm [1 – 3].

The article is dedicated to the development of the NIR images of periodontal tissues processing method for quantitative estimation of periodontal tissues lesion stage.

Materials and methods

The NIR images of the periodontal tissues contain the areas of the hyperemia and edema that are the symptoms of the early lesion stages, attached gingiva and tissue surface (Fig.1).

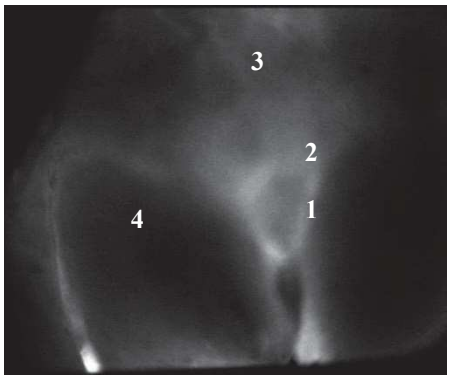

Fig. 1 Example of the NIR image of the periodontal tissues: 1 – hyperemia area, 2 – **edema** area, 3 – attached gingiva, 4 – tissue surface

The probability of the inflammation area visual detection depends on the contrast coefficient C_a, defined by the equation:

$$C_a=(I_{max} - I_{min})/ (I_{max} + I_{min}) \quad (1)$$

where I_{max} is intensity of the epithelium attraction loose pixels, I_{min} is intensity of the hyperemia area pixels.

There were 36 pairs of the visible and NIR images analysed. The visible images were registered in the reflected irradiation of the wavelength range 400..440 nm, 440 ..480 nm, 480..520 nm, 520..560 nm, 560..640 nm, 640..700 nm. The NIR images were registered in the forward scattered irradiation of the wavelength 890±75 nm [2, 3].

According to the research results, maximum values of the inflammation area contrast coefficient C_a achieved for the NIR images of the periodontal tissues.

For the automatic detection of the inflammation areas on the NIR images possibility research there was automatic segmentation of the inflammation areas conducted.

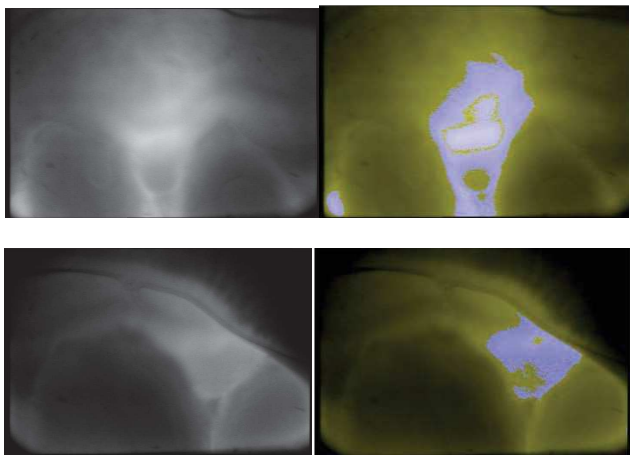

References

[1] Kolpakov. A. Infrared Diaphanoscopy of Soft Tissues in the Mouth Cavity// Proceedings of the 2–nd Russian-German Conference on Biomedical Engineering: LETI, St. Petersburg, 2014.P.144-147

[2] Kolpakov A.V., Spiridonov I.N., Makarov A.L. The Absorbtion of Optical Radiation by Soft Periodontal Tissues Process Research. Science and Education of the Bauman MSTU, 2014, no. 11, pp. 444 – 457. DOI:10.7463/1114.0735264

[3] Kolpakov A.V., Makarov A.L., Spiridonov I.N. Use of an infrared diaphanoscopy method for estimating the condition of mouth cavity's soft tissues in dentistry. Nauka i obrazovanie MGTU im. N.E. Baumana, 2013, no. 12, pp. 297-306. DOI: 10.7463/1213.0669704

Application of multispectral acousto-optic image processing for medical diagnostics

K.V.Zaichenko, B.S.Gurevich

State university of aerospace instrumentation, Department of Medical radio electronics, 190000, St.Petersburg, Russia

The multispectral processing of different biological objects images is very common and necessary task for medical diagnostics and some adjacent areas. This kind of image processing means the polychromic image transformation (preferably in real time mode) into the series of monochromic images, each of which corresponds to the certain narrow spectral interval. The traditional devices providing such analysis contain a turret of interference filters. It allows to select the separate spectral components of the image with rather high selectivity: the transmission bandwidth of an interference filter is less than 10 nm. However, the presence of mechanically moving parts in this configuration, introduces the serious limitations into the processing speed, and the device based on the interference filters turret cannot operate in the real time mode. From the other hand, the amount of the selected spectral components is defined by the number of interference filter in the turret. These filters are rather expensive because they contain many decades layers of different materials deposited one over another. The reliability of the devices containing mechanically moving parts is rather low as well.

The alternative method must contain the possibility to control the wavelength interval switching for the sub-images by means of software. It can be performed by using of wide-aperture acousto-optic tunable filters (AOTF) [1]. This device can be considered as a spectrally selective component because it contains running phase diffraction grating (acoustic wave) which provides Bragg light diffraction. The light wavelength to be selected, is defined by the frequency of electric signal which comes on AOTF's piezoelectric transducer. In its turn, this frequency can be controlled by means of software, and provide the real time mode. The AOTF productivity is limited by the acoustic beam velocity, i.e., by the time of acoustic beam crossing the light beam aperture.

As for operation with images of biological objects, the spectrometric device based on AOTF, developed by Spanish specialists and intended for the multispectral processing in visible and near infrared areas, is of a significant interest [2,3]. For example, by means of the newly elaborated device, these authors have found accurately the chlorophyll distribution across the Canadian poplar leave as well as across the bean leave processed by herbicide.

The devices which perform the multispectral processing of biological objects images and contain AOTF, can be characterized by the maximum values of spatial and spectral information amounts which can be transmitted by the devices. These values are connected with the characteristics of Bragg cells, on the basis of which the devices are designed. Moreover, the limitations regarding amounts of spectral and spatial information, are mutually dependent.

Indeed, in the device described above, the limitation of spatial resolving power is defined by AOTF ability to transmit images. This ability is caused by wide angular aperture formation in AOTF in the conditions of anisotropic Bragg diffraction. As for wide-aperture AOTF, its transmission band by light wavelength can be defined as [4]

$$\delta\lambda \approx 0{,}8\frac{\lambda^2}{l}[\Delta n - \lambda\frac{\partial\Delta n}{\partial\lambda}]\sin^2(\theta_i + \alpha),$$

where α is angle between acoustic wave front in Bragg cell and the crystal optical axis, l – Bragg cell spatial aperture, θ_i – angle of light beam incidence into acoustic beam, Δn – value of the crystal birefringence. It can be found from expression above, that it can be simplified significantly if the birefringence dispersion is small enough.

Spatial resolving power of the pattern transmitted through AOTF can be defined by AOTF angular aperture. It can be approximately considered that (according to the commonly accepted Raleigh criterion) the total amount of the resolved elements in the pattern is equal to relationship between angular aperture of AOTF and angular diffraction divergence of the parallel light beam with the same aperture. On a level with that, as it has been shown [5] spatial resolving power depends on the same parameters as AOTF transmission bandwidth does, which defines the amount of spectral information. It follows from all listed above that increasing of the spectral information amount (decreasing of the transmission bandwidth) requires the angular aperture decreasing, and, correspondingly, decreasing of the transmitted spatial information amount. The problem of the device information optimization is not yet solved, and the solution can be expected in near future.

The experimental implementation of the multispectral processing device is shown in figure 1.

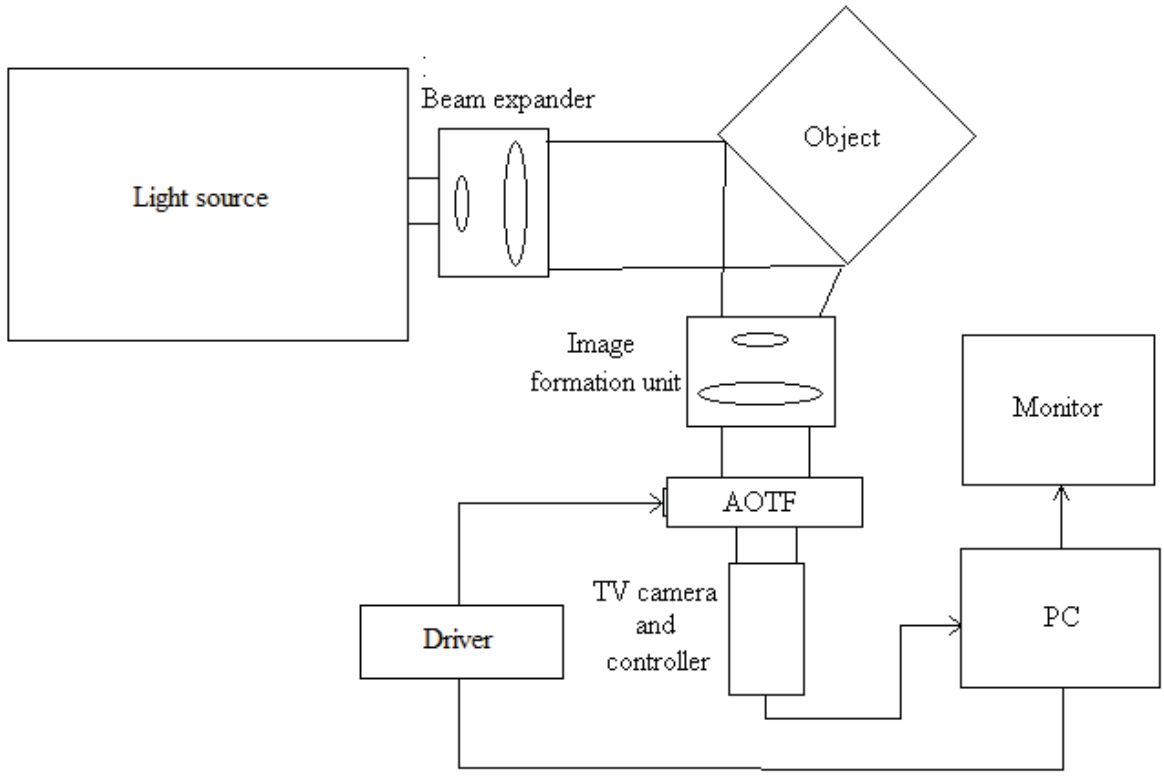

Fig. 1 Schematic configuration of the system intended for multispectral processing of the images for the purposes of medical diagnostics

The light source produces the beam of white light which is expanded to the necessary size to illuminate the object. It represents either the part of patient's body or the tissue mount,

depending on the kind of medical diagnostics to be performed. The light reflected from the object and scattered by it comes to optical unit which forms the object image. The light beam further passes through AOTF and forms a monochrome sub-image of the object in 1st diffraction order, in the plane of TV camera. The selected wavelength of this monochrome sub-image is defined be the control signal frequency which is formed by electronic driver controlled by PC. The signal from the camera comes to PC which demonstrates the sub-image in the monitor display together with the value of the selected wavelength. Hence, laboratory assistants and doctors can estimate some areas which includes the certain colors. They can conclude which areas are in the most danger of the certain disease.

We have used in our experiments the AOTF (see figure 2) based on tellurium dioxide single crystal in which the anisotropic acousto-optic diffraction was performed using the shear acoustic wave propagating into approximately [110] crystallographic direction [6]. Piezoelectric transducer made with lithium niobate single crystal, was connected to the TeO_2 crystal by means of vacuum cold welding.

Fig 2 AOTF used in the experiments

We have found that the sub-image spatial resolution of approximately 200x200 elements is attainable whereas the number of sub-images was about 25…30 in the total spectral range of 400…700 nm. Of course, if necessary, the spectral range can be shifted either in near UV area or in near IR area. It can be achieved using the same AOTF with slightly deteriorated spatial and spectral resolution.

We express our gratitude to Russian Foundation of Basic Researches for their financial support (grant No. 16-07-00533A).

References

[1] N. Gupta, “Acousto-optic-tunable-filter-based spectropolarimetric imagers for medical diagnostic applications: instrument design point of view,” J. Biomed. Opt., **10**, 05180 (2005).
[2] Vila-Frances J., Ribes-Gomez E., Ibañez-Lopez C., et al., “Configurable-bandwidth imaging spectrometer based on acousto-optic tunable filter,” Proc. SPIE **5953**, 59530S-1 – 59530S-12 (2005).
[3] Calpe-Maravilla J., Vila-Frances J., Ribes-Gomez E., et al., “400- to 1000-nm imaging spectrometer based on acousto-optic tunable filters,” Journal of Electronic Imaging **15**, 023001-1 – 023001-8 (2006).
[4] Chang I.C., “Tunable acousto-optic filtering: an overreview,” Proc. SPIE **90**, 12-22 (1976).
[5] K.V.Zaichenko, S.B.Gurevich, and B.S.Gurevich, “Application of optical freedom degrees principle to acousto-optic devices”, Physics Procedia **70**, 774-778 (2015)

[6] K.V.Zaichenko, B.S.Gurevich, “Multispectral image processing by means of acousto-optic devices” [in Russian], Biomeditsinskaya radioelektronika No.9, 70-76 (2013)

Data mining in EEG wave trains in early stages of Parkinson's disease

***O.Sushkova*[1], *A.Morozov*[1,2], *A.Gabova*[3], *A.Karabanov*[4]**

[1]*Kotel'nikov Institute of Radio Engineering and Electronics of RAS, Mokhovaya 11, Moscow 125009, Russia*

[2]*Moscow State University of Psychology & Education, Sretenka 29, Moscow 107045, Russia*

[3]*Institute of Higher Nervous Activity and Neurophysiology of RAS, Butlerova 5A, Moscow 117485, Russia*

[4]*Research Center of Neurology, Volokolamskoe shosse 80, Moscow 125367, Russia*

A method of analysis of electroencephalograms (EEG) based on wave trains is developed. In physics, a wave train (or a wave packet) is a short “burst” or “envelope” of localized wave action that travels as a unit. In this paper, we use the “wave train” term to denote a signal localized in time, frequency, and space. The wave train is a typical pattern in a background EEG and detecting / analyzing such signals gives useful information about the brain activity. Alpha spindles (sleep spindles) and beta spindles are the best known examples of the wave trains in EEG; several methods based on Fourier spectra, wavelets, autoregressive models, adaptive filtering, etc. have been developed for detecting and analyzing these EEG patterns (see surveys in [1,2]).

The idea of our method of EEG analysis is in that we detect and analyze the wave trains in a wide frequency band including theta, alpha, beta, and gamma EEG. We detect the wave trains as local maxima in a wavelet spectrogram of EEG record and compute various attributes of these signals. Then we implement a statistical analysis on the base of these attributes. In the paper [3], we have demonstrated that our method reveals a new statistically significant regularity in a group of de novo Parkinson's disease patients. Namely, the Mann-Whitney statistical test indicates a significant decrease of the quantity of the wave trains in the C3 and C4 electrodes in the beta frequency range. In this paper, we consider a problem of searching such wave train features that are appropriate for recognition / diagnosis of early stages and, possibly, a preclinical stage of Parkinson's disease on the base of EEG data.

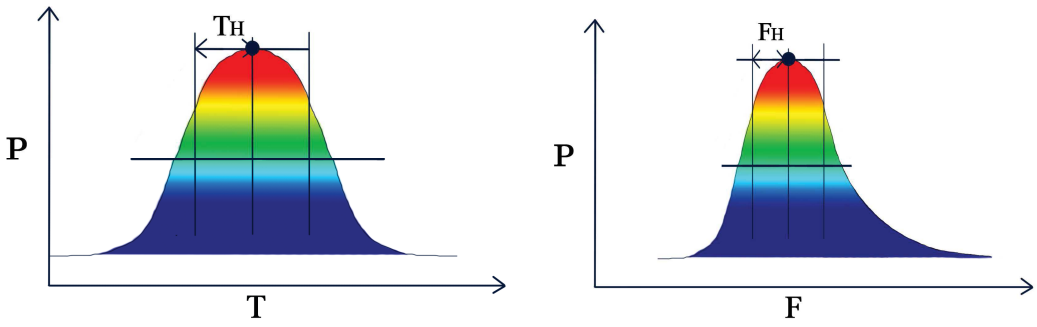

Fig. 1 An example of a spectrogram of a wave train in a time-frequency domain. The diagram on the left shows the spectrogram of the signal in the time plane. The abscissa indicates a time and the ordinate indicates a power. The diagram on the right shows the spectrogram of the signal in the frequency plane. The abscissa indicates a frequency and the ordinate indicates a power.

Let M be a local maximum in a wavelet spectrogram. We consider M as a case of a wave train if the half width of M (at half maximum) is greater or equal to the T_H threshold in the time plane and greater or equal to the F_H threshold in the frequency plane (see figure 1). The F_H threshold is a constant and the T_H threshold is a function of the f central frequency of the M maximum:

$$T_H = N_P / (2f) ,$$

where N_P is a constant given by an expert. In this paper, we apply the values: $N_P = 2$ and $F_H = 1$ Hz.

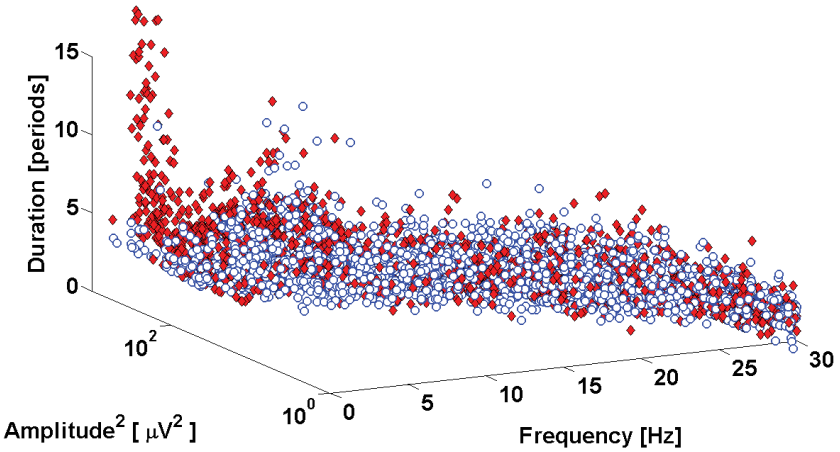

Fig. 2 The set of wave trains detected in the group of de novo Parkinson's disease and the control group. The abscissa indicates frequencies of the wave trains. The ordinate indicates squared amplitudes of the wave trains in a logarithmic scale. The applicate indicates durations of the wave trains. The patients are indicated by dark red diamonds and the healthy volunteers are indicated by light circles.

Let us consider a set of wave trains detected in a group of de novo Parkinson's disease patients and a control group (see figure 2). The group of patients includes 16 subjects with the first stage of Parkinson's disease receiving no treatment. The group of healthy volunteers includes 19 subjects. All patients have a tremor in the right hand. The patients were diagnosed according to the standard Hoehn and Yahr scale. All patients and volunteers were right-handers. EEG was recorded in a non-standard condition [4]. Namely, a subject was instructed to keep a special pose to provoke a tremor: the arms were placed on armrests of the chair; the palms were straightened, placed in a vertical plane, and stretched a bit; the feet were stretched a bit and touched the floor by the heels only. The eyes were closed during the recording. A 41-channel digital EEG system Neuron-Spectrum-5 (Neurosoft Ltd.) was used for the data acquisition. The sampling rate was 500 Hz. The 0.5 Hz high-pass filter and the 50 Hz supply-line filter were used. Three EEG records were acquired for every subject with interruptions for a rest and a relaxation. The duration of every record was about 2 minutes. Then the best of three records was selected that contains a minimal number of artifacts. A standard 10x20 EEG acquisition schema was used. See [3] for details of the experimental setting, data preprocessing, and wavelet analysis. In this paper, the wave trains are considered in the C4 electrode that is ipsilateral to the tremor hand and contralateral to the no tremor hand. We analyze the ipsilateral ("healthy") hemisphere, but not the contralateral ("ill") hemisphere, because our idea is to use the "healthy" hemisphere as a model for exploration of the preclinical period of Parkinson's disease. The wave trains are scattered in a 3D space based on the squared amplitude, frequency, and duration of the wave trains.

Let *MinFreq*, *MaxFreq* are frequency bounds of 3D area S (a parallelepiped S) in the space of the wave trains. Let *MinAmpl*, *MaxAmpl* are amplitude bounds of the area S; and *MinDurat*, *MaxDurat* are duration bounds of the area S. One can calculate a number of wave

trains per second located in the area *S* in every individual patient and healthy volunteer and create histograms of the quantity of the wave trains per second (see an example in figure 3). A statistical difference between the diagrams may indicate that the area *S* contains wave trains that are typical for Parkinson's disease, but not for the control group, or vice versa. A second interesting issue is whether one can specify a threshold (a limit of the number of the wave trains in the area *S*) that separates adequately the histograms, because the presence of such threshold means that the quantity of the wave trains in the area *S* may be used for diagnosis of the preclinical period of Parkinson's disease. For instance, there is a strong statistical difference between the histograms in the figure 3 (the Mann-Whitney test, $p < 0.008$). The diagram demonstrates that a typical number of the wave trains in the control is 0.4 per second and more in the given frequency band. At the same time, a typical number of the wave trains in the patients is less than 0.4.

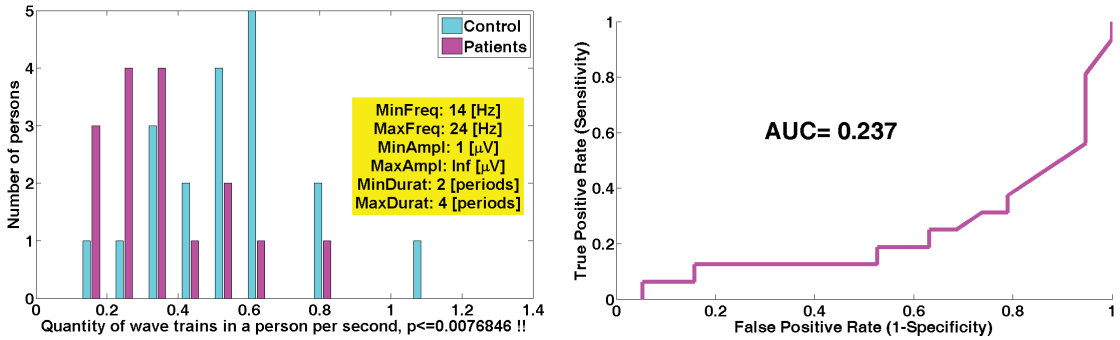

Fig. 3 On the left: histograms of the quantity of the wave trains per second in the patients and the control group. The wave trains are considered in a parallelepiped *S* bounded by the following limits: a frequency range is 14-24 Hz, an amplitude range is 1 uV^2 and more, the duration range is 2-4 periods. The patient histogram is indicated by the dark magenta color; and the control histogram is indicated by the light cyan color. On the right: a ROC curve based on the histograms. The abscissa indicates the False Positive Rate. The ordinate indicates the True Positive Rate. The area under the ROC curve (AUC) indicates whether the area *S* is applicable for separation of the patients and the control group. AUC < 0.5 indicates that the wave trains quantity is greater in the control group than in the patients.

Let us consider a threshold *Q* of the wave trains quantity in the histograms. Let us utilize this threshold as an indicator of Parkinson's disease, that is, a quantity of the wave trains per second greater than Q in a person *N* in the given area *S* will indicate that the person *N* is probably ill. Thus, the True Positive Rate (TPR) indicates the number of the patients that were diagnosed properly using the threshold *Q*; and the False Positive Rate (FPR) is the number of the controls that were mistakenly diagnosed as Parkinson's patients. A ROC curve can be created based on the histograms of the wave trains quantity, that is, a diagram that indicates a relation between the TPR and FPR for various values *Q* (see figure 3). The area under the ROC curve (AUC) is a standard indicator of the quality of the ROC curve; big values of AUC (that are much more than 0.5) and small values of AUC (that are much less than 0.5) indicate that the given area *S* may be prospective for making clinical diagnosis.

Thus, in mathematical terms, the goal of our investigation is searching such areas in the 3D space of the wave trains, where AUC differs sufficiently from 0.5 and is approached to 1 or to 0. AUC > 0.5 indicates that the wave trains quantity is greater in the patients than in the controls. Similarly, AUC < 0.5 indicates that the wave trains quantity is greater in the control group. An exhaustive search of the values *MinFreq*, *MaxFreq, MinAmpl*, *MaxAmpl, MinDurat*, and *MaxDurat* can be implemented to investigate the 3D space, but we prefer an

accurate consideration of different slices of the space using various 2D and 3D diagrams not to miss any interesting regularities in the space of the wave trains. Several examples of this analysis are considered below.

Let us compute AUC values for various frequency ranges. In figure 4 the functional dependence of AUC is shown, where the arguments of the function are the *MinFreq* and *MaxFreq* bounds. The frequency values varied from 0 to 25 Hz (with the 1 Hz step); the *MinAmpl*, *MaxAmpl, MinDurat*, and *MaxDurat* were constant: *MinAmpl* = 1, *MaxAmpl* = infinity, *MinDurat* = 0, *MaxDurat* = infinity. The diagram in figure 4 reveals two interesting frequency ranges that may be prospective for research. The first range is alpha or mu (a red region) and the second range is beta (a dark blue region). This is a confirmation of the regularity (the significant decrease of the wave train number in beta) discovered by a group analysis and reported in [3]. Moreover, a "good" value AUC = 0.18 indicates that the beta frequency range may be prospective for making clinical diagnosis. The peak in the mu frequency range indicates that interesting group differences may exist in this band too, however the value AUC = 0.71 indicates that the mu range is unlikely to be useful for making diagnosis.

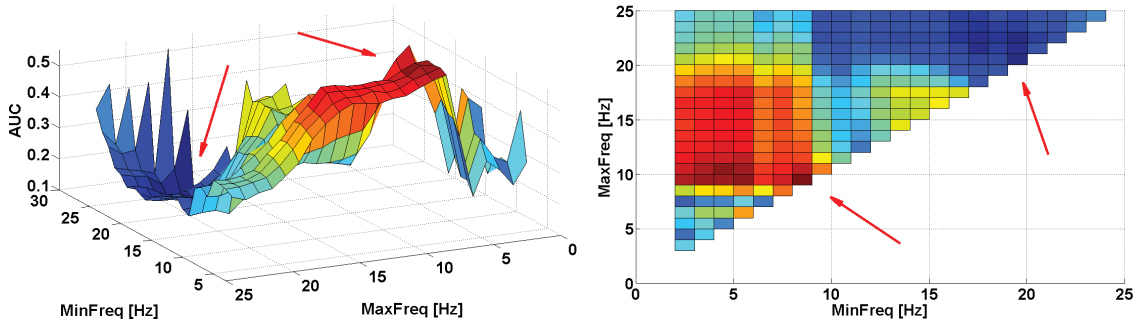

Fig. 4 The diagram of the AUC value calculated for various *MinFreq* and *MaxFreq* bounds. The frequency varied from 0 to 25 Hz with the 1 Hz step. *MinAmpl* = 1, *MaxAmpl* = infinity, *MinDurat* = 0, *MaxDurat* = infinity. Interesting areas in the diagram are indicated by arrows. On the left: a 3D view of the diagram; on the right: the top view of the same diagram.

Let us investigate a *MinDurat–MaxDurat* slice of the AUC values space (see figure 5). The diagram demonstrates that a typical duration of the beta wave trains that are present in the control (but are missed in Parkinson's disease) is 2.9-3.6 periods (these bounds are co-ordinates of a peak in the diagram in figure 5).

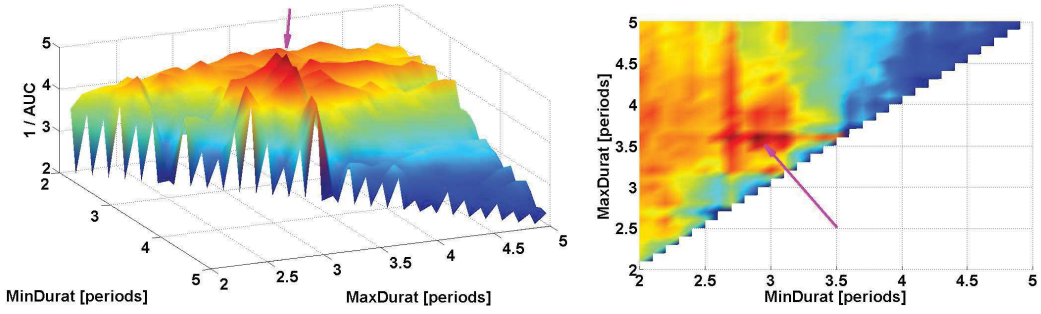

Fig. 5 The diagram of the AUC value calculated for various *MinDurat* and *MaxDurat* bounds. Note that the reciprocal values 1/AUC are shown in the diagram to emphasize minima in the AUC function. The wave train duration bounds varied from 2 to 5 periods; the step was 0.1. *MinFreq* = 14, *MaxFreq* = 24, *MinAmpl* = 1, *MaxAmpl* = infinity. An interesting area in the diagram is indicated by the arrow. On the left: a 3D view of the diagram; on the right: the top view of the same diagram.

The preliminary results of the research give evidence that EEG analysis method based on the wave trains is prospective for: 1) looking for group regularities in the early stages of Parkinson's disease that gives a basic knowledge about the disease and compensatory mechanisms in the cortex; 2) for searching EEG features that are prospective for the early stages and, possibly, the preclinical period of Parkinson's disease diagnostics. The method is implemented in a special software package [5] for analyzing EEG, EMG, and accelerometer signals.

Authors are grateful to Galina D. Kuznetsova and Alexander F. Polupanov for co-operation and a help in the research and Yuriy V. Obukhov for a help in the statement of the problem. We acknowledge a partial financial support from the Russian Foundation for Basic Research, grants 16-37-00426 and 15-07-07846.

References

[1] O'Reilly C., Nielsen T., Automatic sleep spindle detection: benchmarking with fine temporal resolution using open science tools // Frontiers in Human Neuroscience. – 2015. – Vol. 9:353. – http://doi.org/10.3389/fnhum.2015.00353 .

[2] Parekh A., Selesnick I.W., Rapoport D.M., Ayappa I., Sleep spindle detection using time-frequency sparsity // IEEE Signal Processing in Medicine and Biology Symposium, Dec. 2014. – Philadelphia, PA: IEEE. – pp. 1-6.

[3] Sushkova O.S., Morozov A.A., Gabova A.V. A method of analysis of EEG wave trains in early stages of Parkinson's disease // International Conference on Bioinformatics and Systems Biology (BSB-2016), 4-6 March 2016, Allahabad, India. – Allahabad: Indian Institute of Information Technology, 2016.

[4] Andreeva Y., Khutorskaya O. EMGs spectral analysis method for the objective diagnosis of different clinical forms of Parkinson's disease // J. Electromyography and Clinical Neurophysiology. – 1996. – Vol. 36, No. 3. – pp. 187-192.

[5] Certificate No. 2015660136. A program for signal processing and statistical analysis of parameters of peaks of envelopes of EEG, EMG, and accelerometer signal for experimental investigation of Parkinson's disease: a certificate of a government registration in the Computer program register / O.S. Sushkova, A.A. Morozov; declarants and rightholders: O.S. Sushkova, A.A. Morozov. – No. 2015617150; claimed 28.07.2015; registered 22.09.2015.

Early breast cancer detection by using radar aids

***I.L. Alborova*[1], *L.N. Anishchenko*[1]**

1. Biomedical Engineering Department, Bauman Moscow State Technical University, 5, 2-d Baumanskaya str., Moscow 105005, Russia

Breast cancer is the most common cancer in women worldwide, with nearly 1.7 million new cases diagnosed in 2012 (second most common cancer overall). This represents about 12% of all new cancer cases and 25% of all cancers in women [1]. This is due, first of all, late diagnosis of this disease, delayed treatment of patients, and the lack of highly sensitive methods for establishing early (pre-clinical) stages of mammary gland cancer, insufficiently quality of metastases diagnosis in regional lymph nodes.

The most effective way to increase treatment success and reduce mortality from breast cancer is the additional application of non-invasive methods allowing to detect the tumors at the earliest stages of tumorigenesis.

This paper describes the possibility of solving this problem through the use of radar. Emitted by the radar electromagnetic wave is scattered and absorbed in the media (breast tissue) due to the differences in the dielectric properties between tumors and normal tissues [2]. This principle is a base for the radar usage in visualization the breast internal structure.

The possibility of using this method to determine the dielectric inhomogeneities in the breast tissue has been investigated in experiments using breast phantom. It consisted of the following materials: adipose and muscular tissues of animal origin. We did not use the breast

phantoms based on gelatin, due to it unstable in time dielectric properties. For the phantom proposed in the present paper they remain stable for much longer period in contrast to gelatin phantoms. In addition, this type of materials is convenient to create different configurations of phantoms, and it allows localization the inclusions at any place and depth (see. Fig. 1).

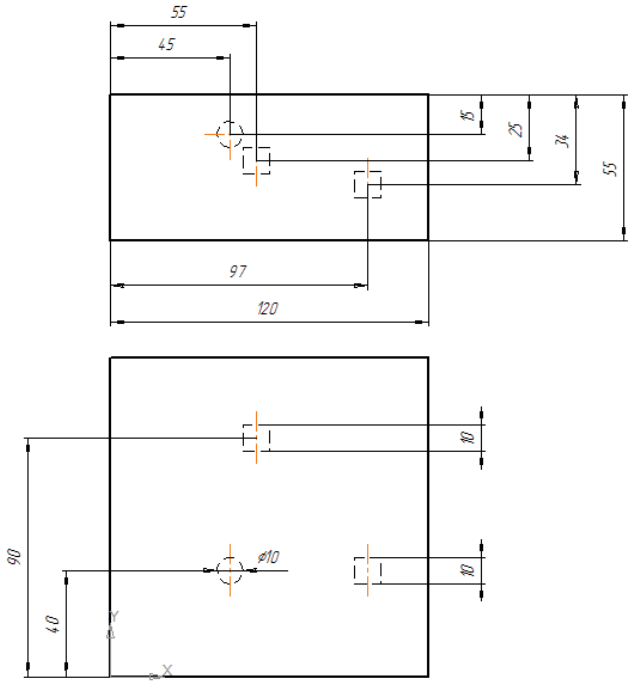

moved on the platform. Figures 3-5 show the results of the experiment. Located inclusions were marked with a red line.

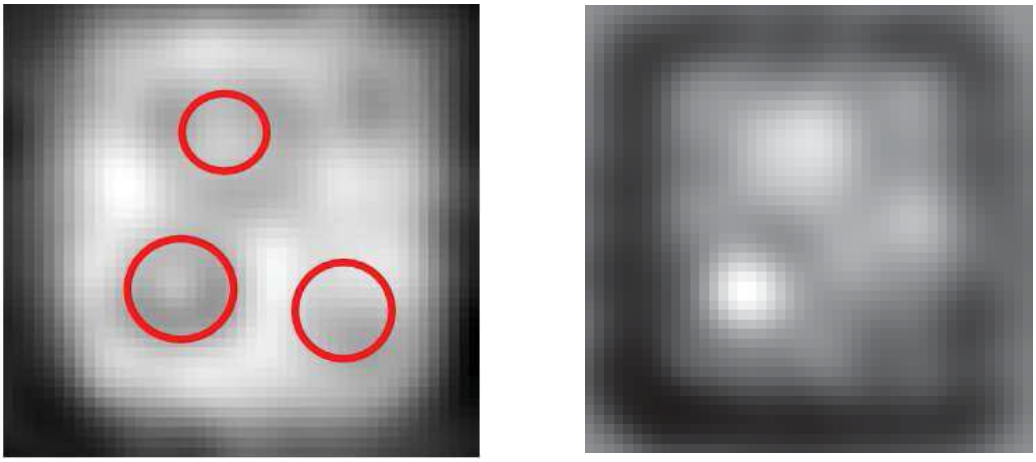

I-quadrature Q-quadrature

Fig. 3 Image of the phantom with inclusions on probing frequency at 6,1 GHz

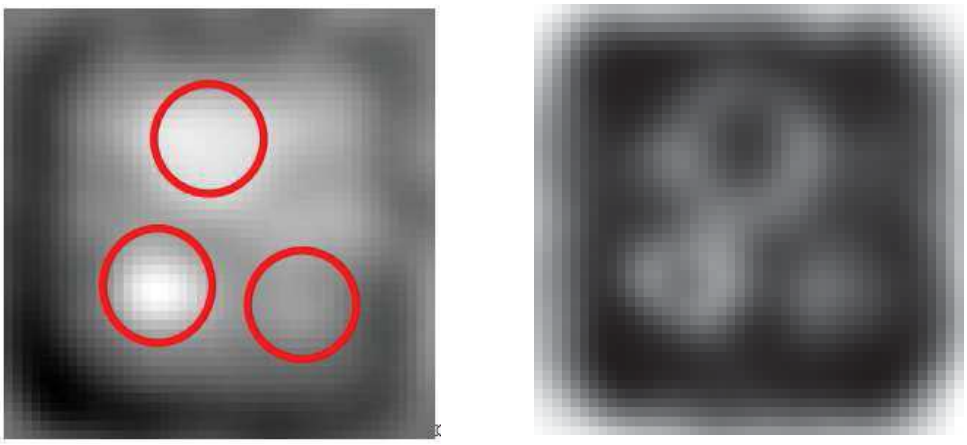

I-quadrature Q-quadrature

Fig. 4 Image of the phantom with inclusions on probing frequency at 5,5 GHz

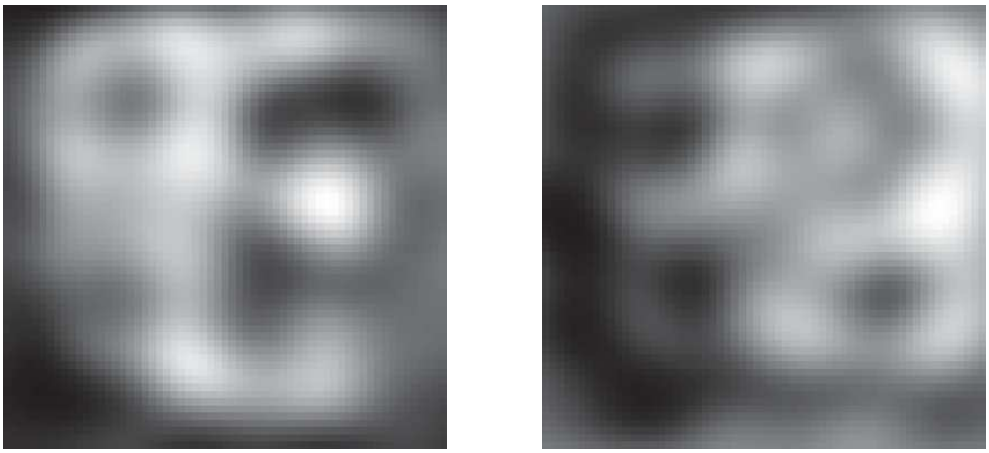

I-quadrature Q-quadrature

Fig. 5 Image of the phantom without inclusions on probing frequency at 6,1 GHz

There are artifacts on image caused by the edge effect. To solve this problem in the future work we plan to conduct experiments with the use of models with larger geometric dimensions.

References

[1] Ferlay J, Soerjomataram I, Ervik M, Dikshit R, Eser S, Mathers C, Rebelo M, Parkin DM, Forman D, Bray, F. GLOBOCAN 2012 v1.1, Cancer Incidence and Mortality Worldwide: IARC CancerBase No. 11 [Internet]. Lyon, France: International Agency for Research on Cancer; 2014. Available from: http://globocan.iarc.fr, accessed on 16/01/2015

[2] M. Lazebnik, L. McCartney, D. Popovic, C.B. Watkins, M.J.Lindstrom, J. Harter, S. Sewall, A. Magliocco, J.H. Booske, M.Okoniewski, and S.C. Hagness, "A large – scale study of the ultrawideband microwave dielectric properties of normal breast tissue obtained from reduction surgeries", Physics in Medicine and Biology, Vol. 52, 2637-2656 (2007).

Human emotions valency and level change monitoring by means of the eeg and speech signals analysis

***N.N. Filatova*[1], *K.V. Sidorov*[1]**

1. Tver State Technical University, 22 Afanasy Nikitin Emb., 170026 Tver, Russia

The problem of human emotions monitoring is important for many areas of human activity including medicine. The estimates of patient's emotional states can be used for phylactic or treatment purposes (e.g., when estimating psychomatic, psychomotor and somatovegetal disorders; neurosis-like and neurotic syndromes; emotionally affective and depressive disorder, etc.). In this context, recently various Russian branch enterprises and companies (Speech Technology Center, Medicom MTD, Neurosoft, Neuromatix, RusBITech et al.), as well as research and educational companies and institutes (Volgograd State Technical University, Southern Federal University, Tomsk Polytechnic University, Moscow State Technical University, Institute of Higher Nervous Activity and Neurophysiology of RAS, Institute of Control Sciences of RAS et al.) have developed and implemented specific software and instrumental complexes, as well as information-measurement systems. The systems are focused on human emotions monitoring and diagnostics using biomedical signal interpretation recorded in a contact and/or non-contact way using various instrumental biosensors. Such technologies, as well as foreign researchers' developments [1-3] allow generating regularity descriptions and forming sets of production rules, which describe human emotions according to different components (valence, arousal, dominance et al.) using the analysis of biomedical signals [4] (electrophysiological signals (EEG, EMG, ECG, EOG, GSR et al.); speech signals; video fragments of facial expressions and postures or gestures; biochemical indicators of circulatory and respiratory systems; parameters of typing or handwriting, etc.).

The initial data for customizing and testing developed complexes and systems are instrumental signal databases [5-7], that display changes in testees' emotional states when applying various stimulants (audio-visual, gustatory, somatosensory or olfactory). In most cases emotions in signal samples, their valence and level are defined based on expert estimation. As the processes of human emotianal perception is subjective, databases usually include signal samples with strong emotions of testees.

This paper presents the research results obtained using a bioengineering system "*EEG/S*" [8, 9]. The system is used for examination and monitoring of testees' emotional reactions

changes according to various physical stimuli. A pilot model of "*EEG/S*" system is a software and instrumental tool that includes verified and gauged recording and processing means for EEG patterns and speech signal samples. "*EEG/S*" system involves audio auditory, visual and olfactory human analyzers and enables parallel recording of biomedical signals (EEG as contact recording, speech signals as non-contact recording).

"*EEG/S*" system allowed creating a multimodal database (*MDB*) of emotions, which contains accurate samples of two types of biomedical signals recorded with objective assurance of changes in testees' emotional response valence and level. Formed experimental sampling of EEG patterns and speech samples were used to create a mathematical model and production rules for interpretation of emotional valence and level.

In order to describe samples of speech signals and EEG patterns the authors use characteristics of a reconstructed attractor y_n (Takens' theorem) [10] that is invariant to a signal type:

$$y_n = (x_n, x_{n+\tau}, ..., x_{n+(m-1)\tau}), \quad n = 0, ..., s-1, \quad s = N-(m-1)\tau, \tag{1}$$

where N is a total number of time series elements (x_1, x_2, …, x_N); τ is a time delay between time series elements; m is an embedding dimension (Fig. 1, a).

An optimal value of τ (1) corresponds to a temporal value when the autocorrelation function $B(\tau)$ crosses zero mark for the first time. An optimal value of m (1) is defined from a perspective of saturation (we use determining values of a correlation integral $C(E)$ and correlation dimension D_2) [11]. The paper proposes an algorithm for rough estimation of attractors' m-dimensional projections sizes, e.g., when m=3 (Fig. 1, b) and m=2 (Fig. 1, c). For all m-projections with four quadrants we calculate a maximum length vector. Based on such estimates with all quadrants we determine an average vector for one (i-th) attractor's projection $\overline{A}^i_{\max} = 0{,}25\sum_{j=1}^{4} A^{i,j}_{\max}$, $A^{i,j}_{\max} = \max\{\sqrt{x_h^2 + x_{h+\tau}^2}\}$, where x_h, $x_{h+\tau}$ are time series values for h-th and $h+\tau$-th moments of time; i is a projection number; $i = \overline{1,3}$ (i=1 when x_n–$x_{n+\tau}$; i=2 when x_n–$x_{n+2\tau}$; i=3 when $x_{n+\tau}$–$x_{n+2\tau}$); j is a projection quadrant number; $j = \overline{1,4}$. Each description of EEG pattern and speech sample is represented as follows [9]:

$$A(z) = \bigcup_{i=1}^{3} \overline{A}^i_{\max} \bigcup_{j=1}^{4} A^{i,j}_{\max}, \; B(k) = |b_w|_{p\times 1}, \; b_w = \bigcup_{i=1}^{3} \overline{B}^i_{\max} \bigcup_{j=1}^{4} B^{i,j}_{\max}(w), \; w = \overline{1,P}, \; P \le 8, \tag{2}$$

where $A(z)$, $B(k)$ are descriptions of attractor's characteristics that are reconstructed according to speech signals and EEG, respectively; $A^{i,j}_{\max}$, $B^{i,j}_{\max}$ is a maximal vector length of j-th quadrant in i-th projection; $\overline{A}^i_{\max}$, $\overline{B}^i_{\max}$ is a length of an aggregate vector of i-th projection; z is a number of speech signal object; $z = \overline{1,270}$; k is a number of EEG object; $k = \overline{1,270}$; w is a number of EEG lead (the EEG patterns analysis has been carried out in 8 most informative leads of the right hemisphere [9]).

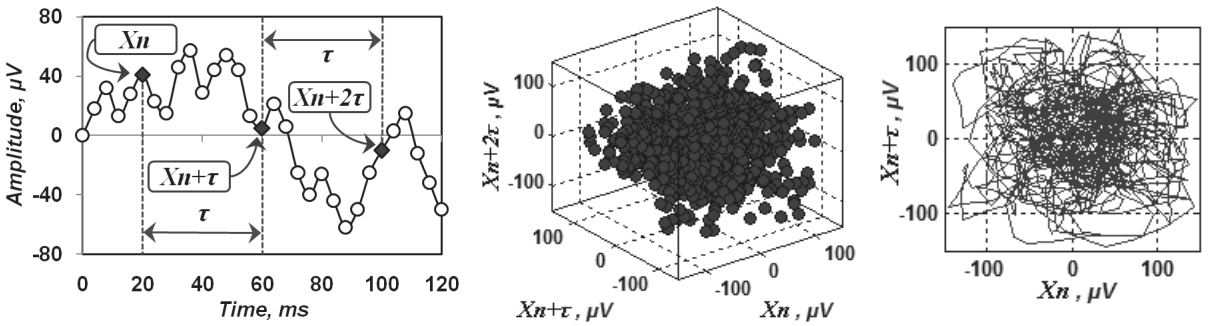

(a) (b) (c)

Fig. 1 Attractor reconstruction.

Therefore, according to the description (2) every speech signal object in *A(z)* form is described by 15 characteristics (Fig. 2, a), every EEG object in *B(k)* form is described by 120 characteristics (Fig. 2, b).

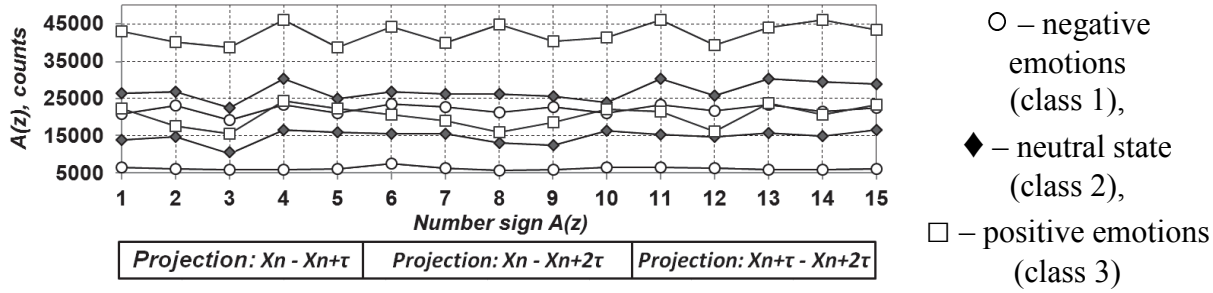

(a) – a range of *A(z)* characteristics according to speech signals

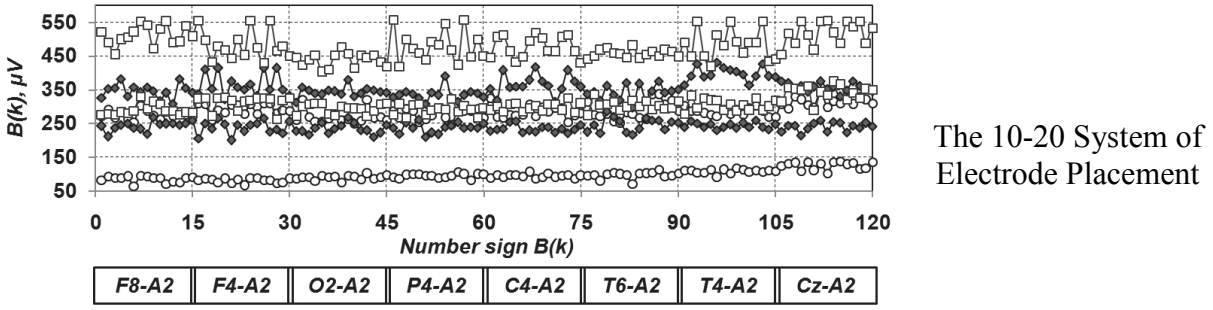

(b) – a range of *B(k)* characteristics according to 8 EEG leads in the right hemisphere

Fig. 2 A range of characteristics of *A(z)* and *B(k)* descriptions (2) according to the classes of emotions.

The obtained characteristic curves (Fig. 2, a and Fig. 2, b) show the lack of linear split classes (class 2 and class 3), as well as significant classes intersections (class 1 and class 2) according to speech signals and all EEG leads. Description of characteristics (2) is transferred into a linguistic scale and are applied to monitor human emotions valence.

In order to monitor the changes of human emotional reactions level we use a description of characteristics for attractor's trajectory density. In this case every projection (x_n–$x_{n+\tau}$, x_n–$x_{n+2\tau}$, $x_{n+\tau}$–$x_{n+2\tau}$) is covered by a regular grid in increments of $\delta=const$. Based on a grid model we form a density matrix M_P (*i* is a row number; $i=1,2,\ldots,N$; *j* is a column number; $j=1,2,\ldots,M$) (Fig. 3, a). We can calculate a density of a certain *i*,*j*-cell using the equation $P_{i,j}=(H_{i,j}+K_{i,j})/S_{i,j}$, where $H_{i,j}$ is a number of points inside the cell; $K_{i,j}$ is a number of points at the boundary of the cell; $S_{i,j}$ is a cell area; $S_{i,j}=\delta^2$. For central cells of M_P matrix are of special interest (Fig. 3, b) due to the fact that they can be used for constructing a characteristic curve of sign $P_{i,j}$ (Fig. 3, c). Characteristic curves (Fig. 4, a and Fig. 4, b) show $P_{i,j}$ density variation of four central cells in the matrix M_P for corresponding classes of emotions. In order to display cell padding uniformity in the matrix M_P we introduce an additional characteristic *F*, which describes the number of zero cells of attractor's projections (Fig. 4, c and Fig. 4, d).

Testing of an emotion interpreter from "*EEG/S*" bioengineering system has been carried out in two educational institutions (Tver State Technical University and Tver State Medical Academy). Students, postgraduates, teachers and staff members of the institutions were the testees. They had age and gender differences (a multimodal database of emotions, *MDB*). In order to estimate interpreter efficiency independently, we tested it using speech samples from the German database *Emo-DB* [6], which presents seven emotion classes. Quantitative estimation involves an information bias indicator $Q=(N_{error} / N_{all})*100$ %, where N_{error} is a quantity of incorrectly classified objects; N_{all} is a total number of objects. As a result, we obtain the following information bias values according to emotional valence monitoring:

1) Q=8 % for EEG patterns from *MDB*; 2) Q=5 % for speech samples from *MDB*; 3) Q=13 % for speech samples from the database *Emo-DB*.

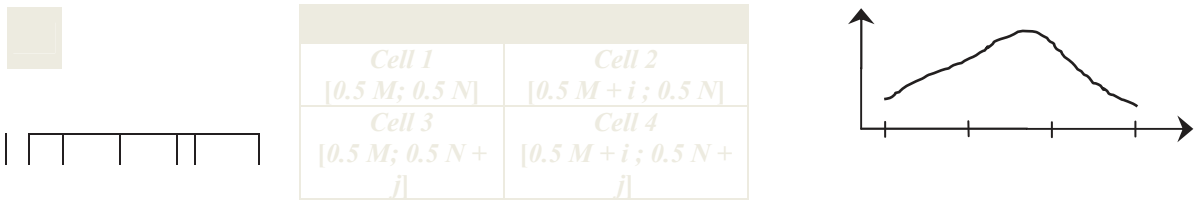

(a) (b) (c)

Fig. 3 Attractor's density.

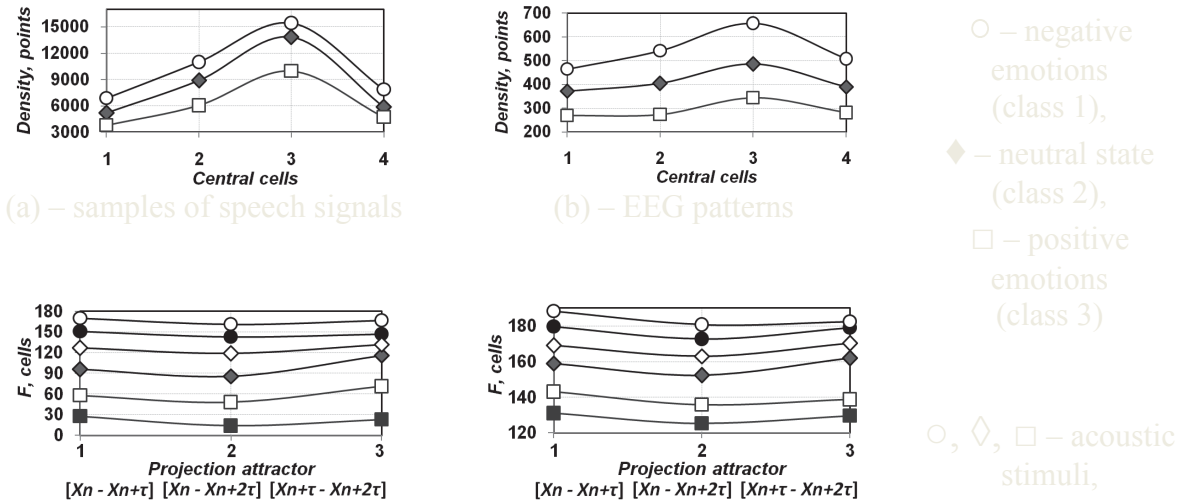

(a) – samples of speech signals (b) – EEG patterns

○ – negative emotions (class 1),
♦ – neutral state (class 2),
□ – positive emotions (class 3)

○, ◊, □ – acoustic stimuli,
●, ♦, ■ – visual stimuli

(c) – samples of speech signals (d) – EEG patterns

Fig. 4 The centers of emotional classes for x_n–$x_{n+\tau}$ projection of an attractor.

To sum up, the research results showed high accuracy of automatic interpretation of human emotion valence and level. It determined a concurrence with testees' self-assessment. It also defined correlation with results and facts from foreign independent sources [12, 13].

This work is partially supported by the Russian Foundation of Basic Research (project no. 14-01-00719-a).

References

[1] P. A. Abhang and B. W. Gawali, "Correlation of EEG Images and Speech Signals for Emotion Analysis", British Journal of Applied Science & Technology (BJAST) **10**, 1–13 (2015).

[2] S. Lokannavar, P. Lahane, A. Gangurde, and P. Chidre, "Emotion Recognition Using EEG Signals", International Journal of Advanced Research in Computer and Communication Engineering (JARCCE) **4**, 54–56 (2015).

[3] Z. Lan, O. Sourina, L. Wang, and Y. Liu, "Real-Time EEG-Based Emotion Monitoring using Stable Features", The Visual Computer **32**, 347–358 (2016).

[4] R. M. Rangayyan, *Biomedical Signal Analysis*, 2nd. ed., (IEEE Press–Wiley, New York, 2015).

[5] S. Koelstra, C. Muhl, M. Soleymani, J.-S. Lee, A. Yazdani, T. Ebrahimi, T. Pun, A. Nijholt, and I. Y. Patras, "DEAP: A Database for Emotion Analysis using Physiological Signals", IEEE Transactions on Affective Computing (TAC) **3**, 18–31 (2012).

[6] F. Burkhardt, A. Paeschke, M. Rolfes, W. Sendlmeier, and B. Weiss, "A Database of German Emotional Speech", in Proceedings of the 9th European Conference on Speech Communication and Technology (Interspeech'2005), 4-8 Sept. 2005, Lisbon, PRT, 1517–1520 (2005).

[7] V. Makarova and V. A. Petrushin, "RUSLANA: A Database of Russian Emotional Utterances", in Proceedings of the 7th International Conference on Spoken Language Processing (ICSLP'2002), 16-20 Sept. 2002, Denver-Colorado, USA, 2041–2044 (2002).
[8] N. N. Filatova and S. A. Terekhin, "Bioengineering System for Research on Human Emotional Response to External Stimuli", in Proceedings of the International Conference on Biomedical Engineering and Computational Technologies (SIBIRCON), 28-30 Oct. 2015, Novosibirsk, Russia, 13–17 (2015).
[9] N. N. Filatova, K. V. Sidorov and L. V. Iliasov, "Automated System for Analyzing and Interpreting Nonverbal Information", International Journal of Applied Engineering Research (IJAER) **10**, 45741–45749 (2015).
[10] F. Takens, "Detecting Strange Attractors in Turbulence", Lecture Notes in Math. **898**, 366–381 (1981).
[11] J.-P. Eckmann and D. Ruelle, "Ergodic Theory of Chaos and Strange Attractors", Rev. Mod. Phys. **57**, 617–655 (1985).
[12] Y. Liu, O. Sourina and M. K. Nguyen in, *Transactions on Computational Science XII: Special Issue on Cyberworlds*, M. L. Gavrilova, C. J. K. Tan, A. Sourin, O. Sourina eds. (Springer–Verlag, Berlin Heidelberg, 2011).
[13] Y. Liu, O. Sourina in, *Transactions on Computational Science XXIII: Special Issue on Cyberworlds*, M. L. Gavrilova, C. J. K. Tan, X. Mao, L. Hong eds. (Springer–Verlag, Berlin Heidelberg, 2014).

Artificial images for leukocyte classification using convolutionnal neural networks

J. V. Stadelmann[1]

1. European Medical Systems (BME-1) dept, Bauman Moscow State Technical University (BMSTU)
2nd Baumanskaja St. n°5, bld 1, Moscow, 105005, Russian Federation

Blood count is one of the most frequently required analysis that are required by physician during their clinical activities [1, 2]. During a complete blood count, thrombocytes and other blood cells, including leukocytes are counted. Leukocytes are the immune system's main agent, therefore assessment of their formula is used in the numerous diseases' diagnostics. Both its quantitative and qualitative changes are representative features for diagnosis (Fig.1) [2, 3].

In order to assess the leukocyte formula, one may make use of flow cytometry methods. Those methods are based on the analysis of the leukocytes' impedance and scattering properties. As a results, those apparatuses present the overall leukocyte number for every class and as well their relative concentration. However the analysis of leukocyte morphological markers using flow cytometry apparatuses is impossible. And if the received results are different from haematological norms, a visual confirmation is generally made under the microscope [4].

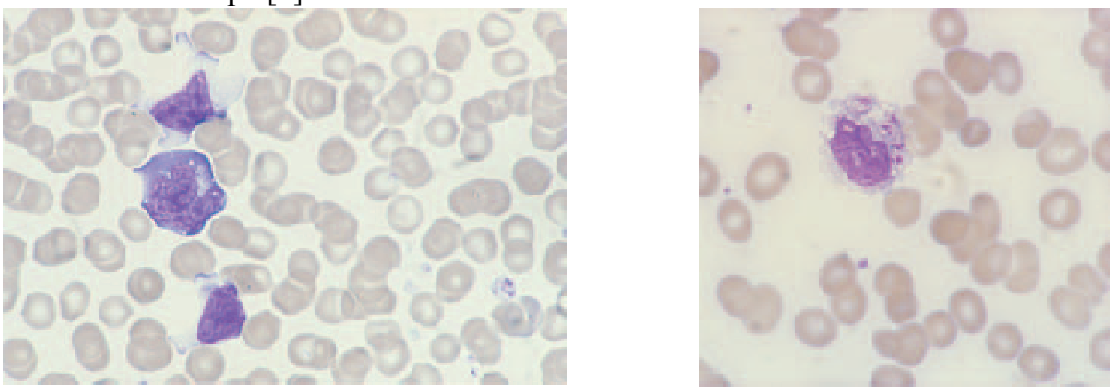

a b

Fig. 1 Blood smear images showing morphological markers of (a) mononucleosis and (b) HIV [2]

The second method for blood formula assessment is the blood smear visual exploration under a microscope. In order to use this method, one has to prepare a blood smear that will be analyzed by a laboratory technician under a microscope. The standard procedure states that this analysis take in account a hundred cells [5, 6]. In consequence this method lacks of statistical significance. Therefore the development of automatic visual system for blood formula assessment is deemed necessary.

The usual procedure for automatic visual analysis includes several steps such as the image quality analysis. [5, 7, 8] Leukocyte detection, in result of which every leukocyte is shown in the center of a subimage. Segmentation separates the leukocyte from surrounding erythrocyte fragments and background. Segmentation is time consuming and its quality difficult to evaluate objectively. It results in separated images of leukocyte nucleus and cytoplasm [7, 8]. After segmentation, the process goes onto the evaluation of the feature vector that is used for multidimensional logistic regression, thus achieving classification.

The comparison of the different steps in visual blood smear exploration with its automated counterpart yields that two automated steps that are detection and segmentation do not find their reflection in visual exploration. Therefore an efficient method for better leukocyte classification lays in the development of classificators working without segmentation.

Artificial neurons are simple computation units that evaluate the weighted of their inputs. Afterwards artificial neurons apply a given function, usually sigmoid or arctangeant, to the weighted sum in order to compute their outputs [9, 10].

The use of those computation units in groups, called networks, allows to approximate complex function. For instance the approximation of the identity function between the networks' input and output is a very efficient method for dimensionality reduction and input description [9, 10]. It requires the definition of the network's topology and weights. Topology is generally left to the experimentator's choice. The weight definition is usually achieved by means of error backpropagation [9].

Convolutionnal neurons are a variant on artificial neurons for which the input is not a vector but a matrix. The neurons compute a convolution of this matrix with a convolution kernel determined beforehand. This allows for the highlighting of feature inside the matrix and thus minimize the dimensionality of the input [10, 11]. Since spatially close point output similar convolution results, the best results are separated by means maximum pooling neurons after the convolution layer.

The network used for classification consited in three convolution and pooling layer pairs to which two identity autoencoders were appended. Convolution layers maintained dimensionnality using zero-padding on the images boundaries. The dimensionnality reduction was performed in the pooling stages and with the help of restricted bolzmann machine inspired autoencoders. In order to add robustness, the first autoencoder was overdefined with 64 hidden units. The network is illustrated on figure 2. The image database used for training and scoring is presented in the table 1. The scoring results are in table 2.

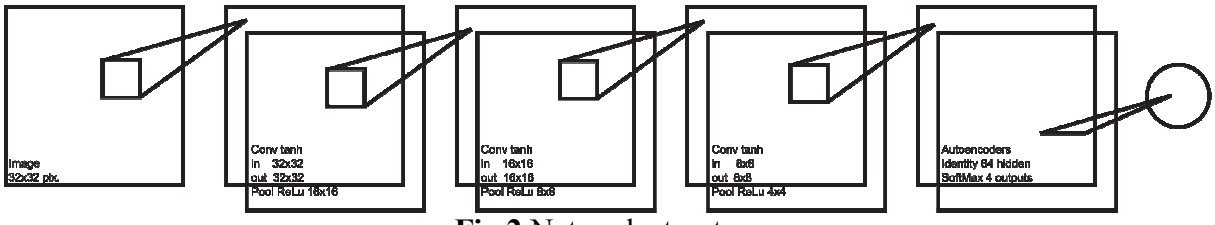

Fig.2 Network structure

Table 1 – Database composition

	Training	Control
Eosinophiles	18	19
Lymphocytes	100	185
Monocytes	24	24
Neutrophiles	100	233

Table 2 – Network scoring results

	Number	Scoring results			
		Eosinophiles	Lymphocytes	Monocytes	Neutrophiles
Eosinophiles	19	3	4	5	7
Lymphocytes	185	0	172	5	8
Monocytes	24	1	6	16	1
Neutrophiles	233	1	9	0	223

The probability of correct classification was 89,8%. The low classification rates for eosinophiles and monocytes are caused by their number in the training sets. Having at hand large amounts of data for classification is often a prerequisite for low error rates. Both classical database for pattern recognition algorithm control, MNIST and CIFAR-10, both consist in more than 50 000 images for training and in 10 000 examples over all class for control. Although it is not made clear for the CIFAR-10 database, it is known that the MNIST database is partially formed of artificial images that have been skewed, rotated and compressed [11, 12]. Thus image distortion and rotation may be used in order to provide enough images to form balanced training sets. Figure 3 provides an example of distorted images obtained from the same source lymphocyte. However, as shown on figure 3, the creation of new images requires the reoccurring visual verification of the database.

a b c

Fig. 2 Original lymphocyte image (a), mildly distorted image (b), lymphocyte distorted beyond recognition (c)

The leukocyte classification task may be characterized as a completely defined and closed classification task. The number of different classes is known and can not be changed once the system is trained. Moreover images of blood cells are well available and allow the fast creation of decent datasets. Those characteristics of this specific classification task make it a perfect candidate for the development of method for open and under-defined classification methods. Using the data reduction capability of autoencoders, one can imagine the dimensionality reduction to four unlabelled classes. And afterward applying labels to the image using an extremely reduced labeled set.

References

[1] G.I. Kozinets, Blood and bone marrow cell atlas. – Moscow, Triad-X, 1998, 150p.
[2] Bain B.J. Blood Cells – A Practical Guide. Malden: Blackwell Publishing Ltd, 2006. 476 p.
[3] A.I. Vorobyev, Clinicl-diganostic values of laboratory indicators in haematology. Russian Academy of Medical Science, 2001, 17p.
[4] B.H. Hyun, G.L. Gulati, J.K. Ashton Differential Leukocyte Count: Manual or Automated, What Should It Be? Yonsei Medical Jounal. 1991. Vol. 32. №. P. 283 – 291.
[5] A.V. Samorodov, Biotechnical system for erythrocyte morphometry analysis. PhD Dissertation, Moscow, 2002, 168p.
[6] J.V. Stadelmann, Biotechnical system for automatic white blood formula assessment, PhD Dissertation, Moscow, 2012, 96p.
[7] A.V. Samorodov Building intelligent systems for the analysis of microscopic images in medicine and biology. Pattern Recognition and Image Analysis. (Advances in Mathematical Theory and Applications). 2013. Т. 23. № 4. С. 508-511.
[8] J. V. Stadelmann, I.N. Spiridonov. Automatic leukocyte classification on blood smear images. Biomedical Engineering, 2012, n°2, pp. 43-47
[9] A. Ng, J. Ngiam, C.Y. Foo, Y. Mai, C. Suen. Unsupervised Feature Learning and Deep Learning Tutorial. Standford University Ressources, Режим доступа : http://ufldl.stanford.edu/wiki/index.php/UFLDL_Tutorial (дата обращения 01.04.2016)
[10] Y. Bengio, Practical Recommendation for Gradient-Based Training of Deep Architectures arXiv:1206.5533v2, 2012 Режим доступа : http://arxiv.org/pdf/1206.5533v2.pdf (дата обращения 01.04.2016)
[11] A. Krizhevsky. Learning Multiple Layers of Features from Tiny Images // Computer Science Department, Toronto University, Toronto, 2009, 60p.
[11] Y. LeCun, L. Bottou, Y. Bengio, and P. Haffner. "Gradient-based learning applied to document recognition." Proceedings of the IEEE, 86(11):2278-2324, November 1998

$$F_{test\ name} = \alpha x_1 + \beta x_2 + \gamma x_3 + \cdots + \omega x_n + C$$

scaling is not merely a procedure, but rather the way the most efficient placement of objects observed approximately preserving the distance between them.

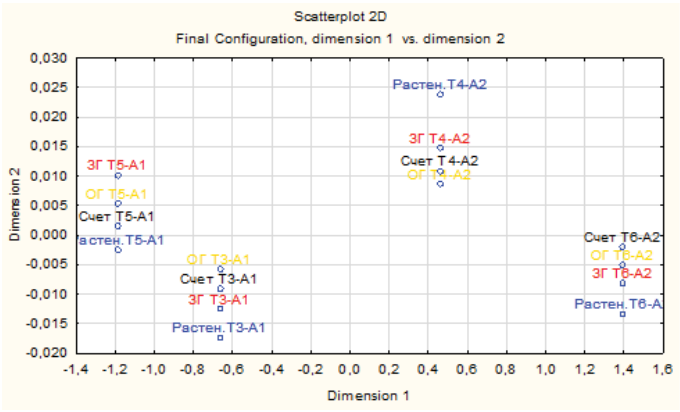

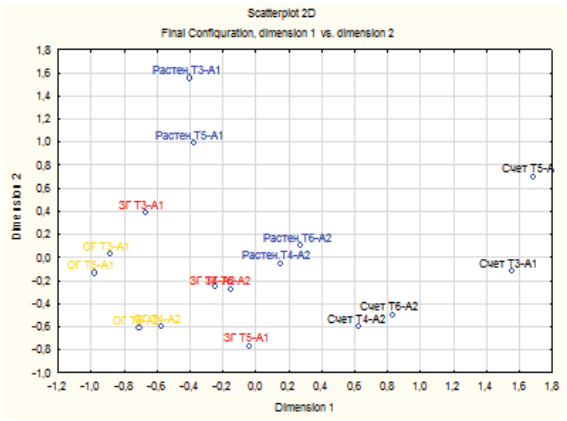

References

[1] Kizhevatova, E. A. Omelchenko, V.P. *Information technology in the study of cognitive functions* //

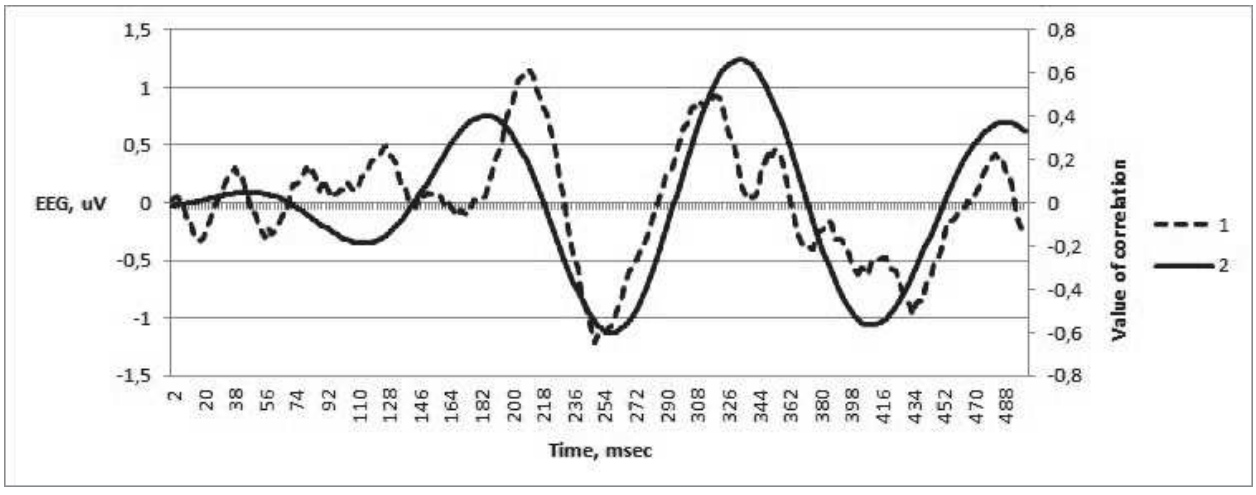

International 10-20 system with ipsilateral aural electrodes was used in experiments. Derivations Pz, Cz, Fz,[2] Fpz for extraction P300 was considered. Simple threshold function was used for classification in time interval from 250 msec after the beginning of stimulation to 500 msec (the end of epoch). If correlation more than determine threshold, which was selected in a range of max correlation in EEG record (0.6) to weak correlation (0.1), then corresponding to EEG stimulus are considered as relevant.

Two experiments conducted with various conditions of photostimulation. Stimuli were generated with frequency 2 Hz and time duration – 40 msec. In the first experiment the probability of appearance relevant stimuli was 10%. In the second experiment the dynamic probability of appearance target stimulus was used. First two stimuli always were non-target, further probability of appearance target stimuli increase on 10% for each subsequent. Thus, probability of 4-th stimulus as target is 20% in series and 8-th is 60%. Next stimulus can be target with 10% more probability, after this stimulus new series begins with 2 non-target stimuli. Thus, set series of stimulation was formed with time interval between the target stimulus in 0.5 sec (two target stimuli are nearby), if between relevant stimuli 2 and more irrelevant stimuli, then more 1.5 sec but less 6 sec. So, the influence expectation relevant stimulus on P300 amplitude was determined [5].

In first experiment the accuracy is 15-25% with 3-4 averaging, if 8 averaging, then maximum of accuracy is about 50%. For 10 averaging maximum of accuracy is 67% in range at 0.375 to 0.35 value of threshold.

In second experiment for 3-4 averaging the accuracy of classification stimuli is 20-30%. Results for 10 averaging of signal in Pz derivation are presents in fig.2. The graph shown that maximum of accuracy discrimination stimuli is in a range of 0.3 to 0.225 value of threshold. If the number of averaging increases to 12, then accuracy is 100% (at 0.28 to 0.26 value of correlation), for 20 averaging accuracy is 100% in more widely range of correlation threshold at 0.3 to 0.22. Problem of selection threshold can be solved with using algorithm of classification such as linear discriminant analysis, vector support machine and artificial neural networks [2-4].

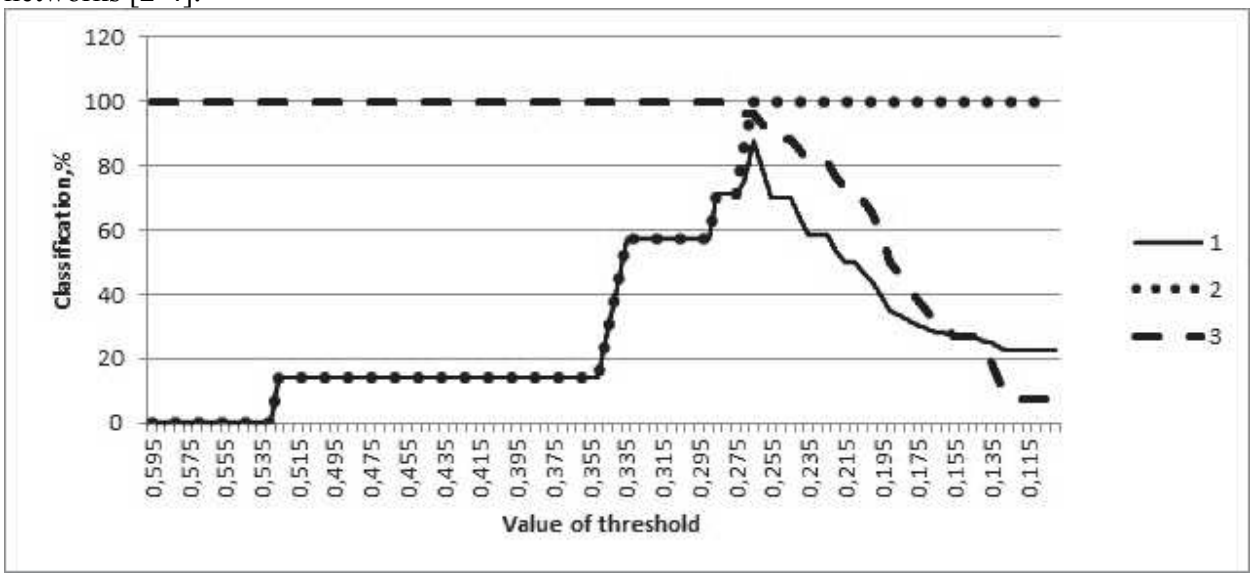

Fig.2. Dependence of value classification targets stimuli at the threshold value. 1 – accuracy, 2 – specificity, 3 – sensitivity.

Reference

[1] Brahim Hamadicharef. "Brain-Computer Interface (BCI) Literature - a Bibliometric Study.", ISSPA, inria-00511189 (2010).

[2] Heloisa Veiga1, Andréa Deslandes, Maurício Cagy, Kaleb McDowell, Fernando Pompeu, Roberto Piedade, Pedro Ribeiro. "Visual Event-Related Potential (P300)", Arq Neuropsiquiatr, 62(3-A):575-581 (2004).

[3] Sandra Mara Torres Muller, Wanderley Cardoso Celeste, Teodiano Freire Bastos-Filho, Mario Sarcinelli-Filho, "Brain-computer Interface Based on Visual Evoked Potentials to Command Autonomous Robotic Wheelchair", J. Med. Biol. Eng., Vol. **30** No. 6 (2010).
[4] Fazel-Rezai R1, Allison BZ, Guger C, Sellers EW, Kleih SC, Kübler A,"P300 brain computer interface: current challenges and emerging trends," Front Neuroeng. **5**, 10.3389 (2012).
[5] Gonsalvez C.J., Polich J. "P300 amplitude is determined by target-to-target interval.", Psychophysiology, 10.1017.S0048577201393137, Vol. **39**, № 3. P. 388–396 (2002).

Definition of a herniated disc based on the measurement of electrical impedance signal.

Blinow A.A.[1], Shchukin S.I.[1]
1. Bauman Moscow State Technical University, Moscow, Russia

The aim of this study is to determine the changes in the impedance of the biological tissue in the area of the damaged intervertebral disc. One of the main problems of the spine diagnostics is the impossibility in measurement of the base impedance, it is caused by a set of factors: the wettability of the electrodes, the high arrangement depth of the intervertebral discs, a human factor arising in the process of positioning the assembly. These factors do not allow to conclude that the value of the base value of the impedance with repeated application of the electrode assembly in the region of interest will be the same. Method for determining the impedance of the pulse, muscle tissue, located in the area of pathology can be used to solve this problem. [3].

Measurement of biological tissue impedance can be concluded to restructurization of biological tissue. This article consists the result of measuring the impedance of the biological tissue in the lumbosacral spine.

The aim of this study is to determine the changes in the impedance of the biological tissue in the area of the damaged intervertebral disc. One of the main problems of the spine diagnostics is the impossibility in measurement of the base impedance, it is caused by a set of factors: the wettability of the electrodes, the high arrangement depth of the intervertebral discs, a human factor arising in the process of positioning the assembly. These factors do not allow to conclude that the value of the base value of the impedance with repeated application of the electrode assembly in the region of interest will be the same. Method for determining the impedance of the pulse, muscle tissue, located in the area of pathology can be used to solve this problem. [3].

To confirm this hypothesis, the following experiment was conducted: On the human spine have been attached electrodes size 60-30mm, where 60 is the distance between the current electrodes, and 30 is the distance between the potential electrodes [2]. After that happened, pulse impedance values had been measured. The electrode assembly was imposed in two ways:

1)The electrode assembly is along the line of the spine at a distance of 10 mm from the axis of the spine, measurements were made in increments of 5 mm with assembly motion parallel to the axis of the spine from the neck to the waist;

2)The electrode assembly was placed across the spine, the center electrode assembly coincides with the axis of the spine, the measurements were performed with a 5 mm pitch when driving assembly axis parallel to the spine from the neck to the waist;

Measurements were carried out on two volunteers, one of whom was a patient with a herniated disc L0 / L1. As a result of measuring the presence of a herniated disc in a patient, it was confirmed patient with an accuracy of 5 mm (fig 1).

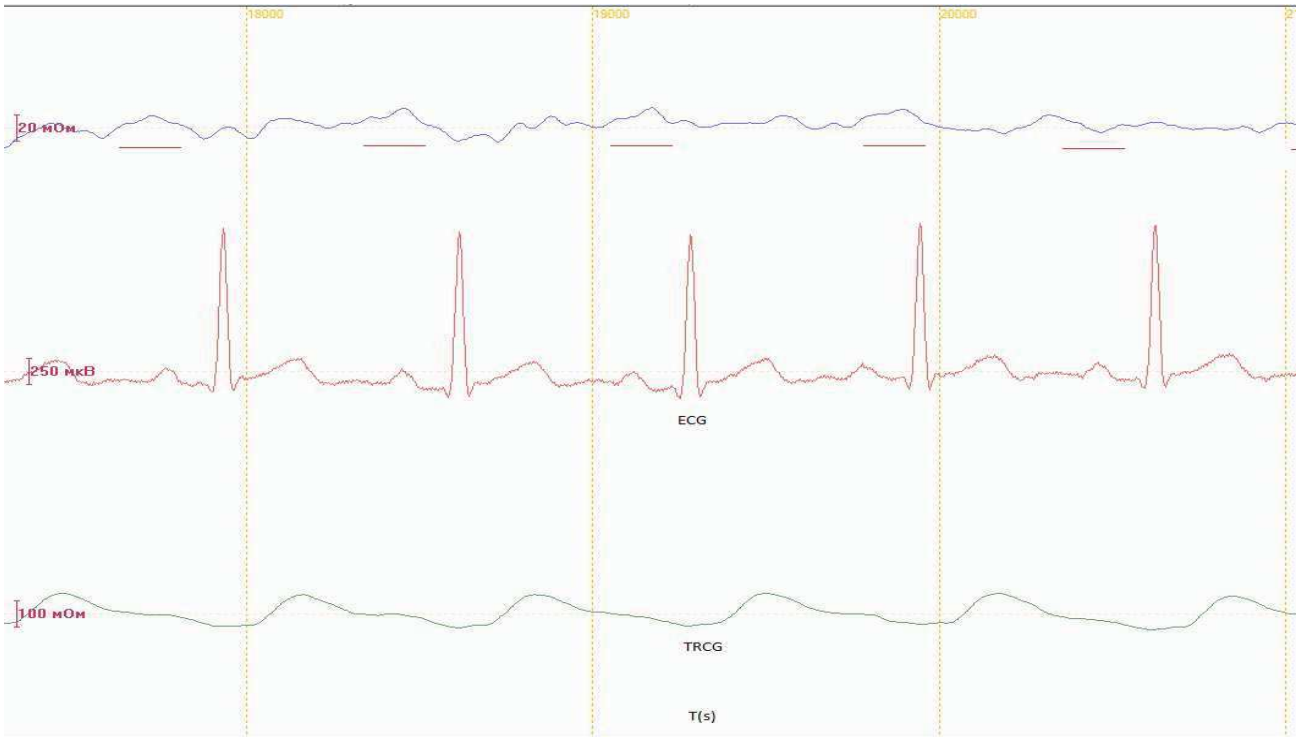

Fig.1. The signal pulse impedance in hernia longitudinal overlay electrode assembly

As a result, the measurement was made up of pulse impedance map for each of the two methods of imposing electrode assembly (Figure 2).

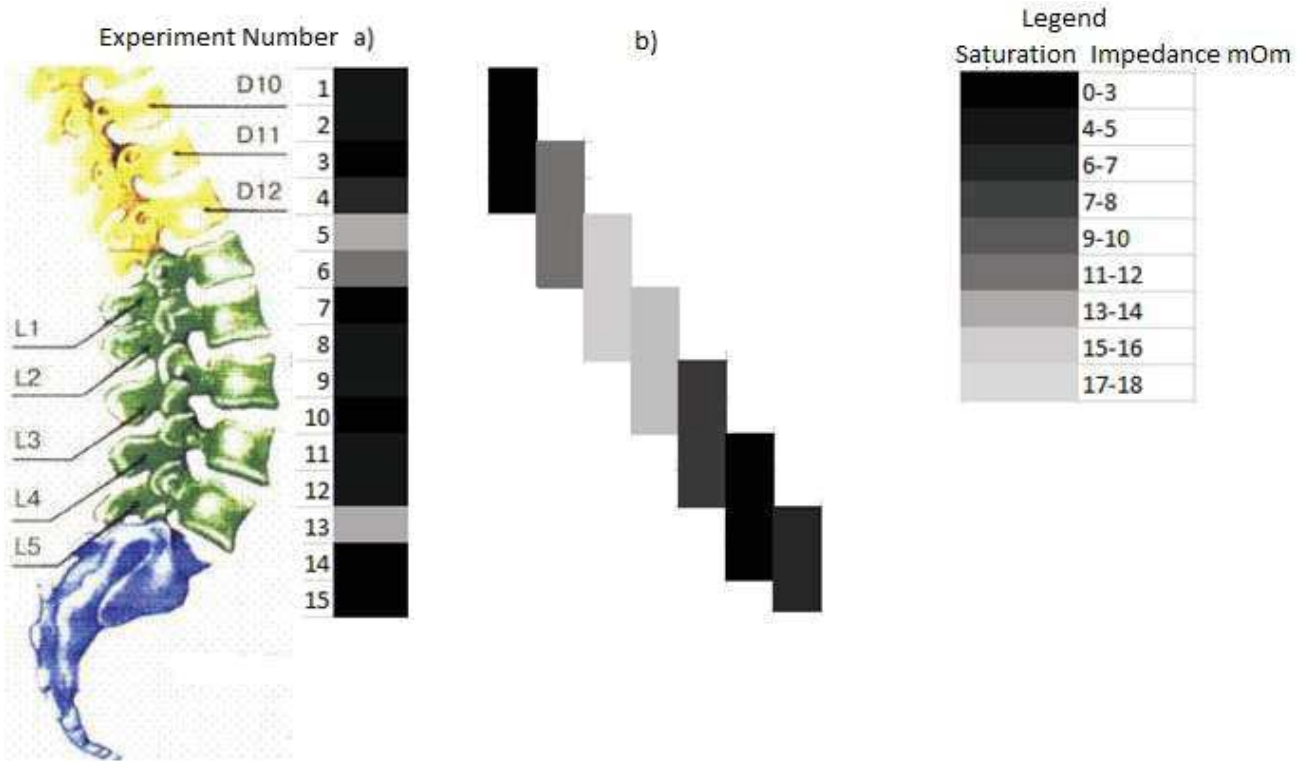

Figure 2. Map of the changes in pulse impedance for (b) and longitudinal (a) cross-electrode application

On the map, the pulse impedance perpendicular to overlay the electrode assembly in the field of hernia found falling impedance of 10 milliohms;

On the map, the pulse impedance for longitudinal overlay of the electrode assembly in the

field of hernia found falling impedance of 20 milliohms;

Reference

[1] О.С. Левин. “Полинейропатии. Клиническое руководство.”, Медицинское информационное агентство (2005).
[2] LI, John K-J. Series on Bioengineering & Biomedical Engineering – Vol. 1. Dynamics of the vascular system. World Scientific Publisher Co. Pte. Ltd 2004, ISBN 981-02-4907).
[3] M.N. Lebedeva, D.S. Lukjanov, M.V.Novikova, V.V. Novikov, I.P. Vereshchagin «Feasibility of impedance cardiography and impedance pletysmography in spine surgery» Хирургия позвоночника, №2,P58-66 (2011).
[4] Неврологический статус и его интерпретация»

When muscle contracts its impedance reduces due to the physics of the process. If we imagine the muscle as conductor with cylindrical shape, in accordance with the formula resistance is directly proportional to length and inversely proportional to transverse section. In addition, while muscle contracts the width of the electrode-skin-muscle transition decreases. It explains the impedance change. [6,7]

Thus, impedance changes describe the degree of muscle tension, as well as the nature of the implemented movement.

B. Experiment

For the purposes of registration control signals researches have been conducted on male and female volunteers.

The electrode systems were set in accordance with the places for recording control signals that are used in modern bioelectric forearm prosthetic. In the experiments two-channel recording system was used. Electrodes were placed on antagonist's muscles - flexor muscles and extensor muscles of fingers. Example electrode systems placement shown in figure 1.

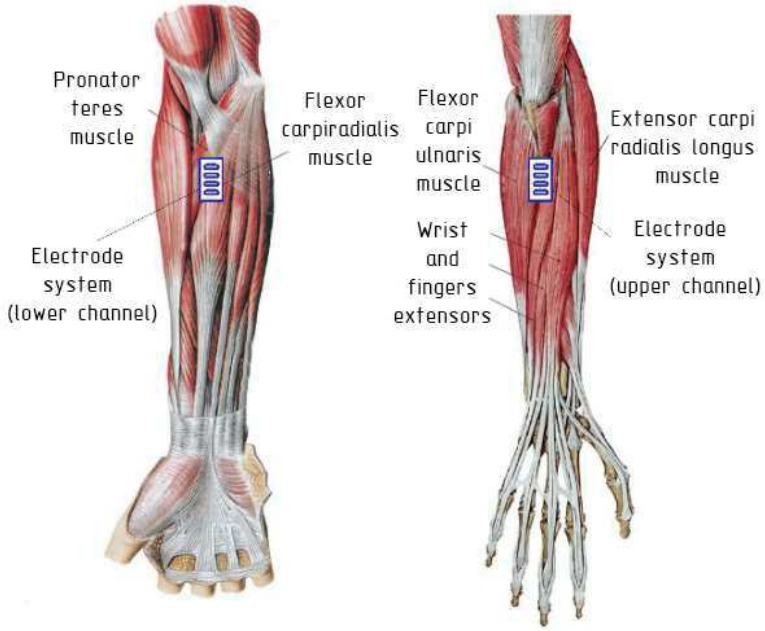

Fig. 1 Electrode systems placement.

As an electrode system were used reusable electrodes arranged according tetrapolar exhaust system (two current electrodes on the edges and two measuring electrodes in the middle), spaced apart by a distance of 10 mm. Such system can reduce the polarization effect.

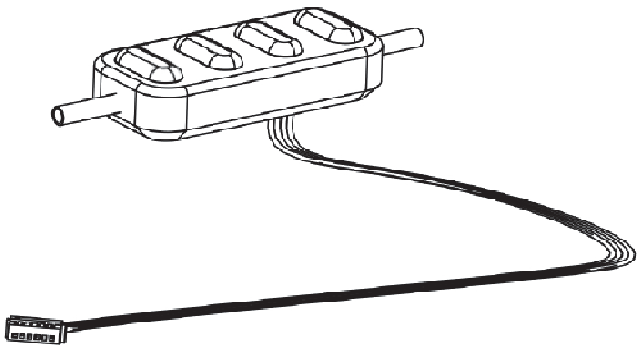

Fig. 2 View of electrode system.

The volunteers performed hand movements: tong, grabbing and rotation with power and in relaxed ways.

The signals were recorded simultaneously from two channels with a sampling frequency of 1 kHz. The surface of the skin under the electrode systems has been pre-treated with a scrub, the electrodes were lubricated by electrode contact substance.

Signals have been processed; the network disturbance has been removed.

C. Results

By now, it is difficult to find examples of the analysis of various signal parameters for controlling the bioelectric forearm prosthesis in the literature about rheography, but impedance changes in big muscles or muscle groups were considered. [1,2,4,5,9,10] However, in the published literature was used an unacceptable number of channels for accurately and quickly determination of action type.

When you release tong flexor muscles, which are located on the rear side of the forearm, contracts, this lead to impedance decrease. When you release grabbing flexor muscles relaxes, the impedance increases.

For the extensor muscles (they are antagonists muscles), which are located on the outer side of the forearm, the situation is reversed. Thus, the upper and lower channel signals at grasping and grabbing follow in antiphase.

When brush rotation was registered, it was observed that rheogram signals, unlike the gripper-grabbing situation, followed in phase. It can also explain the movements physiology.

In our method, to distinguish this kind of movement is supposed to use a special way. The recorded two-channel rheogram signal from antagonistic muscles should be submitted to the phase plane: the horizontal axis plotted values of the lower electrode impedance, on vertical axis plotted values of the upper electrode impedance values. Thus, each point of the phase portrait characterizes the impedance at each point. According to the movement pattern of the point the kind of action could be determined. Patterns of movement are shown in figure 3.

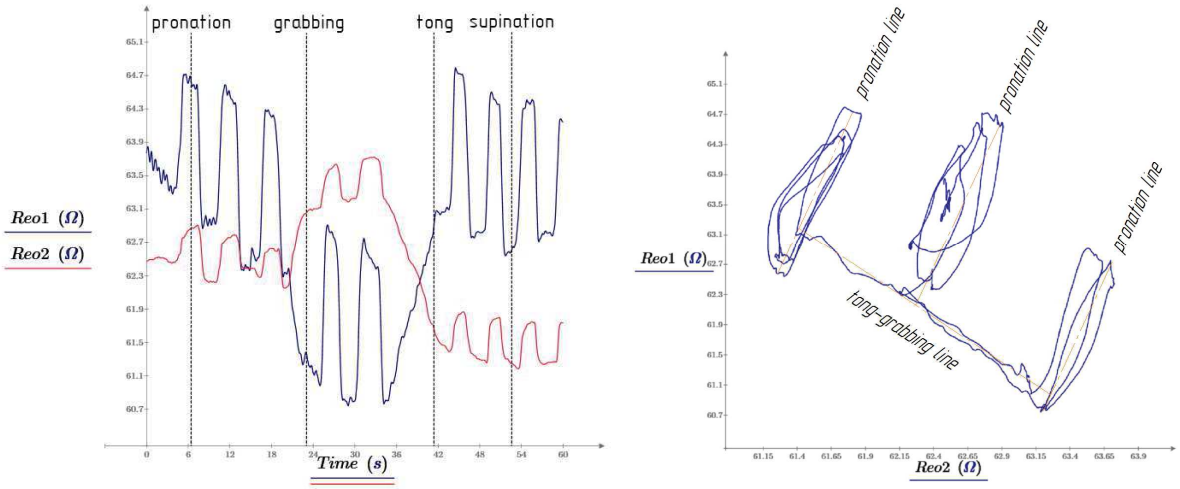

Fig. 3 Dual Channel rheogram during tong-grabbing and brush rotation (left) and phase portrait (right), where Reo1 – first channel rheogram, Reo2 – second channel rheogram.

Brush actions can be approximated by the defined lines which are perpendicular to each other. "Full tong" system condition characterized by the left point of the tong-grabbing line. The state of "full release" is characterized by extreme right point of the tong-grabbing line.

Pronation and rotation is determined by the extreme points on the pronation line. Thus, using the pattern of movement type of natural action can be determined.

To describe the degree of tong-grabbing and rotation of the brush, special parameter could be offered. When phase portrait point position changes along the lines parameter values will be between -1 and 1, where 0 - relaxed state of the brush, -1 - grabbing (supination), 1 - tong (pronation). The intermediate position of the phase portrait point will correspond to an intermediate stage of action. Positions of extreme points will be determined by the first calibration run.

III. Conclusions

From this study, we can conclude that the most accurate method of determining the action type with a force analysis is based on the joint registration of EMG and rheogram. By dint of electromyogram of the power of contraction could be analyzed [3] and kind of action could be analyzed by rheogram.

The proposed method for determining the type of movement by the dual-channel phase rheogram porter is an informative and a new real time method with low time delay and can be used in modern bioelectric prosthetic forearm control systems.

References

[1] K.S. Kim, D.Y. Yoon, Y.K. Yang, J.H. Seo, K. Kim, C.G. Song "A New Bio-impedance Sensor Technique for Leg Movement Analysis" IEEE 0-7803-8894-1/04 (2004).
[2] S.C. Kim, K.C. Nam, D.W. Kim, C.Y. Ryu, Y.H. Kim, J. C. Kim "Optimum electrode configuration for detection of arm movement using bio-impedance" Medical & Biological Engineering & Computing Vol. 41 (2003).
[3] M.V. Markova, A.N. Briko, A.V. Kobelev, S.I. Shchukin "Evaluation of informative parameters of the EMG signal for controlling of prosthetic arm in real time", Proceedings of the 11th German-Russian-Conference on Biomedical Engineering (2015).
[4] T. Nakamura, T. Kusuhara, Y. Yamamoto "Motion discrimination of throwing a baseball using forearm electrical impedance" J. Phys.: Conf. Ser. 434 012070 (2013).
[5] T. Nakamura, T. Kusuhara, Y. Yamamoto "Motion Discrimination Using Parameters of Bioelectrical Impedance" IFMBE Proceedings 17 (2007).
[6] V.I. Polishuk, L.G. Terehova, *Technique and methodology rheography and reopletizmography*, (Medicine, Moscow, 1983).
[7] R.M. Rangayan, *Analysis of biomedical signals*, (FIZMATLIT, Moscow, 2007).
[8] Y.L. Slavucky, *Physiological aspects of bioelectric control of prostheses* (Medicine, Moscow, 1982).
[9] C.G. Song, K.S. Kim, K. Kim, J.H. Seo "A New Approach for Detection of Leg Movement Using Bio-impedance Measurement", IEEE 1-4244-0437-1/06 (2006).
[10] T. Zagar and D. Krizaj "Electrical impedance of relaxed and contracted skeletal muscle", Hermann Scharfetter, Robert Merva (Eds.): ICEBI 2007, IFMBE Proceedings 17 (2007).

The influence analysis of geophysical factors on the people's morbility standart and road-transport incidents

L. Grunskaya., I.Leshchev, M.Makarova, I.Snigina
Vladimir State University named after Alexander and Nikolay Stoletovs,Vladimir, Russia

The system of multichannel synchronic monitoring was created on the physical experimental station of Vladimir State University. This station is created for monitoring, storing and processing of data of geomagnetic and electric boundary level fields. Since 2009 together with Departament of the Russian consumer supervision in the Vladimir region use statistical data on mortality of the population, and also on negotiability of children with deseases of respiratory system from July, 2004 till December, 2006 in Vladimir. Operation on

research of influence of space and geophysical factors on indexes of health of the population is carried out.

The experimental data point out for certain the ecological significance of the natural Earth EMF in the range of infralow frequences. The intensity level of these EMF-s and their spectrumare effectively controled by solar activity through the variations of solar wind parameters, interplanetary magnetic field and changes of hard radiation flow disturbing ionosphere current systems.

The investigations of interconnection of children's organ breathing deseases with geophysical characteristics have been done using data basis of Russian Requirement Inspector Departament(RRID) in

Vladimir region and data basis of electrical field monitoring results, air temperature, atmospheric pressure and relative humidity of the VSU physical experimental proving ground [1-3]. When analysing there have been taken data of the number of treatments to doctors by baby-patients with deseases of bronchial asthma, obstructive bronchitis and loryngotracheitis for the time period from July, 2004 till December, 2006 in Vladimir region which were confronted with the synchronous data of the geophysical parameters. Using the investigation results there have been analysed the correlative connections of the taken factors. The coeficient of the electrical field intensity vertical component correlation and the number of baby-patients treatments having obstructive bronchitis from September, 2005 till December, 2006 in Vladimir was 0,44 with probability of error $\leq 0,1$.

The investigations showed a direct connection between the morbidity standart of bronchial asthma, obstructive bronchitis and loryngotrancheitis and the level of atmosphere boudnary layer electrical field intensity of the showed factors (a correlation coefficient was 0,01 – 0,3). It has been revealed, the level of atmosphere boundary layer electrical field intensity influences on the ratio between the borbidity standarts showed above.

In the space of time from 2, July till 27, September of 2003 and from May, 21 till October, 30 of 2005 investigations were carried out on the base of mortality number of people in Vladimir region. The data information are got from the medical information analytical centre of the administration health departament if Vladimir region. The synchronous data of the physical experimental proving ground about electrical field intensity, air temperature, atmospheric pressure, relative humidity, radiation background were also taken in the space of time from July, 2 till September, 27 of 2003 and from May, 21 till October, 30 of 2005. The correlation coefficients of the electrical field intensity vertical component and people mortality in space of time from July, 2 till August, 1 of 2003 in Vladimir region was -0,52($p\leq0,1$); in space of time from July, 2 till July, 11 of 2003 was -0,62($p\leq0,1$); in space of time from September, 1 till September, 27 of 2003 was 0,31($p\leq0,1$); in space of time from july, 1 till August, 31 of 2005 was 0,33($p\leq0,1$), At some sections of time series(fig.4) we can see high correlation for the electrical field intensity component and for mortality of the population in Vladimir region. The analysis of the mortality srandart interconnection in 2003 in space of time from July to August when changing air temperature (fig.3) means high enough dependence of these factors (correlation coefficient was 0,49). The correlation coefficient of air temperature and people mortality in space of time from July,2 till August,19,2003 in Vladimir region was 0,49 ($p\leq0,001$); in space of time from July,23 till August,19,2003 in Vladimir region was 0,61 ($p\leq0,001$).

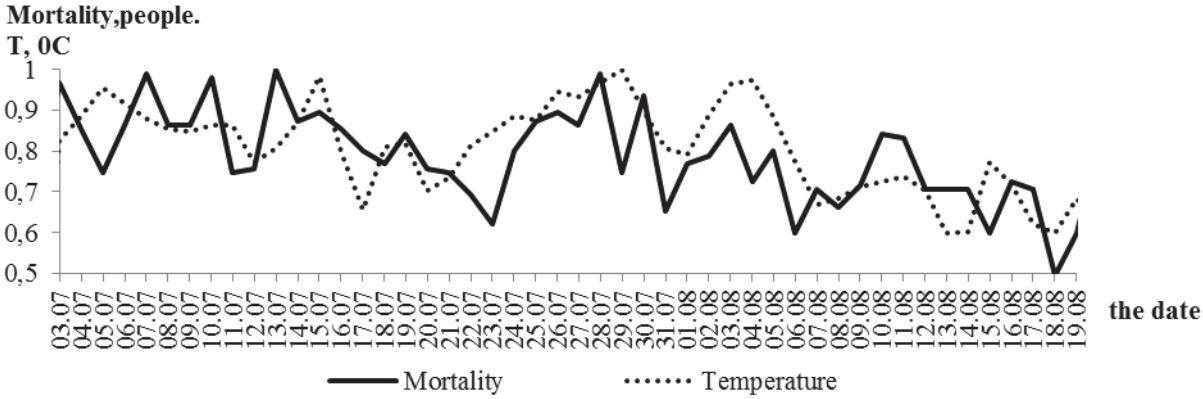

Fig.3. People mortality and air temperature in space of time from July,2 till August,19,2003 in Vladimir region.

Fig.4. People mortality and the electrical field intensity(fluxmeter №2) in space of time from July, 2 till July, 24, 2003 in Vladimir region.

The analysis of interconnection of heliophysical and geophysical factors (Wolf number, the Earth electrical field, the Earth magnetic field) with the road and transport accidents in Vladimir region was carried out using data information of the medical departament of Russia Ministry of Internal Affairs (MIA) of Vladimir region, street traffic safety state inspection departament of Russia MIA of Vladimir region and first medical aid city hospital of Vladimir. At some sections of time series significant correlation was revealed among the electrical field intensity vertical component, the Earth magnetic field, Wolf numbers and the number of RTA in Vladimir region (fig. 5-11). There has been revealed significant correlation between the number of killed and injured as a result of RTA in Vladimir region and Wolf number [4].

Table 1 Correlation coefficients of mistake probability p for a number of RTA, killed, injured as a results of RTA, their sum in Vladimir region and Wolf numbers for 2001.

Analysed processess	the dates	correlation coefficients	P
Road and Transport Accidents(RTA) and the Earth electrical field	28.06-24.07	-0,45	≤0,02
RTA and geomagnetic field	28.06-08.08	0,40	≤0,01
RTA and Wolf number(s)	28.06-29.08	0,45	≤0,001
Killed as a results of RTA and Wolf number	19.07-19.09	-0,46	≤0,001
Injured people as a results of RTA and Wolf number	19.07-19.09	0,39	≤0,01

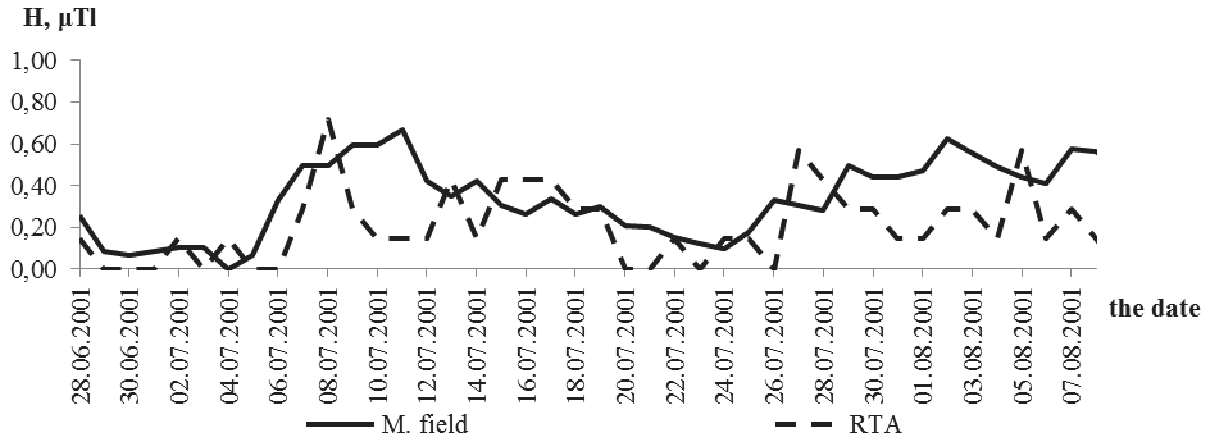

Fig.6. The number of RTA and magnetic field round Vladimir region in the space of time from June, 28 till August, 8, 2001.

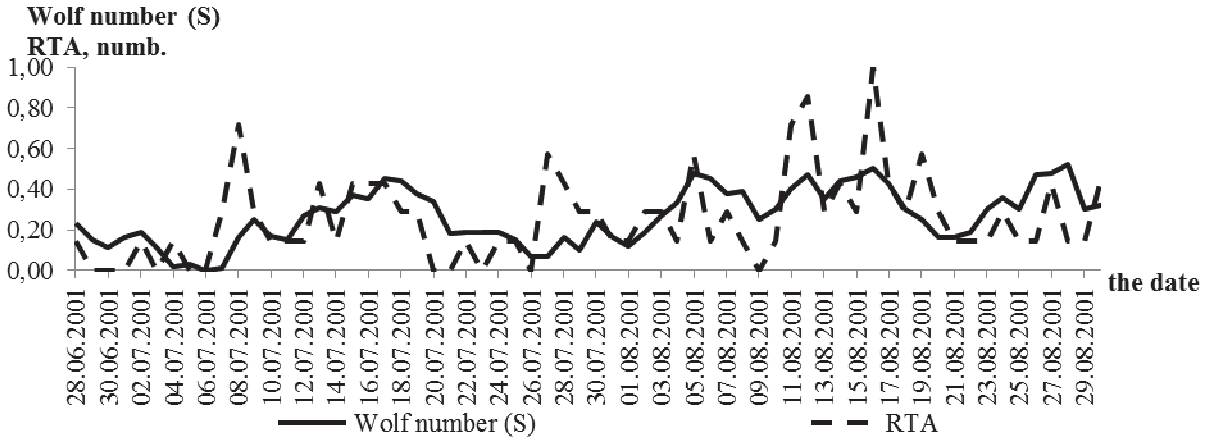

Fig.7. The number of RTA round Vladimir region and Wolf number in the sun southern hemisphere in the space of time from June, 28 till August, 29, 2001.

Table 2 Correlation coefficients of mistake probability p for a number of RTA, killed, injured as a results of RTA, their sum in Vladimir region and Wolf numbers for 2003.

Analysed processess	the dates	correlation coefficients	P
Injured people as a results of RTA and Wolf number (N)	11.07-11.08	-0,46	≤0,01
Injured people as a results of RTA and Wolf number (N)	11.08-11.09	0,46	≤0,01
Injured people as a results of RTA and Wolf number (S)	11.08-11.09	-0,41	≤0,02

The works are done with support of State Task 2014/13,2871, RF grant №14-07-97510\14.

References

[1] Grunskaya L.V. A mobile receiving and registrating system for monitoring atmosphere boundary layer electromagnetic field /L.V.Grunskaya [and others] // Projecting and technology of electronic means. -2005. -№2 pp. 69-74.

[2] Grunskaya L.V., Isakevich V.V., Yefimov V.A. Development of a program-divece system to investigate influence of geophysical and man-triggered factors on the atmosphere boundary layer electrical field // Biomedical radio electronics, 2008, №6, pp 87-93.
[3] Grunskaya L.V. Influence of geophysical characteristics of the atmosphere boundary layer on some index of population's health. / L.V. Grunskay, V.N. Burenkov, L.T. Sushkova, E.Y. Rizhova, I.A.Leshchev, M.I. Degtereva // Biotechnosphere – 2011, №5.
[4] Grunskaya L.V. Investigation of road and transoprt accidents interconnection round Vladimir region with geophysical and heliophysical characteristics / Grunskaya L.V., Leshchev I.A., Isakevich V.V., Shirobokov A.V., Sushkova L.T. // Biotechnosphere. St.Peterburg: Issue "Polytechnic'. 2013-№3(27) pp. 26-34.

The study of rheocardial atrial signals formation mechanisms

Malakhov A.I. [1], ***Shchukin S.I.*** [1], ***Tikhomirov A.N.*** [1], ***Soboleva V.Y.*** [1], ***Levando A.M.*** [1]
1. Bauman Moscow State Technical University, ul. Baumanskaya 2-ya, 5, Moscow, Russian Federation

In most cases, the atria work deflection are not considered as life-threatening. However, the violations in the atrial electromechanical characteristics can become a cause of complications and have serious consequences. The main reason for the problems with the atrial work is atrial fibrillation (AF). AF leads to disruption of cardiac hemodynamics and blood supply of the whole organism and to formation of blood clots that can cause pulmonary embolism or stroke. The death risk in patients with stroke associated with AF occurs 2 times more often [1].

At the first research stage we analyzed MRI data of 3 healthy volunteers. Volunteers parameters are shown below:

- Gender - Male;
- Age - 25 ± 3 years;
- Tilt angle axis of the heart - 45 ± 10 °;
- Thorax perimeter - 92 ± 4 cm;
- The depth of heart occurrence - 24 ± 4 cm.

It was found that the main motion at the time of atrial reduction is fibrous ring (atrium-ventricular septum) movement. Normally, according to the literature [2] fibrous ring movement throughout the cardiac cycle must be greater than 10 mm. According to the MRI studies analysis we found that at the time of atrial reduction fibrous ring movement may reach 7 mm and the maximum movement of the free atria wall is achieved less than 5 mm in the right atrium anterior region.

We created the heart motion during atrial contraction model to evaluate the heart structures motion effect to changes in electro impedance derived from the right atrium projection on the chest region. Figure 1 shows the heart model created in the software environment Ansys.

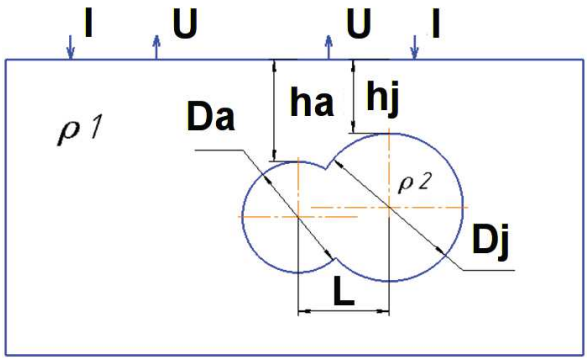

Fig. 1 Heart model for Ansys study. Where I – current electrodes, U – potential electrodes, Da – atrial size, Dj – ventricles size, ha – atrium occurrence depth, hj – ventricular occurrence depth, ρ1 – soft tissues resistivity, p2 – blood resistivity, L – the distance between the spherical models centers.

The model parameters are shown below:

- The size of the electrode assembly: 140 mm between the current electrodes and 70 mm between potential electrodes;
- Ventricular size: Djb = 100 mm;
- Size of ventricular after fibrous ring movement caused by atrial contraction: Dje = 90 mm;
- Ventricular occurrence depth: hj = 30 mm;
- The atria size during diastole: Dab = 50 mm;
- The atria size at the systole end: Dae = 40 mm;
- Atrium occurrence depth: ha = 60 mm;
- The distance between the spherical models centers: L = 60 mm;
- The soft tissues resistivity: ρ1 = 5 Ohm * m;
- The blood resistivity: ρ2 = 1,35 Ohm * m;
- Mid assembly located above fibrous ring.

According to the simulation results it was showed that **the atria walls movement and moving fibrous ring movement lead to the same absolute value of the impedance changes, but different in sign**.

In view of the studies based on electro impedance measurements [3] we can show that fibrous ring movement makes the main contribution to rheocardiography signal. Further work on the analysis of precordial electro impedance signals will allow to control the heart mechanical motion at monitor mode.

Reference

[1] Atrial fibrillation diagnosis and treatment. Recommendation CSC, VNOA and SUVs. (The National Preventive Medicine Support Foundation "PROFMEDFORUM", Moscow, 2012).

[2] A.F. Safarova, E.P. Korovina, J.D. Kobalava, V.S. Moiseev, *Ultrasound diagnosis of myocardium and coronary arteries morpho-functional state disorders at various heart diseases* (PFUR, Moscow, 2008).

[3] A. Malakhov, A. Tikhomirov, S. Shchukin, S. Otstavnov, A. Nickolaev, “Investigation of right atrium hemodynamics via the electro impedance methods for patients with atrium fibrillation”, Biomedical radioelectronic, №7, 2015.

Adaptive filtration of the EMG signal in prosthesis control.

***N. Rudnyi*[1]**

1. Bauman Moscow State Technical University, 2nd Baumanskaya str., 5, Moscow Russia.

During the everyday usage of the myoelectric prosthesis appears a large amount of different noises that affect on the movement detection. The most common of them are: power supply noise 50/60 Hz and multiple of it 100/120 Hz and the white noise. If the first two of them easily removed with the simple band-stop filter, the white noise cannot be removed by the conventional filter and it seriously affects on the signal noise.

During this work was carried out the research on the influence of contact ”electrode-skin“ on the EMG-signal noise degree Research was divided into three stages.

At the first stage the signal electrode was located on the anterior compartment of the forearm, in 1 cm from the line passing through the middle of the cubital fossa, on the side of the line passing through the center of the forearm from the side of little finger. In the first spot the electrode was tightly pressed to the skin surface while the tested one made three grasp movements. In the second part of the dusted one made the same movements but the signal electrode was not tightly pressed to the skin surface.

At the second stage the signal electrode was shifted by 3 cm perpendicular the axis passing through the middle of the forearm towards the thumb. The stage was divided into two parts similar the first stage parts. The tested one also made three grasp movements.

At the third stage the signal electrode was moved along the hand till the middle of the forearm from the initial position. Otherwise, this stage was similar to the first two stages.

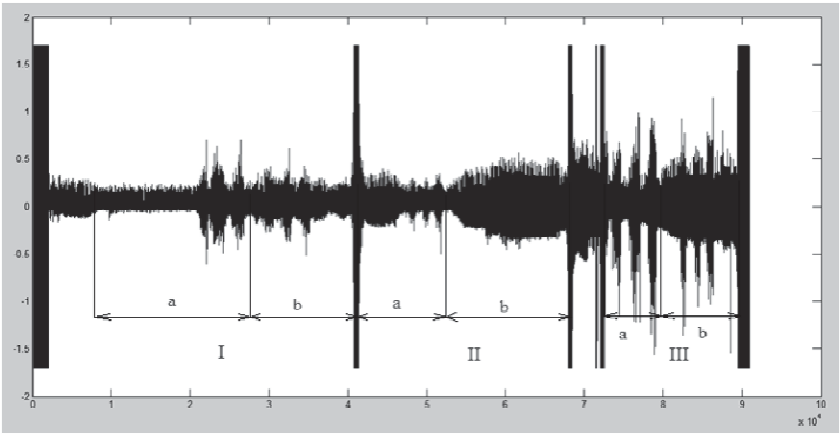

Fig. 1 Influence of the contact ”electrode-skin“ on the EMG-signal noise degree (a – electrode is tightly pressed to the surface of the skin, b – not tightly pressed).

As you see from the recorded EMG signal, when the electrode is not tightly pressed to the skin surface, the signal noise is too high at all three stages that affects on the movement detection.

Adaptive selective filter allows significantly cut the white noise. During the work was simulated Gaussian noise with dispersion of 60% EMG signal dispersion in motion and noise with linearly increasing dispersion. It was added to a normal EMG signal, recorded from flexor muscles during 11 “flexion movements”. When movements are detected with simple double-threshold method, a lot of false movements appear and initiation of movements is detected incorrectly.

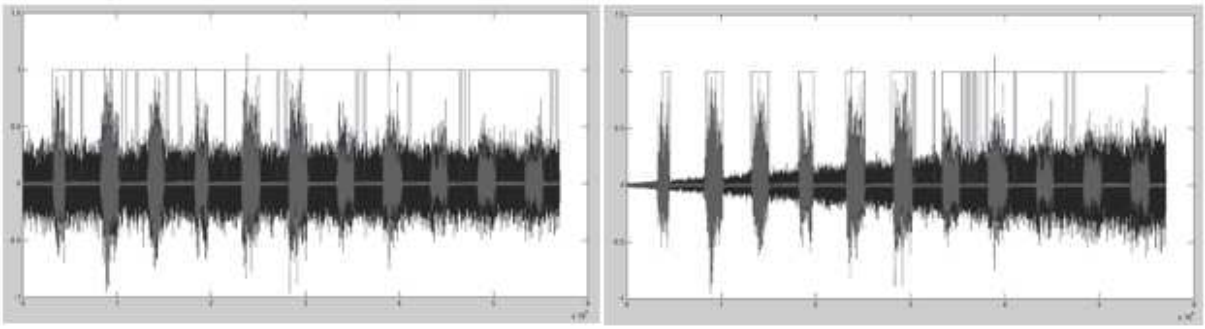

Fig. 2 Movement detection in noisy EMG signal with constant dispersion (left) and linearly increasing dispersion (right). Rectangles show detected movements.

The filter circuit is shown in figure 3. Adaptive selective filter operates as follows:

- First it works as usual windowing wilter,
- Then counts the filter output

  $\hat{n}_k = \sum_{i=0}^{N-1} w_k(i) x_{k-i}$,
- Performs error estimation

  $e_k = y_k - \hat{n}_k$,
- Updates the set of weighting coefficients

  $w_{k+1}(i) = w_k(i) + 2\mu\, e_k\, x_{k-i}$.

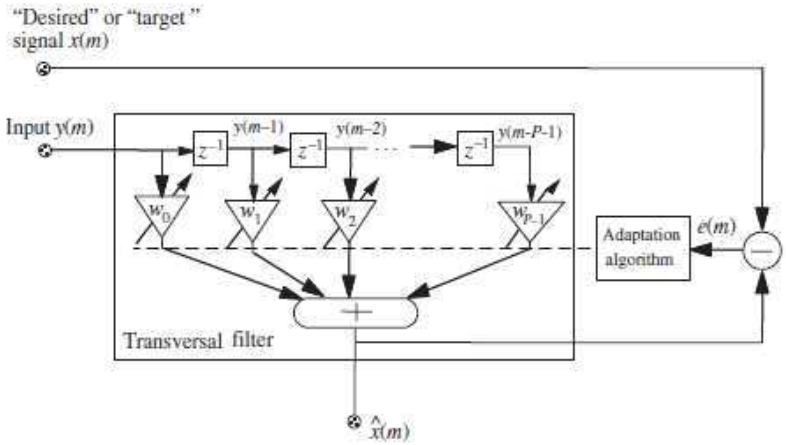

Fig. 3 Adaptive selective filter circuit.

Adaptive selective filter was realized in Matlab 2011 computer environment. The optimal coefficient μ has been chosen as 0.0002.

As a result, a number of falsely detected movements was reduced.

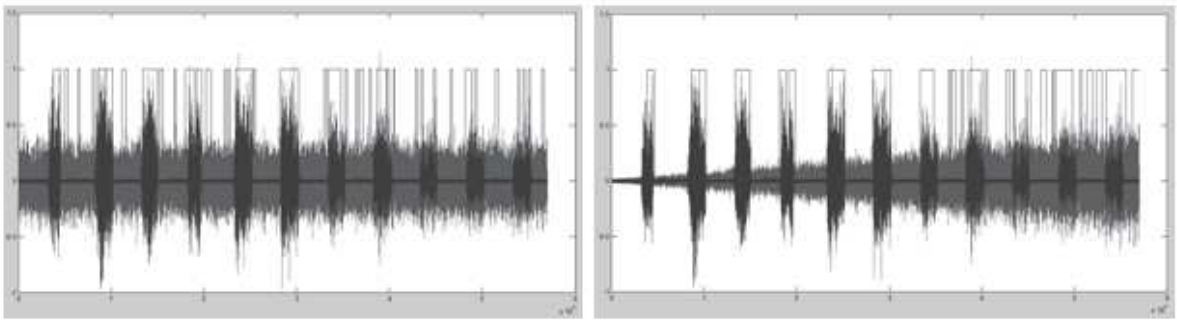

Fig. 4 Movement detection in EMG signal after adaptive selective filter (left – constant dispersion, right – linearly increasing dispersion). The darkest signal is ideal recorded EMG signal.

Author would like to thank Anton Dogadov and Artyom Maslov (Bauman Moscow State Technical University) for providing and processing EMG data. This work was supported by the Foundation for assistance to small Innovative enterprises in Science and Technology under Grant No. 6937ГУ2/2015

References

[1] P. Bonato, T. D'Alessio, M. Knaflitz. A Statistical Method for the Measurement of Muscle Activation Intervals from Surface Myoelectric Signal During Gait. IEEE TRANSACTIONS ON BIOMEDICAL ENGINEERING, VOL. 45, NO. 3, MARCH 1998, pp. 287-289.
[2] E. C. Ifeachor, B. W. Jervis. Digital Signal Processing: A Practical Approach, 2nd. ed. (Prentice Hall, 2001).
[3] S. V. Vaseghi. Advanced Digital Signal Processing and Noise Reduction, 4th. ed. (Wiley, UK, 2008).

Analysis of gait parameters obtained by contactless measurement.

L.O. Akulenko, J.V.Stadelmann

Biotechnical Medical Systems (BME-1) dept, Bauman Moscow State Technical University
2 nd Baumanskaja St. n°5, bld 1, Moscow, 105005, Russian Federation

Osteoarthritis of the knee is a chronic joint disease of degenerative nature. The disease is caused by the destruction of the cartilage surface of the joint structure. Those morphological changes disturb the functionality of the knee, thus deteriorating the patient's quality of life eventually leading to the development of cardiovascular disease, diabetes, and disability [1, 2].

Existing hardware and software systems and methods for visual assessment of gait quality have a number of disadvantages, such as the subjectivity of the analysis, the dependence to the quality of diagnostics to the experience of the rheumatologist or inaccessibility caused by high cost and a large number of peripheral elements of hardware and software [3, 4].

Preliminary research on the development of a biotechnical system of determination of gait parameters has proven the efficiency of contactless methods of measuring the angle of flexion-extension of the knee joint. On the basis of this method curves of the angle of flexion-extension of the knee joint were analyzed and thereafter modeled [5, 6].

The registration the angle of flexion-extension of the knee joint extension was carried out on the test setup (Fig. 1) which consists of:

1. camera with tripod;

2. three IR-markers;
3. treadmill.

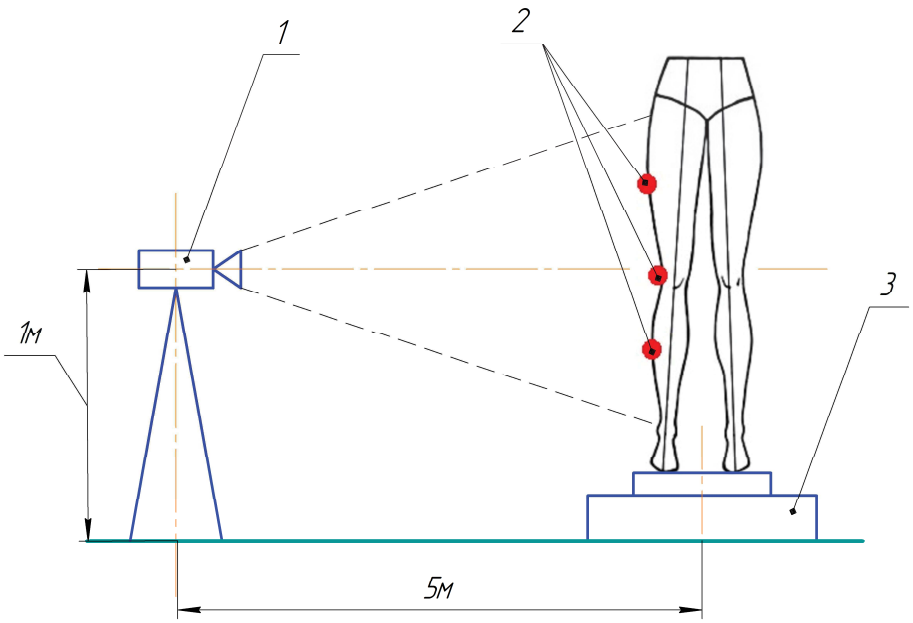

Fig. 1 The test setup for the registration of the angle of flexion-extension of the knee joint.

The lab assistant sets on the patient's leg three IR-markers in the knee area. The patient starts moving on a treadmill at a speed of 4.5-5 km/h. The lab assistant records the video of the patient's walking on the treadmill. The video is loaded up onto the PC for post-processing and analysis of received data.

The obtained data is presented in the form of a trajectory of the angle of flexion-extension of the knee (Fig. 2).

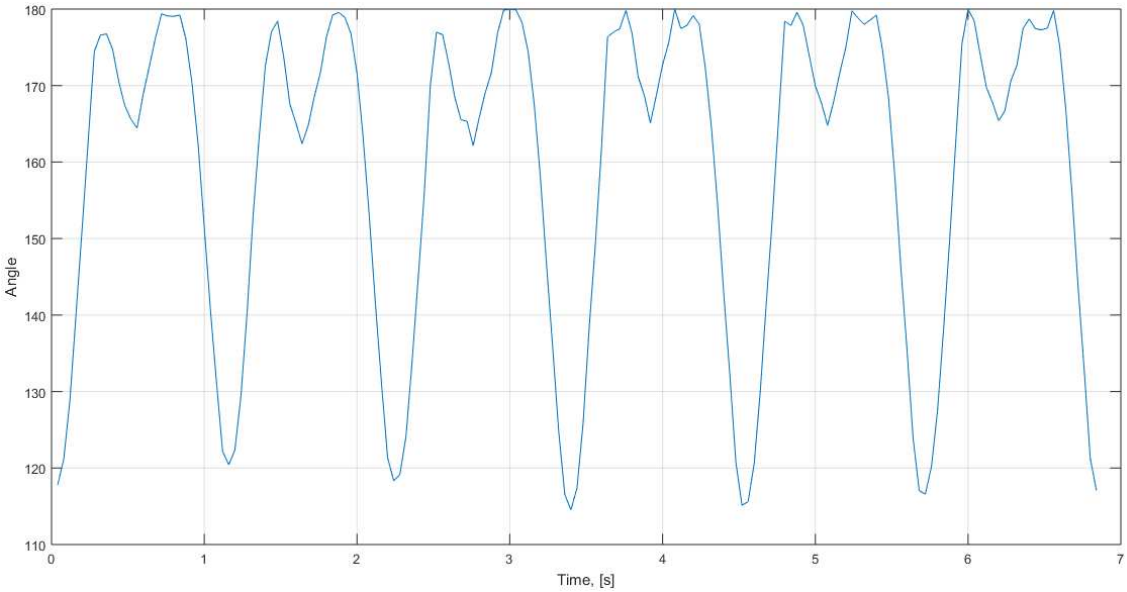

Fig. 2 Trajectory the angle of flexion-extension of the knee joint.

Analysis of the spectral characteristics of the received signal (Fig. 3) indicates that the detected signal is composed of the main components constituting 95% of the signal energy and lying in the range from 0 to 2 Hz.

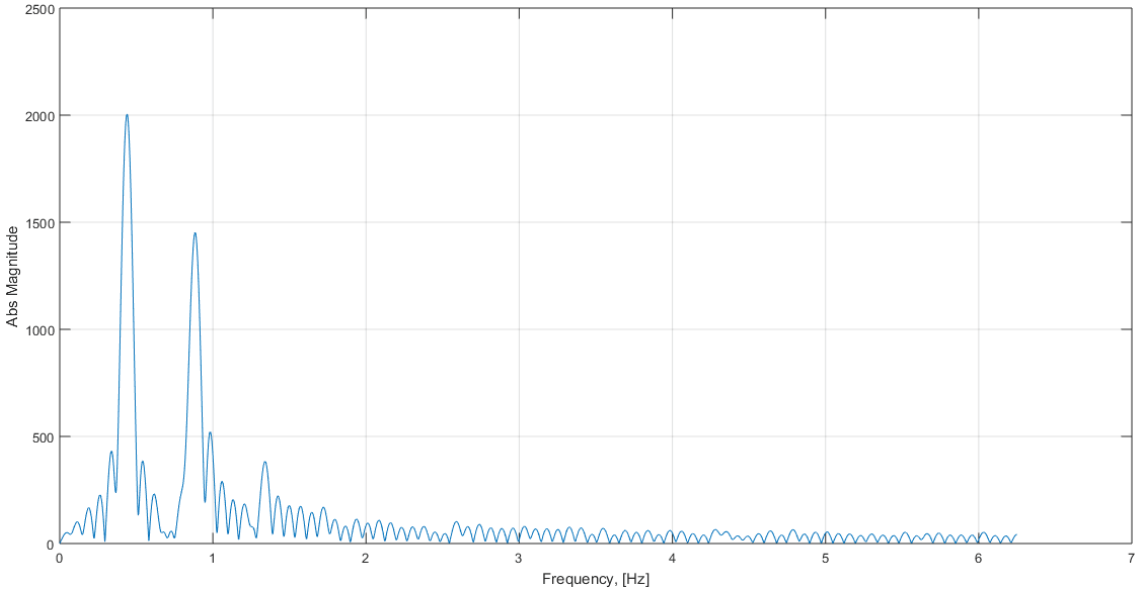

Fig. 3 Spectral characteristics the angle of flexion-extension of the knee joint.

Each harmonic in the spectrum of the recorded angle was represented with a sinusoidal function. Correlation analysis showed that the use of three harmonics is enough for effective modeling of the original signal (Table 1).

Table 1. Correlation values for different number of harmonics.

ID of research	Number of harmonics			
	1	2	3	4
1	0.8321	0.9590	0.9734	0.9722
2	0.8059	0.9667	0.9778	0.9626
3	0.8666	0.9475	0.9843	0.9444
4	0.7005	0.9562	0.9582	0.9510
5	0.8157	0.9375	0.9613	0.9589
6	0.8069	0.9453	0.9887	0.9721
7	0.8336	0.9347	0.9863	0.9850
8	0.8444	0.9655	0.9746	0.9683
9	0.8885	0.9555	0.9721	0.9660
10	0.7958	0.9678	0.9822	0.9812

The modelling results of the original signal are shown in figure 4.

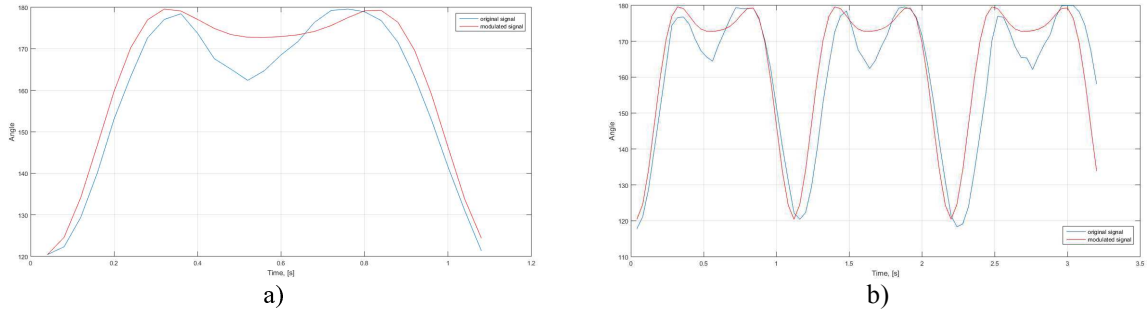

a) b)

Fig. 4 The modelling results: a) for one step, b) for three steps.

The analysis of gait patterns showed that it may be modeled as a sinusoidal sum of three harmonics. Since pair in the knee joint is likely to hinder movement amplitude and affect the speed at which movements are performed, those three harmonics are likely to be not only key parameters for data dimensionality reduction, but as well indicators of the patient's joint's state. This supposition is to be confirmed in the future by means of registration of patients with clear diagnoses of the knee joint diseases.

References

[1] Gray H. Anatomy of the Human body. New York: Bartleby, 2000. 1576p.
[2] World Health Organization. WHO Disease and injury country estimates. 2009.
[3] Vicon Motion Systems, Technical Report, Motion Analysis & Instrumented Treadmill Laboratories, Department of Physical Therapy, University of Delaware, 2002.
[4] Walsh M., Woodhouse LJ, Thomas SG, Finch E. Physical impairments and functional limitations: a comparison of individuals 1 year after total knee arthroplasty with control subjects //Journal of the American Physical Therapy Association. 1998. №78. 248-258p.
[5] Soya D.M., Zhuk D.M. Modeling of the athlete's locomotion // Engineering gazette. BMSTU. Electronic journal. 2014. № 7.
[6] Message C.A., Stadelmann J.V., Spiridonov I.N. Method of contactless measurement of gait's parameters // Biomedical engineering. 2015. №5.

Research segmentation algorithms endoscopic images of blood vessels in the brain tumor removal

K.G Maximova[1], A.V. Kolpakov[1], I.N. Spiridonov[1], A.N. Shkarubo A.N[2]
[1] Bauman Moscow State Technical University/Department of Biomedical Techniques, chair BME-1 "Biotechnical system and devices"
Moscow, Russian Federation
[2] Scientific Research Neurosurgery Institute named after N.N. Burdenko
Moscow, Russian Federation

Introduction

Surgical intervention is one of the main methods of treatment of brain tumors. A risk of vascular damage arises because of the great complexity of the endoscopic surgery to remove a brain tumor [1]. Consequently, the risk of deterioration of the patient's quality of life and the risk of death. These risks may reduce with methods of automatic detection of blood vessels in the endoscopic image is possible.

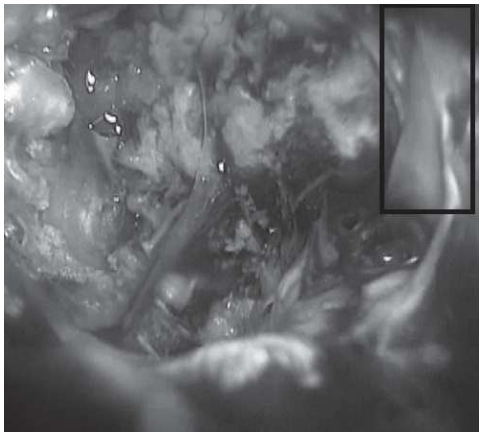

Fig.1 An example of an endoscopic image

Due to a bimodal type histogram views local intensity of the image-background boundary vessel (Figure 2) a threshold segmentation algorithm is applied for endoscopic blood vessel images in removing brain tumors [3].

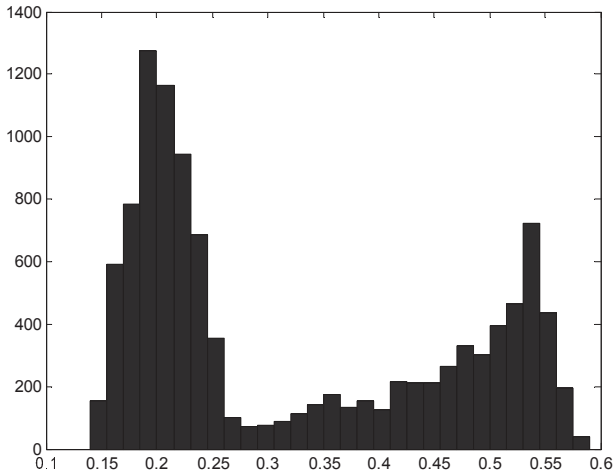

Fig. 2 Local image histogram vessel background border

Threshold segmentation is performed on each channel RGB color code average error of threshold image segmentation has been calculated by the channel RGB color code. Accuracy was calculated by imposing vessel mask as a benchmark in the segmented image according to the formula:

$$\delta = (|mask - I_{out}| / mask)\cdot 100\%$$

where δ- error, mask - the area of the vessel in the image, I_{out} - the area of the vessel in the

Table. 1 The value of the average error on channels RGB color coding

Canal	R	G	B
error δ of segmentation without pre-processing the image	19%	19%	18%
error δ of segmentation using the gamma correction (gamma = 0.5)	16%	18%	17%
error δ of segmentation using the gamma correction (gamma = 1)	17%	18%	17%
error δ of segmentation using the gamma correction (gamma = 1.5)	19%	21%	22%
error δ of segmentation using histogram equalization	15%	14%	14%

The research has proven that the smallest error of threshold segmentation in color channels R, G and B is achieved by using histogram equalization.

Conclusion

According to the research informative parameters are chosen on the basis of database vascular imaging in removing brain tumors such as image intensity values for each of the channels in the RGB color code. According to the research pre-processing method using the image histogram equalization to reduce the error segmentation of blood vessels in the endoscopic image by removing a brain tumor was proposed.

In the future for increasing the accuracy of the segmentation of images of vessels in removing brain tumors is necessary to apply additional informative parameters.

References

[1] "Damage of the cavernous part of internal carotid artery during endoscopic transsphenoidal removal of
pituitary adenomas (4 cases from practice)." // The Burdenko Neurosurgery Journal. - 2013. - № 6 (Volume 77) - p. 28-37. (PL Kalinin, Sharipov OI , Shkarubo AN, Fomichev DV, Kutin MA, Alekseev SN, Kadashev BA, Yakovlev SB, P Dorohov, Bukharin EY, Kurnosov AB, Popugaev KA).

[2] Website of KARL STORZ. Access: https://www.karlstorz.com/ba/ru/fi.htm (Reference date: 10.10.2015)

R time intervals of the (ECG). This is a more robust method since the R—R time intervals are less affected by the noise.

Many algorithms have been proposed over previous years for automatic cardiac arrhythmia detection, in this paper we use support vector machines.

The support vector machine is an elegant and highly principled learning method for the

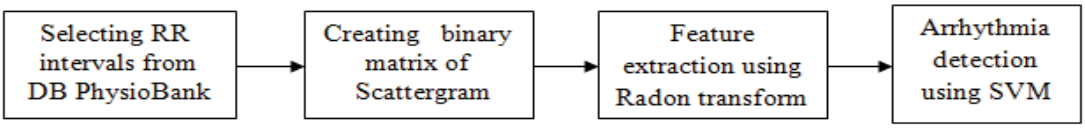

. The

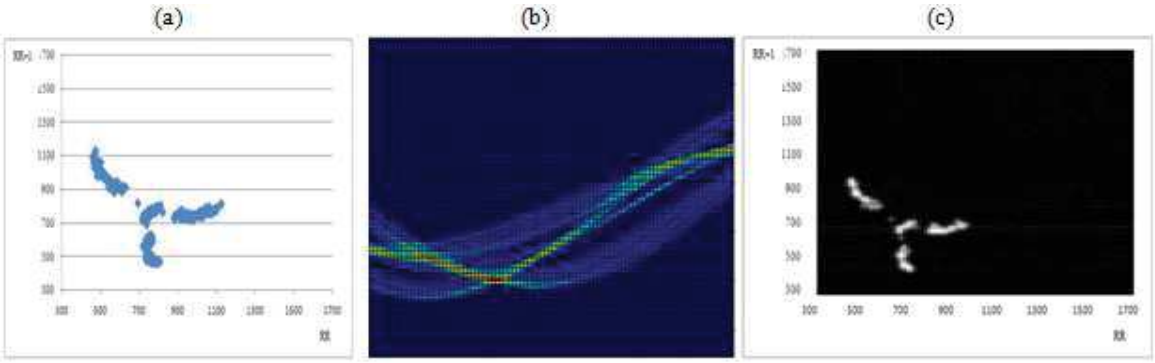

Fig. 2 a) The scattergram b) crating feature we used Radon transform from the binary matrix of scattergram

Next we created the database from the features that where obtained from the Radon transform of the binary image of scattergram. The database was divided in to training and testing database.

2.2 Support vector machine

As mentioned in the interdiction in this paper for arrhythmia detection we used SVM which is the most common use for the diagnostic of cardiovascular disease.

Simply stated, the SVM identifies the best separating hyperplane (the plane with maximum margins) between the two classes of the training samples within the feature space by focusing on the training cases placed at the edge of the class descriptors. In this way, not only an optimal hyperplane is fitted, but also less training samples are effectively used; thus high classification accuracy is achieved with small training sets [5].

The support vectors are the data points that are closest to the separating hyperplane; these points are on the boundary of the slab. The following figure illustrates these definitions,

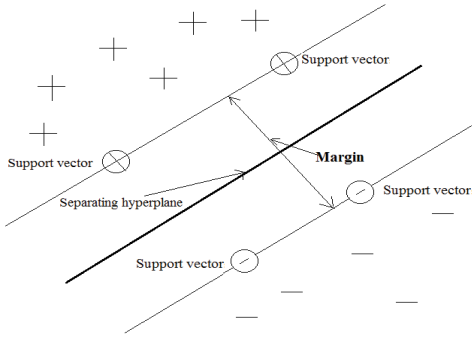

Specificity is evident less immediately. It refers to the ability of the examination to identify the absence of a given disease, given by the ratio

In this work we have presented a SVM algorithm for arrhythmia detection, which is associated with Radon transform for feature extraction from binary matrix of scattergram.

Result obtained by using SVM for arrhythmia detection using the Radon transform

the visualization of nuclear and cell membrane markers (Ki-67, HER2, etc.). The presence or absence of these markers influence on the treatment scheme, and helps to identify predictive and prognostic factors. It is especially important to separate the contribution of dyes in the case when the intensity of DAB staining contains diagnostic information (for example, for determining ER/PR-status of breast cancer), and H staining is supplementary and its intensity should be excluded.

The proposed method is based on the Beer-Lambert-Bouguer law [4] which takes into account the following spectral characteristics: transmittance spectra of dyes H and DAB ($\tau^H(\lambda)$ and $\tau^{DAB}(\lambda)$), the emission spectrum of light source of the microscope ($I_0(\lambda)$), the spectral sensitivity of CCD sensors of the digital camera ($m_A(\lambda)$):

$$I_i = \int I_0(\lambda) \cdot m_i(\lambda) \cdot \tau(\lambda) d\lambda, \quad (1)$$

where i denotes one of RGB-coordinates, I_i is intensity value or camera response.

Considering the known spectral sensitivities of CCD sensors and the emission spectrum of light source it's possible to derive the system of linear equations for each image pixel with unknown transmittance spectrum [5]. The system of linear equations is solved using the method of least squares with Tikhonov regularization [6] resulting in the estimation of transmittance spectrum for one pixel.

The transmittance spectrum of pixel could be presented as the product of the transmittance spectra of the dyes H and DAB if pixel is located in dyes co-localization:

$$\tau(\lambda) = \tau^H(\lambda) \cdot \tau^{DAB}(\lambda). \quad (2)$$

Usually, there are regions in the specimen stained only with H, so the solution of the equation (1) for these regions give $\tau^H(\lambda)$. So considering (2) $\tau^{DAB}(\lambda)$ could be estimated. From $\tau^{DAB}(\lambda)$ the final value of DAB staining intensity is calculated:

$$I^{DAB} = \int \tau^{DAB}(\lambda). \quad (3)$$

This parameter is analogous to the RGB-coordinates with excluded spectral sensitivity of CDD sensors and the emission spectrum of light source. This becomes evident when substituting in (1) $I_0(\lambda) = 1 = const$ and $m_i(\lambda) = 1 = const$.

The value of I^{DAB} calculated using (1-3) is influenced by the intensity of H staining. The transmittance spectrum $\tau^H(\lambda)$ as well as intensity of H staining I^H, calculated similar to (3), differs from one specimen to another. The purpose for this is difference of concentration of this dye in different specimens. Moreover, intensity I^H usually changes within one specimen. The study of the error value of I^{DAB} depending on the mean intensity of H staining (I^H) and the variability of H staining intensity (ΔI^H) within one slide was provided in this work. ΔI^H was determined as difference between maximal and minimal intensity of H staining. The initial data for the study were transmittance spectra of concentrated dyes H and DAB and emission spectrum of the light source of the microscope measured using spectrophotometer, as well as the spectral sensitivities of CCD sensors that were obtained from camera specification. The dependences of the error of the I^{DAB} from the average intensity and variability of H staining are presented in figure 1.

The obtained dependence of the relative error of I^{DAB} allows to determine the mean intensity I^H and the maximum allowable variability of H staining for which the error of I^{DAB} does not exceed a predetermined value. Separated spectral component of DAB characterizing intensity of staining, which corresponds to the concentration of a particular biological marker in cellular and tissue structures, can be further associated with diagnostic scores used by pathomorphologists.

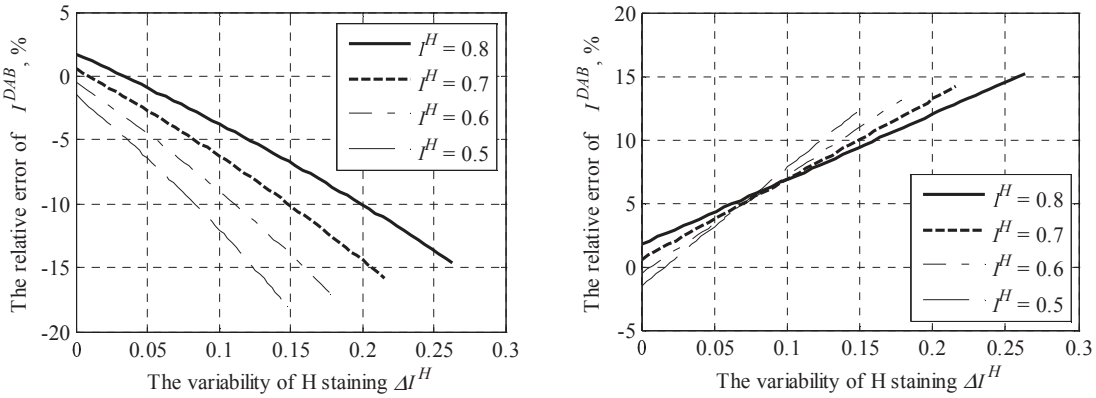

Fig. 1 The dependence of the error of the T^{DAB} from average intensity T^H and variability of H staining. The left plot shows the situation when the actual intensity of H staining in particular image pixel area is less than the average intensity and the right plot shows the situation when the actual intensity is more than the average intensity.

References

[1] D.E. Korzhevsky, O.V. Kirik, E.S. Petrova, et al, *The Theoretical Basis and Practical Application of Techniques of Immunohistochemistry: Guidelines*, 2nd ed., (SpecLit, St. Peterburg, 2014). [in Russian]
[2] R. Levenson, P.J. Cronin, K.K. Pankratov, "Spectral Imaging for Brightfield Microscopy," Proc SPIE **4959**, 27-33 (2003).
[3] C.M. Van der Loos, "Multiple Immunoenzyme Staining: Methods and Visualizations for the Observation with Spectral Imaging," J. Histochem. Cytochem. **56**, 313-328 (2007).
[4] T. Abe, Y. Murakami, M. Yamaguchi, et al, "Color Correction of Pathological Images Based on Dye Amount Quantification," Opt Rev **12**, 293-300 (2005).
[5] T. Harifi, S.H. Amirshahi, F. Agahian, et al, "Recovery of Reflectance Spectra from Colorimetric Data Using Principal Component Analysis Embedded Regression Technique," Opt Rev **15**, 302-308 (2008).
[6] G.I. Vasilenko, *The Theory for Signal Recovery: On the Reduction to Ideal Device in Physics and Engineering*, (Soviet Radio, Moscow, 1979). [in Russian]

The results of denoising algorithms comparison on magnetic resonance images

***A. Abdulraqeb*[1], *L. Sushkova*[1], *M. Abounassif* [2], *P. Parameaswari* [2], *M. Muteb*[2]**
[1] *Vladimir State University, 87, Gorky St., Vladimir, Russia*
[2] *King Saud Medical City, Al Imam Turki Ibn Abdullah Ibn Muhammad, Ulaishah, Riyadh, Saudia Arabia*

Introduction: Magnetic resonance image (MRI) is the result of a complex multi-component technical system and displays different physical aspects in the internal tissues of the body together with noise such as Gaussian noise, thermal noise, salt and pepper noise, multiplicative noise etc.[1, 2]. Noise reduction (smoothing) is usually the first stage (pre-processing) in image processing before the application of the post-processing procedures such as segmentation, classification, image analysis, etc.[3]. Filtering methods used in digital image processing can be divided into two groups: Spatial filtering (performed directly on the pixels of an image), and frequency filtering (the image is transferred to the frequency domain and filtered, later transferred back to the spatial domain) [4].

The aims of this research were to

1. Compare the existing (average, Gaussian, Wiener, median, Haar wavelet) filters on the two datasets.
2. Identify the optimal filter which enhances the effectiveness of noise removal from the MRI for the pre-processing stage.

The present study was approved by the Institutional Review Board, KSMC, Riyadh. The denoising algorithms are presented in table 1.

Table 1. The comparison of denoising algorithms

No	Filter	Principle of work	Note
1	Average	Replace pixels value in the image by the average of all the values in the local neighborhood	The default mask (3, 3)/9 was applied in this study.
2	Gaussian	Convolve the image with the 2-D Gaussian distribution, first combining with a 1-D Gaussian in the x-direction, and then with another 1-D Gaussian in the y-direction.	A 2-D Gaussian smoothing kernel with a standard deviation of 0.5 was used here.
3	Wiener	Estimate the local mean and variance around each pixel. It is more selective than a comparable linear filter, preserving edges and other high-frequency parts of an image, and affects the image adaptively.	For a large variance, little smoothing is performed and for small variance, more smoothing is performed.
4	Median	Replace each pixel value by the median value of local neighborhood.	Nonlinear filter preserves edges while removing noise.
5	Haar Wavelet	Starts with the selection level of decomposition, type (soft and hard) of thresholding and the value of thresholds, Modify the noisy wavelet coefficients according to a thresholding rule, finally reconstructing the denoised image.	This work used a 2 level decomposition - soft thresholds 4.937 at 1st level and 4.648 at 2nd level.

Comparison criteria: Two commonly used measures are Mean-Squared Error (MSE) and Peak Signal-to-Noise Ratio (PSNR) for comparing filtration's results. Since MSE depends strongly on the image intensity scaling, [5] we used PSNR which avoids scaling and can be calculated from the following formula:

$$PSNR = 10\log_{10}\frac{I_{\max}^{2}}{MSE},$$

where I_{max} - is the maximum pixel value in the input image [6].

$$MSE = \frac{1}{MN}\sqrt{\sum_{i=1}^{N}\sum_{j=1}^{M}(h(i,j)-f(i,j))^{2}},$$

where f (i,j) – is the original image; h(i,j) – is the denoised (filtered) image; i,j – is the pixel position of the M×N image.

Methodology: Dataset 1 with 18 MRI from Government hospital in Vladimir, Russia (they were obtained using a Philips Intera scanner with 1.5 T magnetic field induction), Dataset 2 with 56 MRI from Government hospital in Riyadh, Saudi Arabia (they were obtained using GE SIGNA scanner with 1.5 T magnetic field induction). Many of the current techniques assume the noise model to be Gaussien [7]. A Wiener filter is a minimum mean square error filter[8]. The images were experimented individually by adding Gaussian noise with zero mean and 0.01 variance, multiplicative noise with zero mean and 0.04 variance, salt and pepper noise with zero mean and 0.05 variance. The result of an image on experimentation and filtration is shown in Fig 1.

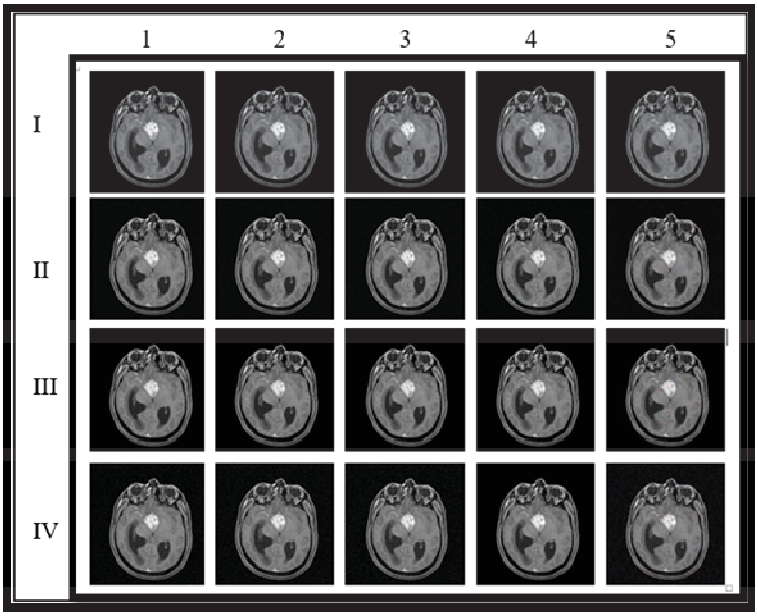

Fig. 1 Sample image after denoising: I-without noise, II-Gaussian added noise, III-Multiplicative added noise, IV-Salt & Pepper added noise; & Filters: 1-Average, 2-Gaussian, 3-Wiener, 4-Median, 5- Haar Wavelet.

Table 2. Descriptive Statistics for PSNR of all images in 1st and 2nd data sets

Type of Noise	Filters	Mean		Standard Deviation		Minimum		Maximum	
		Dataset 1	Dataset 2	Dataset 1	Dataset 2	Dataset 1	Dataset 2	Dataset 1	Dataset 2
Without noise	Average	19.988	17.572	2.462	2.679	**16.913**	12.932	24.292	22.903
	Gaussian	**24.715**	**22.155**	2.495	2.791	21.560	17.270	**29.001**	27.710
	Wiener	22.850	20.826	2.172	2.811	20.138	16.265	26.577	**28.407**
	Median	21.515	18.966	2.754	3.115	18.159	**12.334**	26.668	25.433
	Wavelet Haar	21.391	19.857	**0.818**	**1.499**	20.283	16.996	22.842	23.792
Gaussian noise	Average	13.688	14.240	0.155	0.747	13.457	12.127	13.934	**16.141**
	Gaussian	12.349	13.628	0.059	**0.153**	12.249	13.150	12.491	13.842
	Wiener	13.011	14.363	**0.027**	0.314	12.962	13.701	13.062	15.339
	Median	**14.357**	**14.491**	0.268	0.718	13.955	11.876	**14.907**	15.486
	Wavelet Haar	12.260 6	12.107	0.093	0.798	**12.124**	**6.493**	12.516	12.760
Multiplicative noise	Average	**16.567**	16.661	1.048	2.269	14.999	12.845	**18.237**	**21.502**
	Gaussian	14.632	**16.719**	0.780	1.451	13.314	14.569	15.936	20.215
	Wiener	14.194	16.549	**0.495**	**1.299**	13.292	14.625	15.045	19.688
	Median	15.271	16.502	0.893	2.017	13.842	**12.295**	16.701	20.843
	Wavelet Haar	14.309	15.072	0.828	1.451	**12.913**	13.093	15.691	18.485
Salt and Pepper noise	Average	12.644	13.593	**0.065**	0.571	12.569	11.963	12.823	14.956
	Gaussian	10.231	11.914	0.086	**0.218**	10.062	11.190	10.366	12.754
	Wiener	9.320	11.599	0.125	0.222	**9.075**	11.093	9.522	12.032
	Median	**19.952**	**17.597**	2.113	2.489	17.518	12.333	**23.747**	**22.475**
	Wavelet Haar	9.776	9.960	0.080	0.322	9.573	**9.190**	9.889	11.796

The results of this study are given in Table 2 and the Bar diagram in Fig 2, shows the Mean [9] PSNR with the Standard Deviation of the Five denoising algorithms for two data sets.

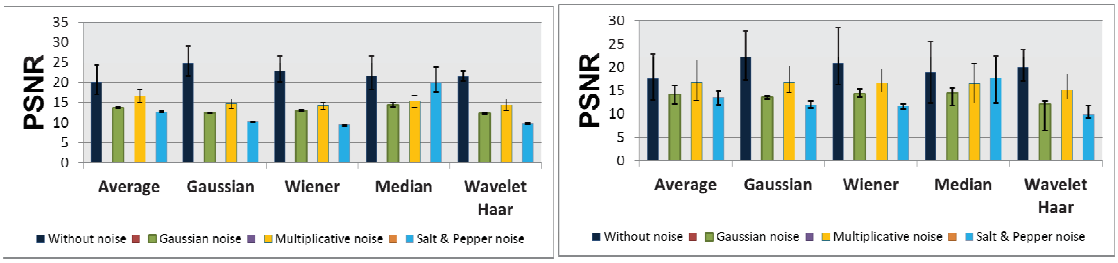

Fig. 2 Mean PSNR for Dataset 1(left) and Dataset 2 (right)

Discussion and Conclusion: Denoising algorithm is to reduce noise levels by preserving the image features and Visual perception is an essential part in diagnosing the brain tumors [10]. In our present study, among the original images without noise, the Gaussian filter had the maximum average of PSNR as 24.715, 22.155 for the 1st & 2nd dataset where the Wavelet Haar produced the minimum standard deviation of 0.818 respectively. Generally the quality of image can be measured by the peak signal-to-noise ratio (PSNR). However, sometimes a denoised image with a high PSNR value does not have satisfactory visual quality [11]. In the case of added Gaussian noise to original images, we observed that median filter produced the maximum average of PSNR as 14.357, 14.491 for the 1st & 2nd data set and the minimum SD by Wiener filter as 0.027. In those of multiplicative noise added to the original image, the Average filter showed the maximum average PSNR as 16.567, 16.719 for the 1st & 2nd data set and the minimum SD of 0.495 produced by Wiener filter. Different noise models include noise as additive and multiplicative type. They include Gaussian noise, salt and pepper noise (impulsive noise), Brownian noise and speckle noise. Salt and pepper noise [12] is an impulse type of noise, which is also called as intensity spikes. The basic Concept behind Image Restoration is digital Convolution using linear filters and moving window principle. From the Salt and Pepper noise added to original images, the median filter produced the maximum average of PSNR=19.952, 17.597 for the 1st & 2nd data set and the minimum standard deviation was noticed in average filter SD=0.065. The median filter is popular because of its ability to reduce random impulsive noise without blurring edges. It often fails to perform well as linear filters in providing sufficient smoothing of non impulsive noise components such as additive Gaussian noise. The main drawback of median filter is that it is not location variant in nature, and thus also tends to alter the pixels not disturbed by noise. The mean filters find applications where the noise is concentrated in the small portion of the image [13]. In our study there existed a statistically significant difference between the filters as tested by ANOVA- $F(4,275) = 24.94(P=0.000)$. Hence Median PSNR was considered to be the ideal tool for measurement. Filtering scheme has been proposed to eliminate impulse noise using global and local statistics [14]. Image Denoising has become a very essential exercise in Image Restoration. The wavelet transform has recently entered the arena of image denoising and it has firmly established its stand as a powerful denoising tool. Experimental results show that our noise reduction algorithm exhibits much better performance in both PSNR and visual effect. [15]

Qualitative analysis shows that the average filter tends to blur image more than the others filters, followed by median, Gaussian, Wiener and wavelet Haar. From the results above it can be recommended using the Gaussian filter in the case of images without noise and images with multiplicative noise and it's recommended to use it with a standard deviation of 0.5, to remove the noise and to keep the edges without blurring. In the case of Gaussian and Salt and Pepper noises, it can be recommended using the median filter because it well removes the noise and preserve the edges which are important for further image processing.

References

[1] S.R. Anisha. Krishnan J.Venugopala. "Comparison of various filters for noise removal in MRI brain image," ICFTCC. 68−73, (2015).

[2] H. Oulhaj. A. Amine. M. Aziza. D. Aboutajdine.,"Noise reduction in medical imaging - comparison of noise removal algorithms," ICMC. 344 – 349, (2012).
[3] Siti Noraini Sulaiman. Siti Mastura Che Ishak. Iza Sazanita Isa. Norhazimi Hamzah. " Denoising of Noisy MRI Brain Image by Using Switching-based Clustering Algorithm" /EEED-Bio.**05**. 33−39, (2014).
[4] Rafael C. Gonzalez. Richard E. Woods. Steven L. Eddins. *Digital image processing using MATLAB*. 2nd. Ed. (Gatesmark. LLC. 2009).
[5] Ramesh Jain. Rangachar Kasturi. Brian G. Schunck. *Machine vision*. (McGraw-Hill. Inc.1995).
[6] K.Sidhu, B.Khaira, I.Virk. "Medical Image Denoising In The Wavelet Domain Using Haar And DB3 Filtering," IRJES.**1**. 01-08, (2012).
[7] R.Pavithra. R.Ramya. G.Alaiyarasi. "Wavelet Based Non Local Means Algorithm for Efficient Denoising of MRI Images". IJARCCE.**4**. 388–392, (2015).
[8] Betty R.K.,Jonathan A.C., *Essential Medical Statistics*, Blackwell publishing, 2nd edn, , Pg :33-41.(2009).
[9] http://www.mathworks.com/help/images/ref/fspecial.html (date of access 01.03.2016).
[10] A. Anilet Bala, Chiranjeeb Hati, CH Punith, " Image Denoising Method Using curvelet Transform and Wiener Filter ," IJAREEE, **3**, 6943-6950, (2014).
[11] M. Amirmazlaghani, Hamidreza Amindavar, "A Novelwavelet Domain Statistical Approach for Denoising SAR Images" ICIP, (2009).
[13] Bhumika Gupta1, S. S. Negi, 'Image Denoising with Linear and Non-Linear Filters: A REVIEW', IJCSI, **10**, 1694-0814, (2013).
[14] R. Pushpavalli, G. Sivarajde, 'Image Denoising Using A New Hybrid NeuroFuzzy Filtering Technique', IJST.**2**, (2013).
[15] Yong-Hwan Lee, and Sang-Burm Rhee, 'Wavelet-based Image Denoising with Optimal Filter', IJIPS.**1**, (2005).

Back projection method for multiplexed measurement systems with hexagonal coded apertures

I.S. Burnaevskiy[1], M.A. Antakov[1], G.F.Fedorov[2], S.A.Tereshchenko[1]

[1] *National Research University of Electronic Technology, Russia, Moscow*

[2] *Department of Radiation Physics and Safety of Nuclear Technologies, National research nuclear university «MEPhI», Russia, Moscow*

The single photon emission computed tomography (SPECT) is well-known nuclear medicine imaging technique using gamma rays [1-4]. 3D object is typically presented as a stack of 2-D cross-sectional slices. Multiplexed measurement systems (MMS) are widely used in gamma- and X-ray astronomy, time-of-flight neutron spectrometry, optical spectroscopy, radiation introscopy and other areas [5-7].

To use the exponential Radon transform for emission computed tomography it is needed the possibility observing the object in all directions [6, 7]. If this assumption is not valid there is the fundamental problem of the object reconstruction from the incomplete projection data set (the problem of the limited solid angle), which is not solved to the present time. Typical examples are environmental monitoring of the ground layer with a radioactive contamination and a remote control of a nuclear reactor operation [8].

The way to resolve this problem is methods of longitudinal emission computerized tomography. One of these methods is the use of flat coded apertures [3-5].

The main method of the reconstruction for radiation sources space distributions with the use of MMS is the focal plane method (FPM) [3, 4, 9], which reduces this problem to solving of a high order system of linear algebraic equations. The criterion to estimate reconstruction quality is the mean-square deviation (D), which is computed as:

$$D = \frac{1}{M}\sum_{k=1}^{M}\sum_{i=1}^{V}\sqrt{\frac{1}{V}(\tilde{x}_i^k - x_i^k)^2}\ , \qquad (1)$$

where M is the number of planes in FPM, V is the number of elements in the hexagonal coded aperture, $\tilde{x}_i^k$ is the element of the reconstructed spatial distribution, x_i^k is the element of the given spatial distribution.

FPM implementation gives the next result (figure 1).

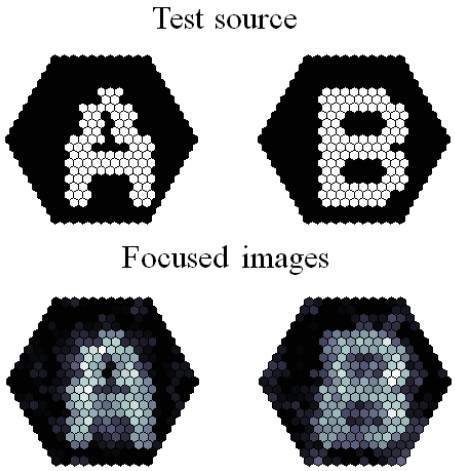

Fig. 1. Test source containing 2 planes and focused images in FPM.

However there is a necessity to improve the reconstruction quality. To achieve this goal iterative algorithms are used. Well known iterative methods are steepest descent method (SDM) and directed divergence method (DDM) [9].

It can be proposed a new iterative algorithm for the reconstruction of the radiation sources spatial distribution in SPECT. This algorithm based on an idea of the back projection (figure 2). The iteration formula corresponding this idea is:

$$\vec{s}^{(k+1,1)} = \vec{p}^{(k)}, \tag{2}$$

$$\vec{s}^{(k+1,i)} = \vec{s}^{(k+1,i-1)} + \alpha_{ik} \frac{q_i - \vec{h}_i^{\mathrm{T}} \vec{s}^{(k+1,i-1)}}{\vec{h}_i^{\mathrm{T}} \vec{h}_i} \vec{h}_i, \; i = 2,3,..., Mv \tag{3}$$

$$\vec{p}^{(k+1)} = \vec{s}^{(k+1,Mv)}, \tag{4}$$

$$\alpha_{ik} = \beta \cdot \tau_k, \tag{5}$$

where $\vec{h}_i^{\mathrm{T}} = \left[(h_i)_1, (h_i)_2, ..., (h_i)_{Mv}\right]$ is the i-th row of matrix $\hat{H}$, $\hat{H}$ is the matrix describing encoding process, τ_k is an empirical relaxation coefficient, β is the inverse squared distance between the source and the i-th cell of the detector.

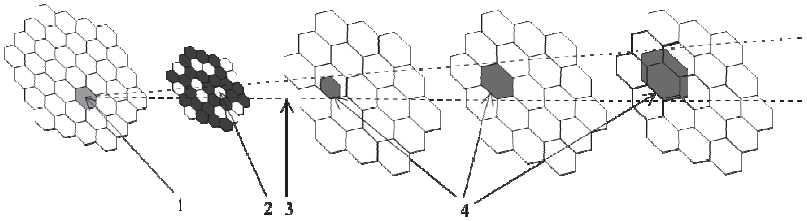

Fig. 2. Back projection method: 1 is a cell of the detector, 2 is the corresponding open pinhole of the coded aperture, 3 is a cone of the back projection, 4 is the object cells, which lie in the cone of the back projection

Comparison of SDM, DDM and BPM after 100 iterations for test source from figure 1 is presented on figure 3.

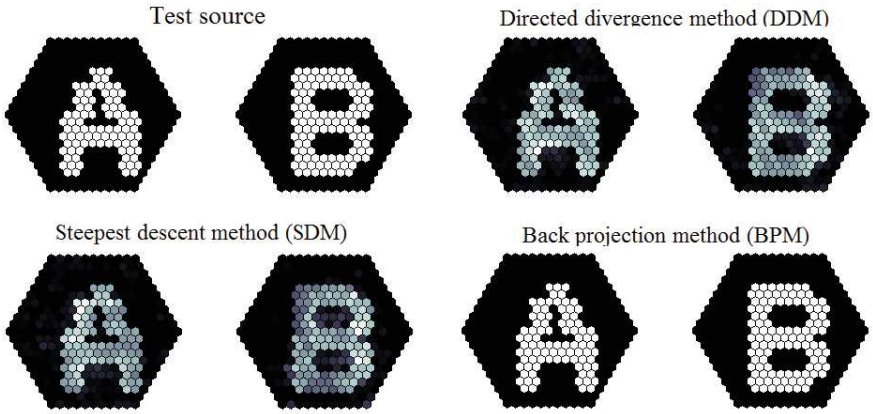

Fig. 3. Comparison of SDM, DDM and BPM after 100 iterations

On figure 4 presented 3 planes of the Modified Shepp-Logan Phantom used as a test source and reconstructed images after 100 iterations for SDM, DDM and BPM. Dependence of D on the number of iterations for SDM, DDM and BPM is presented on figure 5.

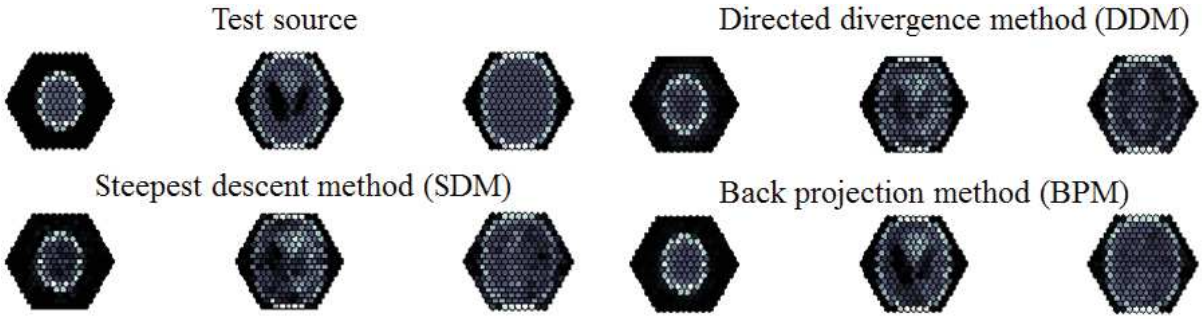

Fig. 4. Comparison of SDM, DDM and BPM

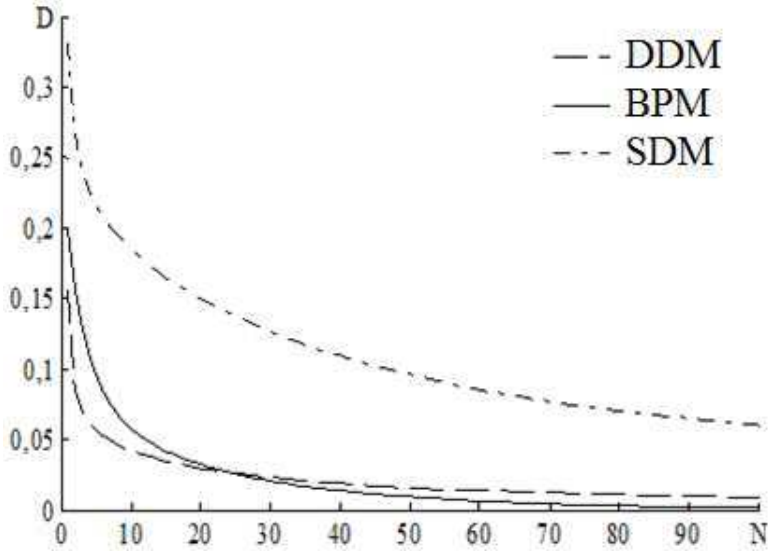

Fig. 5. Dependence of D for number on iterations of SDM, DDM and BPM

Mean-square error and images after 25, 50, 75, 100 and 250 number of iterations are presented on figure 6.

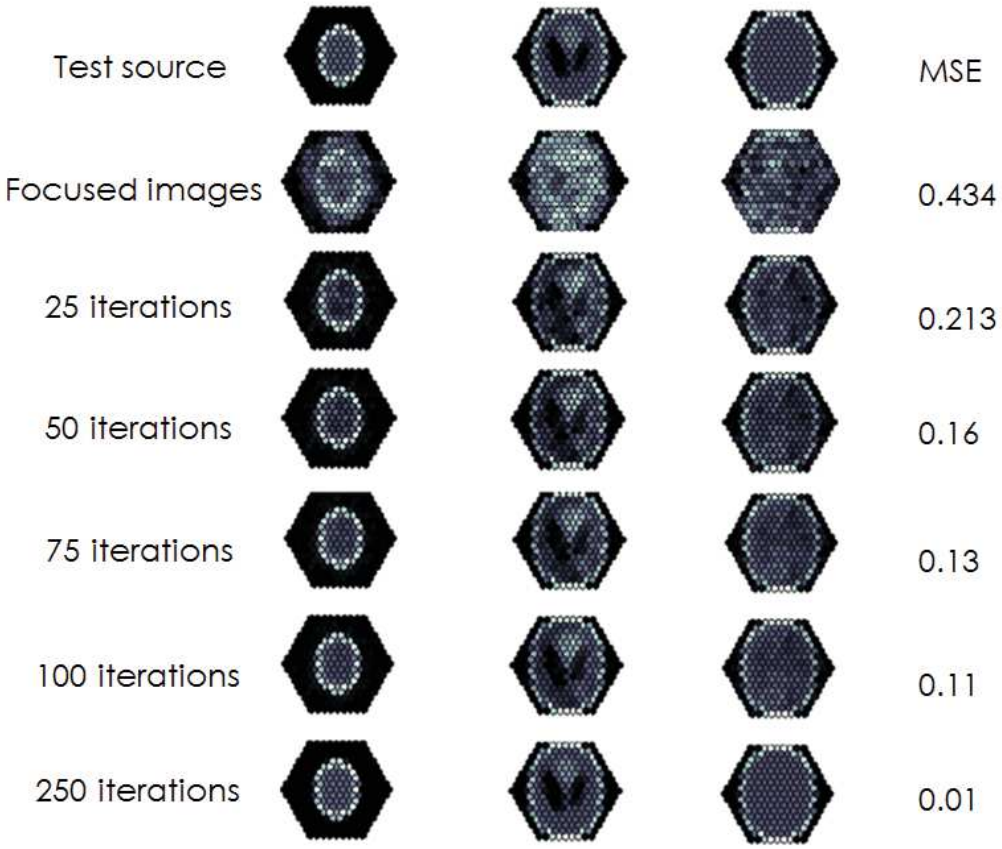

Fig. 6. The mean-square error and the reconstructed images after 25, 50, 75, 100 and 250 number of iterations

The back projection method has a rapid convergence in all cases (a different transparency, a different size of coded aperture, different types of test distributions). The proposed algorithm can be used with hexagonal coded apertures. In terms of the convergency the BPM is highly improved and it is better than DDM and SDM. As a conclusion the BPM is preferred in future investigations.

This work was financially supported by the Ministry of Education and Science of the Russian Federation (agreement № 14.575.21.0090, identifier RFMEFI57514X0090).

References

[1] The Special Issue on Computerized Tomography (1983), Proceedings of the IEEE, V.71, No.3
[2] Wernick M.N., Aarsvold J.N. (2004) Emission tomography: the fundamentals of PET and SPECT. Amsterdam, Elsevier
[3] Fedorov G.A., Tereshchenko S.A. (1990) The Computed Emission Tomography. M.: Energoatomizdat [in Russian]
[4] Terechenko S.A. (2004) Methods of the Computed Tomography. Moscow [in Russian]
[5] MacWilliams, F.J.; Sloane, N.J. (1976) A. Pseudo-random sequences and arrays. Proceedings of the IEEE, V.64, No.12, P.1715-1729
[6] Soroko L.M. (1980) Multiplexed measurement systems in physics. M.: Atomizdat [in Russian]
[7] Cook W.R., Finger M., Prince T.A., Stone E.C. (1984) Gamma-ray imaging with a rotating hexagonal uniformly redundant array. IEEE Tr. On Nuclear Science. V. NS-31. No. 1. P. 771-775
[8] Louis A.K.; Natterer F. (1983) Mathematical problems of computerized tomography. Proceedings of the IEEE, V.71, No.3, pp. 379 - 389
[9] Fedorov G.A., Tereshchenko S.A. (2001) Integral Code Systems for Recording Ionizing Radiation: Iterative Image Reconstruction Algorithms for Focal Plane Processing. Measurement Techniques. V. 44. No. 4. P. 422-427

Smoking determination by conventional camera with IR filter and image processing algorithm

***A.N. Briko*[1], *E.N. Rimskaya*[1], *I.A. Deshin*[1]**

1. Bauman Moscow State Technical University, 5 building 1, Baumanskaya street, Moscow, Russia

Introduction

One of the most today common social problems is smoking. Smoking is one of premature death causes and various diseases. Today it causes more than 5 million deaths each year. Effective and systematic tobacco epidemic tracking mechanism is one of the significant components of fighting against smoking.

According to WHO report in 2008 the prevalence of tobacco smoking among Russian men aged over 18 is about 60.4%, among women older than 18 years - 15.5%, among boys (13-15 years) - 30.1% and for girls (13-15 years) - 24,4% (Global Adult Tobacco Survey).

Smokers can be divided into two types: active (who smoke) and passive (who breathes smoke from a cigarette). Active smokers inhale an average of one-fourth part of tobacco smoke through the filter. And three-quarters of smoke are formed during the cigarette smoldering and fall in the ambient air. This smoke is the most dangerous, because it does not pass through the filter. Thus, passive smokers are exposed to similar harmful effects as active smokers, but without their own desires.

In May 21, 2003, the World Health Organization adopted a document "The WHO Framework Convention on Tobacco Control". It was signed and ratified by many states. Thus, smoking in public places was prohibited by law in many countries.

Following the trend of smoking bans as a fight with smoking and ensure the protection of non-smokers from smoking in public places, registration of smoking facts has become an urgent problem. This will allow not only to prevent offenses, but also help to track the number of smoked cigarettes.

This paper presents one of the variants to identify the smoking fact, which is applicable in the public places, or just for recording this fact (for example, for insurance coverage).

IV. Research

D. Smoke detectors

Produced detectors for registration smoke primarily developed as a fire safety measure, thus they have some limitations. Detector register scattered light is transmitted through the working chamber. Such detector cannot unequivocally distinguish suspended in the air different particles and smoke. Also it is required air constant circulation between the working chamber and room. Thus, as a result of air circulation fume concentration may be not enough for sensor operation.

The video surveillance using can be an alternative to smoke detectors. Thus, it increases the area of surveillance and have ability to identify smoke source (for our problem – to register smoking).

E. *Method*The cameras allow to respond to IR illumination sources. Lighted cigarette is such source. Thus, based on the blackbody model, we can approximately estimate the radiation wavelength and intensity.

For thermal radiation estimating it is necessary to use the relation between the wavelength and intensity of radiation that is derived for blackbody: Planck's law (figure 1). [1]

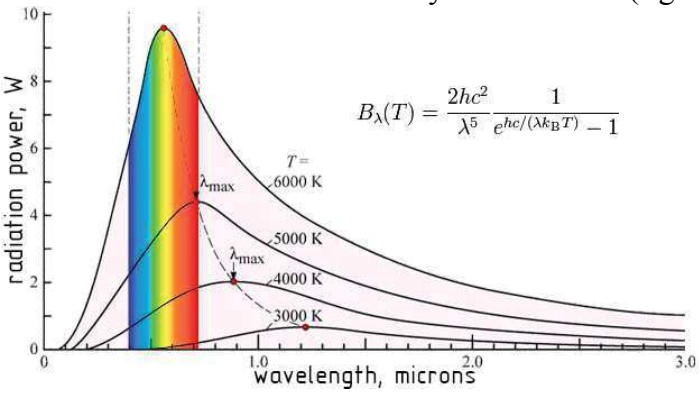

Fig. 1 Planck's formula and the radiation power dependence of the wavelength.

The wavelength at which the blackbody radiation energy is maximum is determined by Wien's displacement law: λmax = 0.0028999 / T, where T - temperature in Kelvin, λmax - the wavelength of maximum intensity in meters.

Assuming in the first approximation that the human skin close in properties to a completely black body, the emission spectrum peak at 36°C (309 K) is at a wavelength of 9400 nm (in the infrared region).

The temperature of tobacco smoldering temperature is 300°C and during puffing on the cigarette reaches 900-1100°C. After calculation wavelengths at which radiation energy has maximum value by the formula Wines, we obtain the following values for the 300°C - 5,061 microns; to 900°C - 2,472 microns; 1100°C - 2,112 microns.

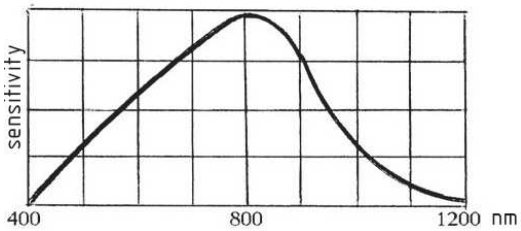

Fig. 2 Spectral sensitivity of the CCD matrix.

Figure 2 shows the spectral sensitivity of the CCD matrix. According to this curve it is evident that it comes at the beginning of the IR, but does not include the required wavelengths. However, according to Figure 1, the camera must register part of the necessary radiation. Despite the fact that digital matrix cameras are sensitive to infrared radiation, their sensitivity to visible light in hundreds or even thousands times more, therefore, it is necessary to block visible light. Infrared filters are used to solve this problem. Thus, to ensure the possibility of realization, the experiments were conducted.

F. Experiment

To implement the detection method experiment was performed using 2 cameras. One of the cameras was a Sony HDR-CX550 with the NightShot function. This function is designed to shoot in low-light conditions through the infrared light using and using special matrix. In order to cut the excess range of frequency the special infrared filter Falcon Eyes IR 950 with a bandwidth of 950 nm was used.

As a second camera the webcam Canyon CNR-WCAM420 with removed manually hot-mirror filter (a filter that blocks infrared radiation and is glued to the matrix) was used. Thus a camera that also records the IR was obtained. Special film Kodak Wratten # 87C was used to cut unnecessary frequency band with a bandwidth of 850 nm.

Fig. 3 Cameras and filters used in experiments (left) and the resulting image (for example the heated soldering hot air gun was used)(right).

G. Results

The obtained images from the cameras were needed to be processed. As a system for image processing mathematical package Matlab was used, because it contains built-in functions for image processing. A method of growing areas was used for segmentation processing of the objects. [2,3]

First, the image transferred in shades of gray with preliminary uninformative components removal in order to simplify the computation tasks. The next step was object detection. At this stage, there is recognition of the key points of the image, i.e. the definition of the points with a border of a sharp gradient difference.

Thereafter, the method of areas of cultivation. Morphological expansion of the image produces - building areas related to the key points. Also internal filling gaps performed - fill the area inside the object.

The final stage is an object smoothing - the alignment of the object edges. Below there are examples of processed images.

Fig. 4 An example of image processing with the Sony camera with a filter at the cigarette smoldering (the original image on the left preconditioning image in the center, highlighted contrasting object on the right).

Fig. 5 An example of image processing with the Sony camera with a filter at the cigarette inhaling (the original image on the left preconditioning image in the center, highlighted contrasting object on the right).

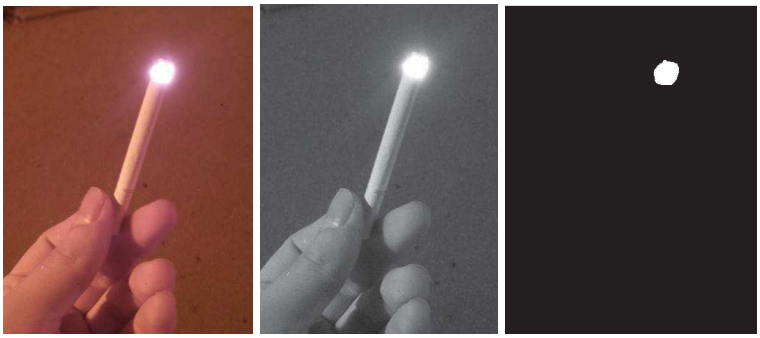

Fig. 6 An example of image processing with the webcam with a filter at the cigarette smoldering (the original image on the left preconditioning image in the center, highlighted contrasting object on the right).

V. Conclusions

Based on the study, it can be concluded that the detection of infrared radiation sources can locate signs of smoking, as well as to record other sources of heat radiation. This registration can be carried out using conventional cameras (after modifying them a bit) with the IR filter, which is a cheap alternative to currently used smoke detectors.

The highest characteristics of the matrix and the image quality is not a priority because the aim is recording only the smoking fact. For software images post-processing is necessary to obtain a contrast spot areas of high temperature.

In this article was shown optimal and fast version of the image processing algorithm, which has shown good results. Thus, it is necessary to produce a further modification of the algorithm for determining smoking in real-time.

References

[1] R. Gonsales, R. Vuds, *Digital image processing*, (Tehnosfera, Moscow, 2005).
[2] R. Gonsales, R. Vuds, S. Eddins, *The world of digital processing*, (Tehnosfera, Moscow, 2006).
[3] L.K. Martison, E.V. Smirnov, *The quantum physics*, (BMSTU, Moscow, 2004).

Analysis of psychophysiological indicators of the functional state of a human operator during monotonous activity

A.A. Petrenko[1], V.S. Kublanov[1]

1. Research Medical and Biological EngineeringCentre of High Technologies, Ural Federal University, 32 Mira Str., Yekaterinburg, 620002, Russian Federation

I. Introduction

The problem of human functional states in labor, physiology, and psychophysiology, various fields of medicine requires urgent attention now, as indeed it has for many decades. Constructive solutions to the question of how to assess and analyse human functional states during the undertaking of practical tasks in various spheres of human activity in special or extreme circumstances is of great importance [1, 6].

Studies of the human functional state of an operator performing complicated tasks are of most interest since a monotonous workload increases the risk of making mistakes, which can in turn have unpredictable consequences.

The functional state of a human operator depends on such individual characteristics as temperament, emotional stability, agility, concentration and maintenance of attention, etc. [2].

The aim of this study is to determine the significant personal and other parameters which are responsible for the regulation of the nervous system, which together determine the efficiency and stability of the human operator.

II. Methods

The study involved 67 healthy subjects between the ages of 18-25 years who gave their informed consent to participate in the study.

In order to reach the monotony state the subjects were asked to perform the Bourdon-Wiersma test for 10 minutes. The test is aimed at assessing productivity, sustainability, distribution and switching of attention [3]. The quality of the test was evaluated by the number of errors, the number of gaps, the number of scanned characters and productivity indicator.

The Standardized Minnesota Multiphasic Personality Inventory MMPI in the Russian modification by Sobchik L.N. – SMIL was used to assess the individual and psychological characteristics of subjects.

The SMIL test methodology contains 10 major scales and 3 basic reliability scales [4].

The heart rate variability (HRV) signal was used as a physiological indicator of the dynamics of the human functional state. The signal was recorded by means of psychophysiological complex "REHACOR" by Medicom MTD. HRV enables the discovery of regularities in physiological and psycho-emotional human states [5]. Analysis of the spectral components of HRV data was performed using the program implemented in MATLAB.

"STATISTICA 10.0" software applications were used for statistical analysis.

The study consisted of 4 stages. ECG was recorded in course of 2-4 stages. The sequence diagram of the experiment is shown in Fig. 1

I.	II.	III.
MMPI-test	**Background**	

III. Results

Table 2: Classification Functions

	3	9	6	0	8	F	K	L	Constant
first - p=,52239	0,173	1,838	-0,134	2,479	-1,314	1,899	2,524	0,693	-239,163
second - p=,47761	0,197	1,738	-0,078	2,358	-1,207	1,803	2,38	0,797	-229,203

These discrimination functions can be used to classify new objects in cases where it is not known in advance which of the existing classes they belong to.

The classification matrix is the overall result in the assessment of the quality of the current function classification. The classification matrix contains the number of samples correctly classified (on the matrix diagonal) and those which occurred in the wrong group. The classification matrix is shown in Table 3.

Table 3: Classification Matrix

Observed\Predicted	Percent-Correct	first - p=,52239	second - p=,47761
first	80,00000	28	7
second	71,87500	9	23
Total	76,11940	37	30

Thus the classification accuracy of the first group is equal to 80%, the second group - 72%. The accuracy of the general classification is 76%.

Later on, the analysis of the HRV spectral components (HF, LF and VLF) was carried out.

According to the previously selected method of dividing subjects into 2 groups (according to productivity) the variance analysis of the HRV spectral components at each stage of research was carried out. The results are shown in Fig. 2.

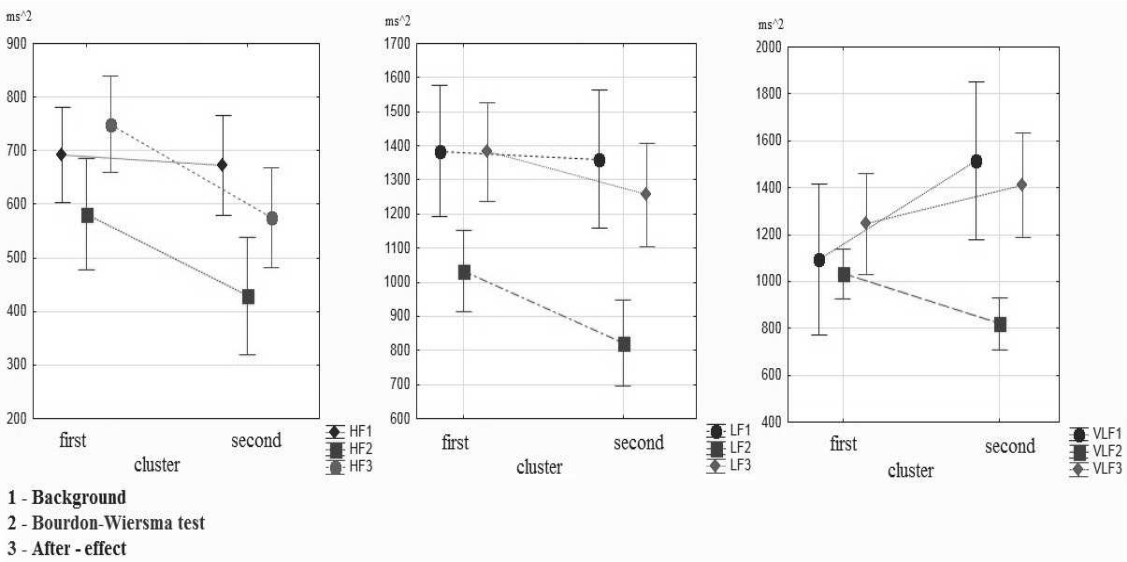

Fig. 2 Variance analysis of the HRV spectral components at each stage of research

According to the received data the significant difference in the groups is not observed at the initial background stage of research, but at the stage of the Bourdon-Wiersma test the averages of HRV indices decrease in the second group in comparison with the first. At the third stage of after-effect the averages are closer to the original data, and the significant differences between the groups were not observed.

Thus, during the course of the stress test a different response from the autonomic nervous system can be observed.

The HF index is an indication of the power of respiratory waves of heart rhythm. The LF index characterizes the state of the sympathetic division of the autonomic nervous system, in particular, the system of vascular tone regulation. The spectral component of the VLF is closely related to psycho-emotional stress and functional state of the cerebral cortex. VLF power of HRV is a sensitive indicator of the control of the metabolic processes, and reflects well the energy deficient state [5].

IV. Conclusion

While this work was carried out, experimental research data analysis of the functional state psychophysiological parameters of a human operator in a monotonous activity was conducted. During the course of this analysis, the discriminant function was found. This enables the classification of the subjects according to their productivity, using the results of standardized

processes with energy. Breath and blood circulation – the main links of oxygen transport system, define both providing an organism with energy, and its reserve opportunities. At the same time, at rest and at loadings of different intensity interaction of breath and blood circulation significantly differ. So, in our researches it was shown that at rest at breath function strengthening warm activity decreases a little, showing the retsiprokny relations between these physiological systems [1]. At physical activities, since power level is 1vt/kg body weights, the increase in function of breath occurs together with increase in warm activity that reflects a synergy of these physiological systems. At persons with the low level of functional reserves reaction from cardiovascular system at physical activity prevails over reaction from breath, at persons with high reserves of function of these systems change synchronously. Therefore, estimating an orientation of reciprocal adaptive reactions to functional loadings expediently along with a traditional quantitative assessment of dynamics of the studied scalar indicators to apply and the vector analysis of the combined reactions of breath and blood circulation.

Other aspect of use of vectors for an assessment of functional reserves and, perhaps, durations of the forthcoming life appears in the analysis of the loops of a hysteresis describing behavior of cardiorespiratory system in MOD-MOK coordinates. The phase curve of changes of a vector of the intersystem relations of breath and blood circulation at the increasing loading and during restoration [2] will show an open condition of phase curve what will testify to loss or decrease in reserves, and return of a vector to an initial state (isolation of a phase curve) – about process of training and about high reserve opportunities of an organism. The offered approach will allow to estimate better quality of providing an organism with energy through an assessment of regulation of interaction of breath and blood circulation, considering complexity and variety of the regulatory relations between physiological systems in different living conditions.

References

[1] Severin A.E., Rozanov V.V., Torshin V. I., Schukin S. I. The simultaneous analysis of a warm rhythm and breath for expansion of opportunities of functional diagnostics. // Biomedical radio electronics, 2011, No. 10, 96 - 102.

[2] Severin A.E., Rozanov V.V., Batotsyrenova T.E., etc. Hysteresis loop as indicator of ability of an organism to adaptation and functional reserves of an organism. // XI International scientific conference "Physics and Radio Electronics in Medicine and Ecology" Vladimir 2014, S.330-331.

The electrical impedance method of peripheral vein localization

***M.B. Al-harosh*[1], *S.I. Shchukin*[1]**

1. Bauman Moscow Technical University, Moscow, Russia

The electrical impedance method of peripheral vein detection is a novel approach, which offers the advantages of being not expensive and capability of minimizing and reducing the difficulty of achieving intravenous access in many patients, especially pediatric and obese patients. This work represents the quality of this method to achieve intravenous access in patients.

The electrical impedance method of peripheral vein detection is based on the measurement of electrical impedance using the 4-electrode technique by applying a known alternating current of frequency 100 kHz and constant amplitude to a current electrodes and measuring the resulting surface potential at the two separate electrodes.

To perform electrical impedance measurements a special electrode system was designed to be attached to the study area. The electrode system, which is an array of surface electrodes,

has four channels of tetra-polar electrode configurations. The electrode system has a distance between electrodes and a diameter of 3.5 mm. The ambulatory of electrical impedance system of peripheral vein detection system depends on the development of small dry electrodes that can provide good signal quality in a variety of conditions, and the ability to retain their characteristics during the whole procedure. However, due to the small contact area with the skin of such electrodes, it's requiring so long time to stabilize the transient resistance of skin-electrode contact. The stability of the skin-electrode contact can also be achieved by pressing the electrode system to study area but pressing on the patient's skin with the electrode system can cause the vein to collapse. This is not desirable in such measurement, thus the collapsed vein can't be detected. This paper represents the new electrode system shown in figure 1. In this electrode system the surface of the current electrodes became larger and thus the stability of the skin-electrode contact improved so measurements were much more reliable and feasible for larger time periods.

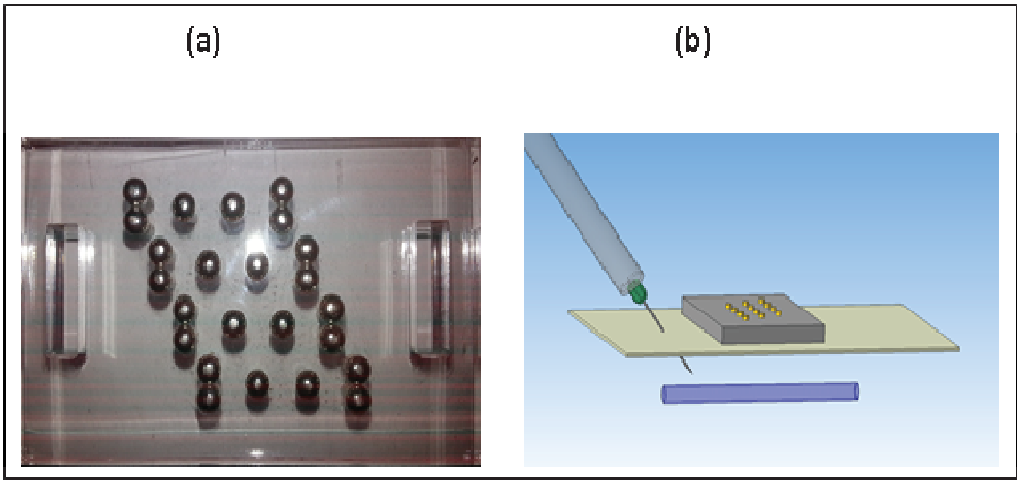

Fig. 1 The designed electrode system (a), the method of electrode system setting (b).

The impedance was recorded with the multichannel system (REO-32) which is developed at the department of medical and technical information technology at Bauman Moscow state technical university [1]. The measurements on participants show that it is so hard to detect the peripheral veins by the absolute impedance values, due to the heterogeneity of soft tissue. So factors affecting the absolute impedance are eliminated by only measuring relative impedance changes, rather than absolute impedance values. To display the relative impedance changes in our work we used the venous occlusion impedance plethysmography as a method of vein cross-sectional changes [2].

The principle of the methodology is that the venous return from the forearm is briefly interrupted by inflating a cuff, placed around the upper arm, to well above venous pressure but below diastolic pressure [3].

For this examination the patient is after the cuff is placed around the upper arm, an inflation pressure of around 60 mmHg is used for intervals of 2 min, then the cuff are deflated

Figure 2 shows the change of electrical impedance during two-minute arm cuff occlusion from different channels of the electrode system. The maximum decrease of electrical impedance occurs during the occlusion corresponds to the filling phase of the vein that we need to detect. After the filling phase is completed the cuff is deflated so the venous flow can flow out and this change corresponds to the increase of electrical impedance in the curve.

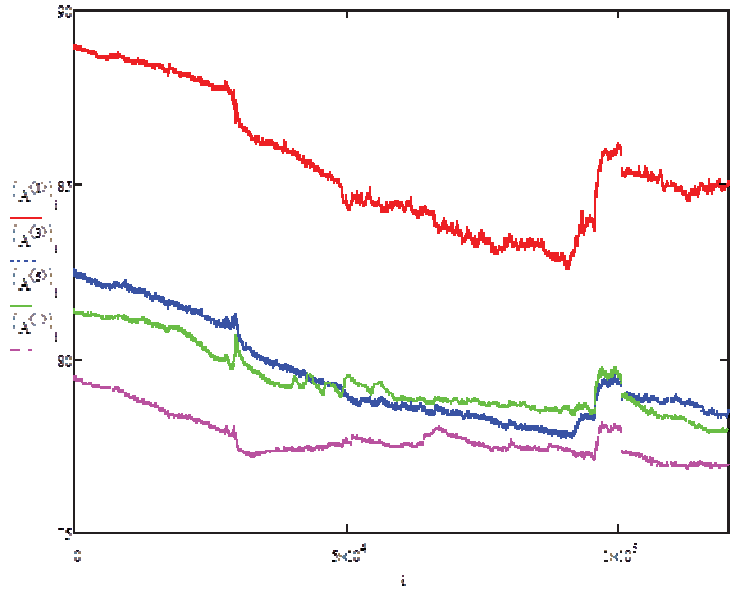

Fig. 2 The electrical impedance signals obtained by the electrode system.

The next step after obtaining the signals is to improve the signal to noise ration. The signals are filtered in order to reduce the noise component due to hand's operator movements during the measurement. The results of filtering are shown in figure 3.

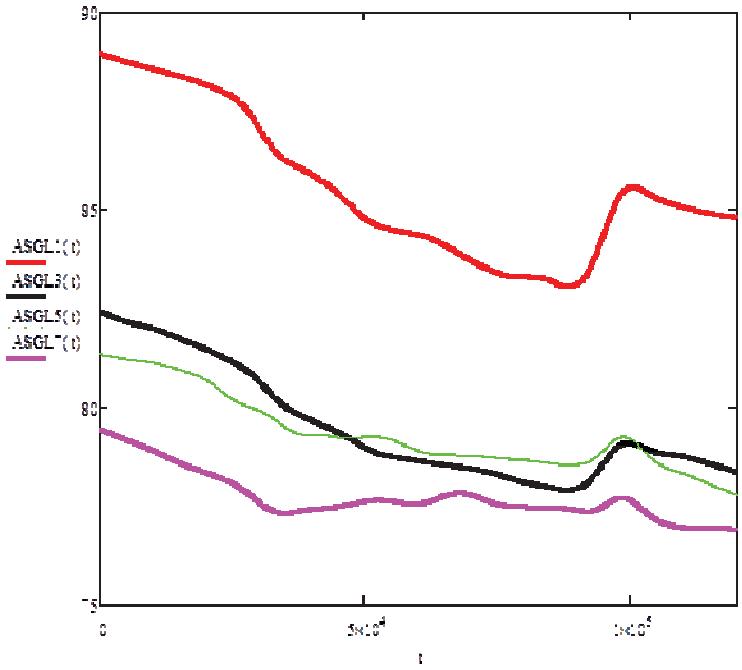

Fig. 3 The electrical impedance signals after filtering.

Figure 4 shows the first derivative of signals. The minimum peak during inflation and the maximum peak during deflation have been used as an algorithm to detect peripheral veins, which can be located on the reign of interest.

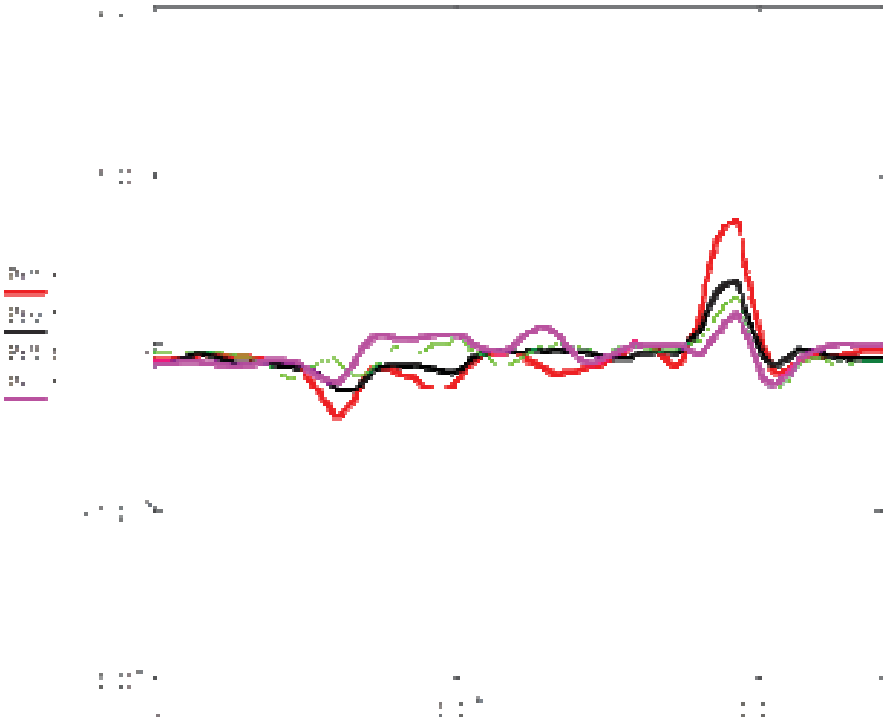

Fig. 4 The first derivative of the electrical impedance signals.

The corresponding peak of the impedance value shown in the derivative signals depends on difference of electrical properties of soft tissue and vein, the diameter of vein and the vein depth in soft tissue.

References

[1] AL-Harosh, M. B., and S. I. Shchukin"Numerical Modeling Of The Electrical Impedance Method Of Peripheral Veins Localization." World Congress on Medical Physics and Biomedical Engineering. **51**, 1683-1686 (2015).
[2] R. Nils Planken, Xavier H. Keuter, Alfons G. Kessels, Arnold P. Hoeks, Tim Leiner, Jan H. Tordoir" Forearm cephalic vein cross-sectional area changes at incremental congestion pressures: towards a standardized and reproducible vein mapping protocol." J Vasc Surg. **44(2)**, 353–358 (2006).
[3] Wilkinson, I. B. and Webb, D. J " Venous occlusion plethysmography in cardiovascular research: methodology and clinical applications." British Journal of Clinical Pharmacology. **55** 631–646 (2001).

Sleep stage classification using respiratory effort signals

A. Tataraidze
Bauman Moscow State Technical University, 5, 2nd Baumanskaya str., 1050005, Moscow, Russia

Sleep architecture consists of alternating cycles. Each of them is divided in Rapid Eye Movement (REM) and non-REM (NREM) sleep. Then, NREM is subdivided into 3 stages. Frequently, first two NREM stages are united into Light Sleep (LS) while the third stage is called Deep Sleep (DS).

Polysomnography (PSG) is a gold standard for sleep architecture evaluation. Usually, an expert classifies epochs (30s. intervals) as one of the sleep stages or wakefulness (W) based on the manual analysis of signals acquired during PSG, namely electroencephalogram, electrooculogram and electromyogram. Due to inapplicability of using PSG as a screening tool, sleep architecture evaluation based on the cardiorespiratory analysis has drawn attention over the last decade. Nevertheless, sleep stage classification using respiratory effort signals only has been poorly investigated, although respiratory activity might be easier registered by non-contact manner than heartbeats.

This paper describes a method for W-REM-LS-DS (WRLD) classification based only on respiratory effort signals registered both contact and non-contact methods. The study is a continuation of our previous works aimed at W-REM-NREM classification based on BRL [1] and RIP [2] signals.

Two datasets were used in the study. The first one consists of 628 subjects from the Sleep Heart Health Study (SHHS) [3, 4] database whose respiratory effort was registered by Respiratory Inductance Plethysmography (RIP). Data of 32 subjects from the second dataset were obtained in V.A. Almazov Federal North-West Medical Research Centre during simultaneous bioradiolocation (BRL) monitoring and PSG.

The bioradar and the signal preprocessing methodology were the same as in our previous works [1, 2]. Each epoch was described by the following features: the length and the energy of an artifact period; median, interquartile range (IQR) and median/IQR ratio of peaks, troughs, breathing cycle amplitudes and widths; the median respiratory volume during inhalation, exhalation and their ratio over an epoch [4]; the median respiratory volume and flow during breathing cycle, inhalation and exhalation over 25 epochs [4]; the mean and the standard deviation (SD) of breath-by-breath correlation [5]; spectral powers and their logarithms in the very low frequency band between 0.01 and 0.05 Hz, the low frequency band (LF) between 0.05 and 0.15 Hz, the high frequency (HF) band between 0.15 and 0.50 Hz, and LF/HF ratio; the peak frequency and its power in HF; the minimum of standard, constrained and parametric dynamic time and frequency wrapping between the target epoch and its four nearest neighbours; sample and approximate entropy of the respiratory effort signal; the mean and SD of multiscale permutation entropy of the signal; sample entropy of peaks and troughs over an epoch; SD and variation of breathing frequency during 3, 5, 7, 9 and 11 epochs [5]; the normalized index of epoch over total record time.

The probability that epoch corresponds to a certain stage was estimated using Gradient Boosted Machine classifier. Then, these probabilities were used as features for Linear Discriminant Analysis classifier. Classifiers were trained and tested by 5-fold cross-validation and leave-one-subject out cross-validation for SHHS and BRL datasets, respectively. Classification results were compared with PSG epoch annotations and estimated by Cohen's kappa coefficient of inter-rater agreement.

The kappa of 0.54 ± 0.14 (mean ± SD) and 0.49 ± 0.12 was achieved for SHHS and BRL datasets, respectively. To the best of our knowledge, the results outperforms those reported in literature for WRLD classification based only on the analysis of RIP signals as well as BRL signals. The performance of sleep stage classification using BRL is comparable with this obtained using RIP. Thus, using BRL is a promising way for sleep monitoring.

The research was supported by Russian Foundation for Basic Research grant # 15-07-02472 A and grant of President of Russian Federation # MK-7812.2015.7.

References

value of biasing resistor should be at least 10^{10} Ω for the reliable reception of low-frequency harmonics. Unfortunately, the resistors with ultra-high value are pretty expensive and hard-to-buy goods.

II. The Feedback Loop for Biasing of the Input Instrumentation Amplifier

In [3] an original circuit, which appears as an equivalent to the ultra-high value biasing resistance, was described. This circuit contains only inexpensive general purpose components (Fig. 1).

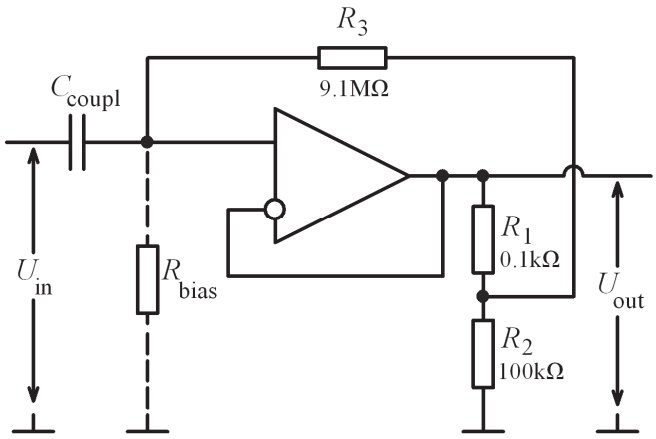

Fig. 1 Circuit diagram of the feedback loop around operational amplifier

A resistive divider with the transmission factor of $a = R_2 / (R_1 + R_2) = 0.999$ is connected to the output of the operational amplifier (op-amp). A 9.1 MΩ resistor is connected between the input of op-amp and the output of the resistive divider. The current through the resistor R_3 can be represented as the current through the virtual resistor R_{bias} with resistance value given by the formula

$$R_{bias} = \frac{R_3}{1-a}. \quad (1)$$

The operation of the biasing feedback loop was verified through SPICE simulations and experiments on the breadboard. Then, the biasing circuit was connected to the INA116 amplifier (Fig. 2).

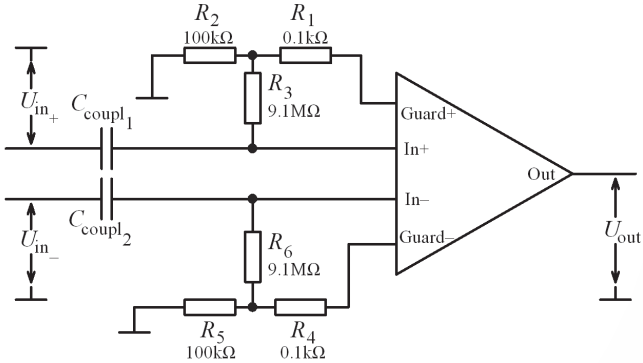

Fig. 2 Feedback loops, connected between signal inputs and guard pins of the instrumentation amplifier.

III. The Narrow-Band Stop Filter

One of the main problems with the reception of the bioelectric signals (such as ECS) is the suppression of various interferences. This problem becomes much more important when the ECS is received via capacitive coupling.

The greatest negative impact on the quality of the ECS is shown by the mains 50/60 Hz hum. Usually a stop filter is used to remove this type of interference. The filter design should provide the convenient adjustment of the quality factor and the notch frequency. In the work [4] a tunable stop filter comprising two cascaded all-pass filters, symmetrical voltage divider and a feedback loop with variable depth (Fig. 3) was designed.

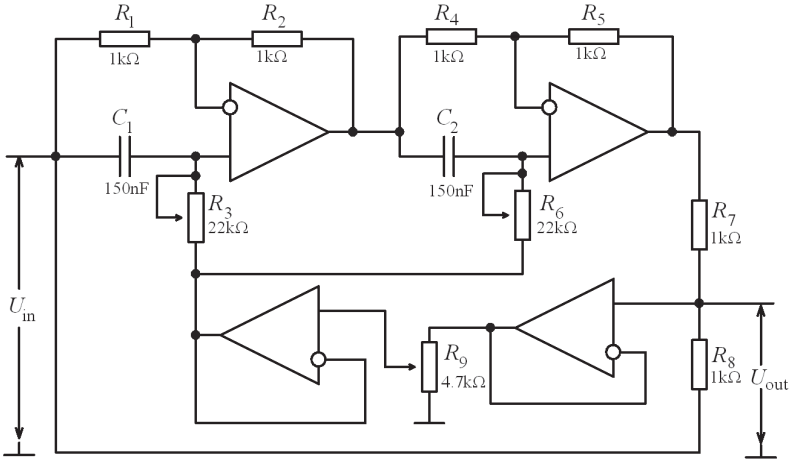

Fig. 3 Circuit diagram of the narrow-band stop filter.

After the signal had passed through the all-pass filters, it is added to its own original by the symmetric divider (R_7, R_8). Herewith the amplitudes of all harmonics of the signal are reduced according to the changes in the phase of the signal. The phase of the harmonic with maximum suppression is changed by 180°. The frequency of the harmonic with maximum suppression is equal to the geometric mean of the two frequencies: $\omega_1 = (R_3 \cdot C_1)^{-1}$ and $\omega_2 = (R_6 \cdot C_2)^{-1}$.This is the notch frequency of the filter:

$$\omega_0 = \sqrt{\omega_1 \cdot \omega_2} \,. \tag{2}$$

The output signal of the filter is applied through buffer op-amps to the potentiometers R_3 and R_6. The resistor R_9 varies the depth of the feedback d (from zero to 100%) and thus changes the quality factor Q, given by the expression

$$Q = \frac{0.5}{1-d} \cdot \frac{2\sqrt{\omega_1 \cdot \omega_2}}{\omega_1 + \omega_2} \,. \tag{3}$$

The gain-transfer characteristic of the rejection filter is

$$H(s) = \frac{s^2 + \omega_0^2}{s^2 + \frac{\omega_0}{Q} \cdot s + \omega_0^2} \,, \tag{4}$$

where $s = j\omega$, $j = \sqrt{-1}$.

IV. The Experimental Results

The experimental setup for the ECS recording includes:

- cotton T-shirt with two capacitive coupled sensing plates embedded (Fig. 4);
- two analog stages: the input stage, based on IA with feedback loops and the narrow-band stop filter;
- sound card, acquiring filtered analog signal;
- personal computer with Audacity software installed.

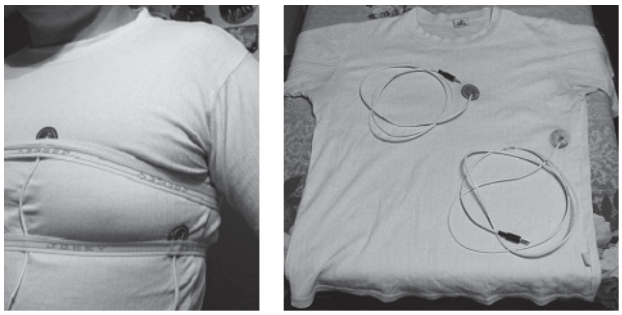

Fig. 4 T-shirt with the capacitive coupled sensing plates.

The output signal from the stop filter is acquired by sound card and digitized with a 24-bit resolution and 44.1 kHz sampling rate. The digital signal is recorded on a personal computer using the Audacity software. The higher harmonics of the 50/60 Hz interference are removed by the digital processing. The form of the processed ECS in 1–100 Hz frequency range is represented on Fig. 5. The QRS complex, T-wave and P-wave [5] are more or less visible on the ECG recording.

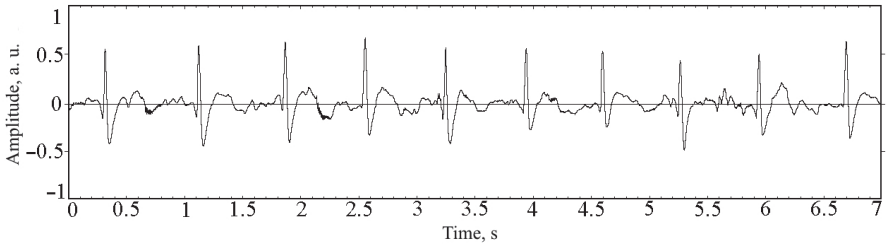

Fig. 5 Recorded ECS with 1–100 Hz frequency band.

V. Conclusion

The method of the bioelectric signals registration via capacitive coupling is useful for real-time monitoring as well as for continuous data collection. This method can be used for monitoring the health status of people working in stress conditions (rescue workers, firefighters, etc.), in sport medicine and fitness.

References

[1] M. Chi Yu, G. Cauwenberghs, “Micropower Non–contact EEG Electrode with Active Common–Mode Noise Suppression and Input Capacitance Cancellation”, Proceedings of the 31st Annual International Conference of the IEEE EMBS, pp. 4418-4421 (2009).

[2] A. Aleksandrowicz, S. Leonhardt, “Wireless and Non-contact ECG Measurement System – the “Aachen SmartChair”, Acta Polytechnica, vol. 47, no. 4-5, pp. 68-71 (2007).

[3] V. A. Gerasimov, P. V. Afanasjev, O. S. Bokhov et. al., “Research of systems for contactless obtaining of electrocardiograms creation possibility”, Biotekhnosfera, no. 3, pp. 2-6 (2015).

[4] A. A. Uhov, V. A. Gerasimov, L. M. Selivanov et. al., “A Method of Cardiac Signal Registration Through a Capacitive Coupling Between Sensors and Patient’s Skin”, Proceedings of the 2016 IEEE ElConRusNW, pp. 797-799 (2016).

[5] A. Gacek, W. Pedrycz, *ECG Signal Processing, Classification and Interpretation: A Comprehensive Framework of Computational Intelligence*, (Springer Verlag, New York, 2011).

Significance of segmentation methods in assessing brain tumor magnetic resonance images

***A.R. Abdulraqeb*[1], *L. Sushkova*[1], *M. Abounassif* [2], *P. Parameaswari* [2], *M. Muteb*[2]**

[1]*Vladimir State University, 87, Gorky St., Vladimir, 600000, Russia*

[2]*King Saud Medical City, Al Imam Turki Ibn Abdullah Ibn Muhammad, Ulaishah, Riyadh, Saudia Arabia*

A great effort in the field of research, medical imaging was focused on brain tumors segmentation in recent years[1]. After obtaining Magnetic resonance imaging (MRI), radiologists measure the mass of the tumor manually by scaling the two extreme points, which is a time-consuming task. Several methods were proposed and developed for accurate segmentation [2,3,4,5,6,7] such as thresholding, region based, edge based, and clustering methods etc. In this work, thresholding, region grow and proposed method (region growing + active countour) were experimented on two datasets (the first one includes 18 images from a governmental hospital in Vladimir and the second data set of 52 images from a governmental hospital in Riyadh). Table 1 provides the comparison of segmentation algorithms.

Table 1. The comparison of Segmentation Algorithms

Segmentation method	Principle of work	Note
Thresholding	Based on threshold value selection which can be divided into global (one threshold) and local (two or more thresholds). The threshold can be selected as the lowest point, which is located between two peak values of the histogram.	Global threshold method of various thresholds for different images followed by the erosion procedure with a disk to remove the small objects which passed the threshold was used in this study.
Region growing	Based on seeds selection, seeds represent the centres of objects to be segmented. The region is iteratively grown by comparing all neighboring pixels to the seeds. This process continues until all pixels are allocated to a region and stops when the difference between region mean and new pixel become larger than a certain threshold.	The difference between a pixel's intensity value and the region's mean is used as a measure of similarity. The pixel with the smallest difference measured is allocated to the respective region.
Proposed (region growing + active countour)	Based on two methods: region growing and active contour methods. By using region growing method we get the initial contour of tumour, after that based on the partial differential equation solution, It can change own shape, topology and location to cover the object boundaries to be segmented.	The initial contour tries to move to the position where energy function is minimized. Energy function consists of internal and external forces to measure the contour of the object.

The images have been subject to segmentation using software MATLAB 2013 [8]. The similarity between two finite sample units of the images are measured by Jaccard Index and Dice Coefficient. [9]

Dice Coefficient: is the main validation metric of spatial overlap between the segmented object (tumor segmented by the method) and the ground truth (tumor segmented by Radiologist) and it can be defined as a ratio of the number of matching pixels multiplied by two to the sum of the segmented image and the ground truth. Dice Coefficient D can be calculated from the following formula: $D = 2A(G \cap R)/A(G+R)$.

Jaccard index: is region-based metrics, which measure the similarity between the segmented object and the ground truth and it can be defined as a ratio of the number of matching pixels to the total number of both matching pixels and mismatching pixels [9]. Jaccard index J_{ind} can be calculated from the following formula: $J_{ind} = A(G \cap R)/A(G \cup R)$, where G ground truth, R is segmentation result and A(.) is the operation of counting amount.

Sensitivity: is the proportion (percentage) of tumor tissue pixels that are correctly segmented as a tumor. Sensitivity can be calculated from the following formula: $Sensitivity = TP/(TP+FP)$.[10]

Specificity: is the proportion (percentage) of normal tissue pixels that are correctly segmented as a normal (non-tumor). Specificity can be calculated from the following formula: $Specificity = TN/(TN+FN)$.

Accuracy: is the proportion of both tumor tissue pixels and normal tissue pixels which are correctly segmented among the total number of cases examined. Accuracy can be calculated from the following formula: $ACCuracy = TP+TN/(TP+FP+TN+FN)$

Methodology: The initial step in processing the Brain MRI was to remove the non-brain tissues. We applied Gaussian filter [11] for denoising the images and then administered the segmentation algorithms. The data was analysed using SPSS 21 [12] and compared with the ground truth. The Sample images after applying the segmentation algorithms to the data sets are provided in Figure 1.

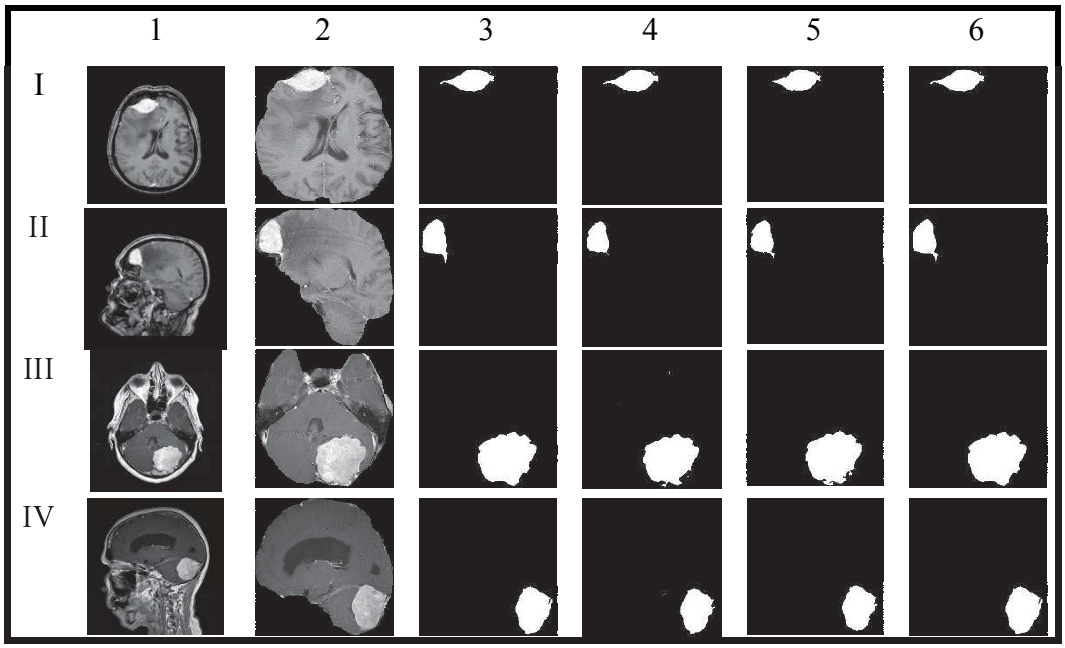

Fig 1. Sample images before and after segmentation: I-axial, II-sagittal, III-axial, IV-sagittal; 1-initial image, 2-image after removal of non-brain tissues, 3-ground truth, & segmentation algorithms: 4- thresholding, 5-region growing, 6-proposed method.

Results: From Figure1, it's observed that the thresholding and region growing methods have over-segmentation in the III image, unlike the proposed method which segments the tumour boundaries very well. The Descriptive Statistics [13] of segmentation methods for all images in 1st and 2nd data sets are presented in Table 2. The Sensitivity 85.2 % and Accuracy 99.43% of the proposed segmentation method was observed to be high compared to Threshold and region contour methods [14]. Specificity of 99.3% was noticed in Threshold method. The proposed method further showed high mean Dice coefficient of 0.9151 and Jaccard index of 0.8459 with an ANOVA , F(2,153) = 0.225, was statistically insignificant from the other two methods is presented in Figure 2.

Table 2. Descriptive Statistics for Outcome Parameters

Segmentation Methods	Dice Coefficient		Jaccard index		Sensitivity (%)		Specificity (%)		Accuracy (%)	
	Dataset		Dataset		Dataset		Dataset		Dataset	
	1	2	1	2	1	2	1	2	1	2
Threshold	0.7332	0.7664	0.5881	0.6561	59.65	69.74	**99.96**	**99.31**	98.61	**96.90**
Region	0.8718	0.7736	0.7747	0.6818	78.19	76.46	99.93	97.75	99.19	95.98
Proposed	**0.9151**	**0.7769**	**0.8459**	**0.6865**	**85.27**	**77.34**	99.95	97.70	**99.43**	96.01

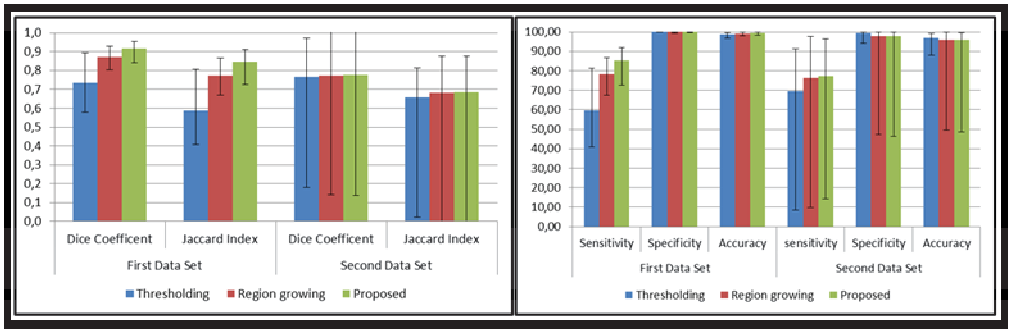

Fig 2. The Bar diagrams for Jaccard index and Dice coefficient (left); Sensitivity, Specificity and Accuracy (Right)

Discussion and Conclusion: Brain tumor is curable and treatable if it is diagnosed in earliest stages of disease. MR images are generally more sensitive in detecting brain abnormalities during the early stages of disease, and is excellent in early detection of cases of cerebral infarction, brain tumors, or infections. [1] Like thresholding, region growing is seldom used alone but usually within a set of image-processing operations, particularly for the delineation of small, simple structures such as tumors and lesions. [15]

The Specificity and Accuracy was observed to be maximum for threshold method with not much difference from the other two methods in this study. 3D image segmentation helps in automated diagnosis of brain diseases and helps in qualitative and quantitative analysis of images such as measuring accurate size and volume of detected portion [16]. The LSD Posthoc test for multiple comparison also did not show much significant difference in the mean values of Jaccard index and Dice coefficient between the three segmentation methods. The present study confirmed that the proposed method had the maximum average for the

parameters – Jaccard Index & Dice Coefficient irrespective of the source of images, thus giving efficient end results.

References:

[1] Priyanka, Balwinder Singh, 'A review on Brain Tumor detection using Segmentation', IJCSMC, Vol. 2, Issue. 7, July 2013, pg.48 – 54.
[2] Priyanka, Balwinder Singh, "A review on brain tumor detection using segmentation," IJCSMC. **2**, pg.48 – 54, (2013).
[3] Priyanka, Balwinder Singh, "A review on brain tumor detection using segmentation," IJCSMC. **2**, pg.48 – 54, (2013).
[4] D. Selvaraj, R. Dhanasekaran, "MRI Brain Image Segmentation Techniques - A Review, " IJCSE, **4,** pg.364 – 381, (2013).
[5] R.Yogamangalam, B.Karthikeyan, "Segmentation Techniques Comparison in Image Processing, " IJET, **5**, pg.307 – 313, (2013).
[6] P.K.Srimani. Shanthi Mahesh. "A Comparative Study of Different Segmentation Techniques for Brain Tumour Detection," IJETCAS, **4**, pg. 192-197, (2013).
[7] J. Mikulka, E. Gescheidtova, K. Bartusek, and D. Nespor. "Comparison of Segmentation Methods in MR Image Processing," Progress In Electromagnetics Research Symposium Proceedings, KL, MALAYSIA, (2012).
[8] *Rajesh C. Patil, A. S. Bhalchandra,* "*Brain Tumour Extraction from MRI Image Using MATLAB,*" *IJECSCSE, **2**,* pg.1 – 4, (2011).
[9] Ran SHI, King Ngi NGAN, Songnan L.I. "Jaccard index compensation for object segmentation evaluation," IEEE ICIP, pg. 4457 – 4461, (2014).
[10] Betty R.K.,Jonathan A.C., Essential Medical Statistics, Blackwell publishing, **2nd** edn, Pg. 33-41,(2009).
[11] Bhumika Gupta, Mr. Shailendra Singh Negi, "Image Denoising with Linear and Non-Linear Filters: A Review", IJCSI. **10**, pg.149-154, (2013).
[12] http://www.spss.com date of Access 20.03.2016.
[13] P. S. S. S. Rao and J. Richard, Introduction to biostatistics and research methods, **5th** ed. New Delhi: PHI Learning Pvt. Ltd, (2012).

SECTION 3

MODELING AND COMPUTER AIDED MEDICINE

Prediction of heart cycle lengths in a myocardial infarction animal model

C. Hoog Antink, D. Rüschen, S. Leonhardt, M. Walter

Philips Chair for Medical Information Technology,

RWTH Aachen University, Pauwelsstr. 20, 52074 Aachen, Germany

Introduction: Left ventricular assist devices (LVADs) can significantly improve survival rate and quality of life for patients suffering from end-stage heart failure [1]. Several strategies to control LVADs exist, over which an overview is presented in [2]. As of today, rotational LVADs are commonly operated at constant rotational speed. However, this strategy has a decreasing effect on the pulsatility in the arterial tree. This can be alleviated by employing a synchronized pulsatile speed control strategy [3]. In this scenario, a speed profile synchronized to the heart cycle is applied to the rotational LVAD. Usually, the R-wave of the electrocardiogram (ECG) is used as a trigger for a specific profile. To implement such a strategy with optimal precision, the length of the current heart cycle I_i has to be known in advance, that is, at the time point of the R-wave. As this is impossible, the objective of this study is to analyse different methods to predict the current heart cycle length I'_i based on the history of previous heart cycles I_{i-n} on data recorded in a myocardial infarction animal model. In this study, the cycle length I is defined as the temporal distance between consecutive end-diastolic pressure (EDP) time points.

Materials and Methods: The data used in this study was recorded in 11 experiments. Animals used in these experiments were adult sheep (Ovis aries, Rhön, female, approx. 63 kg) under general anaesthesia. Myocardial infarction was induced by occlusion of the left anterior descending artery with a balloon, followed by an injection of microspheres into the occluded vessels. A rotary blood pump LVAD (*Impella CP, Abiomed Inc., Danvers, USA*) was implanted directly after the first symptoms of a myocardial infarction were noticeable. The study was approved by responsible authority *(Landesamt für Natur, Umwelt und Verbraucherschutz NRW (LANUV)*) in accordance with national and international standards.

Trial #	1	2	3	4	5	6	7	8	9	10	11	all
n_{ann}	2381	19150	19721	23154	19744	21614	929	13611	18133	23635	40981	∑ 203053
t_{ann} [h]	0,8	3,8	3,7	3,6	3,3	4,6	0,2	2,4	3,3	5,4	6,4	∑ 37,4
mean(I) [ms]	1162	724	680	561	593	760	706	638	661	820	558	ø 664
sd(I) [ms]	195	187	122	127	152	48	52	92	235	68	171	ø 181

Tab. 1 Number of annotated EDP time points (n_{ann}), total amount of annotated time (t_{ann}), mean cycle length (mean(I)) as well as standard deviation of cycle lengths (sd(I)) for each trial as well as gross statistics.

The left-ventricular pressure (LVP) signal was recorded and the EDP was manually annotated by a medical expert. Table 1 lists the Number of annotated EDP time points (n_{ann}), total

amount of annotated time (t_{ann}), mean cycle length (mean(I)) as well as standard deviation of cycle lengths (sd(I)) for each trial as well as gross statistics.
Three different strategies to predict heart cycle lengths were employed. First, the cycle length was predicted by averaging over the last n_{mean} cycle lengths,

$$I_i^{'} = \frac{1}{n_{\text{mean}}} \sum_{n=1}^{n_{\text{mean}}} I_{i-n} \ .$$

The second strategy determines the cycle length based on the median of the preceding n_{median} cycle lengths,

$$I_i^{''} = \text{median}(I_{i-1}, I_{i-2}, \ldots, I_{i-n_{\text{median}}}) \ .$$

Finally, the third approach predicts the cycle length based on a linear prediction coefficients (LPC)

$$I_i^{'''} = -a_2 \cdot I_{i-1} - a_3 \cdot I_{i-2} - \ldots - a_{n_{\text{LPC}}+1} \cdot I_{i-n_{\text{LPC}}} \ .$$

Here, n_{LPC} is the number of filter coefficients that were trained on the preceding n_{train} cycles. To evaluate the quality of estimation, the absolute estimation error is calculated,

$$E_i = \left| I_i - I_i^{'} \right| .$$

Statistical analysis is performed in terms of mean, median as well as the 95th percentile (P95) of the absolute estimation error.

Results: In the following, the influence of the number of cycles used to train the linear predictor, n_{train}, as well as the number of previous cycle lengths considered in the respective strategy, n_{mean}, n_{median} and n_{LPC}, is examined. Results of the gross analysis of all cases for the LPC strategy with varying n_{LPC} and n_{train} is shown in Fig. 1. In Fig. 2, a fixed n_{train} = 1600 was used and the LPC approach was compared to the mean and median predictor for varying n_{mean}, n_{median} and n_{LPC}. Finally, Tab. 2 presents the mean absolute error for all cases individually as well as the gross analysis for n_{mean} = n_{median} = n_{LPC} = 10 and n_{train} = 1600.

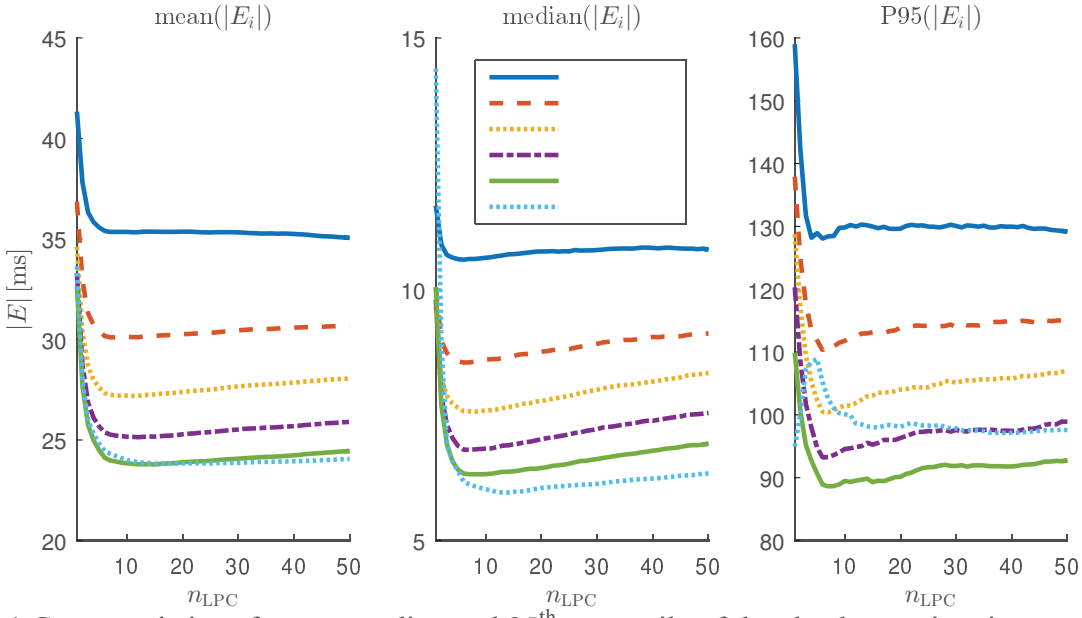

Fig. 1 Gross statistics of mean, median and 95th percentile of the absolute estimation error for different values of n_{LPC} and n_{train}.

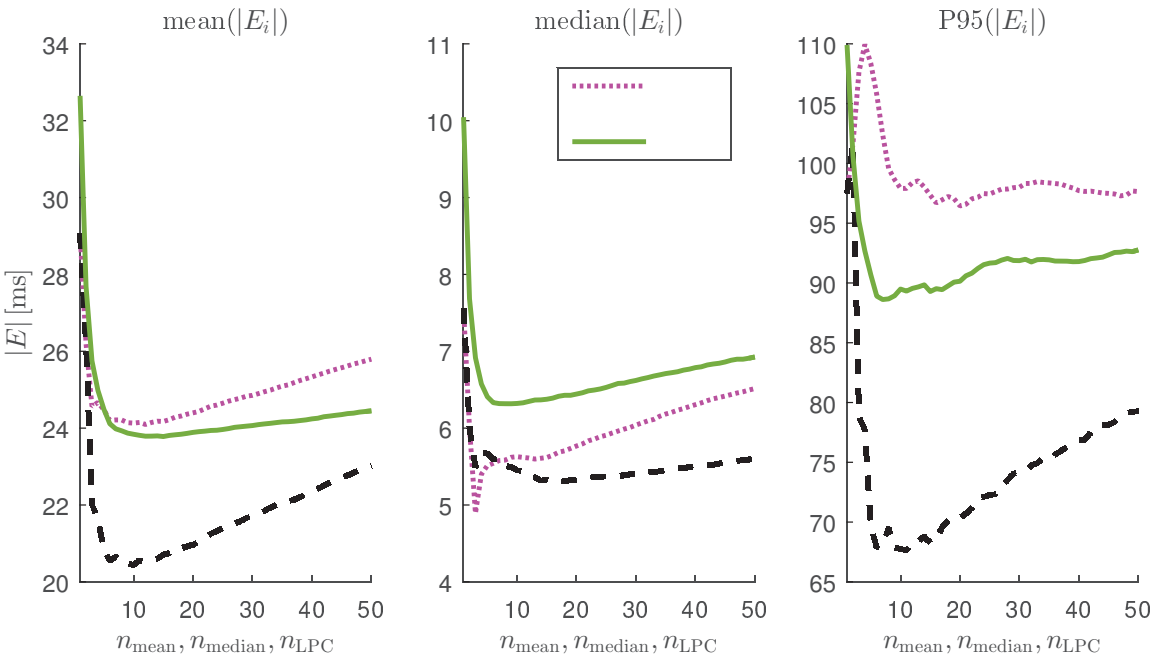

Fig. 2 Gross statistics of mean, median and 95th percentile of the absolute estimation error for mean, median and LPC prediction for different values of n_{mean}, n_{median} and n_{LPC} with fixed n_{train} = 1600.

Trial #	1	2	3	4	5	6	7	8	9	10	11	all
mean|E_{mean}| [ms]	45	38	26	14	42	10	13	31	30	9	24	24
mean|E_{median}| [ms]	31	31	20	11	37	9	10	29	26	9	20	20
mean|E_{LPC}| [ms]	47	32	28	17	41	11	/	30	30	11	22	24

Tab. 2 Mean absolute error when using mean, median and LPC prediction for each case and gross statistics, $n_{mean} = n_{median} = n_{LPC} = 10$, and $n_{train} = 1600$.

Fig. 1 reveals that a linear predictor approach is in principle feasible to predict the length of a cardiac cycle based on past cycle length information as a mean absolute error below 25 ms can be achieved. For this, about 10 filter coefficients are necessary. Here, the minimum error is achieved and an increase in filter coefficients actually increases the absolute error.

It is shown in Fig. 2 that the LPC approach can achieve better results compared to the mean predictor in terms of mean and 95th percentile of the absolute estimation error. However, both approaches are clearly outperformed by the median predictor with $n_{median} = 10$. With it, a mean estimation error of 20 ms is reached. The lowest median absolute error is achieved by a mean predictor (4.9 ms, $n_{mean} = 3$), but the difference to the best median predictor (5.3 ms, $n_{median} = 16$) is small.

Finally, Tab. 1 reveals that differences between individual trials exist. While the mean absolute estimation error using the median predictor is as low as 9 ms in trial 6 and 10, it is 37 ms in trial 5. At the same time, all estimation approaches exhibit a similar performance on each case.

Discussion: Several observations can be made. First, while the LPC approach is capable of reducing the estimation error, its performance strongly depends on the number of previous intervals used for training. To achieve a mean absolute error of 25 ms, a very large training period of $n_{\text{train}} = 1600$, corresponding to approximately 18 minutes, is necessary. This means that, for optimal performance of this approach, the dynamic of the heart cycle length has to be in a steady state.

As a computational inexpensive alternative, the mean estimator exhibits a performance comparable to the LPC approach. Only the preceding 10 intervals are considered, which corresponds to a training or learning phase of approximately 7 seconds. Thus, fast changes in the dynamics of the heart cycle length can be tracked.

The best performance, however, is achieved by the median approach. Again, only the past 10 intervals are necessary for prediction. This strategy is slightly more computational expensive, as a sorting operation is necessary. At the same time, it is inherently robust towards outliers, as they are ignored by the median operation.

It is interesting to note that all approaches exhibit optimal performance when the estimation is based on 10 preceding heart cycles and that performance actually deteriorates when more cycles are considered. This deterioration is least in the LPC approach. The underlying mechanics have to be investigated further, but we assume that the modulation of the heart cycle length caused by the respiratory sinus arrhythmia and other slow rhythms plays an important role.

Conclusion: To conclude, the prediction of heart cycle lengths in a myocardial infarction animal model was investigated. Three prediction approaches based on mean, median and LPC were evaluated on a human annotated dataset obtained from 37.4 hours of animal experiment data. Using a median prediction strategy based on 10 preceding heart cycles, a mean absolute estimation error of 20 ms was achieved.

References

[1] J. Kirklin, D. Naftel, F. Pagani, R. Kormos, L. Stevenson, E. Blume, S. Myers, M. Miller, J. Baldwin, and J. Young, "Seventh intermacs annual report: 15,000 patients and counting", J. Heart Lung Transplant. **34**(12), 1495–1504 (2015).

[2] A. AlOmari, A. Savkin, M. Stevens, D. Mason, D. Timms, R. Salamonsen, and N. Lovell, "Developments in control systems for rotary left ventricular assist devices for heart failure patients: a review", Physiol Meas **34**(1), R1-27 (2012).

[3] R. Amacher, G. Ochsner, and M. Schmid Daners, "Synchronized Pulsatile Speed Control of Turbodynamic Left Ventricular Assist Devices: Review and Prospects", Artif Organs **38**(10), 867-899 (2014).

High-resolution esophageal manometry data processing algorithm

A. Samoilov, D. V. Telyshev

National Research University of Electronic Technology, Bld. 1, Shokin Square, Zelenograd, Moscow, Russia, 124498

The issue of gastrointestinal tract diseases is one of the most frequently discussed question in the medicine nowadays. Such disorders are difficult to find, what can be a reason of non-effective treatment. Commonly for diagnosis are used traditional esophagus manometry, impedance-ph-metry and relatively new promising method – high-resolution manometry (HRM) [1].

This method is similar to the traditional manometry, but the differences make it much more valuable tool. In contradistinction to traditional manometry, where 4 or 8 water-perfused pressure sensors are used, in HRM there are 36 solid-state sensors, located at a special catheter. Each of sensors is circumferentially sensitive, zeroed to atmospheric pressure and placed at 1 cm interval from each other. The HRM assembly is passed transnasally and positioned for record throughout the entire esophagus, and high sampling rate makes possible considering all the processes occurring during the study, in particular the rapid events taking place in the distal esophagus. Amount of sensors eliminates problem of movement-related artifacts that is usual shortcoming of a traditional manometry [2]. Also it prevents strong influence of every single sensor, even if some has been fractured for any reason [3].

In spite of the intuitiveness of this method, for the patient's primary diagnosis it is required interpretation of HRM results. This implies the evaluation of the special pressure topographic parameters such as distal latency, integrated relaxation pressure and others according to the Chicago classification of esophageal motility disorders [4, 5]. Before calculating parameters values it is essential to define temporal and spatial limits: to define areas, that are relevant to upper and lower esophageal sphincters, transition zone, proximal and distal esophagus (figure 1).

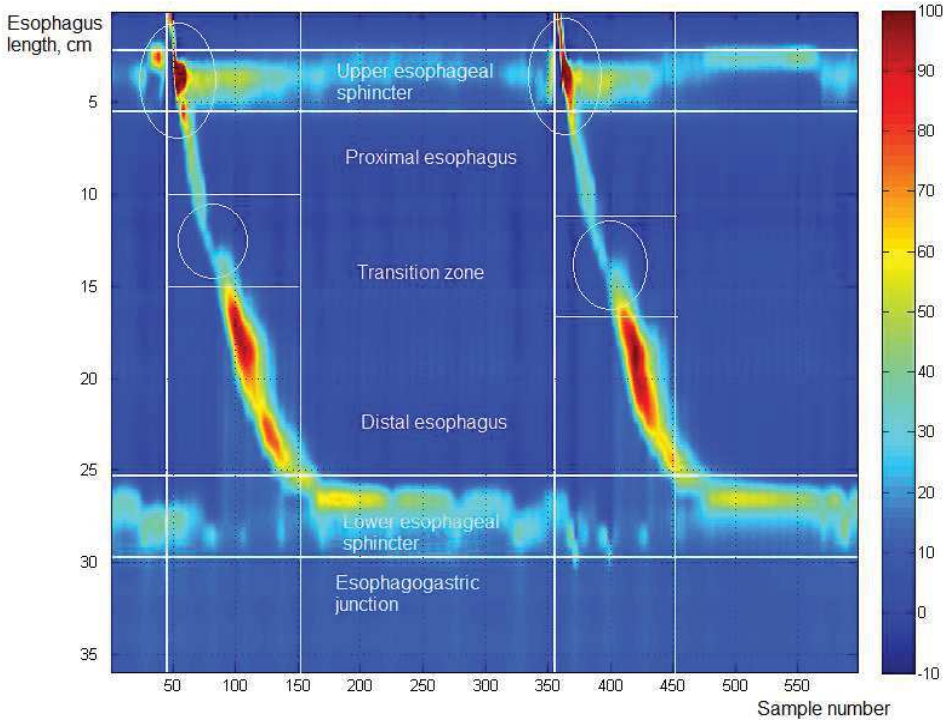

Fig. 1 Topographic colored pressure plot of a normal wet water swallow being made by healthy subject. On plot marked esophageal areas

Swallow is the moment of time when upper esophageal sphincter fully relaxes, but after that it is compressed with new strength and relaxes already to normal state [6]. For its detection plot is constructed based on pressure values of upper esophageal sphincter area. Minimum peak, and then almost instantaneous maximum peak is mandatory criterion. If such values has been found, swallow is detected and marked on topographic pressure plot (figure 2-A).

$$\mathbf{P_i} = \sum_{i=0}^{T} \sum_{j=1}^{N/2} p_{cp} \quad (1)$$

where $\mathbf{P}$ – is an array of average pressure values of sensors corresponding to upper sphincter area, i – sample numbers, j – sensor numbers.

Besides the swallow moment detection, there is a question of compliance between sensors and esophageal areas. To determine the correspondence between the sensor and upper esophageal sphincter area the moment of any swallow is taken and pressure 2D plot is constructed (figure 2-B), where by x-axis are channel numbers and by y-axis are pressure values.

$$P_i = \sum_{i=1}^{N} p_{t,i} \quad (2)$$

Then for defining the beginning and the end of the upper esophageal sphincter the points are searched, where of pressure sharply increasing. It is done for both sides of the maximum peak using pressure 2D plot. Same actions can be implemented for the lower esophageal sphincter area.

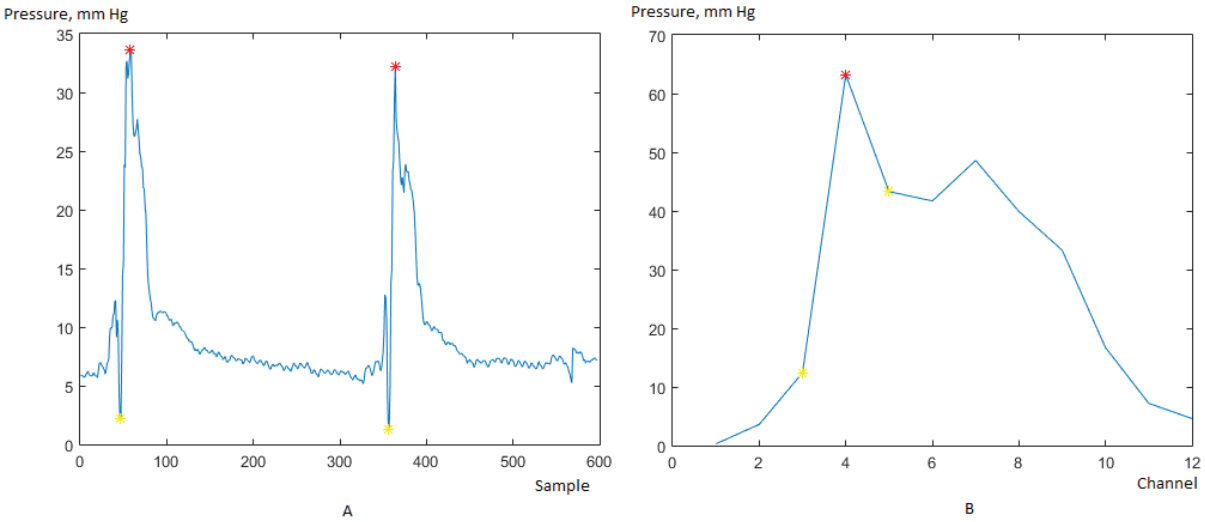

Fig. 2 Defining the swallow moment (A) and channels corresponding to the upper esophageal sphincter area (B)

A transition zone is of particular interest to research, because it is a place of connection of striated (upper esophageal sphincter, proximal esophagus) and smooth muscles (distal esophagus, lower esophageal sphincter) [7]. Feature of this area is that the pressure therein drops, that can be showed by plot construction (figure 3-A).

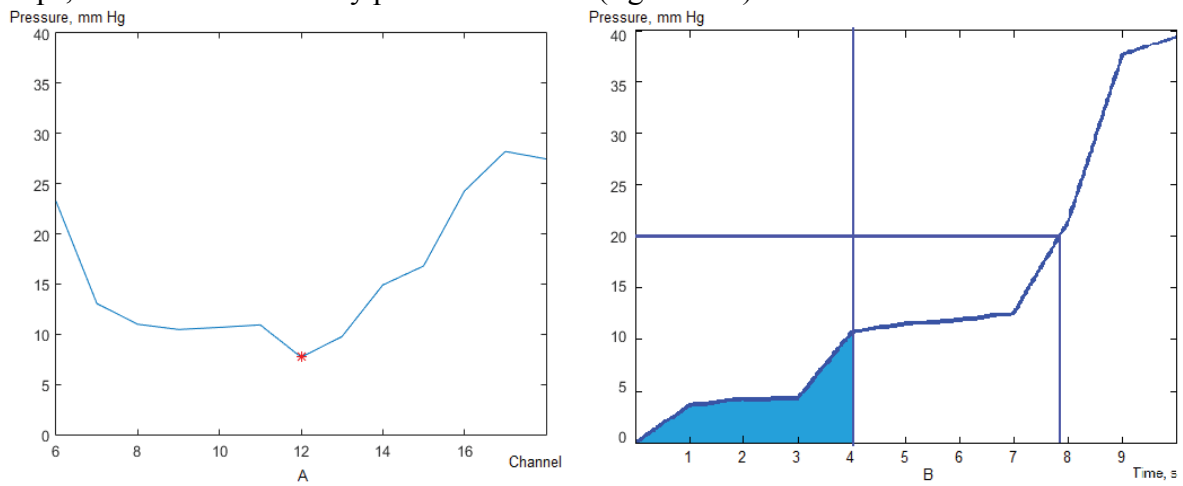

Fig. 3 Defining corresponding to transition zone sensor (A) and evaluating the integrated relaxation pressure (B)

Contractile deceleration point (CDP) is a point reducing velocity of a peristaltic wave passing into the distal esophagus. It is also a point corresponding to the start of a lower esophageal sphincter. Distal latency characterizes the elapsed time till the peristaltic wave will not reach the CDP. The values more than 4.5 seconds are within the normal range.

Esophagogastric junction (lower marginal points of lower esophageal sphincter) is selected to determine the integrated relaxation pressure [8]. The pressure values at these points are then ranked in ascending order and the plot is constructed (figure 3-B).

$$\mathbf{IRP} = \frac{\int_0^t P(t)dt}{t} \ \mathbf{mm\ Hg} \tag{3}$$

The IRP is a curvilinear integral pressure for some temporal limit, divided by it. Usually is taken 3 or 4-second interval. Normal values for IRP do not exceed 15 mm Hg. Also can be determined the time the pressure in the gastrointestinal compound was below a certain value.

Another parameter that is defined by HRM data is pressurization front velocity. For its evaluation on a pressure topographic plot is selected circuit equal to 30 mm Hg and points corresponding to a boundary of the transition zone and an upper boundary of the lower esophageal sphincter. Then the incline of the line, constructed on these points, is calculated, expressed in cm / s.

$$\mathbf{PFV} = \frac{dy}{dx} = \mathbf{cm/s}, \tag{4}$$

where dx - a temporal value, y - the depth of the esophagus, where the pressure sensor is located.

Distal contractile integral characterizes the length of the distal esophagus, the speed and duration of contractions, expressed in mmHg · s · cm. It is necessary for assessing the state of the distal esophagus, as well as the success of the passage of peristaltic waves [9]. Calculated by multiplying the length of the distal parameters, duration of contractions and pressure on this interval. This takes into account only those values that are higher than 20 mm Hg. The normal value of the integral distal is in the range of 5000 mm Hg · a · cm.

$$\mathbf{DCI} = \sum_{x_1}^{x_2} \sum_{y_1}^{y_2} P(x,y)dxdy \ \mathbf{mm\ Hg \cdot s \cdot cm}, \tag{5}$$

where dx - time increment rate, dy - the increment length of the esophagus, P (x, y) - pressure function, x_1, x_2 - the beginning and the end of contractions in the distal esophagus, respectively, y_1, y_2 – the beginning and the end of distal esophagus relative to the total length

Area of high-resolution manometry application is not limited to diagnostics of a gastrointestinal tract. It can be also used in cardiac diagnostics, detection of problems in respiratory system [10]. The usage of this method has improved the understanding of many processes, has facilitated diagnosis of achalasia, functional obstruction and others and has allowed describing new types and sub-types of diseases [11]. The developed algorithm can be integrated in the long-term manometry diagnostics, allowing detecting the events, which cannot be found during the conventional procedure in a short period of time [12].

The goal of the algorithm – to do possible the automatic processing of the HRM researches results, such as defining the spatial temporal limits and evaluating topographic pressure parameters, that allows to decrease the time of manual diagnostics by clinicians, especially in case of long-term (24-hours) research.

References

[1] J. E. Pandolfino, P. J. Kahrilas “AGA technical review on the clinical use of esophageal manometry” Gastroenterology. **128**, 209-224 (2005).

[2] B. F. Kessing, A. J. P. M. Smout, A. J. Bredenoord "Clinical Applications of Esophageal Impedance Monitoring and High-Resolution Manometry" Current Gastroenterology Reports. **14**, 197-205 (2012).
[3] Roman S., Damon H., Pellissier P.E., Mion F. "Does body position modify the results of oesophageal high resolution manometry?" Neurogastroenterology and Motility. **22,** 271–275 (2010).
[4] P. J. Kahrilas, S. K. Ghosh, J. E. Pandolfino "Esophageal Motility Disorders in Terms of Pressure Topography. The Chicago Classification" Clinical Gastroenterology. **42**, 627 – 634 (2008).
[5] Pandolfino J. E., Ghosh S.K., Rice J., Clarke J.O., Kwiatek M. A., Kahrilas P. J. "Classifying Esophageal Motility by Pressure Topography Characteristics: A Study of 400 Patients and 75 Controls" Clinical Gastroenterology **102**, 1–11 (2010).
[6] P. J. Kahrilas, D. Sifrim "High-Resolution Manometry and Impedance-pH/Manometry: Valuable Tools in Clinical and Investigational Esophagology**"** Reviews in basic and clinical Gastroenterology. **135**, 756–769 (2008).
[7] Ghosh S. K., Pandolfino J. E., Kwiatek M. A., Kahrilas P. J. Oesophageal peristaltic transition zone defects: real but few and far between // Neurogastroenterology and Motility. **20**, 1283-1290 (2008).
[8] P. J. Kahrilas, J. H. Peters "Evaluation of the esophagogastric junction using high-resolution manometry and esophageal pressure topography" Neurogastroenterology Motility. **24**, 11-19 (2012).
[9] J. L. Conklin "Evaluation of Esophageal Motor Function With High-resolution Manometry" Journal of Neurogastroenterology and Motility. **19**, 281-294 (2013).
[10] M. M. Machado, P. F. G. Cardoso, I. O. S. Ribeiro, I. Z. Junior, R. J. Eilers "Esophageal manometry and 24-h esophageal pH-metry in a large sample of patients with respiratory symptoms" The Brazilian Journal of Pulmonology. **34**, 1040-1048 (2008).
[11] **R. E. Clouse, A. Staiano, A. Alrakawi, "Application of topographical methods to clinical esophageal manometry" Clinical Gastroenterology. 95, 2720– 2730 (2000).**
[12] Barham CP, Gotley DC, Fowler A, Mills A, Alderson D. "Diffuse oesophageal spasm: diagnosis by ambulatory 24 hour manometry" Gut. 41, 151–155 (1997).

Software and hardware for quality assurance of digital X-ray equipment and ct scanners in clinical conditions

S. Kruchinin[1], M. Zelikman[2]

1. Design Office RoentgenTest Co Ltd, 3, Scherbakovskaya str., Moscow, Russia, 105318

2. Radiology Department of Russian Medical Academy of Postgraduate Education, 2, Barrikadnaya str., Moscow, Russia

Last years changes in radiology equipment which is in use in Russian hospitals lead changes in quality assurance of this equipment in clinical conditions. Given the fact that the changes are mainly concern the data registration by using various modalities (such as digital X-Ray, digital mammography, angiography and computed tomography), differences in quality assurance relate mainly to the evaluation of the imaging quality properties.

It is important to notice that estimation of frequency dependent DQE for digital X–Ray detectors (utilizing MTF) is usually conducted in laboratory conditions since in clinical operating conditions DQE(u,v) estimation is not convenient because of a lot of time required for tests and inability to secure all the requirements established by standards [1-3]. In this case more convenient and easy way is to determine DQE in the region of zero spatial frequencies– DQE(0,0). The corresponding algorithm has been developed and additional software module for DQE(0,0) evaluation has been designed on its basis. No need to determine MTF in this case – it is enough to register a single "clean field" image with given dose and given radiation qualityforexample, RQA 5 (X-Raytubevoltage 70 kV, additionalfiltration 21 mmAl), at the detector's surface. Signal to noise ratio (SNR) at the output of the detector is calculated on the basis of this "clean field" image too. Special arrangements are taken in order to avoid the influence of the input X-ray field non-uniformityon the noise power spectrum evaluation.

Structurally the software consists independent modules for different modalities which can be used as a separate programs also: a module for DQE (u,v) evaluationof digital systems which are utilized in general radiography; a module for DQE (u,v) evaluation of digital mammography units; a module for DQE(u,v) of dynamic imaging devices (angiography) evaluation; a module for DQE(0,0) estimation as well as a module for CT scanners imaging

Medical electrical equipment - Characteristics of digital X-ray imaging devices - Part 1-1: Determination of the detective quantum efficiency - Detectors used in radiographic imaging
[2]IEC 62220-1-2: 2007. Medical electrical equipment - Characteristics of digital X-ray imaging devices - Part 1-2: Determination of the detective quantum efficiency - Detectors used in mammography.
[3] IEC 62220-1-3: 2008. Medical electrical equipment - Characteristics of digital X-ray imaging devices - Part 1-3: Determination of the detective quantum efficiency - Detectors used in dynamic imaging.

Method of automated express diagnostics of pigmented skin lesions

E.N. Rimskaya[1], I.A. Apollonova[1]
[1] Bauman Moscow State Technical University, Department of Biomedical Engineering, Moscow, Russia

1.Introduction

Over the past two decades, incidence of melanoma has increased dramatically worldwide.

According to foreign authors, the average annual growth rate of standardized incidence of melanoma is 3 to 7% [1].

In the Russian Federation ~ 0.3% of the population (about 400,000 people) have a malignant skin tumors. Of these, almost 20% (over 65,000 people) have melanoma of the skin, mortality of patients within 1 year after diagnosis - 15%.

At the present stage in dermatology at diagnosis is common visual inspection and the results of other studies are clarifying nature. The accuracy of this diagnosis depends essentially on the experience of the doctor, his condition at diagnosis and a number of other factors, to some extent affect the process of assessing the severity of the disease. That is, in the diagnosis of a high probability of error of a subjective nature, as well as the error associated with the use of a particular method of diagnosis.

All of the above demonstrates the need for an automated system for the rapid diagnosis of pigmented skin lesions for early detection of pre-cancerous changes in the skin.

2.Clinical parametres of pigmented skin lesions

The main reasons for the appearance of pigmented skin lesions:

• Adolescence is a endocrine changes in the body, especially affecting the increase in the number of tumors.

• Skin diseases (irritation, acne, rashes, etc.) provoke the appearance of new lesions, causing inflammatory changes of the epidermis.

• Excessive sun exposure of the skin is the most powerful catalyst, leading to an increase in the number and growth of tumors.

• Fluctuations in the level of sex hormones in the body of a pregnant woman: a progestin and an estrogen.

• Exposure to adverse factors: toxic substances, various types of radiation.

• Genetic disorders

Under the above influences pigmented skin lesions characterized by changes in parameters such as the border, color, square and shape (Fig. 1) [2].

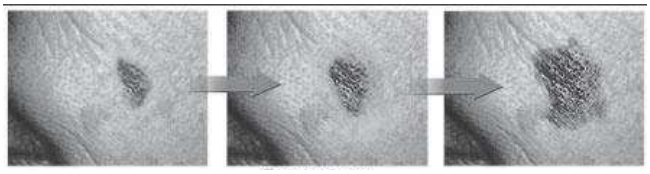

Fig. 1 Changes pigmented tumors under different treatments

3.Diagnostics of pigmented skin lesions

For the diagnosis of precancerous skin lesions, it is important to monitor the dynamics of changes in these parameters. Usually it is the use of the following methods of diagnosis of tumors: dermatoscopy, fluorescence, thermometer and cytology.

Analysis of these diagnostic methods [2] shows that the most common and is used by dermatoscopy.

The sensitivity and specificity for the diagnosis of dermoscopy pigmented skin lesions are very high, so is the most widely used diagnostic tool for the diagnosis, thus avoiding traumatic operations in diagnosis of pigmented skin lesions with a low risk of malignancy.

Fluorescence diagnosis is used as an additional diagnostic method and helps to detect hidden, small in size of tumor lesions on the skin surface.

Coincidence thermometric and histological diagnoses occurs in 94.8% of cases with skin melanoma and 67.9% - in benign tumors of the skin. The accuracy of the thermometric method is limited by the fact that not all melanoma have properties hyperthermia.

From all the above, we can conclude that for the rapid diagnosis of pigmented skin lesions is necessary to develop an automated non-invasive method for the early diagnosis of pigmented skin lesions based on the digital dermatoscope and specialized software.

Structural diagram of the automated method of express diagnostics of pigmented skin lesions is an image registration unit and information processing unit (Fig. 2).

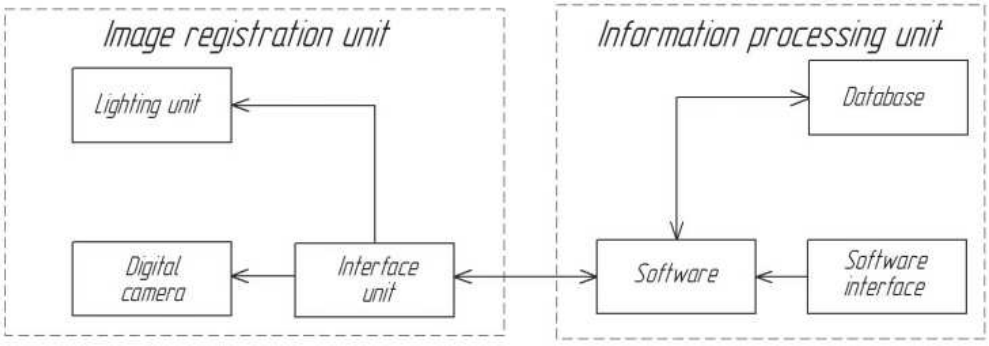

Fig. 2 Structural diagram of the method of automated express diagnostics of pigmented skin lesions

The developed method is to register and subsequent digital processing of images of pigmented skin lesions [3]. Recording is done with a digital camera and the lighting system. After image registration should be pre-treatment imaging: color correction. After that evaluated the image quality: evaluation of brightness, contrast, tone saturation, sharpness of images. After evaluating the image quality to meet the requirements should be detailed image processing, which is to find the standard and its parameters: R-, G-, B-color values, an area of 1 pixel in the image. Further there is a recognition of the tumor and the determination of its parameters, such as the border, area, diameter, color of pigmented skin lesions. Using software interface, the doctor sees all calculated parameters to a computer [4]. All data is stored in the database for each patient, so the doctor can perform a comparative analysis of tumors at regular intervals. Algorithm of the method of rapid diagnosis of pigmented skin

lesions is presented in figure 3. Based on the algorithm and the principle of operation of the complex automated express diagnostics pigmented skin lesions had developed software to measure the parameters of pigmented skin lesions and assembled the layout of the complex automated express diagnostics pigmented skin lesions (Fig. 4 and 5)[5].

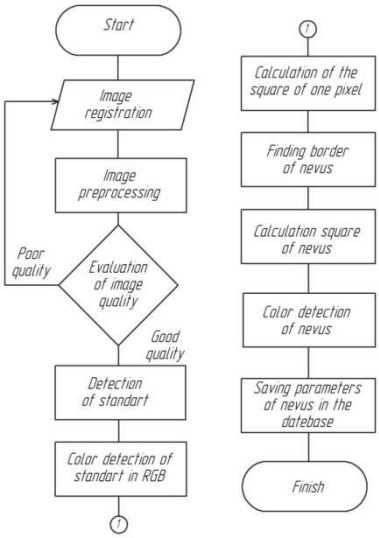

Fig. 3 Algorithm of the method of automated express diagnostics of pigmented skin lesions

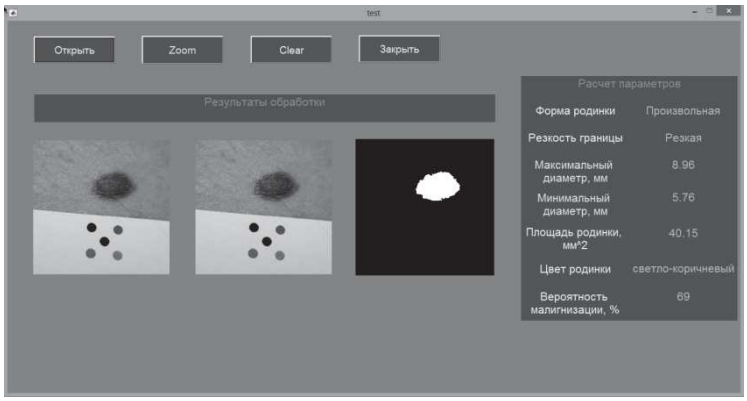

Fig. 4 The software interface for measuring parameters of pigmented skin lesions

Fig. 5 The layout of the complex automated express diagnostics pigmented skin lesions

4.Conclusions

Melanoma - one of the most malignant tumors. In most countries has been steadily increasing the number of cases of melanoma. In this regard, questions clinic melanoma remain highly relevant. Is currently under intensive search for rational forms of detection and primary prevention of melanoma, improved diagnostics. Unfortunately, many aspects of the pathogenesis, diagnosis, finally resolved, so it is advisable to periodically summarize and systematize proven themselves in practice new scientific data, as well as the experience of predecessors. One of the most important aspects of melanoma is to improve early diagnosis, thereby increasing the effectiveness of treatment.

Literary analysis showed that the formation of melanoma affected by the same factors of influence, as in the pigmented lesions: UV and IR-radiation, mechanical and chemical effects, etc. The main clinical signs of melanoma are asymmetry, color, diameter, and their dynamics over time. These clinical signs can be completely described parameters such as area, color, border and shape.

In this article we addressed the following methods of diagnosis of pigmented skin lesions: dermatoscopy, thermometers, cytology and fluorescence. Analysis of these diagnostic methods showed the need for automated non-invasive method of express diagnostics of pigmented skin lesions based on the digital dermatoscope and specialized software.

Formulated medical and technical requirements allowed us to develop a structural diagram and algorithm that implements the method of automated express diagnostics of pigmented skin lesions, as well as software for the measurement of parameters of pigmented skin lesions, compiled the layout of the complex automated express diagnostics pigmented skin lesions.

References

[1] R.J.Friedman, D.S. Rigel, A.W. Kopf. Early detection of maligant melanoma: the role of physician examination and self- examination of the skin // CA Cancer J.Clin.-1985; 35; 130-151.

[2] N.N. Potekaev. Dermatoscopy in clinical practice: a guide for doctors (Moscow: Publishing Group MDV). - 2010

[3] R. Gonzalez, R. Woods. Digital Image Processing.- 2005. Technosphere.

[4] I.N. Spiridonov, K.G. Kudrin, I.V. Reshetov, O.V. Matorin. Modern problems of dermatology, immunology and medical cosmetology **1**(8) 28-33. 2010.

[5] E.N. Rimskaya, I.A. Apollonova. Development of requirements for complex automated express diagnostics pigmented skin lesions. // Modern scientific research and innovation. 2015. №6

Thermoregulation in term and premature infants: the passive system

***C. Barbosa Pereira*[1], *V. Blazek*[1,2], *B. Venema*[1] , *S. Leonhardt*[1]**

1. Chair for Medical Information Technology (MedIT), Helmholtz-Institute for Biomedical Engineering, RWTH Aachen University, D-52074 Aachen, Germany

2. Czech Institute of Informatics, Robotics and Cybernetics (CIIRC), CTU Prague, 166 36 Prague 6, Czech Republic

Motivation: In 2010, approximately 14.9 million babies (11.1%) were born preterm (before 37 completed weeks of gestation) [1]. In contrast to full-term newborns, premature and very low birth weight (VLBW) babies (< 1500 g) have an incompletely developed thermoregulatory system. Therefore, it is important to maintain their body temperature in a small target range, since they are extremely vulnerable to environmental temperature changes [2]. Indeed, thermal stress in neonates has been highly correlated with increased morbidity and mortality [3]. According to clinical guidelines, their skin temperature must be in the range of 35.5 °C to 37.5 °C, and core temperature should be approximately 37 °C (36.8–37.5˚C) [2].

However, in order to keep an appropriated body temperature several complex physiological processes such as lipolysis and gluconeogenesis are involved. Hence, the more energy expended to maintain an adequate temperature, the less energy is available for other crucial processes, for example growth, lung maturation, brain developments [2]. In addition, there are several factors of the neonatal physiology that predispose to increased heat losses, (1) reduced amount of brown adipose tissue, (2) a thin subcutaneous fat layer, (3) increased surface area to body weight ratio, (4) high evaporative losses, among others [4]. Therefore, it is crucial to maintain premature/VLBW babies in a neutral thermal environment (which guarantees minimal metabolic activity) to improve clinical outcome [5-6].

Adapted distributed models can offer a deeper insight into heat transfer processes and body-environment interactions. In addition, they can be used to optimize warming therapies and hyperthermia processes as well as to obtain more detailed knowledge on pathophysiology related to heat transfer processes. In sum, mathematical models allow to simulate and predict clinical situations without involving real patients in clinical studies. In this paper we present a compartment model of the thermoregulatory system of a neonate. With it we intend to predict the core and skin temperature of neonates depending on the environmental conditions (e.g. temperature and relative humidity).

Methods: The model introduced here is schematically illustrated in Fig. 1. It was inspired by Bussmann *et al.* (1998) [7] and Fiala *et al.* (1999) [8]. While the former group developed a thermoregulatory system of a neonate, the latter focused its work only in adults. Our model consists of a main system, i.e. the controlled system (also known as plant or passive system). The passive system models the physical body of a newborn and the heat-transfer processes. It is composed of one spherical and six cylindrical compartments (head, thorax, abdomen, arms and legs). The body compartments are, in turn, constituted of concentric layers. The head is formed by brain, bone, fat and skin; the thorax and abdomen consist of five layers (thorax: lung, bone, muscle, fat and skin (Fig. 1); abdomen: viscera, bone, muscle, fat and skin); and the upper and lower extremities comprise four tissues (bone, muscle, fat and skin). Moreover, the model includes a last compartment, the central blood that stands for large arteries and veins (Fig. 1). It was implemented in the environment Dymola (Dymola 2015 FD01, Dassault Systèmes AB, Lund, Sweden). Note that all parameters in our approach were based on literature.

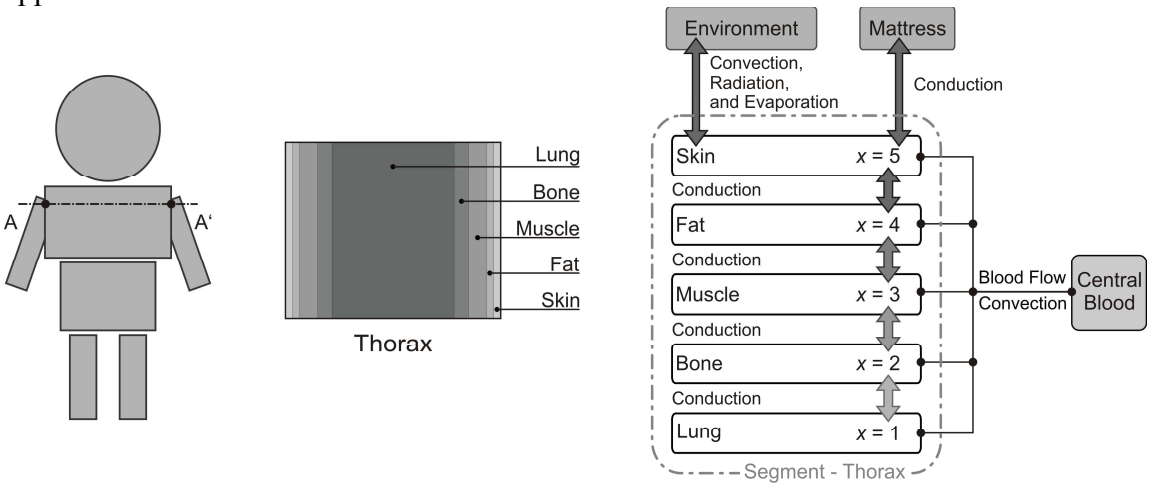

Fig. 1 (a) Illustration of the seven compartments (head, thorax, abdomen, arms and legs) which constitute the whole body. (b) Representation of the body compartment thorax and respective layers (lung, bone, muscle, fat and skin). (c) Graphical illustration of (a) the radial heat conduction across the thorax tissues/layers, (b) vascular convective heat transfer, and (c) heat exchange with the environment via convection, evaporation, radiation and conduction.

In order to describe the heating transfer mechanisms in a tissue (e.g. heat storage or accumulation, conduction, metabolic heat generation/production and blood perfusion), the one-dimensional heat transfer equations was used. For a single layer, the heat transfer by conduction is given by the following mathematical expression:

$$\underbrace{\rho_t c_t \frac{\partial T_t}{\partial t}}_{Accumulation} = \underbrace{k_t\left(\frac{\partial^2 T_t}{\partial r^2} + \frac{\omega}{r}\frac{\partial T_t}{\partial r}\right)}_{Conduction} + \underbrace{M_t}_{Generation} + \underbrace{K_t \rho_{bl} c_{bl} w_{bl,0_t}(T_{bl,a} - T_t)}_{Perfusion}. \quad (1)$$

In the above equation, T_t (K), ρ_t (kg m^{-3}), c_t (J kg^{-1} K^{-1}), k_t (W m^{-1} K^{-1}), K_t (dimensionless) are the temperature, density, specific heat, thermal conductivity and countercurrent factor of the tissue t (brain, bone, fat, lung, muscle, skin or viscera). In addition, ρ_{bl} (kg m-3), c_{bl} (J kg-1 K-1), represent density and specific heat of the blood. The variables $w_{bl,0}$ (s^{-1}), $T_{bl,a}$ (K) are the blood perfusion in thermal neutrality and temperature of the arterial blood. The conduction heat transfer is dependent on the radius r (m), geometry factor ω (dimensionless) [ω=1 for polar coordinates (cylindrical compartments: abdomen, thorax, arms and legs) and ω=2 for spherical coordinates (spherical compartments: head)]. The metabolism term M_t (W m-3) defines the energy generation due to biological processes. It is the main source of heat in preterm/VLBW babies.

The total body surface area (BSA) (m^2) has a great influence on the heat transfer processes, therefore it is one of the input parameters of our compartment model. The BSA was calculated using the equation proposed by Meban (1983) [9]

$$BSA = \left(6.4954 \cdot (W \cdot 1000)^{0.562} \cdot L^{0.320}\right)/10000. \quad (2)$$

Here, W (kg) corresponds to the weight of the newborn and L (cm) to the crown-heel length. BSA was further used to compute the area A of each body compartment (A_{head}, A_{thorax}, $A_{abdomen}$, A_{arm} and A_{leg}).

In contrast to the remaining tissues, skin exchanges heat with the environment by convection, evaporation and radiation. In addition, when the body is in contact with a surface (e.g. a mattress) heat transfer by conduction needs to be also considered. Therefore, the bioheat equation of the skin comprises four additional terms, q_c, q_e, q_r and q_{cd}.

The term q_c models the convective heat exchange between the neonate and the incubator air as defined by

$$q_c = h_c \cdot A_{skin,a} \cdot (T_{skin} - T_{air}), \quad (3)$$

where h_c (W m^{-2} K^{-1}) and $A_{skin,a}$ are the convection coefficient and area of the skin exposed to the air.

Evaporation of water [from the skin (q_{ev}) or from the respiratory system (respiration)] is one of the major forms of heat loss in premature babies. The first (evaporation of water from the skin) is described according to

$$q_{ev} = e_{ev} \cdot A_{skin,a} \cdot TEWL. \quad (4)$$

In the above equation e_{ev} and TEWL (g m^{-2} h^{-1}) are specific enthalpy of the vaporization of water (0.65 W h g$^{-1)}$ and transepidermal water loss.

Radiation, in turn, is the heat transfer by long-wave radiation (q_r). It is dependent on parameters such as mean radiant temperature [T_{MRT} (K)] and radiative heat-exchange coefficient [h_r (W m^{-2} K^{-1})] as given by

$$q_r = h_r \cdot A_{skin,a} \cdot (T_{skin} - T_{MRT}). \quad (5)$$

The conductive heat transport between the neonate and the mattress (q_r) is a scenario that must be also considered in the model. It is defined by

$$q_{cd} = k_m \cdot A_{skin,m} \cdot (T_{skin} - T_m), \quad (6)$$

Where, k_m (W m^{-2} K), T_m (K) and $A_{skin,m}$ (K) are the heat transfer coefficient, the temperature of the mattress, and the area of the skin in contact with the mattress of the incubator.

Our model was validated in thermal neutrality (steady state) by comparing the simulations with measurements carried out by Hammarlund *et al.* (1983) [10] in 10 newborn babies directly after birth. The group was constituted by 4 female and 6 male babies, with a gestational age of 39.60 ± 0.70 weeks [mean ± standard deviation (SD)], a weight of 3.71 ± 0.54 kg and a length of 0.51 ± 0.02 cm.

Results: In this paper we used the work of Hammarlund et al. (1983) [10] to validate the model during stable environmental conditions. Table 1 compares the empirical data (rectal/core temperature and skin temperature) obtained by the latter group with our model simulations. The mean difference in core temperature between measurements and simulation was 0.22 ± 0.19 °C, and that of skin averaged 0.41 ± 0.41 °C. As shown, similar results were achieved. Therefore, we can infer that this approach is able to estimate accurately core temperature and skin temperature in neutral conditions in full-term newborns. Unfortunately, we did not find in the literature similar studies to that of Hammarlund et al. (1983) [10] but dealing with preterm infants. Perinatal and natal research is still a controversial field due to ethical reasons. Premature babies are extremely vulnerable subjects, therefore ethical aspects, such as risks and benefits, clinical equipoise, parental informed consent and assent, must be weighted before clinical studies. In 1998, Bussmann et al. presented a similar approach. In contrast to it, our model includes more compartments and layers, therefore we expect to predict a more accurate global and local physiological responses.

Table 1 Comparison between the measurements performed by Hammarlund et al. (1983) [10] and the results achieved with our simulations

		Hammarlund et al. (1983)			Mathematical model			Temperature difference	
I	**GA**	**T_{amb} ± SD**	**T_{core} ± SD**	**T_{skin} ± SD**	**T_{amb}**	**T_{core} ± SD**	**T_{skin} ± SD**	**T_{core}**	**T_{skin}**
	weeks	**°C**	**°C**	**°C**	**°C**	**°C**	**°C**	**°C**	**°C**
I1	39	34.2 ± 1.5	36.7 ± 0.4	35.4 ± 0.3	34.2	36.8 ± 0.1	35.4 ± 0.1	0.1	0.0
I2	38	34.6 ± 0.4	36.9 ± 0.1	36.0 ± 0.1	34.6	36.8 ± 0.1	35.7 ± 0.1	0.1	0.3
I3	40	34.8 ± 0.2	36.7 ± 0.1	35.7 ± 0.2	34.8	36.8 ± 0.1	35.8 ± 0.1	0.1	0.1
I4	40	34.5 ± 0.3	36.6 ± 0.1	35.5 ± 0.1	34.5	36.9± 0.1	35.8 ± 0.1	0.3	0.3
I5	40	34.1 ± 0.2	36.6 ± 0.1	34.5 ± 0.4	34.1	36.9 ± 0.1	35.7 ± 0.1	0.3	1.2
I6	40	34.2 ± 0.4	36.8 ± 0.1	34.6 ± 0.4	34.2	36.8 ± 0.1	35.6 ± 0.1	0.0	1.0
I7	40	32.6 ± 0.4	36.1 ± 0.0	34.6 ± 0.3	32.6	36.6 ± 0.1	35.2 ± 0.1	0.5	0.6
I8	39	33.2 ± 0.3	36.4 ± 0.2	35.2 ± 0.1	33.2	36.7 ± 0.1	35.3 ± 0.1	0.3	0.1
I9	40	32.5 ± 0.2	36.7 ± 0.1	34.9 ± 0.1	32.5	36.7 ± 0.1	35.3 ± 0.3	0.0	0.4
I10	40	33.6 ± 0.1	36.2 ± 0.2	35.3 ± 0.2	33.6	36.7 ± 0.1	35.4 ± 0.1	0.5	0.1
Mean	39.6	33.83	36.57	35.17	33.83	36.77	35.52	0.22	0.41
SD	0.7	0.82	0.26	0.51	0.82	0.10	0.23	0.19	0.41

I – infant, GA – gestational age, SD – standard deviation, T_{amb} – ambient temperature, T_{core} – core temperature, T_{skin} – skin temperature

Conclusions: We have presented in this paper the passive system of a multi-node model of the thermoregulatory system of newborn infants. A first successful validation of the current model in thermal neutrality was performed by comparing the measurement results of Hammarlund et al. (1983) [10] with our simulations in Dymola. This mathematical approach demonstrated to be able to predict body temperatures (core and skin temperature) during thermal neutrality. The next step should be the implementation of the active system to describe the regulatory mechanisms, i.e. nonshivering thermogenesis (oxidation of brown adipose tissue) and vasomotion (control of peripheral blood flow through vasodilation or vasoconstriction). In addition, the validation of the model should be extended to premature infants (moderate preterm, very preterm and extremely preterm infants).

References

[1] H. Blencowe, S. Cousens, M. Oestergaard, D. Chou, A.-B. Moller, R. Narwal, A. Adler, C. Vera Garcia, S. Rohde, L. Say, and J. Lawn, "National, regional, and worldwide estimates of preterm birth rates in the year 2010 with time trends since 1990 for selected countries: a systematic analysis and implications," Lancet **379**, 2162–2172 (2012).

[2] A. Abbas, K. Heimann, K. Jergus, T. Orlikowsky, and S. Leonhardt, "Neonatal non-contact respiratory monitoring based on real-time infrared thermography," Biomed. Eng. Online **10**, 1–17 (2011).

[3] A. Lyon, A. Pikaar, P. Badger, and N. McIntosch, "Temperature control in very low birthweight infants during first five days of life," Arch. Dis. Child.-Fetal Neonatal Ed. **76**, F47–F50 (1997).

[4] K. Cramer, N. Wiebe, L. Hartling, E. Crumley, and S. Vohra, "Heat loss prevention: a systematic review of occlusive skin wrap for premature neonates," J. Perinatol. Off. J. Calif. Perinat. Assoc. **25**, 763–769 (2005).

[5] S. Waldron and R MacKinnon, "Neonatal thermoregulation," Infant **3**, 101–104 (2007).

[6] H. Asakura, "Fetal and neonatal thermoregulation," J. Nippon Med. Sch. **71**, 360–370 (2004).

[7] O. Bussmann, W. Nahm, and E. Konecny, "A model for simulating heat transfer and thermoregulation of premature infants," Biomed. Tech. (Berl). **43**, 300–301 (1998).

[8] D. Fiala, K. Lomas, and M. Stohrer, "A computer model of human thermoregulation for a wide range of environmental conditions: the passive system," J. Appl. Physiol. **87**, 1957–1972 (1999).

[9] C. Meban, "The surface area and volume of the human fetus," J. Anat. **137**, 271–278 (1983).

[10] K. Hammarlund, G. Sedin, and B. Stroemberg, "Transepidermal Water Loss in Newborn Infants," Acta Paediatr. **72**, 721–728 (1983).

Conducting X-ray researches by portable technical equipment in unspecialized conditions

Y. N. Potrakhov[1], A. Y. Vasilev[2], V. A. Lyubimenko[3], E. N. Potrakhov[4], N. N. Potrakhov[1], V. V. Ryazanov[5], G. E. Trufanov [6], O.M. Alekseeva[2]

1 – Saint-Petersburg State Electrotechnical University «LETI», 5 Professora Popova st., Saint-Petersburg, Russia

2 – Moscow State Medical University of Medicine and Dentistry named after A. I. Evdokimov, Ministry of Healthcare of Russia,
Vucheticha ul., 9a, Moscow, Russia.
3 – «Children's city hospital №1», 14 St. Avant-garde, Saint Petersburg, Russia.
4 – «ELTECH-Med», company, Professor Popov str. 5,A St.Petersburg, Russia.
5 – State budget institution of higher professional education Saint-Petersburg State Pediatric Medical University Ministry of Health of the Russian Federation, 2, Lithuanian street, Saint Petersburg, Russia.
6 – Federal Almazov North-West Medical Research Centre, 15 Parkhomenko street, St. Petersburg, Russia.

As still not defined regulatory framework for medical X-ray diagnostic in unspecialized conditions, such as "at home", the solution of this problem is becoming more acute.

Reasons for conducting X-ray diagnostic studies at home may be different, including:

- somatic "serious" condition in elderly patients who are unable to get to the health facility for suspected pneumonia, fractured limbs, other trauma, etc .;
- availability of financial well-off citizens who do not want to stand in line at the reception, and is therefore ready to pay for X-ray diagnostic, for example, for the purpose of diagnosis and monitoring of inflammatory control in the lungs or the fracture healing process at home.

However, in many cases, X-ray radiography in unspecialized conditions can not be regarded as a method of definitive diagnosis, since there is a number of specific restrictions in carrying out such researches:

- often medical condition of patient does not allow to perform X-ray examination in the standard (at least 2) projections;
- on the size and weight of the X-ray apparatus, X-ray visualisation system and, most importantly, the tripod device;
- on the value of exposure dose of X-rays;
- on the total electric power consumption.

Obviously, the use of traditional stationary tripod devices providing positioning X-ray apparatus relative to the patient, at home is not possible. Therefore, using portable tripods or takes the picture without using a tripod - "in hand." Therefore, special importance becomes the issue of radiation safety for the staff carrying out the study, and to others who may also be involved in the study, such as the laying of the patient. However, the use of stationary means of protection against the unused X-ray radiation, as well as remove others at a safe distance in the home is almost impossible. Therefore it is necessary to use such a technique of X-ray photography, which can significantly reduce the exposure dose of radiation than when using stationary devices. In this case, is extremely important to increase the image quality of the test authority, the necessary and sufficient for a decision on the presence or absence of pathology.

Of particular importance to the issue of X-ray diagnostics in unspecialized conditions gives the important challenges of modern clinic - radiological surveys in neonatology. Additional difficulties in its decision are caused by the small size and weight of the newborn (up 400 g); conditions in which there is a child (incubator, open resuscitation system, operating), as well as the severity of his condition (reanimation, intensive care, rehabilitation). Often, because of the condition of the patient: artificial ventilation, cardiac or infusion therapy, active aspiration - X-ray study can be conducted only in the reanimation..

At the same time the conducting digital X-ray radiography for newborns very claimed. According «City Children's Hospital №1» (Saint-Petersburg) only in its resuscitation units annually around 4500 radiographic procedures in 2 or 3 projections. In total, it is up to 10 thousand X-rays in a year. Currently, these studies are carried out on the domestic or foreign X-ray machines, practically not adapted to the problems and conditions of the resuscitation of newborns with pathologies. Accordingly, the additional radiation load subjected to medical staff and other patients.

Research carried out in collaboration with experts from Federal Almazov North-West Medical Research Centre and «City Children's Hospital №1» showed that virtually all requirements to the organization of the X-ray studies in unspecialized environment and, above all, neonatology, satisfied by method of Microfocus X-ray radiography. [1].

Its main features are:

- using X-ray apparatus with a size of focal spot of x-ray tube is less than 0.1 mm;
- 1.5-2 fold increase voltage on X-ray tube and 3-5 times decrease focal distance as compared to standard X-ray technique [2, 3].

To implement a methodology was developed specialized digital X-ray diagnostic complex "PARDUS-Neo" composed of the X-ray apparatus "PARDUS" in a portable version and X-ray visualisation system on the basis of the screen with the photoluminophore. The

construction of the first domestic portable apparatus "PARDUS-R" allows to obtain X-ray images without the use of a stationary tripod. X-ray lab assistant takes a picture while holding the device in hand, while being in the radiation safety conditions (Fig. 1) [4].

Fig. 1. Portable X-ray apparatus «PARDUS-R».

Figure 2 shows an X-ray image of the preparation of the newborn body obtained by the method of Microfocus X-ray radiography in unspecialized conditions on the X-ray diagnostic complex "PARDUS-Neo".

Fig. 2 X-ray image of the preparation of the newborn body.

On the X-ray image is good visualized structure of bone elements: bone of the skull base, thorax skeleton, spine, pelvis and long bones, and soft tissues, including non-contrast nasotracheal tube.

Figure 3 shows the X-ray images of the thoracic department (patient P., age 7 months, weight 3.5 kg), obtained in a stationary X-ray room in «City Children's Hospital №1» (Fig. 3a), and obtained in unspecialized conditions "at home" of the same patient (Fig. 3b) using the complex «PARDUS-Neo».

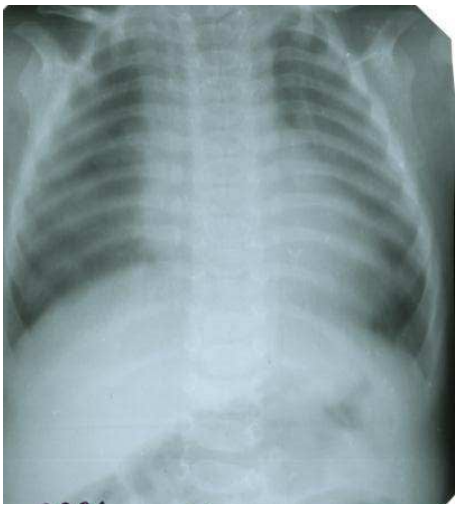

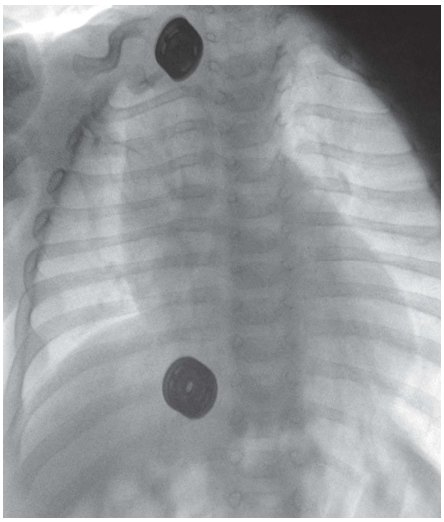

distortions in results. In most studies the results of mathematical modeling are not validated by experiment studies. In the majority of studies. It is not considered in detail the relationship between the global hemodynamic disorders, heart disease and hemodynamics of cerebral aneurysms. Development of methods, models and algorithms for modeling of cardiovascular system for preoperative assessment of hemodynamics of patients with cerebral aneurysms is a topical scientific and practical task. The aim of the study is to improve methods of mathematical modeling of cardiovascular system considering individual characteristics of cardiovascular system and influence of factors of global hemodynamics.

Methods. Multiscale mathematical model of cardiovascular system was used to assess the preoperative hemodynamics of patients with cerebral aneurysms [1, 2]. Multiscale model of cardiovascular system is a set of mathematical models of hemodynamics with different spatial dimension, which are coupled together using corresponding boundary conditions.

Model of global hemodynamics (0D model) is used to describe the hemodynamics of the whole cardiovascular system. With this approach, the entire cardiovascular system is considered as a set of interconnected elements. Each element is described as a lumped parameter model. The advantages of such approach are computational efficiency and a relatively small number of experimentally determined parameters of the model. Developed 0D model describes the main compartments of the cardiovascular system, and includes a description of heart in terms of physiology. In the developed model of the arterial tree hemodynamics (1D model) an arterial tree is described as the set of one dimentional arteries. It is assumed that the blood velocity and pressure in the artery are changed only along the length of the vessel. Cross-section area of artery varies along the length of the artery under the influence of blood pressure. This model allows to investigate the phenomenon of pulse wave propogation through the arterial system. Arterial tree model consists of 48 arteries and represents the upper body arteries, as well as cerebral circulation. For the proper description of the 1D model it is required an assignment of corresponding boundary conditions at the inlet and outlet elements of arterial tree. Such boundary conditions can be obtained by using the 0D model of hemodynamics. Using the developed 3D model of local hemodynamic of cerebral artery it was described a local hemodynamics of cerebral artery with aneurysm. 3D model of local hemodynamics was developed using the Navier-Stokes equations. Non-Newtonian properties of blood were described by power-law approximation. High performance computing techniques were used to solve the 3D model of local hemodynamics of cerebral artery. In addition to the computational cost for 3D model of hemodynamics, there are certain difficulties in obtaining reliable forms of computational domain. For the computation domain definition it can be used methods of clinical research such as magnetic resonance and computed tomography. For 3D model the boundary conditions for velocity and pressure were obtained from model of arterial tree hemodynamics.

Thus, for correct numerical studies of hemodynamics of cerebral artery with aneurysm it is required to develop a set of coupled mathematical models of hemodynamics (0D, 1D and 3D), which together represent a multiscale mathematical model of the cardiovascular system (Fig. 1). Multiscale model of the cardiovascular system allows to couple models of global hemodynamics, hemodynamics of arterial tree and model of local hemodynamics of cerebral artery, which allows to utilize the advantages of each type of model and minimize their weaknesses. For example, when assessing hemodynamics of cerebral artery it is possible to study the influence of global hemodynamic disorders (0D model) on the local hemodynamics of cerebral artery with aneurysm (3D model).

Results and Disscussions. To assess the preoperative hemodynamics of patient it was selected the left internal carotid artery with aneurysm, the geometry of which is shown in Fig. 2. The length of the test cerebral artery segment is 8 cm, width - 40 mm. The lateral size of the aneurysm is 12 x 10 x 7 mm. The diameter of the input segment is 8 mm. Diameter of

output segments - 4 and 6 mm, respectively. For a preliminary assessment of preoperative hemodynamics of the selected cerebral artery a series of experiments using CT angiography was conducted in the department of Neuroradiology of Klinikum Rechts der Isar of Technical University of Munich (Munich, Germany). The experimental studies were conducted using a modified experimental setup located in the laboratory of interdisciplinary research of Klinikum Rechts der Isar [3]. Patient's cardiac cycle was simulated using the experimental setup. Physician uniformly inject a radiopaque substance in the model of cerebral artery. Fig. 2 and Fig. 3 shows an angiogram obtained during the experiments. Such images are used in clinical practice for a preliminary assessment of hemodynamics in cerebral arteries, but they do not allow to assess blood velocity for the cerebral artery with acceptable accuracy.

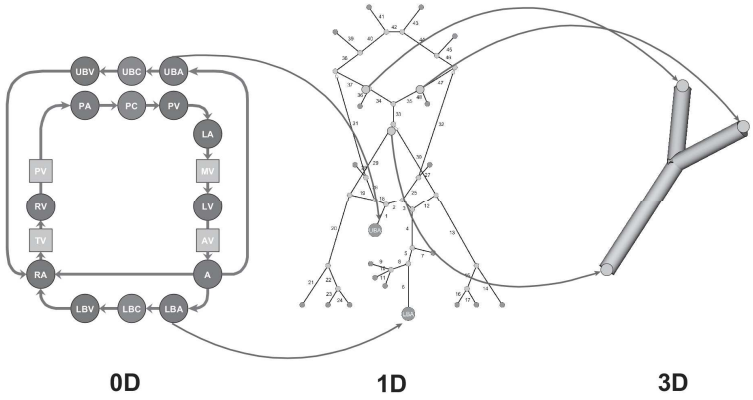

Fig. 1 Structure of multiscale mathematical model of cardiovascular system.

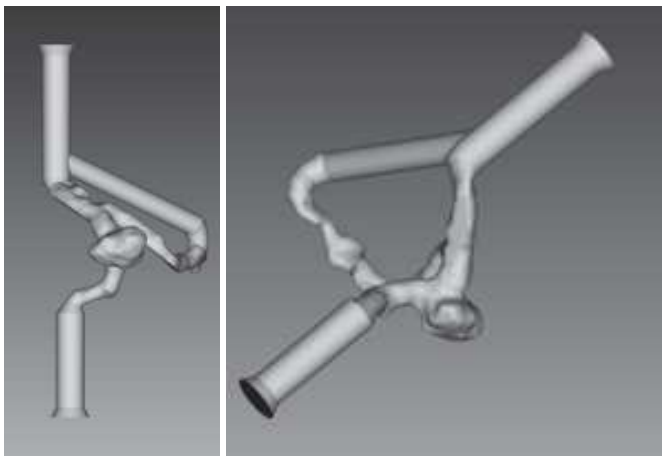

a) b)

Fig. 2 Individual geometry of cerebral aneurysm: a) XY-plane; b) perspective view.

To assess the preoperative hemodynamics of cerebral artery it was used the developed multiscale mathematical model of the cardiovascular system. The advantage of this approach is that the velocity and pressure in aneurysm model can be determined with high precision in a reasonable time (about 6 hours). It was prepared a computational mesh consisting of 2 million elements. The simulated time was 5 seconds. As a result of simulation the velocity and blood pressure were determined, particle tracks and streamlines were computed. Computed particle tracks in the anterior-posterior (AP) and lateral (LAT) projections at time $t = 2.789$ s are shown in Fig. 5. Computed streamlines are shown in Fig. 6.

Conclusion. According to the numerical results, the presence of unstable vortex can lead in consequence to thrombus formation. In the inlet segment a blood flows at a maximum velocity of 1.27 m / s; in the output segment a blood velocity does not exceed 0.75 m / s.

Blood velocity magnitude inside the aneurysm changes in range of $\left[4 \cdot 10^{-4}; 0.5\right]$ m/s. The smallest value of wall shear stress were found in the dome of the aneurysm, which might cause further growth and rupture of cerebral aneurysm. Numerical results show a good agreement with experimental studies. The relative error doesn't exceed 10%, so it can be concluded that proposed multiscale mathematical model of cardiovascular system can be used for preoperative assessment of hemodynamics of patients with cerebral aneurysm.

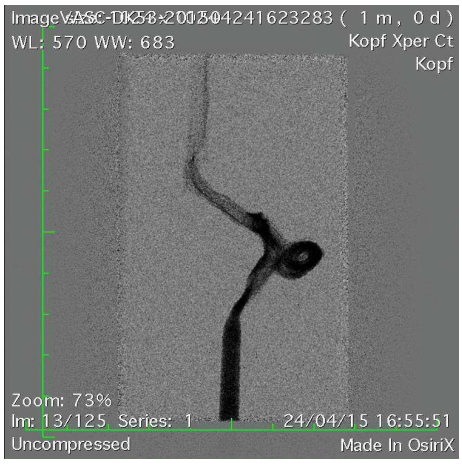

Fig. 3 Angiography of cerebral aneurysm – AP projection.

Fig. 4 Angiography of cerebral aneurysm – LAT projection.

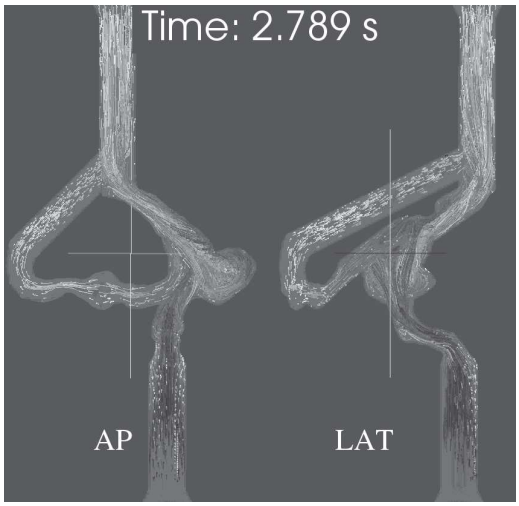

Fig. 5 Particle tracks for cerebral aneurysm at moment $t = 2.789$ s, computed using multiscale mathematical model of cardiovascular system.

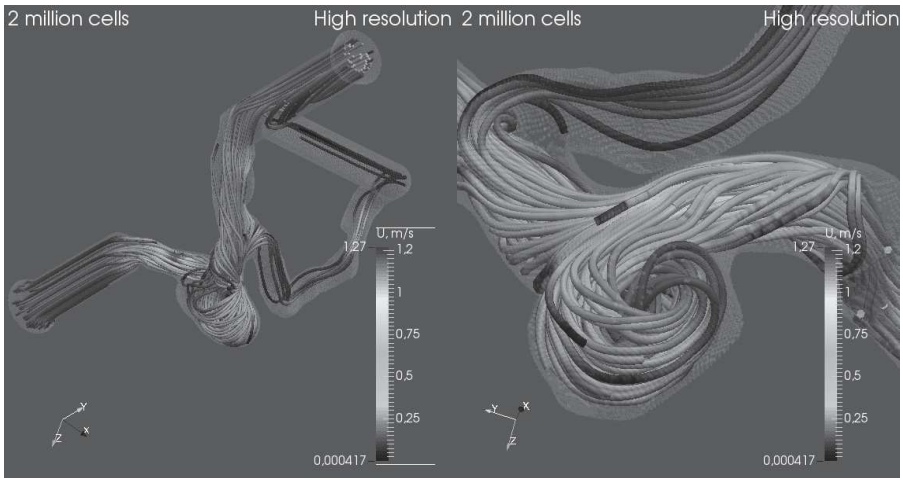

Fig. 6 Computed streamlines for bloow flow in cerebral aneurysm model at moment $t = 2.789$ s.

References

[1] S. V. Sindeev, S. V. Frolov. "Multiscale mathematical of cardiovascular system for evaluation of cerebral circulation". Fundamental research. **12(5)**, 950-954 (2015).
[2] S. V. Frolov, S. V. Sindeev, V. A. Lischouk, D. Sh. Gazizova, D. Liepsch, A. Balasso. "Development of multiscale hemodynamics model for research of basilar artery circulation". Contemporary Science and Practice. Vernadsky University. **4(48)**, 46-53 (2013).
[3] D. Liepsch, A. Balasso, H. Berger, J. Mclean and G. Thurston. "Blood modelling and flow studies in models of the cardiovascular system". Series on Biomechanics. **25**(1-2), 7-22 (2010).

Theoretical justification of numerical algorithms for fluorescence diagnostic systems

I. Guseva[1,2], D. Rogatkin[1], E. Beliaeva[1,3]

1 Moscow Regional Research and Clinical Institute "MONIKI" named after M.F. Vladimirsky, Moscow, RF

2 National Research Nuclear University MEPhI (Moscow Engineering Physics Institute), 31 Kashirskoye Highway, Moscow, 115409, RF

3 M.V.Lomonosov Moscow State University (MSU), Leninskie Gory, Moscow, 119991, RF

Introduction

Today, there is a large number of different promising optical diagnostic techniques in medicine, one of which is a laser fluorescence spectroscopy (LFS) [1].To date, the most famous area of its application is oncology [2]. LFS is often used for "highlighting" the neoplastic tissues. The patient is injected with photosensitizer that selectively accumulates in tumours. By analysing the fluorescence signal a physician visually estimates the presumed border of pathology [3]. However, it should be noted that such diagnostic method is very subjective and it depends on the investigator's perception. The quantitative criterion for evaluating the tissue's state by LFS is the intensity of the fluorescent signal. However, the spectrum of the secondary radiation does not carry any diagnostic information to the physician. Also it is worth noting that the power of incident radiation and the properties of tissue have a strong effect on the detected signal. Accordingly, other methods of signal estimating have been proposed [4], but presented values are also unclear to the physicians. In

this case, the detected signal intensity has to be translated into a diagnostically more significant value such as fluorophore concentration in the tissue. Previously, it was shown that the relationship between the fluorescence signal intensity and the concentration of fluorophore is nonlinear and this non-linearity is manifested at low concentrations of fluorophore [5].Thus, the goal of our research is to develop a magnitude which will linearly depend on fluorophores concentrations with high accuracy for biological objects.

Theory

Since it is very important to obtain the information by LFS method in real time, it is impossible to use numerical methods. Therefore, analytical solution obtained in [5], which is based on a modified two-flux Kubelka-Munk and Kokhanovsky's method [6], was taken as a basis. There were only two directions in the medium for light propagation – forward and backward. The forward-directed flux at excitation wavelength λ_e was assumed to be denoted by i(x), and the backward-directed one was denoted by j(x). Let the corresponding fluorescent fluxes at the wavelength of fluorescence λ_f be denoted by I(x) and J(x), respectively. Also, let the coordinate axis "x" be directed forward (from left to right, see Fig. 1). In the task we assume that the incident monochromatic light with excitation flux F_0 at wavelength λ_e illuminates the left surface (x=0) of the tested light-scattering medium. Inside the medium some part of the excitation flux induces fluorescence at the wavelength λ_f, so that both the pure backscattered radiation j(0) at λ_e and the fluorescent backscattered radiation J(0) at λ_f can be detected from the left surface of the medium. Also we assume that the medium is a semi-infinite medium.

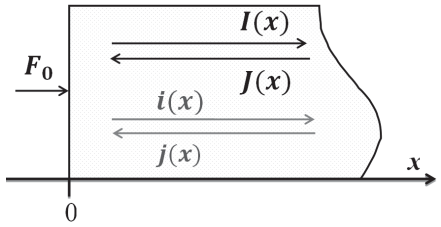

Fig. 1 Formulation of the 1D problem of light propagation in the light-scattering medium with fluorescence.

In used approach the examined 1D light-scattering medium is characterized by its local optical properties: absorption coefficient $\mu_a(\lambda)$ [mm^{-1}], reflection (Fresnel's) coefficient $R(\lambda)$ characterizing the reflection on the boundaries of the homogeneities, and the average density of the homogeneities μ_ρ [mm^{-1}] inside the medium. According to [5] all these statements can be written mathematically as the basic system of differential equations describing the forward I(x) and backward J(x) fluorescent fluxes as follows:

$$\begin{cases} \frac{dI(x)}{dx} = -\beta_1(\lambda_f)\cdot I(x) + \beta_2(\lambda_f)\cdot J(x) + F_{ef}(x) \\ \frac{dJ(x)}{dx} = \beta_1(\lambda_f)\cdot J(x) - \beta_2(\lambda_f)\cdot I(x) - F_{ef}(x) \end{cases}, \quad (1)$$

where $\beta_1(\lambda_f)$ [mm^{-1}] and $\beta_2(\lambda_f)$ [mm^{-1}] are the local attenuation and backscattering coefficients of the tested tissue at the wavelength λ_f, respectively. They are determined for any wavelength λ by formulas [7]:

$$\beta_1(\lambda) = \omega(\lambda)\cdot\frac{\mu_a(\lambda)-\mu_\rho\ln(1-R(\lambda))+\mu_\rho\ln\left(1-\omega(\lambda)+\sqrt{\omega^2(\lambda)-R^2(\lambda)e^{-2\mu_a(\lambda)/\mu_\rho}}\right)}{\sqrt{\omega^2(\lambda)-R^2(\lambda)e^{-2\mu_a(\lambda)/\mu_\rho}}} \quad (2)$$

$$\beta_2(\lambda) = R(\lambda)e^{-\mu_a(\lambda)/\mu_\rho}\cdot\frac{\mu_a(\lambda)-\mu_\rho\ln(1-R(\lambda))+\mu_\rho\ln\left(1-\omega(\lambda)+\sqrt{\omega^2(\lambda)-R^2(\lambda)e^{-2\mu_a(\lambda)/\mu_\rho}}\right)}{\sqrt{\omega^2(\lambda)-R^2(\lambda)e^{-2\mu_a(\lambda)/\mu_\rho}}}, \quad (3)$$

where $\omega(\lambda) = \frac{1-(1-2R(\lambda))e^{-2\mu_a(\lambda)/\mu_\rho}}{2}$.

Function $F_{ef}(x)$ in Eq. (1) describes the effect of enhanced fluxes due to the fluorescence effect at the wavelength λ_f under the excitation of the fluorescence at the wavelength λ_e. It can be calculated as [5]:

$$F_{ef}(x) = \frac{1}{2} A_f(\lambda_e)\varphi(\lambda_e,\lambda_f)F_0\left(1 + r_{\infty\lambda_e}\right)e^{-\alpha(\lambda_e)x}, \quad (4)$$

where $\varphi(\lambda_e,\lambda_f)$ is a quantum efficiency of the fluorescence yield, $\alpha(\lambda_e) = \sqrt{\beta_1^2(\lambda_e) - \beta_2^2(\lambda_e)}$ and $r_{\infty\lambda_e} = \frac{\beta_2(\lambda_e)}{(\beta_1(\lambda_e)+\alpha(\lambda_e))}$. Coefficient $A_f(\lambda_e)$ [mm^{-1}] in Eq. (3) characterizes a part of the excitation fluxes {i(x)+j(x)} absorbed by fluorophore inside the elementary path-length"dx"of the medium [5].

To introduce into consideration a concentration C_f of the fluorophore in relative units ($0<C_f<1$) the total absorption coefficient $\mu_{a\Sigma}(\lambda_e)$ of the medium at the excitation wavelength λ_e was expressed as the sum: $\mu_{a\Sigma}(\lambda_e) = \mu_{af}(\lambda_e)C_f + \mu_{at}(\lambda_e)(1 - C_f)$, where $\mu_{at}(\lambda_e)$ is the absorption coefficient of the medium without any fluorophores. The same approach was used to describe the total density of scatterers in the medium: $\mu_{\rho\Sigma} = \mu_{\rho f}C_f + \mu_{\rho t}(1 - C_f)$. In a practical situation with a semi-infinite medium at a noninvasive (*in vivo*) LFS the registered fluorescence signal is J(0). Resolving the system (1) with the use of Eqs. (2)-(6) for the asymptotical semi-infinite case with boundary conditions I(0)=0, i(0)=F_0, J(∞)=0 and j(∞)=0, one can obtain:

$$J(0) = F_0 \cdot A_f(\lambda_e) \cdot \varphi(\lambda_e,\lambda_f) \cdot \frac{(1+r_{\infty\lambda_e})(1+r_{\infty\lambda_f})}{2(\alpha(\lambda_e)+\alpha(\lambda_f))} \quad (5)$$

The resulting dependence of J(0) on the concentration C_f for different medium optical parameters is presented on Fig. 2. It was assumed that Φ_0=1, φ=1, $\mu_{\rho t}=\mu_{\rho f}$. Obviously, this relationship is not linear.

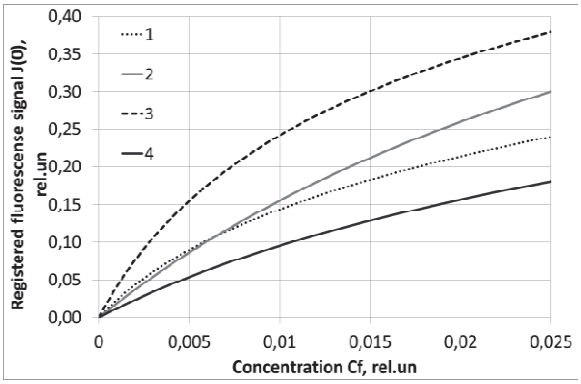

Fig. 2 Registered fluorescence signal J(0) versus relative concentration of the fluorophore C_f.

1. $\mu_{af}(\lambda_e)$=200 mm^{-1}; $\mu_{at}(\lambda_e)$=1 mm^{-1}; $\mu_{\rho\Sigma}$=200 mm^{-1}; $R(\lambda_e)$=0,2; $\mu_{a\Sigma}(\lambda_f)$=0,2 mm^{-1}; $R(\lambda_f)$=0,005.
2. $\mu_{af}(\lambda_e)$=200 mm^{-1}; $\mu_{at}(\lambda_e)$=5 mm^{-1}; $\mu_{\rho\Sigma}$=200 mm^{-1}; $R(\lambda_e)$=0,04; $\mu_{a\Sigma}(\lambda_f)$=0,2 mm^{-1}; $R(\lambda_f)$=0,02.
3. $\mu_{af}(\lambda_e)$=300 mm^{-1}; $\mu_{at}(\lambda_e)$=1 mm^{-1}; $\mu_{\rho\Sigma}$=150 mm^{-1}; $R(\lambda_e)$=0,04; $\mu_{a\Sigma}(\lambda_f)$=1,5 mm^{-1}; $R(\lambda_f)$=0,02.
4. $\mu_{af}(\lambda_e)$=300 mm^{-1}; $\mu_{at}(\lambda_e)$=5 mm^{-1}; $\mu_{\rho\Sigma}$=150 mm^{-1}; $R(\lambda_e)$=0,2; $\mu_{a\Sigma}(\lambda_f)$=1,5 mm^{-1}; $R(\lambda_f)$=0,05.

As mentioned above, to implement the possibility of quantifying the fluorophore concentration in tissue by results of measurements, it is necessary to find a value depended on the detected intensity and other measured parameters, which changes linearly with the concentration, regardless of the optical parameters of the medium.

Results

This value is

$$\alpha(\lambda_e) = \mu_a(\lambda_e) - \mu_\rho \ln(1 - R(\lambda_e)) + \mu_\rho \ln\left(1 - \omega(\lambda_e) + \sqrt{\omega^2(\lambda_e) - R^2(\lambda_e)e^{-2\mu_a(\lambda_e)/\mu_\rho}}\right) \quad (6)$$

where β_1 and β_2 are calculated using the Eq.(2) and Eq.(3). Here, the first term is responsible for the absorption, the second one takes into account single scattering, and the third is responsible for multiple scattering. This statement is not obvious and it was

empirically derived, so we decided to check it out. This lines were drawn (dashed lines, Fig.3), approximating the dependences of $\alpha(\lambda_e)$ on C_f. All of the optical parameters which affect the received value (Eq.6), were varying in the range of typical values for biological tissue. Also, determinacy factor (D^2) was identified for each straight line. It is clear that $\alpha(\lambda_e)$ depends on C_f approximately linear with 98-99% accuracy (Fig.3).

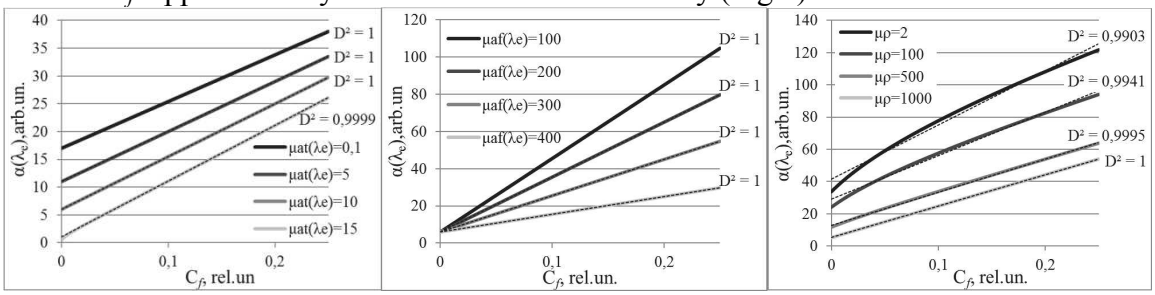

a b c

Fig. 3 Dependence of $\alpha(\lambda_e)$ on the concentration of the fluorophore C_f at different optical parameters of the medium.

a - $\mu_{af}(\lambda_e)$=200mm^{-1}; $\mu_{\rho\Sigma}(\lambda_e)$=100mm^{-1}; $R(\lambda_e)$=0,1; b - $\mu_{at}(\lambda_e)$=5mm^{-1}; $\mu_{\rho\Sigma}(\lambda_e)$=100mm^{-1}; $R(\lambda_e)$=0,1; c -$\mu_{af}(\lambda_e)$=200mm^{-1}; $\mu_{at}(\lambda_e)$=5mm^{-1}; $R(\lambda_e)$=0,1;

As $\alpha(\lambda_f)$ does not depend on the concentration of the fluorophore, the ratio $\frac{\alpha(\lambda_e)}{\alpha(\lambda_f)}$ can be also approximated by a straight line with high accuracy. By expressing this ratio from (5), we get:

$$\frac{\alpha(\lambda_e)}{\alpha(\lambda_f)} = \frac{F_0\varphi(\lambda_e,\lambda_f)(1+r_{\infty\lambda_e})(1+r_{\infty\lambda_f})\left\{\frac{\alpha(\lambda_e)}{\alpha(\lambda_f)}\frac{1-r_{\infty\lambda_e}}{1+r_{\infty\lambda_e}}\right\}_{C_f=0} + 2J(0)}{F_0\varphi(\lambda_e,\lambda_f)(1+r_{\infty\lambda_f})(1-r_{\infty\lambda_e}) - 2J(0)}. \quad (7)$$

It is necessary to normalize measured *J(0)* to prevent the influence of incident power. For saving near to linear dependence (7), let's normalize *J(0)* as $J(0)|_{\lambda=\lambda_f} = F_0 r_{\infty\lambda_f}$ and denote normalized *J(0)* by *J''(0)*.

$$\frac{\alpha(\lambda_e)}{\alpha(\lambda_f)} = \frac{\frac{1}{r_{\infty\lambda_f}}\varphi(\lambda_e,\lambda_f)(1+r_{\infty\lambda_e})(1+r_{\infty\lambda_f})\left\{\frac{\alpha(\lambda_e)}{\alpha(\lambda_f)}\frac{1-r_{\infty\lambda_e}}{1+r_{\infty\lambda_e}}\right\}_{C_f=0} + 2J''(0)}{\frac{1}{r_{\infty\lambda_f}}\varphi(\lambda_e,\lambda_f)(1+r_{\infty\lambda_f})(1-r_{\infty\lambda_e}) - 2J''(0)} = kC_f + b. \quad (8)$$

This equation with 98-99% accuracy is linear in relation to the concentration of the fluorophore in the tissue. Now in order to make the line going through point (0, 0), we have to subtract the value $b = \left.\frac{\alpha(\lambda_e)}{\alpha(\lambda_f)}\right|_{C_f=0}$ from Eq (8), and then denote the resulting expression by $Y(C_f)$.

Considering $Y(C_f)$, we can now have some ideas about the dynamics of fluorophore concentration in the tissue: we denote $Y(C_f)$ at the moment t_1 by $Y_1(C_f)$ and at the moment t_2 by $Y_2(C_f)$. If we take into account that the same area is being investigated, their ratio can be represented in the following way:

$$\frac{Y_2(C_f)}{Y_1(C_f)} = \frac{C_f(t_2)}{C_f(t_1)} \quad (9)$$

Thus, considering the ratio of $Y_2(C_f)$ to $Y_1(C_f)$,we can deduce we can determine the concentration ratio. Basing on the analytical solution of the problem of light propagation through biological tissues, we can conclude that the Eq. (9) should be used for quantitative comparison of the concentration of fluorophores between the tested region and the control one.

Conclusion

This paper is focused on the problem of mathematical data processing for laser fluorescence spectroscopy. In our research we offered the algorithm for an approximate estimate of the concentration of fluorophores in tissue. This approach can be applied for

quantifying the concentration of fluorophores in the tissue for obtaining more diagnostically significant information.

References

[1] M. A. Calin, S. V. Parasca, R. Savastru, M. R. Calin, S. Dontu, "Optical techniques for the noninvasive diagnosis of skin cancer," Cancer Res. Clin. Oncol. **139(7)**, 1083–1104 (2013).
[2] D.C.G. De Veld, M.J.H. Witjes, H.J.C.M.Sterenborg, J.L.N. Roodenburg, "The status of in vivo autofluorescence spectroscopy and imaging for oral oncology," Oral Oncol. **41(2)**, 117-131 (2005).
[3] J. P Belloch, V. Rovira, J. L Llacer, P. A Riesgo, A. Cremades "Fluorescence-guided surgery in high grade gliomas using an exoscope system, " Acta Neurochir (Wien). **156(4)**, 653-660 (2014).
[4] Д. А. Рогаткин, "Физические основы лазерной клинической флюоресцентной спектроскопии in vivo. Лекция,"Медицинская физика **4,** 78–96 (2014).
[5] D. Rogatkin, I. Guseva, L. Lapaeva "Nonlinear Behavior of the Autofluorescence Intensity on the Surface of Light-Scattering Biotissues and its Theoretical Proof," J Fluoresc. **25(4)**, 917-924 (2015).
[6] A. A. Kokhanovsky "Radiative properties of optically thick fluorescent turbid media," J. Opt. Soc. Am. **A 26,** 1896-1900 (2009).
[7] Д. А. Рогаткин "Об особенности в определении оптических свойств мутных биологических тканей и сред в
расчетных задачах медицинской неинвазивной спектрофотометрии" Медицинская техника. **2**, 10–16 (2007).

Measurement of nose tip temperature using IR imaging

L. Leicht, J. Ferch, S. Leonhardt and D. Teichmann

Philips Chair for Medical Information Technology, Helmholtz-Institute for Biomedical Engineering, RWTH Aachen University, Pauwelsstr. 20, D-52074 Aachen, Germany

Introduction

Driver distraction is an important factor in road safety. According to the U.S. department of transportation, 10 percent of all fatal crashes, 18 percent of all injury crashes and 16 percent of all police reported crashes occurred while the driver was distracted. [1]

Driver distraction can be subdivided into four classes: Visual distraction, auditory distraction, mechanical distraction (e.g. driver is adjusting the radio) and mental distraction.

Visual distraction can be monitored by analysing the driver's gaze direction and auditory distraction can be assessed by measuring the noise level inside the vehicle. Mechanical distraction can be monitored by evaluating the amount of interaction between driver and vehicle interfaces (HMI). In contrast, mental distraction is difficult to assess since this type of distraction takes place inside the drivers head. Evaluation of mental distraction must therefore look for projections of the inner, distracted driver state onto measureable variables, for example behaviouristic and physiological variables.

For example, other research groups have reported that mental distraction leads to a narrow field of view and fixation. [2] However, visual fixation of an object does not imply that the object is perceived, since the visual information from the eyes might not be properly processed in the human brain ("driver looked but did not see").

Therefore, detection of a narrow field of view can indicate distraction, but a normal visual scanning profile of the surrounding area does not mean that the driver is not distracted. Thus, other indicators of distraction should be used, for example physiological parameters. A popular example is heart rate, usually derived from ECG data [3], since distraction will usually also lead to a certain degree of increased workload and stress, which has an effect on heart rate. But also more exotic features such as the temperature of the noise tip, recorded using IR imaging, have been reported. [4] However, these finding have been produced under laboratory conditions and are possibly not comparable to real world conditions. Also, while

driving, driver movement is unavoidable and the nose position is not fixed in the image data stream. Thus, tracking of the nose is required.

In this work, we present a tracking algorithm for the nose position and an exemplary temperature recording of 10 min under real world driving conditions.

Materials and Methods

As a first step, IR image data was recorded from the vehicle driver. For that, an Optris PI 230 IR camera (**Fig. 3**, manufacturer: Optris GmbH, Berlin, Germany) was placed on the dashboard of a test vehicle, directly in front of the driver. Since the body temperature is approx. 37°C, the dynamic range of the camera was set to a range from 20 to 40°C. An example of the raw data acquired by the camera is presented in **Fig. 4**.

In the next step, the nose was located. In image processing, the Viola-Jones-Algorithm is a popular algorithm used for face detection. However, the algorithm is intended for image data from the visual spectrum. Performance for IR image data was found to be poor, most likely due to different and less prominent image features. Using detectors available in Matlab based on this algorithm was found to be unreliable for nose detection.

However, the face contour could be detected with high reliability using the pre-trained detector FrontalFaceLBP in Matlab, given the restriction that the driver was looking ahead. An example for the detected outer boundary box is given in **Fig. 5**. The red crosses indicate detected facial features which are tracked over time so a consistent head box is maintained. The nose is located centrally in the face, so a smaller box containing the nose can be constructed around the center of the outer box. Using this smaller box, the subsequent search for the nose can be facilitated.

Isothermal areas inside the smaller box are identified using a contour plot. The contour polygons are assessed by their size, weighted by the Euclidean distance to the box center. The best match is taken as the nose contour. **Fig. 6** shows the contour as a bold line. From the contour plot, a bit mask is created which only selects the image pixels which are located inside the contour. The nose temperature can then be calculated as given in Equation 1. n_i, n_j denote the image dimensions, I_{IR} the pixel intensity and M_{Nose} the bit mask for the nose. The calculated nose temperature was recorded over time while driving the test vehicle.

Results

Fig. 7 presents the detected nose temperature during a 10 min long recording. The majority of measurement values lies around 33°C, which is a reasonable value for the skin temperature, but there are several deviations to both lower and higher temperatures. During the experiment, it was noticed that the tracking of the nose is lost in case the driver turns his head too much to the side. Then, another region of the face is taken for the temperature calculation which gives different temperature values.

Since the nose temperature changes only slowly over time, this error can be easily compensated by rejecting the outliers using an appropriate filter. In **Fig. 7**, the compensated nose temperature is presented as a dotted line.

Discussion and Conclusion

In this work, a method to detect the nose tip temperature of a vehicle driver under real world driving conditions has been presented. Preliminary results indicate that the nose tip temperature can be measured in case the driver has turned his head towards the camera. Rotations of the head will disrupt the nose tracking and results in erroneous temperature readings. However, the error can be compensated using filter algorithms.

In the preliminary setup, no reference sensor for the nose tip temperature is present so the correctness can only be verified as being physiologically sound or unsound. In future work, the accuracy and reliability of the measurement system should be assessed by comparing the reference temperature sensor data with the temperature derived from the IR images.

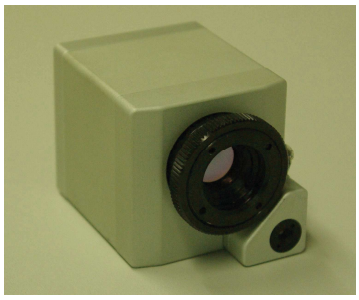

Fig. 3 Optis PI 230 IR camera

Fig. 4 Raw IR image, recorded by the Optris PI 230 IR camera

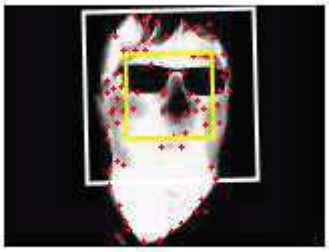

Fig. 5 IR image with boxes denoting the detected boundaries of the driver's face

Fig. 6 Detected nose contour

$$T_{nose} = 20°\mathrm{C} + \frac{1}{n_i n_j}[\sum_j \sum_i (\boldsymbol{I_{IR}} \circ \boldsymbol{M_{Nose}})_{i,j}] * (40 - 20)°\mathrm{C}$$

Equation 1 : Equation for the calculation of the nose temperatur from the IR image data

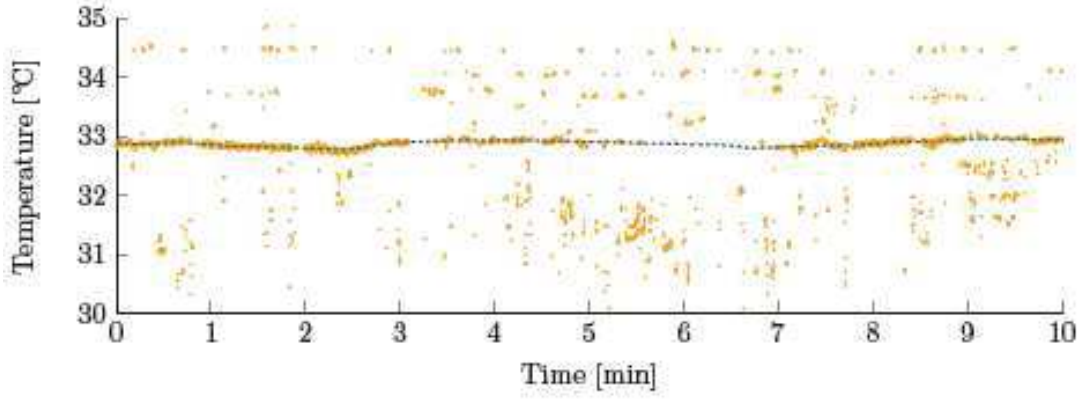

Fig. 7 Scatter plot of the extracted raw nose temperature and interpolated curve

Acknowledgement

The authors would like to thank Ford Motor Company for funding the project from which this publication originates.

References

[1] Traffic Safety Facts Research Note: “Distracted driving 2013”, National Highway Traffic Safety Administration, U.S. Department of Transportation, 2015

[2] Masahiro Miyaji, Haruki Kawanaka and Koji Oguri, “Driver's cognitive distraction detection using physiological features by theadaboost”, 12th International IEEE Conference on Intelligent Transportation Systems , St. Louis, MO, 2009

[3] Erin T. Solovey, Marin Zec, Enrique Abdon Garcia Perez, Bryan Reimer and Bruce Mehler,Classifying driver workload using physiological and drivinf performance data : two field studies

[4] Makoto Itoh, “Individual Differences in Effects of Secondary Cognitive Activity during Driving on Temperature at the Nose Tip”, International Conference on Mechatronics and Automation, Changchun, China, 2009

New results for the PVC / SPB detection using based on the MCA heart rhythm estimation method

V.E. Antsiperov, I.V. Zabrosaev

Kotel’nikov Institute of Radio Engineering and Electronics of Russian Academy of Sciences, Mokhovaya 11-7, Moscow, Russia

At the last RGC conference, we proposed a new method and first results for the PVC (premature ventricular contraction) and SPB (supraventricular premature beats) – shortly – extrasystoles detection [1]. Proposed algorithm is based on heart rhythm multiscale correlative analysis (MCA) for the purpose of searching for signal fragments containing sequences of sharp decrease followed by sharp increase of the interval between cardiac contractions corresponding to extrasystoles and compensatory pauses that follow after them accordingly.

The conventional methods for evaluation of the cardiac contraction period are usually based on detection of R-peaks [2]. However, since these methods need to look for signal peaks (or zeros of signal derivative), they appear to be unstable while processing signals with large number of interferences and distortions.

The proposed cardiac rhythm (CR) detection method is based on the correlation approach, which uses inherent to the signal periodicity. Numerical implementation of the method admits a fast algorithms due to the two special features of the method. First, a fragment of the signal which is selected to evaluate the autocorrelation function (ACF) covers only a small interval of analyzing time moment. Second, using the analytical spectra technique [3] allows boiling evaluation of ACF down to several Fourier transformations and one multiplication of arrays with a size that is a half of that used for calculation of the basic section. If fast Fourier transformation procedures are used for implementation of Fourier transformations, then the ACF calculation algorithm becomes fast.

Detection of heart disorder by our method is based on selecting the cardiac rhythm and finding its abrupt changes. The analytical spectra technique based on multi-scale correlation analysis (MCA) [3] is used for rhythm estimation. Its application is supported by the property of ECG-signal repetition. Because QRS complex of cardiac contractions has quite complex but repeating shape, the ACF evaluation takes on maximal values when the signal shifts right to the distance between neighboring QRS-complexes, i.e. the period of cardiac contractions. This period changes from beat to beat and can considerably vary at moments divided by long periods of time. In order to determine the variable repetition period of such signals we earlier proposed [3] to use ACF estimation of the following type:

$$r_x(t,\tau) = \int_{-\infty}^{+\infty} \varphi(t-\upsilon,\tau)x(\upsilon+\tau/2)x(\upsilon-\tau/2)d\upsilon \quad (1)$$

where t – moment of time for which ACF is calculated, τ – variable scale of ACF. For adequate evaluation of varying period of ECG signal, kernel φ is selected in such a way that it allocates integration interval so that several cardiac contractions are placed on it, but the value of period does not change noticeably. Otherwise, ACF peaks will be smeared, which results in reduction of the method's precision. In order to increase precision of the method when processing noisy ECG, it is suggested that a locally averaged version of ACF estimate be used [3]:

$$R_x(t,\tau) = \int_{-\infty}^{+\infty} r_x(t,\tau')w_\sigma(\tau',\tau)d\tau' \quad (2)$$

where $w_\sigma(\tau',\tau)$ is a narrow window function, its width is σ. The averaged window function can ensure precision increase during analysis of a noisy signal if width of the window is more than the time of noise correlation [3]. In this case, the use of a too wide window, as was noted above, decreases precision of the method. Therefore, σ is an adjustable parameter and should be chosen according to the analyzed signal features.

Note that (2) can be interpreted as some generalized spectral presentation of the function $r_x(t, \tau')$, the basis of which is a set of window functions $w_\sigma(\tau',\tau)$ corresponding to various values of τ.

The final structure of the quadratic form proposed in [3] as local estimate of ACF is the following:

$$R_x^+(t,\tau) = \frac{1}{\tau}\int_{-\infty}^{+\infty} \exp(2\pi if\tau)\cdot\exp\left(-\frac{1}{2}(2\pi\sigma f)^2\right)S_{Ft}(f)S_{Pt}(f)df \quad (3)$$

where $S_{Ft}(f)$ and $S_{Pt}(f)$ – analytical spectra of local future and local past of signal (relative to the current time moment t) accordingly:

$$\begin{cases} S_{Ft}(f) = \int_0^{+\infty} x(t+t')\exp(-2\pi if t')dt' \\ S_{Pt}(f) = \int_0^{+\infty} x(t-t')\exp(-2\pi if t')dt' \end{cases} \quad (4)$$

The use of the analytical spectra technique makes it easy to find the dynamics of the heart rhythm period. Namely, we will find estimate of the current local period by forming, for example, with a certain step by t analytical spectra (4), then evaluating ACF (3) and determining the position of its highest side (not central) peak.

Program implementation of the spectrum calculation algorithm (3) boils down to calculation of the product of analytical spectra (4) weighted with Gaussian window and subsequent (inverse) Fourier transformation. Analytical spectra (4), in turn, are in the result of the Fourier transformation of local future $x(t + t')$ and past $x(t – t')$ signals. It is worth noting that relatively small time interval – a couple of periods duration interval that is symmetrical in relation to the current moment of time – can be used for calculation of analytical spectra (4) and generalized spectrum (3). If fast algorithms of Fourier transformation are used in the calculations (3) and (4), then the whole spectrum calculation algorithm will appear to be fast.

The method of detection in the estimated rhythm of episodes that correspond to extrasystoles is based on the following known factors. Most of extrasystoles resemble QRS complexes in the shape. Therefore, on the generalized spectrum (3), they are also displayed as side maxima, but ones that have somewhat smaller displacements compared to the maximums, which correspond to the preceding QRS complexes of normal contractions. As a result, characteristic structures consisting of abrupt decrease of the local period, which are followed by its abrupt increase corresponding to the compensatory pause, normally correspond to the extrasystoles.

In order to select the episodes of abrupt change of the heart rhythm, it is suggested that the initial sequence of cardiac contraction values should be processed first with a median filter with a band of ~2 sec. This allows smoothing out all abrupt changes of the rhythm, and then, from the sequence smoothed in this way, subtracting the initial one, which will allow selecting all abrupt changes. Then to emphasize just extrasystoles, maximum and minimum of the period in a small interval of ~2 sec. that encircles each point of the resulting sequence are calculated and the value of their difference is attributed to the points. Thus, reduction of the period before an extrasystole and its increase after it are summed, and the probability of detecting exactly the episodes that are characteristic for extrasystoles and eliminate episodes with abrupt change of rhythm but only in the higher or lower side, which do not correspond to them, increases.

It should be noted that this approach appears to be more effective than the one which was developed by the authors earlier [1].

In our work, records from NSRDB and SADB MIT-BIH databases [4] were used for experimental testing of the algorithm proposed. Extrasystoles detected using our method were compared to the annotations, which accompanied all records of these databases. This permitted to evaluate efficiency of the algorithm having compared the results with a well-checked data. The total of 20.5 hours of ECG-records were processed in the course of the experimental inspection.

Based on the consideration of convenience, the algorithm was tested in Matlab software system. Such implementation of the method allows assessing its characteristics like efficiency and noise immunity. However, operation speed performance demonstrated by such implementation is obviously far from the limit.

The first part of the algorithm responsible for selecting the heart rhythm was tested separately. Testing was carried out using records from the database of normal sine rhythms NSRDB. It consisted in comparison of values of cardiac contraction periods determined by the program with RR-interval values taken from the annotations where moments of all cardiac contractions are specified. Standard script coming with the database attributes each ECG-record data count a value of the RR-interval equal to the distance between the heart contractions, between which this count is located. Thus, in each point, where our program calculates the value of the period, it can easily be compared with the control value.

It proved that our algorithm has quite high precision in determining the values of the periods in the normal rhythm. Considering that the sample rate of the record is 128Hz, the time interval between consecutive data samples will be 8 milliseconds. This value can be considered as time precision of initial data. Moreover, deviation of the calculated periods from the RR-intervals from annotation does not exceed 16 milliseconds, i.e. it is not more than two minimal samples in terms of the time. This, apparently, is connected with the periods computed by the program and periods calculated based on the abstract set with the sample rate of 8 milliseconds. This means that errors of the period estimations are connected, evidently, for the most part with signal discretization, but not errors of the method.

This assumption is also confirmed by a bigger amount of data. Such comparison of the calculated periods with RR-intervals was made for all ten records used for the testing.

Distribution of the frequency of deviations of the calculated period from RR-interval by their value was used as a quantitative indicator of period determination precision. Relative deviation was also calculated on each step where the period was calculated:

$$\lambda = \frac{|t' - RR|}{RR} \quad (5)$$

where t' – estimate of the current period, and RR – duration of RR-interval in the annotations. Comparison results of periods obtained by the algorithm with ones from the annotations are summarized in Table 1 where parameters of sampling distribution of relative deviations λ (5) are shown. As seen from the table, the average relative precision of cardiac contraction period determination is 1-2%. This at the value of the period being about 1 sec. means, that the error is about 0.01 sec. This means that, during the period of all records, the error of the period estimation is approximately equal to the precision limit, which only initial data allow.

Table 1. The diviations of the periods estimation from RR-interval values

Record number	Center of a distribution	Sampling distribution width
16265	1%	2%
16273	0%	2%
16240	0%	2%
16483	1%	2%
16539	1%	2%
16773	0%	1%
16786	0%	1%
16795	0%	1%
17052	0%	2%

When testing the second part of the algorithm responsible immediately for detection of extrasystoles, we focused first of all on its most common types – ventricular and supraventricular. The testing was carried out both on the records of NSRDB database, and the records from SADB. The testing showed that the algorithm quite reliably detects extrasystoles. From the processed 40 ventricular and 39 supraventricular, 36 and 37 were detected accordingly. Note that episodes where extrasystoles are arranged one after another with an interval of 1-2 sec. occur quite often in the records of SADB database. Our algorithm, because it is based on the analysis of a single section of ~4 sec., cannot obviously select them, so we reckoned the extrasystole to be detected always when the program gave a corresponding signal in a section of 4 sec. around it. If there were several extrasystoles in the section, all of them were considered as detected. Unfortunately, such approach does not allow counting their number in the record.

Testing of actual ECG by proposed in the report algorithm showed that it is good at determining ventricular and supraventricular extrasystoles (36 of 40 of the former and 37 of 39 of the latter were found) and demonstrates high precision of cardiac contraction period estimation. Regarding precision, our algorithm does not lose to the precision of the classic threshold methods based on R-peak selection. Moreover, the most important quality of the proposed algorithm is its reasonable demand for computing resources: the heart rhythm calculation program implemented in the Matlab environment on PC with a 3 GHz CPU processes an hour ECG record only in three minutes. This opens possibilities for using the developed algorithm not only in stationary conditions but also on mobile and personal medical devices intended for automatic monitoring of heart rate or for control of common types of extrasystoles. Such devices could considerably simplify and make more common, for example, the holter monitoring of patients.

The authors acknowledge financial support of this work from Russian Foundation for Basic Research, grant № 14-07-00569 A.

References

[1] V.E. Antsiperov et al., "A new PVC detection method for long ECG recordings," Proc. of the 11th German-Russian Conference on Biomedical Engineering, Germany, Aachen, pp. 131-134 (2015).

[2] Z. Piotrowski, K. Rózanowski, "Robust Algorithm for Heart Rate (HR) Detection and Heart Rate Variability (HRV) Estimation," Acoustic and Biomedical Engineering, Vol. 118 , No. 1 (2010).

[3] V.E. Antsiperov et al., "Using analytical spectra technique for automatisation of heart rate monitoring," Achievements of Modern Radioelectronics, N.8., C. 28-36 (2014).

[4] AL Goldberger et al., "PhysioBank, PhysioToolkit, and PhysioNet: Components of a New Research Resource for Complex Physiologic Signals,"/ Circulation 101(23):e215-e220 [Circulation Electronic Pages; http://circ.ahajournals.org/cgi/content/full/101/23/e215]; (2000).

Radiography with image magnification

A. I. Mazurov[1], N. N. Potrakhov[2]

1 – NIPK «Elektron», St. Petersburg, Russian Federation

2 – Saint-Petersburg State Electrotechnical University «LETI», 5 Professora Popova st., Saint-Petersburg, Russia

Introduction

Recently, in clinical practice we can see the use of radiology with microfocus X-ray sources and direct manifold magnification [1, 2]. Practice has demonstrated, that with magnification with focal spot sizes of 0.1 mm and less, it is possible to see the detail of the object of interest which is more fine than detector blur. This fact disagrees with commonly accepted methodology of imaging, which states that to obtain a sharp image the detecor has to be positioned as close to the object as possible.

The technique of contact imaging is based on the equation for the total blur H_Σ:

$$H_\Sigma = \sqrt{H_d^2 + H_g^2 + H_v^2}\,, \qquad (1)$$

where H_d, H_g, H_v – blur of a detector, blur of imaging geometry and dynamic blur respectively. Equation (1) can be found in many textbooks, including [3, 4], and it implies that total blur is always greater than any of its individual components. This conclusion, which contradicts the practice of microfocal imaging, can be desregarded, if in the equation (1) the magnification of the object of interest is taken into account.

The aim of the present work is to determine H_d, H_g and H_v in explicit form taking into account the magnification of the object of interest and also to determine the total unsharpness as a function of magnification.

Materials and Methods

Let's determine the blur H_d, H_g, H_v in the detector's plane.

Detector blur.

Because the technical specifications of a detector usually specifies the resolution R_d, when calculating H_d we would consider R_d, which is determined by contrast-frequency characterisctics (MTF) of a detector. We would consider MTF of a detector as being normally distributed.

$$A(\nu) = \exp(-2\pi^2\sigma_d{}^2\nu^2)\,, \qquad (2)$$

where ν - spatial frequency (mm^{-1}), σ_d – standard deviation of detector's spread function. Assumption of normality of detecotor's MTF follows from its multi-stage nature. Digital X-

ray imaging detectors have MTF consisting of at least four components, hence the line spread fucntion for a detector as a whole can by rather precisely approximated by the gaussoid [5].

Resolution of a detector can be directly estimated from (2), assuming $A(\nu = R_d) = \triangle$, where $\triangle$ - base level of the detector's MTF. In this case resolution of a

$$R_d = \frac{\sqrt{\ln \Delta}}{1.41\pi\sigma_d}. \quad (3)$$

In TV systems the base level is taken as $\triangle = 0.12$ [6]. In this case resolution of a detector would be $R_d = 0.33 / \sigma_d$. For a system with normally-distributed MTF the blur $H = 3\sigma$; hence detector's blur would be $H_d = 1/R_d$.

Geometrical blur

Geometrical blur is the blur caused by the point details of the object being imaged creating in the detector plane images of the X-ray tube's focal spot rather than points (fig. 1). According to fig. 1, geometrical blur equals:

$$H_g = f\frac{a}{F-a} = fm_f = f(m-1), \quad (4)$$

where m_f - magnification of the X-ray tube's focal spot, m – magnification of the object.

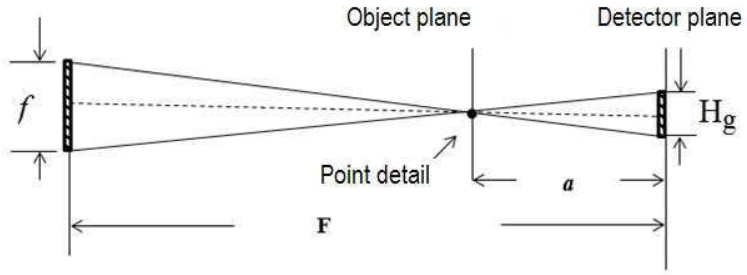

Fig. 1. Origin of the geometrical blur in the detector plane. f – size of the focal spot of the X-ray tube, H_g – geometrical blur in the detector plane, F – focal distance, a –object-to-detector distance.

Dynamic blur

Dynamic blur takes place during imaging of the moving objects, e.g. heart, lungs or gastro-intestinal tract. Dynamic blur also depends on the movement of the emitter relative to the detector during an exposure. This component of the dynamic blur depends on the rigidity of the linkage between the X-ray emitter and the detector, or on the absence of such linkage. Evaluating the dynamic blur, it is necessary to account for only the projection of the velocity which is parallel to the detector plane. For example, if the object moves along the line perpendicular to the detector plane, then the dynamic blur would be absent. Dynamic blur in the detector plane is determined by the following relationship:

$$H_v = mVt \quad (5)$$

where m – magnification of the object, V – projection of the velocity vector on the detector plane, t – exposure time.

Substituting equations (3), (4) and (5) into equation (1), we get

$$H_\Sigma = \sqrt{\left(\frac{1}{R_d}\right)^2 + (m-1)^2 f^2 + (mVt)^2}. \quad (6)$$

Relationship (6), which discloses eq. (1) is confirmed by the experimental evidence quite acceptably when m is close to unity, i.e. when the object is placed as close as possible to the detector (contact imaging). During imaging with high magnification, calculations with eq. (6) give considerable errors. This is due to the fact that with increasing distance the object and the

detector, the spectrum of frequencies forming the image is decreased by the factor of m, and therefore it simplifies its representation. Simultaneously the resolution is increased by the factor of m, and the blur is decreased by the same factor:

$$H_{\Sigma}(m)=\frac{1}{m}\sqrt{\left(\frac{1}{R_d}\right)^2+(m-1)^2 f^2+(mVt)^2}=\sqrt{\left(\frac{H_d}{m}\right)^2+\frac{(m-1)^2}{m^2}f^2+(Vt)^2}\,. \quad (7)$$

Equation (8) coincides with (1) if detector , geometrical and dynamic components of the blur are calculated accordingly to the following equations:

$$H_d(m)=\frac{1}{mR_d},\qquad H_g(m)=\frac{m-1}{m}f,\qquad H_V(m)=Vt\,.$$

Fig. 2 shows the results of calculation of the total blur $H_{\Sigma}(m)$ and its components as functions of magnification for a microfocus system and for a system for contact imaging.

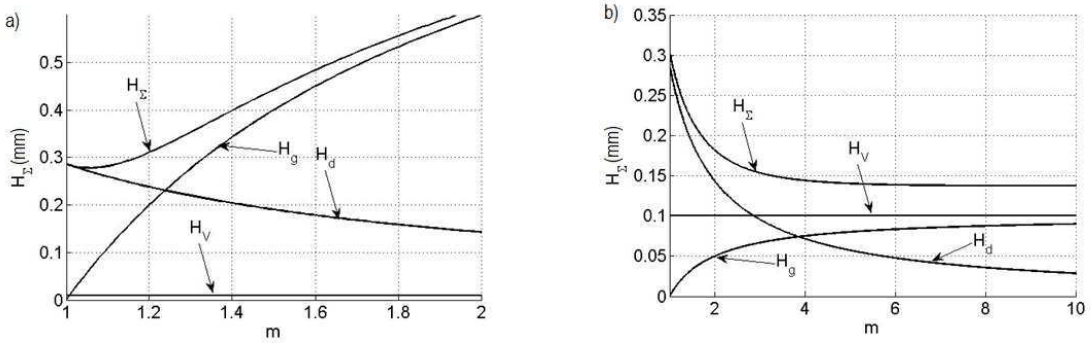

necessary. Time of exposure is determined not only by the mobility of the organ being imaged, but also by the spatial frequency spectrum, contained in that organ. For example, it is possible to immobilize extremities, guaranteeing that $V < 1$ mm/s, but to preserve the fine structure of bone tissue exposure time should not exceed 50 ms [7]. There are two radical methods of dynamic blur reduction: increase of the power of X-ray source (and corresponding reduction of the exposure time) and automatic compensation for the dynamic blur by means of digital image processing. Both methods are used in the interventional radiology in angiographic systems.

From eq. (7), taking $H_\Sigma R_\Sigma = 1$ and $H_d R_d = 1$, it is possible to get the formula for evaluation the imaging system's resolution:

$$R_\Sigma = \frac{1}{H_\Sigma} = R_d \frac{m}{\sqrt{1+(m-1)^2\left(fR_d\right)^2+\left(mR_dVt\right)^2}}.$$

Conclusion

Total blur of X-ray images can be either larger or smaller than its components. It depends on imaging geometry, relationship between the focal spot of the X-ray tube and the detector blur and also on the mobility of organs being imaged.

References

[1] A. Yu. Vasiliev, Radiography with direct multiple magnification in clinical practice, NTPK Logos; Moscow, 1998.

[2] N. N. Potrakhov, editor, Microfocus radiography in medicine. SpBGETU LETI; St. Petersburg, 2015.

[3] V. V. Dmokhovsky, Fundamentals of radiotechnics. Medgiz; Moscow, 1960.

[4] N. N. Blinov, editor, Fundamentals of radiodiagnostic techniques. Meditsina; Moscow, 2002.

[5] J. LLoyd, Thermal imaging systems. Mir; Moscow, 1978.

[6] Ya. A. Ryftin, Television system. Sovetskoye Radio; Moscow, 1967.

[7] S. Nudelman, Kh. Rerikh, M. P. Kepp, Electro-optical digital radiography, TIIER, 70(7), 33-48, 1982.

Development of a universal software for visualizing data of medical devices

I. N. Rodionov[1], K. V. Pozhar[2]

1. National Research University of Electronic Technology, Bld. 1, Shokin Square, Zelenograd, Moscow, Russia, 124498

2. OJSC "ESDIAR", D. 8, Solnechnaya alleya, Zelenograd, Moscow, Russia, 124527

Rapid development of the modern technique allowed to expand considerably a line of the medical equipment applied in medical institutions. However, such a variety of devices has led to the emergence of a large number of complex software systems, which need to work doctor. An example may be a program for analyzing ECG and EEG data, the program of information processing about operation of artificial heart. They all have similar functionality, but they can only work with one specific device. For lowering of time necessary for training on the medical equipment is offered the universal software allowing not only to reduce time for training of medical staff, but also to reduce costs of software development for the specific equipment.

The basis of the program architecture is a pattern Model-View-Controller (MVC) [1]. Its main feature is that the model of application and the user interface are partitioned into separate components so that a change in one of them has a minimal impact on the other. There are several varieties of MVC. Among them the scheme with passive model was selected, i.e. the model has no opportunity to influence representation (figure 1).

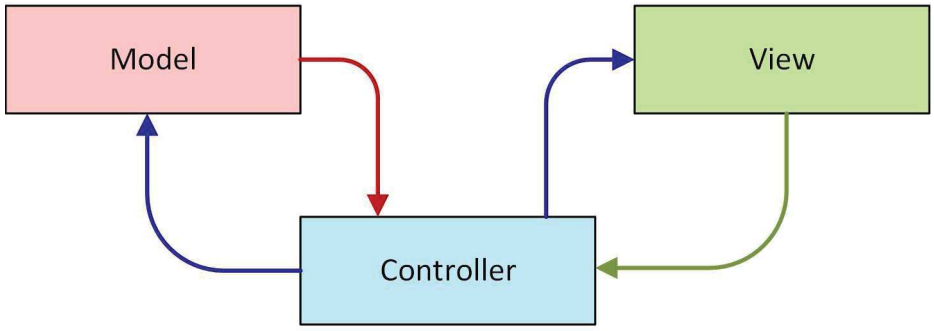

Fig. 1 The general scheme of interaction of the basic template modules Model-View-Controller, with a passive model

In order to ensure greater flexibility of architecture it is decided that each of MVC modules realizes a pattern "Bridge" (figure 2.a) [2]. Its essence lies in the fact that the basic module is an abstraction, whose main task is redirection of all the received requests to other elements, in this case to dynamically connected elements – plug-ins. In turn in plug-ins are implemented special cases for each of the possible queries.

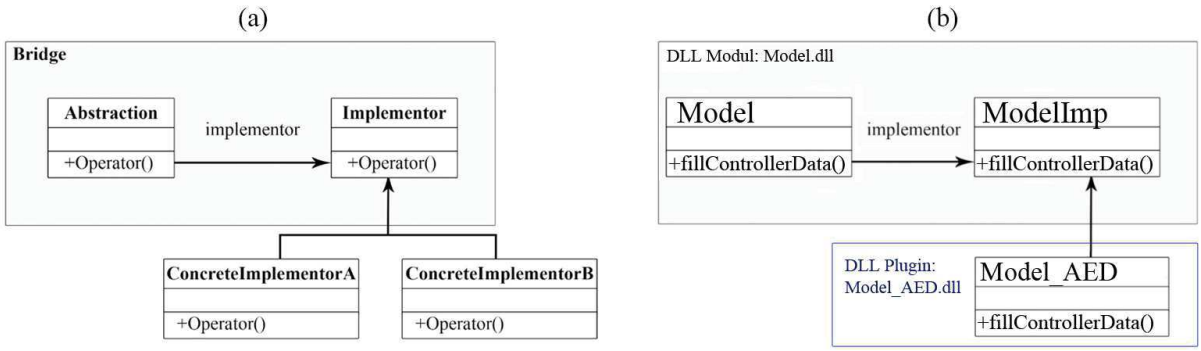

Fig. 2 (a) Scheme of the structural template "Bridge". (b) Implementation of the "Bridge" pattern on the example of "model" module

We will consider it on the example of the Model module. (figure 2.b). In it there is a method "fillControllerDate()" – responsible for filling of data for the controller, in which is called the appropriate method of the internal pointer and the returns result of its operation. This internal pointer is a virtual function table [3], which is the interface, with which operates the Model, and an interface that should override all plug-ins for the model.

Currently developed a plugin for "Model_Heart" model, which is responsible for access to the data generated during the operation of the device of the long mechanical substitution of function of heart. It defines the necessary interface for the model, including method "fillControllerDate()" in which data for the controller are formed from the data read from the file.

In summary, using different plug-ins, depending on model parameters, the user obtains data from different devices. Moreover, data can be taken both from the file, and from a remote server, or to be read out directly from the device. As a result to add support of the new device it is necessary to write the appropriate plug-in for model. At the same time it isn't necessary to recompile all system since plug-ins are connected dynamically – i.e. in the course of operation of application.

Each of modules realizes the "Bridge" template, i.e. they supports system of plug-ins. Including the module "View" for which plug-ins are responsible for the user interface. One of

them is "View_QT" – the plug-in based on a framework of Qt [4]. The area of data mapping which is available in it is based on the "QtCharts" library, designed to draw graphs. The majority of similar libraries work by the following principle: in the beginning to them all available data array is provided, further there is their processing and display, and only then the user can interact with available information [5]. The problem of this scheme is that there is a duplication of information. These models may have changed over time, but because stored in the interface of the old data copy, then it does not reflect the changes occurred with the data. It was therefore decided to use other algorithm of operation. Every time there is a change in the data display area: the application window size is changed, changed the scale, triggered a timer update - this field is redraw. But before this new data is requested from the model for the new desired area. Only on the basis of the newly received data is repainted. Model offers not all data, but only a part. Selects the available information, based on the parameters of the request. It provides data only from the required area - ie what a user wants to see at particular time.

But happens that there is too much data for necessary area in model. For example if conditionally to take area of 100x100 pixels on a display element of diagrams, then for this period the model can have 10 000 samples (figure 3). But for obvious reasons we could display only 100 points. Therefore in model there is data filtering. on the basis of different methods – decimations or approximations. Data is actually formed for the specific screen resolutions. For this example on an output receive 100 points which need to be displayed on a graphics. Besides, always realized is one case - the complete data update.

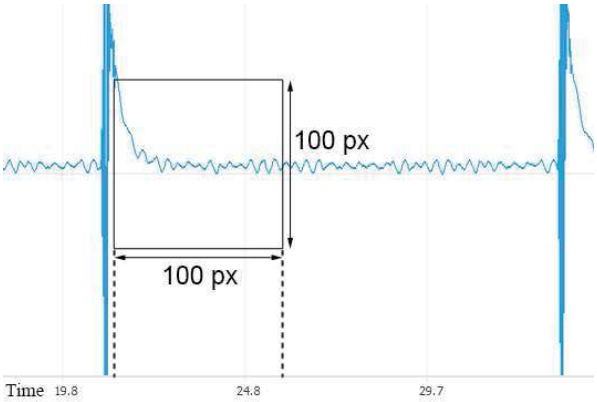

Fig. 3 Illustration of data samples for 100x100-pixel area, on the display field

In the provided scheme, the model completely is responsible for information obtained by the user. Therefore at the different scale it is possible to show the different or changed data. For example, "events" - their icons are displayed in the upper part of the area of visualization of data. At the certain scale of an icon will strongly superimpose each other (figure 4.a), worsening their perception. Therefore the model assembles events into groups and presents them in the form of one event, when you click on that you can is possible to receive the complete list of the hidden data (figure 4.b). Uploading of contents of group occurs only while the user demands this information.

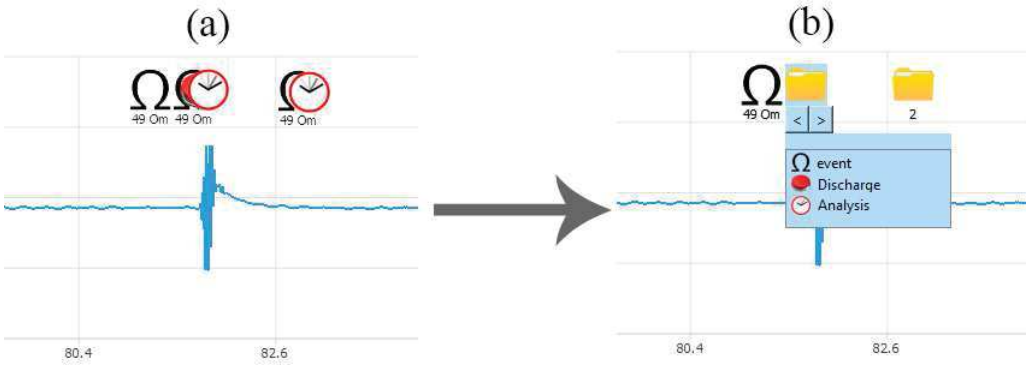

Fig. 4 (a) Superimposing event icons on each other. (b) Packing events close group and access group data

As a result, this system makes it easy to work with large amounts of data, which is essential, as the target medical equipment, for which developed the software package: sensors ECG and EEG, the device long mechanical replacement heart function - are high-frequency devices that generate data with a large frequency and, consequently, in large volumes.

In the controller, and specifically in its plug-in of "Controller_Standard" there is a data conversion created by "Model" into a form perceivable by "View" and also transmission of requests from "View" in "Model" (figure 5). In addition in this module there is additional data filtering as well as correction parameters incoming requests [6].

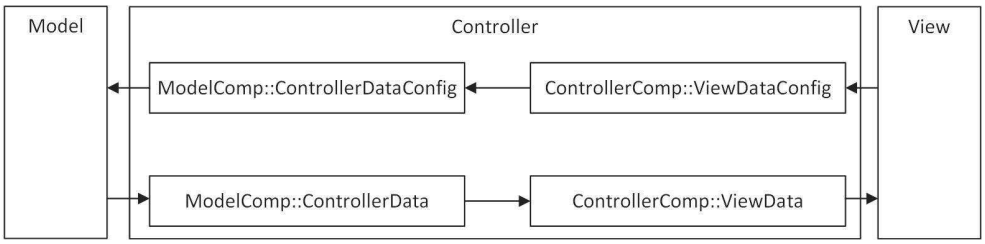

Fig. 5 Scheme of destination of the Controller module

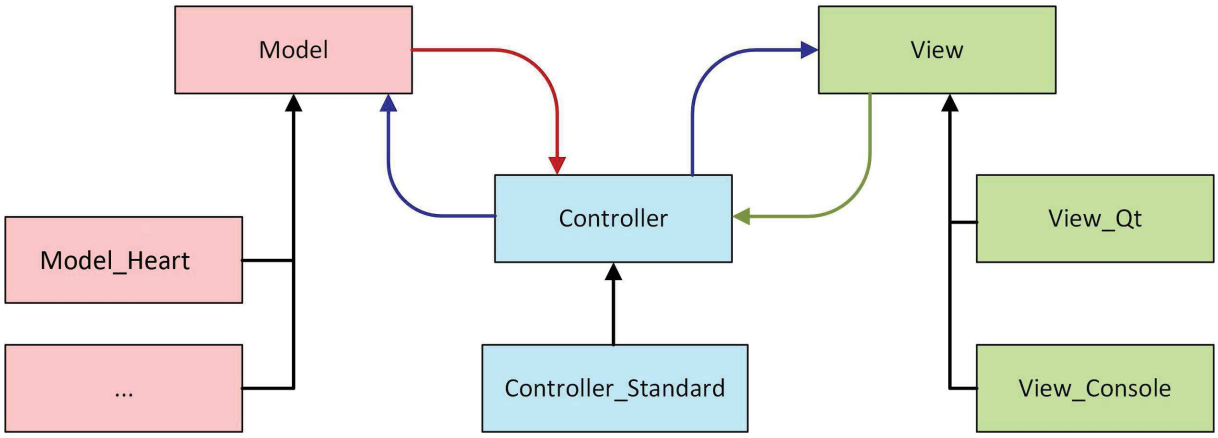

Fig. 6 The final scheme of architecture of the developed program complex

As a result, we get quite a flexible architecture in which each element of the MVC is implemented through a plugin system (figure 6). This makes it easy to add support for new devices, and secondly allows multiple user interfaces. For example, in addition to "View_Qt" is created the plug-in for the console interface – "View_Console". So far it is used for testing

of the developed system, but in the future it can work with third-party software, which only the data from the instruments will be required, without the graphical user interface.

The present software allows you to view data received from various devices. This will significantly reduce the time of training of medical personnel, as will no longer need to work with a number of programs designed for specific devices. Markedly reduced the time to create software for the new hardware. Developers will need to write only a part of the system - a module that provides access to specific data, and then connect it to the submitted software.

The work was supported by the Ministry of Educational and Science (project ID RFMEFI57915X0102).

References

even more intensity of useful Doppler signal thereby creating noise in the input signal of device. For today this effect of amplitude modulation is not considered in existing methods and models of signal processing in the LDF. Its description does not exist in the literature so this fundamental aspect of formation of the LDF output signal studied today is very poorly. The aim of our study is to study theoretically the effect of amplitude modulation of light flux incident on a photodetector applied to LDF.

Model. The studied biological tissue is represented in the form of a semi-infinite layer of turbid medium filled with blood. The absorption coefficient μ_a and the scattering coefficient μ_ρ (the average density of scattering inhomogeneities) of such layer are written as sums [9]:

$$\mu_a = \mu_{at} + \mu_{ab} C_b$$
$$\mu_\rho = \mu_{\rho t} + \mu_{\rho b} C_b \,, \tag{1}$$

where μ_{at} and μ_{ab} are absorption coefficients of bloodless tissue and blood, $\mu_{\rho t}$ and $\mu_{\rho b}$ are the average density of scattering inhomogeneities of bloodless tissue and blood respectively, C_b is relative level of tissue blood volume ($C_b = 0\ldots1$).

The intensity of backscattered flux for a single layer of semi-infinite turbid medium in the approximation of single scattering is written as [10]:

$$I_{BS} = \frac{I_0 R \cdot \exp(-\mu_a / \mu_\rho)}{1-(1-R)\cdot\exp(-2\,\mu_a/\mu_\rho)} \tag{2}$$

where R is reflection coefficient of Fresnel on the border of inhomogeneities inside the medium. Since C_b <1 and $|\mu_a/\mu_\rho| << 1$ by using (1) the expression (2) is decomposed in a Taylor series by C_b limited of the two terms. After all transformations we have:

$$I_{BS} = Y\left[1 + Z\left(\frac{\mu_{at}\mu_{\rho b}}{\mu_{\rho t}^2} - \frac{\mu_{ab}}{\mu_{\rho t}}\right)C_b\right], \tag{3}$$

where

$$Y = \frac{I_0 R \cdot \exp(-\mu_{at}/\mu_{\rho t})}{1-(1-R)\cdot\exp(-2\,\mu_{at}/\mu_{\rho t})}\,,\quad Z = \frac{1+(1-R)\cdot\exp(-2\,\mu_{at}/\mu_{\rho t})}{1-(1-R)\cdot\exp(-2\,\mu_{at}/\mu_{\rho t})}\,. \tag{4}$$

The total intensity of light flux incident on a photodetector is presented as:

$$I_{BS} = I_S + I_d \,, \tag{5}$$

where I_S is intensity of reference flux without Doppler shift and I_d is intensity of Doppler-shifted flux scattered on moving RBCs. I_S is determined as intensity of total flux in the absence of light scattering on the RBCs:

$$I_S = I_{BS}(\mu_{\rho b} = 0) = Y\left[1 + Z\left(-\frac{\mu_{ab}}{\mu_{\rho t}}\right)C_b\right]. \tag{6}$$

I_d is determined as difference between total and reference flux:

$$I_d = I_{BS}(\mu_{\rho b} \neq 0) - I_{BS}(\mu_{\rho b} = 0) = YZ\frac{\mu_{at}\mu_{\rho b}}{\mu_{\rho t}^2} C_b \,. \tag{7}$$

Consider the amplitude modulation of C_b caused by fluctuations of blood volume in tissue due to various rhythmic processes in the microcirculation system, i.e.:

$$C_b(t) = C_{b0}(1 + k_{Cb}\cos\Omega t) \,, \tag{8}$$

where C_{b0} is average level of C_b, k_{Cb} is the modulation depth of C_b, Ω is the frequency of modulation. Substituting (8) in (6) and (7) gives the time dependencies of I_S and I_d:

$$I_S(t) = Y\left(1 - ZC_{b0}\frac{\mu_{ab}}{\mu_{\rho t}}\right) + YZC_{b0}k_{cb}\frac{\mu_{ab}}{\mu_{\rho t}}\cos(\Omega + \pi)t \,,$$
$$I_d(t) = YZC_{b0}\frac{\mu_{at}\mu_{\rho b}}{\mu_{\rho t}^2} + YZC_{b0}k_{cb}\frac{\mu_{at}\mu_{\rho b}}{\mu_{\rho t}^2}\cos\Omega t \,. \tag{9}$$

As can be seen, fluxes I_S and I_d consist of some constant components and components fluctuating in accordance with blood volume changes which are in antiphase. So according to (9) the modulation amplitude of reference and Doppler fluxes intensity can be presented as:

$$AM_{Is} = YZC_{b0}k_{cb}\frac{\mu_{ab}}{\mu_{\rho t}},\ AM_{Id} = YZC_{b0}k_{cb}\frac{\mu_{at}\mu_{\rho b}}{\mu_{\rho t}^2}. \quad (10)$$

The results of theoretical modeling and discussion. The dependencies of the AM_{Id} and AM_{Is} from the modulation depth k_{Cb} are interesting. These dependencies were modeled and graphs are presented in figure 1.

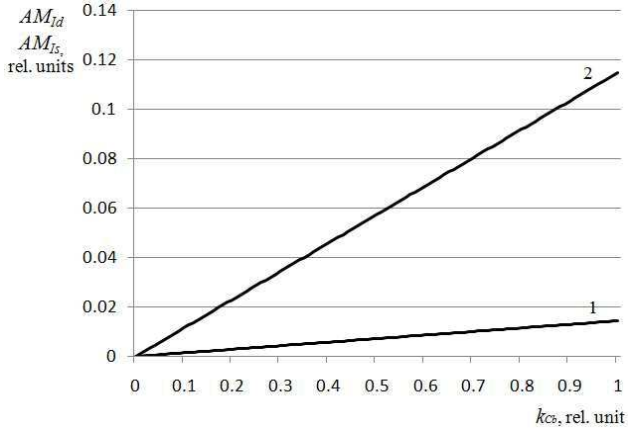

Fig. 1. The dependence of the modulation amplitude of the Doppler flux AM_{Id} (1) and reference flux AM_{Is} (2) from the modulation depth of blood volume k_{Cb}.

In the calculations it was used that I_0 = 1. The absorption coefficient was taken from [11] as function of wavelength in the form μ_{at} =27exp(–0,006λ). All calculations were performed for λ = 800 nm. The absorption coefficient of blood was determined as $\mu_{ab} = \mu_{aHBO2}S_tO_2 + \mu_{aHB}(1- S_tO_2)$, where μ_{aHBO2} is the absorption coefficient of oxyhemoglobin, μ_{aHB} is the absorption coefficient of deoxyhemoglobin, S_tO_2 (S_tO_2 = 0...1 relative units) is the average value of tissue oxyhemoglobin saturation [9] (in calculations typical value for the mixed arterio-venous blood S_tO_2 = 0,7 was used). The typical for human skin values of average density of scatterers in tissue and blood were taken from [12]: $\mu_{\rho t} = \mu_{\rho b}$ = 100 cm^{-1}.

The dependency of relation AM_{Id}/AM_{Is} from the scattering properties of media is also interesting. Graphs of these dependencies for different values of $\mu_{\rho t}$ and $\mu_{\rho b}$ (100, 500, 1000 cm^{-1}) are presented in figure 2.

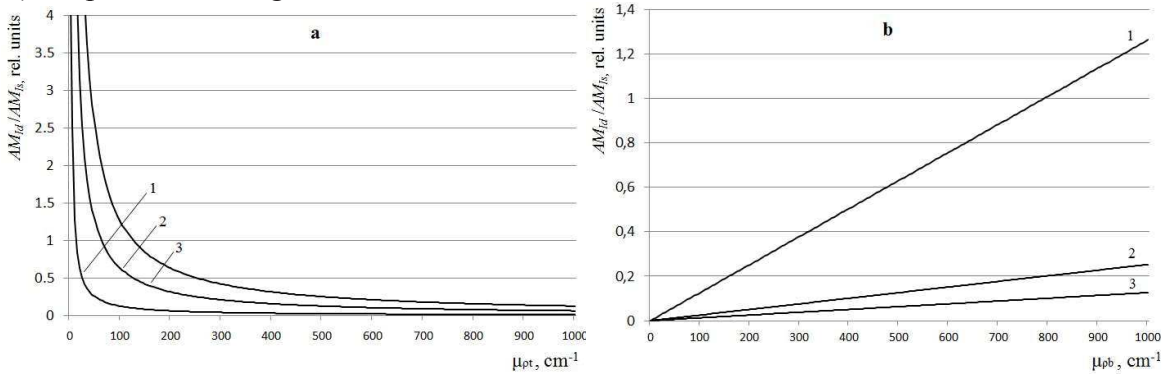

Fig. 2. The dependency of relation AM_{Id}/AM_{Is} from the density of scatterers in the tissue $\mu_{\rho t}$ for different values of the density of scatterers in the blood $\mu_{\rho b}$ = 100 (1), 500 (2), 1000 (3) (a). The dependency of relation AM_{Id}/AM_{Is} from $\mu_{\rho b}$ for different $\mu_{\rho t}$ = 100 (1), 500 (2), 1000 (3) (b).

So the analytical expressions related the modulation depth of tissue blood volume with the modulation depth of backscattered fluxes applied to LDF method were obtained. This effect of modulation of light flux intensity incident on a photodetector is further transferred along path of signal processing in the LDF instrument and eventually is superimposed on the measured value of perfusion.

References

[1] Rajan V., Varghese B., Leeuwen T. G. and Steenbergen W. Review of methodological developments in laser Doppler flowmetry // Lasers Med Sci, 2009, V.24, pp.269–283.
[2] Bonner R.F., Nossal R. Model for laser Doppler measurements of blood flow in tissue // Appl. Opt. 1981. V.20. pp.2097–2107.

spring and summer due to the reservoir refill because of the melt surface water and the water temperature increase with current velocity reduction.

For the study we selected 17 chemical parameters that influence the development of the disease (Table 1). Each indicator is characterized by its own maximum permissible concentration (MPC).

According to the sanitary regulations 5 groups of diseases are singled out (Table 2). Diseases are determined by the weight coefficient, number of indices causing the development of the disease. The given weight coefficient will be necessary for creating a probable procedure of the identification systems assessment. Then the given scheme of the influence of water chemical indicators on the development of diseases will be used as the basis while forming the identification system of diseases.

Table 1. Chemical data

Number	Chemical index	Maximum permissible concentration mg / l
1	ammonia nitrogen	0,4
2	nitrites	0,02
3	nitrates	9,1
4	chlorides	300
5	sulphates	100
6	iron	0,1
7	manganese	0,01
8	copper	0,001
9	cadmium	0,005
10	nickel	0,01
11	cobalt	0,01
12	phenols	0,001
13	arsenic	0,05
14	fluorides	0,75
15	potassium	50
16	sodium	120
17	magnesium	40

Table 2. The influence of chemical indicators on the disease

Number	Disease	Chemical indices exceeded	Weight coefficient
1	Methemoglobinemia (cyanosis)	phenol, nitrites, nitrates, ammonia nitrogen	4
2	Blood diseases	nitrates, chlorides, cadmium, phenols, ammonia nitrogen	5
3	Cardiovascular deseases	nitrates, chlorides, sulfates, cobalt, iron, manganese, arsenic, potassium, sodium, nickel ammonia nitrogen	11
4	Genitourinary deseases	copper, arsenic, potassium, magnesium, chlorides, nitrates, nitrites	7
5	Anemia	nitrates, copper, nickel, fluoride, manganese, ammonia nitrogen	6

The task of creating of the identification system of diseases (ISD) according to water quality indices is classified as difficult to formalize (difficult for algorithmization) the

mathematical model of which has uncertainties. Therefore, for the synthesis of ISD the mathematical apparatus based on artificial neural networks (ANN) is selected, it has a number of advantages compared with other methods (operation parallelism, automatic adaptation, work resistance, etc.).

Along with the advantage of neural networks methods there are certain difficulties of using ANN apparatus because their use does not give the desired accuracy of the procedure of the identification of diseases. These difficulties are connected with the wrong choice of ANN architecture which is understood as its structural, topological and analytical description. Therefore, it is an urgent task to choose the optimal ANN architecture increasing the probability of the identification of diseases. To do this it is necessary to consider various ANN models based on the same training sample and to compare identification probabilities.

For the analysis of neural networks techniques we compared probabilities of the identification [3,4] to solve the problems of determining diseases according to water chemical parameters. The created scheme of water chemical indicators influence on the development of diseases was used as a training set for training neural networks. The list of ANN analyzed to solve the problem of the identification of diseases according to water chemical indicators is shown in Table 3.

Table 3. List of ANN analyzed

Number	Name of ANN	Specification
1	Perceptron 8	Three-layer perceptron using 8 neurons in the intermediate layer
2	Perceptron 10	Three-layer perceptron using 10 neurons in the intermediate layer
3	Probabilistic neural network	Probabilistic Neural Network (PNN)
4	Regression neural network	Generalized Regression Neural Network (GRNN)

Each neural network consists of 17 inputs corresponding to uniform chemical characteristics (Table 1) and 5 outputs. The output of each neuron characterizes the degree of belonging to the relevant disease (Table 2). The regression and probabilistic networks architecture does not involve the use of several intermediate layers. The learning algorithm for these ANN is also simplified because the procedure of learning is based on the "memorizing" of the training set, and then evaluating of the degree of similarity between the new indicators and "stored" data.

The analysis of ANN functioning for the generalizing ability was carried out with the use of the theory of probability and mathematical statistics. For this we developed an assessment algorithm of ANN work. ANN performance test was conducted according to the real water chemical indicators in the Penza region in 2012 – 2014. The assessment algorithm consists of a sequence of the following actions:

1. Select the chemical parameters (H_m) for the current month (m);

2. Perform the unification of rates by the formula 1 and receive the plurality of input values H'_m, where m is a month;

$$x_i = \frac{x_i^l}{D_{max}}, \quad (1)$$

where x_i – a unified chemical indicator;

x_i^l – a real chemical indicator;

D_{max} – the maximum permissible concentration of the chemical indicator;

3. Mark the indicators approaching to or above 1;

4. Form, in accordance with the SanPiN [2] (Table 2), a list of the most probable diseases T_m;

5. Specify the number of the indicators exceeded n_i for each item (i) of the list of probable diseases. This value determines the weight coefficient of the disease;

6. Choose ANN from the list of ANN analyzed;

7. Feed the plurality H'_m to the input of ANN and get the plurality of diseases as a result of ANN work T_m. This plurality is produced by the selection of those diseases in which the respective neuron output value is above the predetermined threshold F. In order to solve the current problem we should determine this threshold by the formula 2:

$$F = \frac{K_з}{K_п}, \tag{2}$$

where $K_з$ – the number of diseases;

$K_п$ – the number of indicators;

As $K_з$=17, $K_п$=24, то F≈0,7;

8. Calculate the probability of the identification of the disease in ANN P_m by the formula 3:

$$P_m = \frac{\sum_{i=1}^{k} s_i w_i}{\sum_{i=1}^{k} w_i}, \tag{3}$$

where k – the size of the list of the most probable diseases T_m;

w_i – the weight of the i-th disease;

s_i – a sign of the presence of the i-th disease in T_m list;

9. Perform steps 6-7 for each of ANN analyzed from Table 3;

10. Save probabilities P_m for each ANN and go to the next month.

Thus, it is necessary to fulfill the following condition (4) for the analysis of ANN:

$$\begin{cases} t_{training}(j_{ANN}) \longrightarrow min \\ P_{detection\ i\ index}(j_{ANN}) \rightarrow max \end{cases}, \tag{4}$$

where $t_{training}(j_{ANN})$ – training time of j-th ANN (should strive for a minimum);

$P_{detection\ i\ index}(j_{ANN})$ – detection probability of i-th index of j-th ANN (should be maximum).

Having calculated the probability of the identification of the ANN for each month you can create a graph of the probability distribution (Figure 1) in which on the vertical axis there is the probability of the identification, and on the horizontal one – months of 2012 – 2014. Figure 1 shows 4 graphs corresponding to ANN analyzed (Table 3).

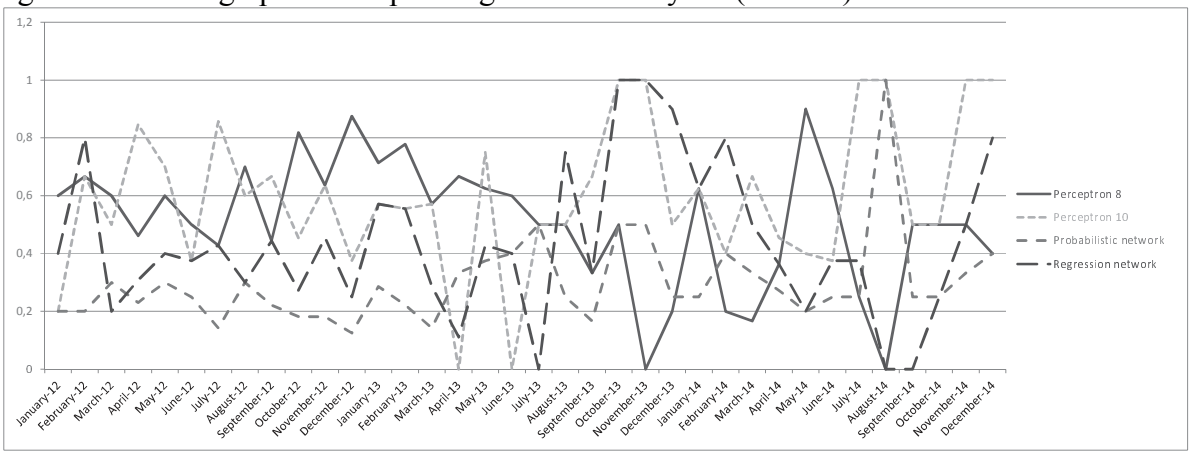

Fig. 1 Graph of the probability distribution of the identification according to months

According to the schedule of the probability distribution of the identification (Figure 1) it can be determined that ANN "Perceptron 10" shows the highest probability. This is

confirmed by Table 4 which shows the average value of the probability of the identification of diseases (*P'*) calculated by the formula 5.

$$P' = \frac{\sum_{M1=1}^{C} P_{M1}}{C}, \quad (5)$$

where *P'* – the average value of the probability of the identification of diseases;
C – the number of months under study.

Table 4. Identification Probability

Number	Artificial neural networks (ANN)	The probability of the identification
1	Three-layer perceptron using 8 neurons in the intermediate layer	**0,52**
2	Three-layer perceptron using10 neurons in the intermediate layer	**0,68**
3	Probabilistic Neural Network (PNN)	**0,35**
4	Generalized Regression Neural Network (GRNN)	**0,41**

In spite of the fact that multilayer nets indicate the higher probability of the identification the probabilistic neural network (PNN) should be noted. The graph (Figure 1) shows that this ANN has no null values. Additionally, when identifying the given network is focused on the issue of one result, and, as a consequence, identifies the most probable disease. Along with this, the learning time of the probabilistic neural network is minimal.

Thus, the proposed approach to building of the system for the identification of diseases according to water chemical indicators can increase the probability of the identification. This approach is based on the use of multi-layer ANN trained on standardized data. We suggested the assessment algorithm of the efficiency of ANN performance which allowed to justify the choice of the neural network with the structure in the form of a three-layer perceptron with 10 neurons in the intermediate layer.

References

[1] Konovalova O.E., Konovalov A.V., Istomina T.V. The analysis of the chemical indicators of water quality and their impact on human health // XXI century: the results of past and present problems plus. 2016. Number 01 (29). P. 120-125.
[2] Sanitary-epidemiological rules and norms "Drinking water: hygiene requirements for water quality of centralized drinking water supply systems. Quality control. SanPiN 2.1.4.1074-01"
[3] Konovalov A.V. Neural networks probabilities of the signals detection // Collected papers of the International Scientific Technical Conference. Penza. 2005.
[4] Istomin T.V., Istomin B.A. Application of neural network technology for analysis electrocardiosignal// Neurocomputers: development, application. 2010. № 11. S. 11.

Development of a cardiovascular system model for investigation of biventricular circulatory support

D. Petukhov
National Research University of Electronic Technology, 1 Shokin square, 124498 Zelenograd, Russia

Currently continuous flow left ventricular assist devices (LVAD) considered as one of the efficient ways for chronic heart failure treatment along with the heart transplantation [1–3]. While many patients can be successfully managed with LVAD only, up to 30% of patients developing right ventricular failure [4]. These patients have significantly higher mortality and

greater end organ compromise compared to LVAD recipients [5, 6] and require biventricular circulatory support if medical treatment strategies failed [7, 8].

The contemporary way of biventricular circulatory support is to implantation of a second LVAD to mechanically support the right ventricle as in [9, 10]. It poses technical challenges due to different ventricular geometries, ventricular interaction and different systemic and pulmonary vascular resistances. A speed variation of both pumps significantly alternates patient hemodynamics and exacerbate the problem of flow balance between systemic and pulmonary circulation.

The aim of this work is to developing of a mathematical model of cardiovascular system, which should characterize hemodynamics of biventricular heart failure and describe hemodynamic changes during biventricular circulatory support with two VADs.

Methods

A model of circulatory system is based on previously described lumped patameter models of circulation [11, 12]. A heart model is based on elastance heart model [13] and takes into account ventricular interaction.

The fig. 1 demonstrates complete cardiovascular model, represented by an electrical circuit.

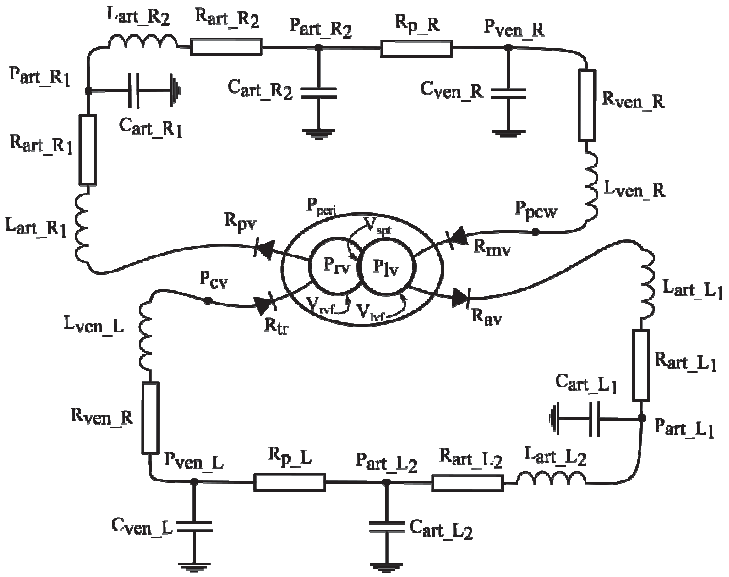

Fig. 1 Cardiovascular system model; P – pressures, R – resistances, L – inertances, C – capacitances, Pperi – pericardium pressure, P_{lv} – left ventricular pressure, P_{rv} – right ventricular pressure, V_{lvf} – left ventricular free wall volume, V_{rvf} – left ventricular free wall volume, V_{spt} – septum free wall volume.

Systemic and pulmonary segments of circulation are modeled with constant resistances R, inertances L, and capacitances C. Systemic and pulmonary artery divided into two segments to obtain site for a ventricular assist device connection. The tricuspid, pulmonary, mitral and aortic valves are modeled as ideal diodes [12].

The cardiac mechanics is modeled by a time varying pressure–volume relationship that simulates the contraction and relaxation of the ventricle walls according to [13, 14]. To enable simulation of ventricular interaction, the two ventricles are divided into three parts: left ventricle wall (lvf), the right ventricle wall (rvf) and the septum wall (spt), as shown at fig. 1. The corresponding free wall volumes are not physical volumes, but are defined to capture the deflection of the cardiac free walls relative to the ventricular volumes in order to evaluate pressure in the ventricles [13].

The reference parameters of circulatory model are derived from [11, 12] and parameters of heart model are based on [14]. The cardiovascular system state with biventricular failure are based on [9, 15]. Target hemodynamic indices and corresponding simulated values are listed in table 1. In order to obtain accordance between simulated and target hemodynamics all model parameters were adjusted by an optimization routine on the basis of Levenberg–Marquardt method.

Table 1 List of target and simulated hemodynamic indices

Hemodynamic index	Target value	Model value
Systolic arterial pressure (SAP, mmHg)	96	88.0
Diastolic arterial pressure (DAP, mmHg)	52	41.2
Left Ventricular Stroke volume (LV SV, mL)	45	45.9
Right Ventricular Ejection Fraction (RV EF, %)	32	56
Pulmonary systolic arterial pressure (PSAP, mmHg)	48	39.9
Pulmonary diastolic arterial pressure (PDAP, mmHg)	25	18.4
Central venous pressure (CVP, mmHg)	11	-0.38
Pulmonary capillary wedge pressure (PCWP, mmHg)	21	15

A baroreflex model was implemented according to [16] in order to reflect the influence of ventricular assist devices on the heart rate. A regression pump model of HeartMate II LVAD (Thoratec, USA) is used as ventricular assist device. It describes as $Q_{VAD} = a(\Delta P)\omega + b(\Delta P)$, where the pump flow ($Q_{VAD}$, L/min) depends on the pressure head across the pump (ΔP, mmHg) and the pump speed (ω, rpm), and a-b are coefficients [11].

Results

Initial hemodynamics in the cardiovascular system with biventricular failure is shown at fig. 2. One can see that state characterized by elevated inlet pressures for the both ventricles and rightward shift in the pressure-volume curves due to the ventricular dilatation. The septum volume (V_{spt}) changes similar to the [14].

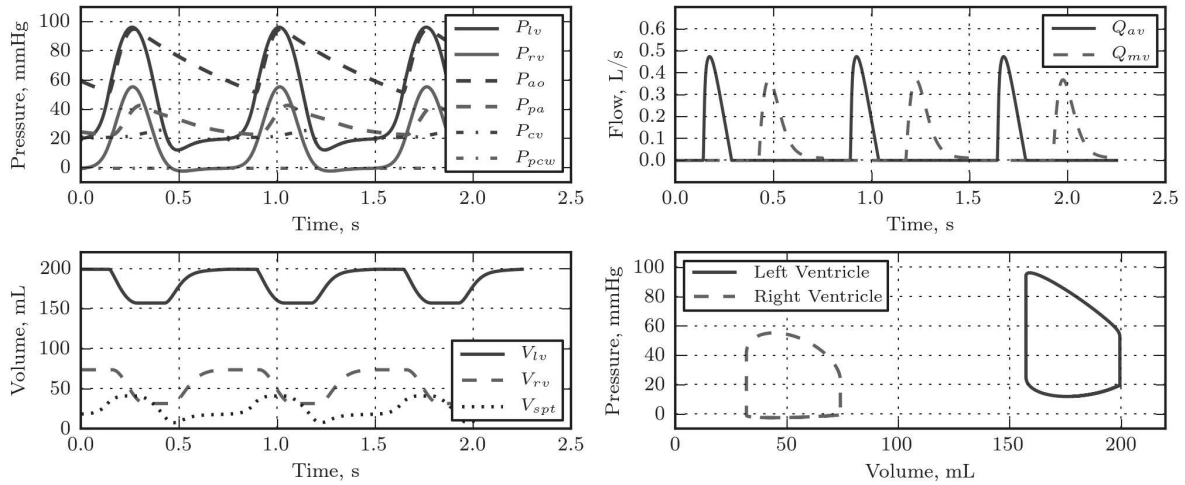

Fig. 2 Initial hemodynamics in the cardiovascular system; P_{ao} – aortic pressure, P_{pa} – pulmonary artery pressure, P_{cv} – central venous pressure, P_{pcw} – pulmonary capillary wedge pressure, Q_{av} and Q_{mv} – aortic valve and mitral valve flows, V_{lv} – left ventricular volume, V_{rv} – right ventricular volume, V_{spt} – septum volume.

The general hemodynamics in the cardiovascular system with two VADs as biventricular assist device is shown at fig. 3. The dashed lines represent initial values for the systemic circulation without ventricular assist devices. The speed of pumps increased simultaneously from 5600 rpm to 8800 rpm.

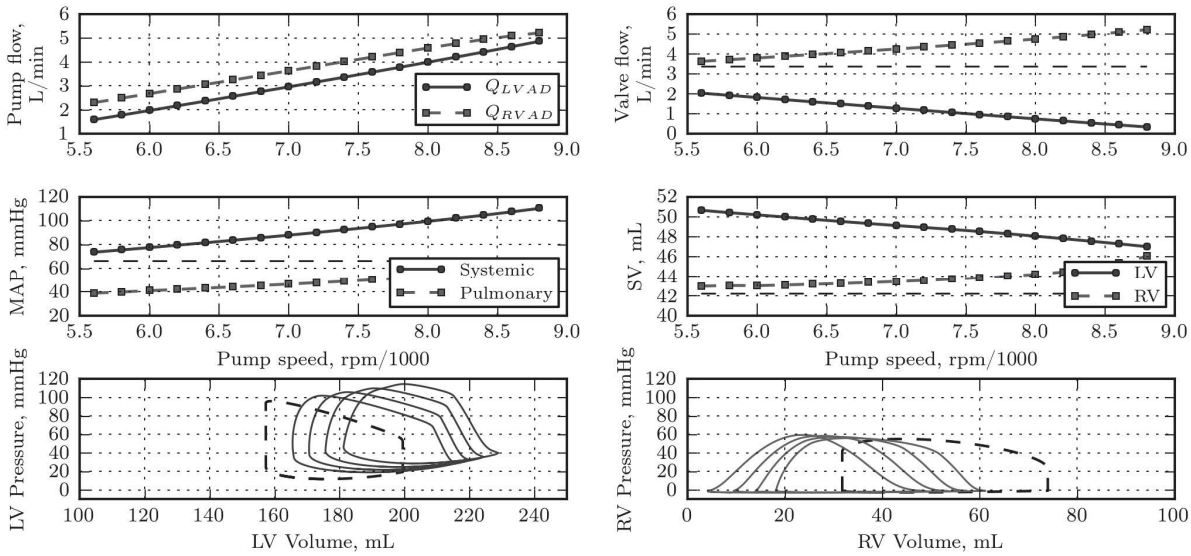

Fig. 3 Hemodynamics in the cardiovascular system with two ventricular assist devices; LVAD – left ventricular assist device, RVAD – right ventricular assist device, AV – aortic valve, MV – mitral valve, MAP – mean arterial pressure, SV – stroke volume.

Conclusion

This work proposes the mathematical model of the cardiovascular system with biventricular failure state. It based on the lumped-parameters models of circulatory system and heart model taking into account ventricular interaction. The proposed cardiovascular system model is tested with two VAD models as biventricular assist device and general hemodynamics is demonstrated for this case.

For the future addition of several features, such as atrium models and coronary circulation, is expected for more accurate evaluation of biventricular circulatory support.

References

[1]. Mancini D., Colombo P. C. Left Ventricular Assist Devices: A Rapidly Evolving Alternative to Transplant // Journal of the American College of Cardiology. 2015. Vol. 65, no. 23. P. 2542–2555.

[2]. Patel C. B., Cowger J. A., Zuckermann A. A contemporary review of mechanical circulatory support // The Journal of Heart and Lung Transplantation. 2014. Vol. 33, no. 7. P. 667–674.

[3]. Garbade J., Barten M. J., Bittner H. B., Mohr F.-W. Heart Transplantation and Left Ventricular Assist Device Therapy: Two Comparable Options in End-Stage Heart Failure? // Clinical Cardiology. 2013. Vol. 36, no. 7. P. 378–382.

[4]. Kirklin J. K., Naftel D. C., Kormos R. L. et al. Second INTERMACS Annual Report: More Than 1000 Primary LVAD Implants // The Journal of Heart and Lung Transplantation. 2010. Vol. 29, no. 1. P. 1–10.

[5]. Cleveland J. C., Naftel D. C., Reece T. B. et al. Survival after biventricular assist device implantation: An analysis of the Interagency Registry for Mechanically Assisted Circulatory Support database // The Journal of Heart and Lung Transplantation. 2011. Vol. 30, no. 8. P. 862–869.

[6]. Morgan J. A., Paone G., Nemeh H. W. et al. Impact of continuous-flow left ventricular assist device support on right ventricular function // The Journal of Heart and Lung Transplantation. 2013. Vol. 32, no. 4. P. 398–403.

[7]. Aissaoui N., Morshuis M., Schoenbrodt M. et al. Temporary right ventricular mechanical circulatory support for the management of right ventricular failure in critically ill patients // The Journal of Thoracic and Cardiovascular Surgery. 2013. Vol. 146, no. 1. P. 186–191.

[8]. Schmitto J. D., Burkhoff D., Avsar M. et al. Two axial-flow Synergy MicroPumps as a biventricular assist device in an ovine animal model // The Journal of Heart and Lung Transplantation. 2012. Vol. 31, no. 11. P. 1223–1229.

[9]. Krabatsch T., Potapov E., Stepanenko A. et al. Biventricular Circulatory Support With Two Miniaturized Implantable Assist Devices // Circulation. 2011. Vol. 124, no. 11. P. 179–186.
[10]. Saito S., Sakaguchi T., Miyagawa S. et al. Biventricular support using implantable continuous-flow ventricular assist devices // The Journal of Heart and Lung Transplantation. 2011. Vol. 30, no. 4. P. 475–478.
[11]. Cox L. G., Loerakker S., Rutten M. C. et al. A Mathematical Model to Evaluate Control Strategies for Mechanical Circulatory Support // Artificial Organs. 2009. Vol. 33, no. 8. P. 593–603.
[12]. Martina J. R., Bovendeerd P. H., de Jonge N. et al. Simulation of Changes in Myocardial Tissue Properties During Left Ventricular Assistance With a Rotary Blood Pump // Artificial Organs. 2013. Vol. 37, no. 6. P. 531–540.
[13]. Smith B. W., Chase J. G., Nokes R. I. et al. Minimal haemodynamic system model including ventricular interaction and valve dynamics // Medical Engineering & Physics. 2004. Vol. 26, no. 2. P. 131–139.
[14]. Smith B. W., Chase J. G., Shaw G. M., Nokes R. I. Simulating transient ventricular interaction using a minimal cardiovascular system model // Physiological Measurement. 2006. Vol. 27, no. 2. P. 165–180.
[15]. Drakos S. G., Janicki L., Horne B. D. et al. Risk Factors Predictive of Right Ventricular Failure After Left Ventricular Assist Device Implantation // The American Journal of Cardiology. 2010. Vol. 105, no. 7. P. 1030–1035.
[16]. Sun Y., Beshara M., Lucariello R. J., Chiaramida S. A. A comprehensive model for right-left heart interaction under the influence of pericardium and baroreflex // American Journal of Physiology. 1997. Vol. 272, no. 3. P. 1499–1515.

Diagnostics of the organism on biomedical signals based on reinforcement learning

N. Kalugina
South-West state University, Kursk, Russia

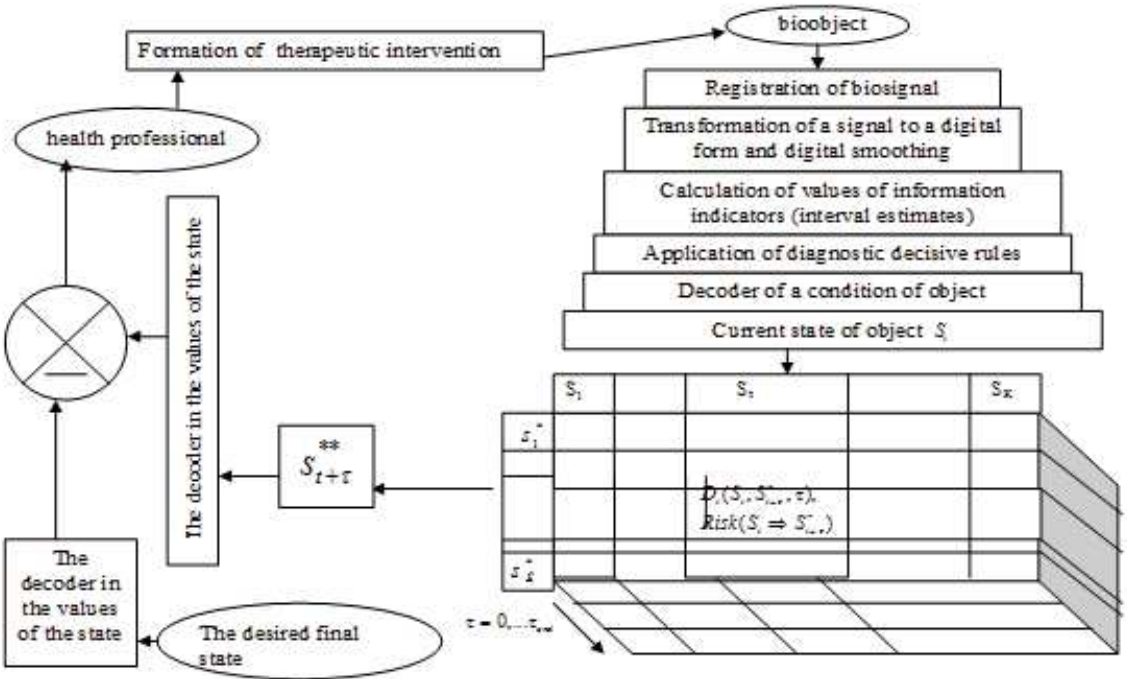

$\{TE_{t,\tau} = \{S_t, D_t(S_t, S^*_{t+\tau}\tau), Risk(S_t \overset{D_t}{\Rightarrow} S^*_{t+\tau})\}\}$ S_t

$D_t(S_t, S^*_{t+\tau}\tau)$ S_t

$S^*_{t+\tau}$ $Risk(S_t \overset{D_t}{\Rightarrow} S^*_{t+\tau})$ S_t

$S^*_{t+\tau}$ $D_t \equiv D_t(S_t, S^*_{t+\tau}\tau)$ D_t

$S^*_{t+\tau}$ S_t $S^*_{t+\tau}$ D_t

$TE_{t,\tau}$

$TE_{t,\tau}$

$S^*_{t+\tau}$

f_{min}, f_{max}

$[f_{min}, f_{max}]$ $[f_{max}, 2 \cdot f_{max} - f_{min}]$

$$\hat{y}(t) = F(\varphi_{t-1}(t-1), \varphi_{t-2}(t-2), \ldots, \varphi_{t-\tau_1}(t-\tau_1), \varphi_{t+1}(t+1), \varphi_{t+2}(t+2), \ldots, \varphi_{t+\tau_2}(t+\tau_2))$$

$\varphi_{t\mp i}(t \mp i)$ $(t \mp i)$

τ_1 τ_2

$$\hat{y}(t) = F(\varphi_{t-i1}(t-\tau_{i1}), \varphi_{t+i2}(t+\tau_{i2}))$$

τ_{i1} τ_{i2}

$y(t)$ $\hat{y}(t)$

$y(t)$

$$\tau_{i1} = \tau_{i2} = d$$

$$\varphi_{t\mp i}(t \mp i) = a_{t\mp i} + b_{t\mp i} \cdot y(t \mp i)$$

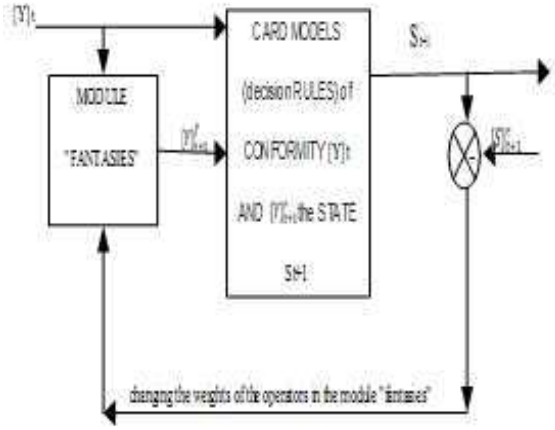

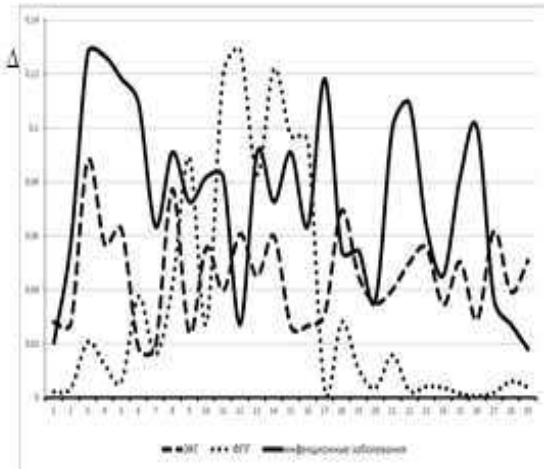

$\{Y\}_{t+1}^{f}$

$\{S\}_{t+1}^{Y}$

$F(y(t-1), y(t+1))$

$$y_{t+1} \approx 2 \cdot y_t - y_{t-1}$$

Study of the impact of the number and electrodes arrangement on the results of the reconstruction of an equivalent electric heart generator

M.N.Kramm[1], A.I.Chernikov[1]
1. National Research University «MPEI», Russia

Electrocardiographic signals of leads (the ECS - electrocardiosignals) are projections of electrical processes in the myocardium. We study inverse problem of electrocardiography – the reconstruction of equivalent electrical heart generator (EHG) [1], based on the records of the ECS on the surface of the human torso. Parameters of spatio-temporal EHG dynamics provide additional information for the diagnosis of ischemia and conductivity disturbances. In this study we examined the impact of the electrodes amount and method of placement of the electrodes on the results of the reconstruction of EHG. We examined the standard nine

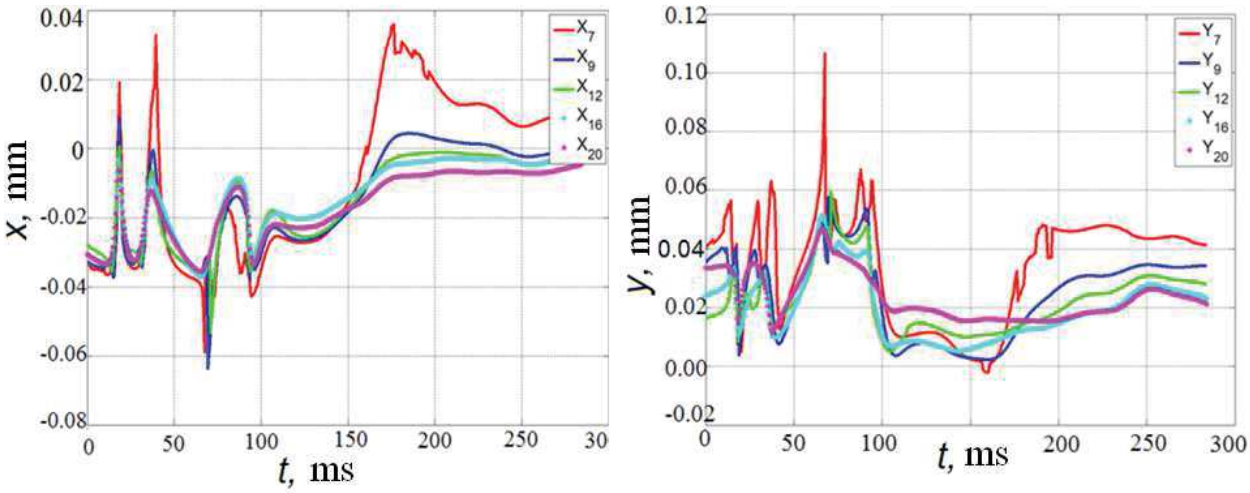

Fig. 1 Time dependencies of EHG coordinates x and y for a variety of selected electrode systems

References

[1] L.I.Titomir, V.G.Trunov, E.A.I.Aidu. – Moscow: Nauka, 2003. - 198 p.
[2] G.Zhikhareva, M.Kramm. *Reconstruction of current sources of heart in the ECG inverse problem*, (LAP LAMBERT Academic Publishing GmbH & Co. KG, Saarbrücken, 2012).


Value
5
4
3
3
4
5

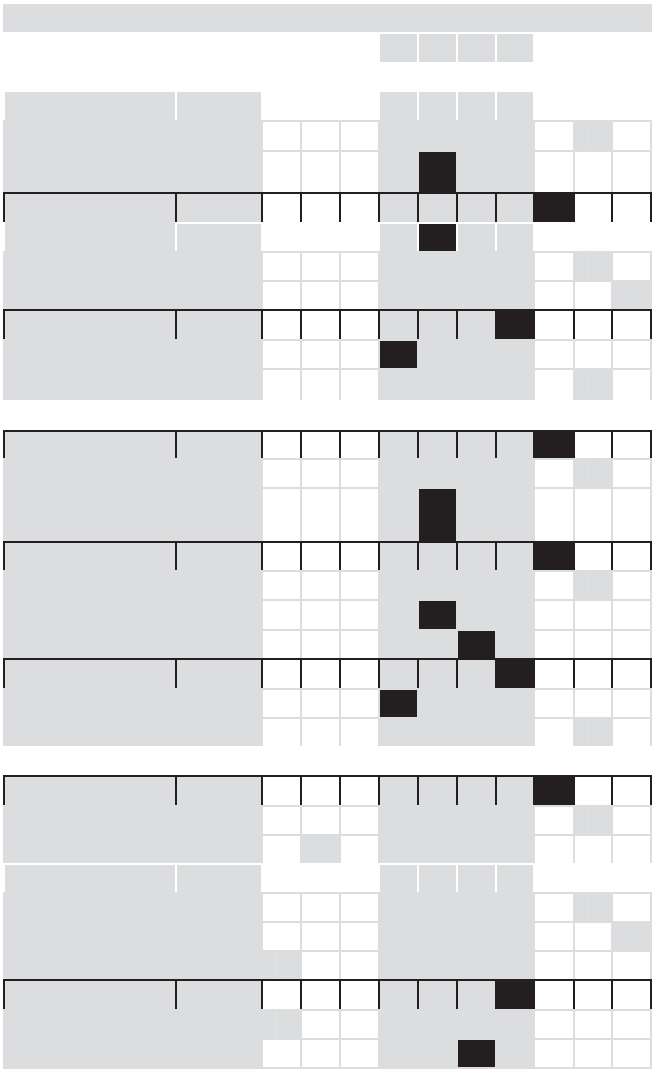

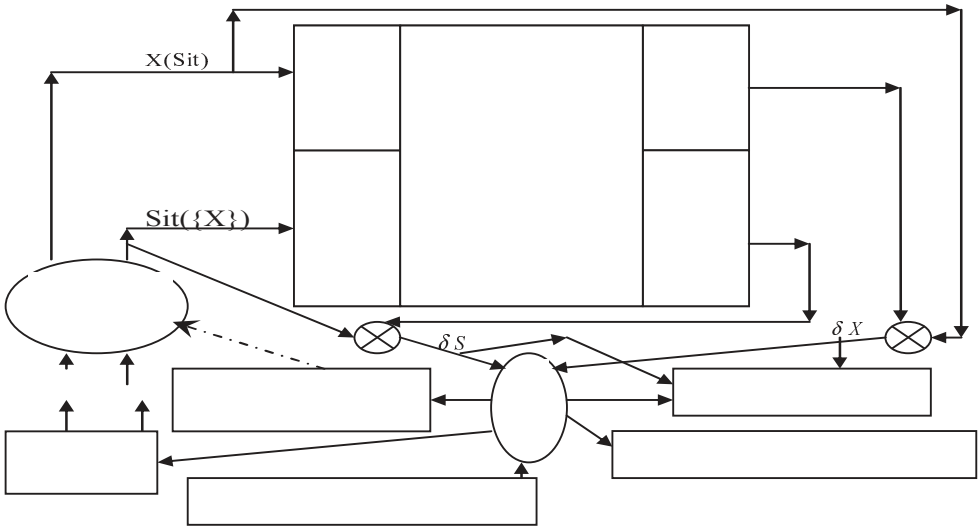
X(Sit)
Sit({X})
δ S
δ X

Where: X - the set of informative characteristics, S(X) - the patient' state obtained by decisive implication rules $X \Rightarrow S(X)$; X(S) – set of values X, necessary to identify a state S through implications $X \Rightarrow S(X)$; {X} is the set of values of informative features X of a virtual patient; Sit({X}) is the virtual patient's state according to the trainee's opinion; Sit – the state of the virtual patient (the situation); δX - mismatch between X(Sit) and X(S): δS - mismatch between Sit({X}) and S(X).

The educational process (according to the scheme) is carried out under the supervision of a teacher. On the basis of information about the action error of the trainee in response to the correct assessment of the situation (δX and δS) the teacher can influence the trainee by means of the corrective module of the acquired knowledge and skills, besides he estimates the degree of professionalism and forms the statistical reporting. When training active testing of the subject (trainee) is carried out by means of test generation. It consists of either the property values of the virtual patient's state X, or his hypothetical state Sit.

On the basis of the obtained information, his own experience and intellectual opportunities the subject (trainee) generates respectively Sit({X}) or X (Sit), which come into the AMESDD module. On the basis of direct and inverse decision rules AMESDD [4] either diagnoses a state of the virtual patient (forms S(X)) or detects the presence of his diagnostic informative features (X (S)). Mismatch assessment blocks between the correct ("reference") decisions (created by AMESDD) and those proposed by the trainees form the corresponding values of the error signals (δS and δX), according to which the TEACHER controls and manages training.

The error signals are calculated according to the formulas: $\delta X = \frac{\sum_{i=1}^{N}(true(x_i^*))}{N}$, $\delta S = \frac{\sum_{i=1}^{N}(true(x_i(S)))}{N}$

x_i x_i^* x_i

$true(x_i^*) = 1$ $x_i^* \subset (x_i \pm \Delta x_i)$

$true(x_i(S)) = 1$ $x_i(S) \subset (x_i \pm \Delta x_i)$

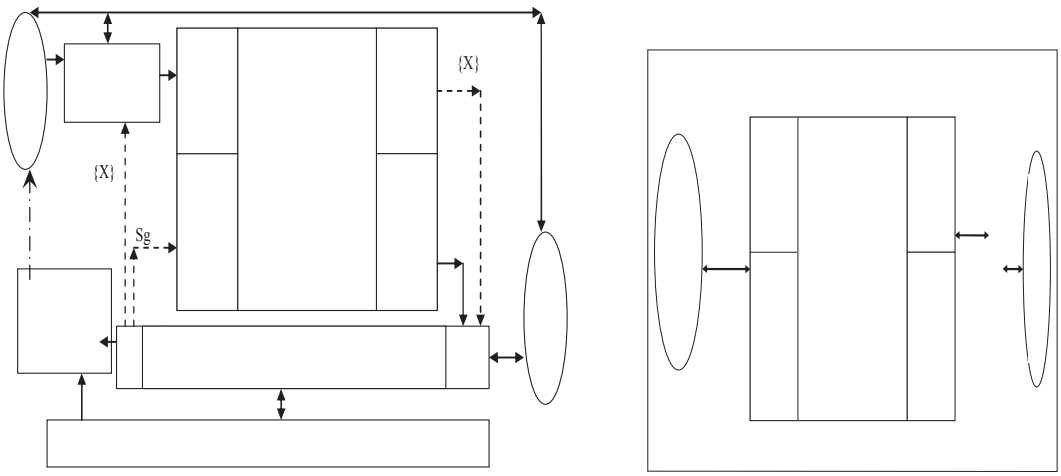

$B(\delta)$ $B(\delta)$

$Risk(B(\delta)$

$Rg_m, m = \overline{1, M_g}$ M_g

Rg_m

w_l

$OR_{g_m} = 1 - \prod_{j1=1}^{j_m}(1 - \frac{B_{m,j1}}{\max_{j1=1,\dots j_m}(B_{m,j1})}) \cdot Rg_m$ $Risk\left(B(\delta)\right) = 1 - \prod_{m=1}^{M_g}(1 - OR_{g_m})$

OR_{g_m}

Biomedical Engineering". 2008, Vol. 42. № 6. pp. 317-319.
[12] M. V. Artemenko, I. I. Dobrovolsky, "Automated decision support based on the application of direct and inverse decision rules //Fundamental and applied studies in the modern world", "Proceedings of the XII International scientific and practical conference 15 may 2015", Vol. 1, pp. 78-83
[13] M. V. Artemenko, I. I. Dobrovolsky, V. N. Mishustin, "Informational and analytical support of the automated classification on the basis of direct and inverse decision rules on the example of prediction of thromboembolic disease", " Modern high technologies",2015,N12-2, pp. 199-205; URL: http://www.top-technologies.ru/ru/article/view?id=35237

The complex of decision support algorithms when selecting a treatment strategy for patients with serious liver damage

E. Semenova

Saint-Petersburg state electrotechnical university "LETI"n. a. V.I. Ulyanov (Lenin), Saint-Petersburg

Applicability

Nowadays the information technologies are of a great concern in the modern medicine, allowing to get high quality person diagnostic information. A must of such technologies, which get opportunities in the operational efficiency of making decisions when setting a diagnosis and a further patient treatment, is arising in case of a medical treatment of patients with a damage of abdominal cavity organs, a liver in particularly.

For increasing of the operational efficiency in getting an emergency surgery response for patients with a serious liver damage, the creation of surgeon decision support system (DSS) has been proposed.

The emergency surgeon decision support system for a treatment of patients with serious liver damage

The emergency surgeon decision support system is a computer-based system which provides the emergency surgeon information support when making decisions for selecting the treatment strategy and extra surgeon approach.

The surgeon DSS consists of five modules: the user interface, the data accumulation, selecting of a treatment strategy, determination of extra surgeon approach, information analysis.

The main modules are: the Module of selecting of a treatment strategy and the Module of determination of extra surgeon approach, which must include the group of **Decision Support** algorithms.

The methodology for information content of the emergency surgeon DSS has been developed for creating the group of the emergency surgeon decision support algorithms when selecting a treatment strategy based on the analytic hierarchy process.

The methodology for information content of the emergency surgeon DSS when selecting a treatment strategy for patients with a liverdamage

The methodology for information content of the emergency surgeon DSS when selecting a treatment strategy for patients includes the following stages:

Stage 1. Expert review of factors to consider when selecting a treatment strategy for patients.

For finding out sets of factors to consider when selecting a treatment strategy for patients, the methodology of extraction of medical knowledges was developed, which consists of 3 stages: finding out the main factors to consider when selecting a treatment strategy for patients, a questionnaire survey to explore and specify, and an interview to more detailed learning of each factor.

Fig 1-3 shows the developed complex of the hierarchically structured factors models to consider when selecting a treatment strategy for patients.

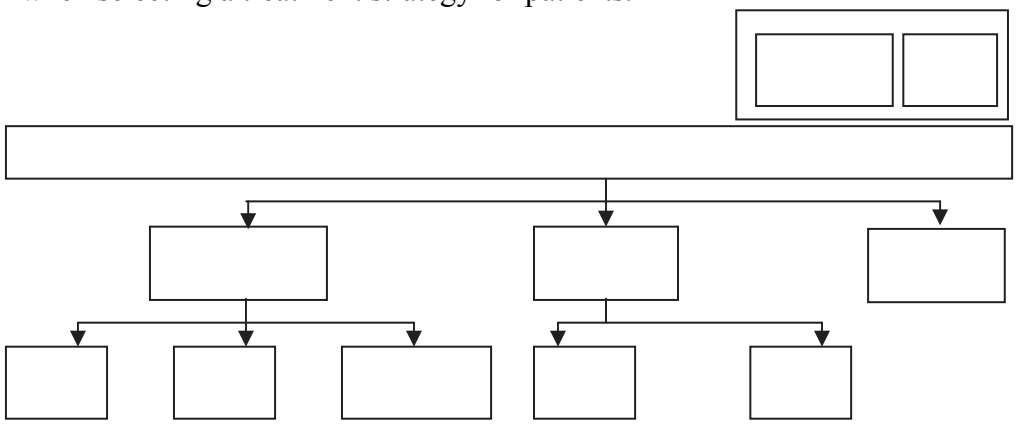

Fig. 1 The hierarchically structured factors models to consider on the need for applying the “Damage control” method. Keys: K_{d11} – hemodynamic blood parameters, K_{d12} – level of hemorrhage, K_{d13} – seriousness of injury, K_{d111} – systolic blood pressure, K_{d112} – pulsus, K_{d113} – rate of pulsus change, K_{d121} – hemoglobin, K_{d121} – hematocrit, K_{d1MPI} – coefficients, characterizing organization capability of medical preventive institution, K_{d1S} – coefficients, characterizing the surgeon professional competence.

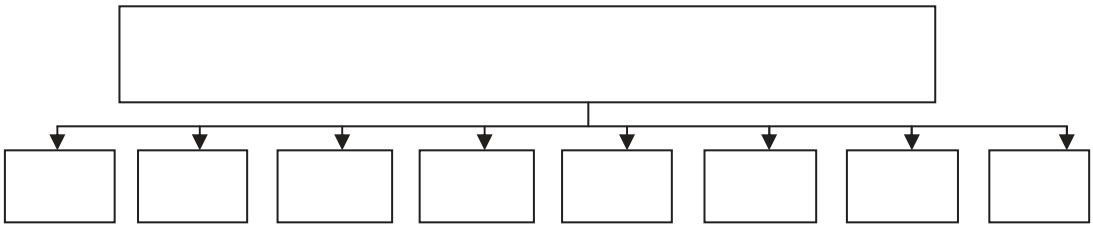

Fig. 2 The hierarchically structured factors models to consider when making decision about the necessity for providing an extra surgeon approach. Keys: K_{d21}– I liver segment, K_{d22} – II liver segment, K_{d23} – III liver segment, K_{d24} – IV liver segment, K_{d25} – V liver segment, K_{d26}– VI liver segment, K_{d27} – VII liver segment, K_{d28} – VIII liver segment

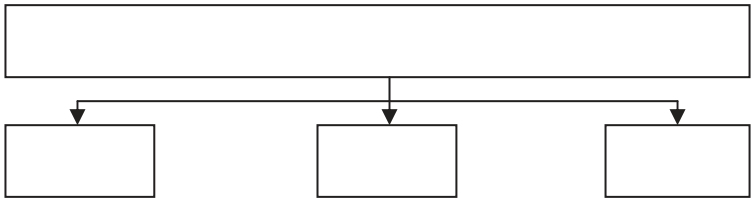

Fig. 3 The hierarchically structured factors models to consider when choosing the most suitable surgical approach.
Keys: K_{d31} – 3 degree of liver damage, K_{d32} – 4 degree of liver damage, K_{d33} – 5 degree of liver damage

By applying the paired comparison method, the importance of these factors was determined.

Stage II. The professional competence evaluation of each expert.

Nowadays there are a lot of methods for the experts professional competence evaluation: the self-evaluation according to objective factors, the mutual evaluation, the evaluation by independent experts, so on. The most suitable method is the experts professional competence evaluation using the independent evaluation method. In this research the analytic hierarchy process was applied for these purposes.

Fig. 4 shows the developed complex of hierarchically structured factors models to consider for the experts professional competence evaluation. Using the paired comparison method, the importance of these factors was determined, on the basis of which the algorithms of experts professional competence evaluation was made.

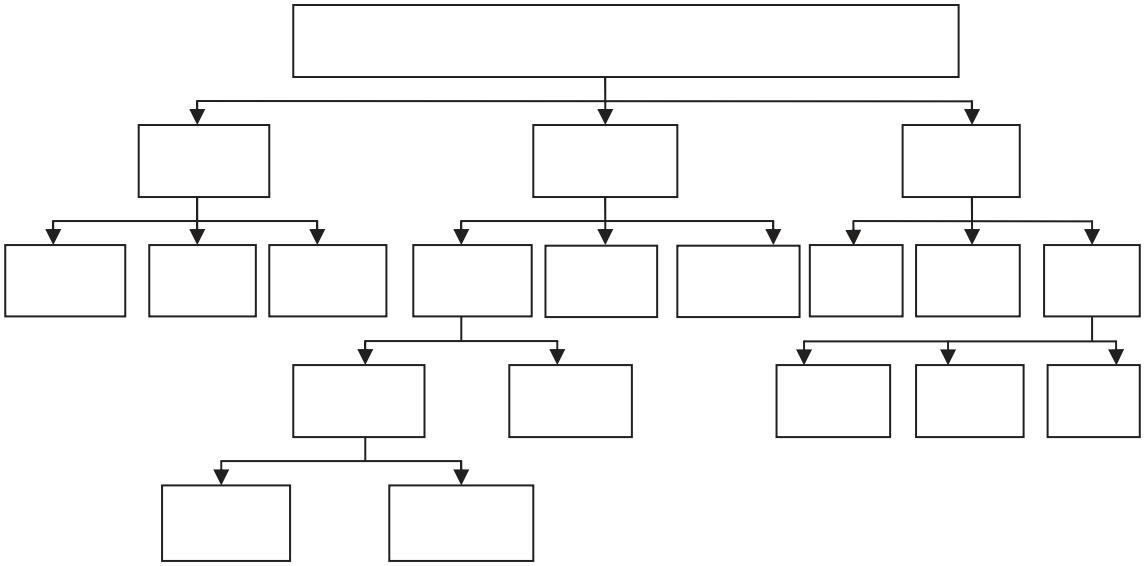

Fig. 4 The hierarchically structured factors models to consider for experts professional competence evaluation.

Keys: K_{e1} – the experience, K_{e2} – previous done emergency surgeries, K_{e3} – the academic work for the last 5 years, K_{e11} – years of experience in the emergency surgery, K_{e12} – total years of experience in the surgery K_{e13} – rank, K_{e21} – the quality of done surgeries for the last 3 years, K_{e22} – the quantity of done surgeries for the whole surgical practice, K_{e23} – the quantity of done surgeries for the last 3 years, K_{e31} – the academic status, K_{e32} – the teaching and guiding, K_{e33} – the results of the academic work, K_{e211} – the treatment results, K_{e212} – the postoperative course, K_{e331} – the scientific efforts, K_{e332} – the intellectual property, K_{e333} – honorary degrees, prizes, awards, K_{e2111} – short-term, K_{e2112} – long-term

Stage III. The integration of experts opinions on the basis of their competence.

The integration of experts opinions on the basis of their competence was carried out, in virtue of such integration the group of decision support algorithms when selecting a treatment strategy for patients was produced.

Conclusion

The implementation the surgeon DSS in the form of the application program “SLIDSS”, representing the developed group of decision support algorithms when selecting a treatment strategy for patients, can increase the operational efficiency in getting an emergency surgery response for patients with a serious liver damage.

SECTION 4

BIOMEDICAL ENGINEERING AND BIOMATERIALS

"Symbiotic" hemofiltration: new principle and hardware system for chronic renal failure compensation

Yumatov E.A.[1,2], Glazachev O.S.[2], Dudnik E.N.[2], Pertsov S.S.[1] Raevskiy V.V.[3]

[1] P.K. Anokhin Research Institute of Normal Physiology, Russian Academy of Sciences. Moscow, Russian Federation. 125009, Russian Federation, Moscow, ul. Mohovaya, 11.
[2] I.M. Sechenov First Moscow State Medical University. Moscow, Russian Federation. 119991, Russian Federation, Moscow, ul. Trubetskaya 8, bld.2.
[3] Research Institute of Higher Nervous Activity and Neurophysiology, Russian Academy of Sciences.
Moscow, Russian Federation. 117485, Russian Federation, Moscow, ul. Butlerova 5a.

Clinically proved methods of chronic renal failure (CRF) compensation based on hemodialysis, hemofiltration, kidney transplantation are widely used in medical practice, but they are sometimes (15-25%) complicated by possible water and electrolyte dysbalance in cronically treated patients [1-5].

Well known nowadays techniques of hemodialysis and hemofiltration can not replace completely renal excretory function, which carries out all its activities in natural conditions and is regulated physiologically. Previously we proposed «Method of chronic renal failure (CRF) symbiotic "compensation in humans» [6, 7] is based on the use of natural physiological function of healthy human kidney for CRF patient's blood purification from waste substances subjected to be excreted. CRF patients blood purification from excessive metabolites is based on the periodic temporary association of a healthy person's and CRF patient's circulations. This method has certain limitations associated with the necessity of a careful selection of partners (donor and recipient) with an absolute blood compatibility.

We have developed a completely new method and apparatus for CRF patient "symbiotic" compensation based on hemofiltration and natural physiological functions of healthy human kidneys, but exclude mixing partners circulating blood [8, 9].

"Symbiotic" hemofiltration is based on mutual exchange of equivalent blood ultrafiltrate of healthy person and CRF patient who need blood purification from metabolites. At the same time donors and recipients blood circulatory systems are divided by hemofilter and therefore there is no blood mixing of the patient and healthy person.

During CRF patients blood purification from metabolic products separated hemofiltration of the patient's and a healthy person's blood plasma takes place in equal volumes. In this case the patient's blood ultrafiltrate flows into the bloodstream of a healthy person, and also the blood ultrafiltrate from a healthy person in the same extent enters the CRF parient's circulation. Remaining (after hemofiltration) patient's and healthy donor's blood components (formed blood elements) are returning simultaneously in their bloods circulations respectively (**Fig. 1**).

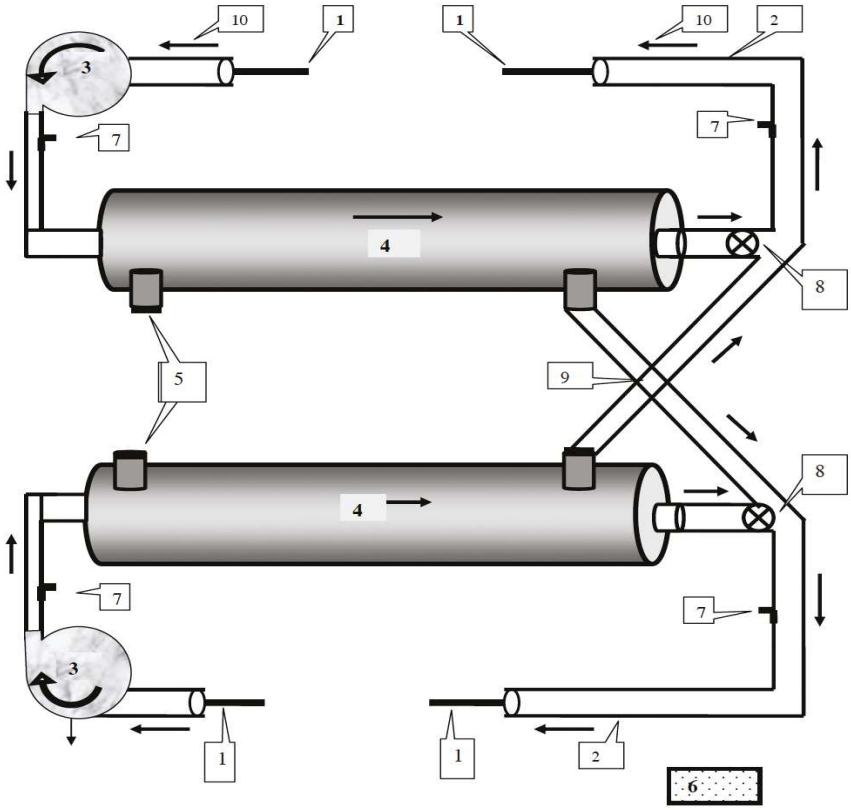

Fig. 1. The Device for "symbiotic" hemofiltration, which consists of two separate circuits for healthy and sick person blood circulation. Legend: 1 - catheters, 2 - Plastic pipes, 3 - blood perfusion pumps, 4 - hemofilters, 5 - plugs, 6 - electronic operation and control unit, 7 - blood pressure sensors, 8 - valves, 9 - exit of the ultrafiltrate from hemofilter, 10 - arrow indicating the direction of blood and fluids movement.

The hardware complex for "symbiotic" hemofiltration includes: blood pumps, which are used in hemodiafiltration [10], hemofilters [11], the electronic operation and control unit, pressure sensors, plastic catheter tube [7, 8].

Currently, many well-known companies produce hemofilters with different characteristics [11]. Filtration characteristics of hemofilter membranes related to «high-flux» droop, are very close to the parameters of glomerular filtration rate of a healthy person's kidneys. Mentioned hemodiafilters are designed for high-volume hemodiafiltration (HDF) with maximum pressure of 500 mm Hg and replacement volume of more than 15 liters per 1 procedure. Based on the manufacturer's data, it is possible to define the hemofilter's functional capacities and to choose the best hemofilter for procedures of "symbiotic" hemofiltration.

Calculated data for blood plasma clearance from urea and creatinine show high efficiency of "symbiotic" hemofiltration. Scheme 2 shows calculated in model dynamics of urea concentrations changes in the blood of CRF patient and healthy person during a "symbiotic" hemofiltration. At the initial period of "symbiotic" hemofiltration procedure the concentration of uremic substances in healthy human blood, due to the receipt of metabolites from the patient's blood slightly increases. Kidneys of a healthy person will «respond» by increasing of their functional capacities to remove excessive wastes. With the increase of uremic metabolites in healthy person's blood plasma due to more intense glomelural clearance their concentrations will increase in primary urine and there will be an increase of their

excretion with the final urine. Subsequently, fewer all uremic substances enter into healthy person's blood due to lowering of their concentration in CRF patient 's blood (**Fig**. 2).

Entering into healthy person's blood of patient's urea and other nitrogenous metabolic products will not lead to an increase in their content in blood plasma, and the procedure of partners filtered blood plasma interchange does not cause any complications in healthy person.

Applied result of "symbiotic" blood plasma clearance is to reduce the level of nitrogen-containing metabolites in CRF patient's blood plasma due to more intensive physiological function of healthy partner's kidneys.

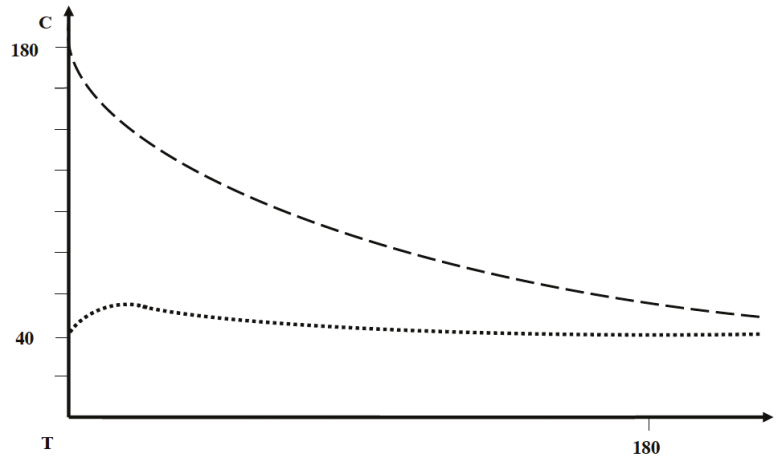

Fig. 2. Urea concentration changes in healthy person's (lover curve) and in CRF patient's (upper curve) blood plasma during the procedure of "symbiotic" hemofiltration. Legend: ordinate: C - the concentration of urea in the blood plasma in mg%, one notch - 20 mg%; abscissa axis: T - time (in min).

Advantages of "symbiotic" hemofiltration over hemodialysis and hemofiltration.

Fundamentally important advantage of "symbiotic" hemofiltration is that the CRF patient's blood plasma clearance from uremic metabolites is produced due to the natural physiological functions of healthy human kidneys.

1. The method is more physiological than hemodiafiltration. As a result of continuous mutual hemofiltration procedure kidneys of healthy person effectively purify CRF patient's blood plasma from uremic substances.

2. The method is less expensive, does not require expensive equipment and complex schemes of hemofiltration. There is no need to prepare and obtain a special dialysis fluid, in performing of predilution and postdilution (common practice in hemodialysis).

3. In contrast to hemofiltration, whereby it is difficult to provide an equivalent ultrafiltrate volume replacement, the method of "symbiotic" hemofiltration provides equal "cross-" ultrafiltrate exchange that maintains a constant circulating blood volume in partners circulation.

4. Due to the natural physiological function of healthy person's kidneys, used as a basis for patient's blood plasma clearance, the potential for complications development arising from hemodiafilration, such as acid-base dysbalance, dehydration and so forth, is reduced.

Thus, "Symbiotic" hemofiltration is highly effective method of CRF patients blood plasma physiological purification from uremic metabolites. Nevertheless each patient and doctor have a choice – what to prefer under specific clinical settings and individual patient's comorbidities and conditions: hemodiafiltration or "symbiotic" hemofiltration for blood plasma purging from metabolites in case of decompensated chronic renal failure.

References
[1] Henderson L.W., Colton P.K., Ford C. Kinetics of hemodiafiltration. II Clinical characterization of a new blood cleansing modality. J. Lab. Clin. Med. 1975, 85, p. 372.
[2] Smirnov A.V. Renal replacement therapy. Nephrology, 2011; 15(1): 33-46. (Rus)
[3] Handbook of Dialysis. Eds J.T. Daugirdas, T.S. Ing. - 2nd ed. Little, Broun, 1994.
[4] Fomin V.V., Paltseva E.M., Kozlovskaya L.V., Mukhin N.A. Nephrology. Emergency conditions. Edited by N.A. Mukhin. 2010. (Rus)
[5] Stetsyuk E.A. Fundamentals of hemodialysis. Ed. Prof. E.B. Mazo. Moscow: GEOTAR-Med, 2001. (Rus)
[6] Yumatov E.A., Sudakov K.V. Symbiotic "method of chronic renal failure compensating in humans. J. Clinical Nephrology. 2012; 5-6: 68-70. (Rus)
[7] Yumatov E.A., Sudakov K.V. Method of chronic renal failure (CRF) "symbiotic" compensation in humans. RF Patent № 2506956. 2014. (Rus)
[8] Yumatov E.A., Glazachev O.S., Dudnik E.N., Pertsov S.S., Rayevsky V.V. The method and the device of "symbiotic" hemofiltration for chronic renal failure compensation. Inventions and Utility Models: Rospatent Official Bulletin. 2015; 25. (Rus)
[9] Yumatov E.A., Glazachev O.S., Dudnik E.N., Pertsov S.S., Rayevsky V.V. "Symbiotic" hemofiltration for chronic renal failure compensation. Research and Practice in Medicine. 2015; 2 (3): 69-75. (Rus)
[10] The pump roller, for perfusion. Model JHBP-2000 A / B. http://www.bbmed.ru/ji-hua/blood-pump.html
[11] Product hemofilters: Catalogue. http://www.tehnomedservis.ru/katalog-tovarov/dializ.html http://www.fresenius.ru/files/DialyserCatalog.pdf http://www.tehnomedservis.ru/katalog-tovarov/dializ/26-sureflux-dializatori.html

Assistive control of extracorporeal oxygenation systems

M. Walter[1], C. Brendle[1], J. Kühn[2], T. Janisch[3], R.Kopp[3], A.Stollenwerk[3], S. Leonhardt[1]

1. Chair for Medical Information Technology, RWTH Aachen University, D-52074 Aachen, Germany

2. Informatik 11 - Embedded Software, RWTH Aachen University, D-52074 Aachen, Germany

3. Department of Intensive Care and Intermediate Care, RWTH Aachen University Hospital, D- 52074 Aachen, Germany

Motivation:

In cases of severe lung failure and lung injury conventional artificial ventilation may not be sufficient in maintaining gas transfer. Even when applying modern therapy guidelines in protective lung ventilation required pressure levels may lead to even increased lung damage and subsequent loss of lung areas [1, 2]. One option to break this vicious circle and to maintain sufficient gas transfer is to support gas transfer by extracorporeal circulation. As a consequence it is now possible to relieve ventilation to healthier pressure levels [3]. In the past this treatment option was limited to emergency cases as complication rate was rather high and the required technical, medical and operational skill to operate such devices challenging. With the advent of improved oxygenator and pump technology many of the mentioned problems are relieved. However, the scenario of operating such complicated life saving machines 24/7 remains critical. In the operating theatre supervision and optimal setting of an extracorporeal circulation requires permanent attention of a specially trained cardiovascular

perfusionist/technician. When transferred to the intensive care unit (ICU) the operating scenario (see Fig. 1 left) changes significantly and machine operation is reduced to intermittent/alarm driven supervision and control. In order to provide similar levels of control performance, reliability and safety, ICU devices should provide advanced autonomous functions. In our interdisciplinary project "ECLA-VENT" we developed patient oriented control strategies to address this issue.

Methods:

We developed a full electronic extracorporeal gas exchange system based on standard components enhanced with extended patient monitoring (see Fig. 1 right). Our proposed extracorporeal lung assistance (ECLA) consists of two femoral venous cannulaes where venous blood is collected, a centrifugal blood pump (DP3; Medos Medizintechnik AG; Heilbronn; Germany), an oxygenator (Hilite® LT 7000; Medos Medizintechnik AG) as well as a jugular vein cannula for blood reinfusion. A MicroAutoBox (dSPACE GmbH; Paderborn; Germany) is used for central processing and control prototyping. Actuators are a self designed electronic gas blender and a self designed pump control unit. Sensor components are pressure sensors (at pump inlet, pre oxygenator and return cannula), online blood gas measuring system (CDI® Blood Parameter Monitoring System 500, pre and post oxygenator; Terumo Cardiovascular Systems Corporation; Ann Arbor; Michigan; USA), a blood flow meter in the external circuit (HT110 flow meter and H9XL flow probe, Transonic Systems Inc., Ithaca, USA), patient gas monitors (Dräger Medical GmbH, Lübeck; Germany) for gas analysis pre- and post- oxygenator, as well as a fully equipped patient monitor (A/S3 Datex Ohmeda Inc.; Madison; Wisconsin; USA) including ventilator gas monitoring and continuous cardiac output monitor. Additionally, we use a Ventilator (Servo Ventilator 300; Siemens-Elema AB; Solna; Sweden) which is modified so we can set user input settings (e.g. pressures, tidal volume, respiratory rate or FIO2) electronically. Each actuator and sensor component is connected to the CAN based data bus via microcontroller based network nodes [I11 et al.], which implement data protocol translation.

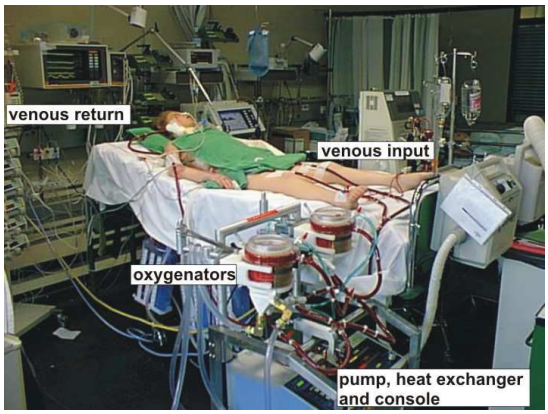

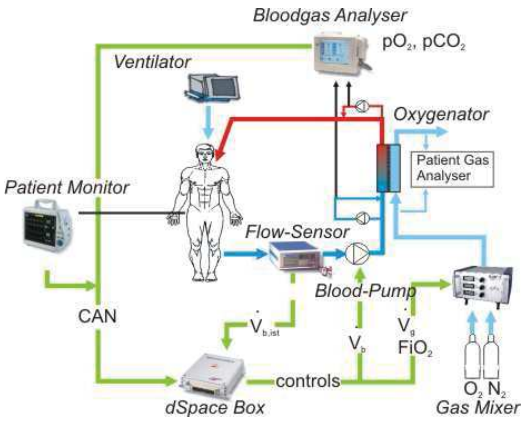

From a technical viewpoint both ventilation and extracorporeal gas exchange act on the same target value (blood gas concentrations) inside the patient body. Thus, from a treatment point of view the control strategy has to solve a MIMO control problem with constraints regarding actuators. In consequence, the following list provides the main goals of the automation system:

- Provide sufficient amount of gas exchange of O_2
- Control of arterial oxygen levels within physiological limits

- Provide sufficient amount of gas exchange of CO_2
- Control of venous CO_2 levels
- Operate ventilation at least invasive levels
- Operate extracorporeal circulation at least invasive levels maintaining optimal operating conditions

This can be achieved by a cascaded control structure as shown in Fig. 2:

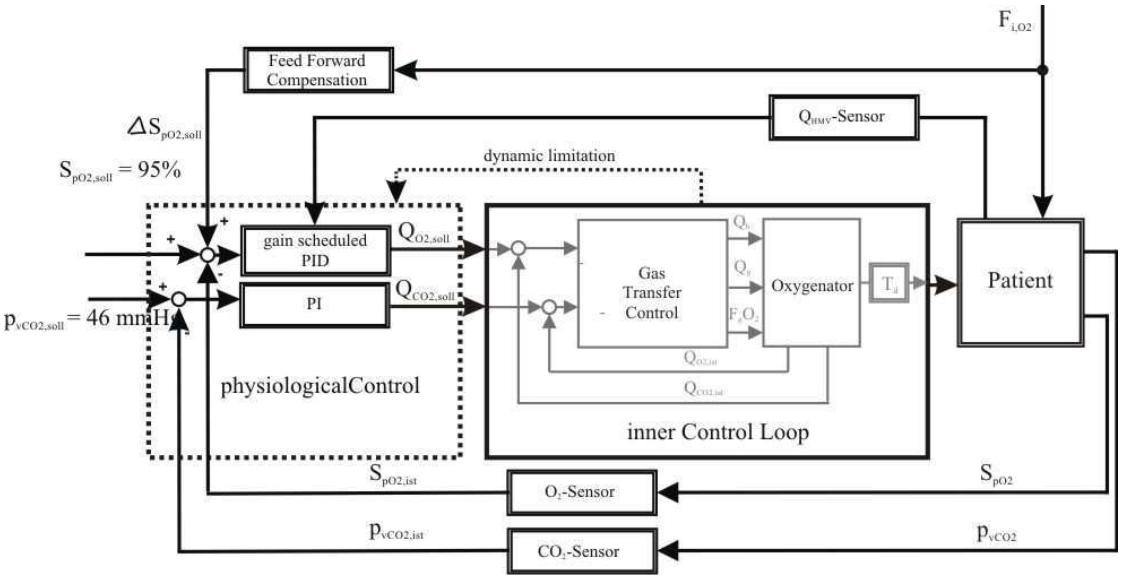

Fig. 2 Cascaded control scheme of an automation system for control of extracorporeal circulation and artificial ventilation. Adapted from [4]

An inner loop controls gas exchange in the oxygenator independently for O_2 and CO_2. This enables a decoupling of the control quantities and independent control. It also compensates for changes in gas exchange capacity of the oxygenator over time. Ventilation parameters are set in an independent feed forward concept. Here we implemented an automatic maximum compliance search strategy to optimize the point of ventilation. All other parameters were set according to the protective ventilation scheme of the ARDS-Net protocol [2]. Physiological target values of peripheral oxygen saturation S_pO_2 and venous CO_2 partial pressure P_vCO_2 are controlled using the outer control loop manipulating oxygenator gas transfer as well as ventilator oxygen fraction (see Fig. 2). One safety feature is included for oxygen transfer. In case of a sudden life threatening hypoxic crisis the control is reconfigured to create maximum O_2 gas transfer until a safe oxygen saturation is reached. Subsequently, the autonomous system switches back to the optimal control maintainig the new safe state.

Results:

To validate the designed control structure, we performed a series of animal experiments (55-75 kg domestic pigs , approved by LANUV NRW; Recklinghausen; Germany 84-02.04.2014.A113;). After instrumentation and connection to the extracorporeal circuit, varying degrees of lung failure were introduced by lung lavage with saline solution. In all cases moderate to severe ARDS could be created (P_aO_2 / F_IO_2 < 200 mmHg). After steady state at the initial operating point, control was activated and several setpoints for S_pO_2 and P_vCO_2 were selected. Intermittent identification of lung parameters and operating point search optimized ventilation. Figure 3 shows results for both S_pO_2 and P_vCO_2 control during a section of the trial. As can be seen, target values could be established and maintained as required. Under normal operating conditions the controller was able to reach the desired

physiological target concentrations within 20 Minutes for CO_2 and 3-5 Minutes for O_2. Even with extreme disturbances hypoxic episodes with S_pO_2<85 could be prevented. Only in cases where venous wall suction at the inlet cannulae prevented further increase of blood flow control targets could not be met (not shown).

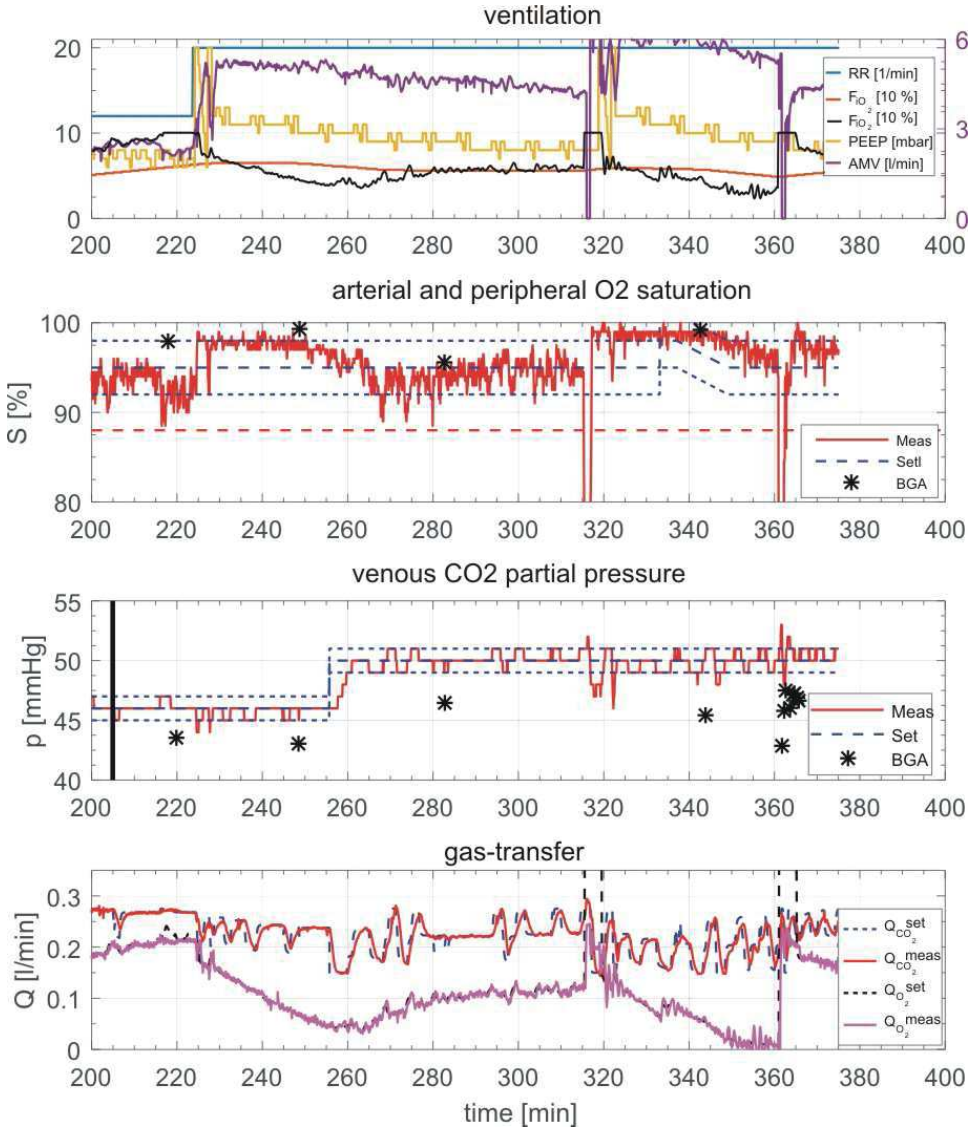

Fig. 3 Target control of S_pO_2 and P_vCO_2 during an animal trial, adapted from [4]

Conclusions:

Our experiments could prove efficacy and performance of the designed control system. Combined with advanced safety functions (not presented here) we show the feasibility of next generation ECLA devices enabling routine application in demanding hospital situations.

References

[1] V. Marco Ranieri et.al. Acute respiratory distress syndrome: The Berlin definition. Journal of the American Medical Association, 307(23):2526–2533, 2012.

[2] Roy G. Brower, et. al. Ventilation with lower tidal volumes as compared with traditional tidal volumes for acute lung injury and the acute respiratory distress syndrome. the acute respiratory distress syndrome network. New England Journal of Medicine, 342(18):1301–1308, 2000.

[3] Tài Pham, et al.. Extracorporeal membrane oxygenation for pandemic influenza A(H1N1)-induced acute respiratory distress syndrome: a cohort study and propensity-matched analysis. American journal of respiratory and critical care medicine, 187(3):276–285, 2013.

[4] Thorsten Mülders, Robuste Mehrgrößenregelung des Patienten für die Therapie mit der extrakorporalen Membranoxygenierung, Master Thesis, RWTH Aachen, 2015

A new device for the rapid assessment of the cardiovascular system

V.V.Shapovalov,

[2] Shapovalov, Fuzzy method for constructing decision rules in the diagnosis of screening systems, "Medical electronics», №1, 2013, s.64-66.

Sensitivity analysis for dual belt electrical impedance tomography

J. Orschulik, ***T. Menden***, ***S. Leonhardt***, ***D. Teichmann***

Philips Chair for Medical Information Technology, Helmholtz-Institute for Biomedical Engineering, RWTH Aachen University, Pauwelsstr. 20, D-52074 Aachen, Germany

Introduction

Electrical Impedance Tomography (EIT) is a biomedical imaging technique. By injecting non-harming currents into the body and measuring voltages at its surface, EIT can visualize impedance changes inside the body. Typically, EIT is used in the field of ventilation monitoring to detect pathological conditions such as atelectasis. Additionally, in mechanically ventilated patients, EIT is can visualize the impact of changing ventilation parameters as it is real time capable. Besides ventilation monitoring, cardiac monitoring is a promising field for EIT. Unfortunately, the separation of cardiac and breathing activity is not straightforward, as the impedance changes obtained from heart activity and perfusion are roughly one magnitude smaller than impedance changes from ventilation activity [1]. Thus, simple filtering in the frequency domain fails due to ventilation harmonics, especially in mechanically ventilated patients.

Current EIT systems use 16 or 32 electrodes placed in a single sectional plane. Additionally, these systems use adjacent injection and measurement patterns, which leads to a high current density close to the body surface. It has been shown before, that the sensitivity to central areas can be improved when using different patterns [2]. Additionally, we demonstrated in an experimental study that using two electrode belts instead of one increases the power of the cardiac signal [3]. In this paper, we quantify this increase and show that dual belt EIT is a promising approach to increase the sensitivity of EIT measurements in the center of the body.

Materials and Methods

The methods that are used in this paper to evaluate different injection and measurement patterns are based on the electrical sensitivity. In general, when using two injection and two measurement electrodes, the measured impedance can be calculated as

$$\underline{Z} = \int_{\nu} \frac{1}{\sigma(\nu)} \vec{J}_{\mathrm{LE}}(\nu) \cdot \vec{J}_{\mathrm{LI}}(\nu) \mathrm{d}\nu ,$$

where $\sigma(\nu)$ is the local electrical conductivity and $\vec{J}_{\mathrm{LE}}(\nu)$ and $\vec{J}_{\mathrm{LE}}(\nu)$ are the normalized current density distribution of the current injecting and voltage measuring electrodes. The sensitivity $S_i(\nu)$ for a given impedance measurement i is then defined as the dot product of the two current density distributions:

$$S_i(\nu) = \vec{J}_{i,\mathrm{LE}}(\nu) \cdot \vec{J}_{i,\mathrm{LI}}(\nu) \text{ [4].}$$

With this definition, it is possible to quantify the contribution from each volume element $\mathrm{d}\nu$ on the measured impedance $\underline{Z}$. Conductivity changes in areas with a high sensitivity will

be strongly visible in the measured impedance, whereas changes in areas with a zero sensitivity do not have any impact on the result. Fig. 1, left, demonstrates a sensitivity distribution in a sectional plane. In order to evaluate different injection and measurement configurations in terms of their capability to monitor cardiac activity, we investigate their sensitivity distribution in the heart region.

In EIT, we have multiple impedance measurements which are used to reconstruct an image. In 16 electrode systems, a total of 208 impedance measurements are performed per frame, while 32 electrode systems provide 928 impedance measurements per frame. Thus, we do not evaluate single impedance measurements but normalize the sensitivity on the total absolute sensitivity of an EIT frame:

$$S_{i,\mathrm{norm}}(v) = \frac{|S_i(v)|}{\sum_i \sum_v |S_i(v)|}.$$

The normalization factor $\sum_i \sum_v |S_i(v)|$ describes the total absolute sensitivity for a given EIT setup.

As we aim to evaluate the configurations in the heart region, we define a region of interest (ROI), as shown in Fig. 2. The focusing index is then defined as the ratio between the total absolute sensitivity in the region of interest and the total absolute sensitivity in the whole model:

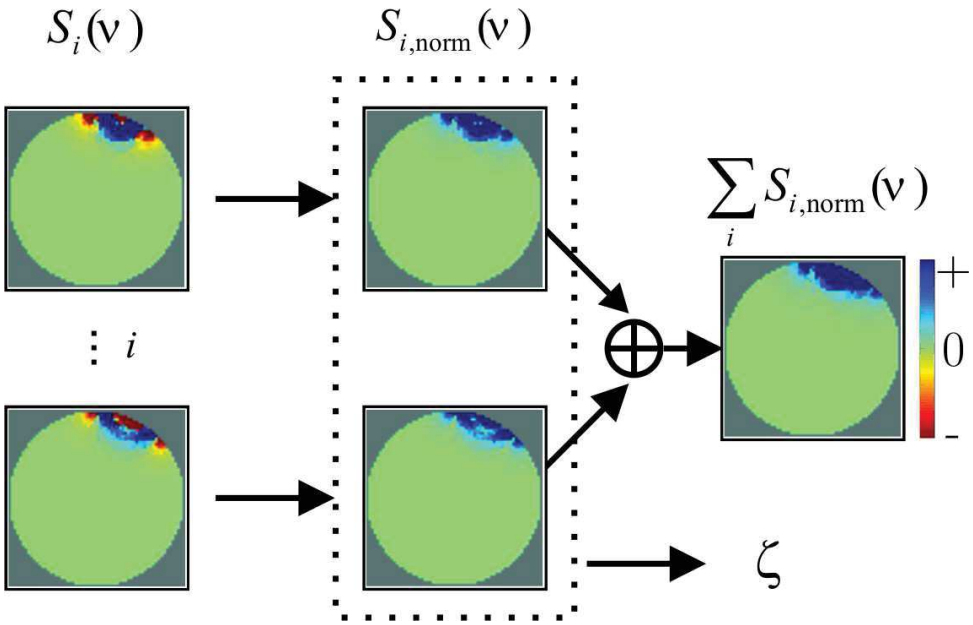

Fig. 1 Evaluation principle. Sensitivity distribution (left) and normalized sensitivity distribution (middle) for two impedance measurements. All normalized distributions are summed up, to create a total sensitivity image as depicted on the right side for these two measurements. Furthermore, the normalized distributions are used to calculate the index ζ.

$$\zeta = \frac{\sum_i \sum_{v \in \mathrm{ROI}} S_{i,\mathrm{norm}}(v)}{\sum_i \sum_{v \in \mathrm{all}} S_{i,\mathrm{norm}}(v)} .$$

The evaluation pipeline is demonstrated for two impedance measurements in Fig. 1. On the left side, the sensitivity distributions of two adjacent impedance measurements are depicted. These sensitivity distributions are then normalized and used to calculate the focusing index ζ. The normalized sensitivity distributions are used to calculate the local total sensitivity, which is defined as

$$S_{\mathrm{local,tot}}(v) = \sum_i S_{i,\mathrm{norm}}(v) .$$

This measure can be used to visualize the local total sensitivity distribution of multiple impedance measurements and will be shown for different EIT setups in the results. Green areas have a sensitivity of zero and do not contribute to the impedance data, while red and blue areas have an influence on the data.

Results

The results in this paper were calculated in Matlab (MathWorks, Inc., USA) using the EIDORS framework [5]. We compare a dual belt EIT configuration to the state-of-the-art adjacent single belt EIT. Fig. 2, left, shows a finite element model (FE-model) of the single belt setup while Fig. 2, right, shows the FE-model of the dual belt configuration. In this study, both FE-models use a cylindrical geometry for the body with a sphere in the center as the region of interest. Current densities and sensitivity distributions are simulated for all 928 impedance measurements. While the single belt configuration uses the typical adjacent injection and measurement pattern, we use a skip-9 pattern for the dual belt setup. This pattern skips 9 electrodes, so that electrodes are used for injection and measurement that are further apart. The total absolute sensitivity for these two configurations is shown at three image planes.

For the single belt configuration, we observe the expected results. The total absolute sensitivity at the electrode height is high in areas close to the surface and low in the center (Fig. 2, b). Additionally, the absolute total sensitivity in slices above and below the electrode plane is very low (Fig. 2, a, e). This results in a focusing index $\zeta = 0.00198$ for this configuration. In contrast, the dual belt approach shows a higher and more homogeneous absolute sensitivity distribution in the center (Fig. 2, e). Furthermore, the dual belt configuration does also provide a higher total absolute sensitivity in higher and lower regions, so that a three-dimensional analysis is possible (Fig. 2, d, f). The focusing index for the dual belt configuration is $\zeta = 0.00276$, which is roughly 40% higher than in the single belt configuration.

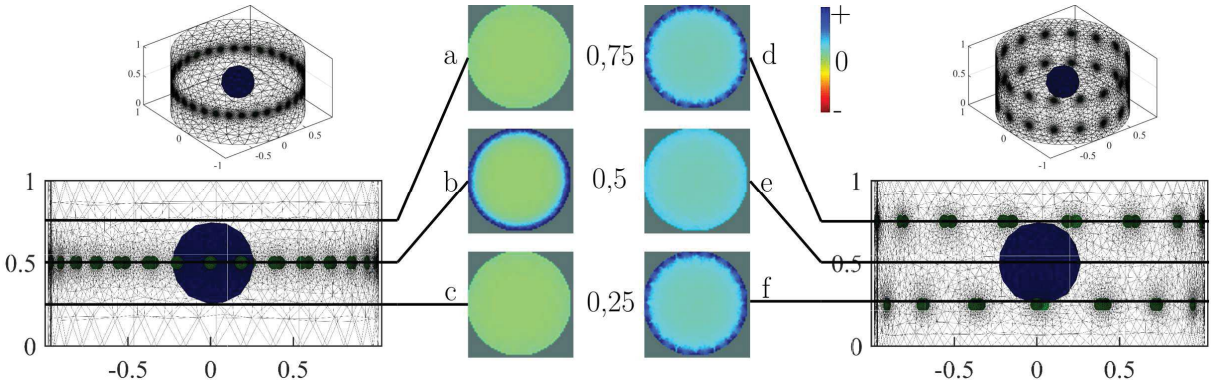

Fig. 2 Sensitivity distribution in multiple image planes with one electrode belt (left) and two electrode belts (right). While state-of-the art configuration with one belt and adjacent injection and measurement patterns is mainly sensitive to areas close to the body surface, the two belt configuration with a skip-9-pattern provides a higher sensitivity in the central area. The ROI used to calculate the index ζ is depicted in blue.

Discussion and Conclusion

The results show that dual belt EIT is promising for future applications for several reasons. For example, dual belt EIT might be able to reconstruct images in multiple planes. In single belt EIT, images can only be reconstructed in one plane, as it cannot be distinguished between impedance changes occurring above the electrode belt and those occurring below. In contrast, in dual belt EIT this becomes possible, as impedance values are acquired at different heights. By accordingly adjusting the reconstruction algorithm, images could be reconstructed at any height in between the two belts. Especially in systems with 32 electrodes, this is promising as the usual 16 electrode reconstruction approach can be used for each individual belt height. In addition, dual belt EIT provides a higher sensitivity in the center than single belt EIT. Current EIT applications mainly focus on ventilation monitoring. However, as mentioned in the introduction, cardiac monitoring is an interesting field for EIT. By using dual belt EIT, it might be possible to increase the power of the cardiac signal. This is important for signal separation, as high amplitude harmonics from ventilation are one major challenge in current approaches.

Some points need to be addressed in future research. In this work, two setups were investigated in a cylindrical model. More setups and more complex models could be used to achieve even higher focusing indices. Even setups with three or four electrode belts could be investigated. Additionally, to reconstruct images at different planes, reconstruction algorithms have to be adjusted. Nevertheless, this study gives an impression on how much dual belt EIT can improve the measurement sensitivity and demonstrates the impact of dual belt EIT on the sensitivity distribution.

References

[1] S. Leonhardt and B. Lachmann “Electrical impedance tomography: the holy grail of ventilation and perfusion monitoring?” Intensive Care Med **38**(12), 1917–1929 (2012).
[2] A. Adler, P. O. Gaggero, and X Maimaitijiang , “Adjacent stimulation and measurement patterns considered harmful.”, Physiol Meas **32**(7), 731–744 (2011)
[3] J. Orschulik, C. Hoog Antink, “Multi-Layer Electrical Impedance Tomography: An Experimental Study”, Proceedings of the student POSTER conference (2015)
[4] J. Malmivuo and R. Plonsey, *Bioelectromagnetism: principles and applications of bioelectric and biomagnetic fields* (Oxford University Press, USA, 1995)
[5] A. Adler and W.R.B. Lionheart “Uses and abuses of EIDORS: an extensible software base for EIT”, Physiol Meas **37**(5), 25-42 (2006)

Multichannel radiophysical complex for functional studies of the human brain

V.I. Borisov, V.S. Kublanov

Ural Federal University named after first President of Russia B.N. Yeltsin, 620002, Yekaterinburg, Rissian Fedeartion

Introduction

In paper, a variant of Radiophysical complex construction in which one of the informational channels is a contact microwave radiothermograph is proposed. This complex provides registration of the electromagnetic field fluctuation of the brain deep structures in the monitoring mode of the functional processes in its tissues. This mode allows continuous record of the biomedical signals for an observational interval. The duration of the interval is determined by the formation of a physiological phenomenon, investigated during the studies. In this context, a special role in such studies belongs to the functional-loading tests, which to some extent may affect the homeostasis of the cerebrospinal fluid circulation and hemodynamic in brain tissues and induce physiological changes that are the subject of the study.

According to this, the following tactical and technical requirements of the Radiophysical complex were formulated: the length of the studies were limited from 5 to 30 minutes. During the study, the complex must be capable to simultaneously register biomedical signals of the radiometric information channel and of the information channels of standard functional diagnostics (*e.g.* electroencephalography, electrocardiography, electrodermal activity, photoplethysmography, *etc*). In order to obtain the integrative assessment of the regulation quality for different regulatory systems of the body, that provides the brain homeostasis. Creation of such multi-channel Radiophysical complex is the urgent task that would improve the quality of early diagnosis of the brain processes regulation disorders.

Methodology

This paper analyses the features of the of brain microwave radiation in 650-850MHz range, which reflects the dynamics of fluid in tissues and dynamic thermoregulation processes, that are indicators of changes in physiological processes in the brain tissues.

According to the provisions of the Planck's radiation law and bio-heat equation, signals of the brain microwave radiation fluctuation is the result of modulation of thermal Brownian motion of functional processes in the brain tissues. However, the mechanisms of this modulation are not well understood. This approach is consistent with the hypothesis of academician Y.V. Gulyaev and professor E.E. Godik: physiological processes in tissues can be modulated by natural physical field. [1].

The Radiophysical complex is considered as part of the bio-technical system (BTS), microwave radiothermograph is one of the informational channels. The brain microwave radiation is caused by the thermal Brownian motion of charged particles that are modulated by functional processes in tissues. As a result, the signal is likely to have self-similar fractal nature, caused by the cyclical processes of dynamic regulation of homeostasis [2].

In the state of art works, statistical, spectral, and correlation information methods are usually applied to assess the characteristics of the signals of the brain microwave radiation. These methods do not take into account the fractal properties of the investigated process. Therefore, in this study of the BTS, it is advisable to apply the methods of multifractal analysis. The structure of such BTS is shown in Fig. 1.

The heart rate variability (HRV) signal is one of the examples of information channel formed by standard instruments of functional diagnostics. Choice of such signals in this study

is not accidental. The segmental divisions of the autonomic nervous system are involved in the organization of the cerebral circulation [3].

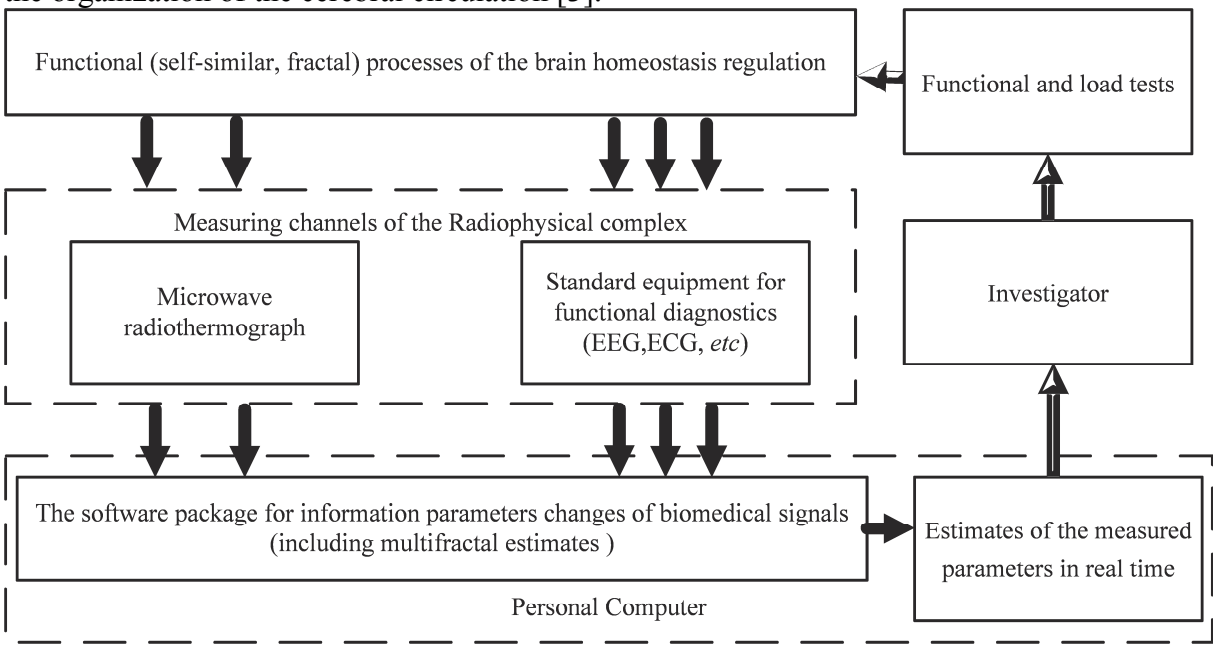

Fig. 1 The structure of BTS.

The collective analysis of the heart rate variability (HRV) and brain microwave radiation signals was performed based on studies that were conducted in the Sverdlovsk Clinical Hospital of Mental Diseases for Military Veterans (Yekaterinburg, Russian Federation). For investigation of cross-correlation between two time series, one can use method of the Multifractal cross-correlation Analysis (MFCCA). Application of this method for biomedical signal evaluation was described in [4].

The studies were conducted on the following groups of patients: the first group was 20 neurologically healthy patients volunteers aging 18-20 years, the second group was 14 patients suffering from ischemic stroke (prior to the treatment), the third group was 7 patients from the second group after treatment processes, for whom the improvement was clinically proved.

Measurements of biomedical signals were carried via the Radiophysical complex in two functional states of patients volunteers: functional rest (F) and during the passive antiorthostatic load (A). The time of each of the functional states was equaled to 300 seconds. Record of the brain microwave radiation was conducted simultaneously the left and right brain in the parietal hemispheres. HRV data was recorded at the same time.

The MFCCA method can be applied for detection of long-term multifractal cross-correlation between two different biomedical signals recorded simultaneously. The HRV signals are not equidistant in comparison to signal of the brain microwave radiation. So, it is advised to use cubic spline interpolation prior to the HRV signals investigation. For summary multifractal estimate, evaluation of the HRV and brain microwave radiation signals, the interpolation was implemented with the same sampling frequency equaled to 10 Hz.

One of the features of the MFCCA method is the possibility to perfom caculations in particular time windows. The following time windows were used to investigate the multifractal properties of short-term biomedical signals: 1–10, 10–20, 20–30, 30–40, 40–50, 50–60, 60–70, 70–80, 80–90 and 90–100 seconds. The lower boundary of time windows is limited by interpolation noise (below one second). The upper boundary is defined by the N/3 ratio, where N is the length of time series [4].

The role of the autonomic regulation in the formation of functional processes in the brain tissue is poorly understood. Although clinical trials of its activity depends on the effectiveness of rehabilitation of vascular lesions of the brain. Moreover there is no data on the effect of the autonomic regulation on the brain microwave radiation signals. Evaluation of nonlinear dynamical laws of the brain microwave radiation signals and HRV, including the temporal synchronisation of the processes, in order to forecast the patient's condition requires the application of a variety of specific analysis tools.

Results and discussions

Diagnostic possibility of the obtained multifractal features of selected biomedical time windows for two functional states was determined by the Bland-Altman criterion [5]. Firstly, the systematic discrepancy is counted as difference of each for each pair of exponents $h_F^{signal} - h_0^{signal}$. After that, the mean value <Δ> and standard deviation σ for the differences are obtained. The standard deviation characterizes the scatter degree of results.

The final estimates of modulus of systematic discrepancy of the Hurst exponents obtained by the method MFCCA for each time window for three group of patients are presented in the tables below. Here, the estimates are shown in bold type that have:

- low level of systematic discrepancy between two functional states for patients of the first group;
- high level of systematic discrepancy between two functional states for patients of the second group;
- reduction of this level for patients of the third group.

The estimates of modulus of systematic discrepancy obtained via the Bland-Altman criterion for difference of the cross-correlation Hurst exponent $h_{xyF}^{HRV-BMR} - h_{xy0}^{HRV-BMR}$ and calculated for the HRV and brain microwave radiation (BMR) signals between two functional states are shown in Table.

Table: Mean and standard deviation of systematic discrepancy of cross-correlation Hurst exponent of the HRV and brain microwave radiation signals.

	$h_{xyF}^{HRV-BMR} - h_{xy0}^{HRV-BMR}$					

According to the data presented in Table, the estimates of differences of the cross-correlation Hurst exponent in time windows 20-40 and 60-70 seconds for patients in the first group have low level of systematic discrepancy. In other cases, for different nosology and functional tests, results may differ from those obtained in the present study.

Conclusions

The BTS based on the Radiophysical complex estimates of the human brain functional processes is suggested. Main pecularities of this BTS are complexation of the microwave radiothermograph with standard equipment for functional diagnostics of the autonimic and central nervous systems. Method MFCCA is proposed for collective analisys of the biomedical signals.

Analysis of the short-term HRV and brain microwave radiation signals with the methods of the cross-correlation multifractal analysis allowed to obtain new knowledge about the studied biomedical signals, which indicate that:

1. for the "time windows" 20-40 and 60-70 seconds in the function rest and during the passive antiorthostatic load systematic divergence of the difference for the Hurst exponent of biomedical signals are minimumal for healthy patients volunteer. For patients suffering from ischemic stroke, these values are substantially greater before the rehabilitation treatment. After rehabilitation treatment for patients from this group, who have been clinically proven to improve, the systematic divergence of the difference for the Hurst exponent of the biomedical signals decreases.

2. application of multifractal formalism allowed to prove that the minimal level of systematic discrepancy between signals of the HRV and brain microwave radiation characterizes the similarity of dynamic changes in these signals. In this case one can conclude that role of the autonomic regulation defined by the parameters of HRV signal in the formation of the brain microwave radiation is high.

The considered BTS allowes to monitor changes in functional processes of the brain homeostasis regulation. The proposed approach can be used for the medical diagnostics.

References

[1] E.E Godik, Y.V.Gulyaev,. “Functional imaging of human body,” IEEE Engineering in Medicine and Biology, **10(4)**, 21–29 (1991).
[2] A.A. Potapov, “Fractal paradigm and fractal-scaling methods in fundamentally new dynamic fractal signal detectors,” Proc. Int. Kharkov Symp. on Ph. and Eng. of Microwaves, Millimeter and Submillimeter Waves MSMW, article number 6622151, pp. 644-647, (2013).
[3] Yu.E. Moskalenko, “Cerebral Circulation, Cardiovascular Diseases” [in Russian]. Meditsina, vol. 1 (1992).
[4] V.S. Kublanov, V.I. Borisov A.Yu. Dolganov, “Summary Processing of Radiophysical Complex MRTHR Signals” Proceedings of the 9th International Joint Conference on Biomedical Engineering Systems and Technologies Vol 4: BIOSIGNALS, pp. 143-149, (2016).
[5] S.A. Glantz “Primer of Biostatistics”: Sixth Edition. McGraw-Hill Professional: New York, p. 520, (2001).
[6] A.M. Syskov, V.I. Borisov, V.B. Parashin, V.S. Kublanov “Information Analysis of Radio Brightness Temperature Fluctuations in Brain Tissues,” Biomedical Engineering, **46(3),** 100-103 (2012).

X-ray microtomography in biomedical applications

A.Yu. Gerasimenko, I.V. Pyanov

National Research University of Electronic Technology, Biomedical Systems Department, Moscow, Russia

Methods of optical or electron microscopy allow to visualize the two-dimensional image of the sample surface or thin sections. However, in most cases, the conclusion of the three-dimensional the structure of the object can't be made on the basis of two-dimensional information.

X-ray tomography system allows visualization and measuring the three-dimensional structure of the object without prior training. Typically, the spatial resolution of medical CT scanners is in the range from 1 to 2.5 mm corresponds to the size of a voxel (volume element)

in the 1 - 10 cubic mm. Computerized x-ray microtomography gives opportunity to improve spatial resolution for the 7-8 orders of magnitude in volume terms. System SkyScan 1174 allows to achieve a spatial resolution less than 10 μm, according to the voxel size $1x10^{-6}$ cubic mm (Fig. 1) [1].

Microcomputed tomography (CT) or "micro-CT" is x-ray imaging in 3D, by the same method used in hospital CT scans, but on a small scale with massively increased resolution. It really represents 3D microscopy, where very fine scale internal structure of objects is imaged non-destructively. No sample preparation, no staining, no thin slicing - a single scan will image sample's complete internal 3D structure at high resolution. As in "macro" CT scanners, the interior structure may be restored and analyzed fully without destroying the object.

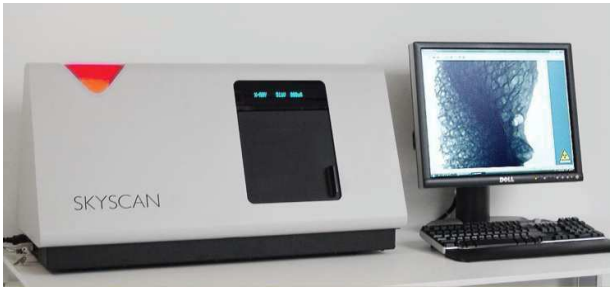

Fig. 1 X-ray microtomography system SkyScan 1174 (Bruker, Belgium)

This scanner uses an x-ray source with adjustable voltage 20÷50kV and a range of filters for versatile adaptation to different object densities. A sensitive 1.3 megapixel x-ray camera allows scanning of whole sample volume in several minutes Camera coupled to scintillator by lens with 1:6 zoom range. Variable is combined with object positioning for easy selection of the object part to be scanned. The spatial resolution of microtomography system SkyScan 1174 is 6÷30 μm pixel size, approximately 10 μm low-contract resolution. With the help of SkyScan we can investigate objects 5÷30mm in diameter and 50mm in length. SkyScan supplies multithread reconstruction by Feldkamp algorithm [2].

We started series of experiments on biological samples, bulk nanocomposites and biocompatible materials (Fig. 2-5).

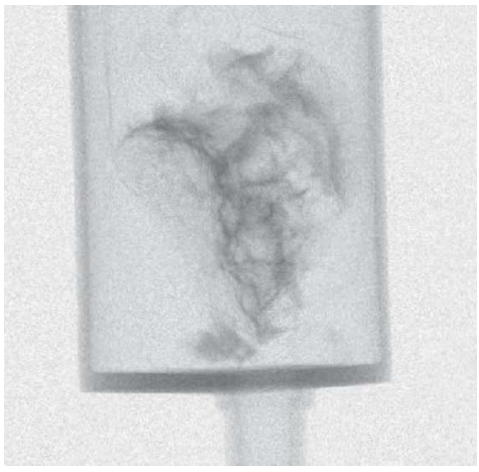

Fig. 2 Tomogram of aqueous suspension of protein albumin with carbon nanotubes

The most common ingredients of the nanocomposites include aqueous suspensions of protein albumin since the latter has good biological and photothermal properties (albumin – a transport protein being a part of blood serum and cytoplasm of human and animal cells) [3].

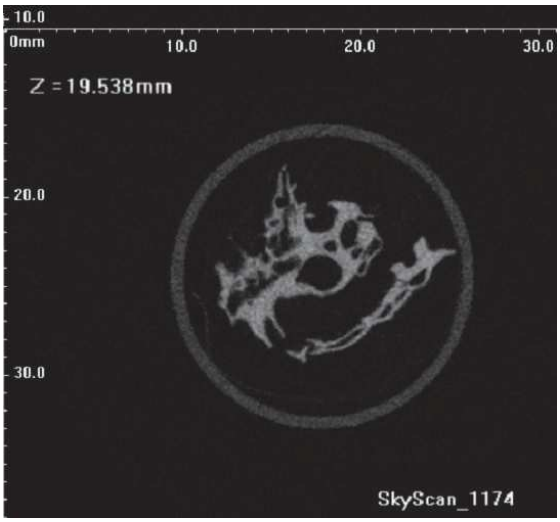

Fig. 3 Single tomography slice of aqueous suspension of protein albumin with carbon nanotubes

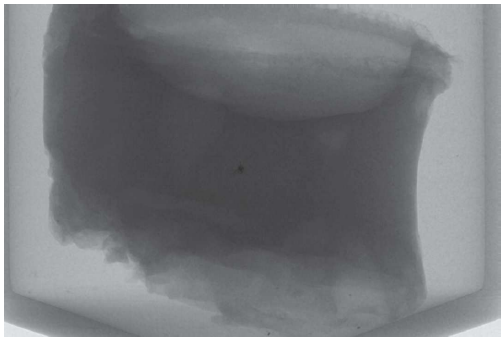

Fig. 4 Tomogram of bulk nanocomposite for biomedical applications

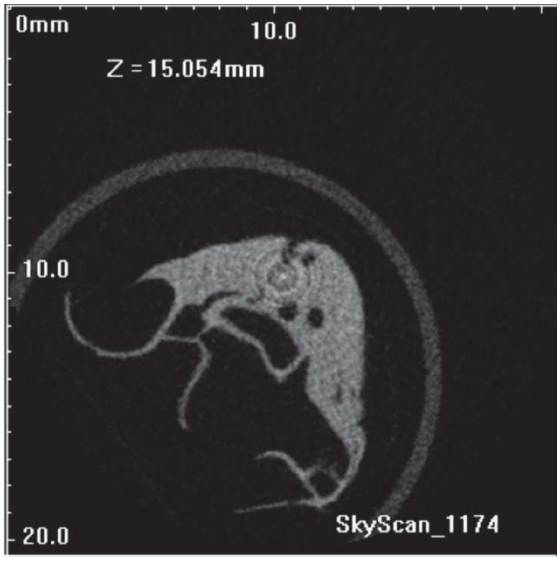

Fig. 5. Single tomography slice of bulk nanocomposite

The surgical experience confirms how important is the nanocomposites tensile strength during the first stages after a laser operation [4]. The strength of nanocomposites based on nanocomposites containing conventional aqueous albumin solutions does not always comply with medical requirements [5]. Therefore, we developed the composition of the nanocomposites based on aqueous albumin dispersion (concentration of 25 % wt) with carbon nanotubes (CNT, concentration of 0.1 - 0.3 % wt). Moreover, multi-walled (MWCNT) and single-walled (SWCNT) carbon nanotubes were used. MWCNT had a diameter (d) of 50-60 nm and a length (l) of 3-7 μm. In case of SWCNT d = 1.2-1.6 nm, l = 0.5-1.5 μm.

The CNT-based laser nanocomposite solder has been developed and analyzed [3, 5].. It is applied on the tissue to be weld before its welding. The effect of the electric field of laser irradiation on CNT orientation leads to the three-dimensional scaffold formation inside the nanocomposite solder. Irradiation electric field can increase at the edges of nanotubes and depends on their sizes.

Results of tomographic reconstruction can be use in the sphere of creating nanocomposites and biocompatible materials for medical application for example for restoring of the integrity the dissected biological tissues by laser welding [6].

In conclusion it should be mentioned that the initial stage of orientation of CNTs which are not placed too close to each other provides conditions for forming the three-dimensional nanoscaffold inside nanocomposite solders and may be feasible. This nanotube scaffold can produce the effective self-assembly of cellular material.

This work was provided by the Ministry of Education and Science of the Russian Federation (Agreement 14.575.21.0089) and the Stipend of the President of the Russian Federation for young scientists and graduate students (SP-70.2015.4).

References

[1] SkyScan 1174 at http://www.skyscan.be

[2] L.A. Feldkamp, L.C. Davis, J.W. Kress Practical cone-beam algorithm // J. Opt. Soc. of America, 1984. – Vol. 1. – № 6. – P. 612-619.

[3] Gerasimenko A.Yu., Ichkitidze L.P., Podgaetsky V.M., Selishchev S.V. Laser nanoformation of biocompatible volume nanocomposites. The International conference on Coherent and Nonlinear Optics (ICONO 2013) and Lasers, Applications, and Technologies (LAT 2013) at the Presidium Bldg (new) of the Russian Academy of Sciences (Russia, Moscow, June 18–22, 2013) p. 67-68.

[4] Gerasimenko A., Ichkitidze L., Podgaetsky V., Selishchev S. Composite nanobiomaterials for compounds biological tissues. Fourteenth international conference on the science and applications of nanotubes (Finland, Espoo, June 24-28, 2013).

[5] Gerasimenko A.Y., Ichkitidze L.P., Ponomareva O.V., Selishchev S.V. / The Use of Composite Nanobiomaterials based on Carbon Nanotubes for Compounds Biological Tissues // International conference "Advenced Carbon Nanotubes" ACNS`2013, July 1-5, 2013, St. Peterburg, Russia. Abstracts of Invited Lectures & Contributed Papers, p.114.

[6] Gerasimenko A.Yu. Restoring of the integrity the dissected biological tissues by laser welding. Exhibition-conference of Ministry of Education and Science of Russian Federation «New nanostructured biocompatible materials» (Czech Republic, September10-14 2012), p. 16-18.

Bioradar parameters informativeness in fall detection for elderly

M.K. Dremina[1] , E.S Smirnova, L.N. Anishchenko[1]

[1]Biomedical Engineering Department, Bauman Moscow State Technical University, 5, 2d Baumanskaya str., Moscow 105005, Russia

Russian Federation like many other countries, is facing the problem of an ageing society

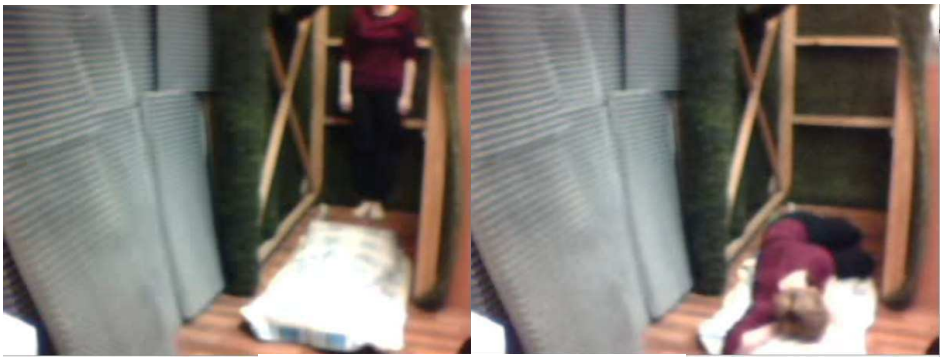

Table 1. Resulting informativness.

	Assessment of informativeness			
Features	**t**	**ΔA**	**C**	**PC**
Cumulative frequencies method	29	21	34	30
Shennon method	0,588	0,326	0,72	0,593
Kullback divergence method	3,285	0,981	6,829	6,96

The results generally show a predominance of frequency domain parameters over the time domain parameters . But any single feature alone is not enough to provide comparable fall detection performance. Thus we conclude that for better performance classifier should be based on both frequency and time domains parameters. Although the results are preliminary, they may be useful for the development of non-contact fall detection system.

References

[1] United Nations, Department of Economic and Social Affairs, Population Division (2013). World Population Prospects: The 2012 Revision, CD-ROM Edition.
[2] Russian Federal State Statistics Service «Demographic features of the population in the Russian Federation»
[3] L. Anishchenko, M. Alekhin, A. Tataraidze, S. Ivashov, A. Bugaev, F. Soldovieri, "Application of step-frequency radars in medicine," Proc. SPIE 9077, Radar Sensor Technology XVIII, 90771N (May 29, 2014)
[4] Golovanova I. «The selection of informative features. Assessment of informativeness» — Tomsk: TPU, 2003. – 18 p.

The investigation of the tensile strength of composite based on carbon nanotubes and the AFM structure of composite

D.I. Ryabkin[1], A.Yu. Gerasimenko[1], L.P. Ichkitidze[1], V.M. Podgaetsky[1], I.V.Pyanov[1], Ya.A. Shimarova[1], M.S. Savelyev[1], A.A. Pavlov[2], E.M. Eganova[2], S.V. Selishchev[1]

[1]*National Research University of Electronic Technology MIET, Bld. 1, Shokin Square, Zelenograd, Moscow, Russia, 124498;*

[2]*Institute of Nanotechnology of Microelectronics of the Russian Academy of Sciences, 18 st.Nagatinskaya, Moscow, Russia, 115487*

3-D bioconstructions were created using the evaporation method of the water-albumin solution with carbon nanotubes (CNTs) by the continuous and pulsed femtosecond laser radiation. It is determined that the volume structure of the samples created by the femtosecond radiation has more cavities than the one created by the continuous radiation. The average diameter for multi-walled carbon nanotubes (MWCNTs) samples was almost two times higher (35-40 nm) than for single-walled carbon nanotubes (SWCNTs) samples (20-30

nm). The most homogenous 3-D bioconstruction was formed from MWCNTs by the continuous laser radiation [1]. The hardness of such samples totaled up to 370 MPa at the nanoscale. High strength properties and the resistance of the 3-D bioconstructions produced by the laser irradiation depend on the volume nanotubes scaffold forming inside them. The scaffold was formed by the electric field of the directed laser irradiation. The covalent bond energy between the nanotube carbon molecule and the oxygen of the bovine serum albumin aminoacid residue amounts 580 kJ/mol. Thus, the 3-D bioconstructions that are nanostructured by the pulsed and continuous laser radiation can be applied as implant materials for the recovery of the connecting tissues of the living body. High strength properties and resistance of 3-D bioconstructions produced by laser irradiation depend on the 3-D nanotube scaffold forming inside them. The scaffold is formed by the electric field of the directed laser irradiation. The authors of N. V. Kamanina et al. have shown the possibility of CNTs structuring (perpendicular to the template surface) using the electric field of the CO_2 laser with the power of 30 W, the light electric-field strength being E_{mean}= 10-20 kV/m.

The technology of 3-D bioconstructions laser formation has several steps. First step is the preparation of the water-albumin dispersion. BSA is dissolved in the distillated water in ~25 % concentration to receive the albumin solution. Next the composition is dispersed in the ultrasonic bath for 1-2 hours to receive the homogenous medium. Second step is a preparation of the working medium with CNTs. CNTs are added in the water-albumin dispersion in 0.1-1 g/l concentration. Then the solution is dispersed in the ultrasonic bath for 3-5 hours to receive the homogenous colloidal black-colored solution. It is necessary to preliminary interfuse 3-D bioconstructions with the powerful probe homogenizer (30-40 minutes, 30 W) while receiving them from SWCNTs [2].

The usage of the unfocused laser beam that falls on the working water-albumin CNTs dispersion is a specialty of this 3-D bioconstruction formation technique as opposed to the laser stereolithography, polymerization and sintering. It gives the possibility to receive volume materials without inhomogeneities of solid material through pointed moving of laser beam on the surface of the working medium. The solid material formation results by the liquid evaporation under the laser radiation. The falling beam profile has Gaussian distribution and its diameter equals the diameter of container with water-albumin CNTs dispersion (~ 5 mm). And the layer thickness of the solution is 5 mm. The intense radiation absorption followed by heating of single CNTs and its conglomerates occurs during the laser radiation of the water-albumin CNTs dispersion. Next the local boiling of water-albumin matrix happens around CNTs and its conglomerates that causes BSA denaturation. The dispertion level (size of CNTs and its conglomerates) affect the size of the developed inner pores and cavities. So, if the size of CNTs conglomerates in the initial solution is normalized then the inner structure of 3-D bioconstructions become more homogenous.

The two types of lasers i.e. the continuous diode laser and the pulsed solid-stated laser (Ti:Sa) were used to create 3-D bioconstructions based on CNTs in the water-albumin matrix with the laser nanostructuring method. The basic characteristics of the radiation of both lasers were equal i.e. the generation wave length - 810 nm, power – 2 W. The impulse duration of the Ti:Sa femtosecond laser amounted 140 fs and the frequency - 80 MHz. The radiation of the both lasers was brought into the optic fiber and the needed diameter was adjusted with the collimator at the output.

The particular study of the sample I and III porosity (Table 1) by the capillaceous nitrogen adsorption-desorption has shown following results. The specific surface for the samples with SWCNTs made about 0.03 m^2/g. The specific surface values for the MWCNTs samples received by the continuous radiation (0.009 m^2/g) were significantly lower than for the samples received by the femtosecond radiation (0.07 m^2/g). Meanwhile the value of the specific pore volume for the all samples have the one degree of order. The average pore

diameter for the SWCNTs samples is 20-30 nm and for the MWCNTs totals almost two times higher (35-40 nm).

Table 1. The investigated properties of the samples

Number of the 3-D bioconstruction	CNTs type	Type of laser radiation	Specific surface, m^2/g	The specific pore volume, ml/g	Average diameter of pore, nm
I	SWCNTs	Continuous	0.03	0.0005	28.802
II	SWCNTs	Femtosecond	0.031	0.0004	23.044
III	MWCNTs	Continuous	0.009	0.0006	39.413
IV	MWCNTs	Femtosecond	0.07	0.0009	35.792

The mechanical characteristics research was carried out after the inner structure studying of the samples. The scanning probe indentation method was used for this purpose. The method is based on the analysis of the pressing dependency while the hardness indentation in the material surface versus the depth of penetration. The indentor of Berkovich type was used i.e. the tree-sided diamond pyramid with an angle of 65° at the top. The hardness of the linear sizes in the nanometer scale was measured. The nanohardness of the SWCNTs samples formed by the femtosecond radiation totaled up to 370 MPa, the modulus of elasticity made up to 4.2 GPa and the elastic restitution of the original form after the indentor puncture was up to 40 %. The mass of the initial water dispersion of BSA with CNTs totaled 0.938-0.986 g at the water density. The material at the solid phase state after the laser radiation had the mass of 0.147-0.153 g and the density of 1.24 – 1.28 g/cm^3. For example, the density of the human pore bone is 500 MPa over the 1.930 g/cm^3 density.

Then the structure of the 3-D bioconstruction surface was studied using the atomic force microscopy before the *in vitro* studies. The research of the film samples nanostructured by the laser radiation on the silicon substrate was carried out. As seen on figure 5, the bright areas at the 3-D topograms represent the hills and the dark areas represent the cavities. The pore sections are observed with the sizes from 50 to 100 nm (the dark spots). The nature of the taken topograms is defined by the presence of the pores in the samples. The form and the amount of the pores depend on the technological parameters of the sample preparation (CNTs concentration, time of the processing and the capacity of the laser radiation). The amount of the pores and its size reduces as a rule when adding CNTs in the BSA matrix. It may be related to the reinforcing action of CNTs when the scaffold is building under the laser radiation. With the increase of the CNTs concentration the amount of pores also reduces.

There are seen low (-11 nm) and high (6 nm) regions on the AFM topograms of the samples based on SWCNTs (figure 1a). Figure 5 has the 2D view of the samples at the top and the inverted 3-D view at the bottom. The level difference made 17 nm. The surface structure is seen enough homogenous with the periodically repeated cavities in the form of the pores. The level difference for MWCNTs made 15 nm but the observed surface structure was less homogenous (figure 1b).

When the power concentration of the semiconductor lasers operating in various modes within different wave lengths was 10-20 W/cm^2, Emean was equal to 5-10 kV/m. These conditions may allow CNTs orientation and nanoscaffold formation inside the 3-D bioconstruction.

.

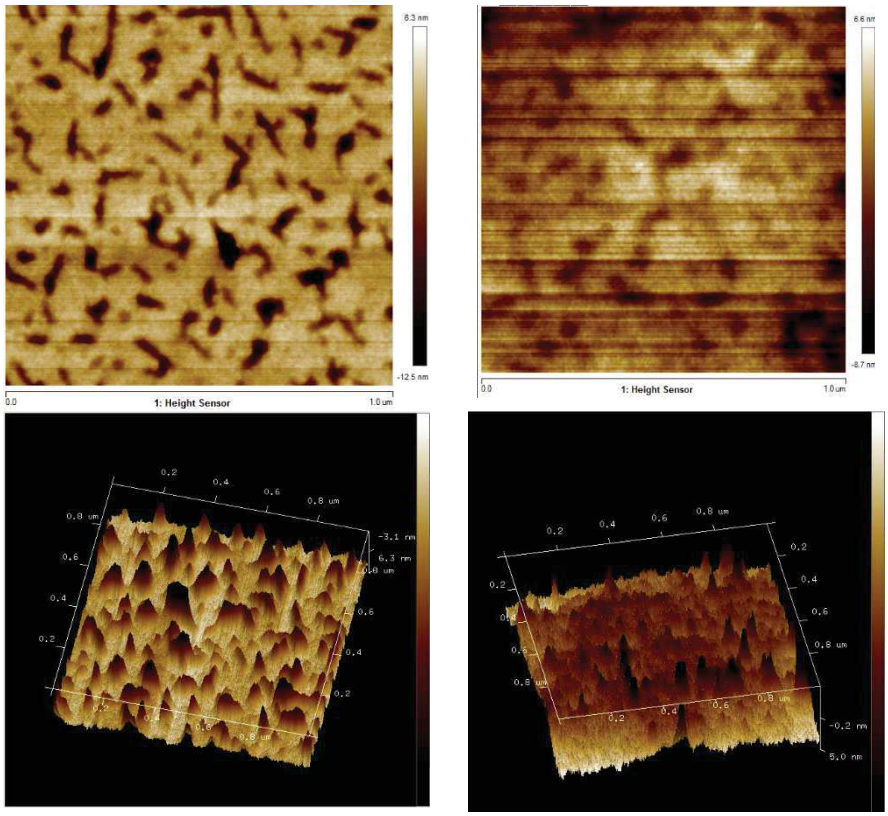

a b

Fig. 1 AFM topograms (2D view of the above, inverted 3-D view of the below) of a film samples based on SWCNTs (a) and MWCNTs (b) formed by continuous laser radiation.

CNTs-orienting electric irradiation field may increase at the end of the nanotube depending on the CNTs sizes and the mode of the set structuring. Near the CNTs end the optical field intensity (ma+b) times higher than Emean, where the aspect ratio is a = l/d, b ≈ 30, while l and d are the CNTs length and diameter, respectively. Coefficient m is ≈ 0.7 for isolated nanotubes and decreases when approaching the CNTs. In case of used nanotubes a ~ 1000 (SWCNTs) and 50 (MWCNTs).

In 3-D bioconstructions the CNTs and BSA bonding comes through the Glu and Asp amino acid residues. The acidic amino acid radical has the additional carboxyl group that can create the chemical bond. The calculated energy of CNTs and neutral molecule of BSA interacting makes 3.7 kJ/mol which corresponds with Van der Waals' energy for the protein aminoacid intermolecular interaction. The covalent bond energy between the carbon nanotube molecule and the oxygen of the BSA aminoacid residue (CNT-BSA) amounts 580 kJ/mol. The increasing amount of the oxygen atoms lead to the reduction of CNTs and BSA energy of interaction. The more oxygen atoms connect, the stronger the deformation. One can change the CNTs configuration by the oxygen to tube connection points changing and it can be used to produce the scaffold of the required tube form

The inner structure of the samples, that were received using the femtosecond laser, has a large amount of cavities. It doesn't depend from the amount of nanotubes. The most homogenous structure of the sample for 3-D bioconstruction with MWCNTs was received under the influence of the continuous radiation. Meanwhile the average pore diameter for the SWCNTs samples was 20-30 nm and for MWCNTs totaled almost two times higher (35-40 nm). The hardness of the linear sizes in the nanometer scale was measured. The specific

surface of 3-D bioconstuctions appeared some times smaller than the starting material, i.e. SWCNTs and MWCNTs. Such structure of the samples provides hardness up to 370 MPa over the density of 1.24 – 1.28 g/cm^3.

This work was provided by the Ministry of Education and Science of the Russian Federation (Agreement 14.575.21.0044 RFMEFI57514X0044).

References

[1] K. Hung, C. Tseng, L. Dai, S. Hsu, "Water-based polyurethane 3D printed scaffolds with controlled release function for customized cartilage tissue engineering", Biomaterials 83, 156-168 (2016).

[2] A. Gerasimenko, A. Dedkova, L. Ichkitidze, V. Podgaetsky, S. Selishchev, "A study of preparation techniques and properties of bulk nanocomposites based on aqueous albumin dispersion," Optics and Spectroscopy 115(2), 283-289 (2013).

Adaptive stress control method used in remedial action complexes for human respiratory system

N. Ivakhno, S. Fedorov

Tula State University, 92 Lenina pr., Tula, Russia, 300012

Depending on the type of exposure, condition of human respiratory system is characterized by relevant parameters acquired by the analysis of pressure curve with the use of methods discussed in articles [1, 2, 3].

During the analysis of the matrices of conditions the correspondences between each parameter depending and the stress/shift pressure are obtained as a result of diagnosis of the respiratory system [2, 3], and the intermediate points can be calculated using interpolation methods.

In this case, it is necessary to find the exposure level that will provide the result, closest to the reference characteristic of the selected effectiveness parameter. Biotech complex of remedial action, including the respiratory system, is characterized by the evaluation of a number of particular indices of quality, differentiated by dimensions and values:

– in case of relay action [1, 3] (with different shift pressure $P_1,...,P_N$) it is the duration of inspiration/expiration phases - $T_1,...,T_N$, the slope angle of the approximating curve [1, 3] on the first observed interval – $\alpha_1,..,\alpha_i..,\alpha_N$, approximating function coefficient [1.3] on the third observed interval $k_1,...,k_N$, the rise time of the pressure curve to its maximum $t_{н1},...,t_{нN}$, pressure curve characteristics in case of eupnoea– $\alpha_0, k_0, t_{н0}, T_0$;

– in case of choking action (with different resistance of the breathing circuit $R_1,..., R_N$) it is [2, 3] duration of inspiration/expiration phases - $T_1,...,T_N$, the slope angle of the approximating curve on the first and second observed intervals $-\alpha_1,..,\alpha_i..,\alpha_N$, $\beta_1,...\beta_i,...\beta_N$, the rise time of the pressure curve to its maximum $t_{н1},...,t_{нN}$, the pressure curve characteristics in case of eupnoea– $\alpha_0, \beta_0, t_{н0}, T_0$, where N - number of stress levels, *i* - stress level.

In accordance with the principle of the uniqueness, the effectiveness index in whole as an optimality criterion should be expressed as an overall index, including particular indices [5]. To calculate practically optimal variant of the complex biotechnical system, the

effectiveness index function, if its analytical expression is unknown, can be replaced by a linear function, including all basic particular indices of quality with restrictions on each index [4, 5]. This requires a comparison of relative values, which are formed as correspondences for each index. If the overall effectiveness index of the optimal system should be minimal, the indices with values, that tend to decrease when the system is approaching to the reference one [5], can be selected as particular indices of quality.

Having set each parameter of conditions matrix M [3] of the respiratory system as *y*, parameter number as *k*, the level of exposure as *i*, we obtain the expression for calculation of the relative value of the index at each stage of the stress (resistance/pressure):

$\frac{yp_{ik} - \overline{yp}_{ik}}{\overline{yp}_{ik}}$ where $\overline{yp}_{ik}$ – the reference value of the parameter *k* when *I* is the stress level.

This function is used to select practically optimal variant of stress/shift pressure.

The optimal parameters of an individual are defined as average on the basis of processing of the results of the study of a large number of patients with different types of diseases, as well as of healthy patients and of those who need trainings (athletes). Thus, the reference values are different for different classes of systems.

The root-mean-square deviation of the measured system parameters from the reference ones is used as a particular index of the objective function of automatic remedial action complexes.

Calculation of this characteristic at no-stress (eupnoea) and the choking action will be described with the following objective function:

$$Q_0 = \sqrt{\frac{\left(T_0 - \overline{T}_0\right)^2}{\overline{T}_0^2} + \frac{\left(t_{н0} - \overline{t}_{н0}\right)^2}{\overline{t}_{н0}^2} + \frac{\left(\beta_0 - \overline{\beta}_0\right)^2}{\overline{\beta}_0^2} + \frac{\left(\alpha_0 - \overline{\alpha}_0\right)^2}{\overline{\alpha}_0^2}},$$

The generalized function in this case is describe with the equation:

$$Q_i = \sqrt{\sum_{k=0}^{S-1} c_k \frac{\left(M_{ik} - \overline{yp}_{ik}\right)^2}{\overline{yp}_{ik}^2}}.$$

where *i* – stress level, $i = 0,.., N-1$, *S* – number of parameters, *N* – number of stress levels, *M* – matrix of the respiratory system.

Then the algorithm of selection of stress/shift pressure will be based on the search for the minimum value of this generalized function (Fig. 1). Wherein the starting level can be set in two ways: during the analysis of the characteristics of each person, stress/shift pressure value, corresponding to the minimum value Q_i, will be calculated, the second method provides a gradual transition from the initial stress to a level at which the minimum value Q_i is reached.

Having established at the set level, the system operates in the search mode. Finding of the optimal stress can be based on the use of different gradient methods.

To build a model, the target values were set, and the algorithm of stress search and adaptation to the changing parameters of the human respiratory system was considered, using the gradient method.

The experimental results of the study of the algorithm of adaptation and finding of the value of the objective function are illustrated by the graphs, where step number is put on the *x* axis, and *y*-axis shows the stress and values of Q_i.

The observation on Fig. 1 was carried out within 2-3 minutes. Q_i takes the maximum value of 0.345, and the minimum of 0.27. At first, the minimum value is fixed at 10th observation step at the stress of 0.35, with a gradual change in the state of the human respiratory system the stress has increased up to 0.55. Further increase of the stress leads to a considerable fall of the objective function Q_i, so the stress is set at the value of 0.5-0.55.

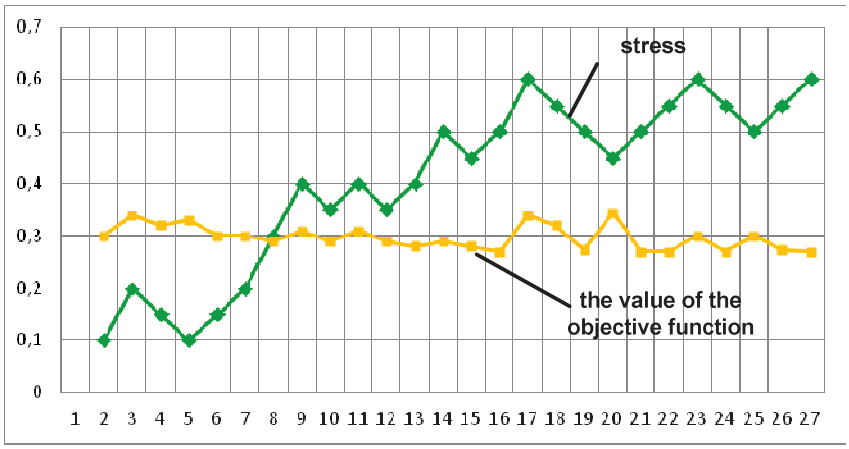

Fig.1. Experimental characteristics of the result of the adaptation algorithm, observation 1 (the stress in the form of resistance)

The observation on Fig. 2 was carried out within 3.5 minutes. The minimum value is 0.68 at the stress of 0.5. From 17th to21st step the system tries to increase the stress, causing an increase of value of the criterion Q_i, and the stress returns to the acceptable level of 0.5-0.55.

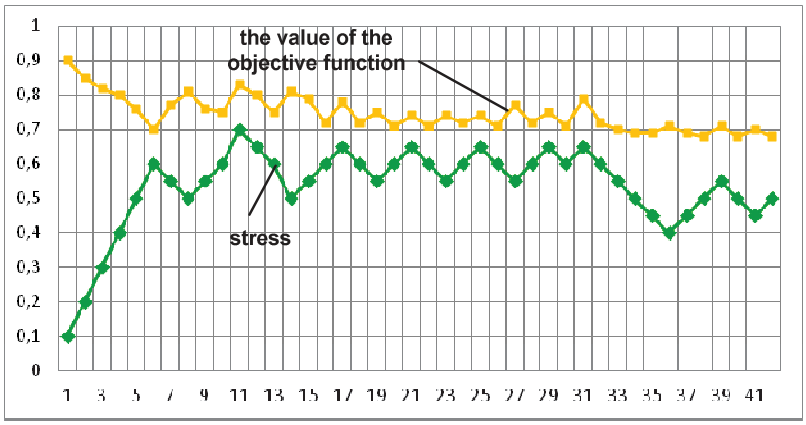

Fig.2. Experimental characteristics of the result of the adaptation algorithm, observation 2 (stress in the form of resistance)

In a real system, taking into account the restrictions imposed on the remedial action complexes, we can only discuss the minimization of the functional Q_i. When choosing between two options of the stress in which the effectiveness criterion is the same, the greater stress is preferably chosen, which is caused by the need for training [4, 5].

To ensure the safety of the remedial action procedure, restrictions on the values of the some characteristics of Q_i functionality are introduced.

The designed algorithm for finding the best stress/shift pressure values allows the remedial action to adapt to the changing condition of the respiratory system. The restrictions on the parameter's values of the objective function, characterizing the effectiveness of adaptation, provide the safety of the systems and the stability of the algorithm.

The research was sponsored by RFBR and the Administration of Tula Region within the framework of a research project No. 15-48-03247 «r_tsentr_a".

References

[1] Ivakhno N.V., Antsibor S.V. Parametric analysis of respiration characteristics under the relay action //Proceedings of the Tula State University. Technical sciences. Issue 5: 2 vol. 2015. Part 2. Pp. 78-84.
[2] Ivakhno N.V. The method of diagnosis of the respiratory system under the choking action // Proceedings of the Tula State University. Technical sciences. Issue 5: 2 vol. 2015. Part 2. Pp. 92-97.
[3] Ivakhno N.V. Formation of a common set of informative signs to identify the condition of the respiratory system. // Proceedings of the Tula State University. Technical sciences. Issue 5: 2 vol. 2015. Part 1. Pp. 106-111.

The possibility of using micro focus computed tomography in biomedical engineering

V. B. Bessonov, N. N. Potrahov, A. V. Obodovsky, A. Y. Gryaznov, K. K. Zhamova
Saint-Petersburg State Electrotechnical University «LETI», 5 Professora Popova st., Saint-Petersburg, Russia

The first X-ray tomography was developed in 1969 this discovery opened a new era in medical diagnostics. Thanks to the invention by G. Hounsfield we have the possibility to look at internal structure of human body and to determine the relative location of different organs with high precision.

The first tomographic experiments had considerable limitations in the resolution and the amount of time for building of the image of internal structure of the object; it is called reconstruction of the object. Now, high computer power and modern visualization systems allow to significantly reduce time spent and improved the quality of diagnostics.

We can select two opposite trends of X-ray computed tomography for medical diagnostics. The first trend is the using of relatively narrow X-ray beam that record by detector arrays. Wherein, X-ray source and detector arrays rotate synchronously around the patient who moves along the rotation axis. Movement trajectory of X-ray system looks like the spiral shape in relation to the patient. Such process of the projection data acquisition and corresponding algorithms of reconstruction are called the spiral tomography. Similar type of equipment is developed by way of increasing the number of detecting lines. Now, X-ray tomograph has 128 slices of detecting lines. These scanners are used extensively in diagnostic practice.

The second trend is the using of cone-beam x-ray that is recorded by XY receivers, for example the flat panel detectors. This design of tomograph allows to produce the projection data in the incomplete turn (180 degrees). It allows to reconstruct of the investigated area with high precision very easily. The method described have the wide application in dentistry for diagnostic of dental systems and X-ray studies of animals.

The using of micro focus X-ray tubes and schemes with direct geometric magnification images of objects [1] allowed identifying a new class of equipment for medical diagnostics – micro-focus X-ray computed tomographs. Such tomographs give the possibility to study the visualization of structures in size from micrometers units. It is possible due to features of the projection increase. The natural limitation in this case is the value of focal length that limits the maximum magnification of the object. X-ray tubes are used with remote anode for minimization of the value of focal length [2].

The educational and scientific laboratory of X-ray systems was organized by Saint-Petersburg State Electrotechnical University for testing structures and methods of using this tomograph. One of the first Russian models of micro focus X-ray computed tomograph was developed by the team of laboratory (Fig. 1).

The main feature of this design is the using of a sealed X-ray tube (Fig. 2). The combined electrostatic and magnetic focusing system is used for decrease of the electron beam cross-section (tube focal spot).

The multicam receiver is applied for receiving of x-ray image. This receiver was built according to the sheme of "luminophore-optic-CCD" and it has the pixel size of 200 micrometres.

Accuracy of positioning and moving elements of the system is achieved by the using step motors. Motor control scheme allows to divide the step.

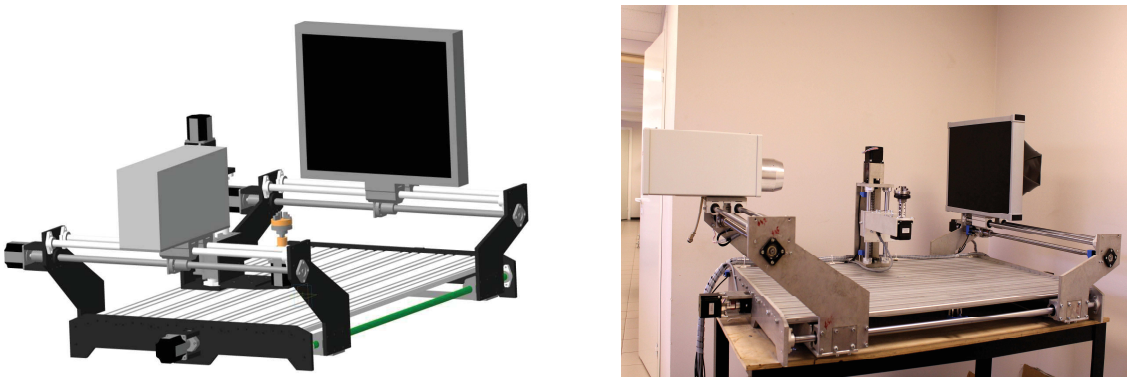

a B

Fig. 1. Micro focus X-ray computed tomograph (MFCT-01):
a – computer model; b – appearance.

Fig. 2. Sealed micro-focus X-ray tube with remote anode

The main specifications of developed tomograph is shown in Table 1.

Table 1. Main specifications.

№	Specification		Value
1	Anode voltage		from 20 to 130 kV
2	Anode current		from 10 to 150 uA
3	Size of the focal spot		less 5 um
4	Number of projections		from 100 to 4000
5	Ratio zoom		from 1,5 to 200
6	Maximum resolution in the reconstruction		2 um

As an example of the possible application of this tomograph is shown in figure 3. This is sections of tooth in the several projections for assess the depth of the defects [3]. Sections of the object observed allow to diagnose the defects of cleaning root canal. Contrast in this research is much higher than with conventional radiographic research (Fig. 3).

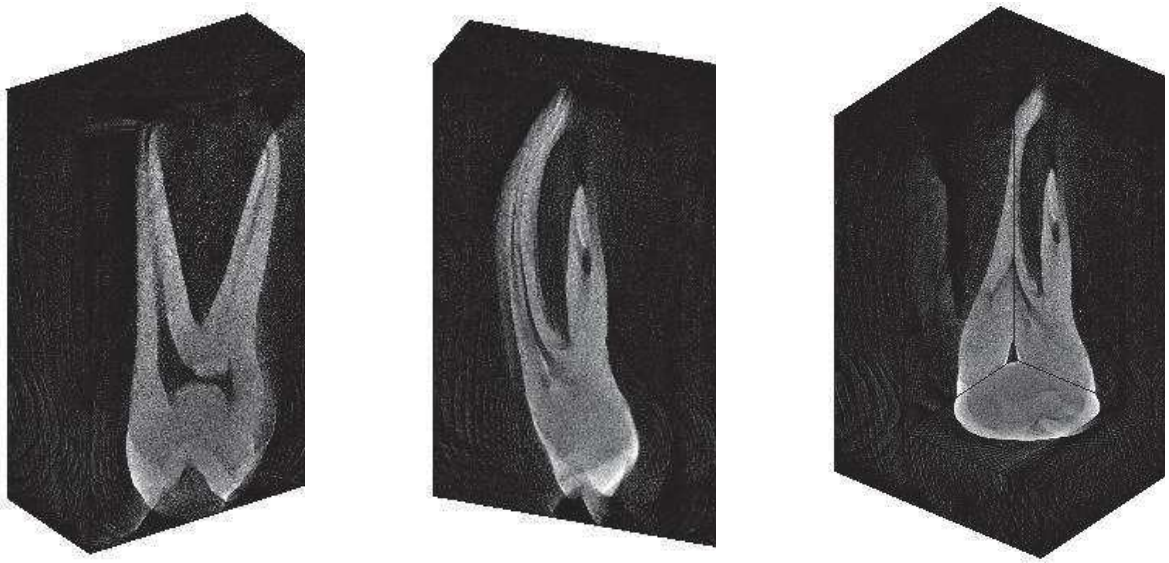

a b c

Fig. 3. Cross sections of research object in the different planes

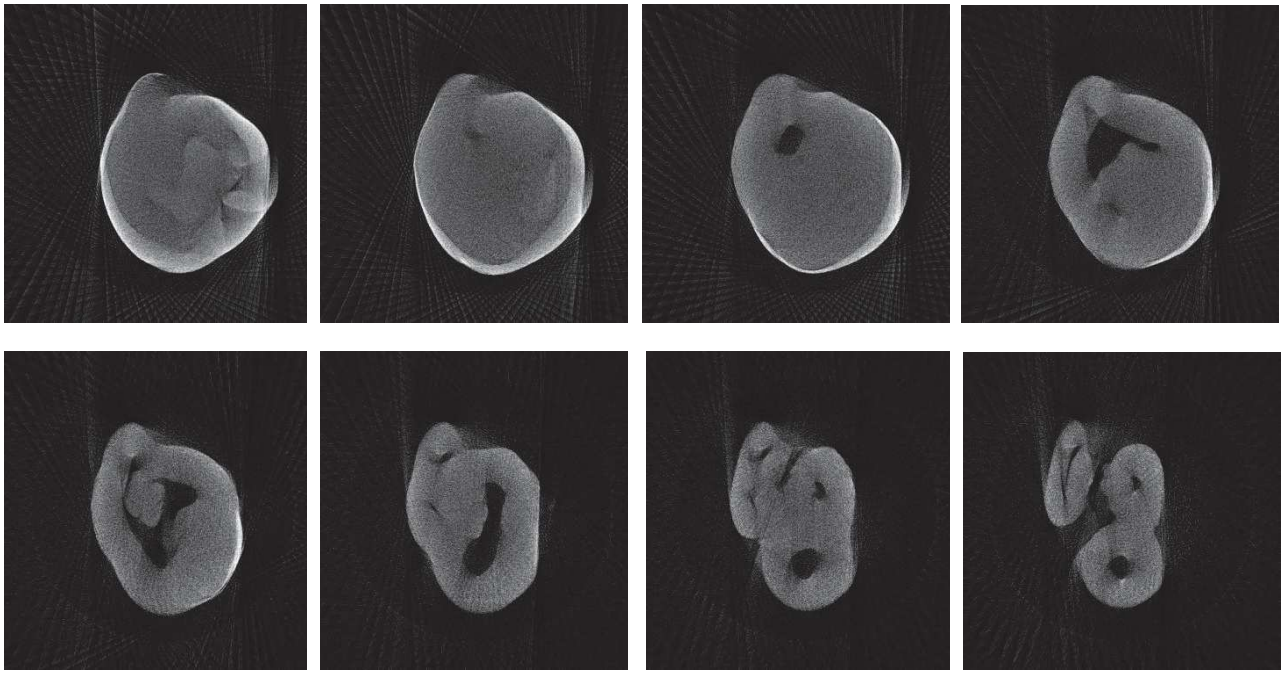

Fig. 4. Cross sections of research object at different depths

Results confirm the perspectives of using micro focus X-ray computed tomography in the medical diagnostics. Research of bioengineering objects with the technology of 3-dimensional print successfully solves the task of developing new methods of treatment, prosthetics, as well as the construction of the maintenance of vital functions of the human body systems.

References

[1] N.N. Potrahov, A.Y. Vasilyev, A.I. Mazurov, I.M. Baranov, V.B. Bessonov, Y.A. Vasilyev, A.Y. Gryaznov, K.K. Zhamova, V.V. Petrovskaya, E.N. Potrahov, Y.N. Potrahov. Micro focus X-rays in medicine / SPb.: publishing SPbETU «LETI», 2015. 91 s.

[2] S.A. Ivanov, Y.K. Ioffe, S.V. Kirienko, G.A. Shchukin. Miniature X-ray sources. Reviews of electronics. Series 4. Electrovacuum and gas equipment / Moscow: CRI «Electronics», 1987. 55 s.

[3] N.N. Potrahov, G.E. Trufanov, A.Y. Vasilyev, D.Y. Anohin. Microfocus X-ray in clinical practice: a tutorial / SPb: ELBI-SPb, 2012. 80 s.

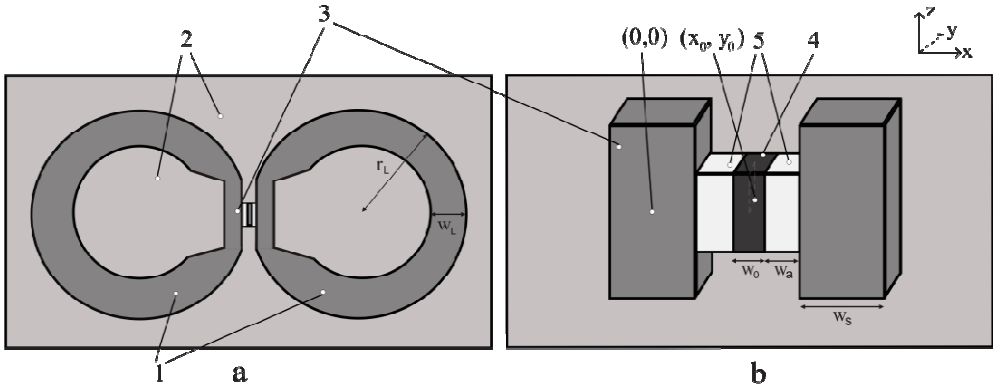

$I_S = \phi/(L+M)$, where L is the ring inductance and M is the sum of

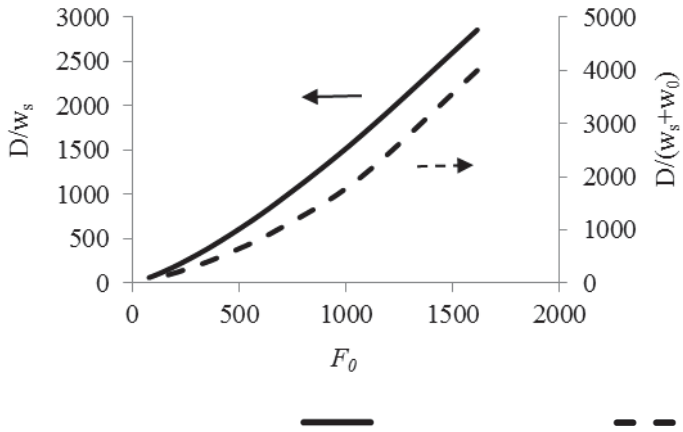
3000
2500
2000
1500
1000
500
0
D/w_s
5000
4000
3000
2000
1000
0
D/(w_s+w_0)
0
500
1000
1500
2000
F_0

It should be noted that in real superconducting films, the I_S distribution can be less uniform or different from the case of the Meissner effect. In addition, the depth of magnetic field penetration in the film $\lambda_\perp = \lambda^2 / h$ can be much more than λ, which should be taken into account when estimating F_{0m}. Owing to these factors and the possibility of nanostructuring of the magnetic field concentrator [3], the F_0 value can be enhanced and brought closer to the potential F_{0m} value. This approach is suitable for wide active strips (e.g., $w_S \geq 4$ μm, as in our case).

The threshold sensitivity of the sensor depends on the concentration coefficient as $\delta B_0 \sim 1/F_0$ [3]; therefore, the high F_0 value undoubtedly affects the MFS efficiency. Hence, the MFCs based on LTSC films can be considered more effective than the MFCs based on HTSC films.

concentrations: 0,001%, 0,01%, 0,02%, 0,05%, 0,1%, 0,15% и 0,2%. SWCNT-90A have been used as CNTs (Ltd. "Carbon Chg", Russia). Water-albumin CNT solution was created as a result of BWA powder (25% of water mass) addition in water CNT solution. Next the solution was mixed by magnet shaker and ultrasound bath. Also the water-albumin dispersion without the CNT content was obtained. Next, 3 different samples were obtained for each dispersion: the thin film on a silicon substrate (for Raman spectroscopy study), obtained by laser irradiation of biocompatible nanocomposite at 810 nm, the sample in the form of a powder obtained by grinding of 810 nm laser dehydrated biocompatible nanocomposite (for infrared (IR) spectroscopy study), and the sample in the form of a compressed biocompatible nanocomposite (for Raman spectroscopy study). Biocompatible nanocomposite samples for Raman spectroscopy study are shown on Fig. 1.

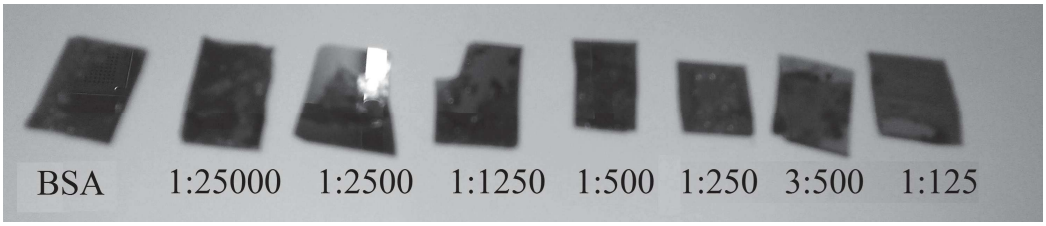

a

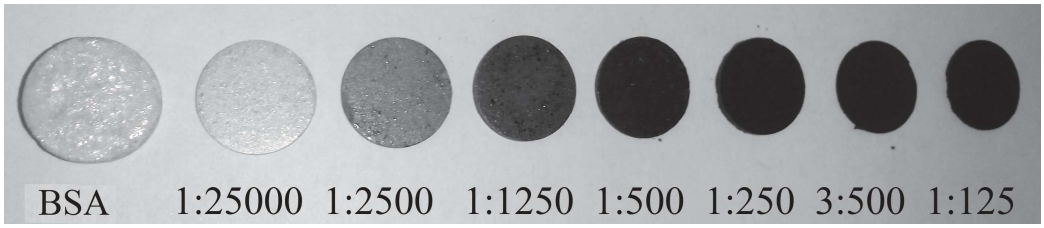

b

Fig. 1 Biocompatible nanocomposite samples for Raman spectroscopy study: in the form of a thin film (a) and in the form of a compressed biocompatible nanocomposite (b)

Raman spectroscopy is a type of vibrational spectroscopy and is very often used in the studies of carbon nanotubes and other allotropic modifications of carbon because of its extensive features. This method shows such parameters of CNTs as diameter and defectiveness. [4]. Also, as CNTs have a high intensity of Raman scattering, the concentration of CNTs can be measured in the case of the thin film sample by the intensity of G-band.

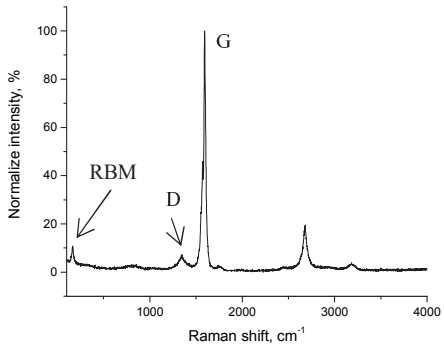

a

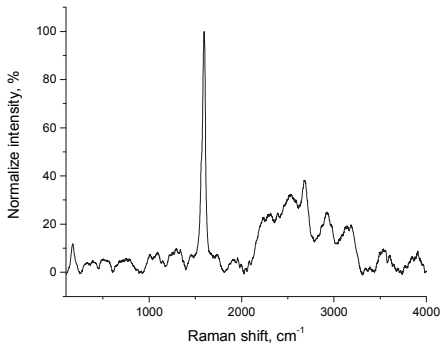

b

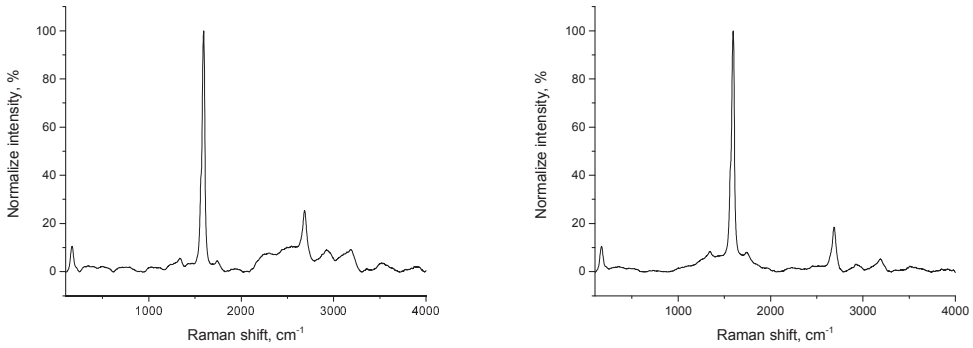

c **d**

Fig. 2 Raman spectra of CNT (a) and biocompatible nanocomposite with next CNT and BSA mass proportions: 1:500 (b), 1:250 (c) and 1:125 (d)

In this work, the Raman spectrometer LabRAM HR Evolution (Horiba, France) was used. As an excite source the 514nm argon laser (Melles Griot, USA) was used. Raman spectra were obtained for two types of samples: in the form of a thin film (Fig.3a) and in the form of a compressed biocompatible nanocomposite (Fig.2b,c,d). A range of CNTs alone, used in the manufacture nanocomposite (Fig.2a) was also obtained.

All spectra of biocompatible nanocomposite samples have the following bands that are characteristic for CNTs: radial breathing mode (RBM), D-band and G-band. Frequencies of radial breathing mode are connected with the diameter of the nanotubes by the following formula: ωRBM = 234/d + 10. The ratio of the intensities of D-band/ G-band characterizes the defectiveness of CNTs. Frequencies ωRBM remain unchanged for biocompatible nanocomposite samples regardless of the 165 cm-1 concentration, which corresponds to a CNT diameter of 1.5 nm. Also the ratio of the intensities of D-band/ G-band remains constant (~1/10). This indicates that CNTs do not undergo structural changes during the preparation of biocompatible nanocomposite under the influence of factors such as laser light and powerful ultrasonic mechanical effect.

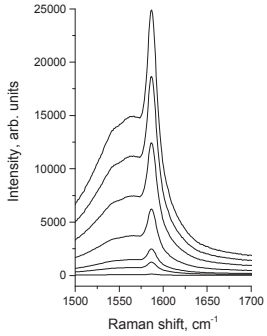

Intensity of G-band, arb. units	CNT and BSA mass proportions
23883	1:125
19582	3:500
13441	1:250
6000	1:500
2788	1:1250
1244	1:2500
144	1:25000

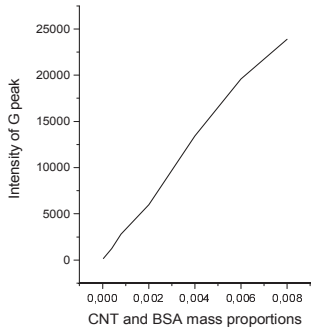

a **b** **c**

Fig. 3 Raman spectra of range 1500-1700 cm-1 of thin films of biocompatible nanocomposite with next CNT and BSA mass proportions (from bottom to top): 1:25000, 1:2500, 1:1250, 1:500, 1:250, 3:500 and 1:125 (a), table (b) and graph (c) dependence of the intensity of G-band and CNT and BSA mass proportions

The analysis of the Raman spectra of thin films of biocompatible nanocomposite on silicon substrates and the concentration of the CNTs in these films showed a linear dependence of the intensity of G-band from the mass concentration of CNTs. This method works in the case of the same conditions of collecting the spectral data.

Infrared (IR) spectroscopy is a technique based on the vibrations of atoms of a molecule. An IR spectrum is commonly obtained by passing IR radiation through the sample and determining what fraction of the incident radiation is absorbed at a particular energy. The energy at which any peak in an absorption spectrum appears corresponds to the frequency of a vibration of a part of a sample molecule. Fourier transform infrared (FTIR) spectroscopy has dramatically improved the quality of IR spectra and minimized the time required to obtain data [5]. This method allows to find the structure of molecules of various substances with relatively short molecules: antibiotics, enzymes, alkaloids, polymers, complex connections, etc using absorption spectra. The number and position of peaks in the IR absorption spectra can show the nature of the substance (qualitative analysis) and the intensity of absorption bands — the number of substances (quantitative analysis). FTIR spectroscopy can be used to detect the presence of carbon nanotubes (CNTs) in the biocompatible nanocomposite samples, as well as to establish interaction between the carbon nanotubes and bovine serum albumin.

Biocompatible nanocomposite powders with different CNT and BSA mass proportions were grounded with highly purified KBr crystal in an agate mortar and the mixtures were pressed to form a pellet. The FTIR spectra were measured by a FTIR spectrometer Nicolet iS50 (Thermo Scientific, USA) in 400-4000 cm-1 frequency range (Fig.4).

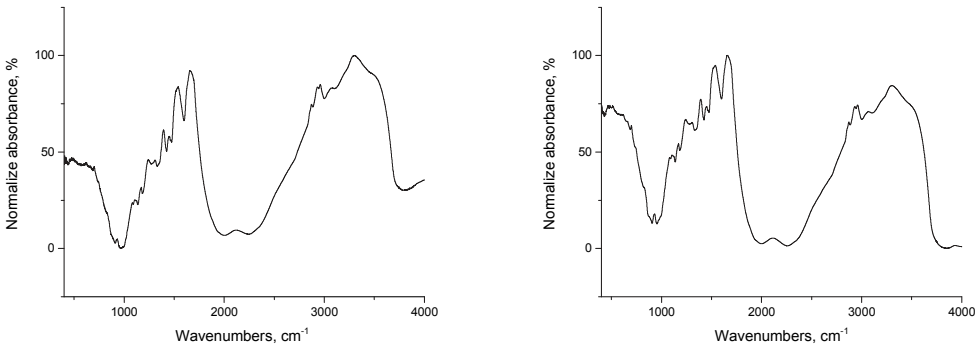

a **b**

Fig. 4 FTIR spectra of bovine serum albumin (a) and biocompatible nanocomposite sample with 1:250 CNT and BSA mass proportions (b)

In the spectra of bovine serum albumin and biocompatible nanocomposite samples there are absorption bands typical for proteins, which are associated with the following vibrations: the peak near 1650 cm-1 is the Amide I band. It results from the C=O stretching vibrations of the peptide bond. Similarly, the peaks near 1540 cm-1 (N-H bending vibration/C-N stretching vibration) and 1240 cm-1 (C-N stretching vibration/N-H bending vibration) are the Amide II band, and Amide III band, respectively. The peak near 3300 cm-1 is thought to be N-H bending vibration and the peak near 1400 cm-1 to result from protein side-chain COO-.

As the absorption peak position and shape of the amide I band differ according to the secondary structure, peak analysis can yield information on the secondary structure. Also, depending on the concentration of CNTs in the biocompatible nanocomposite there is a change in the shape and intensity of the main peaks, which indicates the influence of CNTs on bovine serum albumin.

In this work, the samples of biocompatible nanocomposite with different concentrations were produced and were studied using the methods of Raman and infrared spectroscopy. It was established using Raman specroscopy that CNTs do not undergo structural changes during the preparation of biocompatible nanocomposite under the influence of factors such as laser light and powerful ultrasonic mechanical effect. There was also a linear dependence of

the intensity of G-band from the mass concentration of CNTs in the biocompatible nanocomposite. Also, depending on the concentration of CNTs in the biocompatible nanocomposite the shape and intensity of the main peaks are changing, which indicates the influence of CNTs on bovine serum albumin. Studies conducted in this work indicate the applicability of Raman and infrared spectroscopy to study biocompatible nanocomposite protein-based and carbon nanomaterials.

References

[1] A. A. Dedkova, A.Yu.Gerasimenko, L.P. Ichkitidze, V.M. Podgaetsky, S.V. Selishchev, "A study of preparation techniques and properties of bulk nanocomposites based on aqueous albumin dispersion", Optics and Spectroscopy. **115(2)**, 283-289 (2013).
[2] A.Yu. Gerasimenko, O.V. Gubarkov, L.P. Ichkitidze, V.M. Podgaetsky, S.V. Selishchev, O.V. Ponomareva, "Nanocomposite solder for laser welding of biological tissues", Semiconductors. **45(13)**, 93–98 (2011).
[3] N.N. Zhurbina, U.E. Kurilova, L.P. Ichkitidze, V.M. Podgaetsky, S.V. Selishchev, I.A. Suetina, M.V. Mezentseva, E.M. Eganova, A.A. Pavlov, A.Yu. Gerasimenko, "Investigation of cell proliferative activity on the surface of the nanocomposite material produced by laser radiation", Proc. of SPIE. **9917**, 991718-1 - 991718-7 (2016).
[4] M. S. Dresselhaus, G. Dresselhaus, R. Saito, A. Jorio, "Raman spectroscopy of carbon nanotubes", Physics reports. **409(2)**, 47-99 (2005).
[5] B. Stuart, *Infrared spectroscopy,* (John Wiley & Sons, New York, 2005)

Using of hydrogels in 3D-bioprinting

S.A. Peleshok, M.V. Titova, M.I. Eliseeva, V.S. Sheveleva, A.F. Mullashev, A.K. Astanina

Military Medical Academy named after S.M. Kirov, 194044, Academician Lebedev street, 6, Saint-Petersburg, Russia

3D-bioprinting is a complex multifunctional process, depending on the interaction of a number of factors, determining of which is the right choice of matrix or substrate for printing-hydrogel [1].

The analysis of literature for the period from 2012 to 2016 was conducted with the aim to determine the choice of hydrogels among the variety of biocompatible natural or synthetic hydrogels with the most relevant physical and chemical properties for cells and tissues.

The elaboration of functional biocompatible materials assumes the deep understanding of biology of cells and tissues formed by cells; the knowledge of functions of extracellular matrix, which keeps up the cells and tissues, the essential factors of growth and differentiation. Uniform seeding density of the cells is crucial for the perfect bioink [2]. General morphological characteristics of the tissue structure depend on this homogeneity.

non-toxicity and non-toxigenicity, biocompatibility (non-immunogenicity), ability to neovascularization and neoinnervation, ability to perform the function of a frame and nutrient for cell components (hydrogels may contain the growth factors to maintain cells proliferation in 3D-format) to stimulate the proliferation[5]. It is important to take into account the physicochemical characteristics: material must have adequate fluidity, but retain adequate viscosity to keep up the selected shape, have strength, possess adhesive properties to cell cultures, contain certain amount and length of cross-links, which impart volume to hydrogels, possess the necessary porosity[6,7].

One of the main tasks in the field of hydrogels creation for 3D-bioprinting is the choice of materials, which should be compatible with biological materials and the printing process, providing required mechanical and functional properties of tissue constructions [8-10].

The analysis of literature allowed to get information about physical and chemical properties, methods of synthesis of hydrogels, the mechanisms of their formation and their structure. The literature about the hydrogels using in 3D-bioprinting is represented.

References

[1] R. DeVolder, H.J. Kong, *Wiley Interdiscip Rev Syst Biol Med.* , 2012 Jul-Aug;4(4):351-65.
[2] J. Jia, D.J. Richards, S. Pollard, Y. Tan, J. Rodriguez, R.P. Visconti, T.C. Trusk, M.J. Yost, *Acta Biomater* , 2014 Oct; 10(10): 4323–4331.
[3] S. Kapoor , S.C. Kundu , *Acta Biomater.,* 2016 Feb;31:17-32.
[4] F. Chen, S. Yu, B. Liu, Y. Ni, C. Yu, Y. Su, X. Zhu, X. Yu, Y. Zhou, D. Yan., *Sci Rep.,* 2016 Jan 28;6:20014.
[5] J. Shan, Q. Chi , H. Wang, Q. Huang, L. Yang, G. Yu, X. Zou., *Cell Biol Int.,* 2014 Nov;38(11):1233-43.
[6] J. Liu, H. Zhen, P.S. Poh, H.G. Machens, A.F. Schilling., *Int J Mol Sci.,* 2015 Jul 14;16(7):15997-6016.
[7] B. Duan, E. Kapetanovic, L. A. Hockaday, J. T. Butcher, *Acta Biomater.*, 2014 May; 10(5): 1836–1846.
[8] C. Mandryck, Z. Wang, K. Kim, D.H. Kim., *Biotechnol Adv. ,* 2015 Dec 23. pii: S0734-9750(15)30066-5.
[9] A. Skardal, A. Atala., *Ann Biomed Eng.,* 2015 Mar;43(3):730-46.
[10] M.M. Stanton, J. Samitier, S. Sánchez , *Lab Chip.,* 2015 Aug 7;15(15):3111-5.

Investigation of optical limiting properties of J-type phthalocyanine dimer of Zn and it conjugate with single-walled carbon nanotubes

M.S. Savelyev[1], A.Yu. Tolbin[2,3], A.A. Polokhin[1], I.B. Rimshan[1], A.Yu. Gerasimenko[1], L.G. Tomilova[2,3]

1. National Research University of Electronic Technology, 124498, Zelenograd, Moscow, Russia

2. Institute of Physiologically Active Compounds, Russian Academy of Sciences, 142432, Chernogolovka, Moscow Region, Russia

3. Department of Chemistry M. V. Lomonosov Moscow State University, 119991 Moscow (Russian Federation)

The development of lasers, accompanied by an increase in laser intensity, enhances the interest in the study of optical limiters. Since the effect of radiation with a sufficiently high intensity can damage the photosensitive optical device and organs of vision. Spectral filters cannot be used to protect, if the wavelength of hazardos laser radiation coincides with the operating wavelength. In addition, short duration of laser pulses makes it practically impossible to apply controlled shutter, including automatic LCD shutter. Creation of effective means of protection from laser radiation of high power requires the development of optical materials (working substance), with their transparence being decreased sharply above a

certain critical value of the laser intensity (limiting threshold) due to the appearance of non-linear optical properties.

Among the large number of nonlinear optical absorbers that have been studied, phthalocyanines and their derivatives could have promising application due to their high nonlinearities and ultrafast response times [1-3]. Chemical modification of phthalocyanines results in altering their nonlinear optical response, and thereby influences the optical limiting. The advantage of phthalocyanine is the possibility to functionalize carbon nanotube [4], which allows you to vary the parameters of nonlinear optical limiters, and improve their efficiency.

In our study dimeric phthalocyanine complex of Zn of J-type (ZnPc) [5] in tetrahydrofuran (THF) and conjugates of Zn with single-walled carbon nanotubes (SWCNTs) [6] in water were used. Linear transmittance of the prepared samples was 70%. Aqueous dispersions of conjugate were prepared while using an ultrasonic homogenizer.

In the experimental study of the threshold effect under nonlinear limitation we used the focusing of the input laser radiation, that allows to obtain the input intensity required for significant demonstration of nonlinear effects. A detailed description of the experimental setup is given in [7]. In this study, an experimental setup was improved by the introduction of an additional lens, which allows to form a Kepler telescope and conduct studies for the construction of the optical limiter as a whole, not only to control the transmitted laser radiation. The obtained results of measurements were processed on the basis of radiation-transfer equation, in which the specific mechanisms of laser interaction with the nonlinear medium were not taken into account [8]. It is assumed that interaction of laser radiation is limited to its absorption by the nonlinear medium. Attenuation of the radiation due to, e.g., scattering, is a substantially more complex problem that does not currently have satisfactory solution.

The solution of the radiation transfer equation for intensity (power density) of laser radiation $I(\rho, \varphi, z, t, d)$ after passing through a limiter (output intensity) of thickness d can be written in implicitly form:

$$\int_{I_0(\rho,\varphi,z,t)}^{I(\rho,\varphi,z,t,d)} (I\mu(I))^{-1}\, dI = -d\ . \tag{1}$$

where $I_0(\rho, \varphi, z, t)$ – intensity of an initial laser pulse, $\mu(I)$ – dependence between nonlinear absorption coefficient and power density, z – sample displacement relative to the lens focus.

It is known that interaction of laser radiation with conjugates of phthalocyanines with SWCNTs have threshold type [9] i.e. they start to operate at intensity values above certain threshold value I_c. That's why it is reasonable to use the model in which absorption coefficient $\mu(I)$ has threshold type. This model allows to obtain optical properties the working substances with a threshold effect, what is very important for the development of effective optical limiters. For the threshold model, the dependence between nonlinear absorption coefficient and intensity is described by the expression:

$$\mu(I) = \alpha + \beta(I - I_c)\eta(I - I_c), \tag{2}$$

where $\eta(\bullet)$ is the Heaviside step function. Working substance of the optical limiter for the threshold model is characterized by three parameters: the coefficient of linear absorption α [m^{-1}], the coefficient of nonlinear absorption β [$m \cdot W^{-1}$] and the limiting threshold I_c [$W \cdot m^{-2}$].

The optical characteristics of the limiters determine by use of z-scan technique, which measures the value of the normalized transmittance passing through the limiter at the displacement z of the sample relative to the focus of the lens. Experimentally normalized transmittance $T(z, d)$ can be found according to the results of z-scan:

$$T(z,d)=\frac{U(z,d)}{U_0}\exp(\alpha d)\,. \qquad (3)$$

where z is the displacement of the sample, $U(z,d)$ is output pulse energy, U_0 is input pulse energy, α is linear absorption coefficient, d is the thickness of the layer.

The solution of equation (1) by substituting the expression (2) made it possible to find an analytical representation for the function $I(\rho,\varphi,z,t,d)$, and the theoretical value of the total energy transmitted pulse $U(z,d)$ through the limiter was calculated using the formula:

$$U(z,d)=\int_{-\infty}^{+\infty}\int_{0}^{2\pi}\int_{0}^{\infty} I(\rho,\varphi,z,t,d)\rho\,d\rho\,d\varphi\,dt\,. \qquad (4)$$

Substituting equation (4) into formula (3) allowed to obtain function $T(z,d)$ for fitting the experimental values of normalized transmittance and obtaining unknown parameters β and I_c.

We calculated values of the nonlinear absorption coefficient β and the limiting threshold I_c and radius beam waist w_0 from the z-scan data. These results are summarized in the table 1. Experiments with the fixed location of the optical limiter was used for obtaining the dependence output (peak) fluence vs input (peak) fluence. This output characteristic describes the basic properties of optical limiters on the sample for optical materials based on ZnPc in THF and conjugate ZnPc with SWCNTs in water are shown in figure 1.

Table 1. The calculations of the working substance parameters of the limiter using z-scan data

Working substance	**λ, nm**	***U*₀, mJ**	**α, cm⁻¹**	***d*, cm**	***w*₀, μm**	**β, cm·GW⁻¹**	***Ic*, MW/cm²**
ZnPc in THF	532	1.6	1.5	0.2	64	330	1.6
Conjugate ZnPc with SWCNTs in water		1.6	1.5	0.2	55	340	2.6
ZnPc in THF	1064	1.6	0.5	0.2	120	0	–
Conjugate ZnPc with SWCNTs in water		1.6	1.5	0.2	120	388	10.2

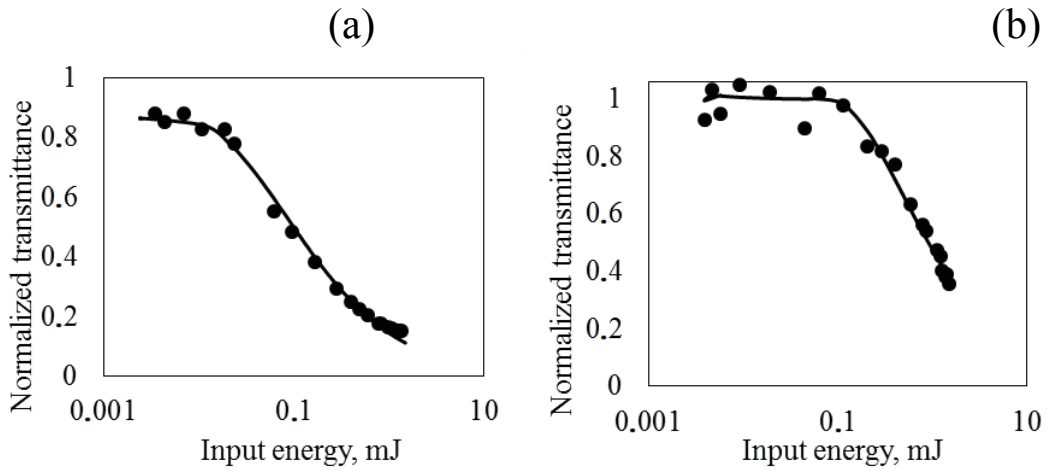

Figure 1. Experimental dependence output (peak) fluence vs input (peak) fluence (●) and approximation by threshold model for conjugate ZnPc with SWCNTs in water: wavelengths 532 nm (a) and 1064 nm (b)

Proposed threshold model characterizing limiters of intensity laser radiation takes into account the threshold nature of nonlinear interaction of irradiation with the nonlinear optical material. The threshold model allow obtaining the dependence of absorption coefficient against the radiation intensity of substance in accordance with z-scan data and to do approximation of output characteristics (dependence output (peak) fluence vs input (peak) fluence).

Samples ZnPc in THF do not exhibit the nonlinear effects on the wavelength of 1064 nm, since neither an organic solvent nor the dye do absorb laser light at this wavelength. Thus, this working substance can be used as a working substance of the optical limiter at the wavelength 532 nm as at 1064 nm nonlinear effects were not found. To create a limiter of laser radiation in a wide spectral range, conjugate ZnPc with SWCNTs was used. It was found that when it is used as a working substance of the limiter we can achieve high nonlinear absorption coefficient values at a wavelength of laser radiation 532 nm and 1064 nm. However, it is worth noting that functionalization of phthalocyanine by nanotubes improves the characteristics to limit the laser radiation at a wavelength of 532 nm, which follows from the minimum values of the normalized transmittance of 0.1 and 0.3 for wavelengths of 532 nm and 1,064 nm, respectively.

The Studies indicate the possibility to apply the dispersed materials based on carbon nanotubes in comprising optical limiters of high power laser radiation. This work was provided by the Ministry of Education and Science of the Russian Federation (Agreement 14.575.21.0089, RFMEFI57514X0089)

References

[1] Chen J, Zhang T, Wang S, Hu R, Li S, Ma J. S., Yang G, "Intramolecular aggregation and optical limiting properties of triazine-linked mono-, bis- and tris-phthalocyanines," Spectrochim Acta A Mol Biomol Spectrosc. **149**, 426 (2015).

[2]Nyokong, T., Fashina, A., "Nonlinear optical response of tetra and mono substituted zinc phthalocyanine complexes," Journal of Luminescence **167**, 71 (2015).

[3]Tuhl, A., Manaa, H., Makhseed, S., Al-Awadi, N., Mathew, J., Ibrahim, H. M., Nyokong, T., Behbehani, H., "Reverse saturation absorption spectra and optical limiting properties of chlorinated tetrasubstituted phthalocyanines containing different metals," Optical Materials **34**, 1869 (2012).

[4] He, N., Chen, Y., Bai, J., Wang, J., Blau, W. J., Zhu, J., "Preparation and Optical Limiting Properties of Multiwalled Carbon Nanotubes with π-Conjugated Metal-Free Phthalocyanine Moieties," J. Phys. Chem. C **113**, 13029 (2009).

[5]Tolbin, A. Yu., Pushkarev, V. E., Balashova, I. O., Dzuban, A. V., Tarakanov, P. A., Trashin, S. A., Tomilova, L. G., Zefirov, N. S., "A highly stable double-coordinated 2-hydroxytri(tert-butyl)-substituted zinc phthalocyanine dimer: synthesis, spectral study, thermal stability and electrochemical properties," New. J. Chem **38**, 5825 (2014).

[6] Tolbin, A. Yu., Khabashesku, V. N., Tomilova, L. G., "Synthesis of phthalocyanine tert-butyl ligand conjugates with fluorinecontaining single-walled carbon nanotubes having mobile ether bonds," Mendeleev communications **22**, 59 (2012).

[7] Tereshchenko, S. A., Podgaetsky, V. M., Gerasimenko, A. Yu., Savel'ev, M. S., "Investigation of Nonlinear Characteristics of Intensity Limiters of High_Power Laser Radiation," Optics and Spectroscopy, **116**, 454, (2014).

[8]Tereshchenko, S. A., Podgaetsky, V. M., "Determining the parameters of the laser radiation intensity limiter based on a time-dependent equation of radiative transfer in a nonlinear medium," Quantum electron **41**, 26 (2011).

[9]Tereshchenko, S. A., Podgaetskii, V. M., Gerasimenko, A. Yu., Savel'ev, M. S., "Threshold effect under nonlinear limitation of the intensity of high-power light," Quantum electron **45**, 315 (2015).

The mechanical and structural characteristics of the compounds of laser biological tissue using solders based nanoparticles and an organic dye

I.B.Rimshan, D.I.Ryabkin, M.S. Savelyev, L.P. Ichkitidze, V.M. Podgaetsky, E. S. Piyankov, E.N. Shimarov, A.Yu. Gerasimenko

National Research University of electronic technology, 124498, Moscow, Russia

Fastening of the biological tissue is necessary for rapid healing process after surgery or trauma. The heat from the laser makes it possible to connect the tissue in a contactless manner. This avoids foreign body reaction, to reduce the risk of inflammatory reactions and tissue scarring.

It has been experimentally proved that with the right set of radiation parameters and the composition of the solder used, it is possible to obtain a solid, tight connection and alete laser biological tissue of various types. In [1] presented data on the use of Nd:YAG-laser, connected by a small intestinal injury in rabbits[2]. In [3] the histological study of the laser connection rabbit facial nerve have shown positive results. laser adhesion method may also be effective in restoring the integrity of the damaged tendon [4].

Addition of bovine serum albumin (BSA) in the solder can improve adhesion tissues inactivate hepatitis viruses and HIV and to reduce inflammation and thrombus formation on the coupling portion. The use of carbon nanotubes (CNT) contribute to the cultivation, propagation and branching of cells on the surface of the nanotubes and ensures the regeneration of biological tissue. The dye indocyanine green (ICG), can increase the intensity of the absorption of laser radiation in the impact zone, thereby reducing damage to surrounding healthy tissue.

In this paper we investigate the dependence of the strength of the laser connection bovine tendon on the type of solder. Five solder compositions were used. Solder represented the aqueous protein dispersion with the addition of the BSA, and two types of CNTs: multiwalled and single-walled and ICG (figure1).

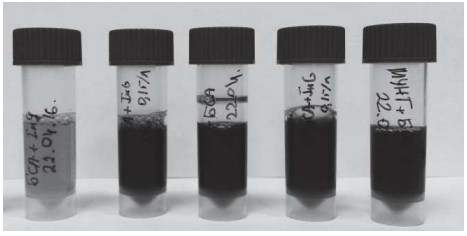

Fig.1 Five solder compositions used in laser connection.

The laser system for welding of biological tissues includes a radiation unit, a laser guidance system, and an adaptive thermal stabilization system (figure2).

The laser system includes a power supply connected to the diode laser head, operating at a wavelength of 810 nm. For the guidance of the laser beam includes a pilot laser with a lasing wavelength of 532 nm. The radiation from the laser head to the site of welding is transmitted through an optical fiber. At its end is a collimator lens. When laser heating is emitted thermal infrared radiation from place of fabric connections and recorded the IR sensor. With an output from the temperature information is supplied in the microcontroller unit. Temperature control of tissue welding place of by means of PID algorithm [5].

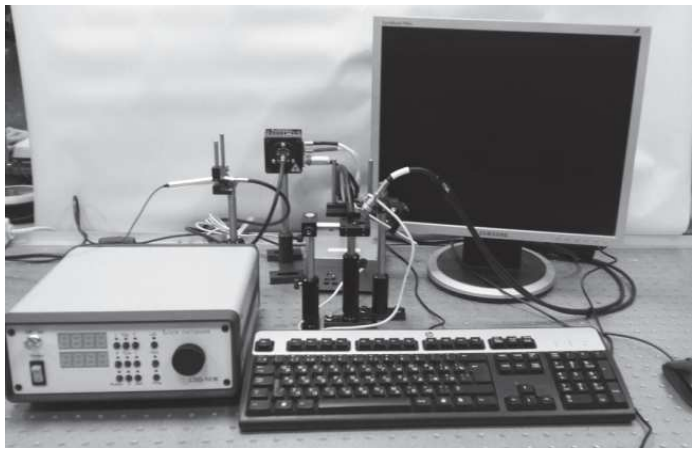

Fig.2 The laser system for welding of biological tissues.

For laser adhesion used bovine tendon. The tendon was divided into samples with a length of 2-2.5 cm and a thickness of 1-2.5 mm. For each of the solder composition was prepared 3 experimental sample. Prior to surgery the samples were stored at -21 ° C. Samples were scattered in the middle. Then place covered with solder connection. Adhesion samples occurred in spot mode. Each point of demanding compliance with equal conditions of its formation. Time of receipt of a adhesion point was 60 seconds. Investigation of tensile strength was performed with a digital dynamometer. Comparing the strength of the laser connections carried out with respect to whole tendon samples. The results of strength measurements are shown in table 1.

Table 1 The dependence of the strength of the composition of the solder.

Solder	Strength, MPa
BSA+MWCNs	0,41
BSA+MWCNs+ICG	0,82
BSA+SWCNs	0,14
BSA+SWCNs+ICG	0,38
BSA+ICG	0,54

Maximum strength was achieved using solder BSA+MWCNT+ICG. The lowest strength had samples obtained with BSA+SWCNT. However, this and previous studies indicate a weak dependence of the strength of the laser connections on the type of biological tissue. Typically, this value does not exceed the strength of 1 MPa. At the same time, the magnitude of the relative strength (bonding strength to the strength of whole tissue) is largely dependent on the tissue type. According to observations, the relative strength is less for solid tissues (such as skin, tendon and bone). It is on contrary for delicate tissues (such as internal organs tissues). The stomach pig muscular layer strength was σ_1 = 0,982 MPa, and at this research the bovine tendon strength was σ_2 = 11,63 MPa. The corresponding laser weld strength wereσ_{1weld} = 0,57 MPa and σ_{2weld} = 0,41 MPa. The relative strengths were σ_{1abs} = 58%, σ_{2abs} = 7,1%.

Structural studies of laser compounds were conducted using optical microscopy. Studies have revealed partially or completely unconnected areas and hot spots (figure.3)

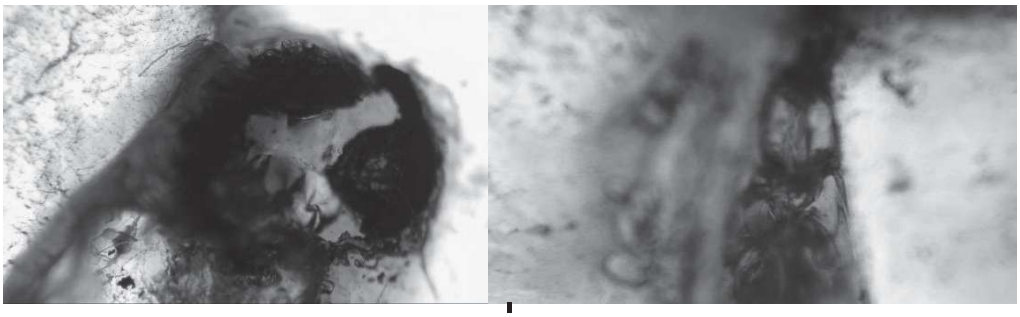

a b

Fig.3 Microscopic image (zoom - 50x) of the sample structure with uneven adhesion (a) and hot spots (b).

Analysis of the results of the structural and mechanical characteristics revealed that in addition to the solder MWNT prepared most uniform across the width of the samples with a high strength. In the case of the addition of SWNTs, the majority of the samples were not connected over the entire thickness. This is probably due to the most severe degree of aggregation of SWCNTs under the influence of a covalent bond. Consequently, the formation of the spatial frame of the SWCNT aggregates under the influence of laser radiation was less pronounced. It is accordingly affected the results of strength. Using the dye in each of the formulations with MWCNTs or SWCNTs possible to avoid the presence in the structure of the connection terminals from overheating, increasing the strength of the samples. Samples prepared without the addition of nanotubes in the solder, uniform structure yielded a greater number of samples, and only one case was observed in the connection portion is not along the whole thickness. Accordingly, the solder composition showed the second result of strength. Thus, the addition of MWNTs into the protein solder and / or ICG to obtain the best structure and mechanical results.

This work was provided by the Ministry of Education and Science of the Russian Federation (Agreement 14.575.21.0044 RFMEFI57514X0044).

References

[1] D. T. Dempsey, D. Showers, P Valente, R. Sterling, and J. V. White, "Tissue fusion of the rat stomach with the CO_2 laser", Surgical forum. **38**, 118-120 (1987).
[2] J. V. White, "Laser instrumentation-A microtenaculum for laser tissue fusion", Lasers in Surgery and Medicine. **8**, 433-434, (1988).
[3] J. Bloom, B. Bleier, S. Goldstein, P. Carniol, J. Palmer, N Cohen, "Laser Facial Nerve Welding in a Rabbit Model", Archives of Facial Plastic Surgery. **40**, 52-58 (2012).
[4] F. El-Wakil Tarek et. all, "Tendon Repair by Suturing Vs Carbon Dioxide Laser Welding: An in-Vivo Study in Rabbits", Egyptian Journal of Plastic and Reconstructive Surgery. 27, 295-303, (2003).
[5] A. Yu. Gerasimenko, L. P. Ichkitidze, A. A. Pavlov, E. S. Piyankov, D. I. Ryabkin, M. S. Savelyev, S. V. Selishchev, I. B. Rimshan, N. N. Zhurbina, V. M. Podgaetskii, "Laser System with Adaptive Thermal Stabilization for Welding of Biological Tissues", Biomedical Engineering. **49**, 344-348, (2016).

Mobile device for adequate control of the human adaptation abilities by means of the neuro-electrostimulation

M.V. Babich, V.S. Kublanov
Ural Federal University named after the first President of Russia B.N. Yeltsin 620002, 19 Mira str., Yekaterinburg, Russia

Introduction

In the process of life, the human body is constantly exposed to various influences of environmental factors and must, in turn, adapt to these factors. The constancy of the internal environment (homeostasis) depends on the body ability to adapt. According the modern theory of health, the adaptive ability of the human body should be considered as a measure of the health [1]. Transition from healthy state to disease goes through a series of transitional, so-called prenosological, states. Decrease of functional reserves and the increase of tension of regulatory systems cause evolution of the prenosological states.

Abnormalities correction during prenoslogical states usually cost less compared to disease treatment. Therefore, the identification of such abnormalities and the development of methods for their correction is an actual task.

As an indicator of prenosological states, many authors suggest the application of the autonomic nervous system (ANS) characteristics [2,3]. Therefore, it is possible to correct prenosological state by means of methods intended for the control of the ANS parameters.

Currently, there are a number of methods that can solve such task. Let us consider only drug-free methods, the most effective devices are the "SYMPATHOCOR-01" [4], the PONS [5] and the GammaCore [6].

The PoNS device produce electrical current stimulation of the tongue by means of 143 electrodes. It is hypothesized that usage of the PONS results in a change in the activity of the brain stem nuclei, due to electrical stimulation of the trigeminal and facial nerves [5].

The GammaCore device implements the technology of non-invasive transcutaneous stimulation of the vagus afferent pathways in the neck. Vagus nerve stimulation allows one to modulate the parasympathetic tone of internal organs [6].

The unique feature of the "SYMPATHOCOR-01" device is the application of a spatially distributed field of current pulses for stimulation of the upper and middle cervical ganglia. Ganglia belongs to the sympathetic division of the ANS. Time-frequency characteristics of this field of current pulses are similar to characteristics of endogenous processes, which include nerve impulse propagation speed in myelinated and unmyelinated fibers [4]. In the treatment process with application of the "SYMPATHOCOR-01" device, dynamic correction of the sympathetic nervous system technique is realized. This technique allows either block or stimulate the activity of the sympathetic nervous system (SNS). Effect of the technique application depends on the autonomic balance, determined by the ratio of activity of the sympathetic and parasympathetic divisions of the ANS [7]. The "SYMPATHOCOR-01" device was developed over 20 years ago, was included in the State Registry of medical devices in Russia (registration certificates №FSR 2007/00757 from 09.29.2007). The Ministry of Health recommended the "SYMPATHOCOR-01" device for serial production and application in clinical practice. Its manual was approved in August 1999 by the head of the State Control Department for Quality, Efficiency, and Safety of Pharmaceuticals and Medical Equipment of the Russian Ministry of Health.

The necessity of development of the mobile device for adequate control of the human adaptation abilities, to be referred as the neuro-electrostimulation device, is determined on the one hand, by the fact that the technical realization of the "SYMPATHOCOR-01" device is

obsolete nowadays. On the other hand, according to the World Health Organization data, there is growing number of diseases associated with cognitive disorders and neurodegenerative processes. In process of the neuro-electrostimulation device development, we made a number of technical solutions that will be useful in the treatment of these diseases.

Materials

Block diagram of the neuro-electrostimulation device is shown in Fig. 1. The device includes a neuro-electrostimulatios subsystem, an electrocardiogram (ECG) registration subsystem, a microcontroller unit and a control unit.

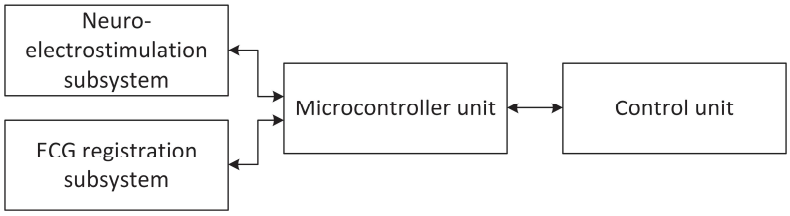

Fig. 1 Block diagram of the neuro-electrostimulation device.

The neuro-electrostimulation subsystem creates spatially distributed field of current pulses, used for ANS activity correction. The ECG registration subsystem records ECG using first lead scheme for further heart-rate variability analysis and ANS activity assessment. The microcontroller unit receives and processes control commands, controls the neuro-electrostimulation and the ECG registration subsystems, and coordinates functioning of these subsystems.

The microcontroller unit collects and wraps informational messages, sends messages to the control unit. Informational messages contains current patient ANS activity assessments and current device subsystems states.

The control unit displays current device state and patients ANS activity assessments. Doctor may change current biotropic parameters of spatially distributed field of current pulses during medical procedure. As the control unit, one can use either personal computer or tablet device.

Neuro-electrostimulation subsystem

Block diagram of the neuro-electrostimulation subsystem is shown in Fig. 2. The neuro-electrostimulation subsystem includes:

- two multielement electrodes, one is used as anodes system, other – as cathodes system;
- voltage controlled current source, which is controlled by the microcontroller digital-to-analog converter (DAC);
- anodes multiplexor MUX1, which connects one of the partial anodes with positive pole of current source;
- cathodes multiplexor MUX2, which connects one of the partial cathodes to the ground.

The microcontroller controls neuro-electrostimulatrion procedure by either switching-on, switching-off or changing current partial electrodes by two enable lines (EN) and two address buses (A0-A3), or changing current level by the built-in DAC.

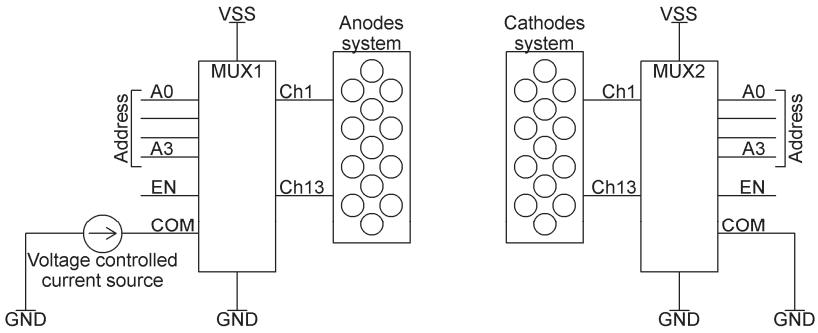

Fig. 2 The neuro-electrostimulation subsystem block diagram.

During neuro-electrostimulatrion procedure microcontroller performs two steps:

- connects one of the partial anodes to the voltage controlled current source;
- sequentially connects the partial cathodes to the ground.

After that in the space between the anodes and the cathodes, the partial field of current pulses with the partial duration τ is formed. After completion of the partial cathodes connection cycle, the microcontroller turns off all partial cathodes and, after the time interval (T_K), starts new cathodes connection cycle. T_K is the time interval between same partial cathode in two successive switching cycles of the partial cathodes. Frequency $\nu_K=1/T_K$ is called a frequency of the pulses.

In accordance with the information about patient's current condition and the control program, the microcontroller can change the currently connected partial anode. The ratio between the time of switching the partial anode (T_A) must satisfy the condition $T_A \gg T_K > \tau$.

At the anodes location in the neck area of the patient, a space-centered structure is formed with a maximum current density of a current, disposed at the center of the anode. The ability to switch allows the anodes to move the spatially distributed current structure, which increases the neuro-electrostimulation possibility by augmenting the number of influence targets in the neck region. Neuro-electrostimulation improvement is achieved by the involvement in the regulatory process in addition to the ANS, the brain structures responsible for motor, visual, auditory, vestibular, and other functions. Clinical studies have shown the improvement of the cognitive function [7].

ECG registration subsystem

For the ECG registration, first-lead scheme is used. During ECG signal registration, the following steps are performed: analog noise filtering with 2 kHz cut-off frequency by the RC-filter, differential signal gaining by the differential programmable gain amplifier, and analog-to-digital conversation by the 24-bit sigma-delta analog-to-digital converter (ADC).

The ECG registration subsystem is based on TI ADS1292 chip, which includes input analog signal multiplexor, 2-channel 24-bit ADC, reference voltage source, and clock signal generator. ADS1292 chip works at 8 kSPS sampling rate and resamples digital signal according to the chip configuration. During ECG registration resampling rate equals to 500 Hz. At this condition resampling digital filter -3dB cut-off frequency equals to 131 Hz. This frequency is sufficient for ANS characteristics assessments.

The microcontroller unit performs ADS1292 chip configuration at the start of the neuro-electrostimulation device, test of the chip, and control signal generation during the device functioning.

Results

Test of the neuro-electrostimulation device electrical characteristic was perofrmed using standard laboratory equipment, which included osciloscope Tektronix DPO2012B and power

supply units. Resistor assembly, that connected all cathodes and all anodes at the same point, was used as biological tissue equvivalent.

Comaprsion of the main characteristics of the "SYMPATHOCOR-01" device and the neuro-electrostimulation device is shown in Tab. 1.

Table 1. The "SYMPATHOCOR-01" device and the neuro-electrostimulation device characteristic comparison

Characteristic	"SYMPATHOCOR-01"	neuro-electrostimulation device
Number of cathodes	12	13
Number of anodes	1	13
Weight	1.5 kg	200 g
Dimensions	186.0x116.0x60.0 mm	90.0x50.0x18.5 mm
Impulse amplitude	0 – 25 V	0 – 15 mA
Frequency of the pulses	15 – 100 Hz	5 – 150 Hz
Partial impulse duration	35 – 50 uS	15 – 60 uS
Set of the field's parameters	Switchers on the panel of the device	PC software via USB
Electrode sequence changing ability	No	Yes
ECG registration ability	No	Yes

Table analysis shows that the ranges of the electrical characteristics of the field of the current pulses, such as impulse amplitude, frequency of the pulses, partial impulse duration exceeds corresponding characteristics of the "SYMPATHOCOR-01" device.

Increase of the anodes number from 1 to 13, as well as the possibility of changing their sequence, augments the number of local targets in the neck. This in turn, increases the efficiency of neuro-electrostimulation due to involvement in the regulatory process, in addition to the ANS, the brain structures responsible for motor, visual, auditory, vestibular, and other functions.

Reduction of the neuro-electrostimulation device weight and size enhance the capabilities of the device for the neurorehabilitation: it is possible to provide simultaneously nerve stimulation and load of motor, cognitive, and vestibular systems.

Addition of the ECG registration subsystem allows to generate biofeedback on the basis of information about the functional state of the ANS. Biofeedback based information allows one to adjust the parameters of the biotropic field of the current pulses and to change local target in the neck.

References

[1] N.A. Agadzhanyan, R.M. Baeevsky, A.P. Berseneva, *Problemy adaptacii I uchenie o zdorovie* [In Russian] (RUDN, Moscow, 2006).

[2] W. B. Mendes in *Methods in social neuroscience*, E. Harmon-Jones and J.S. Beer ed. (Guilford Press, New York, 2009).

[3] V.M. Baranov, R.M. Baevskiy, A.P. Berseneva, V.M. Mihaylov, "Evaluation of adaptive abilities of an organism and tasks of healthcare effectiveness increase" [In Russian], Human Ecology, **6**, 25-29, (2004).

[4] V. S. Kublanov, "A hardware-software system for diagnosis and correction of autonomic dysfunctions", Biomedical Engineering, **42**, 206-212, (2008).

[5] Y.P. Danilov, V.S. Kublanov, "Emerging Noninvasive Neurostimulation Technologies: CN-NINM and SYMPATOCORECTION", Journal of Behavioral and Brain Science, **4**, 105-113, (2014).

[6] P. Barbanti, L. Grazzi, G. Egeo, A. Padovan, E. Liebler, G. Bussone, "Non-invasive vagus nerve stimulation for acute treatment of high-frequency and chronic migraine: an open-label study", The Journal of Headache and Pain, **16**, 1-5, (2015).
[7] V. S. Kublanov, T.S. Petrenko, M.V. Babich, "Multi-Electrode Neurostimulation System for Treatment of Cognitive Impairments", 37th Ann. Int. Conf. of the IEEE Engineering in Medicine and Biology Society, 2091-2094, (2015).

Investigation of geometric attenuation on the reconstruction quality in emission tomography

S.A. Tereshchenko, A.Y. Lysenko
National Research University of Electronic Technology, 124498, Moscow, Russia

Emission computed tomography can be divided into two main items: single-photon emission computed tomography (SPECT) and positron emission tomography (PET) [1, 2]. In SPECT the single gamma-quantum of a radiopharmaceutical radioactive decay is registered. In PET the pair of gamma- quanta of a positron annihilation for positronic radiopharmaceutical is registered.

In contrary to transmission tomography in emission tomography a distance between an each elementary source and the detector is different. Therefore a geometrical attenuation of a radiation is an additional distortion factor [2, 3].

Usually the influence of the geometrical attenuation is neglected in comparison with the radiation absorption in an object substance. Nevertheless it is interesting to investigate the influence of the geometrical attenuation on the quality of reconstructed tomograms.

Let $s(x, y)$ is the spatial sources distribution in the fixed coordinate system (x, y), $s_\theta(\xi, \zeta)$ is the spatial sources distribution in rotational coordinate system (ξ, ζ) turned at the angle θ relative to the motionless coordinate system. Then in SPECT the data registered by the position sensitive detector (PSD) can be described in rotational coordinate system by the next expression [2] including the geometrical attenuation (Fig. 1):

$$p(\xi, \theta) = \mathrm{e}^{-\mu L_2} \int_{l_1}^{l_2} \frac{s_\theta(\xi, \zeta)}{(R - \zeta)^2} \mathrm{e}^{\mu \zeta} d\zeta \,, \tag{1}$$

where $p(\xi, \theta)$ is the measuring data (projections), R is the rotation radius of the system, l_1, l_2 are the boundaries of the spatial sources distribution area at the projection line, L_1, L_2 are the boundaries of the absorption coefficient spatial distribution area at the projection line, μ is the absorption coefficient of the object substance.

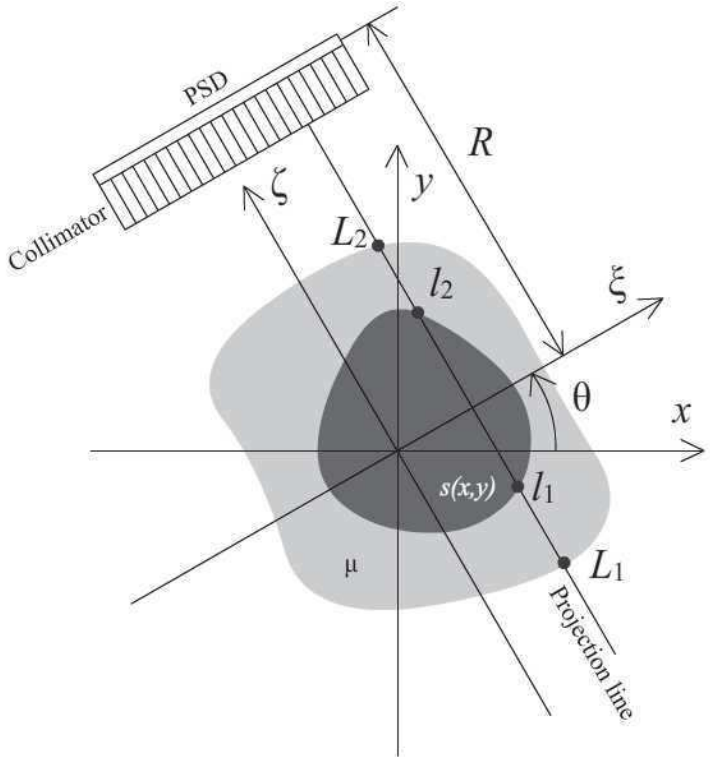

Fig. 1 The geometrical scheme of measurements in SPECT.

In PET the data registered by detectors connected into the coincidence scheme can be described in rotated coordinate system (ξ,ζ) by the next expression including the geometrical attenuation (Fig. 2):

$$p(\xi,\theta)=\mathrm{e}^{-\mu(L_2-L_1)}\int_{l_1}^{l_2}\frac{s_\theta(\xi,\zeta)}{\left(R^2-\zeta^2-\xi^2\right)^2}d\zeta\,, \tag{2}$$

where notations are analogous to the Fig.1.

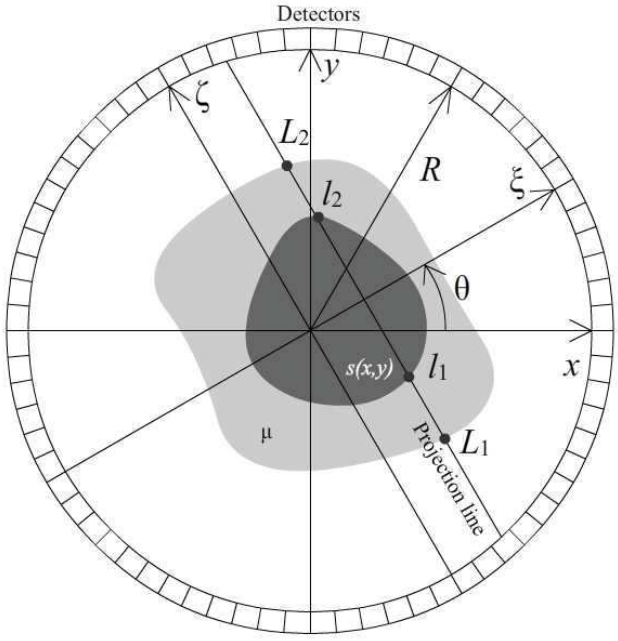

Fig. 2 The geometrical scheme of measurements in PET.

To evaluate the reconstruction quality the uniform deviation of the reconstructed distribution from the original distribution is used in the correspondence with the next formula:

$$R = \frac{1}{N_x N_y} \sum_{i=1}^{N_x} \sum_{j=1}^{N_y} \left| s(x_i, y_j) - s'(x_i, y_j) \right|, \quad (3)$$

where $s(x_i, y_j)$ is the discrete original spatial source distribution, $s'(x_i, y_j)$ is the reconstructed discrete source spatial distribution, N_x is the number of discrete elements along x-axis, N_y is the number of discrete elements along y-axis.

There is investigated the influence of geometrical attenuation on the reconstruction quality depending on the gabarit of object, the system rotation radius and the absorption coefficient for SPECT and PET.

To correct the distortion from the geometrical attenuation the method is developed that is based on the concept of the correction matrix [2, 4].

References

[1]. Emission Tomography: The Fundamentals of PET and SPECT. Ed. by M.N Wernick, J.N.Aarsvold. San Diego, CA: Elsevier Academic Press, 2004. 580p.
[2]. Tereshchenko S.A. Methods of computed tomography. Moscow, Fizmatlit, 2004. 320 p. [In Russian].
[3]. Image Reconstruction from Projections: Implementation and Applications/ Ed. by G.T.Herman. Berlin and New York: Springer–Verlag, 1979. 252 p.
[4]. Chang L.-T. A method for attenuation correction in radionuclide computed tomography. IEEE Tr. on Nuclear Science, 1978, Vol. NS-25, p.638-643.

Investigation of hemolytic activity and biodegradation of nanocomposite materials

U.E. Kurilova[1], N.N. Zhurbina[1], I.A.Suetina[2], M.V. Mezentseva[2], L.I. Russu[2], A.Yu. Gerasimenko[1]

[1]National Research University of electronic technology, 124498, Moscow, Russia
[2]Ivanovsky Institute of Virology, 123098, Moscow, Russia

Today tissue engineering is an actively developing field of science and technology. Special structures – scaffolds are creating to improve adhesion and proliferation of cells seeded on their surface. To achieve the same purpose a biocompatible coating of artificial implant can be created and enhance mechanical characteristics and patient's tissue ingrowth.

Hemolysis (breaking of red blood cells) caused by implant's surface is an important characteristic of its biocompatibility. Moreover, to ensure the possibility of proliferation of patient's living cells material using for tissue engendering purposes must be biodegradable – to decompose on the non-toxic products over time and to be replaced by growing living cells [1]. It is very important to estimate and control biodegradation time of nanocomposite material. On the one hand, it should not to make interference for tissue ingrowth and, the other hand, material should not collapse and lose its mechanical properties (porosity, strength) before the moment of appearance of the new tissue.

For investigation of hemolysis we created three samples of these types: nanocomposite material based on dispersion of bovine serum albumin (BSA) with single-walled (SWCNTs) and multi-walled carbon nanotubes (MWCNTs) treated by laser radiation. Concentration of carbon nanotubes was 0.1 g/l. The dispersion of BSA with carbon nanotubes or without them was coated by ultrasonic method on woven fabric for ligament reconstruction – polyethylene terephthalate (PET). Samples of fabric size of 5×10 mm with dispersion were dried by laser

radiation of 810 nm wavelength at power 5.5 W for 10 minutes and then dried completely on air for 6 days. Two samples of clear fabric were examined too. As a control with basic level of hemolysis a tube with blood was used. Control sample of full blood hemolysis was a tube with blood being freezing and defrosting.

The samples were sterilized by ultraviolet and then were placed in sterile tubes. 1.5 ml of fresh human blood was added in each tube. The samples were placed in a refrigerator until the erythrocyte sedimentation.

To estimate the hemolysis plasma was carefully collected using the pipette and moved into the quartz cuvette 3 mm thick. On average about 400 µl of serum for each of the sample was studied. The spectra of samples of one species were averaged. Between the tests cuvettes were washed with distilled water. Spectra of samples in the range 300-700 nm were obtained with a resolution of 0.2 nm on the spectrophotometer ThermoScientisicGenesys 10S UV-vis (figure 1).

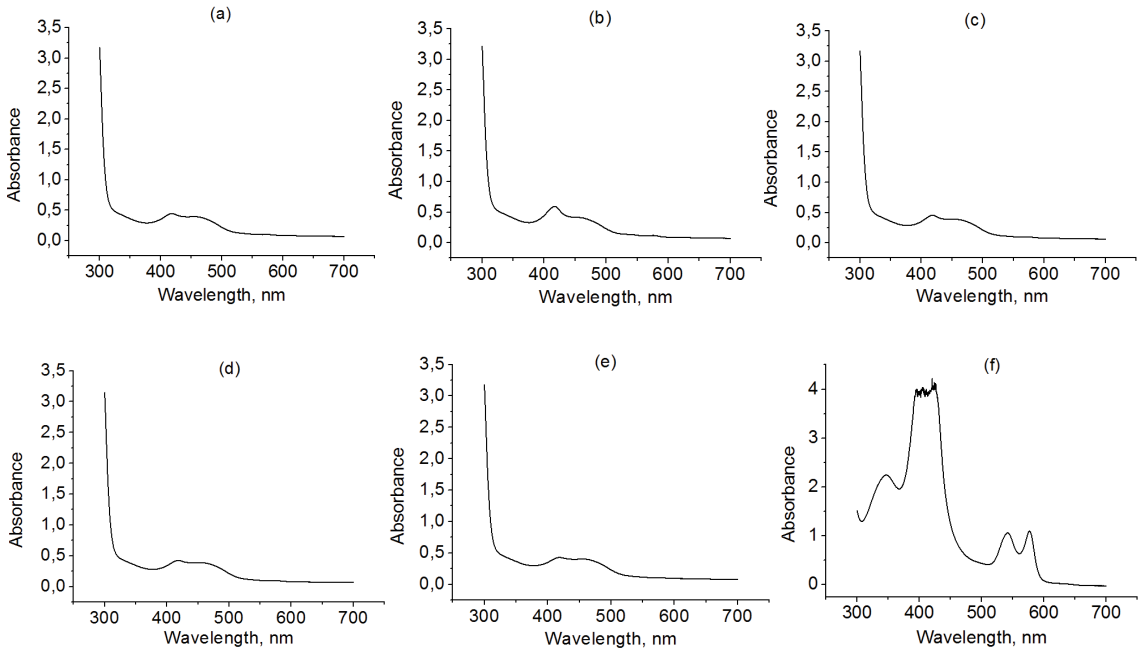

Fig.1 Spectra of plasma from samples with BSA and SWCNT (a), BSA and MWCNT (b), BSA (c), PET (d), control sample without hemolysis (e) and with full hemolysis (f)

Comparison of the obtained spectra with reference data shows that hemolysis is absent in the investigated samples and in the control sample, or its value is insignificant, because there are no peaks corresponding to the compounds of hemoglobin in the range of 450-650 nm [2]. In the samples with full hemolysis nature of the peaks is the same as the peaks of oxyhemoglobin (540 and 578 nm), the most common compound of hemoglobin with environment oxygen [3].

To quantify the value of hemolysis the optical densities of samples of the plasma on a wavelength of 540 nm were obtained. The relative value of hemolysis was calculated in percent by the formula:

$$\delta(\mathrm{h}) = \frac{\mathrm{Ds} - \mathrm{Dc}(+)}{\mathrm{Dc}(-) - \mathrm{Dc}(+)} \times 100\,\%, \qquad (1)$$

where Ds – optical density of plasma on a wavelength of 540 nm after contact with a sample; Dc(+) – optical density of blood samples with basic level of hemolysis (positive control); Dc(-) – optical density blood samples with a 100% hemolysis (negative control). The results are shown in Table 1.

Table 1 - Results of experiments of hemolysis study

Components of a sample	Average value of optical density at 540 nm	Value of hemolysis, %
SWCNT, BSA	0.1154	0
MWCNT, BSA	0.1329	1.2048
BSA	0.1083	0
PET	0.1081	0
Control - 0 % hemolysis	0.1215	0
Control - 100 % hemolysis	1.0513	100

Thus, all samples, except for the sample with the addition of MWCNTs, show the absence of hemolytic activity, in the sample with MWCNTs hemolytic activity is low – 1.2%.

To estimate the biodegradation time of the nanocomposite materials the study of behavior of samples with SWCNTs, MWCNTs and BSA in the blood serum was carried out for one week.

Preparation of samples to explore the biodegradation was analogous to the preparation of samples for measures of the hemolytic activity. Before the beginning of the experiment samples were weighed on the scales VibRAAJH-420 CE. Each sample was weighed three times, the result value was the average value of three measurements.

The samples were placed in the wells of 24-well plate, 1.5 ml of fresh serum was added in each well with a sample. The plate was covered and placed in the refrigerator.

At the end of 7 days samples were took out from the wells and dried for 6 days. Weight of each of the sample was measured, relative value of mass loss was calculated (table 2). Darkening of serum was observed in the two samples with SWCNTs, in all wells with the samples with the addition of nanotubes serum was a little darker than in the wells with the samples of BSA, due to the dissolution of the dark cover.

Table 2 - Results of the biodegradation rate measurements

Sample	Components of a sample	Initial weight, g	Weight after the experiment, g	Difference between initial and final weight, g	Weight loss, %
BSA-7	BSA	0.032	0.025	0.007	21.875
BSA-10		0.033	0.027	0.006	18.182
BSA-11		0.03	0.026	0.004	13.333
S-0.1-9	SWCNT, BSA	0.032	0.03	0.002	6.25
S-0.1-10		0.031	0.026	0.005	16.129
S-0.1-11		0.029	0.025	0.004	13.793
M-0.1-9	MWCNT, BSA	0.034	0.028	0.006	17.647
M-0.1-10		0.028	0.023	0.005	17.857
M-0.1-11		0.033	0.027	0.006	18.182

All samples demonstrated the loss of the weight reaching values of 6.25% (sample S-0.1-9) to 21.875% (sample BSA-7), weight loss in the samples with the addition of SWCNTs on average was less, in the samples with MWCNTs and BSA average weight loss was about the same. The absolute values of weight loss had the least difference in three samples with MWCNTs.

The obtained results of experiments suggests that the study material on the basis of the dispersion of carbon nanotubes with BSA can successfully be used as a cover of the ligaments knee joint implants because it does not cause hemolysis and has an acceptable rate of biodegradation.

This work was provided by the Ministry of Education and Science of the Russian Federation (Agreement 14.575.21.0089, RFMEFI57514X0089).

References

[1] S.Yang, K. F. Leong, Z. Du and C. K. Chua. “The design of scaffolds for use in tissue engineering. Part I. Traditional factors,” Tissue engineering. **7**, 679-689 (2001).

[2] D.V. Kostukov, N. K. Lagutina and L.V. Pavlushkina. “Spectral studies of plasma and blood of newborns” Scientific-Practical Conference "Technology and innovation in laboratory medicine". [In Russian]

[3] G.B. Blakney and A.J. Dinwoodie. “A spectrophotometric scanning technique for the rapid determination of plasma hemoglobin,” Clinical biochemistry. **8**, 96-102 (1975).

Development of matrix photoreceiver based on carbon nanotubes for control optical radiation in medicine

A.A. Polohin[1], A.Yu. Gerasimenko[1], A.A. Dudin[2], L.P. Ichkitidze[1], E.P. Kitsyuk[2], A.P. Orlov[2,3], A.A. Pavlov[2], Yu.P. Shaman[4]

1. *National Research University of Electronic Technology, Bld. 1, Shokin Square, Zelenograd, Moscow, Russia*
2. *Institute of Nanotechnology of Microelectronics of the RAS, Nagatinskaya 18, Moscow, Russia*
3. *Kotel’nikov Institute of Radio-engineering and Electronics of RAS, Mokhovaya 11-7, Moscow, Russia*
4. *Scientific-Manufacturing Complex "Technological Centre”,laneway 4806, Zelenograd, Moscow, Russia*

Nowadays optical radiation is widely used in the variety of fields. Medicine uses a large number of therapeutic equipment based on optical radiation, characteristics of which must be constantly monitored [1]. This indicates the necessity of the development of new radiation receivers, devices that control the characteristics of optical radiation even in extreme conditions. All existing photoreceivers can be devided on 2 main types by operating principle - photothermal and photoelectric. Photothermals have the mechanism of optical to thermal and then to electrical energy transformation. High response delay (and thus, low perfomance) and environmental conditions susceptibility are the disadvantages of this photoreceivers.

The principle of operating mode of the second type photoreceiver (photoelectrical) is a direct optical to electrical energy transformation. This type includes semiconductor photoreceivers that have high perfomance and are less environmental proned then photothermal recivers.

Silicon (Si), Germanium (Ge), gallium-arsenide (GaAs) are as a rule in the basis of the majority of semiconductor photoreceivers. Last studies have shown that carbon nanotubes (CNTs) of semiconductor type can also be used as semiconductor material in photoreceivers. Metallic type CNTs are degenerate as lightning doesn't affect its free charge carriers concentration so the CNTs application in photoreceivers is pointless.

The development of matrix photoreceiver based on CNTs array flows from sensitive elements production based on CNTs array [2]. Matrix photoreceiver based on CNTs and

consisted of 16 sensitive elements on the single semiconductor substrate was developed (Fig.1). Every sensitive element contains 10000 sensitive cells situated as a 100x100 square with 5μm interval. Two-electrode system is a basic topology of sensitive cells. Cells represent the 10x10 μm apertures that go through metallization and dielectric layers to single-crystalline silicone from which the CNT array grows to upper layer. Single-crystalline silicone substrate is a basis of the whole structure. Aluminum metallization is the upper layer. Underneath the metallization is the dielectric layer of thermally oxygenated 0.5 μm silicone.

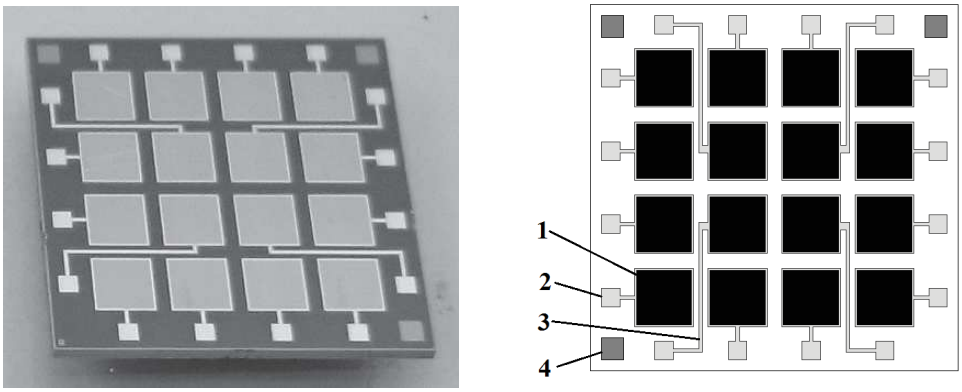

a b

Fig. 1 Layout (a) and topology (b) of matrix photoreceiver based on CNT array: 1-sensitive element, 2 – contact surface of sensitive element, 3 – contact metallization, 4 – contact window of silicon substrate

The parameters of matrix photoreceiver based on carbon nanotubes, such as working wavelength range, perfomance and sensibility were studied using experimental plants (Fig.2), which basic elements are MDR-41 Monochromator (OCB Spectr, Russia) and NI USB-6218 data acquisition (DAQ) device (National Instruments, USA). Research process was automated with process-specialized software-based unit in LabVIEW framework.

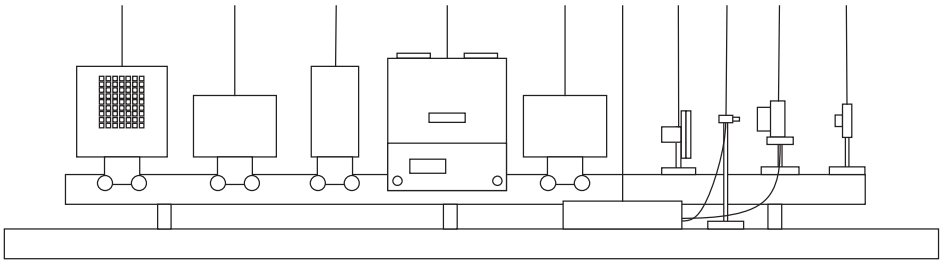

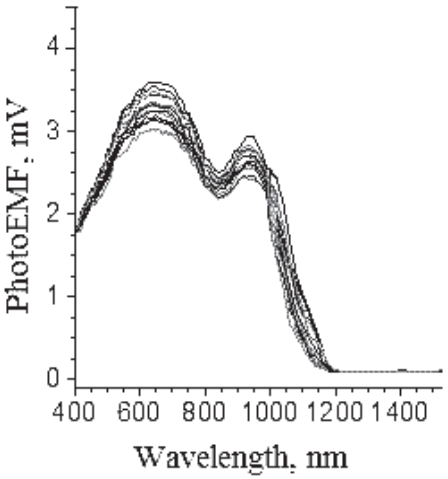

Fig. 3 PhotoEMF of 16 sensitive elements of matrix photoreceiver versus the wavelength of falling radiation

For sensitivity analisys of matrix photoreceiver based on CNTs the dependencies of current rate that each of 16 sensitive elements of photoreceiver generated versus radiation capacity for 3 wavelengths (640, 800, 950 nm) were received. Received characteristics were linearized and sensibility for required wavelengthes was determined as an arithmetical average of 16 slope coefficients of linear functions (Fig. 4). At the wavelength of 640 nm sensitivity of matrix photoreceiver constituted 168 μA/Wt, at 800 nm - 163 μA/Wt, at 950 nm - 88 μA/Wt. The total sensitivity of matrix photoreceiver based on CNTs was 140 μA/Wt.

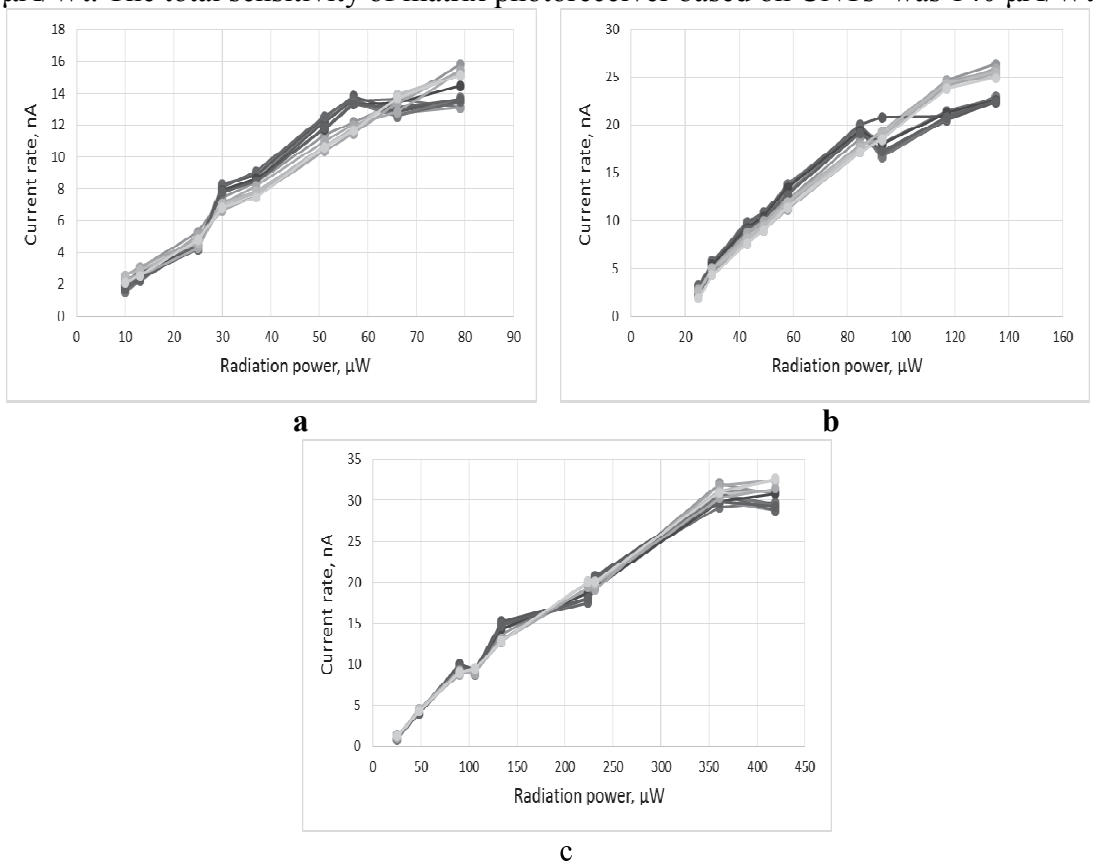

Fig. 4 The of element sensitivity of matrix photoreceiver based on CNT array versus the power of falling radiation on the 640 (a), 800 (b) и 950 (c) nm wavelength

The perfomance of matrix photoreceiver based on CNTs was researched using scheme that measures synchronous signals from transmitter and receiver connected by optical channel. Speed of response was determined by the time of increase to 0.9 of maximal amplitude of photoEMF on sensitive element, that was created after light exposure. It was studied, that speed of response of all sensitive elements and therefore, matrix photoreceiver, was under 30 μs (Fig.4).

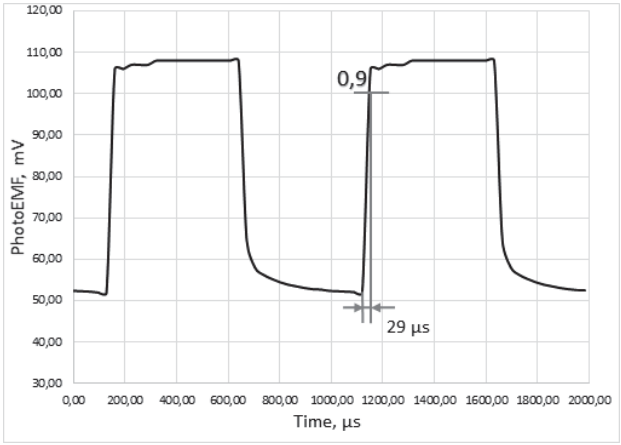

Fig. 4 The oscillogram of one of the 16 sensitive elements of matrix photoreceiver based on CNT array

Further research will be focused on technological parameters optimization with aim to increase the working wavelength range, sensitivity and performance of the matrix photoreceiver based on CNT array. Optimization can be connected with purification of the surface of sensitive elements from unwanted carbon heading and removing defecting layers of multiwall carbon nanotubes which increases the quality of the array and extends the light penetration to the contact CNT-silicon. The extension of the working wavelength can be achieved using the method of thicker tubes synthesis (with higher amount of layers). Developed matrix photoreceiver based on CNT can be used to control the characteristics of optical radiation, which apply in modern medicine.

References

[1] P. Sowa, J. Rutkowska-Talipska, K. Rutkowski, B. Kosztyla-Hojna, R Rutkowski, "Optical radiation in modern medicine", Postepy dermatologii i alergologii. **30(4)**, 246-252 (2013).
[2] E.V. Blagov, A.Yu.Gerasimenko, A.A. Dudin, L.P. Ichkitidze E.P. Kitsyuk, A.P. Orlov, A.A. Pavlov, A.A. Polohin, Yu.P. Shaman, "Development of matrix photoreceivers based on carbon nanotubes array", Proc. of SPIE, **9917**, 99171O-1 - 99171O7 (2016).

Multiplexed measurement systems with coded apertures

M.A. Antakov[1], I.S. Burnaevsky[1], S.A. Dolgushin[1], G.A.Fedorov[2], S.A. Tereshchenko[1]

1. National Research University of Electronic Technology, Moscow, Russia

2. National Research Nuclear University MEPhI, Moscow, Russia

Single photon emission computed tomography (SPECT) is a nuclear medicine tomographic imaging technique using gamma rays. It is able to provide 3D information. This information is typically presented as cross-sectional slices of a 3D object, and can be freely reformatted or

manipulated as required. Myocardial perfusion scan is a nuclear medicine procedure that illustrates the function of the heart muscle (myocardium). It evaluates many heart conditions from coronary artery disease to hypertrophic cardiomyopathy and myocardial wall motion abnormalities. The function of the myocardium is also evaluated by calculating the left ventricular ejection fraction of the heart. This scan is done in conjunction with a cardiac stress test.

Because blood flow in the brain is tightly coupled with local brain metabolism, technetium tracer is used to assess brain metabolism regionally, to diagnose and to differentiate pathologies. Meta analysis of many reported studies suggests that SPECT with this tracer is more sensitive at diagnosing Alzheimer's disease vs. clinical exam (mental testing, etc.).

The main purpose of using multiplexed measurement systems is to replace huge, complicated and expensive rotating diagnostic scheme by more chip translational scheme. Such diagnostic scheme can also be applied in cases, where rotation around object is impossible.

However, there is another method for obtaining images using an obscura-chamber principle [1,2]. This method can be used for the ionizing radiation. In the case of single pinhole an inverted image of flat radiating object is obtained on the position sensitive detector (PSD). If we replace the flat source by the volume source, the image on PSD will be a superposition of images of each 2D slice of the 3D source. Thus, such kind of image is impossible to reconstruct.

If we replace single pinhole by a set of opened and closed pinholes, we will get, so-called, coded aperture (CA) (Fig.1). It has focusing properties, as it is for a lens [3-5]. Thus even for a point source of the radiation which locates in a focal plane, on the detector we obtain difficult superposed image representing a shadow of the aperture. In the case of 3D source the image on the detector is even more difficult. Consequently the image decoding is required. This problem can be solved with multiplexed measurement system (MMS).

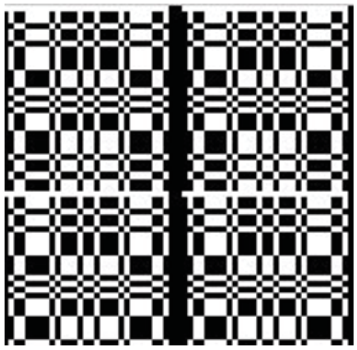

Fig. 1. An example of the coded aperture

2D CA are constructed with 1D pseudorandom sequences (PRS) [3-6]. There are three methods to construct CA from PRS [4,5,7,8]. Line-by-line and diagonal methods construct 2-D CT on the basis of the single PRS. Self-supported method constructs 2-D CT on the basis of two PRS. Total number of possible rectangular and hexagonal CA is more than 1 000 000. It is necessary to investigate tomographical properties of the CA and to select CA with better tomographical properties. To reconstruct the space distribution of radiation sources the focal planes method (FPM) is used [4,5]. Volume source is divided into planes, which sequentially placed in focus of MMS. Obtained images on the detector are used in the decoding algorithm (Fig.2).

It is possible to obtain the focused image from the image on the PSD. In the case of 2D object this focused image is the reconstructed object [4,5]. Using this algorithm in case of the volume source we obtain focused images of focal planes with the contribution of all out-of-

focus planes (Fig.3). At the same time the focused image may be used as the initial approximation for iterative decoding algorithms. The main criterion for comparison of the coding apertures is the point spread function (PSF) which can be computed with FPM [4,5]. PSF shows the contribution of sources in out-of-focus planes to the focused image. If this contribution is less then tomographical properties of CA are better. The only way to get PSF is to calculate it numerically (Fig.4).

There are known iterative algorithms, for example, steepest descent method, directed divergence method [4,5,9]. Their inefficiency has been shown. At the same time, it is known that in the rotational SPECT there are very effective algorithms of ART type [10]. The ART type algorithms use an idea of the back projection. So it was created very more effective iterative algorithm based on the principle of the back projection, which has the significantly better rate of the convergence [11,12].

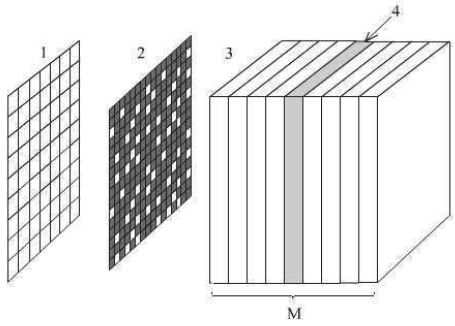

Fig. 2. Focal plane method: 1 – PSD, 2 – CA, 3 – spatial distribution of radiation sources (object) with M planes, 4 – focal plane

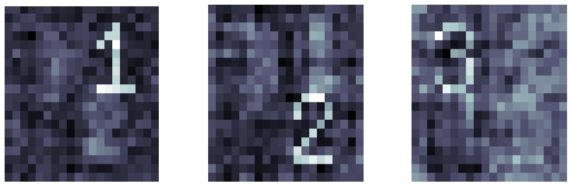

Fig. 3. Focused images in case of 3 planes

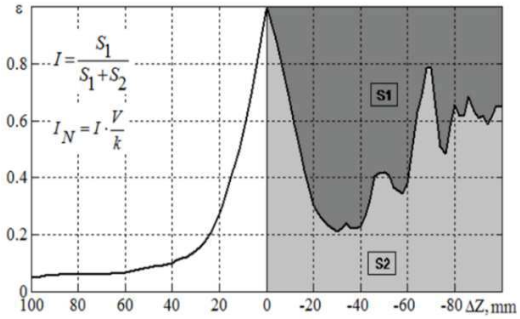

Fig. 4. Example of PSF

Back projection method (BPM) is developed on the basis of an idea of back projecting. The basis of BPM is an information about contributions of sources to every cell of PSD (Fig. 4). Iterations in BPM are performed in accordance with the expressions

$$\vec{s}^{(k+1,1)} = \vec{p}^{(k)}, \quad (1)$$

$$\vec{s}^{(k+1,i)} = \vec{s}^{(k+1,i-1)} + \frac{q_i - \vec{h}_i^{\mathrm{T}} \vec{s}^{(k+1,i-1)}}{\vec{h}_i^{\mathrm{T}} \vec{h}_i} \vec{h}_i ,$$

$$i = 2,3,..., Mv, \quad (2)$$

$$\vec{p}^{(k+1)} = \vec{s}^{(k+1,Mv)}, \quad (3)$$

where $\vec{h}_i^{\mathrm{T}} = [(h_i)_1, (h_i)_2, ..., (h_i)_{Mv}]$ is the i th row of matrix $\hat{H}$, $\hat{H}$ describes encoding process.

Scheme which was described above is called unipolar. This means that we have measurements only at one side of the object . However, we can double the amount of data, if we will have measurements from two opposite directions. Such measurement scheme is called bipolar. It can be used with the same or different coded apertures. Using this measurement scheme the decoding error is averaged. Bipolar measurement scheme can be easily implemented with the unipolar scheme. Thus it is enough to turn the object at 180 degrees.

The degree of improvement can be traced by the dependence of the standard deviation of the iteration number. It was found that the rate of deviation reduction for the bipolar measurement scheme more than for the unipolar scheme about 10 times. Thus a bipolar measurement scheme can be used for a large number of planes. On the Fig. 5 the Shepp-Logan phantom reconstruction is shown using BPM after only 5 iterations.

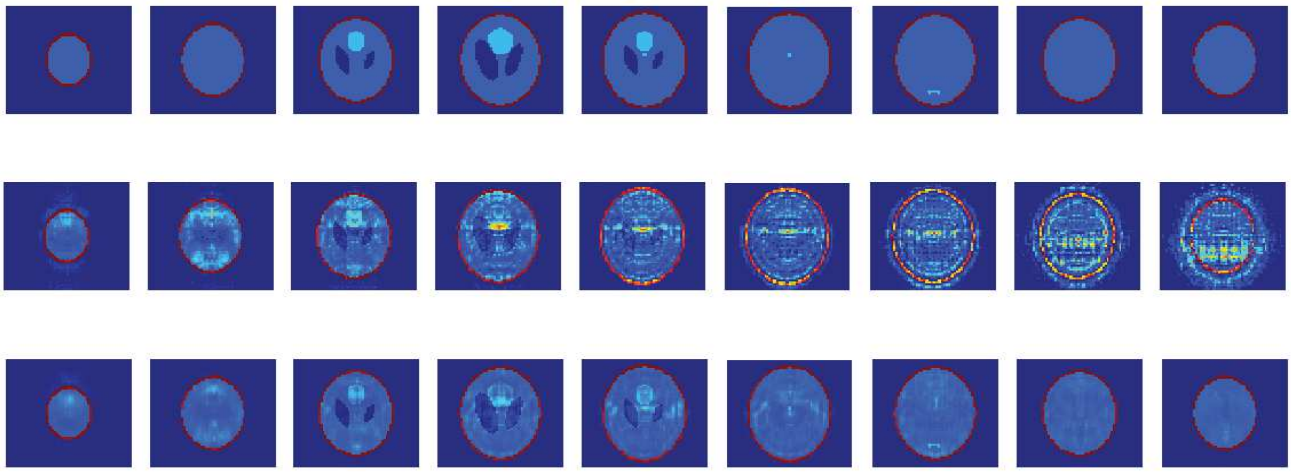

Fig. 5. The real (row 1 from top) and reconstructed images of Shepp-Logan phantom after 5 iterations for BPM in the unipolar (row 2 from top), and bipolar (row 3 from top) scheme.

We have modified decoding algorithms for the case of HCA, and have achieved that in the case of a planar source, there is absolutely accurate decoding [13]. As expected, for the volume source focused images have artifacts due to the influence of out-of-focus sources (Fig.6).

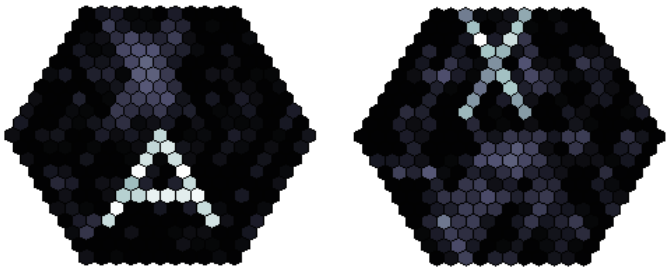

Fig. 6. Focused images in case 2 planes

References

[1] Harwit M., Sloane N.J.A. Hadamard transform optics. New-York, Academic Press, 1979.
[2] Caroly J, Stephen J.B., Di Cocco G. et al. Coded aperture imaging in X-and Gamma-ray astronomy. Space Science Reviews, 1987, vol. 45, Nos. 3/4, p. 349-403.
[3] Fedorov G.A. Radiation introscopy: Coding of information and optimization of the experiment. Moscow, Atomizdat, 1982. [In Russian].
[4] Fedorov G.A., Tereshchenko S.A. Computed emission tomography. Moscow, Energoatomizdat, 1990. [In Russian].
[5] Tereshchenko S.A. Methods of computed tomography. Moscow, Fizmatlit, 2004. [In Russian].
[6] Wilhelmi G., Gompf F. Binary sequences and error analysis for pseudo-statistical neutron modulators with different duty cycles. Nuclear Instruments and Methods, 1970, vol.81, No.1. p.36-44.
[7] Macwilliams F.J., Sloan N.J. Pseudo-random sequences and arrays. Proceedings of the IEEE, 1976, vol.64, No.12, p.1715-1729.
[8] Spann P. A two-dimensional correlation property of pseudorandom maximal length sequences, 1965, vol.53, No.12. p. 2137.
[9] Fedorov G.A. and Tereshchenko S.A. Integral Code Systems for Recording Ionizing Radiation: Iterative Image Reconstruction Algorithms for Focal Plane Processing. Measurement Techniques, 2001, vol.44, No.4, p. 422 - 427.
[10] Gordon R. A tutorial on ART. Algebraic reconstruction techniques. IEEE Tr. on Nuclear Sciences, 1974. vol. NS-21, No. 1, p. 78–93.
[11] Fedorov G. A., Dmitriev A.M., Tereshchenko S. A. and Antakov M. A. The reconstruction of spatial distributions of ionizing radiation sources on the base of iterative back projection in multiplexed measurement systems. ANRI, 2012, No.1, p.62-70. [In Russian].
[12] Fedorov G. A., Tereshchenko S. A., Antakov M. A. and Dmitriev A.M. The algorithm of the back projection for multiplexed measurement systems. Nuclear physics and engineering, 2012, vol.3, No.3, p. 268-278. [In Russian].
[13] Tereshchenko S. A., Fedorov G. A., Antakov M. A., Burnaevskiy I. S.. Reconstruction of radiation source spatial distribution by unipolar and bipolar measuring circuits using hexagonal coding collimators. Biomedical Engineering, 2014, vol.48, No.1, pp. 49-52.

Novel method of fast null-radiometer temperature retrieval

L. Ovchinnikov, S. Vesnin

1. Moscow Bauman Technical University, BMT department, postgraduate student

2. RES Company, chief officer

Accuracy is essential property of a medical radiothermometer, which determine its usage in clinics. It has very special influence on the inverse problem solving limiting stability of the solution. While radiothermometer is a power meter, accuracy is bound with time of measurement, so, we should compare measurement methods by their accuracy within the same time.

Simple theoretical dependency of noise fluctuations deviation versus time of measurement was firstly written by Dicke in 1946 and well known as *Dicke radiometer formula*:

$$\sigma = \frac{m T_{sys}}{\sqrt{B\tau}}$$

regarding T_{sys} is system noise temperature (including measured temperature and amplifiers' additive noise), B is bandwidth, τ is low-pass filter time constant, m is design-dependent constant. Unfortunately, this formula cannot be used to estimate precision as it doesn't consider another sources of error. An example of such source is transient which anyway appears in the beginning of measurement. Additionally, we claim that modern radiometers are more complex than radiometer Dicke used and so his formula doesn't describe their peculiar features.

Let us formulate the problem. Null-radiometer is tracking dynamic system, tending to equal noise temperature of calibrated variable source with noise temperature of measured object. The structure scheme of studied system is shown on Fig. 1.

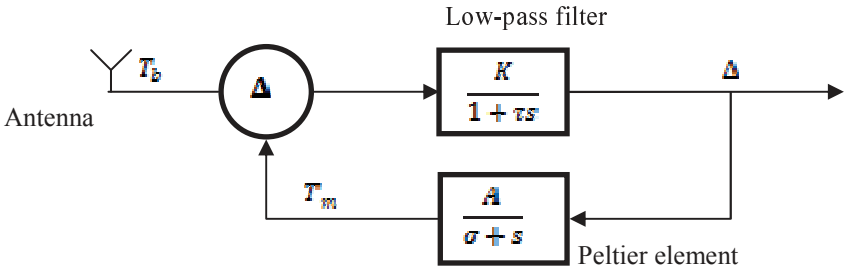

Fig. 1 System-level schematic of null-radiometer

One can find that theoretical dependency of source temperature versus object temperature can be written like this:

$$\frac{T_m}{T_b}(s) = L(s) = \frac{G}{\frac{\tau}{\sigma}s^2 + \left(\tau + \frac{1}{\sigma}\right)s + (G+1)}$$

where $G = AK$ is open-loop amplification coefficient, σ is inertial characteristic of noise source, τ is loop low-pass time constant.

The signal on the input of the system is подается from the RF detector circuit and can be expressed as sum of a constant value, proportional to temperature T_b and a band-limited white noise. A step change of input temperature will output a sum of step transient and colored noise: $L(AH(t) + \xi) = Af(t) + L\xi$.

Thus, the determination of temperature problem can be reduced to the determination of the initial step amplitude. Direct averaging of noise using low-pass filter is not an effective technique because it makes transient longer. The smallest error exist for every given measurement time t and requires specific τ, so implementation of effective algorithm is difficult.

We propose new method, which based on extracting data from transient and noise instead of noise only. One can calculate ideal transient for given system applying Inverse Laplace transform:

$$[K \cdot H](t) = f(t) = k\left(\frac{\omega}{\omega^2 + \alpha^2} - e^{-\alpha t}\frac{\alpha \sin\omega t + \omega\cos\omega t}{\alpha^2 + \omega^2}\right) = 1 - e^{-\alpha t}\frac{1}{\sin\varphi}\sin(\omega t + \varphi)$$

where $\omega = \sqrt{\frac{\sigma(G+1)}{\tau} - \frac{1}{4}\left(\sigma + \frac{1}{\tau}\right)^2}$, $\alpha = \frac{\sigma + \frac{1}{\tau}}{2}$, $k = \frac{\sigma G}{\tau\omega}$. Assuming system parameters are known the problem reduces to minimization:

$$\int_0^t \left((1 - Af(t)) - T(t)\right)^2 dt \to min$$

where A is optimized variable meaning step function amplitude. This problem can be solved with univariate minimization method, e.g. golden ratio method, even in realtime.

System parameters are not usually known accurately enough. In addition, they can change over time.

It is possible to extract unknown system variables from set of transients using multivariate optimization, but it is quiet difficult to obtain such set of transients for every device produced. We propose alternative way to extract the properties using colored noise data. Assuming T_b is constant we can discard the mean value and low-frequency components of noise. Wiener theorem claims that correlation function of such noise will be defined as inverse Fourier transform of its power spectrum. As the source noise is supposed to be band-limited white the spectrum depends firstly on system frequency response. Normalized correlation function calculated from system FR is as follows:

$$R(\tau) = e^{-\alpha\tau}\cos(\omega\tau + \varphi)$$

and α, ω, φ variables are the same with same-named variables of a transient. That's why we can accumulate long enough sample of noise, do a detrending process and calculate correlation function $R_j = \sum T_i T_{i-j}$ (Fig. 2 is an example of such function). With multivariate optimization (e.g. Levenberg-Marquadt method) we can obtain unknown parameters. This process can go while device is standing by and because of this device will keep accuracy even if device parameters changes.

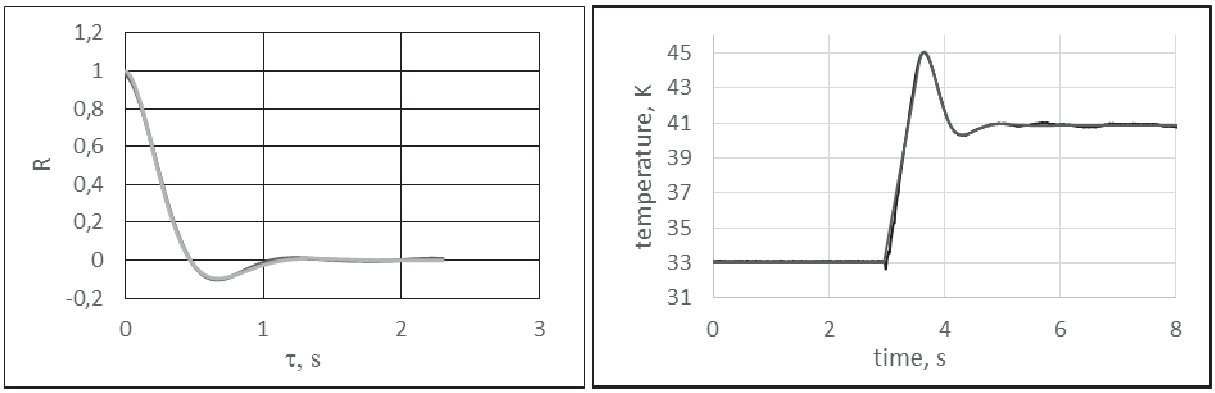

Fig. 2,3 Example of measured normalized correlation function. Example of measured transient

Experimental estimation of method's performance was produced using set of specially measured transients. Step function was modelled by turning on loop switch, while calibrated noise generator was used by noise source. There were $N = 40$ transients from 8 to 12 seconds each, e.g. Fig 3. We also noticed that system parameters determined by proposed method found within 5% deviation the parameters originally designed in circuitry. One of the problems in method implementation was removing the initial part of transient, which was influenced much by non-linearity of the system. Non-linearity was caused by power amplifier which limited the current flows through Peltier element and so limited speed of temperature increase, leading to triangle output signal. To overdo this we determine linear part of signal, then separately apply algorithm described above to "step down" process.

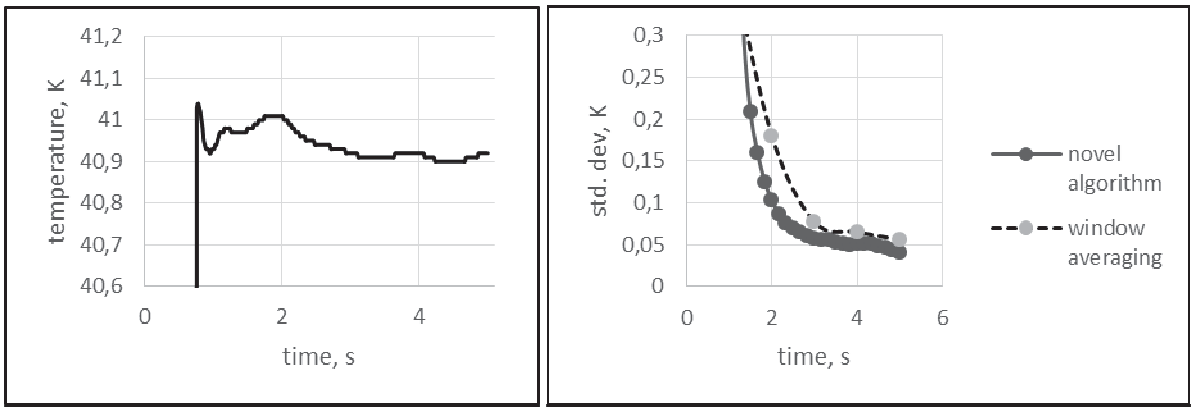

Fig. 4,5 Changes of minimization-based temperature estimation within time. Comparison of measurement error (std. devation), calculated for novel algorithm and traditional averaging.

Described method performs better than traditional averaging method, resulting in at least 30% smaller error, as it is shown on fig. 5. One can see in fig. 4 that it is possible to obtain accurate solution even for 1 or 2 seconds of measurement. Unfortunately, in some cases small-amplitude transient is not visible on background noise and minimization task does not converge. It is useful to revert back to window averaging in such cases. The final algorithm is shown on Fig. 6:

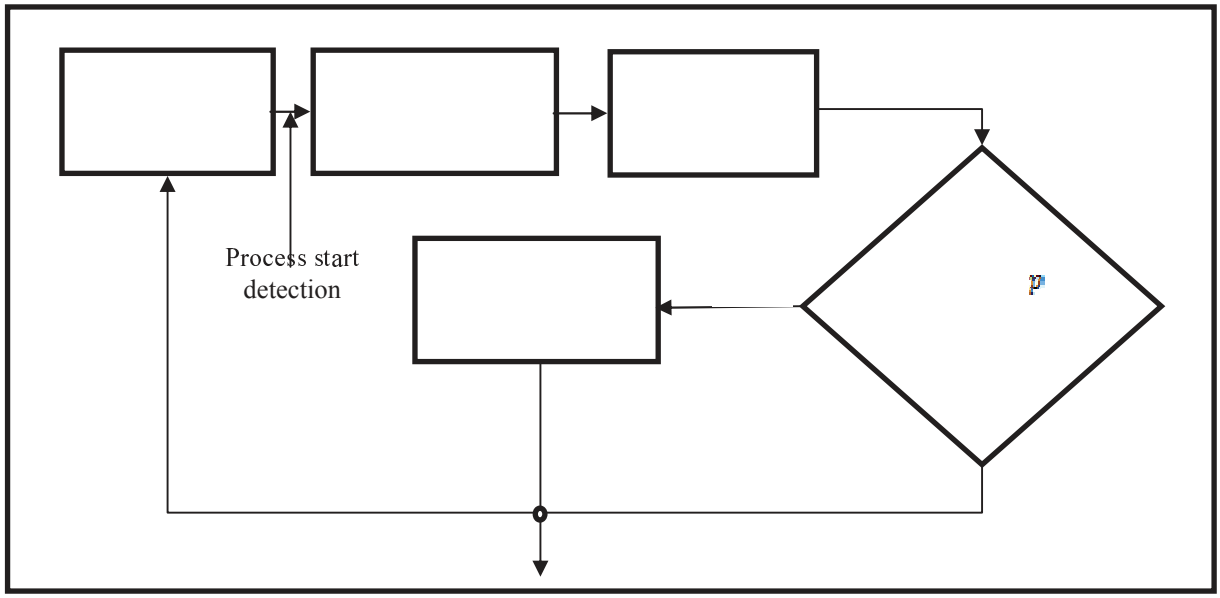

Fig. 6 The final algorithm

Overviewing given results, the new method of null-radiometer signal processing is proposed, which considers its dynamic properties and through this providing smaller time of measurement in comparison to traditional window averaging method.

References

[1] Вайсблат, А. В. *Радиотермография как метод диагностики в медицине*. НЦЗД РАМН, Москва (2003).

Test bench for studying of wireless transcutaneous energy transfer

A.A. Danilov, E.A. Mindubaev

National Research University of Electronic Technology, Biomedical Engineering Department, Zelenograd, Moscow, Russia, 124498

Transcutaneous energy transfer (TET) can be a solution to the energy supplying problem for a variety of implantable medical devices (IMDs) [1-3]. At the same time, there are a number of challenges associated with it. Firstly, relative displacements of the transmitting and receiving coils caused by patient movement and/or postoperative tissue swelling can lead to unstable and inefficient energy transfer. Secondly, operation of the TET system can cause heating, and even burns, of the surrounding tissues. This problem is especially important for IMDs with high power requirements (e.g. ventricular assist devices) [4]. Third issue is existing operating frequency restrictions due to interaction of the electromagnetic field generated by transmitter with biological tissues and its interference with other fields. That said, there are a variety of approaches for solving of these problems: topological (studying of the system on the circuit level), geometrical (study of the coils interactions), a number of optimization schemes, etc. [5, 6]. Experimental studies of the TET system can be a source of quality data about both mentioned problems and solutions. Moreover, such studies can verify numerical calculations and prove concepts of the systems under design. Existing evaluation kits does not provide enough functionality for extensive TET studies [7, 8]. Therefore, the goal of this work was development of the flexible test bench that will allow wide range of the researches specific to the TET.

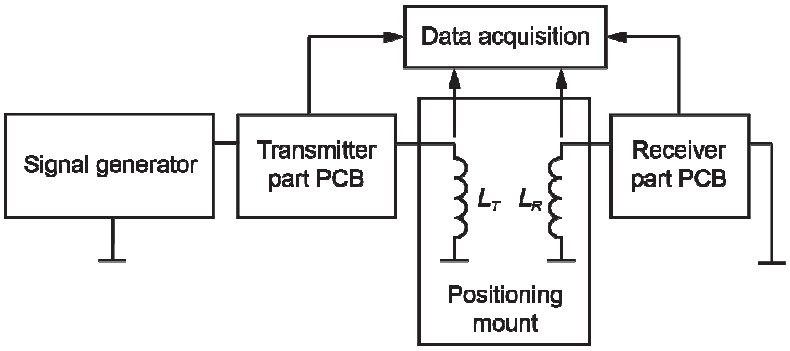

Fig. 1 Schematic representation of the test bench for studying of wireless energy transfer

Schematic representation of the proposed test bench is given in figure 1. The signal generator block includes function generator and high-power radio-frequency amplifier. The power amplifier is used only in cases where transmitted power is of importance (e.g. heating studies). The signal generator generates ideal sinusoidal signal and allows easy regulation of the operating frequency. Frequency range of the generator is from 10 kHz to 230 MHz and, hence, fully covers frequencies of interest in researches of the TET.

Inductances of the transmitting and receiving coils must be compensated to increase efficiency of the energy transfer. There are four different combinations of the compensating circuits known from the literature [9]: primary series secondary series, primary parallel secondary series, primary series secondary parallel, primary parallel secondary parallel. These

schemes have their own properties and it is one of design challenges to choose optimal topology for a specific task. All topologies can be evaluated on the developed test bench. Transmitter part printed circuit board (PCB) includes test resistors and compensating circuit (series or parallel) for the primary inductance L_T. Similarly, receiver part PCB includes load resistor and compensating circuit (series or parallel) for the secondary inductance L_R. Hence, configuration of the compensating circuits can be easily changed by the switching of the PCBs. It allows to extensively study topological approach to the solution of the TET issues. In this work primary series and secondary series compensation will be considered. Principal scheme of the system in this case is shown in figure 2.

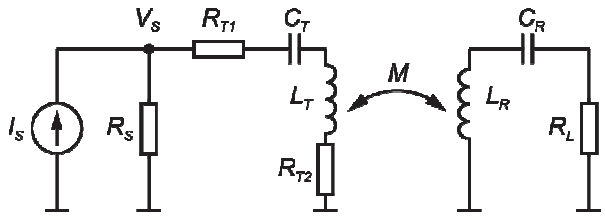

Fig. 2 Principal scheme of the test bench with primary series and secondary series compensation

Table 1 System parameters

Parameter	Value
Output current of the generator I_S, mA	71
Internal resistance of the generator R_S, Ohm	50
Resistance of the test resistors R_{T1} and R_{T2}, Ohm	10
Load resistance R_L, Ohm	20
Capacitance of the C_T and C_R capacitors, nF	1.5
Inductance of the coils L_T and L_R, μH	5.97

In order to be able to test different coils geometries, transmitting and receiving coils are connected to the corresponding PCBs via terminal blocks and, thus, are easily switchable.

The effect of the relative displacement of the coils on the system parameters is expressed in terms of mutual inductance. Mutual inductance is a proportionality factor between the rate, at which current in one circuit changes, and electromotive force around the other circuit due to this current flow. Principal scheme given in figure 2 can be analyzed by Kirchhoff's laws and expression for mutual inductance M can be obtained:

$$M = \frac{1}{\omega}\sqrt{\frac{V_S Z_{trans} Z_{rec} + V_S R_S Z_{trans} - I_S R_S Z_{trans} Z_{rec}}{I_S R_S - V_S}}, \quad (1)$$

here, $Z_{trans} = R_{T1} + R_{T2} - j/(\omega C_T) + j\omega L_T$ is impedance of the transmitting part of the TET system when the coils are not coupled, $Z_{rec} = - j/(\omega C_R) + j\omega L_R + R_L$ is impedance of the receiving part of the TET system when the coils are not coupled, ω is angular operating frequency of the system, I_S is output current of the generator, R_S is internal resistance of the generator, R_{T1} and R_{T2} is resistances of the corresponding test resistors, R_L is load resistance, C_T and C_R is capacitances of the capacitors in the transmitter and receiver, L_T and L_R is

inductances of the transmitting and receiving coils L_T and L_R, V_S is total voltage drop on the system components.

Three basic types of the coils displacement can be distinguished: changing of the distance between the coils, lateral displacement of the coils and angular displacement of the coils. Dependencies of the mutual inductance from any displacement or combination of the displacements can be obtained on the test bench. To demonstrate the accuracy of the measurements, let's consider an experiment, in which dependence of the mutual inductance from a distance between the coils is measured. System parameters are given in table 1. Transmitting and receiving coils is two identical spiral coils with radius 10 cm and 3 turns. Their self-inductances are measured by a RLC-meter. Measured values of the mutual inductance were compared to the corresponding values calculated via finite-element modelling of the transmitting and receiving coils (fig. 3(a)).

Additionally, the effect of the displacements directly on the power transferred to the load can be estimated. For the system shown in figure 2 output power can be calculated as:

$$P_L = \frac{I_S^2 \omega^2 M^2 R_L}{\left(\left(Z_{trans} Z_{rec} + \omega^2 M^2\right)/ R_S + Z_{rec}\right)^2}, \tag{2}$$

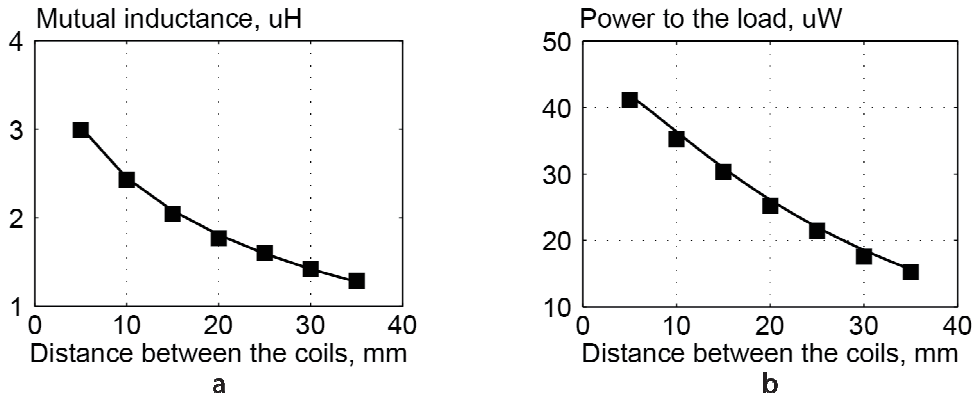

Fig. 3 Comparison of experimental (squares) and calculated (solid lines) values of mutual inductance (a) and power transferred to the load (b) as a function of a distance between the coils

Comparison of the measured and calculated power to the load as a function of the distance between the coils is given in figure 3(b).

Splitting of the resonant frequency into two modes is another major aspect specific to the inductive TET [10]. It greatly affects performance of an inductive TET system. Thus, test bench should be optimized for frequency splitting examination. For this reason, a number of considerations were made in order to minimize value of critical coupling at which frequency splitting appears. In particular case of the primary series secondary series compensation of the transmitter and receiver coils inductances, critical coupling can be derived as:

$$k_{crit} = R_T R_L \sqrt{\frac{C_T C_R}{L_T L_R}}, \tag{3}$$

here, R_T is equivalent resistance of the transmitting part. Low value capacitors were used in the transmitting and receiving parts of the system. Function generator that is basically current

source with parallel internal resistance, and not voltage source with series resistance, was choosen. Transmitting part resistance can be decreased by installing of the low value resistor in parallel. Also, other resistances are minimized. Thus, low value of critical coupling was achieved. Figure 4 shows exemplary frequency sweep at the coupling coefficient between the coils equal to 0.5. Transmitter resistance is 4.5 Ohm, load resistance is 10 Ohm, rest of the parameters are equal to the ones given in table 1. Thus, critical coupling is equal to 0.107. Worth mentioning, that critical coupling could be observed for the coils inductances down to 68 nH if other parameters of the system stay the same.

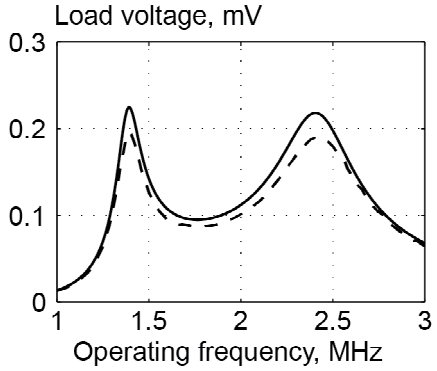

Fig. 4 Load voltage as a function of operating frequency (solid line - PSpice modelling, dashed line – experimental data)

Designed test bench is a flexible system that provides a wide range of possible studies for different configurations of the oscillating circuits. It can be useful for investigation of a physical processes associated with TET as well as for the design of a couple of coils and LC-circuits with defined properties. Particularly, test bench is suited to perform geometric evaluation, to observe and investigate the frequency splitting effect and to compare and choose optimal LC-circuits topology for a given load.

References

[1] R. Puers and G. Vandervoorde, "Recent progress on transcutaneous energy transfer for total artificial heart system", Int. J. Artif. Organs, **25-5**, 400-405 (2001).
[2] A. Yakovlev, S. Kim and A. Poon, " Implantable biomedical devices: Wireless powering and communication ", IEEE Commun. Mag., **50-4**, 152-159 (2012).
[3] A.A. Danilov, G.P. Itkin and S.V. Selishchev, "Progress in methods for transcutaneous wireless energy supply to implanted ventricular assist devices", J. Biomed. Eng., **44-4**, 125-129 (2010).
[4] T.D. Dissanayake, D. Budgett, P. Hu and S. Malpas, "Experimental thermal study of a TET system for implantable biomedical devices" 2008 IEEE Biomedical Circuits and Systems Conference, 113-116 (2008).
[5] Si, P., Hu, A.P., Malpas, S., Budgett, D., "A frequency control method for regulating wireless power to implantable devices", IEEE TBioCAS, **2-1**, 22-29 (2008).
[6] L. Hu, Y. Fu, X. Ruan, H. Xie, X. Fu, "Detecting malposition of coil couple for transcutaneous energy transmission", ASAIO Journal, **62-1**, 56-62 (2016).
[7] [online] http://www.rrc-wireless-power.com/en/rrc-technology/evaluation-kit.html, accessed April 14, 2016.
[8] [online] http://www.ti.com/lsds/ti/power-management/wireless-power-receiver-solutions-overview.page, accessed April 14, 2016.
[9] G.-S. Wang, G.A. Covic and O.H. Stielau, "Power transfer capability and bifurcation phenomena of loosely coupled inductive power transfer systems", IEEE Trans. Ind. Electron., **51-1**, 148-157 (2004).
[10] A.A. Danilov, E.A. Mindubaev, "Space-frequency approach to design of displacement tolerant transcutaneous energy transfer system" PIER M; **44**, 91-100 (2015).

Research of dialysis fluid regeneration methods

N. Bazaev, V. Grinval'd, B. Putrya
National Research University of Electronic Engineering

For last 30 years, development of a wearable artificial kidney (WAK) was a challenge for many research and engineering groups all over the world. At present at least 3 groups of researches are developing wearable artificial kidneys – in Netherlands [1], Singapore [2] and USA [3]. Benefits that such a device can offer are impressive.

1. WAK (in comparison to hemodialysis machine) works all the time and its effect on the human body is closer to native kidney. Hemodialysis cleans human body from metabolites that are produced during 3 days between procedures. Lower rates of metabolites elimination will cause patients on dialysis feel better and live longer [4].

2. WAK is supposed to give patients on dialysis unrestricted mobility. Low weight and portability will let people use the device not only in clinic.

3. WAK will lower expenses on the procedure (from 85k€/year/patient to 50 k€/year/patient [5]).

The work is devoted to results of research in the field of methods for waste dialysis regeneration.

Most metabolites can be eliminated from the waste dialysis fluid via its sorption with activated carbon. The main problem is in effective urea elimination.

Sorption can be expressed in the following way:

$$N_i^{sorp}(j) = A_m \cdot \frac{b_i \cdot [Sub_i](j)}{1 + b_i \cdot [Sub_i](j)} \cdot \frac{\Delta t}{T}, \quad (1)$$

where $N_i^{sorp}(j)$ – amount of substance absorpt by sorption unit during j-th iteration, A_m – amount of substance that can be absorpt by the sorption unit, Δt – duration of one iteration, T – time constant, b_i – constant of adsorption equilibrium for i-th substance, $[Sub_i](j)$ – concentration of i-th substance during j-th iteration.

Experimental result of waste dialysis fluid sorption vs theoretic one is presented in the Fig.

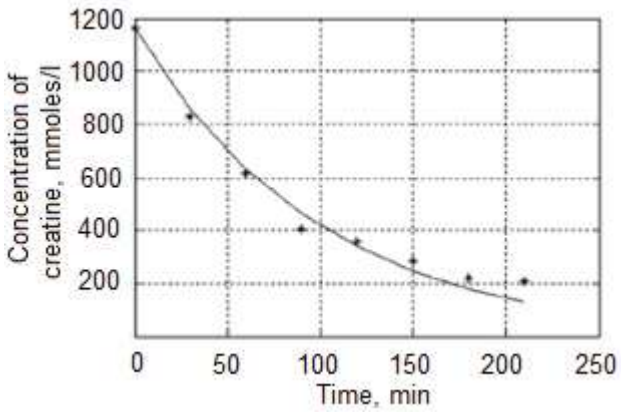

1.

Fig. 1 Creatine sorption with activated carbon

There are several methods that can be used to eliminate urea from waste dialysis fluid: thermal method, enzymatic method and electrolysis (Fig. 2).

Thermal method includes heating of waste dialysis fluid up to 160-250 °C. Under the temperature of more than 100 °C urea undergoes decomposition into ammonia and carbon

dioxide [6]. Experimental results show that urea concentration goes down in an exponential way:

$$C_u(t) = C_{u0} \cdot \exp(-k(T) \cdot t), \quad (1)$$

Where C_u , C_{u0} - concentrations of urea in dialysis fluid at time t and in the beginning of the procedure (t=0), t – time, $k(T)$ - constant of urea elimination rate.

Waste dialysis fluid enters the evaporator (Fig 2c), where some amount of water is evaporated in order concentration of urea in dialysate to be raised. The vapour goes through the parallel circuit where it transforms to the liquid state. Concentrated waste dialysis fluid is set under temperature of 200 °C for about 30 minutes. After that, the gas phase is let out of the circuit, dialysis fluid is cooled and mixed with the water from parallel circuit, and can be used again. Experimental results show that it is possible to eliminate urea from waste dialysis fluid with rates from 2.5 to 10 g/h.

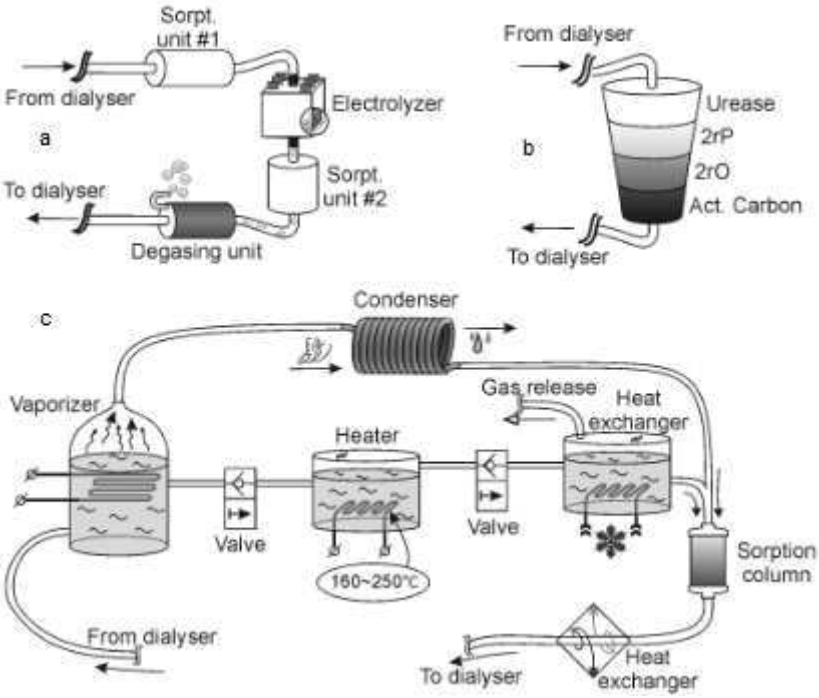

Fig. 2 Methods of urea elimination: electrolysis (a), enzymatic method (b) and thermal method (c)

Enzymatic method uses urease as a catalysis of urea hydrolysis reaction: $(NH_2)_2CO + H_2O \xrightarrow{urease} 2NH_3 + CO_2$. When urease is immobilized on a surface of a solid state carrier, its efficacy becomes 10 times higher. Waste dialysis fluid is transported through sorption unit (Fig 2b) that includes the following layers: activated carbon, immobilized urease, zirconium phosphate, zirconium oxide and activated carbon. Results of the experiment are shown in Fig. 3

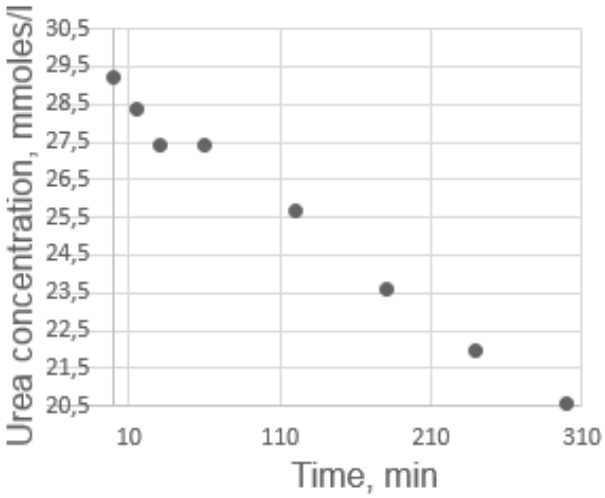

Fig. 3 Urea concentration dynamics in waste dialysis fluid circulating through the sorption unit with 1 g urease (T=37 °C)

Urease activity was also measured in aspect of storage conditions. It was stored in vacuum containers under temperature of 2-4 °C, 20 °C and 37 °C. In all cases, its activity decreased, in particular, 2.8, 3.3, and 3.8 times respectively.

Electrolysis of waste dialysis fluid (Fig. 2a) is another method of urea elimination [7]. Effective electrolysis is a matter of electrodes material and parameters of electrolysis. In our research, we investigated some metals from platinum group: Pt (electrodeposed), Pt (rolled), Rh (electrodeposed) and Ru (electrodeposed). The support plate was Ti for all metals used in the research. In Tab. 1 presented results of electrolysis with different type of electrodes; geometrical square is 150 cm^2.

Tab. 1 Comparison of electro-oxidation activity of some metals from Pt-group

Type of electrode	Urea elimination rate*, mg/h	Comments
Ti-Rh_{eo}	33	Effective time of work ~14 hours, deposition of subproducts on electrode surface
Ti-Pt_{eo}	110	Effective time of work ~40 hours. Pt dissociates into dialysate.
Ti-Pt_r	50	Effective time of work > 200 hours. Pt dissociates into dialysate with much lower rate.
Ti-Pd_{eo}	–	Problems with electrodeposition of Pd on Ti
Ti-Ru_{eo}	0	Ru dissociates into dialysis during 4 hours

Results that were gained during set of experiments show that among metals from Pt-group Pt has the highest electro-oxidation activity. As to the method of its binding with titanium support plate, rolled Pt was the most durable. However, rolled Pt showed twice lower activity in comparison with electrodeposed Pt. It happens because during electrodeposition, surface becomes developed, consequently urea electro-oxidation rate becomes higher.

Tab. 2 Comparison of applicability of urea elimination methods

	Thermal method	Enzymatic method	Electrolysis
Complexity of WAK development	High	Low	Acceptable
Consumption of electricity	High (~5kW)	Low (~7W)	Acceptable (~20W)
Mass-dimensional characteristics of WAK	High (~70×100 cm)	Low (~30×40 cm)	Acceptable (~35×55 cm)
Necessity in expendable materials	No	Yes	Yes
Price of expendable materials	–	100 €/day	1875 €/year + 5 €/day
Time of cycle for expendable materials	–	6-12h	2 years for electrolyser +12 h for sorption units
Complexity of expendable materials storage	–	High (enzyme degrades during several days)	Low (in normal conditions can be stored unlimitedly)

Thermal method can hardly be a good choise for WAK. It has one valuable advantage: it does not need any expendable materials, only electric energy. So that can be a good option for hemodialysis machines with dialysis regenerating unit.

Enzymatic method is a very useful one. On the basis of this method a WAK with very low mass-dimention characteristics can be assembled. But it's very hard to make cheap expendable materials. Moreover it is very difficult to store sets of expendable materials (efficacy of immobilized urease becomes almost four times lower whithin a week).

Electrolysis seem to be the most acceptable option for WAK. However it is also not free from problematic moments: chemical balance during procedure must be controlled and gas phase must be let out from the extracorporeal circuit right after regeneration unit. Electrisity consumption of such a regeneration unit will cause necessity in accumulators exchange several times during 24 hours.

In current research several methods of dialysis regeneration were considered. Experimental results show that all of them has its pros and cons but anyway WAK doesn't seem to be so impossible.

References

[1] www.nanodialysis.nl – Development of a Renal Assist Device (RAD)
[2] www.awak.com – Development of an Automated Wearable Artificial Kidney (AWAK)
[3] V. Gura, A.S. Macy, M. Beizai, C. Ezon, T.A. Golper Technical Breakthrough in the Wearable Artificial Kidney (WAK) Clin. J. Am. Soc. Nephrol 4: 1441-1448, 2009
[4] P. Armignacco, F. Garzotto, A. Lorenzin, and C. Ronco "WAK Engineering Evolution" Blood Purification 2015; Vol. 39, P. 110-114
[5] www.nephroplus.eu – ICT-enabled WAK and Personal Renal Care System
[6] V. Grinval'd, G. Zalko, Ju.Mikhailov, V. Podgaetskij, V. Semin, A. Strelkin, A. Sjulaev. Method of purifying dialyzing solution in apparatus "artificial kidney". – RU 2008927
[7] M. Wester, F. Simonis, N. Lachkar, W.K. Wodzig, F.J. Meuwissen, J.P. Kooman, W.H. Boer, J.A. Joles, and K.G. Gerritsen Removal of Urea in a Wearable Dialysis Device: A Reappraisal of Electro-Oxidation

Bioengineering system used for patients' memory restoration by noninvasive methods in the period after stroke

***D.V. Belik*[1,2], *N.A. Dmitriev*[1,2], *M.S. Zinevskaya*[1,2], *S.A. Pustovoy*[1,2]**

1. Medical Engineering Research Institute

2. Novosibirsk State Technical University (NSTU)

Introduction

The recovery of body functions is of primary importance for the patients suffering from stroke causing pathological processes in the brain areas and memory fields. Based on the theory of long-term memory reservation and its distribution over the brain cortex, the acute problem of memory elements restoration has to be resolved not only with the use of medication but by means of noninvasive physical interventions, which allow us to initiate the processes of memory restoration.

The Problem Formulation

Once recognizing the relevancy of brain activity and memory restoration after stroke, we've set a goal to create a bioengineering system of audio-visual-colour and magnetic brain areas stimulation and to conduct research, which enables us to obtain various simulations of the efficient therapeutic intervention for resolving the problem.

Research Methodology and Implementation

The following approaches to noninvasive intervention for memory field stimulation have been suggested: 1) the impact on vision and auditory system since the receptor areas information is transferred via hippocampus; then processed by hippocampus, the information arrives at brain cortex regions to activate neuron fields and mechanisms responsible for reconstruction of broken links and generation of new ones between the neurons owing to neuroplasticity processes [1]; 2) brain cortex exposure to direct magnetic radiation with the amplitude up to 5mT.

To improve the efficiency of these interventions, the authors had proposed the approaches to affect receptor areas, particularly by the influence on patient's eyes and ears, which were exposed to flash and sound frequencies resolved by the range. The frequency difference of such exposures was equal to alpha, beta, theta and delta patient's rhythms defined by electroencephalograms before starting the simulation. Different colour scales and their combinations were set for colour exposures.

Light and sound exposures with frequency difference (which equals beta and theta rhythms) are characterized by the greatest efficiency because these frequencies are generated by hippocampus neuron fields causing resonances at which rhythm amplitude tends to grow.

In a similar way, it was suggested to expose the brain cortex to several magnetic flows with frequency differences of emitting solenoids, which are equal to alpha and beta patient's rhythms. Frequency content of magnetic flows has to comply with the frequency modulation pulses of interneuronic interaction [2].

The bioengineering system for long-term memory recovery after stroke was developed by R&D institute of Medical Engineering at NSTU. The system functional diagram is presented in Fig. 1.

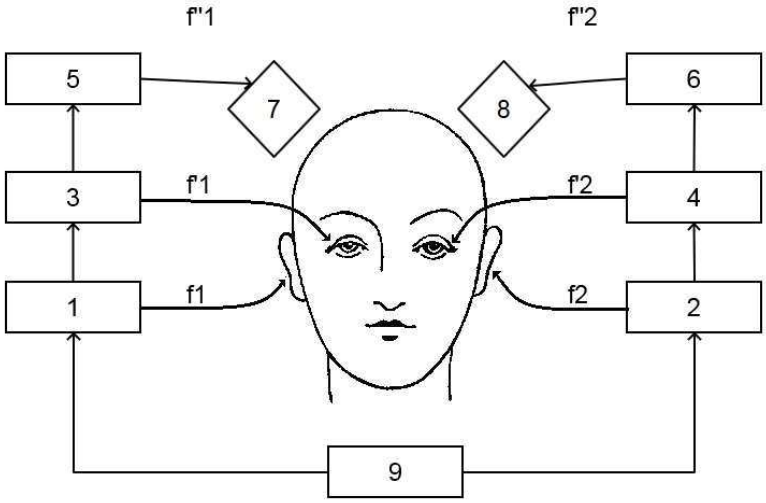

Fig.1. Flow-chart of the research bioengineering system designed for long-term memory restoration after stroke. Where: 1,2 – Audio-exposure units; 3,4 - Flash-colour exposure units; 5,6 – Magnetic field exposure units; 7,8 – Emitters for magnetic flow exposures; 9 – Control unit for interventions synchronization.

$\Delta f = f1 - f2$ – Influence frequency difference complies with alpha, beta, theta and delta rhythms

$\Delta f' = f'1 - f'2$ – Influence frequency difference complies with alpha, beta, theta and delta rhythms

$\Delta f'' = f''1 - f''2$ – Influence frequency difference complies with alpha, beta, theta and delta rhythms

Technical characteristics of the bioengineering system.

1. Light exposure frequency range, from 1 up to 60 Hz.
2. Sound exposure frequency range, from 100 to 2000 Hz with the intensity not greater than 70dB.
3. Colour exposure scale: red, green, dark-blue and combination of these colours with the intensity not less than 300-350 lx.
4. Magnetic field exposure magnitude, from 1 mT up to 5 mT.

Experimental Results

The bioengineering system assigned to long-term memory recovery in the after-stroke period was used for doing research on brain memory field stimulation by means of flash, audio and diverse colour exposures. The degree of changes in brain area activity was assessed with an electroencephalograph and by the topograms obtained. A number of tests aimed at brain activity stimulation were carried out on volunteers. Exposure frequencies were a multiple of the alpha, beta, and delta brain rhythms.

It should be noted that all the volunteers were in good health.

The preliminary approbation outcomes obtained for the bioengineering system used for long-term memory recovery in the after-stroke period confirmed the efficiency of the patient's memory field stimulation by means of the offered techniques, which involve colour/audio eyes and ears exposures at frequency difference being equal to the testee's alpha, beta, theta and delta rhythms.

The outcomes of memory exposures were obtained by the following techniques: the method of the short-term memory assessment, «Short-term memory capacity estimation» method, «TV-set» test, «Visual operating memory assessment» test, and etc. The test results

confirmed the improvement of long-term memory by 15-20% in comparison with the initial memory estimates.

Conclusion

With regard to the results obtained, we can draw the following conclusions:

- Frequency differences of light-colour-audio-magnetic field exposures brought into conformity with the brain rhythms have an effect on the brain area activity and let us reconstruct neuron fields and restore long-term memory.

- The impact of flash-colour exposures with the same frequency difference but diverse colour scales is found to produce various stimulating effects.

- Research findings have proved the advisability of the further research accomplishment by means of the developed bioengineering system and techniques aimed at patients' rehabilitation after stroke and the brain activity recovery.

The authors offer to create two models of the bioengineering system to meet the patients' demands for rehabilitation at home and at hospitals.

References

[1] E.V. Ekusheva, I.V. Damulin. Reabilitaciya posle insulta: znachenie processov neiroplastichnosti i sensornomotornoi integracii // Journal Neurology and Psychiatry, 12, 2013; pp. 44-50.

[2] D.V. Belik. Magnetobiosphere// Novosibirsk: «Sibprint», 2016, pp. 81-87.

electric phenomena which occur during blood coagulation. Nowadays the method is used in INR measurement portable device design.

Impedance measurement system may be divided into following blocks: harmonic signal generator, two-pole voltage and current analyzer and data processing block. As a result having ratio of current and voltage absolute values, it is possible to calculate impedance absolute values and having phase delay between current and voltage it is possible to get impedance argument.

Impedance measuring devices with such a functional structure are technically hard to implement. However there are a number of methods which can be used in developing such a device. They are integrated circuits AD5933 and ADUCM350 from Analog Devices and the basic schematic pattern for current and voltage measurement. The paper reviews mentioned methods, its portable embodiment and evaluation of impedance measurement relative deviation from reference values for the embodiments.

Resistance divider is the basic schematic pattern for impedance measurement. AC voltage source is connected to the unknown impedance. Current, voltage and impedance ratio in this scheme is determined by Ohm's law in the complex form. It is valid also for the absolute values, which are necessary for INR measurements.

As an AC voltage source laboratory an AC signal generator or a DDS can be used, due to its high accuracy and wide frequency range. For current measurement in the form applicable for computer processing the sense combined with unknown impedance into resistance divider is used. The total system is controlled by a microcontroller.

It should be noted that this method requires a time-consuming adjustment, and may also need a selection of individual parameters for each unit due to the electronic components parameters variation. That is why it is worth using meters performed as integrated circuits, which contain all functional blocks needed for impedance meter construction.

measurement relative deviation from reference values, frequency and measuring value ranges. According to [3,4] it is possible to make a conclusion that for INR determination impedance measurement should be performed at the frequency of 10 kHz. Besides in papers [5–7] the possibility of impedance measurements at higher frequencies (several tens kilohertz) is described. It is more difficult to lay down requirements to measuring values, because blood sample impedance at the fixed frequency depends also on the blood volume and electrodes configuration. That is why developed prototypes accuracy evaluation should be performed in wide measuring impedance values range. Accuracy requirements can be laid down due to the results of biological material experiments implemented in ICBFM SB RAS. Thus, during coagulation at the frequency of 50 kHz impedance of 1ul blood sample changes from baseline in several kilo ohms by several tens of ohms. Therefore the deviation of prototypes results must be at the level of 1-2% for the most accurate INR determination.

As a result there were laid down the following requirements for an impedance meter:

- AC signal frequency ranges: 6…14 kHz and 40…60 kHz;
- measuring value ranges: 2000…10000 Ohm, 10000…50000 Ohm, more than 50000 Ohms;
- measurement accuracy not less than 2%.

In order to evaluate impedance meters accuracy according to described requirements there were performed comparison tests with laboratory LCR meter MNIPI E7-20. As measuring samples for the tests radio components, which have ohmic resistance (resistors) as well as reactive resistance (capasitors) were chosen. Measurements were performed at the frequency ranges from 6 to 14 kHz by 2 kHz and from 40 to 60 kHz by 5 kHz. Comparison results consist of two parts: results for resistors (impedance value is equal to nominal value of the resistor) and capacitors (impedance value is calculated by reactive resistance formula). For all components the impedance absolute values were measured at different frequency ranges and comparison of all meters measurement results with the laboratory meter was performed. Average deviation is presented in table 1.

Table 1

Component type	Impedance absolute range, kOhm	Average relative deviation, %					
		AD5933		ADUCM350		Meter based on resistance divider	
		6…14 kHz	40…60 kHz	6…14 kHz	40…60 kHz	6…14 kHz	40…60 kHz
Resistors	2…10	2,0	1,9	0,5	0,5	43,4	-
	10…50	1,7	3,2	0,7	3,3	3,0	60,0
	> 50	1,9	22,5	12,4	-	23,7	25,6
Capacitors	2…10	3,6	3,8	1,7	2,1	20,0	-
	10…50	5,5	8,0	15,6	8,1	23,3	25,2
	> 50	26,7	29,9	-	-	-	25,3

It should be noted, that prototypes accuracy characteristics differ from each other not only in depending on the measuring value range and the generated signal frequency, but also on the component type: deviation increase was noticed during capacitor impedance measurements.

Performed tests showed, that the least deviation (less than 2%) was reached in the impedance absolute values range from 2 to 10 kOhm when the AD5933 and ADUCM350 impedance meters were used at the frequency from 6 to 14 kHz. For the frequency range from 40 to 60 kHz deviation is not higher than 2% for the lower frequency range and 3% for the higher range. However, it should be noted, that these results are valid for samples with ohmic resistance. For samples with only reactive resistance, the deviation is a little higher than 2% for lower impedance values (from 2 to 10 kOhm) for the ADUCM350 impedance meter.

According to test results the best performance has the ADUCM350 meter, as it provides the least deviation from reference values for ohmic as well as reactive impedance component (taking into account capacitor measurements at high frequencies results). The AD5933-based meter development is possible when using it for at low frequency range measurements or with less accuracy requirements. The worst results showed the resistance divider meter. Therefore it was concluded, that the best impedance meter for INR determination is the ADUCM350 meter.

References

[1] 1 MSPS, 12-Bit Impedance Converter, Network Analyzer AD5933 // Analog Devices URL: http://www.analog.com/media/en/technical-documentation/data-sheets/AD5933.pdf
[2] 16-Bit Precision, Low Power Meter On A Chip with Cortex-M3 and Connectivity ADuCM350 // Analog Devices URL: http://www.analog.com/media/en/technical-documentation/data-sheets/ADuCM350.pdf
[3] Bharati S. R., Parvathi C S. and P. Bhaskar Atmel Microcontroller Based Human Blood Conductivity Measurement System // IJEE. 2013. Vol. 5. Num. 2. PP. 115-118.
[4] Kin Fong Lei, Kuan-Hao Chen, Po-Hsiang Tsui, Ngan-Ming Tsang Real-Time Electrical Impedimetric Monitoring of Blood Coagulation Process under Temperature and Hematocrit Variations Conducted in a Microfluidic Chip // Plos One. 2013 / http://journals.plos.org/plosone/article?id=10.1371/journal.pone.0076243
[5] Kin Fong Lei, Kuan-Hao Chen, Po-Hsiang Tsui, Ngan-Ming Tsang Real-Time Electrical Impedimetric Monitoring of Blood Coagulation Process under Temperature and Hematocrit Variations Conducted in a Microfluidic Chip // PLOS ONE.-2013.-Vol. 8.- Iss. 10.-pp. 1-7.
[6] Bharath Ramaswamy, Yin-Ting Tim Yeh, Si-Yang Zheng Microfluidic Device And System for Point-of-Care Blood Coagulation Measurement Based on Electrical Impedance Sensing // Sensors and Actuators B.-2013.-pp. 21–27.
[7] Van Yang, Praveen Aroul, Kevin Wen Impedance Measurement with the AFE4300 // Texas Instrument Application Report SBAA202.-2013.-13 P.

Current source for electrical impedance devices

Y.A. Stryzhak[1]

1. Biomedical Engineering Department, Bauman Moscow State Technical University, 5, 2d Baumanskaya str., Moscow 105005, Russia

A current source is one of the key components in an electrical impedance system. Typical applications of electoimpedance method in medicine, particularly in military or sports medicine require a high quality reliable current source [1]. The main requirement imposed to the current source is a high output impedance at a certain frequency that provides steady current supply to the electrodes throughout bioobject impedance range.

Formed following technical requirements to the current source for military and sports electrical impedance devices:

- A = 5 mA ± 1 μA;
- f = 100 kHz;
- Z_{bo} = 0 – 250 Ω;
- Min Z_{out} = 20 kΩ;

where: A – probing alternating current amplitude, f – probing alternating current frequency, Z_{bo} – base impedance of bioobject, Min Z_{out} – minimal boundary of output impedance.

In MicroCap where simulated six different current source circuits: circuit on two Operational Amplifiers (OpAmp), GIC (general impedance converter), Howland circuit, 3 circuits on Instrumentation Amplifier (IAmp) AD8130, circuit on IAmp LTC2053 [2, 3]. For each circuit was plotted dependence relative current change vs load resistance that is bioobject impedance at constant power supply according to equations (1), (2) (Figure 1).

$$I_{load} = I_0 \cdot Z_{out} / (Z_{out} + Z_{load}) \quad (1)$$

$$Z_{out} = I_{load} \cdot Z_{load} / (I_0 - I_{load}) \quad (2)$$

where: I_{load} – current value at load resistance, I_0 – current at zero load.

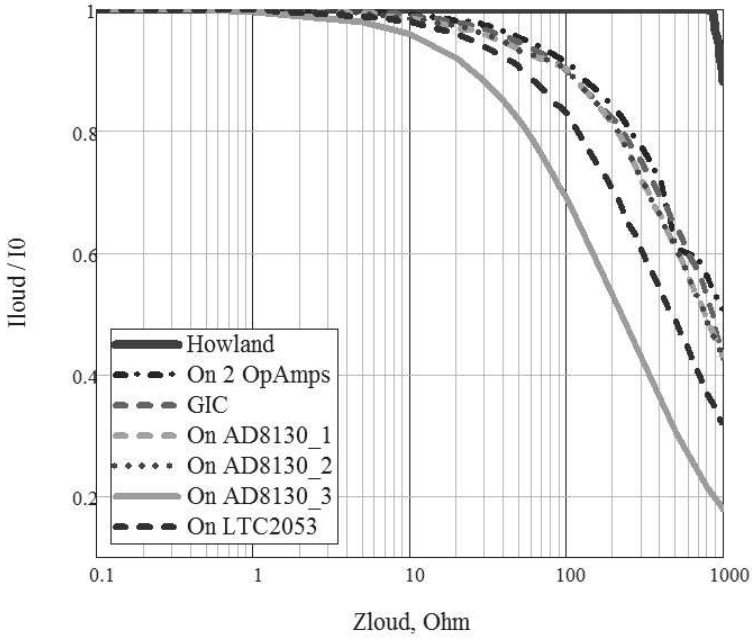

Fig. 1 Relative current change vs load resistance.

Among all circuits, Howland circuit provides the most stable current at different values of load resistance. Therefore, we give dependence output impedance vs voltage supply frequency for Howland circuit (Figure 2). At 100 kHz output impedance is around 15 kΩ that is less than the required minimal boundary, but enough.

Next, we focus on the problem of common-mode signal. In a four-electrode measurement method, contact resistance of current electrodes and skin introduces a common-mode voltage at IA inputs that hides the differential voltage [4]. Standard current source circuit provides unipolar sinusoidal voltage supply from the DAC. One current electrode connected to the ground (GND) of the OpAmp. The value of the common-mode voltage is evaluated relative to this GND and is about 2.5 V. However, the CMRR value of IAmp at the required frequency is not enough.

So then, we provide bipolar current source circuit that initially gets rid of the common-mode voltage appearance. The main thing is that the DAC generates two sinusoidal signals in phase opposition that supply current source. Such circuitry was assembled symmetrically on Howland circuit and was simulated in MicroCap (Figure 3).

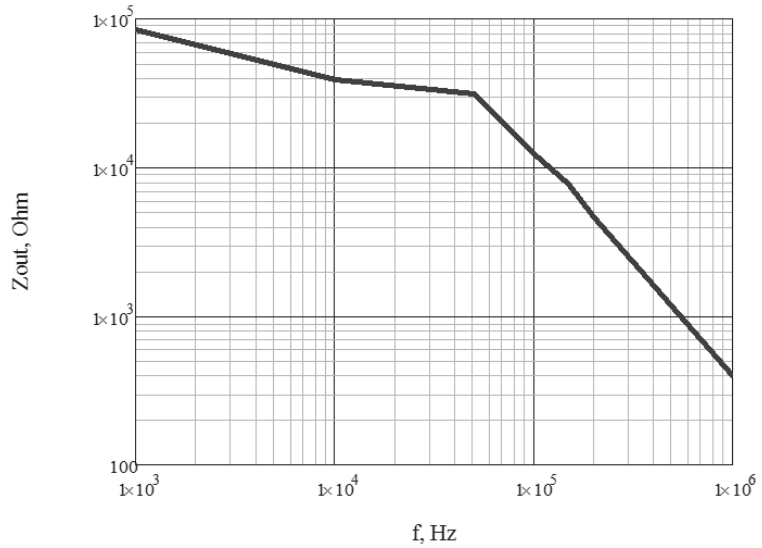

Fig. 2 Output impedance vs voltage supply frequency for Howland circuit.

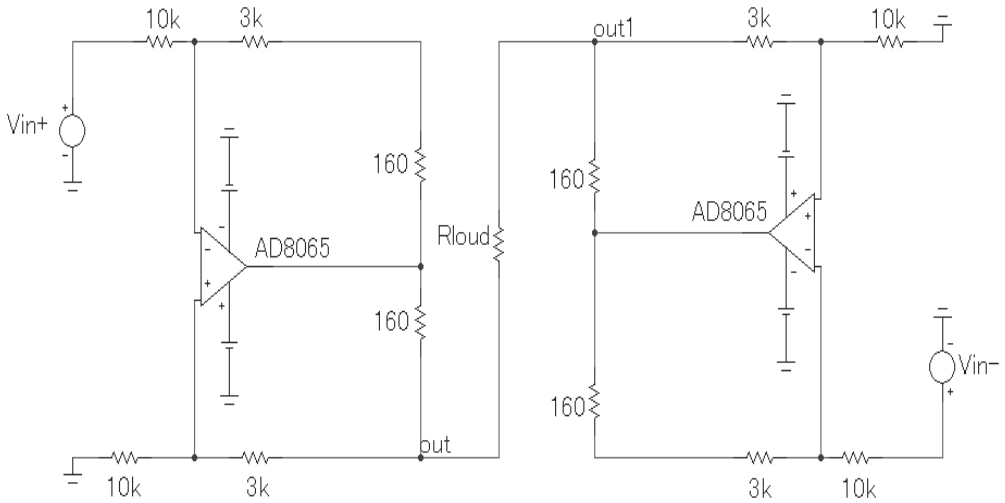

Fig. 3 Output impedance vs voltage supply frequency for Howland circuit.

A comparative analysis of the dependence output impedance vs voltage supply frequency for classic and bipolar Howland circuits is done (Figure 4).

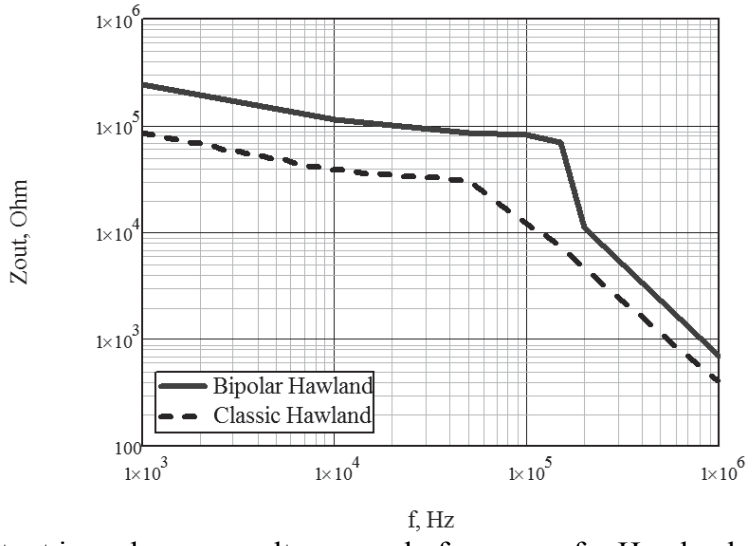

Fig. 4 Output impedance vs voltage supply frequency for Howland circuit.

At 100 kHz, output impedance of bipolar Howland circuit is 8 times higher than that of classic Howland circuit. Thus, proposed bipolar Howland circuit corresponds to the current source requirements.

References

[1] W. Wang, M. Brien, D-W. Gu, and J. Yang, "A Comprehensive Study on Current Source Circuits" ICEBI 2007, IFMBE Proceedings 17, pp. 213–216 (2007).
[2] Xiaosha Zhao, Steffen Kaufmann, and Martin Ryschka, "A comparison of different Current Sources for multi-frequency Impedance Spectroscopy. Preliminary results" Centre of Excellence for Technology and Engineering in Medicine (TANDEM), Lübeck University of Applied Sciences, Stephensonstraße 3, 23562 Lübeck, Germany.
[3] http://kazus.ru/datasheets/pdf-data/3453477/LINER/LTC2053.html.
[4] David Yelamos, Oscar Casas, Ramon Bragos, and Javier Rosell, "Improvement of a Front End for Bioimpedance Spectroscopy" Department of Electronic Engineering, Universitat Politecnica de Catalunya, 08034 Barcelona, Spain.

Programmable current switches for multichannel EEG amplifier with tES functions

***S.V. Zabodaev*[1,2], *A.V. Smoliakov*[2]**

1. National Research University of Electronic Technology (MIET), Bld. 1, Shokin Square, Zelenograd, Moscow, Russia

2. Medical Computer Systems Ltd., Bld. 4-2, passage 4922, Zelenograd, Moscow, Russia

Transcranial electrical stimulation (tES) is a form of noninvasive brain stimulation using a weak electrical current to modify cerebral excitability [1]. It could be done by using the scalp electrodes to stimulate the interest brain area. There are several variations of tES, such as direct current stimulation (tDCS), alternating current stimulation (tACS) and random noise stimulation (tRNS) [2]. The tDCS procedure shifts the resting potential of cortical neurons causing the membrane to depolarize or hyperpolarize [3]. In case of anodal stimulation, depolarization increase spontaneous cell firing, improving excitability of target zone. Cathode stimulation causes the opposite effect.

There are a lot of studies reported about significant effects of the brain stimulation for a range of neurological and psychiatric ills, such as depression or schizophrenia [4,5] and modification of visual, motor, cognitive functions, etc.

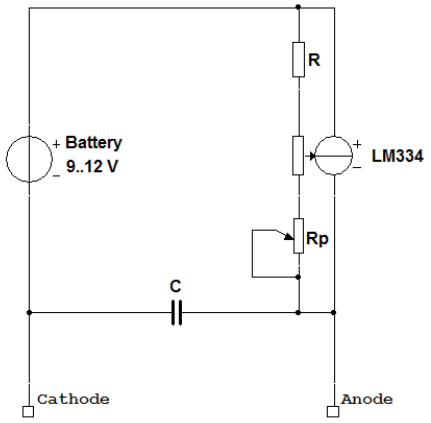

Fig. 1 Circuit diagram of adjustable current source based stimulation device

Special device called electrical stimulator is used for tES. There are many commercially available devices differing in complexity, operating modes and price. The simplest one represents just an adjustable current source with battery power supply (figure 1). This kind of device should not be recommended for clinical purposes, but it is widely used by young researches as tDCS device for cognitive brain function stimulation.

Stimulation device for medical use must meet the safety and essential performance requirements according to IEC 60601-1 and IEC 60601-2-26. Modern clinical devices are able to combine tDCS, tACS and tRNS kinds of stimulation. Maximum amount of stimulation channels of commercially available devices is limited by 16, while the upper frequency of tACS mode does not exceed 1 kHz sample rate.

Conventional tES devices use high voltage analog switches for commutation the current source on stimulation leads. Current source is controlled by digital-to-analog converter, whereas AC-mode realized by changing current source operating mode.

The main purpose of this study is to develop a multichannel medical device that combines both biological signal acquisition and high-speed tES functions. This paper describes benefits of using programmable current switches (PCS) for tACS mode management.

Precision current source with 32 V reference voltage is used for constant current generation. High voltage MOSFET current switches are used for current source direct commutation to EEG outputs (stimulation leads). Field-Programmable Gate Array (FPGA) circuit operates both current source and current switches operation state. Being reprogrammed each time before starting of stimulation procedure, FPGA controls digital-to-analog converter (DAC) values allowing specify custom stimulus shape. During the stimulation, at the moment of intersection the zero level of specified current, FPGA inverts the control levels of current switches. Thus, anode becomes the cathode and vice versa.

Figure 2 shows the simplified circuit diagram of programmable current switches. Presence of feedback line using analog-to-digital converter (ADC) allows impulse value and shape control during the stimulation as well as the value of stimulus current for each electrode. Presence of separate analog acquisition module allows the use of this device also for the EEG signal acquisition for the analysis.

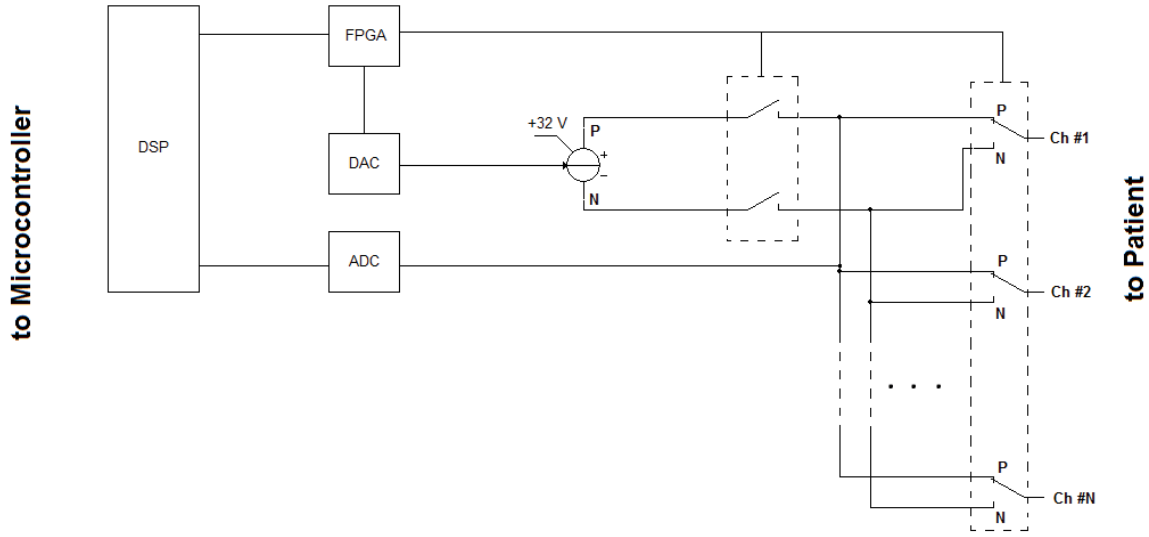

Fig. 2 Simplified circuit diagram of programmable current switches

The main advantage of this approach is obtaining combined device for both EEG acquisition and tES procedure, extension tACS frequency range up to the bound of sound

frequencies, and finally, the price reduction due to implementation of widely used electronic components. Table 1 shows a short list of device technical specification.

Tab. 1 List of technical specification

Characteristic	**Value**
EEG DC monopolar channels	32
EEG dynamic range	±400 mV
EEG channel's input impedance	more 100 MOhm @ DC
EEG channel's noise	less 0.9 uV p-p (0.15 RMS) @ 0,1..30 Hz
Digitalization	24 bit, 6th order delta-sigma modulator with 64x oversampling, one converter per each channel
Sampling rate	250 .. 50000 Hz
Number of stimulation channels	33
Current generator	16 bit, Direct Digital Synthesis (DDS)
Output current ranges in DC mode	0 .. 400 uA, 0 .. 4000 uA
Output current ranges in AC mode	±400 uA, ±4000 uA
Output voltage of current generator	0 .. 32 V
REPEAT MODE: standards stimulus	DC, Sine, Square, Trap, Ramp, Sin(x)/x, Gauss, Lorenz, Haversin, Exp, White Noise
REPEAT MODE: repeating	up to 20 kHz

Currently the stage of making the work prototype has been finished. The next step is appropriate software development.

References

[1] K. Utz, V. Dimova, K. Oppenländer, G. Kerkhoff, "Electrified minds: Transcranial direct current stimulation (tDCS) and Galvanic Vestibular Stimulation (GVS) as methods of non-invasive brain stimulation in neuropsychology—A review of current data and future implications", Neuropsychologia, **48**, 2789–2810 (2010).
[2] W. Paulus, "Transcranial electrical stimulation (tES - tDCS; tRNS, tACS) methods", Neuropsychol. Rehabil., **21**, 602–617 (2011).
[3] M.A. Nitsche, W. Paulus, "Excitability changes induced in the human motor cortex by weak transcranial direct current stimulation", The Journal of Physiology, **527**, 633 (2000).
[4] M. Mondino et al., "Can transcranial direct current stimulation (tDCS) alleviate symptoms and improve cognition in psychiatric disorders?", World J. Biol. Psychiatry, **15,** 261-275 (2014).
[5] S.M. Agarwal et al., "Transcranial direct current stimulation in schizophrenia", Clin. Psychopharmacol. Neurosci., **11,** 118-125 (2013).

The study of the light depolarization in liquid dispersions of nanoparticles

P.V. Shalaev, S.A. Dolgushin, S.A.Tereshchenko

National Research University of Electronic Technology, Russia, Moscow

Nanoscale particles and structures are widely used in various fields [1]. For example, nanoparticles are used for the cancer cell imaging and the photothermal therapy, the targeted delivery of drugs, the detection and the control of microorganisms. Among a plurality of nanoparticles, non-spherical nanoparticles, such as gold nanorods are very interested [2].

There is a problem to measure geometrical parameters of non-spherical nanoparticles. To date the most used method for the nanoparticle shape study is the electron microscopy. Despite of very detailed and sharp images, the electron microscopy method has some significant drawbacks. The main of them is the number of particles which may be analyzed with micrographs. This number seldom exceeds few hundreds, while one milliliter of the typical colloid contains several billions of nanoparticles. In addition, a fundamental restriction is the aggregation of particles in the sample preparation process.

The methods based on the light scattering allow analyzing nanoparticles in a colloidal form without the sample preparation are most suitable for the express analysis in technological processes. In the method of the dynamic light scattering (DLS) the time correlation function is measured, which allows to find the diffusion coefficient and the radii of spherical nanoparticles. All existing devices are based on the assumption of nanoparticles spherical shape. The measurement of geometrical parameters for non-spherical particles is essentially more difficult.

One of the ways which allow determining the geometric parameters of non-spherical particles is the measurement of the polarization characteristics of the scattered light [3].

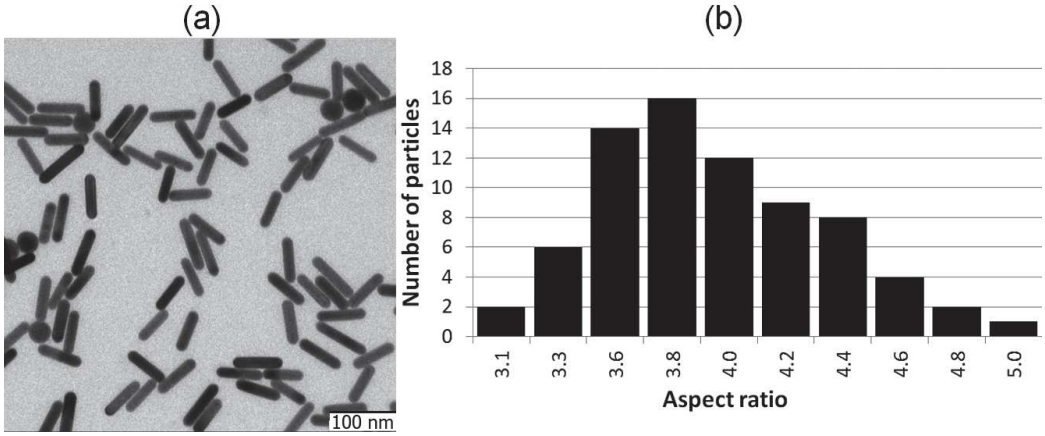

Fig. 1. Gold nanorods: a) transmission electron micrograph of a sample; b) particles aspect ratio distribution in the sample

A number of experiments were carried out to study the light depolarization in liquid dispersions of nanoparticles. In our experiments, the measurement of the scattered light intensity was made for different scattering angles and for different rotation angles of the polarizer. The maximum light intensity corresponds to 0° (VV-polarization) and the minimum light intensity corresponds to 90° (VH-polarization). The diode laser with a wavelength 657 nm was used. The measurements were carried out using the particle size analyzer "Photocor Complex" (Russia). The ratio of VH-intensity to VV-intensity (depolarization ratio) of scattered light was measured.

Samples of gold nanorods water dispersions with aspect ratios ranging from 2 to 10 were studied. The geometric parameters of the samples were previously studied by TEM (Fig. 1).

As a result of the analysis of TEM images, it was found that particles have a spread of the aspect ratios (Fig. 1 b). Each sample characterized by the average aspect ratio. It was also found that there are quasi-spherical impurities in the sample (Fig. 1 a). Moreover, the samples with bigger average aspect ratio contain more quasi-spherical impurities. This is due to the specifics of nanoparticles synthesis.

The studied samples of liquid dispersions have different concentrations of nanoparticles. The dependence of the scattered light intensity (Fig. 2 a) and the depolarization ratio (Fig. 2 b) on the concentration was studied.

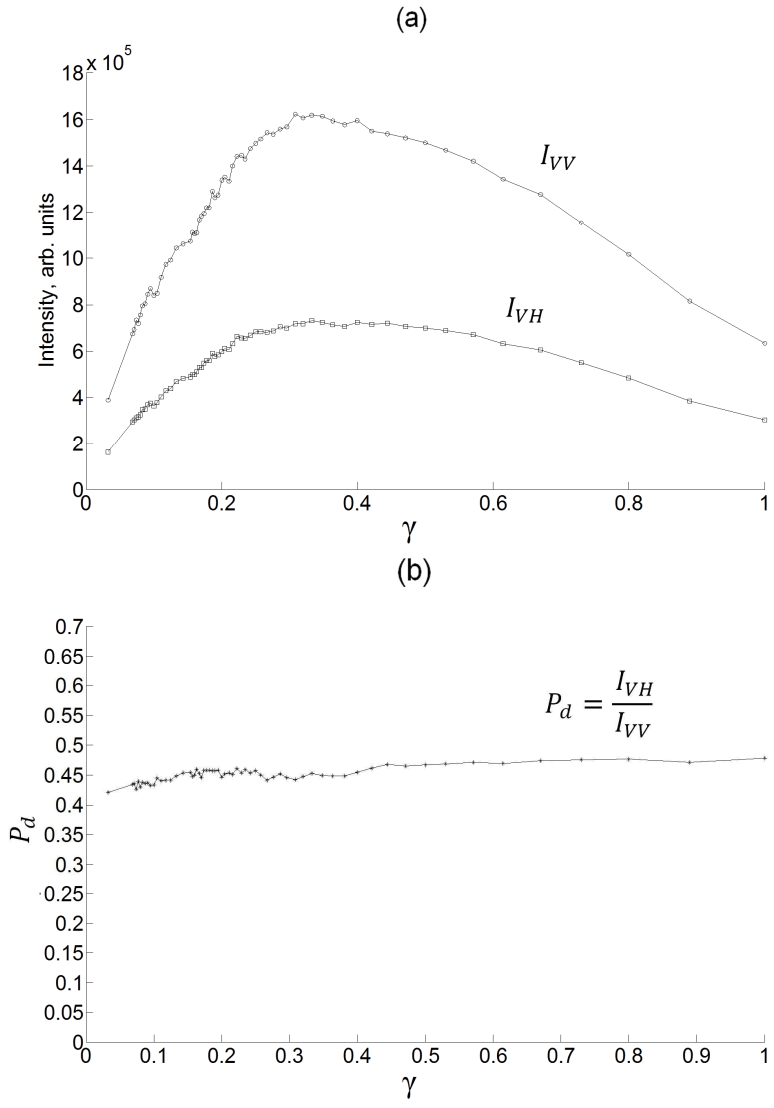

Fig. 2. The dependence of the scattered light intensity I_{VV} for VV-polarization and I_{VH} for VH-polarization (a) and the depolarization ratio P_d (b) on the volume concentration γ of the initial dispersion of nanorods in the diluted dispersion

As seen in Fig. 2a, the scattered light intensity I_{VV} for VV-polarization and I_{VH} for VH-polarization sharply increases, then reaches maximum and then decreases when particle concentration increases. The scattered light intensity near linearly increases at the low concentration of nanoparticles. For bigger concentration of nanoparticles in the dispersion, the

multiple scattering occurs; it decreases the intensity of the singly scattered light reaching the detector. Further increasing of the nanoparticles concentration leads to the near linear decrease of the scattered light intensity. At the same time, as shown in Fig. 2 b, the depolarization ratio P_d remains almost constant.

Therefore, samples of gold nanorods water dispersions with different concentrations can be compared by the depolarization ratio.

The depolarization ratio is almost independent on the scattering angle.

The depolarization ratio was measured for nanorods dispersions with different aspect ratios. As a result, the following dependence of the depolarization ratio on the average aspect ratio was obtained (Fig. 3).

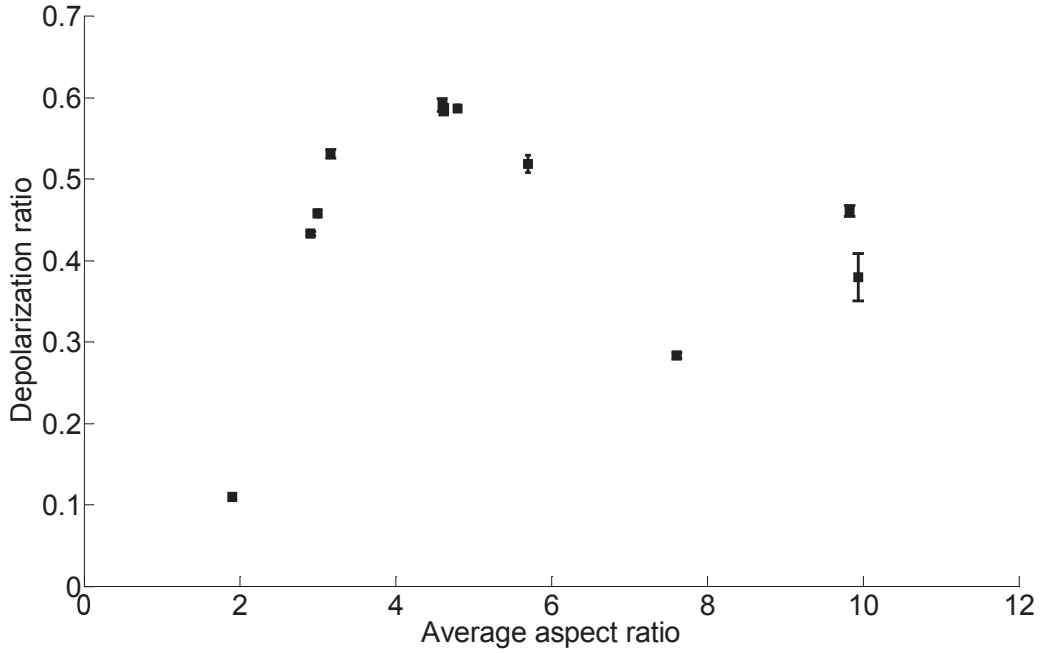

Fig. 3. The dependence of depolarization ratio of the light scattered in liquid dispersions of nanorods on the average aspect ratio

For spherical particles, the depolarization ratio of the scattered light is equal to zero. For non-spherical particles (nanorods) the depolarization ratio is not equal to zero. The depolarization ratio increases with the increasing aspect ratio. As seen in Fig. 3, there is a decrease of depolarization ratio for the samples with average aspect ratio greater than 5. This can be explained by the presence of quasi-spherical impurities. The presence of spherical impurities in the dispersion increases the contribution of the polarized part in the scattering intensity, whereby the depolarization ratio is reduced.

As a result, the influence of the nanoparticle shape on the depolarization ratio of the scattered light was demonstrated. To describe the obtained results a new empirical model was developed. This model allows calculating the depolarization ratio of the light passing through the liquid dispersion of randomly oriented nanorods. The model takes into account the particle aspect ratio distribution and the presence of quasi-spherical impurities.

Obtained results can be used to develop new methods for the determination of geometric parameters for non-spherical particles by the measuring of the depolarization ratio for the scattered light.

This work was financially supported by the Ministry of Education and Science of the Russian Federation (agreement № 14.575.21.0090, identifier RFMEFI57514X0090).

References

[1] Nanoparticles in Biology and Medicine, ed. M. Soloviev, Springer Protocols, vol. 906, 2012.
[2] B.N. Khlebtsov, V.A. Khanadeev, J. Ye, G.B. Sukhorukov, N.G. Khlebtsov "Overgrowth of gold nanorods by using a binary surfactant mixture," Langmuir, vol. 30, pp. 1696–1703, 2014.
[3] S.A. Dolgushin, I.K. Yudin, V.A. Deshabo, P.V. Shalaev, S.A.Tereshchenko, "Depolarization of light scattered in water dispersions of different shape nanoparticles," Biomedical Engineering, vol. 49, pp. 394-397, 2016.

Development of a biotechnical system for rehabilitation of patients with cerebrovascular disturbances

I.Apollonova, V. Stpankevich
Bauman Moscow Technical State University, Moscow, Russia

The challenges of prevention and rehabilitation of myocardial infarct and stroke, along with other diseases having negative impact on physical activity, are of increasing relevance in the world today.

This article presents a solution to this challenge through development of a biotechnical system for rehabilitation of patients with cerebrovascular disturbances, at hospitals and at home. The key feature of this design is that it allows to assess the physical activity of the patient and ability to restore the skills necessary for independent accommodation. Key features of this system also include easy access due to the ease of control and low price, in comparison with the analogues, fast setup and launch, installation of the software on home PC with Windows 8 and higher, with USB 3.0.

The physiological parameters of the patient require control during trainings to avoid overwork and recrudescence. A heart-rate monitor is also included for the assessment of the functional condition of the patient.

The general view of the system (Fig. 1) includes 4 modules: Kinect 2.0 motion sensor, adapter for PC connection, personal computer and heart-rate monitor.

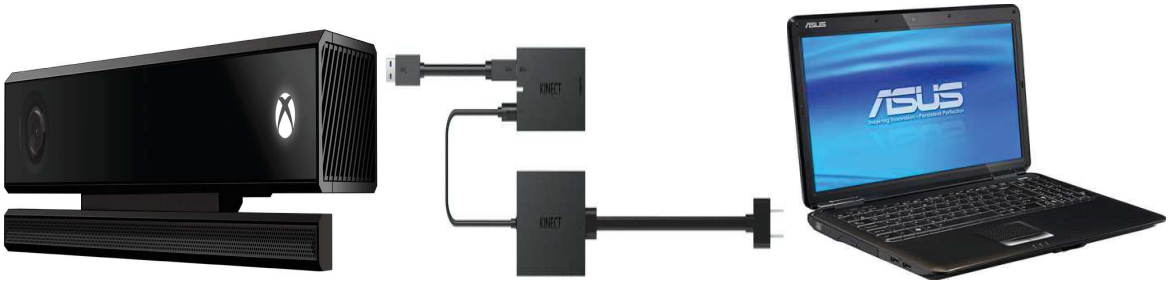

Fig.1 General view of the biotechnical system

A movement standard needs to be created before starting the algorithm of comparison of movement standard to the movement performed by the patient. Recording and processing of movement is done via the SDK Kinect program. At the first stage the standard is registered for the studied movement. After recording the video clip is processed according to correctly and incorrectly performed gestures. After its processing the standard is ready to comparison to the movement carried out by the patient and the further analysis. "The correct performance of

the movement" distinguished in the standard allows the system to deliver the information to the consulting physician more precisely.
The created model of the person in polar coordinate system is presented in Fig.

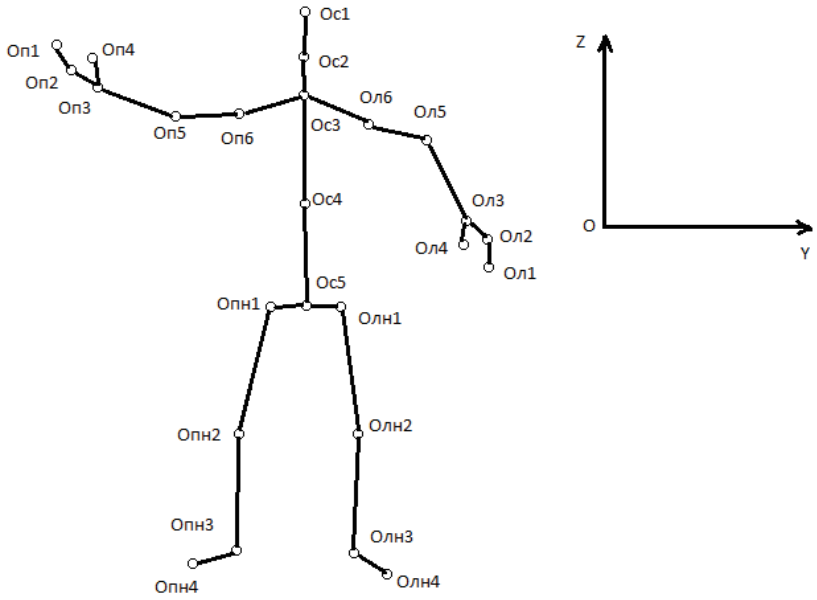

2:

Fig. 2 Model of the person in polar coordinate system

It shows the nodal points, these points and rotation angles (polar and azimuth) denote position of every part of the model.

At the recording of the standard, the system registers the change of position of the model and location in space in each time point. When the patient performs the recorded standard movement, the program superimposes the listed above model parameters on the model of the standard movement.
The following diagram is the direct result of this analysis (Fig. 3):

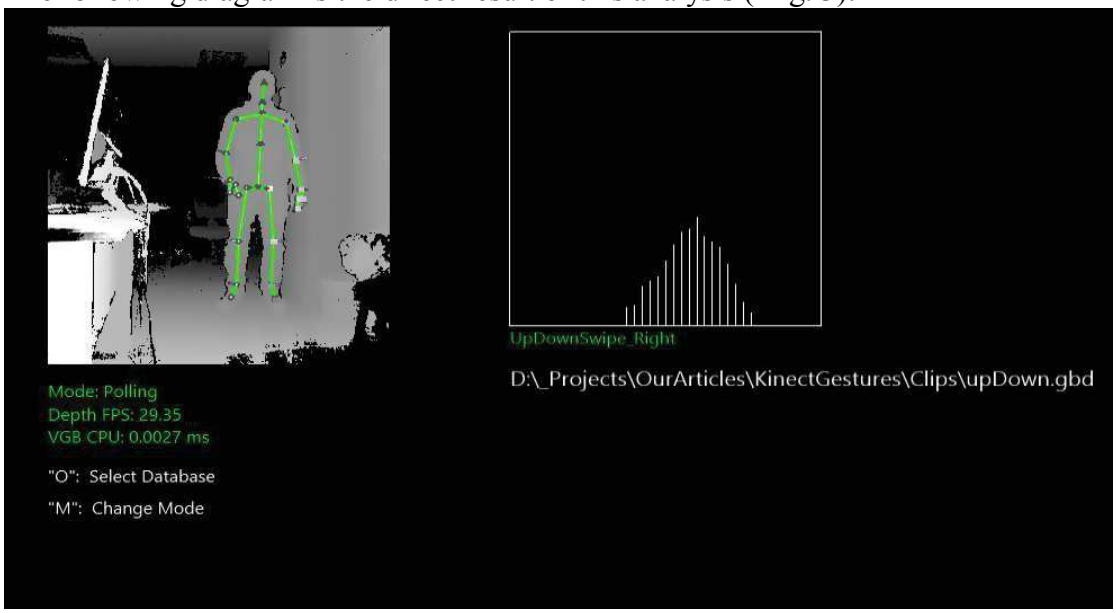

Fig.3 The diagram of motion recognition

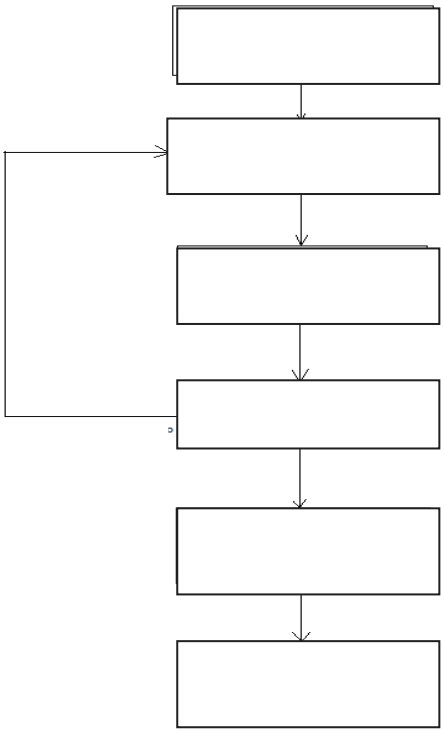

Comprehensive analysis of bulk composites internal structure made from a dispersion of carbon nanotubes and bovine serum albumin by X-ray microtomography

D.Ignatov[1]***, N.Zhurbina***[1]***, A.Guzenko***[1]***, A.Gerasimenko***[1]

1. National Research University of Electronic Technology, Bld. 1, Shokin Square, Zelenograd, Moscow, Russia

Bioresorbable composites are widely used in tissue engineering. Composites should have porosity to replace lost tissues. The porous structure of composites provides sprouting of blood vessels. This requires control over the size of pore spaces and find the optimum combination of the reduction of a certain type of tissue. For this reason, a comprehensive analysis of the microstructure of the composite volume by X-ray microtomography was needed.

Visualization of the structure of the samples was carried out without destroying the bulk composites and their pre-treatment using complex Scyscan 1174. Samples of the bulk composites were formed by laser ablation of an aqueous dispersion of bovine serum albumin (BSA) and single-walled (SWCNTs) and multi-layer (MWCNTs) carbon nanotubes. Different types of irradiation laser was used: pulse and continuous (pulse repetition frequency of 80 MHz, 140 fs pulse duration), but at the same wavelength - 810 nm. Samples 1 and 2 formed on the basis of SWCNTs and MWCNTs, respectively. Their irradiation was carried out by a femtosecond laser. Samples 3 and 4 consisting of SWCNTs and MWCNTs, were irradiated with a continuous laser.

The best resolution X-ray micrographs achieved for the following parameters of the experimental complex: the power of the X-ray tube current (20-30 kV) X-ray tube voltage (400 mA), shutter speed X-ray camera (2000 ms), the camera resolution (smaller pixel size - 1304x1024 on the projections) rotation step (0.1 deg - about 3500 projections).

The picture quality is improved by averaging several shadow projections in one angular position. Reduced quantities of ring artifacts in the reconstruction was performed with the random movement of the sample relative to the rotational axis. Removing zero background before scanning was due to update the state of the light field.

For slicing of bulk composites was carried out the reconstruction of their shadow projections for the following parameters:

• the final alignment of the shadow projections for sample displacement compensation during scanning;
• hardening correction to compensate for the X-ray beam hardening effect;
• correction ring artifacts in order to reduce the appearance of ring artifacts and camouflage pixel defects;
• Smoothing tomograms for reducing signal noise in the shadow projections.

In the two-dimensional and three-dimensional visualization was performed. Figure 1a shows a large number of cavities in the sample 1. This can be explained by a high-energy single laser pulse and inhomogeneous preparation of the initial dispersion. Because SWCNTs form conglomerates intricate and difficult to disperse carbon nanotubes. For sample 2, the number and size of the cavities is much reduced, but remained (Figure 1b). High homogeneity was obtained for a sample 3 (Figure 1c). Sample 4 looks quite homogeneity with a minimal number of cavities (Figure 1d).

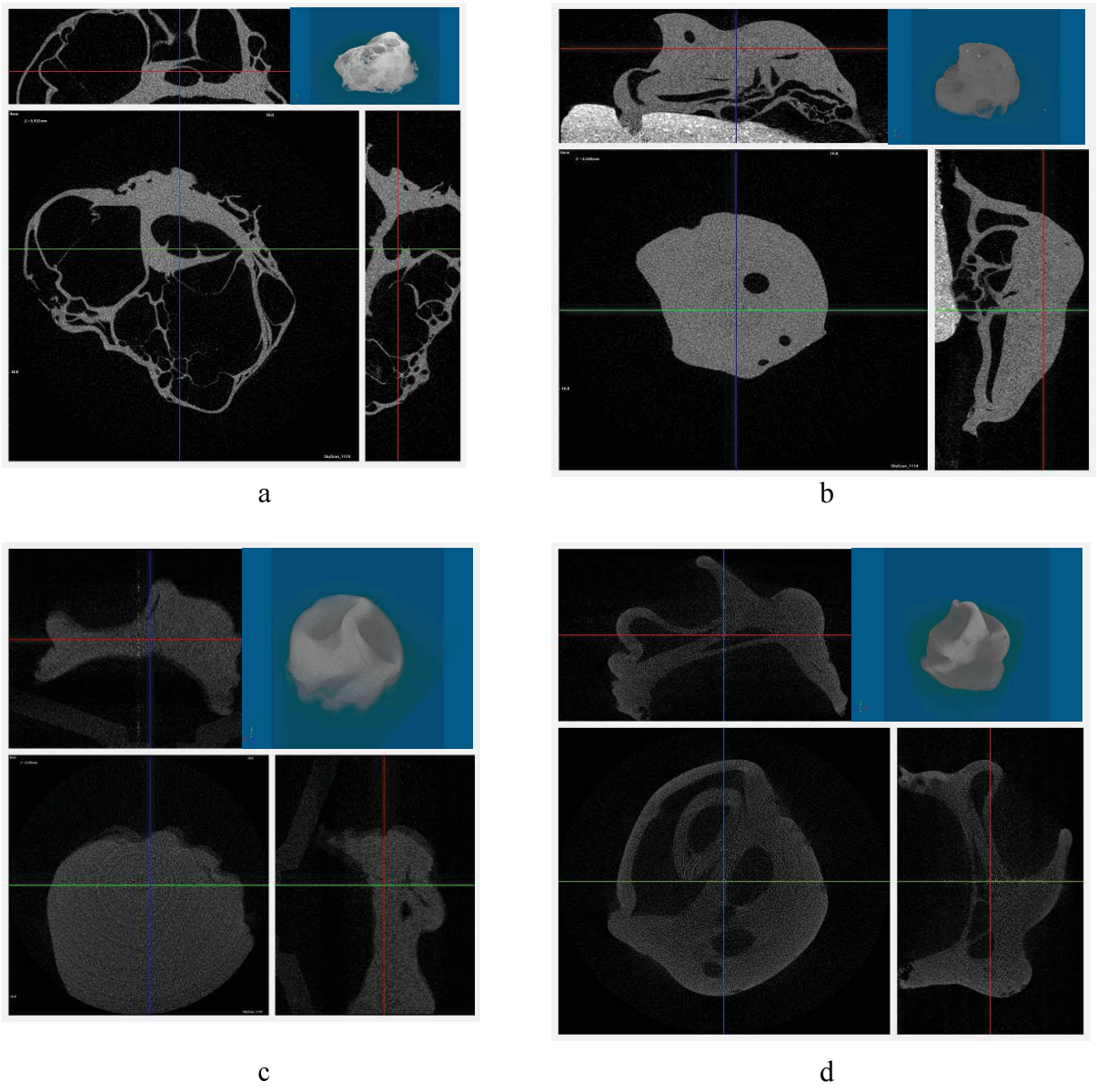

Fig. 1 Slices the shadow projections of bulk composites: a - sample 1, b - Sample 2, c - sample 3, d - Sample 4.

To perform quantitative analysis allocated volume of interest (VOI) on the tomograms. Selecting the VOI was carried out at the site of the most homogeneity of composite. Then we conducted an analysis of the parameters of the VOI (Table 1): total volume of the VOI (the 3D volume measurement is based on the marching cubes volume model of the VOI), object volume (total volume of binarised bulk composite within the VOI), percent object volume (the proportion of the VOI occupied by binarised bulk composite), number of closed pores, volume of closed pores (total volume of closed porosity within the VOI), percent closed porosity (the proportion of the VOI occupied by closed porosity), volume of open pore space (total volume of open porosity within the VOI), percent open porosity (the proportion of the VOI occupied by open porosity), total volume of pore space (total volume of pore space within the VOI), percent total porosity (the proportion of the VOI occupied by porosity), average diameter of pore.

The most homogeneity structure of the sample turned out for the bulk of the MWNT composites irradiated by continuous laser. The average pore diameter for the SWCNTs samples is 20-30 nm and for the MWCNTs totals almost two times higher (35-40 nm).

Parameter	Unit of measure	Sample 1	Sample 2	Sample 3	Sample 4
Total VOI volume	mm^3	1.44	7.46	11.17	7.93
Object volume	mm^3	1.13	4.55	6.78447	3.54
Percent object volume	%	78.73	60.93	60.69	44.72
Number of closed pores		1498	6343	3110	62376
Volume of closed pores	mm^3	0.007	0.005	0.038	0.009
Percent closed porosity	%	0.64	0.11	0.56	0.24
Volume of open pore space	mm^3	0.33	2.91	4.35	4.37
Percent open porosity	%	20.78	38.96	38.95	55.18
Total volume of pore space	mm^3	0.31	2.92	4.39	4.38
Percent total porosity	%	21.29	39.06	39.33	55.29
Average diameter of pore	nm	28.81	23.04	39.41	35.79

Table 1. Quantitative analysis of three-dimensional tomograms bulk composites samples.

Thus, a comprehensive analysis of bulk composites was carried out by X-ray microtomography. Reconstruction of images for shadow projections, two-dimensional and three-dimensional visualization and quantitative analysis allowed estimate the homogeneity, percentage of open and closed pore spaces in bulk composites. As a result, it was found that SWCNt bulk composite in an aqueous albumin matrix formed by using a continuous laser has the highest homogeneity. This sample has excellent mechanical properties: hardness nanoscale reached to 370 MPa, the elastic modulus to 4.2 GPa, and elastic recovery previous form after indenter puncture to 40%. The material in the solid phase state after laser irradiation weighed 0.147-0.153 g, while the density was 1.24 - 1.28 g / cm^3. For comparison, the hardness of the human porous bone is 500 MPa at a density is 1.930 g / cm^3. Consequently, bulk composites can be used in tissue engineering bone. This work was provided by the Ministry of Education and Science of the Russian Federation (Agreement 14.575.21.0044, RFMEFI57514X0044).

Automation hemodynamics assessment of blood

E. Shachneva[1]

[1]*Federal State Educational Institution of Higher Education «Penza State Technology University», Russia, Penza*

Hemodynamics (from the Greek. Haima- blood and dynamis-force), the science of the movement of blood through the vessels. In its basic provisions of hemodynamics. uses the laws of fluid dynamics, the science of fluid motion at all, but the conditions of the natural circulation are so complex and the nature of the blood flow through the vessels is dependent on so many variables that the laws of hydrodynamics suitable for the living organism only within certain limits, with great limitations, and can only be used for approximate orientation [1].

At the moment, there are many systems for the analysis of blood components and devices for automatic collection of blood components, as well as devices and methods for

monitoring and evaluating hemodynamic blood condition. But the process of blood collection and control of blood donor and hemodynamics in patients not sufficiently automated. Currently, in most cases, the blood picks up don a medical worker, which itself controls the process or using the blood separator.
This article considers the possibility of using standard data-measuring systems using the ultrasound transducer to automate the process of blood sampling of the patient or donor, as well as blood transfusion process.

Block diagram of information-measuring system is shown in Figure 1.

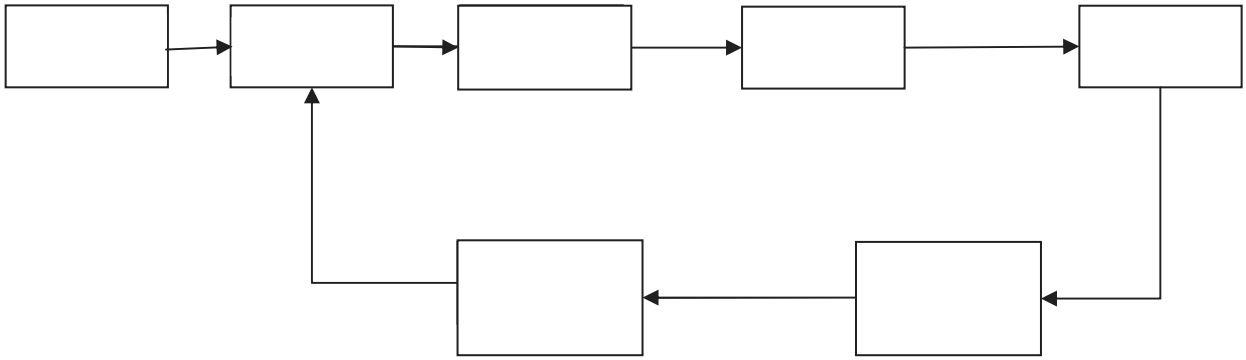

УЗК - blood sampling device; УБП - universal conversion unit; АЦП - analog-to-digital converter,
ЭВМ - electronic computer

Figure 1 - Block diagram of information-measuring system

It is proposed to use this system in the patient's blood drawing, thereby reducing the time to make recordings, and also using an ultrasonic flowmeter to control the process of blood sampling.

Consider the principle of ultrasonic flowmeters. The principle of operation is based on measurement of an effect, which occurs when passing acoustic waves through the flow of the medium. Ultrasonic flow meters include, based on the displacement of the acoustic oscillations moving medium, and converters based on the Doppler effect [2].

The most common flow meters found, based on the measurement of the time difference or the rate of passage of acoustic waves directed downstream and upstream. Such flow meters are used for measuring the flow of liquids and gases. The main requirement for the measured acoustic environment is its permeability.

As emitters and receivers of acoustic vibrations of piezoelectric used. Under the influence of the acoustic oscillations is compressed - the expansion of the crystal, electric charges are formed on its surface. Work receiver acoustic oscillations is based on the direct piezoelectric effect of the radiator - at the inverse piezoelectric effect: when applied to the surfaces of the crystal alternating voltage piezo will expand and contract, exciting environment in the measured acoustic waves [3].

The emitters and receivers of acoustic vibrations are arranged at an angle to the pipe axis. The first ultrasonic flow transducers were performed with two acoustic channels. Most modern ultrasonic transducers run single channel. The piezo elements alternately perform the function of the radiator and receiver. First acoustic waves from the transducer are sent downstream and are perceived by the receiver. Then the receiver becomes emitter, acoustic waves from the transducer are directed against the flow and are perceived by the receiver. The operating principle of the measuring system, ultrasonic transducers are divided into:

1) transit-time;
2) Frequency-pulse;

3) Differential phase.

During transit-time converters is a direct measurement of the time of passage of short pulses from the transmitter to the receiver, designed for upstream and downstream. The travel time pulse from the emitter to the receiver when the current direction:

$$T_1 = \frac{L}{c + v_L \cos\alpha}, \quad (1)$$

against the current:

$$T_2 = \frac{L}{c + v_L \cos\alpha} \quad (2)$$

where T_1, T_2 - transit time of acoustic vibrations directed downstream and upstream;
L - is the length of the acoustic channel;
c - the speed of sound in the measured medium;
v_L - the average speed of the medium along the length of the acoustic channel;
α - angle of inclination of the acoustic channel.

$$v_L = \frac{L}{2\cos\alpha} \cdot \frac{T_1 - T_2}{T_1 T_2}. \quad (3)$$

In the pulse-frequency converters are alternately fed a series of short pulses, directed by and against the flow. If the acoustic signal arrives at the receiver is sent the next pulse, etc. There is a sequence of pulses, the frequency of which is inversely proportional to the time of the pulse from the transmitter to the receiver [3]. The difference frequency pulses directed upstream and against the current, determined by the speed of the medium.

The speed of acoustic waves directed flow:

$$c + v_L \cos\alpha = \frac{L}{T_1}, \quad (4)$$

pulse frequency:

$$f_1 = \frac{1}{T_1} = \frac{c + v_L \cos\alpha}{L}. \quad (5)$$

Acoustic vibrations speed against flow:

$$c - v_L \cos\alpha = \frac{L}{T_2}, \quad (6)$$

pulse frequency:

$$f_2 = \frac{1}{T_2} = \frac{c + v_L \cos\alpha}{L}. \quad (7)$$

Frequency difference:

$$\Delta f = f_1 - f_2 = \frac{2\cos\alpha}{L} v_L. \quad (8)$$

Flow rate:

$$v_L = \frac{L}{2\cos\alpha}\Delta f \quad (9)$$

The differential-phase inverters measured phase shift difference of ultrasonic vibrations occurring when passing the receivers oscillations downstream and upstream:

$$\Delta\varphi = 2\pi f \Delta T = \frac{2L\omega\cos\alpha}{c^2} v_L, \quad (10)$$

where $\Delta\varphi$ - the difference between the phase shifts;

ΔT - the difference in propagation time of acoustic oscillations, and directed against the flow;

f and ω - the frequency and angular frequency of the acoustic oscillations.

The differential phase input converters depends on the velocity of sound in the medium. To eliminate the error caused by the change in the velocity of sound in the medium. To eliminate the error caused by the change in the speed of sound, it is necessary to introduce special compensation scheme. In transit-time and pulse-frequency converters the output is virtually independent of the sound velocity. The presence of this delay time is determined depending on only the signal in the electronic-acoustic path, the non-passage of the signal in the fluid [3].

Analyze the features of the application of ultrasonic transducer with the process of blood sampling. The information-measuring system, one of the components is ultrasonic inspection, which includes an ultrasonic transducer and a blood vessel. quantity measurement range by using ultrasonic testing blood from 0 to 1000 ml. Calculation of SP produced specifically for such a range, since the maximum blood volume which can be collected from the donor is equal to 600 mL and a venous blood loss of 1000 ml may badly affect the human health [5].

The process of blood collection using this transducer, can take place as follows: in human vein needle is inserted, it is fastened silicone tube further transducer (within which there are 6 sources and receivers, each of which is disposed at an angle of 60 degrees), after passing blood through converter, it enters the vessel, whose volume is 1000 mL, from above the receptacle pump which pumps blood from a vein.
Since the speed of blood is approximately 6-14 cm / s, the speed of blood withdrawn by laboratory analysis should be in the aisles of 0.2 cm / s and 1.3 cm / s - it is necessary to oxygen and other necessary in the process of life substances supplied to vessels and the brain [4].

The block diagram of the measuring fluid flow transducer for laboratory analysis. Chose the type of conversion: ultrasound, as this type of transformation is the most secure and provides the most accurate measurements compared to other principles of transformation [5].

On the presented structure (Figure 2) shows the scheme of action transducer principle.

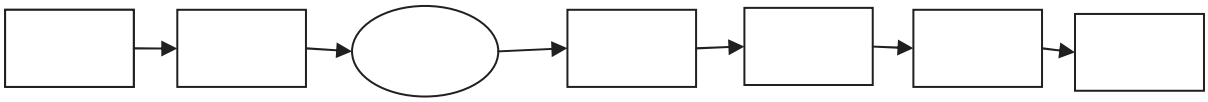

Г - generator ПЭП1,2 - piezoelectric transducer, БО - a biological object, ФУ - shaping power

Figure 2 - Block diagram of the ultrasonic transducer

The ultrasonic transducer starts with the rectangular pulse generation via pulse generator G. The signal produced by the generator is transmitted to the piezoelectric transducer PEP1, PEP2 a signal BO goes to the bioobject. In case of BO signal is distorted, then the distorted signal is applied to PEP2. To return to the previous form of the rectangular signal pulse shaping amplifier used FU. It begins the process of measuring the values of f and Δf, after the measurement converter is shut down. [6]

In this article the possibility of applying the standard information-measuring systems using ultrasonic transducer for automated blood sampling process and evaluating hemodynamic blood condition in a patient or donor on the basis of the analysis operation of the converter can be concluded that the use of such systems is possible [7].

References

[1] Great Medical Encyclopedia. - URL: http://bigmeden.ru/article/гемодинамика. - Hemodynamics. - Treatment date (05/20/2016). - bigmeden.ru

[2] Types of devices and actions flow principle. - URL: http://www.devicesearch.ru/article/rashodomeri - Ultrasound or Doppler transducer. - Treatment date (04/21/2013). - 2010-2014 DeviceSearch.ru

[3] Lepyavko A.P. Flowmeters and fluid and gas meters. Testing and calibration. - M .: ASMS, 2005. - 98 p.

[4] Dmitrienko A.G., Mikheev M.Yu. Yurmanov V.A. Piskaev K.Y. Improving the accuracy of measuring devices of the system of monitoring indicators of quality of electric power of the launch complex./Proceedings of the higher educational institutions. Volga region. - Technical science. 2012. № 2. S. 69-80.

[5] Istomin VV, Istomin TV Rationale for the development of multi-channel system with remote access to research and correction of postural disorders / In: information and management technologies in medicine and ecology collection of articles IX All-Russian scientific and technical conference. Edited TV Istomin. 2015. pp 21-25.

[6] Murashkina T.I., Istomina T.V., Badeeva E.A., Serebryakov D.I., O.V. Yurova, Udalov A.Y., Shachneva E.A. Fluid Flow Measurement in Astronauts Life Support Systems//Biomedical Engineering. – Vol. 49.- No 5.- January 2016. –pp.295-299

[7] Shachneva E.A., Serebryakov D.I., Murashkina T.I. Installation for measuring fluid parameters during laboratory analysis / Proceedings of the International Scientific and Technical Conference (Somputer - based conference). - Penza: Penza State Technology University, 2015, vol. 21. - pp.187-190.

AUTHOR INDEX

Vladimir State University
named after Alexander and Nikolay Stoletovs

Proceedings of the 12th Russian-German Conference on Biomedical Engineering
Suzdal
July 4-7 2016

Published in authors edition

Cover design

Suzdal photo – by Olga and Pavel Shirokovs
Background image - by yugra
RGC logo – by RGC BME'2016 Organizing Committee

Заказ № 1362. Подписано в печать 15 июня 2016 г.
Бумага офсетная: плотность 65 г/м^2. Гарнитура Таймс.
Тираж 100 экз.

Отпечатано в ООО «Графика»
с готовых оригинал-макетов без изменения содержания
г. Александров, Красный пер., 13
Тел.: 8(49244) 3-20-10, 3-20-11
e-mail: algortip@mail.ru

XII RGC

This book is dedicated to contibutions of the 12th Russian-German Conference (RGC) on Biomedical Engineering taking place in Suzdal, Russia from July 4 to 7, 2016.

The Russian-German Conference on Biomedical Engineering was founded 2005 in Munich as the Russian-Bavarian Conference. The conference becomes the actual platform for researchers from Russia and Germany.

The confrence location alternated equally between cities in Russia and Germany. After the successful 11th RGC in Aachen the International Program Committee decided to hold the following conference in Suzdal with a purpose of further scientific experience exchange between researchers in the field of biomedical engineering of both countries